Biaxial Behavior of Ultra-High Performance Concrete and Untreated UHPC Waffle Slab Bridge Deck Design and Testing

Kacie Caple D'Alessandro

Dissertation submitted to the faculty of the Virginia Polytechnic Institute and State University in partial fulfillment of the requirements for the degree of

Doctor of Philosophy
In
Civil Engineering

Carin L. Roberts-Wollmann, Committee Chair
Thomas E. Cousins
Norman E. Dowling
Cristopher D. Moen

August 7, 2013
Blacksburg, VA

Keywords: ultra-high performance concrete, UHPC, biaxial stress, failure criterion, waffle slab bridge deck, digital image correlation

Biaxial Behavior of Ultra-High Performance Concrete and Untreated UHPC Waffle Slab Bridge Deck Design and Testing

Kacie Caple D'Alessandro

ABSTRACT

Ultra-high performance concrete (UHPC) was evaluated as a potential material for future bridge deck designs. Material characterization tests took place to identify potential challenges in mixing, placing, and curing UHPC. Biaxial testing was performed to evaluate behavior of UHPC in combined tension and compression stress states. A UHPC bridge deck was designed to perform similarly to a conventional concrete bridge deck, and a single unit bridge deck section was tested to evaluate the design methods used for untreated UHPC.

Material tests identified challenges with placing UHPC. A specified compressive strength was determined for structural design using untreated UHPC, which was identified as a cost-effective alternative to steam treated UHPC.

UHPC was tested in biaxial tension-compression stress states. A biaxial test method was developed for UHPC to directly apply tension and compression. The influence of both curing method and fiber orientation were evaluated. The failure envelope developed for untreated UHPC with random fiber orientation was suggested as a conservative estimate for future analysis of UHPC. Digital image correlation was also evaluated as a means to estimate surface strains of UHPC, and recommendations are provided to improve consistency in future tests using DIC methods.

A preliminary bridge deck design was completed for untreated UHPC and using established material models. Prestressing steel was used as primary reinforcement in the transverse direction. Preliminary testing was used to evaluate three different placement scenarios, and results showed that fiber settling was a potential placement problem resulting in reduced tensile strength. The UHPC bridge deck was redesigned to incorporate preliminary test results, and two single unit bridge deck sections were tested to evaluate the incorporated design methods for both upside down and right-side up placement techniques. Test results showed that the applied design methods would be conservative for either placement method.

Dedication

This dissertation is dedicated to my husband, Adam D'Alessandro, for his unconditional love and devotion to me, his support throughout my doctoral studies, and his patience during the past 6 years. Thank you for encouraging me to pursue this goal, and thank you for loving me through it all.

Acknowledgements

First, I thank my committee members: Carin Roberts-Wollmann, Tommy Cousins, Norman Dowling, and Cristopher Moen. Thank you for your support and guidance throughout this research project. A special thank you to my primary advisors, Dr. Carin Roberts-Wollmann and Dr. Tommy Cousins, for providing detailed feedback, continued encouragement, helping me develop as an independent researcher, and for patience and guidance as I was teaching throughout the years.

I thank Brett Farmer, Dennis Huffman, and David Mokarem for their repeated help at the Thomas M. Murray Structural Engineering Laboratory. Your guidance and assistance was incredibly supportive, and I am truly grateful and appreciative for each of you.

I also thank Lafarge North America for donating Ductal® premix, steel fibers, and technical guidance for the initial material characterization and biaxial testing phases of the project. Thank you to Radva Corporation for their donation of foam for single cell formwork. Thank you to Conrock for donating aggregate for grout. Thank you to Rettco Steel, LLC for donating prestressing steel. Thank you to Turner Fairbanks Highway Research Center and Benjamin Graybeal for use of steam treatment facilities.

Finally, thank you to my friends and family for support and encouragement. Special thanks to William Collins for lifting heavy objects and cutting steel. Thank you to Kedar Halbe, Marc Maguire, Doug Nelson, Rafic El Helou, Samantha Mingrone, and many others for assisting with UHPC mixes and/or for capturing videos and photographs. Thank you also to Beth Poore, Michael Woodworth, Jonathon Hatlee, Lori Koch, and Ashley (Warren) Johnson for cherished friendships.

All photos are by the author unless otherwise noted.

Table of Contents

List of Figures

List of Tables

Chapter 1: Introduction

1.1 Motivation

With the U.S. facing extensive bridge replacements in the near future (AASHTO 2008), ultra-high performance concrete (UHPC) could be a new solution to reduce maintenance and extend the life of future bridges. The American Association of State Highway and Transportation Officials (AASHTO) has identified the number one problem in U.S. bridges to be age and deterioration (AASHTO 2008). The reason for this problem is that the majority of U.S. bridges are over 40 years old, with an expected life of only 50 years. As transportation officials move toward a time of mass bridge replacement and extensive bridge repairs, they look to the future for solutions that can provide longer lasting bridges. Research has been considered an important solution to improving the current status of U.S. bridges (AASHTO 2008). Specifically, research to provide longer lasting bridges has been identified as an essential component to restoring the nation's bridges. With the advanced strength and durability of UHPC, this material could be the answer.

Ultra-high performance concrete is a relatively new and innovative concrete that exhibits superior strength and durability properties as compared to conventional concrete (Graybeal 2006a; Perry 2005). Because of these properties, UHPC has the potential to significantly reduce maintenance costs throughout the life of a structure and ultimately extend the lifespan. The durability properties of UHPC indicate that it can withstand harsh environments, making it suitable for bridge applications. Because the initial cost of UHPC is considerably higher than conventional concrete (Li 2003), structural members must be optimized based on the high strength of the material in order to use the least amount of material possible. Compared to the potential for high initial costs, the overall benefit of using UHPC can be quantified when the entire life of a structure is considered.

UHPC has been used in several countries including the United States for the construction of pedestrian bridges, roadway bridges, roof structures, and more (Lafarge 2013). The aesthetic possibilities of UHPC are displayed by these unique designs. For instance, the Footbridge of Peace in Korea has a 1-¼ in. thick deck made with UHPC (Lafarge 2013). A conventionally reinforced concrete deck would contain rebar for reinforcing bars, requiring cover thicknesses appropriate for the protection of this reinforcement. Based on these requirements, a bridge deck

with such a thin section is seemingly impossible, but UHPC has shown that it can be possible to achieve required capacities with little material because of its high strength and lack of required reinforcement.

Although UHPC has been successfully implemented in structures, designers and producers continue to question the use of the material. One of the major challenges for the acceptance of UHPC is the lack of design guidelines or codes for using this material in the United States (Perry 2005). Moving toward design guidelines, research must continue to advance the knowledge of UHPC material characteristics and structural behavior. Many of the basic material properties of UHPC have been investigated; however, failure due to multi-axial stress states is still an uncertain subject in need of further clarification. Experimental testing is also needed to validate structural behavior of UHPC bridge decks for roadways.

1.2 Objectives

The purpose of this project is to evaluate UHPC as an alternative for bridge decks by investigating the biaxial behavior of ultra-high performance concrete and to experimentally test and evaluate the structural performance of a UHPC bridge deck. Individual objectives were formed to specifically address the overarching purpose and to aid in determining the feasibility of using UHPC in the construction of future highway bridges. The objectives of the project are:

1. To develop a method for testing biaxial strength of UHPC.
2. To propose a failure envelope to represent biaxial tension-compression stress states of UHPC.
3. To evaluate post-cracking behavior of UHPC in biaxial stress states.
4. To design a UHPC bridge deck considering material properties and placement procedures.
5. To experimentally test a single unit UHPC bridge deck section.

1.3 Summary of Approach

To accomplish the aforementioned objectives, the research was carried out in four phases: material property characterization, biaxial testing, bridge deck design and preliminary testing, and experimental testing of full-scale single unit UHPC bridge deck sections.

Phase 1 was aimed at performing an abridged material property characterization on Ductal®, the specific UHPC used in this study. Since several studies had already been completed specifically on Ductal®, this abridged characterization was primarily aimed at verifying mixing procedures and the obtained material properties for non-steam treated UHPC. In this study, the following properties were examined: compressive strength, tensile strength, modulus of elasticity, Poisson's ratio, and shrinkage. A preliminary biaxial test was examined for feasibility during this study, as well. The preliminary biaxial test used small panels to investigate combined tension and compressive stress states. Referred to as the "bending biaxial test," this test was performed by creating biaxial stresses through bending of the panel.

Phase 2 was focused on establishing a more direct biaxial test method to better establish a biaxial failure envelope. The second test used a modified briquette shape known as the "biaxial dog bone" to subject UHPC to more direct biaxial stresses. Because the stresses were applied directly to the member in a single plane, this test is known as the "direct biaxial test." The influence of curing method and fiber orientation were investigated. Photogrammetric methods were utilized to evaluate strains during biaxial testing. Post-cracking behavior was analyzed to determine the ability of UHPC to withstand increasing stresses beyond the point of crack formation.

Phase 3 was focused on designing an optimized UHPC bridge deck that would utilize the unique material properties of UHPC. Previous studies by Garcia (2007) and Toutlemonde et al. (2008) were used as a guide to begin the design process. Typical U.S. design codes were referenced, including those by ACI Committee 318 (2011), AASHTO (2012), and the Virginia Department of Transportation (VDOT) (2007). Recommendations and design guidelines from other countries, including France (AFGC and Setra 2002), Australia (Gowripalan and Gilbert 2000), and Japan (Japan Society of Civil Engineers 2004), were also referenced for some parts of design. Preliminary testing of the webs of the bridge deck cross section was carried out using a preliminary deck design. Preliminary testing was used to examine design assumptions and potential construction challenges. Since UHPC requires specialized construction processes, an investigation of placement techniques was performed on the specimens. Finally, the UHPC bridge deck was redesigned to consider the results obtained during the preliminary testing.

Phase 4 included the experimental testing of full-scale UHPC bridge deck sections. Two full-scale bridge deck sections were placed using two different placement techniques. Each deck section was experimentally tested under static conditions. Not only was the deck evaluated based on strength parameters, but it was also evaluated based on the adaptability to current industry practices.

Chapter 2: Review of Literature

Ultra-high performance concrete (UHPC) has been called "the next generation of concrete" (Graybeal and Tanesi 2007) because of its superior strength and durability properties. Researchers have merely begun to explore the possibilities of this new material, only used in major structures since 1997 (Blais and Couture 1999). This chapter explores prior research and applications of UHPC, highlighting the need for more knowledge of material properties and behavior in bridge applications. Since Ductal®, a product of Lafarge, was used in this project, an emphasis was placed on studies directly involved with this product.

2.1 Material Composition of UHPC

The unique composition and curing procedures of UHPC provide a logical explanation for its advanced properties. In creating UHPC, researchers sought to make improvements to concrete based on known weaknesses, such as a lack of ductility (Richard and Cheyrezy 1995). The primary improvements include creating a denser and more homogenous microstructure, providing fibers for improved ductility, and adapting a post-set curing regime that accelerates the pozzolanic reaction (Richard and Cheyrezy 1995), a reaction that influences the hardened properties of concrete (Kosmatka et al. 2002).

2.1.1 Dry Ingredients

Coarse aggregates account for approximately 30 to 50 percent of the volume in conventional concretes (Kosmatka et al. 2002). However, in UHPC, coarse aggregate is eliminated from the mix, and only fine aggregate, or sand, is used to achieve a denser and more homogeneous microstructure (Dallaire et al. 1998; Richard and Cheyrezy 1995). To increase density, the particle size of each constituent of the UHPC mix was taken into consideration to create an optimized model (Figure 2-1) (Nishikawa and Morita 2006; Richard and Cheyrezy 1995). In this way, dry ingredients are packed together to form a denser matrix. A high cement and silica fume content increases the binder-to-sand ratio, allowing for sand and quartz to fill voids between the binder, also referred to as the cementitious materials, of the mix. The ground quartz specifically acts as a filling material between silica fume and cement particles (Yang et al. 2010). This optimized model creates an engineered material that is very dense, resulting in increased strength and impermeability.

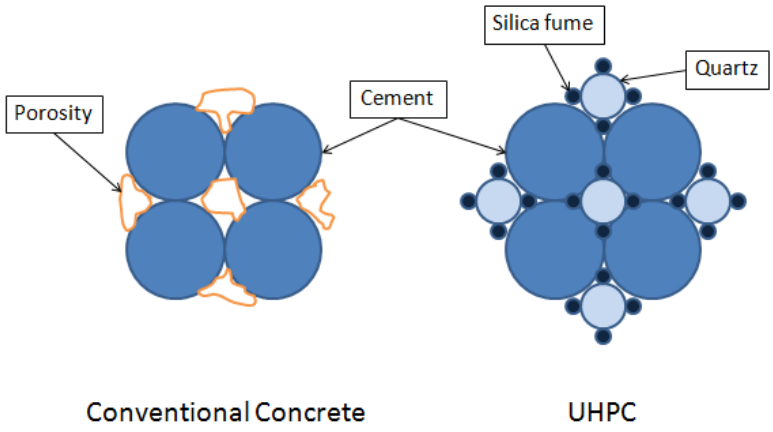

Figure 2-1: Optimized model of UHPC compared to conventional concrete (Nishikawa and Morita 2006).

2.1.2 Wet Ingredients

Little water is added to UHPC, creating a low water-to-binder ratio typically below 0.2 (Graybeal 2008). This is below the minimum water-to-binder ratio for complete hydration of 0.40 as defined by the Portland Cement Association (Kosmatka et al. 2002), indicating that UHPC will have some unhydrated cement. In addition to water, superplasticizer and an optional accelerator are used in UHPC. Superplasticizer, an admixture used to improve the flow of fresh concrete (Kosmatka et al. 2002), is added to counteract the low water content and improve workability. Therefore, superplasticizer makes it possible to reduce the water-to-binder ratio of UHPC to increase strength (Richard and Cheyrezy 1995). The use of an accelerator is optional; however, final setting time can be reduced by approximately half the time when an accelerator is used (Graybeal 2006a). Using an accelerator can be useful in precast applications, where a higher turnover rate is necessary.

2.1.3 Fibers

Fibers of either high strength steel or plastic are used in UHPC to improve ductility (Lafarge 2013; Richard and Cheyrezy 1995) and fracture toughness (Shaheen and Shrive 2007). Fibers improve ductility by providing post-cracking strength through the ability to bridge individual cracks (Figure 2-2). Once the concrete has cracked, the stress required to widen the crack is dependent on three factors: the concrete tensile stress, the tensile stress of fibers bridging

the crack, and the stress required to pull fibers out of the concrete matrix (Mindess et al. 2003; Shaheen and Shrive 2007).

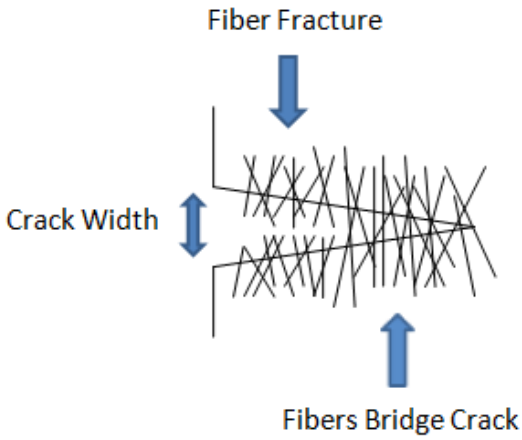

Figure 2-2: Fiber interaction at crack (Mindess et al. 2003).

Fibers used in Lafarge's commercially available UHPC, Ductal®, are composed of either a high carbon steel or poly-vinyl alcohol (PVA) (Lafarge 2013). Lafarge recommends that strength requirements, environmental exposure, rheology requirements, aesthetics, and exposure to human contact should be considered when choosing a fiber type for UHPC. For example, PVA fibers are typically used in applications where a large amount of human contact will occur, because the sharp, needle-like ends of steel fibers can pierce human skin (Lafarge 2013).

Steel fibers are most common in structural applications. The typical steel fibers used are approximately 0.008 in. in diameter by 0.5 in. long, often covered with a brass coating due to the production process (Lafarge 2013; Richard and Cheyrezy 1995; Roux et al. 1996). These fibers are typically added at an amount of 1.5 to 3% by volume, with an optimal quantity being 2% by volume (Richard and Cheyrezy 1995).

2.1.4 Effect of Steam Curing on Composition

A unique post-set curing regime accelerates the pozzolanic reaction, increases the degree of hydration, and refines the microstructure of UHPC, thereby resulting in improved mechanical and durability properties for UHPC (Cwirzen 2007; Richard and Cheyrezy 1995). The pozzolanic reaction leads to the formulation of calcium-silicate-hydrate (C-S-H), a compound that causes bonding in concrete (Richardson 1999), and the post-set curing regime not only accelerates the formation of this compound, but it also results in longer chains of the C-S-H

compound (Zanni et al. 1996). Details of this post-set curing regime and the effects it has on specific material properties of UHPC are discussed in later sections.

2.1.5 Material Composition Summary

The basic material composition of UHPC was formulated based on the aforementioned parameters: increasing density and homogeneity with a unique packing model, improving ductility with the addition of fibers, and accelerating the rate of the pozzolanic reaction with a post-set curing regime. The mix proportions of each constituent in UHPC may vary between producers, but the overall composition is very similar. Table 2-1 indicates the relative percentages by weight of a typical UHPC, including an accelerator (Graybeal 2006a).

Table 2-1: Typical UHPC material composition (Graybeal 2006a).

Material	Percent by Weight
Portland Cement	28.5
Fine Aggregate (Sand)	40.8
Silica Fume	9.3
Ground Quartz	8.4
Super Plasticizer	1.2
Accelerator	1.2
Steel Fibers	6.2
Water	4.4

2.2 Mixing, Placing, and Curing of UHPC

2.2.1 Mixing UHPC

Mixing procedures for UHPC tend to be more complicated than a conventional concrete because ingredients must be added in a specific order at various time intervals. The following instructions are specific to Larfarge's Ductal® (Graybeal 2006a), but may be modified slightly to conform to any UHPC. To begin, all materials should be weighed in advance, and half of the high range water reducer, or super plasticizer, should be added to the water. The Ductal ® premix bags containing all dry ingredients should be mixed dry for approximately two minutes. Then, the water, containing half the super plasticizer, is added slowly to the mixture over a two

minute time frame. After waiting approximately one minute, the remaining superplasticizer is added over a 30 second time frame. If an accelerator is to be used, this should be added approximately a minute after the superplasticizer, pouring slowly into the mixture during one minute. The UHPC is then mixed until it changes to a thick paste. The time for this process will depend on the speed of the mixer, the age of the material in the premix bags, and other minor environmental factors, such as humidity; however, UHPC mixing time is generally longer than a conventional concrete mix. Once the mixture has become a thick paste, fibers can be added slowly over a two minute time frame. Once fibers are completely added, the mixer should continue mixing for about one minute or until the fibers are well distributed into the UHPC (Graybeal 2006a). The complicated mixing procedure is one reason why UHPC is typically used in precast applications rather than cast-in-place applications (Perry 2005).

The type of mixer used for UHPC can have an effect on the mix time and the consistency of mixes. High shear/energy mixers, such as pan mixers, are preferred for UHPC because they produce consistent results in properly mixing UHPC (Hale and Tackett 2010). Pan mixers have rotating blades in a pan holding the concrete. These mixers typically have a blade that scrapes the bottom of the pan, as well as others used to mix the concrete. Low shear mixers, such as rotating drum mixers, are not preferred for UHPC due to inconsistent mix quality. Rotating drum mixers have blades fixed to the interior, and the drum is rotated while often placed on an incline. Inconsistencies in mix quality can result in clumps of unmixed dry materials in the mixture. These inconsistencies can be remedied by using more specialized mixing procedures, such as the half batch method used by Hale and Tackett (2010). In this procedure, half the mix is batched and mixed completely, not including fibers, before the other half of the mix is added and mixed. Fibers are added once the entire mix is workable. A common ready-mix truck is not preferred for UHPC, either, because it can also result in clumps of unmixed dry materials (Hale and Tackett 2010). Despite these inconsistencies, ready-mix trucks have been shown to produce UHPC with adequate strength (Graybeal 2009a).

2.2.2 Placing UHPC

Because UHPC does not behave the same as a conventional concrete in the plastic state, special considerations should be taken during placement to produce optimal results. In the plastic state, UHPC is more viscous than generic concrete, resembling the consistency of putty. Fibers complicate a concrete mixture by providing added frictional effects to workability and

flow (Khayat and Roussel 2000). Workability is also affected by particle sizes. Since UHPC typically lacks coarse aggregates (Dallaire et al. 1998; Richard and Cheyrezy 1995), the overall size of aggregates is reduced resulting in improved workability (Khayat and Roussel 2000). Despite these seemingly counteractive effects, UHPC is considered to be self-consolidating (Sorelli et al. 2006).

Since UHPC is considered to be a self-consolidating mixture (Sorelli et al. 2006), forms must be made with precision to prevent leakage through cracks and crevices. Silicone caulk has been used by some researchers to ensure all formwork edges are sealed (Graybeal 2009a). Special considerations are also made to determine how to place UHPC in a form to facilitate proper fiber orientation and to prevent the material from flowing into itself (Japan Society of Civil Engineers 2004; Nachuk 2008). For instance, flexural members are typically placed to allow UHPC to flow from one end of a form to the other (Graybeal 2009a; Graybeal 2009b). By doing this, fibers will primarily align along the flow path and the principal axis for tensile stresses along the bottom fibers of the beam. This method enables fibers to be in proper alignment to better bridge flexure cracks (Figure 2-3).

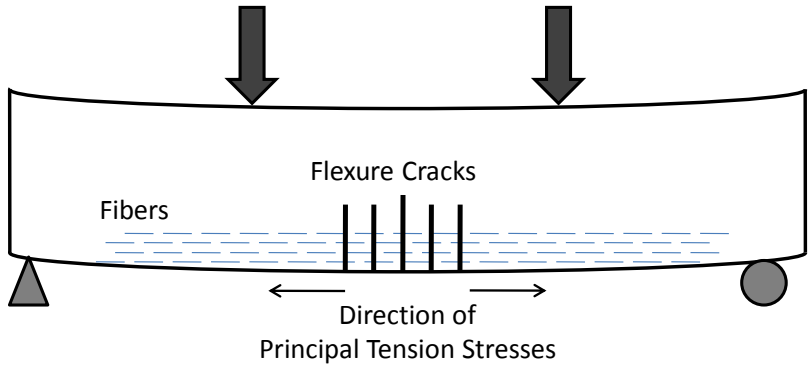

Figure 2-3: Proper fiber alignment in flexural members is affected by placement procedures.

Researchers have also found that UHPC does not consolidate well if it flows horizontally into itself during placement (Japan Society of Civil Engineers 2004; Nachuk 2008) (Figure 2-4). This can negatively affect the fiber alignment by creating a discontinuity in a member at the intersection of the flow paths. Despite problems with mixing across a direct horizontal flow path, no problems have been noted for casting UHPC vertically. Due to the self-consolidating nature of UHPC, it can be placed vertically without any negative effects (Nachuk 2008).

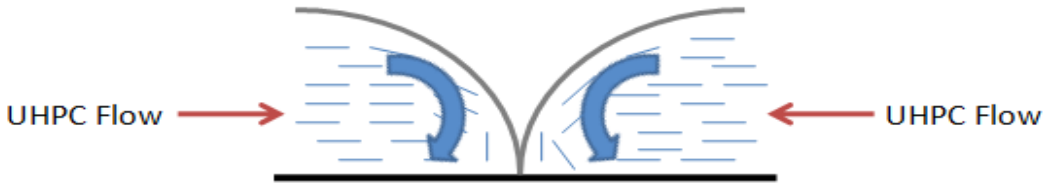

Figure 2-4: UHPC does not mix well if it flows into itself.

The Association Française de Génie Civil (AFGC) and Service d'etudes techniques des routes et autoroute (Setra) (AFGC and Setra 2002) suggest that UHPC should not be dropped from a height greater than 1.64 ft (0.50 m) to prevent fibers from segregating from the binder and clustering. The AFGC and Setra (2002) also suggest that UHPC be poured continuously to prevent exposed surfaces from drying and creating a skin, or a thin dry layer, within UHPC. By preventing this dry layer from forming, there will be no interruption in fiber or binder continuity throughout the structure. During the construction of UHPC girders, water misting and agitation were used when a fresh batch of UHPC was poured on top of older UHPC to better facilitate mixing of the two separate layers (Graybeal 2004). Despite the self-consolidating nature of UHPC, some agitation through external vibration is recommended to ensure smooth surfaces and continuity.

Because complications can result from not carefully planning the placement process of UHPC, special attention was given to placement methods throughout the entirety of this project to best accomplish proper fiber orientation and to prevent discontinuities. In particular, materials were carefully chosen to prevent moisture absorption and to ensure forms are sealed properly. Additionally, adaptation to the precast industry were considered, so as to develop a placement method that could be easily adopted in precast plants.

2.2.3 Curing UHPC

After UHPC specimens are placed, they are typically covered with an impermeable cover, often made of plastic, to prevent moisture loss by evaporation (Graybeal 2004). An initial set may not occur until after 24 hours even when using an accelerator (Graybeal 2004). Due to the long initial setting time, UHPC specimens and structures are not typically removed from molds and formwork as quickly as some conventional concretes. Depending on desired strength gain, form removal time of UHPC structures may vary.

As mentioned previously, UHPC properties are influenced by a unique post-set curing regime. Ductal ® is cured at 95% relative humidity (RH) at a temperature of 194°F for 48 hours following the final set of the material (Graybeal 2006a). This involves two hours of increasing temperature and steam, 44 hours at constant temperature and RH, and two hours of decreasing temperature and steam (Figure 2-5). Following the steam curing, specimens are stored in a lab or outside until they are placed in the field or tested for research purposes. Enhanced properties are achieved without steam-curing; however, optimal results are achieved by using the standard steam-treatment described above (Graybeal 2006a).

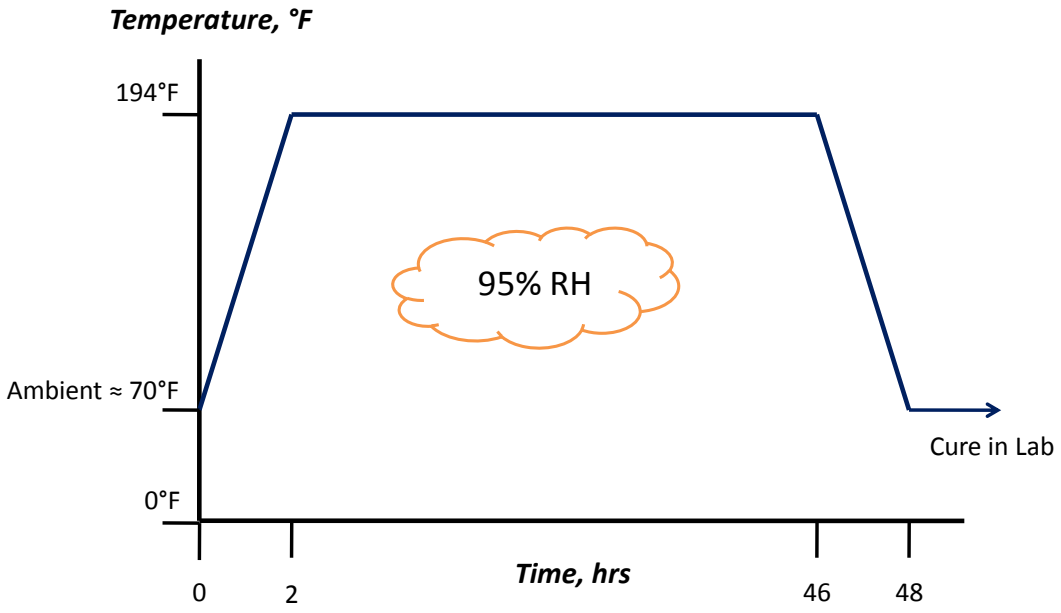

Figure 2-5: Typical steam curing regime for UHPC.

Modifications of this standard curing regime have been researched, including a delayed steam treatment, reduced temperature steam treatment, and untreated curing method. However, best results have been achieved using the standard steam treatment (Graybeal 2006a). Steam treatment was used for some specimens of the current project.

2.3 Material Properties of UHPC

Compared to conventional concrete, UHPC has enhanced mechanical and durability properties. These properties, influenced by the composition described previously, give reason for designers and owners to use UHPC to achieve stronger and longer-lasting structures. This

section describes relevant material properties of UHPC, highlighting the differences between UHPC and conventional concrete.

2.3.1 Compressive Strength

One of the most recognized characteristics of UHPC is its high compressive strength. A typical concrete used for applications such as sidewalks, footings, and foundations has a compressive strength ranging between 3 and 6 ksi. A high strength concrete (HSC), typically used in structural applications, is classified as having a compressive strength ranging from 10 to 18 ksi (Kosmatka et al. 2002). UHPC, however, can achieve compressive strengths ranging between 20 and 116 ksi (Graybeal 2006a; Lafarge 2013; Richard and Cheyrezy 1995; Shaheen and Shrive 2007). Strengths beyond 30 ksi are achieved through pressurization, a process of applying pressure during initial setting (Roux et al. 1996). This process aids in removing entrapped air and excess moisture, as well as reducing porosity present due to chemical shrinkage (Richard and Cheyrezy 1995).

The compressive strength can also be dependent on the type of specimen used in a test, shown by Table 2-2. For instance, a standard 3x6 in. cylinder, typically used in industry for quality control, will provide a slightly lower compressive strength than a 2-in. cube specimen (Graybeal 2006a).

Table 2-2: Specimen geometry can affect compressive strength (Graybeal 2006a).

Test Specimen	Average Compressive Strength (ksi)	Standard Deviation (ksi)
2-inch Cube	31.0	11.7
4-inch Cube	29.1	12.1
2x4 inch Cylinder	29.4	6.9
3x6 inch Cylinder	29.4	4.2
4x8 inch Cylinder	29.3	6.3

All values above based on using the standard steam treatment.

2.3.2 Static Modulus of Elasticity

The static modulus of elasticity is also high in comparison to conventional concrete. The elastic modulus has shown to be as high as 7650 ksi at 28-days for steam-treated UHPC and 6200 ksi for untreated UHPC (Graybeal 2007). Lafarge provides a value of approximately 8500 ksi for standard steam-treated Ductal ® (Lafarge 2013).

According to the ACI 318-11 building code for structural concrete design, a relationship is commonly used to relate the compressive strength to the elastic modulus of normal weight concrete (ACI Committee 318 2011; Pauw 1960). Although the relationship in Equation (2-1) is a reasonably accurate estimation for conventional concrete, UHPC is not accurately represented through this relationship.

$$E_c = 57{,}000\sqrt{f_c'} \text{ (psi)} \qquad (2\text{-}1)$$

Where,

f'_c = specified compressive strength of concrete (psi)

According to a research study by Graybeal (2007), the ACI 363R-92 (ACI Committee 363 1992) and Ma et al. (2004) equations, shown in Equations (2-2) and (2-3) respectively, are fairly accurate predictors for the elastic modulus of Ductal® based on compressive strength. Because the ACI 318-11 (ACI Committee 318 2011) equation was shown to be inaccurate for concrete with compressive strengths above 6,000 psi, the ACI 363R-92 equation was generated based on a collection of data from various researchers and specified for use for concrete with compressive strengths between 3,000 psi and 12,000 psi (ACI Committee 363 1992). Using a large quantity of data from the study by Graybeal (2007), Equations (2-2) and (2-3) were shown to be 95.7 and 88.1 % accurate to test data for Ductal®, respectively. Although these equations were a reasonable fit for most UHPCs, they were not accurate for lower strengths of UHPC. In order to improve this relationship between compressive strength and the elastic modulus, Graybeal (2007) developed an additional equation (Equation (2-4)) that more accurately represents the behavior of UHPC to approximately 96.7 %. This simple equation was based on

modifying the coefficient of Equation (2-1) for conventional, normal weight concrete, to satisfy the relationship between compressive strength and modulus of elasticity (Graybeal 2007).

$$E_{UHPC} = 40{,}000\sqrt{f_c'} + 1{,}000{,}000 \text{ (psi)} \quad (2\text{-}2)$$

$$E_{UHPC} = 525{,}000\sqrt[3]{\frac{f_c'}{10}} \text{ (psi)} \quad (2\text{-}3)$$

$$E_{UHPC} = 46{,}200\sqrt{f_c'} \text{ (psi)} \quad (2\text{-}4)$$

2.3.3 Tensile Strength

The tensile strength of UHPC is considerably higher than conventional concrete, with values above 1.45 ksi (Chanvillard and Rigaud 2003). As with compression testing, tensile strength is also dependent on the testing method. A report by Graybeal (2006a) indicates that the 28-day cracking tensile strength varies by nearly 24 percent among a variety of testing methods (Table 2-3). Also, the ultimate tensile strength is considerably higher than the cracking tensile strengths, as indicated with the splitting tensile strengths in Table 2-3. In this study, the tensile strength from flexural testing of prisms was corrected based on research to account for an overestimation of this testing method (Graybeal 2006a). With this high tensile strength influenced by the ability of fibers to bridge cracks and provide post-cracking strength, UHPC is often considered to carry some post-cracking tensile strength in flexure, whereas conventional concrete is considered to carry zero tension once the concrete has cracked (Garcia 2007; Graybeal 2006a). Further details on flexure behavior are discussed in the following section.

Table 2-3: Reported tensile strengths of UHPC vary depending on testing method (Graybeal 2006a).

Test Method	Tensile Strength, ksi
Splitting Tension of Cylinders, Ultimate	3.51
Splitting Tension of Cylinders, First Crack	1.58
Flexural testing of Prisms, First Crack - Corrected	1.43
Direct Tension of Notched Cylinders	1.60
Direct Tension of Un-notched Cylinders	1.43
Uniaxial Tension of Briquettes	1.22

2.3.1 Durability Properties

Enhanced durability properties of UHPC make it advantageous for use in harsh environments, including those encountered by bridges. UHPC has 100% freeze-thaw resistance (Graybeal 2006a), meaning that it does not exhibit any negative responses to freezing and thawing cycles. This is especially important on bridge decks, which are known to freeze before roads. UHPC is also known to be resistant to alkali-silica reaction, a destructive reaction caused by the interaction of hydroxides and aggregates containing silica or carbonates, and chloride penetration, a common problem in concrete leading to the corrosion of steel (Graybeal 2006a; Kosmatka et al. 2002; Roux et al. 1996).

One of the primary factors in achieving this advanced durability in UHPC is the low porosity, achieved through a low water-to-binder ratio (Roux et al. 1996). Tests have shown that UHPC has no capillary porosity and low air permeability, making it less penetrable to aggressive agents as compared to conventional concretes. Because of these advanced durability properties, the lifetime of a UHPC structure is predicted to be longer than that of a conventional concrete structure. For this reason, UHPC is considered to be a good material for increasing the life of structures and minimizing costs associated with repairs and rehabilitation.

2.3.2 Multi-axial Behavior

Because structures are rarely subjected to pure tension or compression, understanding multi-axial stress states is imperative to implement a material for structural use. A failure criterion is typically established, defining the failure points of a material subjected to multi-axial stresses. Behavior of conventional and high strength concrete in multi-axial stress states is well

documented, including work by Kupfer et al. (1969), Rosenthal and Glucklich (1970), Liu et al. (1972), Ottosen (1977), Tasuji et al. (1978), Gerstle (1981), Chuan-zhi et al. (1987), Su and Hsu (1988), Yin et al. (1989), Belarbi and Hsu (1995), Hussein and Marzouk (2000), Tao and Phillips (2005), and Lü et al. (2007). One of the most complex aspects of generating these models is in the testing method, since a variety of methods have been used to gather data for biaxial behavior of concrete. Many of these methods were complicated and required very specific equipment to perform the experiments. This section discusses several models and methods used to determine biaxial behavior of conventional and fiber-reinforced concretes. Current information on biaxial behavior of UHPC is also discussed, demonstrating the need for more information.

2.3.2.1 *Kupfer-Hillsdorf-Rusch Model for Conventional Concrete*

Kupfer, Hillsdorf, and Rusch (1969) used brushed bearing platens to test small concrete plate specimens in biaxial stress states. The brushed bearing platens were introduced to prevent the effects of end restraints in the members at the loading points often exhibited by solid bearing plates. Kupfer et al. (1969) showed that solid bearing plates exhibited apparent higher biaxial compression-compression results due to the restraint of the member (Figure 2-6). The concrete specimens measured 7.9x7.9x2 in. Three different concretes were tested with three different uniaxial compressive strengths: 2700 psi, 4450 psi, and 8350 psi. The stresses in each direction were normalized according to the unconfined uniaxial compressive strength, β_p, of the prism.

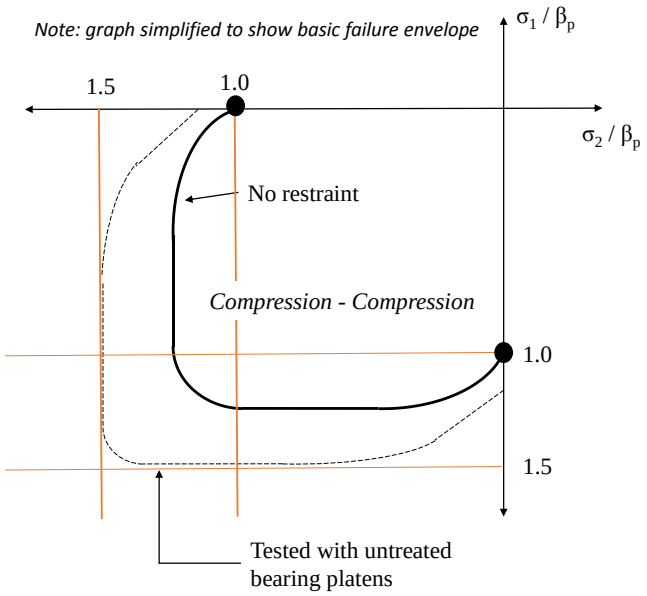

Figure 2-6: Kupfer et al. (1969) proved that loading platen restraint inherently increases the perceived biaxial strength of plain concrete.

The brushes on the platens were created using multiple steel filaments approximately 0.12x0.20 in. in cross section (Kupfer et al. 1969). The length of the filaments varied, depending on the expected stress on the filaments. In general, as concrete strengths increased, the filament lengths were decreased to prevent buckling. For each testing case, the filaments were spaced at 0.0008 in. and soldered together to create a single support for loading. The platens were glued to the specimen using an epoxy resin to provide support during tensile loading.

Five hydraulic jacks were used to perform the experiment, and two individual loading frames were constructed to control the two directions of the tests (Figure 2-7) (Kupfer et al. 1969). A load distributing frame was built to maintain a constant ratio of stresses. One hydraulic jack is applied to a beam that spans two other hydraulic jacks. As the first jack is moved along the beam, the ratio of σ_1 to σ_2 is changed. The two jacks under the beam are used to translate this ratio of stresses to the two jacks controlling the biaxial test.

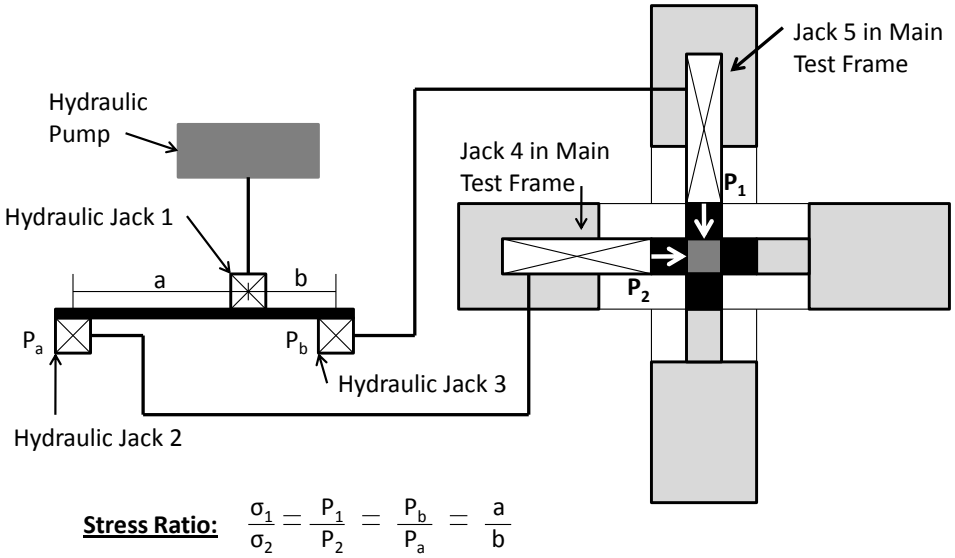

Figure 2-7: Testing apparatus used by Kupfer et al. (1969) to maintain a constant stress ratio in biaxial cases.

For the Kupfer et al. (1969) model (Figure 2-8), the elastic limit and failure stresses under biaxial conditions are given as a ratio of stress to β_p, the unconfined uniaxial compressive strength of the prisms. The biaxial tension stress state showed no significant increase in stress as compared to the uniaxial tensile strength of the concrete. In the combined tension and compression stress state, the compressive strength of a specimen decreases as increasing tensile stress is applied. In the biaxial compressive stress state, the concrete failure stresses increased up to 27 percent above the uniaxial compressive strength of the concrete. At equal compressive stresses, the failure stresses were approximately 16 percent higher than the uniaxial compressive strength of the concrete.

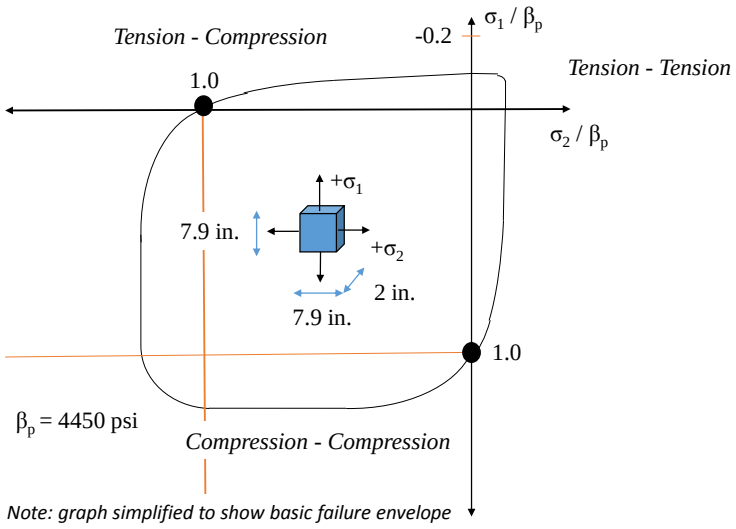

Figure 2-8: Kupfer et al. (1969) biaxial failure model for plain concrete.

The testing apparatus used in this method was reasonable for testing conventional normal strength concrete. However, in the case of ultra-high performance concrete, it may be difficult to implement a glued connection with specimens that are able to withstand higher tensile stress. Additionally, this method requires multiple jacks to control the experiment. Since one of the objectives of the study is to develop a testing method to perform biaxial testing using typical laboratory equipment and minimal load frame fabrication, this testing method may require more equipment than intended.

2.3.2.2 *Ottosen Model for Conventional Concrete*

Ottosen (1977) generated a failure criterion for concrete in triaxial stress states subjected to steady, unsustained loadings. Using mathematical modeling, the new model was generated to better relate experimental data collected from a variety of researchers, including Kupfer et al. (1969). The failure criterion is defined by the following relationship:

$$f\left(I_1, J_2, \cos 3\theta\right) = A\frac{J_2}{\sigma_c^2} + \lambda\frac{\sqrt{J_2}}{\sigma_c} + B\frac{I_1}{\sigma_c} - 1 = 0 \qquad (2\text{-}5)$$

Values A and B are constant parameters with values greater than zero, λ is a function of cos(3θ) that is greater than zero, and σ_c is the uniaxial compressive strength. I_1 is the sum of principal stresses σ_1, σ_2, and σ_3 (Chen 1982). The angle θ is defined by using polar coordinates (ρ, θ) to identify the location of a stress point P in the deviatoric plane (Figure 2-9), where the deviatoric plane is positioned orthogonal to a point (1,1,1) on the principal stress plane (Ottosen 1977). J_2 can be calculated using the principal stresses, as shown in the following relationship (Chen 1982):

$$J_2 = \frac{2}{3}\left(\left(\frac{\sigma_1-\sigma_2}{2}\right)^2+\left(\frac{\sigma_2-\sigma_3}{2}\right)^2+\left(\frac{\sigma_3-\sigma_1}{2}\right)^2\right) \quad (2\text{-}6)$$

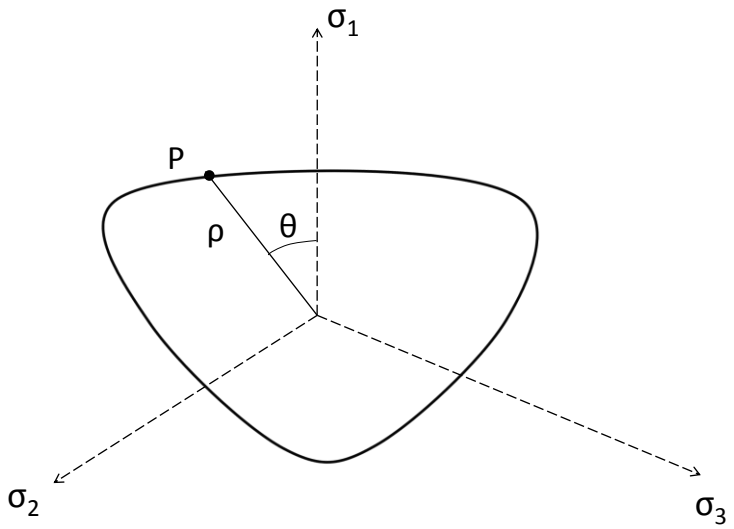

Figure 2-9: Ottosen failure surface in the deviatoric plane (Ottosen 1977).

Using results from other researchers, Ottosen verified that this model was appropriate for concrete in both biaxial and triaxial stress states (Ottosen 1977). This model has smooth, convex, curved surfaces in the deviatoric plane (Figure 2-9). In the case of triaxial compression, the three-dimensional shape of the failure surface is nearly triangular at small stress values, but widens to a more circular shape at large stresses (Ottosen 1977). This creates a narrowing conical shape, similar to an ice-cream cone, with three flattened edges at lower stress values.

2.3.2.3 *Demeke-Tegos Model for Fiber-Reinforced Concrete*

Information is also available to define failure criterion for fiber-reinforced concretes, a conventional concrete with discrete fiber reinforcement. A study by Demeke and Tegos (1994), showed that the addition of discrete fiber reinforcement increases the uniaxial tensile strength of concrete, as well as the strength of concrete subjected to biaxial tension-compression stress states (Figure 2-10). It was also noticed that increasing the fiber volume had very little effect on the uniaxial compressive strength. The same relationship between biaxial tension-compression stress states exhibited by conventional concrete is shown to exist in fiber reinforced concrete; the addition of tensile stress decreases the compressive stress capacity.

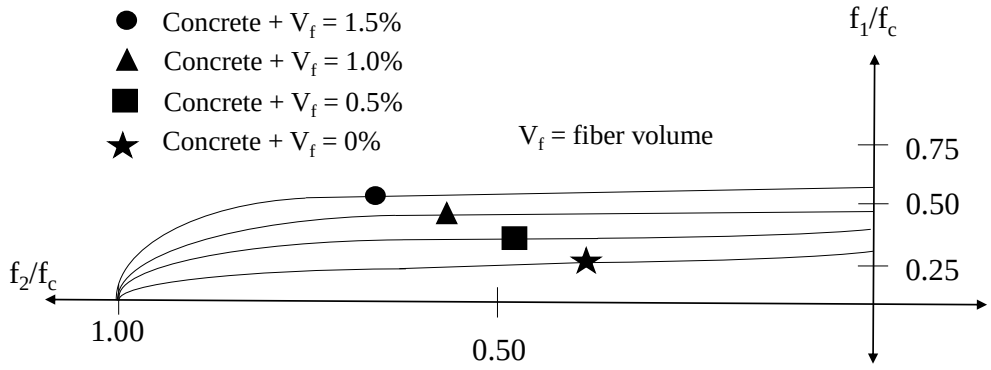

Note: graph simplified to show trend of fiber-reinforced concrete in biaxial tension-compression stress states.

Figure 2-10: Fibers improve biaxial tension-compression capacity (Demeke and Tegos 1994).

The testing method for this study was different from all others mentioned previously. Since only combined tension and compression stress states were considered, the specimens were created with this consideration. Specimens were shaped as prisms, measuring 4x4x11.8 in. (Demeke and Tegos 1994). Each prism was cast with reinforcing bars in the 4x4 in. ends to be loaded in tension (Figure 2-11). These reinforcing bars were also cast into larger reinforced concrete blocks to be used as anchors to load the specimen in tension. Because the reinforcing bars were not extended throughout the entire specimen, there was a small area of unreinforced concrete in the middle intended to experience the biaxial compression-tension stresses.

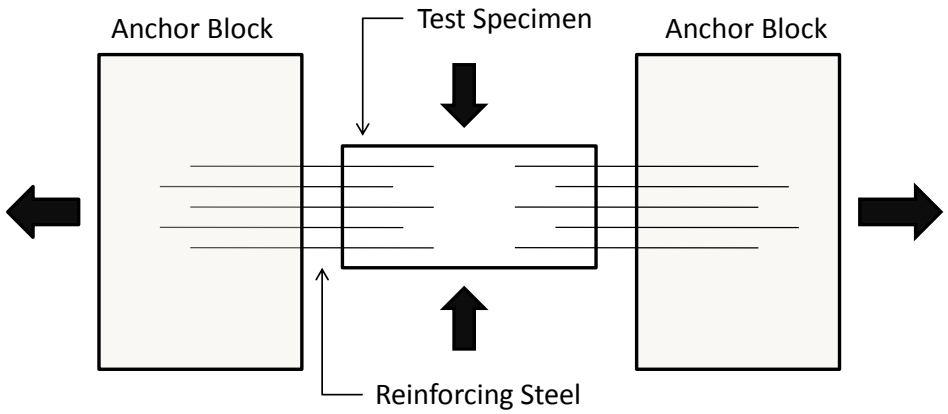

Figure 2-11: Biaxial tension-compression test using reinforcing to transfer tensile loads (Demeke and Tegos 1994).

The specimen was loaded in compression perpendicular to the tension face (Demeke and Tegos 1994). A special layering system using Teflon, plastic, and petroleum jelly was applied to the compression face to prevent shear stress effects on the contact surface (Figure 2-12). The authors tested this layering method against the use of steel ball bearings, proving that the layering method was more effective (Demeke and Tegos 1994).

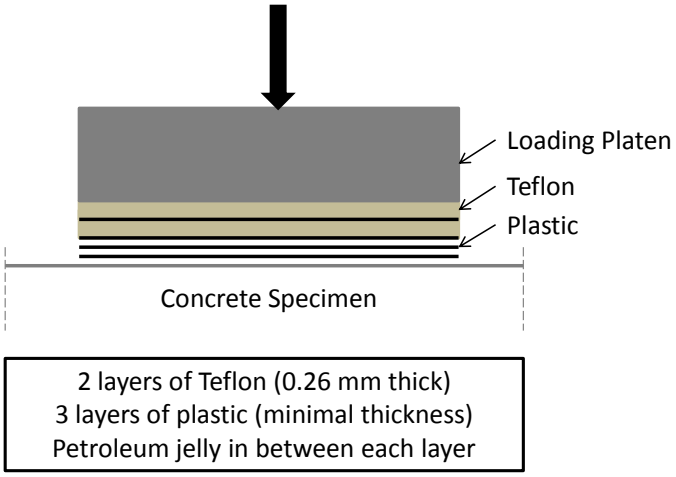

Figure 2-12: Multiple layers of Teflon, plastic, and petroleum jelly were used to eliminate friction between loading platen and concrete specimen (Demeke and Tegos 1994).

This method may have been reasonable for conventional concrete, but complications may arise when using UHPC. Using reinforcing bars to transmit tensile forces to the specimen creates added complications due to the interaction of these bars. Since UHPC has a higher

tensile strength than conventional concrete, increased reinforcement would be needed to transmit the tensile force. Despite possible complications with applying a tensile force, the layering method to prevent shear stresses could be applied to UHPC specimens.

2.3.2.4 *Multi-axial Behavior of UHPC*

With the advanced composition of UHPC and the addition of discrete fiber reinforcement, it is expected that the multi-axial failure envelope would expand beyond the failure surface of conventional fiber-reinforced concretes; however, few studies have investigated multi-axial stress states of UHPC. Research has shown that a type of UHPC known as Compresit exhibits ultimate failure behavior similar to that described by a modified Coulomb model based on triaxial compression tests (Nielsen 1995, Jensen 1999). In a study by Fehling et al. (2008), behavior of UHPC was compared to normal strength concrete (NSC) by testing reinforced panels in biaxial compression-tension stress states. This testing was executed in a sequential manner where the tensile load was applied first. As the tensile load was maintained, the panel was loaded in compression until failure.

Fehling et al. (2008) showed that crack spacing and crack widths decreased and compressive strengths increased by including fibers at 1 % by volume in UHPC. Grünberg et al. (2010) developed models for biaxial and triaxial compression behavior of UHPC with 2.5 % fibers by volume. Typically, UHPC, including Ductal®, contains fibers added at 2 % by volume (Graybeal 2006a); therefore, it is important to understand how the additional fibers affect the biaxial behavior. By understanding biaxial behavior of UHPC, failure of structural components in multi-axial stress states can be predicted more accurately through computer modeling techniques, such as finite element modeling.

2.3.3 Material Property Summary

UHPC exhibits superior strength and durability as compared to conventional concrete. By implementing a post-set curing regime of combined heat and steam, these properties can be enhanced all the more. Many of the material properties have been characterized; however, comprehensive studies of multi-axial behavior have been neglected. Because little is known of combined stress states, this research will focus on defining a new test to examine the biaxial compressive-tensile strength of plain UHPC. The plain UHPC will only contain discrete steel fiber reinforcement with no additional reinforcement.

By taking advantage of high strength and excellent durability properties, UHPC has the potential to be used in a variety of structural applications. In particular, the use of UHPC in bridge applications is of interest because bridges are subject to harsh environmental conditions. Bridges are often subjected to thermal changes including freeze-thaw cycling, degrading concrete and leading to frequent repairs or replacements throughout the lifetime of a bridge. In this study, durability is a primary concern for bridge decks. Additionally, strength of the section will be of utmost importance to ensure that the sections are adequate to resist loadings. For this reason, UHPC will also be explored as a potential solution to extend the life of future bridge decks.

2.4 Structural Properties of UHPC

2.4.1 Stress-Strain Behavior

Conventional design codes in the United States use the Whitney stress block as an approximation for the compressive stress distribution for ultimate limit state analysis and design of concrete structures. Since studies have shown that UHPC behaves differently from conventional concrete, several relationships have been proposed to relate stress and strain for flexure of UHPC structures. This section discusses models for conventional concrete and UHPC, including the ACI/AASHTO Stress Block Model (ACI Committee 318 2011, AASHTO 2012), the AFGC/Setra Model for UHPC (AFGC and Setra 2002), the Australian model for UHPC (Gowripalan and Gilbert 2000), and U.S. FHWA Models proposed for UHPC (Garcia 2007, Graybeal 2008).

2.4.1.1 *ACI/AASHTO Stress Block Model*

Conventional U.S. design codes for concrete, such as the American Concrete Institute (ACI) (ACI Committee 318 2011) and the American Association of State Highway Transportation Officials (AASHTO) (AASHTO 2012), utilize a stress-strain model known as the Whitney stress block for analysis of conventional concrete at an ultimate limit state. The stress block model (Figure 2-13) is equivalent to the actual parabolic stress distribution exhibited by concrete in compression.

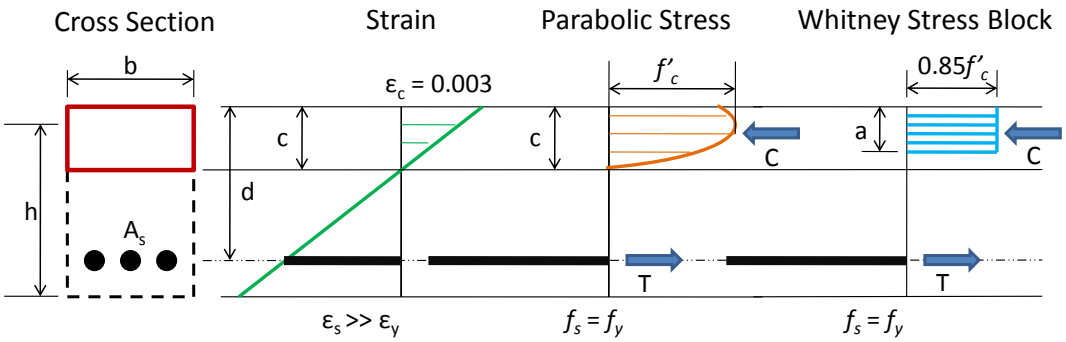

Figure 2-13: The equivalent rectangular (Whitney) stress block typically used by ACI Committee 318 (2011) and AASHTO (2012) design codes at the ultimate stress state of concrete in bending.

The variables in the above diagram (Figure 2-13) are defined as:

h = height of concrete member

b = width of concrete member; width of rectangular stress block

d = depth of reinforcing steel

c = depth of neutral axis

a = depth of rectangular stress block

ε_c = ultimate concrete strain; 0.003

ε_s = strain in reinforcing steel

ε_y = yield strain of reinforcing steel

f_s = stress in reinforcing steel

f_y = yield stress of reinforcing steel

f'_c = specified compressive stress of concrete

C = compressive force contributing to moment resistance of beam

T = tension force contributing to moment resistance of beam

The compression block has a depth of a, a width of b, and a stress of $0.85f_c'$. The depth, a, is determined using Equations (2-7) and (2-8). In this model, concrete strength in tension is neglected, assuming that the concrete is cracked from the extreme tension face to the neutral axis. This assumption is validated by the negligible amount of tension resisted by conventional concrete. The values for the compressive and tensile forces in the beam are given by Equations (2-9) and (2-10) respectively. All values are determined using English customary units.

$$a = \beta_1 c \tag{2-7}$$

$$0.85 \le \beta_1 = 1.05 - \frac{0.5 f_c^{'}}{1000} \le 0.65 \tag{2-8}$$

$$C = 0.85 f_c^{'} b a \tag{2-9}$$

$$T = A_s f_s \le A_s f_y \tag{2-10}$$

Where,

β_1 = factor reducing the depth of the neutral axis to the depth of the equivalent rectangular stress block based on f'_c

Although this method is reasonable for predicting the behavior of conventional concrete, a different model is needed for analyzing UHPC in flexure. A study by Graybeal (2008) explored the flexural capacity of UHPC I-girders. Using the Whitney stress block, the moment capacity of a UHPC I-girder was predicted to be only 73 % of the apparent experimental moment capacity (Graybeal 2008), showing that conventional design methods using the Whitney stress block are not suitable for UHPC because they provide very conservative results compared to the actual behavior. For this reason, a different model should be used to better represent the higher compressive and tensile strength of UHPC.

2.4.1.2 *French Model developed by AFGC and Setra*

The Association Française de Génie Civil (AFGC) and Service d'études techniques des routes et autoroutes (Setra) (AFGC and Setra 2002) proposed a two part stress-strain relationship (Figure 2-14, Figure 2-15, and Equations (2-11) through (2-17)) for UHPC in the *Ultra High Performance Fibre-Reinforced Concretes Interim Recommendations*. These models were developed using bending test specimens, assuming plane sections remain plane and stresses and strains are proportional to stresses in uncracked concrete. The model is formulated for metric units.

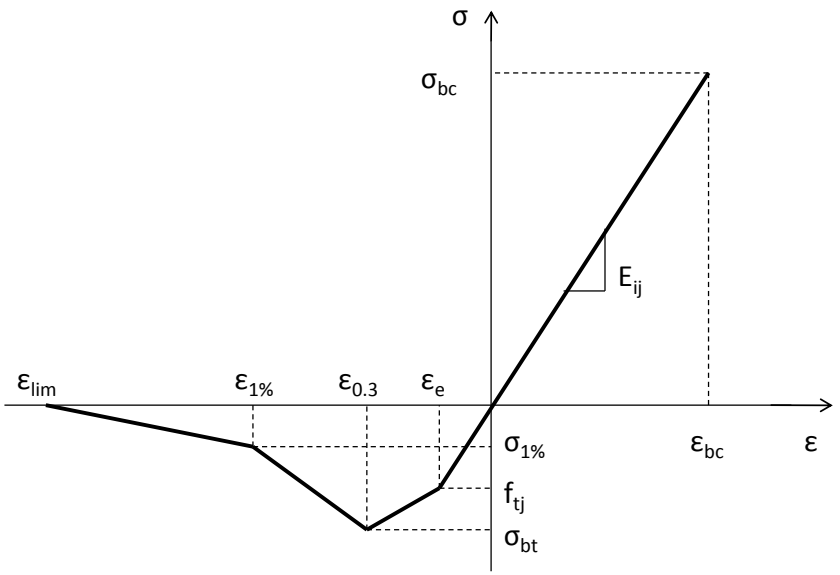

Figure 2-14: Strain hardening law of AFGC and Setra (2002) for UHPC at the serviceability limit state.

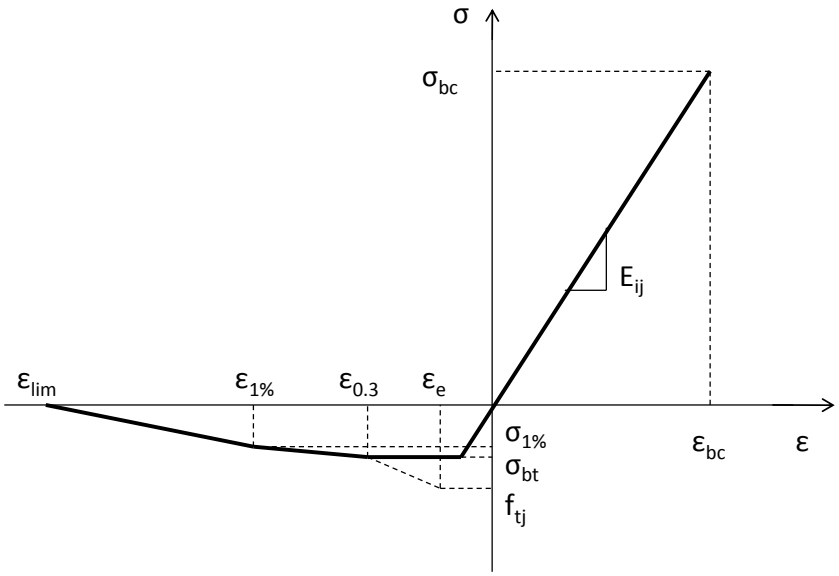

Figure 2-15: Strain softening law of AFGC and Setra (2002) for UHPC at the serviceability limit state.

$$\varepsilon_e = \frac{f_{tj}}{E_{ij}} \tag{2-11}$$

$$\varepsilon_{0.3} = \frac{\omega_{0.3}}{l_c} + \frac{f_{tj}}{E_{ij}} \tag{2-12}$$

$$\varepsilon_{1\%} = \frac{\omega_{1\%}}{l_c} + \frac{f_{tj}}{E_{ij}} \tag{2-13}$$

$$\varepsilon_{\lim} = \frac{l_f}{4l_c} \tag{2-14}$$

$$\sigma_{bc} = 0.6\, f_{C_j} \tag{2-15}$$

$$\sigma_{bt} = \frac{\sigma(\omega_{0.3})}{K} \tag{2-16}$$

$$\sigma_{1\%} = \frac{\sigma(\omega_{1\%})}{K} \tag{2-17}$$

Where,

ε_e = tensile strain elastic limit

$\varepsilon_{0.3}$ = compressive strain; 0.003

$\omega_{0.3}$ = crack width of 0.3 mm

h = depth for a rectangular cross-section (mm)

l_c = characteristic length; typically two-thirds of h (mm)

f_{tj} = tensile stress during construction, in areas subsequently under tension in service (MPa)

E_{ij} = modulus of elasticity (MPa)

H = height of the bending test specimen (mm)

$\sigma_{u1\%}$ = ultimate strain at a crack width of 0.01*H

$\omega_{1\%}$ = crack width of 0.01*H (mm)

ε_{lim} = limiting tensile strain

l_f = length of a fiber (mm)

σ_{bc} = stress in compression (MPa)

f_{Cj} = compressive stress at an age of j days (MPa)

K = orientation coefficient or coefficient for local effects; use 1.25 for all loading other than local effects; use 1.75 for local effects; use 1.0 for thin plates

$\sigma(\omega_{0.3})$ = corresponding stress at a crack width of 0.3 mm (MPa)

$\sigma(\omega_{1\%})$ = corresponding stress at a crack width of 0.01H (MPa)

The strain hardening law is used when proper fiber orientation is utilized in order to achieve strain hardening behavior (Sorelli et al. 2007). The strain softening law is intended to be used when fiber orientation is not utilized properly, resulting in a reduced tensile strength. In both of these models, the concrete has a significant amount of tensile strength, leading designers to utilize this enhanced behavior; however, AFGC and Setra (2002) do mention that designers may neglect tensile strength of the UHPC for prestressed designs.

2.4.1.3 *Australian Model for Stress and Strain*

According to the *Design Guidelines for Ductal® Prestressed Concrete Beams* produced in Australia (Gowripalan and Gilbert 2000), an idealized stress-strain relationship for design was generated for beams (Figure 2-16). In this model, compression is a positive value and tensile strain values, $\varepsilon_{t,p}$ and $\varepsilon_{t,u}$, are represented by Equations (2-18) and (2-19). The fiber content is assumed to be greater than or equal to 2 % by volume, and f_c' is the specified compressive strength of the concrete in MPa.

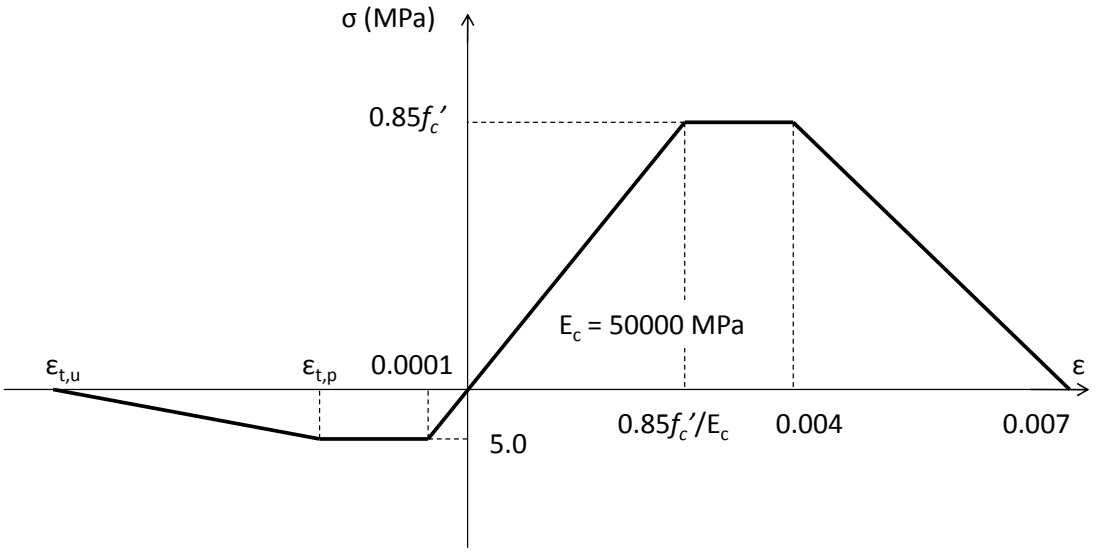

Figure 2-16: Idealized stress-strain relationship according to Australian design guidelines (Gowripalan and Gilbert 2000).

$$\varepsilon_{t,u} = {L_f}/{1.2D} \leq 0.01 \tag{2-18}$$

$$\varepsilon_{t,p} = {0.16L_f}/{1.2D} \leq 0.004 \tag{2-19}$$

Where,

L_f = length of fiber (mm)

D = total depth of member (mm)

For determining the strength of a beam in flexure, two different relationships are given for sections with bonded reinforcement and sections containing no bonded reinforcement (Gowripalan and Gilbert 2000). The stress-strain relationship at an ultimate limit state of a Ductal® section not containing bonded reinforcement is provided below (Figure 2-17). In this diagram, $\varepsilon_{b,u}$ is the ultimate tensile strain at bending, and this value is equivalent to $\varepsilon_{t,p}$ as defined previously in Equation 2-13.

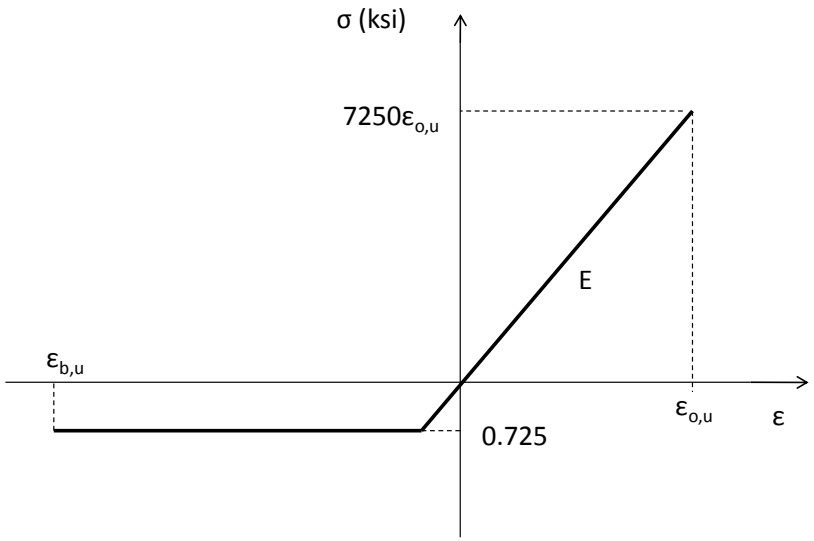

Figure 2-17: Australian stress-strain relationship for pure Ductal® sections in bending (Gowripalan and Gilbert 2000).

2.4.1.4 *U.S. FHWA Models for Stress and Strain*

Two models for UHPC stress-strain behavior in flexure have been developed by the U.S. Federal Highway Administration (FHWA). The first model was developed by Garcia (2007) and the second by Graybeal (2008). The first model by Garcia (2007) was developed to simplify experimental results by researchers at FHWA. In the simplified model (Figure 2-18), a triangular stress distribution was utilized for the compression section of the cross-section, and a uniform stress distribution was assumed for all UHPC in tension. For this model, the value of 28-day compressive strength, f'_c, is assumed to be 28 ksi, and the value of tensile strength, f_t, is assumed to be 1.5 ksi. This simple model was utilized in the design and analysis of waffle slab deck panels, to be discussed in more detail in Section 2.5.2.1 .

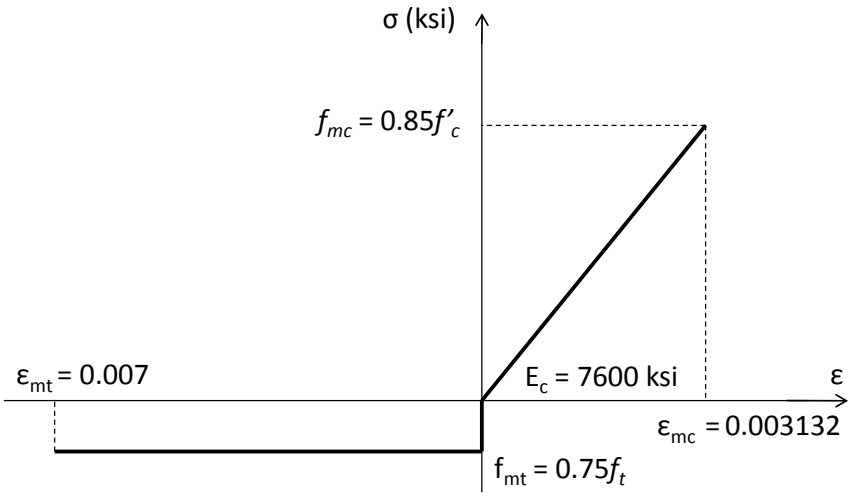

Figure 2-18: Garcia (2007) model for stress-strain behavior of UHPC.

Another conservative design method was proposed for UHPC I-girders through analysis and testing results by the U.S. Federal Highway Association (Graybeal 2008). The triangular compressive stress distribution was shown to more accurately represent the commercial UHPC Ductal®. UHPC was also assumed to carry a portion of tensile stress, due to its high tensile strength in comparison to conventional concrete. By applying results from testing and a conservative design approach, a stress-strain relationship was developed to be used for flexure of UHPC I-girders (Figure 2-19).

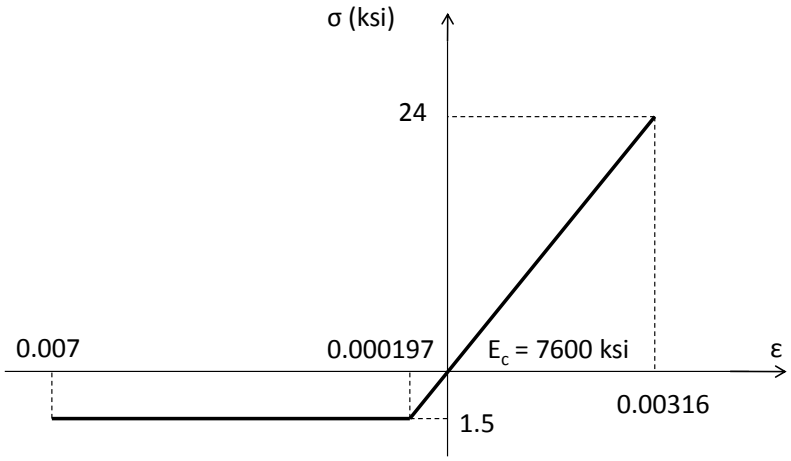

Figure 2-19: Graybeal (2008) stress-strain model developed for Ductal® I-girders in flexure (Graybeal 2008).

In the Graybeal (2008) model, the maximum compressive stress is estimated to be 85% of the 28-day compressive strength, and the maximum tensile stress is 50% of the uniaxial tensile stress as determined from girder testing (Graybeal 2008). The maximum tensile strain is considered 70% of the maximum tensile strain before failure in the girder testing, and the modulus of elasticity used in this model is 7600 ksi (Graybeal 2008). This model does not assume a completely uniform stress distribution for UHPC in tension, as seen previously in the Garcia model. Rather, this modified model extends the elastic behavior in tension to the ultimate tensile stress before applying a uniform stress distribution with increasing strain. This extension is typical to formerly mentioned models, including both the French (AFGC and Setra 2002) and Australian (Gowripalan and Gilbert 2000) models.

2.4.1.5 *Comparison of Stress-Strain Models*

A reliability study by Steinberg (2010) was carried out to compare models used to represent stress-strain behavior of UHPC for flexure members. In this study, Steinberg used Monte Carlo simulations to compare the AASHTO model utilizing the Whitney stress block, the FHWA model by Garcia (Figure 2-18), and a modified AFGC-Setra model developed by Steinberg (Figure 2-20). The modified AFGC-Setra model was developed to provide a more simplified version of the detailed stress-strain model of AFGC-Setra. The new model maintains linear segments without oversimplifying the tensile stress to one constant value. In comparison to the strain hardening model (See Figure 2-14) previously discussed, this model provides a constant stress between $\varepsilon_{u0.3}$ and $\varepsilon_{u1\%}$, whereas the original model has the tensile stress linearly decreasing to a stress of $\sigma_{u1\%}$ (Steinberg 2010).

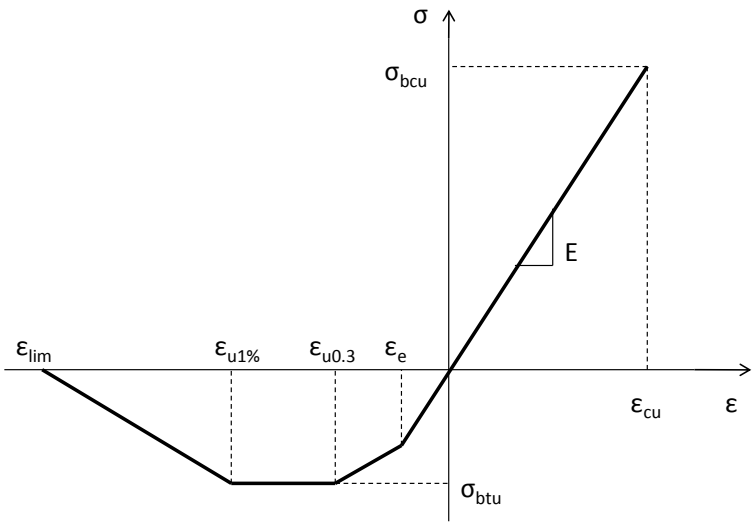

Figure 2-20: Modified AFGC-Setra stress-strain model by Steinberg (2010).

The Monte Carlo analysis method evaluates a variety of parameters to determine when a designed member may be considered unsafe, based on a list of specified parameters (Steinberg 2010). In this study, three shapes were analyzed: a box beam, a modified bulb tee as used in the Wapello County Bridge in Iowa (Section 2.5.1.3), and the second generation Pi-girder (Section 2.5.1.4). The primary parameter evaluated in this study was nominal moment capacity. As a result, the Garcia model was shown to produce higher predicted moment capacities, as compared to the other models. Following the Garcia model, the modified AFGC-Setra model produced the next highest moment capacities, and the AASHTO model gave the lowest values (Steinberg 2010). The conservative values using the Whitney stress block are consistent with results previously discussed in Section 2.4.1.1 by Graybeal (2008) from testing UHPC I-girders.

According to Steinberg (2010), the variability in results from each model was attributed to the type of failure associated with each model. The Garcia model resulted in failures due to tensile strain, causing a lag in compressive stress development. Therefore, the higher moment capacity is likely due to a larger moment arm or a larger tensile force caused by using the Garcia model. Variations in neutral axis location also resulted in some discrepancy, affecting the nominal moment capacities. With little data available, Steinberg (2010) suggests that additional research should be performed to better analyze the performance of these models. In order for this to occur, more full-scale testing should be performed to add to the database of knowledge for flexure of UHPC members.

2.4.2 UHPC in Flexure

Reported flexure strength of concrete members is often misconstrued and misrepresented. The equation for flexural strength is often that shown in Equation (2-20); however, the use of this equation is only valid up to the first crack of concrete. Once the concrete has cracked, the cross section resisting the load has changed, and stresses are redistributed throughout the new cross section. Therefore, the results from this method are inaccurate for reporting actual flexural strength. Despite the invalidity of this equation, it continues to be used to report flexural strength of concrete members since there is no accurate way of determining the actual depth of the cross section resisting maximum stresses. It must be noted that this value is not a realistic value, but can only be used for comparison.

$$f_{flexure} = \frac{My}{I} \tag{2-20}$$

Where,

$f_{flexure}$ = flexural stress; flexural strength at maximum moment (ksi)

M = maximum moment (k-in.)

y = depth to centroid (in.)

I = moment of inertia (in.^{4})

Flexure strength of UHPC is higher than conventional concrete members due to the high compressive and tensile properties. Flexural strength of UHPC can range between 2.9 and 20.5 ksi, with the highest values achieved through pressurization and a high heat steam treatment (Richard and Cheyrezy 1995). More common values for UHPC flexure strength range between 4 and 8 ksi (Lafarge 2013; Shaheen and Shrive 2007). The various relationships in Section 2.4.1 are used to design UHPC structures for flexure and to better represent the behavior of UHPC in bending.

Graybeal (2008) studied the flexural behavior of UHPC I-girders by experimentally testing AASHTO Type II girders made with UHPC to failure. In this study, the UHPC had a 28-day compressive strength of 28 ksi and a modulus of elasticity of 8100 ksi. The girder was prestressed with twenty-six 0.5-in. diameter, low-relaxation prestressing strands and contained

no mild reinforcement typically used for shear. The strands were stressed to 55 % of their ultimate stress, or 148.5 ksi. The girder shape was not optimized to best utilize the properties of UHPC; however, this provided a direct comparison to a familiar and standard conventional concrete girder. The beam was 80 ft long, and it was loaded in a four point bending configuration on a 78.5 ft span using a simple support system. The two point loads were located 3 ft from midspan.

Results from testing, showed that the moment capacity of the UHPC girder was 3,225 kip-ft (Graybeal 2008). Compared to the analysis of a similar concrete girder with a 28-day compressive strength of 8 ksi and a moment capacity of 1700 kip-ft, the UHPC girder moment capacity is approximately 90 % higher. This confirms that UHPC exhibits superior moment capacity over conventional high strength concrete.

Using the modified stress-strain relationship developed by Graybeal (2008) (Section 2.4.1.4 , Figure 2-19), the flexural capacity for the tested I-girder was predicted to be 2440 k-ft, or 76 % of the experimental value (Graybeal 2008). Although this was not a vast improvement compared to values using the Whitney stress block (Section 2.4.1.1 , Figure 2-13), the new model was developed to better represent UHPC with a conservative approach (Graybeal 2008). This conservative approach was considered a reasonable option until more testing has been performed to better understand the complete behavior of UHPC and to gain confidence of designers in using UHPC I-girders.

For this same test, cracking was not visible when loaded below 160 kips. However, at a loading of 78 kips, sounds indicated that the concrete was experiencing tensile cracking. Tensile cracking in UHPC members was shown to be different from conventional concrete members. For UHPC, very closely spaced cracks occurred with relatively small crack widths. Graybeal (2008) produced an equation with a coefficient of variation, R^2, of 0.952 to illustrate the relationship between tensile strains and crack spacing (Eq. (2-21)).

$$\varepsilon = 450 + \frac{500}{\sqrt{s_{cr}}} + \frac{40}{s_{cr}^2} \qquad (2\text{-}21)$$

where, ε = microstrain (in./(10^3 in.))

s_{cr} = crack spacing (in.)

A study by Barnett et al. (2010) showed that the discrete fibers and their orientation affected the flexure strength of small panels, ranging from 1 to 2 in. thick. In fiber reinforced concrete, discrete fibers produce a tension stiffening effect, providing the concrete an ability to carry additional load past the initial cracking point (Bischoff 2003). This same behavior was observed in the UHPC panels, contributing to increased flexure capacity (Barnett et al. 2010). Increased flexural capacity can also result from specific fiber orientation. If fibers are aligned parallel to tensile stresses, fibers can bridge tensile cracks directly. For beams, aligning fibers along the length of the beam is best accomplished by placing UHPC into one end of the beam mold, allowing it to flow toward the opposite end.

2.4.3 UHPC in Shear

Shear strength of UHPC has been proven significantly higher than plain conventional concrete. With the added strength of the fibers, UHPC has the capability of resisting shear cracking without the need for additional reinforcement in the transverse direction (Magureanu et al. 2010). Discrete fiber reinforcement results in the formation of numerous, tightly spaced cracks prior to shear failure (Graybeal 2006b; Voo et al. 2010). The angle of shear cracking has also been shown to be reduced in UHPC beams, showing values below the 45 degree angle commonly exhibited in conventional reinforced concrete (Graybeal 2006b).

The *Interim Recommendations* for *Ultra High Performance Fibre-Reinforced Concretes* by the AFGC and Setra (2002) provides one of the first recommendations for analyzing and designing UHPC structures subjected to shear stresses. Other recommendations can be found in the *Design Guidelines for Ductal® Prestressed Concrete Beams* by Gowripalan and Gilbert (2000), and the *Recommendations for Design and Construction of Ultra High Strength Fiber Reinforced Concrete Structures (Draft)* by the Japanese Society of Civil Engineers (2004). Graybeal (2006b) also recommends a design procedure for prestressed UHPC I-girders in a Federal Highway Administration Report.

2.4.3.1 *Shear Design According to the AFGC and Setra*

The AFGC and Setra (2002) describes the ultimate shear strength of UHPC sections to contain three different components contributing to the shear strength: concrete, fibers, and reinforcement. Both service and ultimate limit state conditions are considered with the criteria when using prestressed UHPC; however, serviceability checks are primarily concerned with

maintaining appropriate stress values. The shear capacity V_u is determined using three components: a contribution from the UHPC (V_{Rb}), a contribution from the fiber reinforcement (V_f), and a contribution from the steel reinforcement (V_a). The following equations outline how to determine shear strength according to the AFGC and Setra interim recommendations.

$$V_u = V_{Rb} + V_a + V_f \tag{2-22}$$

Where,

V_u = total shear resistance of UHPC section (N)

V_{Rb} = shear resistance contribution by UHPC; determined by Equation (2-23) for prestressed concrete or Equation (2-24) for reinforced concrete (N)

V_a = shear resistance contribution by steel reinforcement; determined by Equation (2-27) or (2-28) (N)

V_f = shear resistance contribution by fibers; determined by Equation (2-29) (N)

$$V_{Rb} = \frac{1}{\gamma_E}\frac{0.24}{\gamma_b} k \sqrt{f_{cj}} b_o d \tag{2-23}$$

(for prestressed concrete)

$$V_{Rb} = \frac{1}{\gamma_E}\frac{0.21}{\gamma_b} k \sqrt{f_{cj}} b_o d \tag{2-24}$$

(for mildly reinforced concrete)

Where,

γ_E = safety coefficient, such that $\gamma_E \gamma_b = 1.5$

γ_b = safety coefficient, such that $\gamma_E \gamma_b = 1.5$

f_{cj} = compressive strength of UHPC at time j (MPa)

k = factor indicating a portion of concrete in primarily tension or compression; determined by Equation (2-25) for compression or Equation (2-26) for tension

b_o = width of section (mm)

d = depth to centroid of prestressing tendons (mm)

$$k = 1 + \frac{3\sigma_{cm}}{f_{tj}} \quad (2\text{-}25)$$

(in compression)

$$k = 1 - \frac{0.7\sigma_{tm}}{f_{tj}} \quad (2\text{-}26)$$

(in tension)

Where,

f_{tj} = tensile strength of UHPC at time j (MPa)

σ_{cm} = mean compressive stress in total section of concrete under normal design force (MPa)

σ_{tm} = mean tensile stress in total section of concrete under normal design force (MPa)

$$V_a = 0.9d \frac{A_t}{s_t} \frac{f_e}{\gamma_s} (\sin\alpha + \cos\alpha) \quad (2\text{-}27)$$

(for mildly reinforced concrete)

$$V_a = z \frac{A_t}{s_t} \frac{f_e}{\gamma_s} \frac{(\sin(\alpha + \beta_u))}{\sin\beta_u} \quad (2\text{-}28)$$

(for prestressed concrete)

Where,

z = lever arm at ultimate moment between the centroid of the compression block and the centroid of the tensile reinforcement (mm)

A_t = area of transverse reinforcement (mm^2)

s_t = spacing of transverse reinforcement (mm)

f_e = yield strength of reinforcement (MPa)

γ_s = safety factor; generally taken as 1.15; taken as 1.0 for accidental combinations

α = angle of shear reinforcement measured from the axis of the web

β_u = angle of compression struts as measured from the horizontal; must be greater than or equal to 30°

$$V_f = \frac{S\sigma_p}{\gamma_{bf} \tan \beta_u} \tag{2-29}$$

Where,

S = area of fiber effect; estimated as $0.9b_od$ or b_oz for rectangular or Tee sections (mm^2)

σ_p = residual tensile stress carried by fibers across a shear crack; determined by Equation (2-30) (MPa)

γ_{bf} = partial safety factor; generally taken as1.3 for fundamental cases; taken as 1.05 for accident combinations

$$\sigma_p = \frac{1}{K}\frac{1}{w_{\lim}}\int_0^{w_{\lim}} \sigma(w)dw \tag{2-30}$$

Where,

w_{lim} = maximum of w_u or 0.3 mm (mm)

w_u = ultimate crack width; can be taken as $l_c\varepsilon_u$ (mm)

l_c = characteristic length; generally taken as (2/3)h (mm)

h = depth of section (mm)

ε_u = ultimate strain; 0.003

K = orientation coefficient for general effects

2.4.3.2 *Shear Design According to JSCE*

The Japanese Society of Civil Engineers (JSCE) prepared recommendations for designing and constructing ultra-high strength fiber reinforced concrete structures (Japan Society of Civil Engineers 2004). According to the recommendations, ultra-high strength fiber reinforced concrete (UFC) is defined as "a type of cementitious composites reinforced by fiber with characteristic values in excess of 150 N/mm^2 [22 ksi] in compressive strength, 5 N/mm^2 [0.72 ksi] in tensile strength, and 4 N/mm^2 [0.58 ksi] in first cracking strength" (Japan Society of Civil Engineers 2004). UFC is further defined by having a matrix containing a maximum particle size for aggregates less than 2.5 mm [0.098 in.] and a water-to-cementitious materials ratio less than 0.24. The recommendations also state that UFC contains fibers for reinforcement added at more than 2% by volume and that heat curing is required for UFC (Japan Society of Civil Engineers 2004).

The recommendations by JSCE (2004) consider the contribution of three components to shear strength of UFC structures: the contribution of the member itself without shear reinforcement, the contribution of the reinforcing fibers, and the contribution of longitudinal prestressing reinforcement. The design shear capacity V_{yd} for a structure can be determined using Equations (2-31) through (2-36). If a diagonal compression failure is expected, the shear capacity V_{wcd} can be determined using Equation (2-37).

$$V_{yd} = V_{rpcd} + V_{fd} + V_{ped} \tag{2-31}$$

Where,

V_{yd} = design shear capacity (N)

V_{rpcd} = contribution of the UFC matrix without shear reinforcement; determined by Equation (2-32) (N)

V_{fd} = contribution of the reinforcing fibers; determined by Equation (2-33) (N)

V_{ped} = contribution of longitudinal prestressing reinforcement; determined by Equation (2-36) (N)

$$V_{rpcd} = 0.18\sqrt{f_{cd}^{'}} \cdot b_w \cdot d/\gamma_b \quad (2\text{-}32)$$

Where,

b_w = web width (mm)

d = effective depth (mm)

f_{cd}' = design compressive strength of UFC (N/mm^2)

γ_b = member factor; given generally as 1.3 here

$$V_{fd} = \left(f_{vd} / \tan\beta_u \right) \cdot b_w \cdot z/\gamma_b \quad (2\text{-}33)$$

Where,

f_{vd} = design average tensile strength perpendicular to diagonal cracks of UFC; determined by Equation (2-34)

β_u = angle between member axis and a diagonal crack; must be greater than 30°; determined by Equation (2-35)

z = distance from the location of compressive stress resultant to the centroid of tensile steel; given generally as the value of d/1.15

γ_b = member factor; given generally as 1.3 here

$$f_{vd} = \frac{1}{w_{\lim}} \int_0^{w_{\lim}} \frac{\sigma_k(w)}{\gamma_c} dw = \frac{1}{w_{\lim}} \int_0^{w_{\lim}} \sigma_d(w) dw \quad (2\text{-}34)$$

Where,

w_{lim} = generally 0.3 mm (mm)

$\sigma_k(w)$ = characteristic value of Tension Softening Diagram; considers data scatter

$\sigma_d(w)$ = the value of $\sigma_k(w)$ divided by a material factor

$$\beta_u = \frac{1}{2}\tan^{-1}\left(\frac{2\tau}{\sigma_{xu}^{'} - \sigma_{yu}^{'}} \right) - \beta_0 \geq 30° \quad (2\text{-}35)$$

Where,

τ = average shear stress calculated from design shear force

σ'_{xu} = average compressive stress along member axis

σ'_{yu} = average compressive strength perpendicular to the member axis

β_0 = angle formed by a diagonal crack and a line at 45° from the member axis when not subjected to axial force

$$V_{ped} = P_{ed} \cdot \sin {\alpha_p}/{\gamma_b} \tag{2-36}$$

Where,

P_{ed} = effective tensile force of prestressing steel tendons

α_p = angle formed by prestressing steel tendons and member axis

γ_b = member factor; given generally as 1.1 here

$$V_{wcd} = 0.84 f_{cd}^{'\,2/3} \sin(2\beta_u) \cdot b_w \cdot {d}/{\gamma_b} \tag{2-37}$$

Where,

γ_b = member factor; given generally as 1.3 here

Similar to the AFGC and Setra (2002) recommendations, the JSCE (2004) recommendations also consider the contribution of the concrete matrix and the contribution of the fiber reinforcement separately. The JSCE recommendations also consider that the angle of diagonal cracks in UFC is lower than the typical 45° in conventional concrete, and the 30° limit of diagonal cracks was adopted from the AFGC recommendations. In determining the value for f_{vd}, the JSCE (2004) recommendations alter the AFGC and Setra (2002) methods to account for fiber orientation.

2.4.3.3 *Shear Design According to Australian Guidelines*

According to *Design Guidelines for RPC Prestressed Concrete Beams* (Gowripalan and Gilbert 2000), shear strength is provided to prevent shear cracking under service loads. For this reason, this design code only utilizes the strength limit states. To design for shear strength, the following equation must be satisfied:

$$V^* \leq \phi V_u \tag{2-38}$$

Where,

V^* = design shear force; determined using factored design loads for strength limit states

V_u = shear strength contribution by structural system; determined by Equation (2-39)

ϕ = phi factor; 0.7 for shear according to AS3600 – 1994

$$V_u = V_{uc} + V_{us} + P_v \tag{2-39}$$

Where,

V_{uc} = shear strength contribution of concrete

V_{us} = shear strength contribution of shear reinforcement

P_v = transverse component of prestressing force

The design code also suggests that the shear strength contribution of reactive powder concrete, V_{uc}, be limited to V_t, the shear force required to produce a specified tensile stress σ_t (Gowripalan and Gilbert 2000). Therefore, the principal tensile stress in a beam shall not exceed σ_t, as defined by Equation (2-40).

$$\sigma_t = \left(5.0 + 0.13\sqrt{f_c'}\right) \quad \text{in MPa} \tag{2-40}$$

Where,

σ_t = limiting tensile stress occurring at either the central axis of the beam or at the intersection of the web and the flange (MPa)

f_c' = the specified compressive strength (MPa)

The critical section of a beam represents the location along a beam with the maximum shear force considered in a design. For beams, the design guidelines provide two possible scenarios to determine the critical section. First, the critical section is located at a distance *d* from the support if no diagonal cracking can take place at or into the support (Gowripalan and Gilbert 2000). If cracking can occur at or into the support, the critical section is located at the face of the support.

The *Design Guidelines for RPC Prestressed Concrete Beams* also addresses shear strength of slabs (Gowripalan and Gilbert 2000). If the slab fails in shear across the width, shear design strength is determined as if it were a beam. If the slab fails in shear near a support or a concentrated load, the design strength φV_u is determined according to Equations (2-41) and (2-42). The critical shear perimeter of a slab is similar to the critical section of a beam. The critical shear perimeter is determined by extending the effective area of either a support or a concentrated load by a distance *d/2*. This area is used to determine the design shear strength.

$$V_u = \frac{V_{uo}}{\left[1 + \frac{uM_v^*}{8V^* ad}\right]} \tag{2-41}$$

$$V_{uo} = ud\left(5 + 0.3\sigma_{cp}\right) \tag{2-42}$$

Where,

u = effective length of the critical shear perimeter

M_v^* = bending moment transferred from slab to support in direction considered; zero if considering concentrated wheel loads

d = effective depth of the slab averaged around the critical shear perimeter

a = dimension of the critical shear perimeter measured parallel to the direction of the span producing the bending moment M_v^*

σ_{cp} = average effective prestress around the critical shear perimeter (positive if compressive, negative if tensile)

2.4.3.4 *Shear Design Recommendations by Graybeal (2006b)*

Graybeal (2006b) performed three shear tests on AASHTO Type II girders, each prestressed with twenty-six 0.5-in. diameter 270 ksi low relaxation prestressing strands. Unlike conventional concrete, no mild reinforcement was used throughout the girder. The girders were tested using simple supports, a roller and a rocker, over three different span lengths: 14 ft, 24 ft, and 28 ft. Results showed that the number of shear cracks increased as the load increased. The angle of shear cracking ranged from 35 to 38 degrees, showing that UHPC exhibits shear cracking at a shallower angle than conventional concrete. In the girder tested over a 24 ft span, failure was immediate once fiber pullout began in the diagonal shear cracking. The tensile capacity was greatly reduced by fiber pullout. However, in the girder tested over a 14 ft span, the tendons slipped as the fibers began to pullout. This caused the shear capacity to decrease slowly rather than resulting in a sudden and immediate failure (Graybeal 2006b). Both failures were brittle, and structures should be designed to avoid such failure types.

Graybeal (2006b) recommends that the shear capacity be estimated using the area of the web and an approximate angle of the diagonal tensile failure plane. It is assumed that all shear forces are carried by diagonal tension and compression in the web alone. The concept behind this method is equivalent to the calculation for fiber contribution to shear capacity as proposed in the Interim Recommendations by AFGC and Setra (2002). Manipulating the AFGC and Setra equation shows that the residual stress is multiplied by an estimated shear plane area to provide the shear contribution of fibers (Graybeal 2006b). Graybeal also indicates that the girder should be detailed to maintain small crack widths. This can be accomplished by restraining the top and bottom flanges or by using draped tendons.

2.5 Bridge Applications of UHPC

As previously discussed, UHPC has excellent strength and durability properties, making it suitable for structural applications in harsh environments. Because bridges are exposed to such environments, UHPC is well-suited for bridge applications. This section describes how UHPC has been implemented in existing structures and the research that has begun to investigate the use of UHPC in bridge decks.

2.5.1 Existing Structures

UHPC has been used to construct several pedestrian bridges, including the Sherbrooke Footbridge in Sherbrooke, Quebec (Blais and Couture 1999) and the Footbridge of Peace in Seoul, Korea (Lafarge 2013). Once UHPC reached the United States (U.S.), researchers at the Massachusetts Institute of Technology (MIT) developed an optimized bridge girder concept to take full advantage of the material's strength properties (Graybeal 2009a, Graybeal 2009b). The first UHPC highway bridge to be built in the U.S. is located in the state of Iowa (Lafarge 2013, Graybeal 2009c), but increasing knowledge of UHPC has caused its use to extend beyond the state of Iowa.

2.5.1.1 *Sherbrooke Footbridge (Sherbrooke, Quebec, Canada)*

The Sherbrooke Footbridge, was the first major structure constructed using UHPC (Blais and Couture 1999). This bridge is composed of a space truss, using confined UHPC in steel tubes as diagonal web members. This method of confinement allowed compressive strengths to reach 50 ksi; whereas, the unconfined UHPC was designed for a compressive strength of 29 ksi.

The Sherbrooke Footbridge spans a distance of 197 ft, containing six prefabricated segments that were post-tensioned together (Blais and Couture 1999). In each three chord truss element, the top chord is composed of the unconfined 1-3/16 in. thick UHPC deck and stiffening elements. The deck was designed so that the UHPC could resist shear and punching forces without mild reinforcement. The diagonal chords are composed of confined UHPC encased in stainless steel tubing. Each chord is angled in two directions: 41 degrees in the longitudinal direction and 14 degrees in the transverse direction. Each diagonal chord was prestressed using two tendons and anchored directly against the UHPC. The bottom chord is composed of a UHPC beam that is used to connect the diagonal chord members.

During construction, the Sherbrooke Footbridge was instrumented to monitor the bridge's performance over time (Blais and Couture 1999). The following information is measured and recorded constantly through this system: temperature variations, strains in all chords of the truss, deflections of the superstructure, loads in web members, prestressing force, and vibrations. The results are collected and monitored by researchers at the University of Sherbrooke and Concrete Canada. Results from this long-term bridge monitoring project should provide data to improve UHPC structures in the future.

2.5.1.2 *Footbridge of Peace (Seoul, South Korea)*

The Footbridge of Peace was designed by French architect Rudy Ricciotti and stands as a symbol of the aesthetic possibilities of UHPC (Lafarge 2013). A gift from the country of France to represent friendship, the Footbridge of Peace spans 400 ft to link the city of Seoul to the Sunyudo Island in South Korea (Brouwer 2001). The footbridge contains no passive reinforcement, but only 13.2 tons of prestressed reinforcement was used with the 240 tons of Ductal® (Lafarge 2013). The ability to create slender elements based on the strength and ductility of UHPC is best displayed in the 1- ¼ in. thickness of the bridge's 17 ft wide deck (Lafarge 2013).

The main arch of the bridge is composed of six segments (Brouwer 2001). Each segment is approximately 72 ft long, 14 ft wide, and 4 ft high. On each side, three segments were pretensioned to the foundation, and the foundations served to withstand the horizontal thrust in the bridge. Ductal® was used to fill space between the two ends of the arch. More stress was incorporated into the overall arch by placing a force of 445 kN into each end before pouring the center closure of Ductal®. Transverse ribs were spaced at approximately 4 ft, providing a shock-absorbing system to control vibrations, a concern for slender bridges. As the first project to best take advantage of the superior strength and ductility characteristics of UHPC (Brouwer 2001), the Footbridge of Peace displays new design opportunities available using UHPC.

2.5.1.3 *Highway Bridges in the United States*

As the first bridge built in the U.S. using UHPC, the Mars Hill Bridge, is located in Wapello County, IA (Graybeal 2009c). Standard bulb-tee girders were modified by reducing the section size to take advantage of the high strength of UHPC (Bierwagen and Abu-Hawash 2005). Additionally, traditional reinforcement for shear was eliminated from the bridge because UHPC

alone was able to handle the entire shear demand (Graybeal 2009c). This bridge, built in 2006, is the first of several UHPC structures in Iowa (Keierleber et al. 2010).

Since the opening of the Mars Hill Bridge, other bridges using UHPC have been constructed in the U.S., including the Cat Point Creek Bridge in Richmond County, VA and the Jakman Park Bridge in Buchanan County, IA (Graybeal 2009c). The Jakman Park Bridge was constructed in 2008 (Keierleber et al. 2010). This innovative bridge contains a 50-ft span using specialized Ductal® Pi-girders. The cross-section, discussed in more detail in Section 2.5.1.4 , resembles the Greek letter Pi and takes UHPC's high strength and ductility characteristics into consideration. The overall bridge is 115 ft 4 in. long and 24 ft 9 in. wide. The Pi-girders measured 51 ft 2 in. in length and were supported by neoprene pads. The Cat Point Creek Bridge in VA contains one span of five UHPC I-girders, approximately 80 ft long (Lafarge 2013). A cast-in-place deck was then placed on top of these UHPC girders.

An extensive amount of effort between researchers, designers, and producers made these bridges a reality since there are no standard guidelines for using UHPC in the U.S. As the understanding of UHPC continues to grow, the implementation of UHPC structures can become more common and more accepted among producers and designers.

2.5.1.4 *Pi-girder Test Bridge (McLean, VA)*

The design of the Pi-girder cross-section was inspired by the Footbridge of Peace in Korea (Graybeal 2009a). Researchers from the Massachusetts Institute of Technology (MIT) developed cross-sectional dimensions to optimize for the unique properties of UHPC and to best implement the Pi-girder for use in U.S. highway bridges. Simply, the Pi-girder is a double bulb-tee girder, closely resembling the shape of the Greek letter Pi. Although double tee girders have been previously used for parking decks and bridges in the United States, the innovative Pi-girder features a slender design that would not be possible without the superior strength of UHPC.

The original Pi-girder shape was tested by the Federal Highway Administration, and MIT researchers developed a method to modify dimensions of the girder cross-section based on specified span lengths (Graybeal 2009b). FHWA chose to test a deck designed for a span length between 70 and 100 feet. For this span length, the deck was 3 in. thick and the total girder height was 33 in. The cross-section also featured several distinct edges, resulting in a nearly perpendicular intersection of the webs and the deck. Longitudinal joints were initially bolted together using threaded rods spaced every 3 ft. After joints were connected using bolts, the shear

keys of the joints were filled with non-shrink gout to complete the full connection (Graybeal 2009b).

Results from testing the original Pi-girder provided researchers with valuable information to improve future cross-sections. In the original cross-section, high stress concentrations developed at sharp edges, specifically where the webs met the deck (Graybeal 2009b). The shear strength exceeded the required capacity by AASHTO for the specified girder span length, but the section lacked an excess of flexural strength. Tightly spaced cracks were noticed during flexural testing (Graybeal 2009b), showing the ability of the fibers to provide post-cracking resistance. Transverse flexural strength was improved by strapping the two webs together, and large cracks formed in the deck due to few alternative load paths in the members during transverse flexural testing (Graybeal 2009b). Based on these results, the second-generation Pi-girder was developed to improve the weaknesses of the original cross-section.

The second-generation Pi-girder features several modifications to the original cross-section (Graybeal 2009a). The deck was both widened and thickened. The webs were thickened and shifted inward. Sharp corners were rounded to prevent large stress concentrations. Additionally, overhang blockouts were eliminated, and intermediate diaphragms were included. These differences are most noticeable when comparing the two girder cross-sections (Figure 2-21).

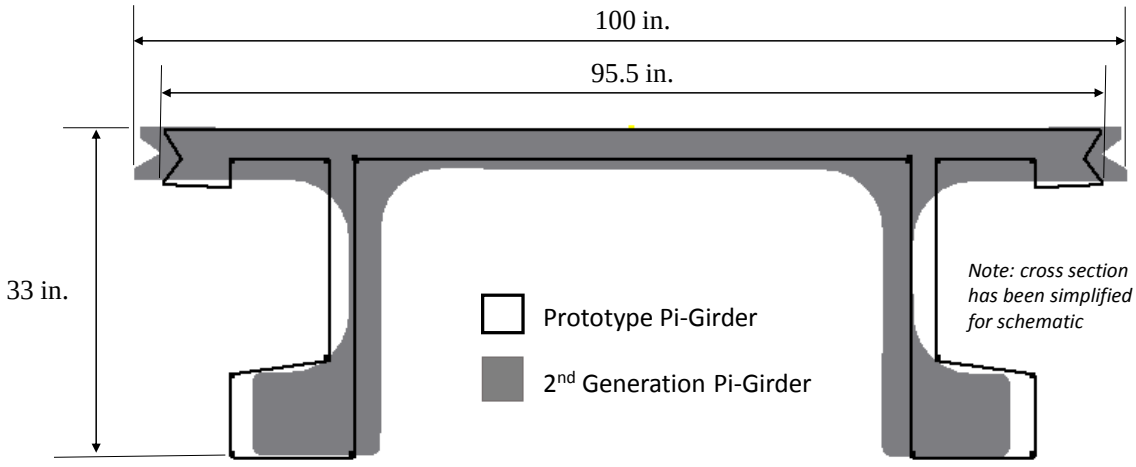

Figure 2-21: Cross-sectional comparison of the original and second-generation Pi-girders (Graybeal 2009a).

Longitudinal joints incorporated a grouted shear key, similar to the original Pi-girder, as well as grouted pockets spaced at 18 in. along the girder (Graybeal 2009a). The shear pockets were 4 in. wide and extended 14 in. into each girder. In each pocket, a No. 8 reinforcing bar was used to strengthen the transverse direction, and two No. 4 reinforcing bars were placed in each girder in the longitudinal direction to strengthen the longitudinal direction of the joint (Graybeal 2009a). As opposed to the bolted joint in the original Pi-girder connection, this connection did not require diaphragm blockouts.

Results from testing the second-generation Pi-girder showed that the cross-section was suitable for spans up to 87 ft (Graybeal 2009a). The flexural capacity was approximately 57,000 kip-in., and the shear capacity was nearly 300 kips. Additionally, the transverse joint connection performed well, resulting in flexural hinging failure similar to that of the deck (Graybeal 2009a). Despite having 42% more weight per unit length than the original Pi-girder (Graybeal 2009a), the second generation Pi-girder has many marked improvements. This innovative cross-section shows the ability of UHPC to take new form as it takes on the ancient challenges of strength and durability battled by preceding bridge girders.

2.5.2 Bridge Deck Research

Bridge decks are continuously subjected to vehicular impact and environmental effects, requiring frequent maintenance and replacement. With the excellent strength and durability properties of UHPC, researchers have recognized the potential of using this material in roadway bridge decks (Garcia 2007; Perry 2005; Toutlemonde et al. 2005). Because UHPC is more expensive than conventional concrete, structures must be optimized to take advantage of the material properties of UHPC while also using the least amount of material possible. With this consideration, the optimized shape for a UHPC bridge deck has been proposed as a two-way ribbed slab (Garcia 2007; Toutlemonde et al. 2005), also referred to as a waffle slab. It is known as a waffle slab because the shape along the bottom of the deck resembles a waffle (Figure 2-22). Because a waffle slab is an unconventional type of bridge deck, typical design and analysis methods cannot be used; however, efforts have been made by researchers to provide possible means of analyzing UHPC waffle slab bridge decks.

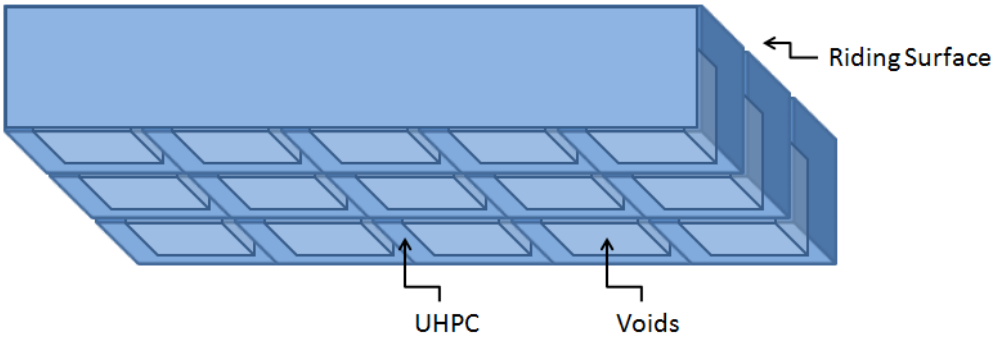

Figure 2-22: Waffle slab bridge deck shape.

2.5.2.1 *FHWA Research on Waffle Slab Bridge Decks*

In the analysis of a UHPC waffle slab bridge deck by the U.S. Federal Highway Administration (FHWA), basic beam theory and strain compatibility methods were applied to design and analyze the section (Garcia 2007). A representative T-beam section (Figure 2-23) was analyzed in flexure with an effective flange width of 24 in. in accordance with Section 4.6.2.6 of the AASHTO LRFD Bridge Design Specifications (2012). Although the UHPC deck is not typical, AASHTO Specifications were used as a guide in the design process. An assumed stress-strain relationship (Figure 2-18) based on previous research was also used in this analysis (Garcia 2007), as previously discussed in Section 2.4.1.4

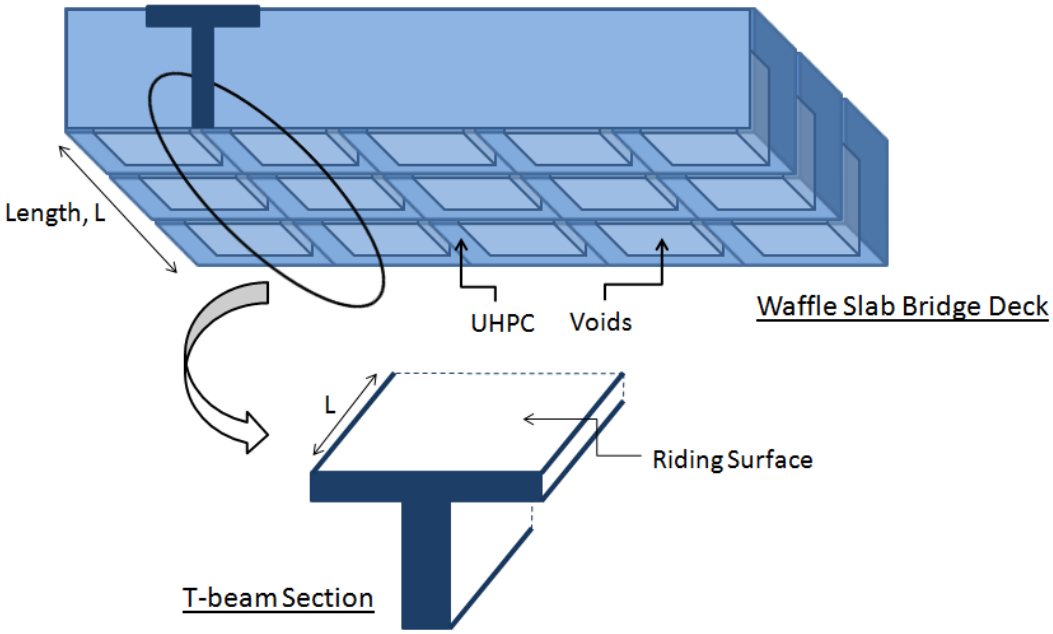

Figure 2-23: Representative T-beam section for flexure analysis by Garcia (2007).

Using the provided relationship for UHPC (Figure 2-18), strain compatibility was incorporated in the analysis to determine the location of the neutral axis of a cross-section (Garcia 2007). Strain compatibility accounts for strain limitations in both compressive and tensile regions. The limiting tension and compression strains used in the strain compatibility were 0.007 and 0.003132, respectively. Using the method of strain compatibility and the modified flexural stress distribution model, the flexural capacity of a T-section was determined using typical beam analysis.

The design dimensions used in the FHWA analysis, as indicated in Figure 2-24 and Table 2-4 (Garcia 2007), reveal that a deck of slender dimensions could be designed using UHPC to withstand design loads of a typical highway bridge. Each panel in the deck was prestressed using two ½ in. prestressing strands in the longitudinal direction and located at depths of 2 and 6.5 in. from the top of the section. The individual panel sections were then designed to be post-tensioned together. Although the ribs were actually tapered (Figure 2-24) the bottom rib width, b_w, was used as a constant width in determining the moment capacity of the deck, providing a conservative assumption in the design process.

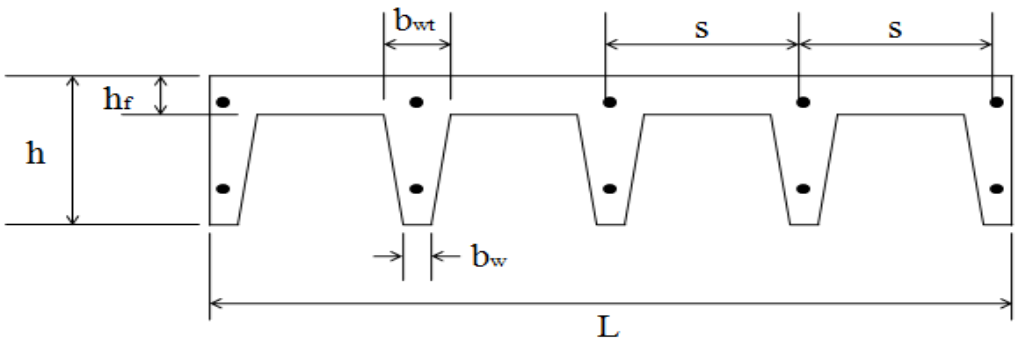

Figure 2-24: Waffle slab bridge deck cross-section (Garcia 2007).

Table 2-4: Waffle slab bridge deck dimensions of FHWA (Garcia 2007) design.

Dimension	Description	FHWA Values
h_f	Slab thickness	2.50 in.
h	Total thickness	8.00 in.
s	Rib spacing	24.0 in.
b_{wt}	Rib top width	4.00 in.
b_w	Rib bottom width	3.00 in.
L	Segment length	8.00 ft

Overall, the design dimensions indicate that the deck contains slender elements compared to a conventionally reinforced concrete deck. In the report by Garcia (2007), two conventional reinforced concrete deck designs were compared with the UHPC waffle slab design. Both conventional decks were designed with a solid 9-in. thick cross-section. Compared to these conventional decks, the UHPC deck was considerably lighter due to the ribbed cross-section that takes advantage of the material's high strength.

Results of the analysis by FHWA showed that the bending capacity of a UHPC waffle slab bridge deck was 10 to 20% higher than a conventionally reinforced concrete deck (Garcia 2007). However, the analysis methods should be experimentally validated in order to confirm these results and to determine whether or not any modifications should be made to analysis techniques. For example the inclusion of other design parameters, such as shear, may be of importance.

2.5.2.2 *French Research*

A similar project was launched by researchers in France to experimentally test a waffle slab bridge deck design (Toutlemonde et al. 2008). French Recommendations for UHPFRC, French Bridge Design codes, and classical beam analysis were used to design and analyze two UHPC waffle slab bridge decks (Toutlemonde et al. 2005). The UHPC decks were designed to connect to two longitudinal steel beams, providing composite action between the beams and deck. The design dimensions for the decks used are indicated in Table 2-5, revealing that the dimensions were similar to those used in the FHWA analysis. The two decks were constructed using two commercially available UHPC's, Ductal® FM and BSI-Ceracem (Toutlemonde et al. 2008). For each deck, individual deck panels were connected by longitudinal post-tensioning with a cast in place cold joint of UHPC with shear keys. Transverse prestressing was provided with two T15S prestressing strands, located within the ribs. Also, no vibration was used during casting due to the self-consolidating properties of UHPC (Toutlemonde et al. 2008).

Table 2-5: Waffle slab bridge deck dimensions of French (Toutlemonde et al. 2008) design.

Dimension	Description	French Values
$\mathbf{h_f}$	Slab thickness	1.97 in.
h	Total thickness	15.0 in.
s	Rib spacing	23.6 in.
$\mathbf{b_{wt}}$	Rib top width	3.94 in.
$\mathbf{b_w}$	Rib bottom width	2.76 in.
L	Segment length	8.20 ft

A portion of the experimental program was aimed at determining the performance of the deck due to local bending and punching shear (Toutlemonde et al. 2008). A typical wheel load was applied at the center of a box cell, simply supported on the four corners of the surrounding ribs. Each wheel load was applied using a 23.6-in. square plate and a 3.54-in. thick polymer material to simulate a bituminous driving layer. Two different wheel load sizes were applied: B-type, measuring 19.7 by 19.7 in., and a narrower A-type, measuring 7.48 by 10.2 in. The design limit for this loading was 33.7 kips, and the deck outperformed the demand from both wheel loads. The B-type loading resulted in narrow bending cracks at 67.4 kips, while no signs of failure were shown up to 157 kips. The A-type loading resulted in failure in punching shear between 78.7 and 94.4 kips, still surpassing the design value of 33.7 kips (Toutlemonde et al.

2008). These results showed that the 1.97-in. slab thickness was well suited to resist punching of wheel loads, resulting in failure at loads well beyond the design values. Also, average shear stresses surrounding the loads were similar to ultimate tensile strengths determined from testing thin plates. For Ductal®, the average shear stresses were 1.42 and 1.33 ksi, and the ultimate tensile strength was determined to be 1.38 ksi. For BSI-Ceracem, the average shear stresses were 1.25 and 1.20 ksi, and the ultimate tensile strength was determined to be 1.20 ksi.

Another portion of the experimental program was performed to simulate 100 years of use through fatigue testing (Toutlemonde et al. 2008). Testing was carried out such that a total of 100 million cycles were simulated through a detailed loading schedule, including the number of cycles, wheel load type, and a loading range (Table 2-6). Two different loading cases were considered, such that testing occurred both near a joint and in the center of a deck panel. In each case, two wheel loads were applied and spaced at 3.94 ft, a standard axle spacing according to the Eurocode. Throughout the testing program, deflections were also measured at 23.6-in. intervals along the deck.

Table 2-6: Fatigue Testing Schedule for UHPC Waffle Slab (Toutlemonde et al. 2008).

No. of Cycles	Wheel Loading Type	Loading Range: Low – High, kips
10,000	B-type*	1.12 – 34.8
2,000,000	B-type	1.12 – 23.6
100,000	A-type**	1.12 – 19.1
100,000	A-type	1.12 – 28.1
100,000	A-type	1.12 – 34.8

*B-type loading refers to a wheel loading area of 19.7x19.7 in.

**A-type loading refers to a wheel loading area of 7.48x10.2 in.

The performance of the deck throughout the experimental program provided reassurance to researchers that UHPC could become a material in future roadway bridge deck applications. Vertical deflections did not exceed 0.079 in., indicating that the deck did not exhibit serviceability problems with deflections (Toutlemonde et al. 2007). At joint locations, the two connected ribs appeared to act as one, generating a higher stiffness at connection locations. This resulted in the majority of loading at the joint locations to be supported by the transverse ribs. First cracking, indicating non-linear stress behavior, appeared at a total load of 180 kips, and

small crack widths at loads up to 224 kips indicated that minimal yielding had occurred in the prestressing steel.

Safety barrier anchorage was another factor tested in this study (Toutlemonde et al. 2008), showing that a connection could be designed such that fuse screws connecting a reinforced concrete barrier to a UHPC deck will fail by yielding without damaging the deck. Maximum loads for the failure of two barrier tests were 55 and 57 kips. With this failure mode, a barrier could easily be replaced if damage occurred, but it would not be necessary to replace a portion of the deck itself.

Overall, the research by Toutlemonde et al. (2007, 2008) indicated that a UHPC waffle slab deck could provide a safe and durable alternative to traditional bridge decks. In general, the narrow wheel loading, or A-Type loading, was more severe than the typical B-Type loading, indicating that more concentrated loads could be more harmful. The safety factors for A-Type and B-Type wheel loadings were approximately 1.15 and 1.25, respectively. Also, the deck segment made of Ductal® generally outperformed the segment made with BSI-Ceracem in both shear and deflections.

2.5.2.3 *Iowa Department of Transportation UHPC Bridge Deck*

The Iowa Department of Transportation completed the design of a UHPC full depth waffle bridge deck in 2009 for future implementation in Wapello County, Iowa (Heimann and Schuler 2010). This bridge deck design was later tested by Iowa State University in 2010 for fatigue and static conditions. This section reviews the design, production, and experimental testing of this bridge deck.

The UHPC waffle deck panels were designed using AASHTO slab deck design provisions (Aaleti et al. 2010). The panels were designed to be 8 ft – 0 in. wide by 9 ft – 9 in. long (Figure 2-25). The design compressive strength of the UHPC was determined to be 24 ksi. The deck was 8 in. deep (Aaleti et al. 2010). Conventional mild reinforcement of Grade 60 was provided in two layers in both the transverse and longitudinal ribs of the panels. In the transverse direction, a No. 6 reinforcing bar was located 1-5/8 in. from the top surface, and a No. 7 reinforcing bar was located 1-1/4 in. from the bottom surface. In the longitudinal direction, a No. 6 reinforcing bar was located 2-3/8 in. from the top surface, and a No. 7 reinforcing bar was located 2-1/8 in. from the bottom surface.

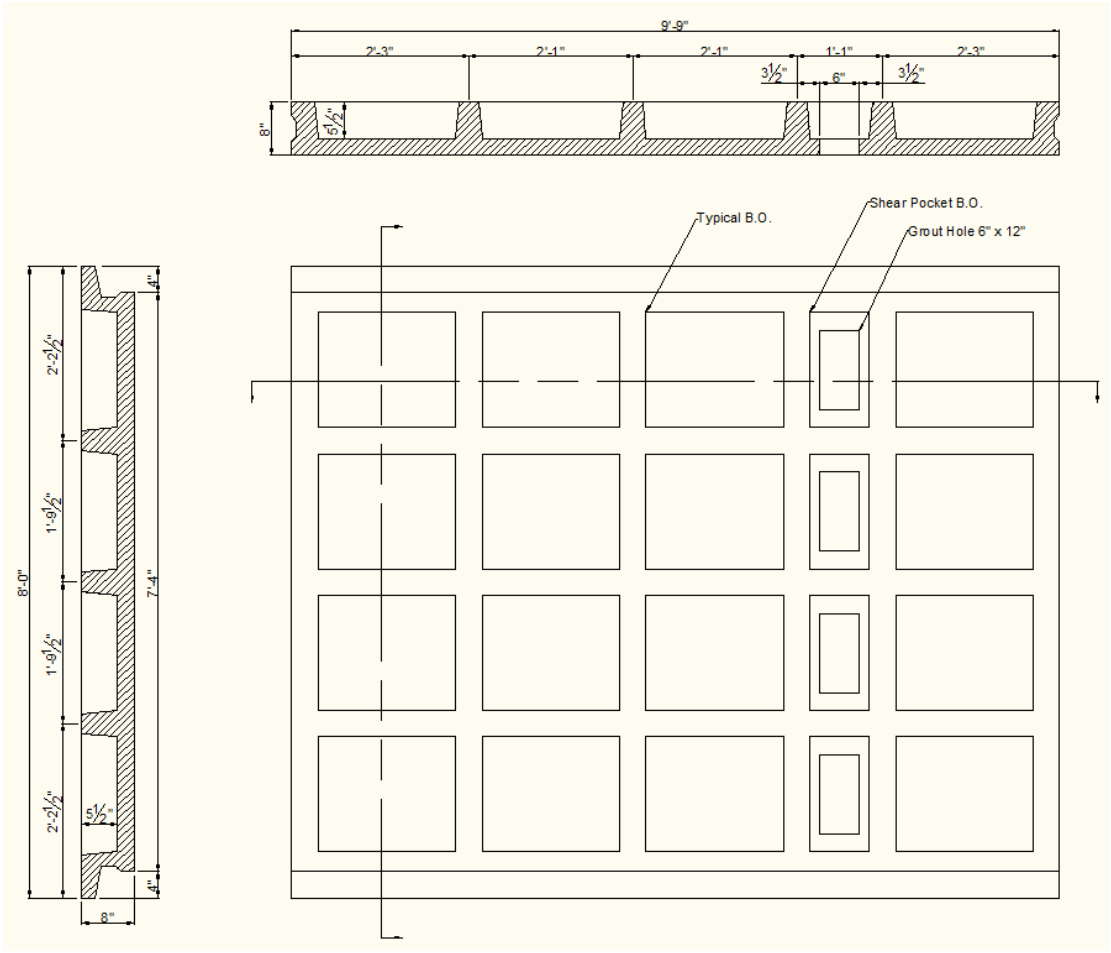

Figure 2-25: Iowa DOT waffle slab bridge deck (Heimann and Schuler 2010).

For fabrication, both Coreslab Structures Inc. and Lafarge North America were consulted (Aaleti et al. 2010). Production took place at Coreslab Structures Inc. in Omaha, Nebraska. For the prototype waffle deck panels, only one cubic yard of Ductal® UHPC was required. The deck was formed upside down, such that the driving surface faced downward. To accomplish this, a larger form was used to create the driving surface and the top flanges. Then, a specially designed form to displace UHPC was pressed into the trough, forming the voids and webs of the waffle shape. First, a predetermined amount of UHPC was placed into the bottom form. A specialized bucket spanning the width of the deck panel was used to place the UHPC into the bottom form, ensuring proper fiber orientation across the length of the deck panel. Then, the top form was placed appropriately and pressed into the UHPC to create the voids.

The upside down placement method for the waffle deck was developed for multiple reasons. First, this placement method prevents fiber alignment segregation due to UHPC folding as two flow paths intersect at a point (Heimann and Schuler 2010), as previously discussed in Section 2.2.2 . Second, this method allows producers to insert a form liner in the bottom form to create a specialized driving surface pattern on the deck panels (Heimann and Schuler 2010). Finally, the upside down placement method allows for early release of the void forms after initial set. Releasing the forms was expected to reduce internal shear stresses by preventing the restraint of shrinkage of the UHPC by the forms before final set.

Once the waffle deck panels were placed, they were covered with a plastic tarp and allowed to cure for two days (Aaleti et al. 2010). During this time, the area within the tarp was heated at a constant 110°F using a propane heater. Once the compressive strength of the UHPC reached 14 ksi, the waffle deck panels were rotated and released from the forms. In order to prevent damage of the panels during rotation, the panels remained inside the bottom form during the rotation. After seven days, the waffle deck slabs were cured according to the producer specified steam treatment for Ductal® concrete: heated at 190°F/±5°F at 100% relative humidity for 48 hours. Prior to the steam treatment, the UHPC had a compressive strength of approximately 15ksi. Following the steam curing process, it was determined that the compressive strength of the UHPC had reached 29.8 ksi. This value was 24% higher than the design compressive strength of 24 ksi. After curing, the waffle deck panels were shipped to Iowa State University for experimental testing.

Experimental testing of the deck panels occurred at Iowa State University (Aaleti et al. 2010). Two deck panels were placed on prestressed concrete girders; one girder simulated an interior girder and the other an exterior. The waffle deck panels were made fully composite with the precast girders. Details of connections used on the prototype bridge are in Section 2.6.6 . Testing was sequenced to test the waffle deck panel section and the panel-to-panel joint at service loads, first. A wheel load was simulated using a 10 in. by 20 in. plate. Then, fatigue testing of the panel section and the joint took place, loading up to one million cycles at a frequency of 2 Hz. Finally, the ultimate load testing took place on the panel section and the joint.

Results from the experimental testing showed that the prototype waffle deck panels exceeded design expectations. Under service conditions, the panels showed maximum crack widths of less than 0.002 in. and displacements of approximately 0.03 in. over a 7 ft - 4 in. span length (Aaleti et al. 2010). Both values were well below the serviceability limits defined by AASHTO. The crack widths exhibited during this testing were also below the 0.012 in. crack width limit defined by AFGC for fiber pull out failure. Under fatigue conditions, the waffle deck panels were shown to experience negligible damage (Aaleti et al. 2010). These results show that the waffle deck panels are adequate for both strength and durability, indicating that the prototype panels should be adequate for the Wapello County replacement project.

2.5.2.4 *UHPC Bridge Deck Research Summary*

UHPC has great potential for improving U.S. infrastructure; however, limited information and funding is preventing this material from reaching its potential in the field. Limited experimental testing has been performed on UHPC waffle slabs, leaving designers with doubts about the capabilities of UHPC as a bridge deck alternative. To aid in this matter, additional testing should be performed to gain the confidence of owners, designers, and fabricators. Specifically, UHPC waffle slabs should be tested against U.S. design criteria to best reflect the capability of a UHPC bridge deck to be used in the U.S. The current project is focused on making additional testing a reality. Both the design and experimental testing of a waffle slab bridge deck section were performed to add to the growing database of research that could be used to develop future design criteria for UHPC structures.

2.6 Connections in Precast Bridge Deck Construction

Precast bridge decks hold many advantages over cast-in-place bridge decks, including more efficient and safe construction practices (Transportation Research Board 2003). Precast bridge decks also have better quality control, as they are manufactured at a plant under more controlled conditions. Despite these advantages, joints connecting precast bridge deck panels can be problematic, making their design and fabrication crucial to achieve optimal behavior. Joints can also determine the efficiency of a construction project (Harryson 2003), making them a vital part of the critical path. This section provides an overview of historical and current practices for connecting precast bridge deck elements as well as innovative connections using UHPC.

2.6.1 Match-Cast Panel-to-Panel Connections

The first type of connection is a non-grouted match-cast shear key connection for joining panels. The ends of the two panels have a male and female shear key that is expected to fit together perfectly with a thin neoprene pad in between (Figure 2-26) (Transportation Research Board 2007). This joint is very simple, requiring only a sealant at the top to prevent leaking; however, a variety of problems were quickly seen with the implementation of these joints. After as little as five years of service, these joints were shown to crack and eventually leak, making them very ineffective. Since this problem was discovered, these joints have not been implemented in new construction due to their poor long-term durability.

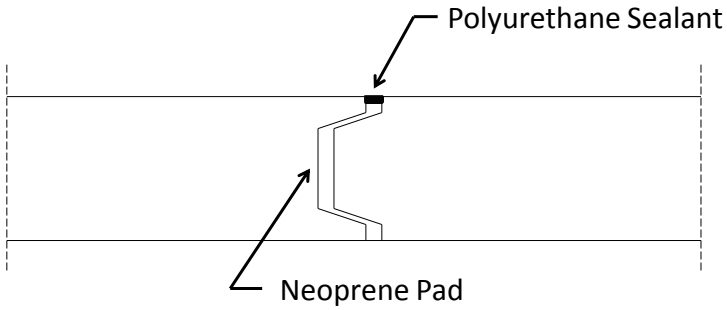

Figure 2-26: Match-cast panel-to-panel connection (Transportation Research Board 2007).

2.6.2 Grout Filled Panel-to-Panel Connections

Grout filled panel-to-panel connections provide additional durability as compared to match-cast connections. These joints contain a female-to-female shear key filled with grout (Figure 2-27) (Transportation Research Board 2007). The inclined surfaces of the shear key improve vertical shear strength of the joint, and a large opening is implemented at the top to facilitate grout placement.

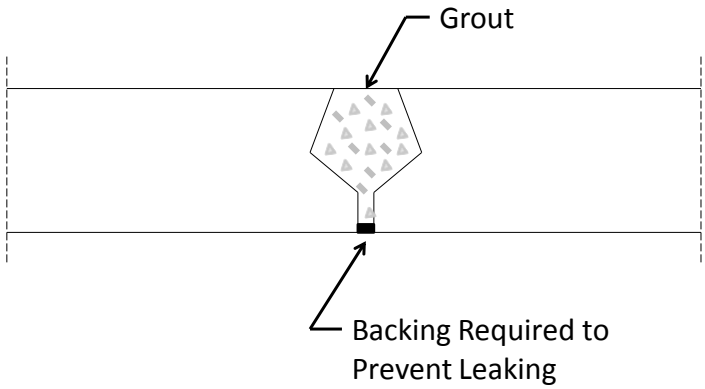

Figure 2-27: Grout-filled Panel-to-Panel Connection (Transportation Research Board 2007).

To fill the joint with grout, temporary backing strips must be placed at the bottom to contain the wet grout until it hardens (Transportation Research Board 2007). Both polyethylene rods and wood forming have been typically used as backing strips. Polyethylene rods have been less successful because they often resulted in half-filled joints due to inconsistent construction. Wood forming is placed underneath panels and hung from the top by threaded rods, providing a consistent construction detail. With wood forming, a consistent spacing is maintained between panels, allowing joints to be filled completely.

2.6.3 Reinforced and Grout Filled Panel-to-Panel Connections

Reinforcement is used in panels to provide continuity in the bridge deck and to better transfer loads from panel to panel (Transportation Research Board 2007). This reinforcement must be spliced at the joints. Since joints are the weakest point in a deck, construction must be very precise in order to accommodate the reinforcement details within the joint. The primary disadvantage of using mild reinforcement is the complicated details associated with providing proper development in the bars within the joint. In order to develop steel reinforcing bars in the small area of the panel-to-panel joint, bars must be hooked (Figure 2-28) (Shim et al. 2001). This type of joint also requires a large amount of reinforcement, making construction precision a high priority to accommodate the high content of hooked reinforcing bars.

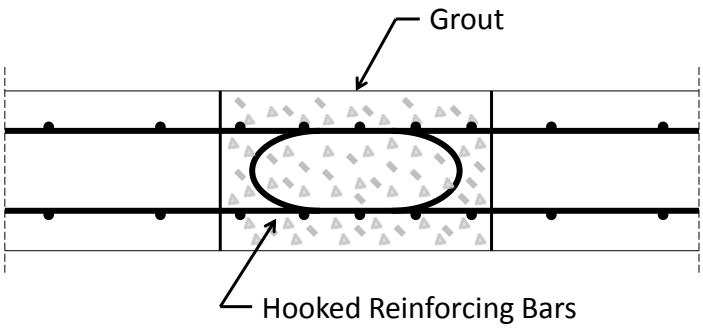

Figure 2-28: Mildly-reinforced Panel-to-Panel Connection (Shim et al. 2001).

Post-tensioning can provide additional benefits to the grouted joints. A simpler reinforcement plan can be implemented by post-tensioning in a joint, as compared to those containing mild reinforcement (Figure 2-29) (Shim et al. 2001). Post-tensioned joints can prevent leakage between panels and provide continuity from panel to panel (Perry and Weiss 2009), but this method still has a number of disadvantages. Post-tensioning requires specialized equipment, raising construction costs. This joint also has a high potential for corrosion, and modeling can be difficult due to a combination of parameters, including long-term creep effects.

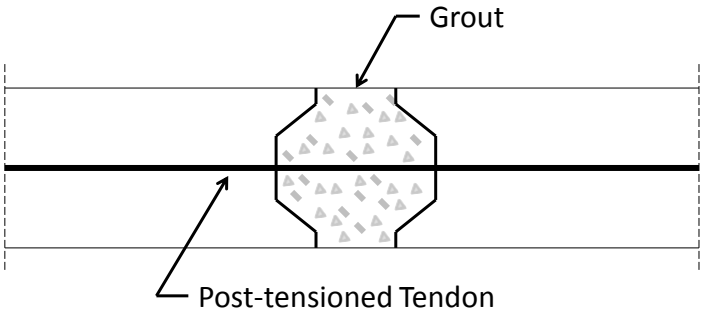

Figure 2-29: Post-tensioned Panel-to-Panel Connection (Shim et al. 2001).

2.6.4 Glued and Bolted UHPC Connections in Gärtnerplatzbrücke

The Gärtnerplatzbrücke was constructed during 2006 and 2007 to replace a timber bridge in Kassell, Germany (Fehling et al. 2009). UHPC was chosen as a material in the new bridge because of its potential to produce relatively light construction elements. This was imperative because the original piers of the timber bridge were to be used to support the new bridge. Featuring an 80 to 120 mm variable deck thickness and a unique three chord truss, this bridge

minimized weight without compromising strength. Part of the uniqueness of this bridge, however, is in the connections.

Both glued and bolted connections were used to produce continuity (Fehling et al. 2009). Glued connections were used in areas where the UHPC was considered too delicate for bolted connections (Figure 2-30). Deck plates were glued to the upper chords of the three-chord truss, and these deck plates were bolted to the steel truss members. Testing showed that the glued connections of this bridge performed as well as UHPC in shear and tensile strength. Additional testing showed that sand blasting the UHPC could improve glued connections.

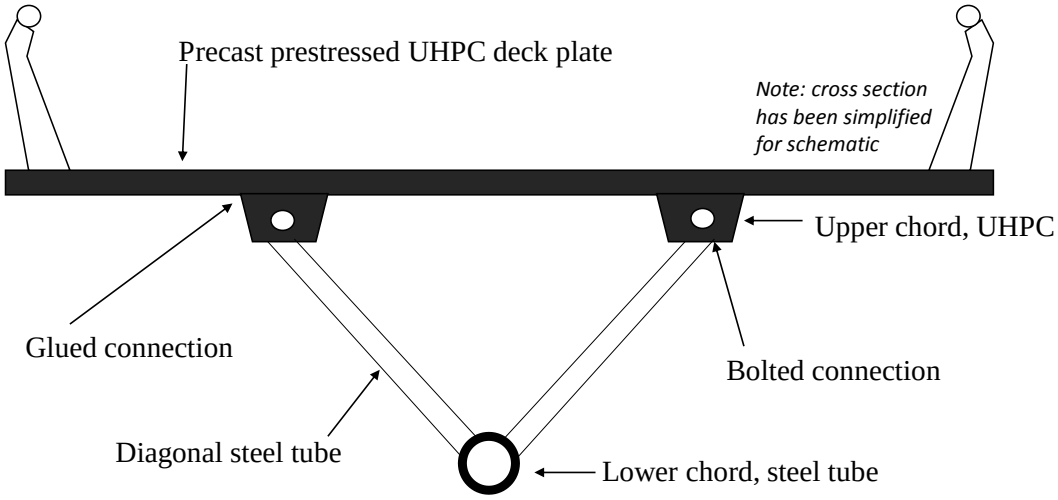

Figure 2-30: Gärtnerplatzbrücke cross-section (Kassell, Germany) (Fehling et al. 2009).

2.6.5 UHPC Filled Joints with Conventional Concrete Structures

UHPC-filled connections were first used by Peter Harryson in Sweden (Harryson 2003). Harryson used a type of UHPC known as Compact Reinforced Composite (CRC) in a mildly-reinforced joint to connect precast panels. CRC has a typical compressive strength of at least 22 ksi, a water-to-binder ratio of 0.16, and a fiber content of 6% by volume. This material exhibits good bond to both steel reinforcement and previously cast concrete, making it an excellent filling material for joints. Jensen (1999) provides a formula to calculate anchorage length required for a reinforcing bar in Compresit, a commercially available CRC. This relationship is given by the following equation:

$$\sqrt{\frac{\tau_\mu}{f_c}} = 0.5 + \frac{17\left(\frac{nA_{st}}{dL}\right)}{0.7\frac{c}{d}\sqrt{\frac{d}{L}}} \qquad (2\text{-}43)$$

Where, L = embedment length of reinforcing bar

d = diameter of reinforcing bar (only mild reinforcement)

f_c = compressive strength of concrete

τ_μ = shear stress; the force in the bar distributed to the surface of the bar

c = thickness of concrete cover

A_{st} = cross-sectional area of reinforcing bar in transverse direction

n = number of reinforcing bars in transverse direction

Equation (2-43) is only valid for mild reinforcing steel (Jensen 1999). On the right side of the equation, the 0.5 represents the roughness contribution of ribs on the steel reinforcing bar. For prestressing steel, this contribution is negated because of the smooth surfaces of reinforcing steel. Therefore, this value would be dismissed for prestressing steel. The numerator of the second half the equation represents the contribution of transverse steel, and the denominator represents the contribution of concrete cover

Using these properties, Harryson (2003) developed a joint using CRC and a simplified reinforcement configuration. The joint (Figure 2-31) is 4 in. wide and contains only straight reinforcing bars, as compared to hooked bars in typical mildly reinforced grouted joints. The joint is fully moment resisting and has shown strength above that of surrounding panels made with conventional concrete with 8 ksi compressive strength. The shear strength of the joint was shown to be 40% higher than the precast panels, indicating that design should be more dependent on flexure strength rather than shear strength. Static testing showed that some bar pull-out failures were possible when adequate cover was not provided. Modifications were made to prevent this by increasing the cover thickness and placing transverse reinforcement on the bottom layer of longitudinal reinforcement. With these modifications, only one reinforcing bar pull-out failure occurred during fatigue testing. Although this joint was successful, quality

control should be a high priority. Harryson (2003) suggests that the joint may be susceptible to construction errors due to the small dimensions of the joint.

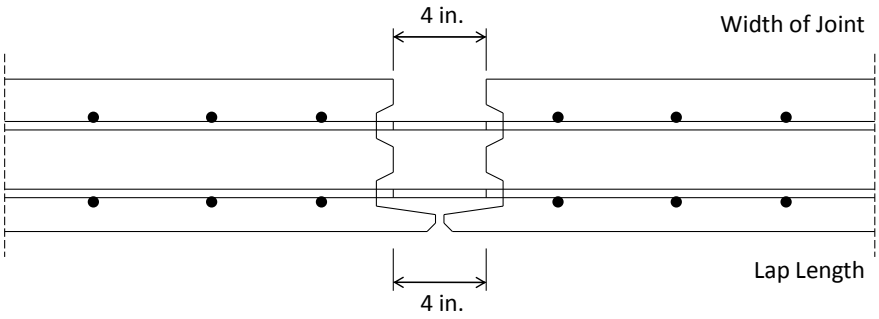

Figure 2-31: CRC filled joint by Harryson (2003).

Expanding on the CRC filled joint by Harryson (2003), Larfarge has recently begun using Ductal® as a filling agent in precast bridge deck panel joints (Perry and Weiss 2009). With a new formulation of UHPC, Ductal® JS1000, Lafarge provides the product through premix bags, a superplasticizer, and steel fibers. Ductal® filled joints have since been used in deck replacements with precast decks in both Canada and the United States. During pilot testing, full-depth 9 in. thick high strength concrete (HSC) panels were used in conjunction with the UHPC filled joints to determine their strength and efficiency.

Both transverse (Figure 2-32) and longitudinal (Figure 2-33) joints were designed to be 8 in. wide (Perry and Weiss 2009), twice as wide as the formerly discussed joint by Harryson (2003). Glass fiber-reinforced polymer (GFRP) reinforcing bars were utilized in the joints because of their durability and resistance to corrosion (Perry and Weiss 2009). These properties were especially important due to frequent use of deicing agents on bridges. Since embedment of GFRP reinforcement had never been tested, Lafarge performed tensile pull-out tests to determine the required development length to fully yield these bars in Ductal® JS1000. These tests showed that slipping did not occur at embedment lengths of 4 and 6 in., making the designated embedment length of 7.5 in. suitable for providing straight GFRP reinforcement to the 8 in. wide joint.

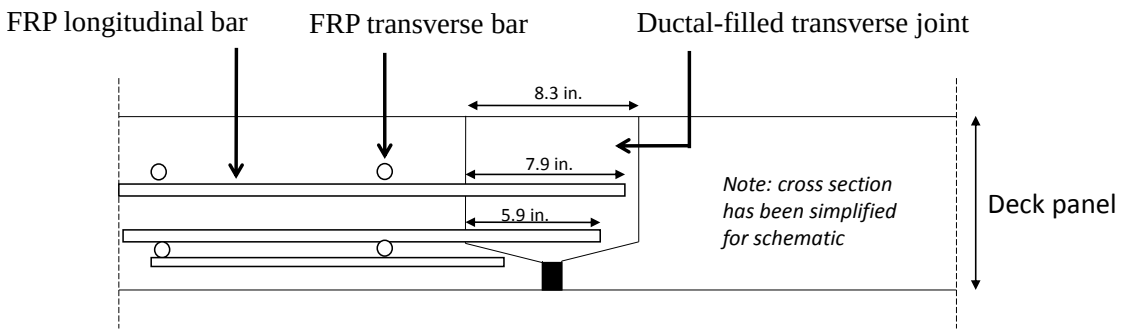

Figure 2-32: Typical Ductal®-filled transverse connection using GFRP reinforcement (Perry and Weiss 2009).

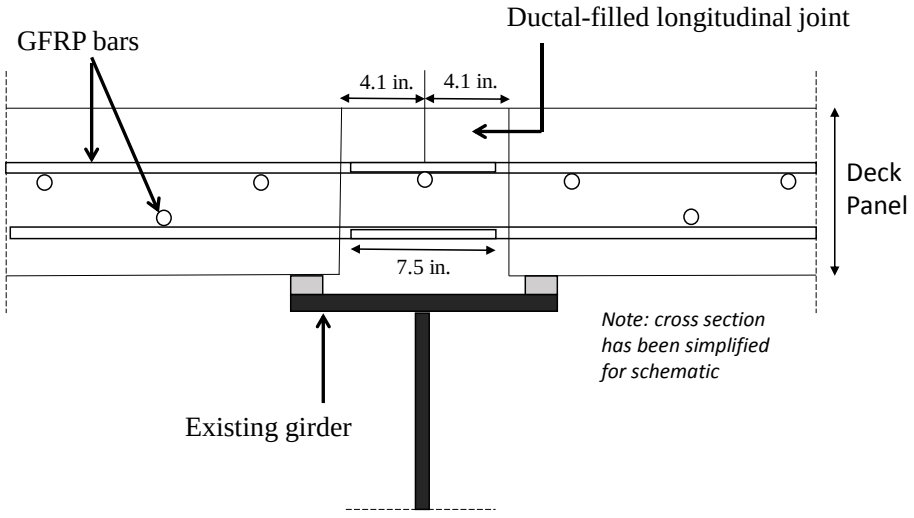

Figure 2-33: Typical Ductal®-filled longitudinal connection using GFRP reinforcement (Perry and Weiss 2009).

Overall, these joints (Figure 2-32 and Figure 2-33) are considered to be a viable option for improving precast panel joints in bridges. Testing at the Federal Highway Administration has showed that under fatigue testing, no signs of leakage were shown to occur when using the Ductal® filled joint in combination with HSC precast deck panels (Perry and Weiss 2009). Construction can be more efficient by phasing the process and making each phase open to traffic after three days of curing. At three days, the Ductal® filled joint typically reaches approximately 14.5 ksi compressive strength. With the strength, durability, and efficiency of a UHPC joint filling material, UHPC filled connections have the potential to provide longer lasting bridge decks.

2.6.6 UHPC Filled Joints with UHPC Structures

The Iowa Department of Transportation designed UHPC filled joints in the Wapello County bridge replacement project to connect UHPC waffle deck panels (Aaleti et al. 2010). All joints were designed to make the panels fully composite with standard Iowa "B" girders. Three different connections were used in this design: shear pocket connections, waffle slab to girder longitudinal connections, and waffle deck panel transverse connections. Ductal® was the UHPC used in all connections, and all connections were placed at Iowa State University (ISU). The UHPC in the connections was cured in the ISU laboratory and had 28-day compressive strength of 18.8 ksi.

The shear pocket connections were in the longitudinal direction along the girders. The shear pockets aligned with the cells of the deck with 6 in. by 12 in. grout holes (See previous figure of deck cross-sections) (Aaleti et al. 2010). The grout hole was filled with UHPC, and a shear hook extending up from the girder allows the connection to create composite action between the girder and deck (Figure 2-34). Shear pocket connections are used along the exterior girders to either side of the central girder. To place shear pocket connections, UHPC was placed in one end of each pocket and allowed to flow to the other end until filled.

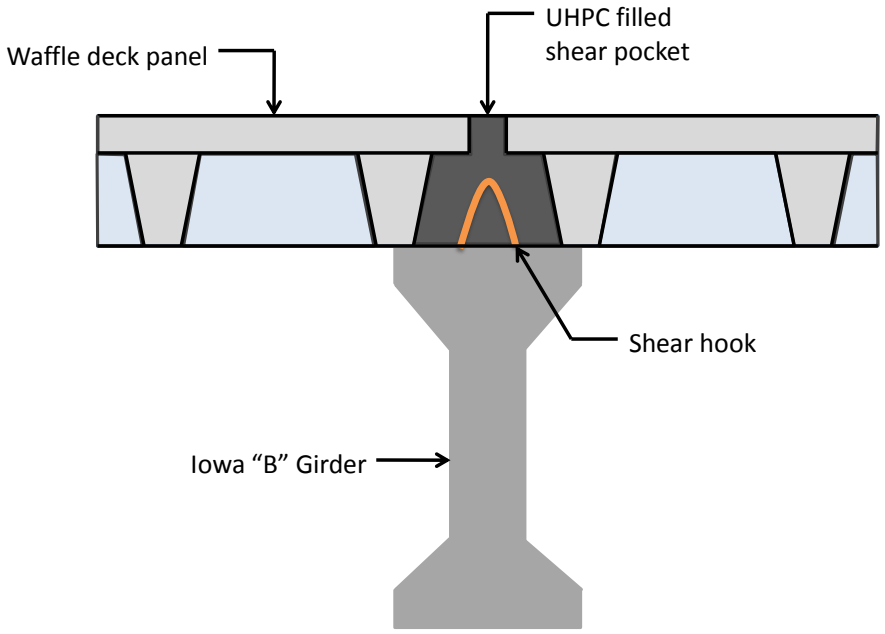

Figure 2-34: Shear pocket connection in Wapello County bridge project (Aaleti et al. 2010).

The second connection in the deck is the longitudinal connection between the waffle slab and the girder. This connection was only used to connect adjoining waffle deck panels to the central girder of the bridge (Aaleti et al. 2010). As with the shear pocket connections, embedded shear hooks extending up from the girder provided composite action between the waffle deck slabs and the girder (Figure 2-35). Dowels extending from the waffle deck panels also contributed to the composite action between the deck panels and girder. The dowels were 12 in. in length and were Grade 60, No. 6 reinforcing steel bars. Additional No. 6 reinforcing bars were placed longitudinally to contribute to the strength of the connection, and the area between the panels and the girder was filled with UHPC. To place the longitudinal connection, UHPC was placed into one end of the joint and allowed to flow to the other end.

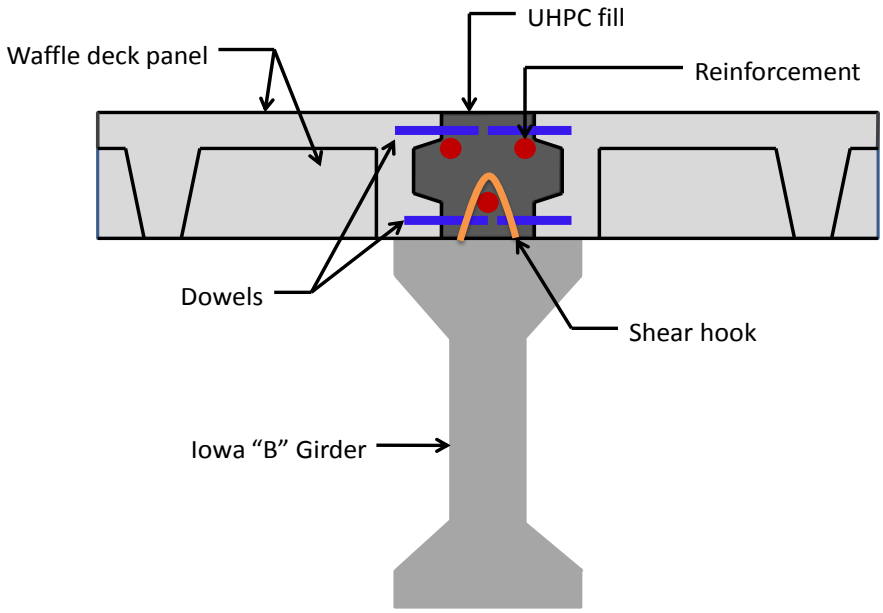

Figure 2-35: Longitudinal connection between deck panels and central girder in Wapello County bridge project (Aaleti et al. 2010).

The final connection in the Wapello County bridge project is the transverse waffle deck panel-to-panel connection. This connection was used to connect adjoining panels placed along the length of the bridge (Aaleti et al. 2010). Dowels extended from the waffle deck panels into the UHPC filled joint (Figure 2-36). The dowels were Grade 60, No. 6 reinforcing steel bars. Two No. 6 reinforcing bars were also used to tie the dowels together. The panel to panel connections served to provide continuity and load transfer between the panels along the length of

the bridge. To place the transverse panel connections, UHPC was allowed to flow from the one end to the other.

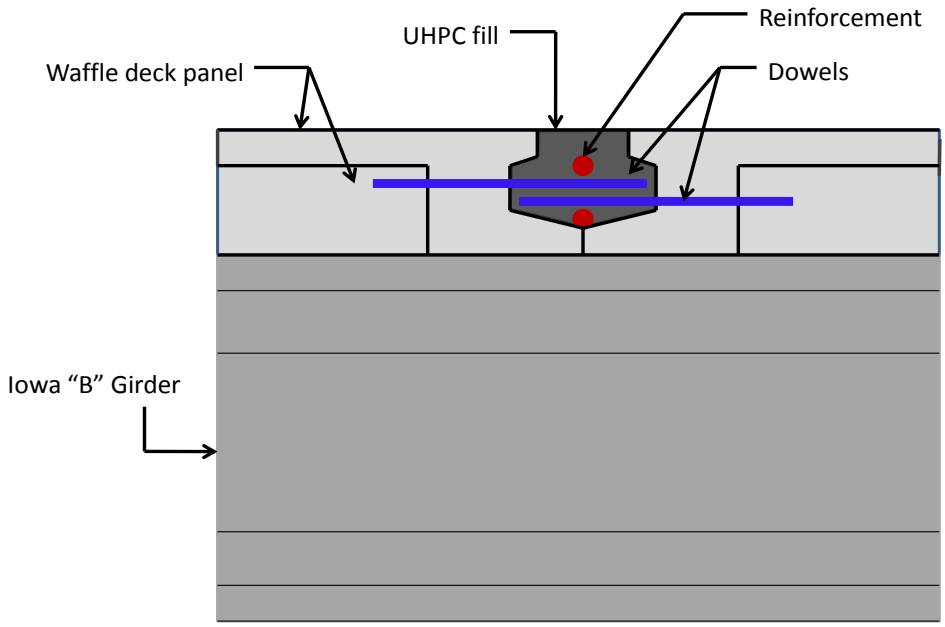

Figure 2-36: Transverse panel to panel connection in Wapello County bridge project (Aaleti et al. 2010).

Testing of this connection in service load conditions showed that both panels on either side of the joint shared load equally, and the connection satisfied the deflection and crack width requirements as recommended by AASHTO (Aaleti et al. 2010). The connection was loaded three times to a peak load of 28 kips. This load was determined by multiplying the AASHTO service wheel load of 16 kips by a factor of 1.75. At 28 kips, a hairline crack was discovered on the transverse ribs forming the connection. This crack was only 0.002 in. wide, which was much smaller than 0.012 in., the width AFGC considers to be the initiation of fiber pull-out and tensile strength loss in UHPC. Due to the small crack width, it was assumed that the connection performed well under service conditions.

Testing of this connection also showed that no significant damage occured due to fatigue testing (Aaleti et al. 2010). The connection was subjected to one million cycles of amplified service load. Static tests were performed intermittently at 168,000, 333,875, and 1 million cycles to determine load-displacement relationships, peak strain in bottom reinforcement, and crack widths in ribs from the transverse panels of the joint. The static tests at these intermittent points showed little variation, showing the ability of the joint to resist fatigue loading.

Finally, the transverse panel-to-panel joint was tested at an ultimate limit state load of 48 kips (Aaleti et al. 2010). This load was determined by multiplying the AASHTO service wheel load of 16 kips by a factor of three. The joint was tested to this load three times, similar to the service load test. At the ultimate load state, minimal damage occurred. A maximum deflection of 0.05 in. occurred, satisfying the AASHTO serviceability limits. The peak strain in the bottom reinforcement of the joint was well below the yield strain of the reinforcement at only 330 με. While testing, hairline cracks developed in the joint with a maximum crack width of 0.003 in. This crack width remained below the 0.012 in. limit defined as the width AFGC considers to be the initiation of fiber pull-out and tensile strength loss in UHPC. Testing results of the transverse panel-to-panel joint indicate that the connection is sufficient for service and was designed well above the required parameters.

2.6.7 Summary of Connections

A variety of connections have been used to connect precast bridge deck panels, including match-cast connections, grout-filled connections incorporating shear keys, and reinforced and grout-filled connections also incorporating shear keys. Although post-tensioned and grout-filled connections can provide a more simplified reinforcement detail, these joints have additional complications in construction and long-term durability.

Although panel-to-panel connections were not designed in this project, future efforts should be made to establish durable connections between UHPC bridge deck panels. This project, however, focused only on the cross-section design of the bridge deck panel, and a connection was designed to make the deck panels fully composite with steel bridge girders.

2.7 Industry Views on UHPC

There are many advantages of using UHPC in bridge decks that have been recognized by researchers and the concrete industry. For instance, optimizing UHPC sections to be slender can result in a lower dead load (Nishikawa and Morita 2006), reducing the cost of transportation and construction. By using precast sections fabricated at a concrete plant and shipped ready for construction, installation time can be reduced, consequently reducing traffic interruptions. The reduction in costs is not only limited to construction aspects, but the life-span of a UHPC bridge is considered to be longer than a conventionally reinforced concrete bridge because of the

advanced durability properties. This advanced durability can potentially lead to lower maintenance costs throughout the lifetime of a bridge, also (Graybeal 2009c; Perry 2005).

Despite the many advantages of using UHPC, designers and producers are still not fully confident that it is better than using well-known, traditional structural materials, such as conventional reinforced concrete or steel. For example, the initial cost of using UHPC is a deterrent because it is much higher than conventional concrete (Bierwagen and Abu-Hawash 2005; Li 2003; Perry 2005). Currently, no design codes are available in the United States for UHPC, causing designs to be driven by modeling and analysis techniques. These techniques often lead to the need for experimental testing before implementation in the field, implying that the duration of the entire process from initial design to implementation is much longer than a normal design project. Concrete producers may also have difficulty introducing UHPC into their facilities because of the special mixing, placement, and curing procedures that must be taken into consideration (Bierwagen and Abu-Hawash 2005). With these hurdles, UHPC may be difficult to implement into current practice; however, by researching new methods to implement UHPC, the advantages and aesthetic possibilities of using this material can lead to future projects that have the ability to last for generations.

2.8 Photogrammetry

Photogrammetric methods have been used by a variety of researchers to measure crack growth, deflection, and strain in concrete (Choi and Shah 1997; Küntz et al. 2006; Lecompte et al. 2006; Whiteman et al. 2002). Photogrammetry, defined as "the science of measuring in photos" (Linder 2009), holds many advantages over traditional strain and deflection measuring methods involving the use of strain gauges or linear variable differential transformers (LVDTs). Because data collection of photos is a non-contact process, specimens remain undisturbed by instrumentation, data collection is uninterrupted during failure (Choi and Shah 1997), and equipment is not harmed if failure is destructive (Whiteman et al. 2002). Data collection can be automated and continuous over an area of interest. This is a major advantage over gauges placed at discrete locations, because these instruments are limited by their placement (Choi and Shah 1997; Robins et al. 2001). Additionally, photogrammetry provides a thorough collection of visual records throughout testing (Whiteman et al. 2002). This can be helpful for concrete researchers, specifically, because images can be post-processed to document crack formation and detailed cracking patterns.

One of the primary disadvantages of photogrammetry is the need for expensive, specialized equipment. Typically, a specialized camera, such as a charged-coupled-device (CCD) camera, is used to achieve best results (Choi and Shah 1997; Robins et al. 2001; Whiteman et al. 2002; Zhang et al. 2006). The viewing range is also limited when using these cameras (Robins et al. 2001), requiring multiple cameras to measure a large area. Despite the limited viewing range and high expense, photogrammetry has proved to be an excellent non-contact method for measuring deflections and strains.

2.8.1 Digital Image Correlation

Digital Image Correlation (DIC) is a form of photogrammetry in which digital images are analyzed to measure strains and deformations. Pixels are tracked as an image deforms, and then strain can be computed by measuring the change in distance between a pixel's original location and the new location of the pixel in the deformed image (Choi and Shah 1997) (Figure 2-37).

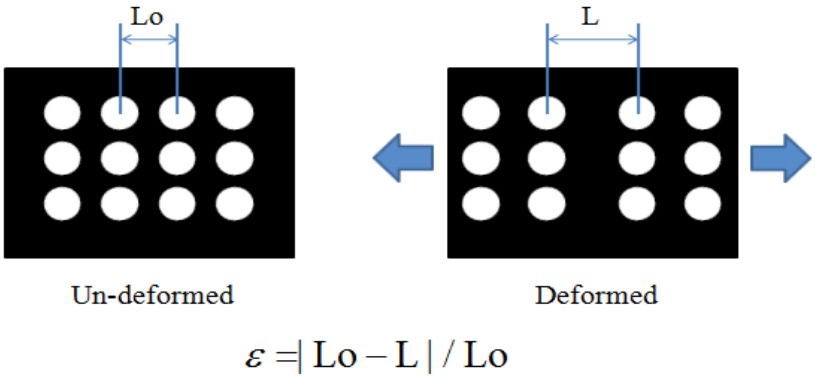

Figure 2-37: Digital image correlation is a method of measuring strains.

A pattern is typically placed onto the surface of the tested object to allow pixels to be tracked more easily using a computer program. These patterns, such as the dot and grid pattern in Figure 2-37, are often applied by using contrasting black and white paint or ink (Choi and Shah 1997; Robins et al. 2001). In some cases, a specialized vinyl overlay is applied to surfaces using epoxy (Sutton 2008). Although some patterns are uniform, the majority of patterns used in DIC are random, speckle patterns. These patterns are most often used because they are easy to apply, and they reduce errors with pattern recognition of the computer. Such errors occur because the computer cannot distinguish movement among very uniform points. For instance, if a dot and grid pattern is used, the computer program may not be able to tell the difference from one dot to another, miscalculating and confusing its location from one image to the next. For

this reason, random patterns are typically used to allow the computer program to better "pattern match" from one image to another, reducing computer error.

Another advantage of random patterns is the ease of application. A common speckle pattern can be applied to a surface with a light mist of spray paint or a light coating of Xerox toner powder (Sutton 2008). Typically, a base layer of white spray paint is applied to the surface, first. Then, the speckle pattern is applied to the surface using either a black spray paint or toner powder, until the proper density of speckling is achieved. A high contrast between the white and black applications is required for best computer recognition. Proper density is also needed to ensure DIC can provide accurate results (Sutton et al. 2009). Robins et al. (2001) experimented with several different methods of stenciling a pattern onto a specimen, including inking with a permanent marker, emulsion painting, and spray painting. For Robins et al. (2001), inking was chosen as the most efficient method to apply a pattern to specimens. This was because ink dried relatively quickly and allowed for a more controlled application of points to be tracked.

Despite the widely accepted use of random speckle patterns, a quasi-uniform dot and grid pattern was best suited for DIC of concrete specimens with multiple cracks by Helm (2008). DIC becomes complicated when cracks produce a discontinuity in a sample, segregating the image into parts. As the image is segregated into parts, each portion deforms inconsistently to one another. In the past, computers were unable to identify cracks, requiring humans to identify cracks and reestablish analyses accordingly to account for the discontinuities. Contrary to this, Helm (2008) produced an analysis technique that was able to identify discontinuities and provide educated guesses to reestablish the analysis of independent regions. For this analysis, Helm found that a quasi-uniform dot and grid pattern was most accurate, despite the common errors previously described.

In any pattern application, adherence to the surface of the tested object is important, especially if high strains are likely to occur (Sutton et al. 2009). Debonding issues are most common with metallic surfaces, requiring more specialized paints to ensure adhesion throughout testing. No problems have been noted with concrete specimens specifically; however, researchers suggest that objects with painted surfaces be tested within one day of application due to poor adhesion over time. Also, toner powder must be applied to a wet painted surface since it

has no bonding abilities of its own (Sutton et al. 2009). As mentioned previously, nylon sheeting requires specialized epoxy to provide full adhesion to the surface of an object.

Once a method is determined for applying the speckling pattern, the next step is to determine the proper density required for an accurate analysis. Sutton et al. (2009) provide a relatively simple approach for determining a required density based on a variety of parameters, including both the tested object dimensions and the analysis capabilities (Figure 2-38). In this approach, the minimum speckle size and pixel subset size for analysis are determined. Then, an appropriate minimum speckle size can be established.

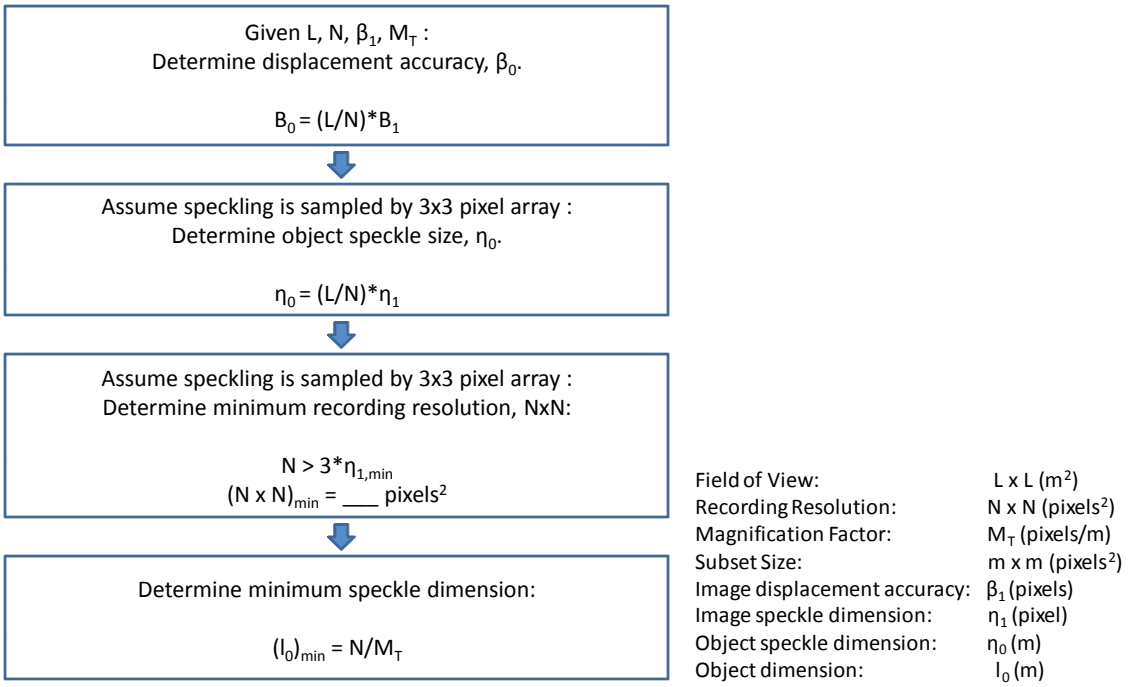

Figure 2-38: Flow chart to determine minimum speckle dimension (Sutton et al. 2009).

2.8.2 Computer Programs for DIC

A variety of computer software and programs are available for performing DIC. Although some code is available free via internet downloads, the software packages executing this code is typically not. This section discusses several options available for performing computer-aided DIC.

VIC 2009 is a specialized DIC software bundle developed by Correlated Solutions, Inc., a company founded in 1998 by researchers at the University of South Carolina (Correlated Solutions 2009). A free trial of this software is available on their website, but an individual

educational license must be purchased for extended use of the product. This software can perform DIC on both planar specimens and three-dimensional specimens to measure deformations and strains. It is capable of performing analyses on high temperature testing and samples experiencing high strain rates.

Digital Image Correlation and Tracking (DIC&T) is a program developed by researchers at Johns Hopkins University to perform DIC in two-dimensions (Eberl 2010). This program is executed using MATLAB, a product of MathWorks™ commonly used for data analysis. Although MATLAB is not a free product, *DIC&T* is free on the file exchange site MATLAB Central. This site is owned and operated by MathWorks™, providing customers with a means of free file exchange. *HighCorr High Temperature Digital Image Correlation (HighCorr)* is another DIC program developed by researchers at Johns Hopkins University (Thompson 2007). *HighCorr*, like *DIC&T*, is executed using the MATLAB software package and is available free on MATLAB Central. *HighCorr* was specially designed to analyze an object exposed to thermal effects, providing a means of relating DIC results with thermal changes.

2.8.3 Summary of Photogrammetry

Digital image correlation (DIC) is a reasonable method to measure deformations and calculate strains on a concrete specimen during testing. The primary disadvantage is the initial investment required to purchase an appropriate camera and a software package to run the analysis. The advantages are in the non-contact method of continual analysis that can be achieved through DIC. To perform DIC, a pattern must be placed on the object to be analyzed in order to allow a computer program to track pixels containing this pattern. Special considerations should be made to produce an appropriate pattern with a proper density for the application considered. These patterns may be either a dot and grid pattern or a random pattern. Pattern application can range from a simple spray paint to a specialized nylon sheet.

For the proposed project, DIC will be used to calculate strains in order to establish stress-strain relationships of UHPC in biaxial conditions. Based on the presented research, both a quasi-uniform dot and grid pattern and a random pattern will need to be explored to determine an accurate method for proper DIC. Additionally, the *DIC&T* (Eberl 2010) MATLAB program will first be explored for performing the DIC. Since behavior of UHPC pre- and post-cracking will be evaluated, DIC methods will aid in exploring a full-range of UHPC behavior in biaxial conditions.

2.9 Literature Summary

It is evident that ultra-high performance concrete has excellent strength and durability properties because of its unique composition. Extensive work has been completed to investigate these properties and to determine how these properties can be used to their complete capacity. Compressive strength, tensile strength, flexural strength, freeze-thaw resistance, and chemical resistance have been tested by many researchers. Using these known properties, several structures have been constructed using this material. Many of the designers for these structures have taken steps to promote UHPC, creating more slender sections than previously possible with conventional concrete. The Pi-girder is an example of this innovation, leading researchers to examine bridges in a new arena. Field-cast UHPC-filled joints for precast bridge deck panels also bring an innovative material into the spot-light to extend the life of future bridges. Further applications in prefabricated bridge deck panels are continuing the expansion of UHPC applications. The proposed waffle deck could provide an opportunity to improve durability of a bridge, leading to reduced maintenance and longer life spans.

It is also evident that there is a definitive need for more research on this relatively new material. The failure criterion of plain UHPC, specifically Ductal®, is still of interest. Little research has been completed to identify the biaxial strength in combined tension and compression stress states. The presented research will address this issue by investigating the biaxial failure of UHPC in combined tension and compression stress states. Additional information will be determined using the methods of photogrammetry and digital image correlation to calculate strains from the biaxial testing. The research will also include additional experimental testing and analysis to determine the feasibility of using a UHPC waffle slab bridge deck in future bridges, specifically looking at the performance of the cross-section and connections.

Results from the current project could provide the industry with additional understanding of UHPC behavior in structures. This knowledge has potential to be utilized in the future production of design guidelines for UHPC structures in the United States. Specifically, a detailed biaxial failure criterion could improve the analysis methods of UHPC. Experimental testing of a UHPC waffle slab could also provide valuable information to both designers and producers, since both performance and casting techniques are being explored in this project.

Despite the current lack of guidelines, UHPC can continue to gain familiarity among designers, producers, and owners as research progresses.

Chapter 3: Methods

This chapter presents the experimental and analytical methods utilized in the project. Preparations for all specimens are included, outlining procedures for mixing, placing, and curing UHPC. These methods also include basic material property testing, biaxial testing, finite element analysis, bridge deck design, and deck section testing. Unless otherwise stated, all experimental testing was performed in the Thomas M. Murray Structural Engineering Laboratory of Virginia Tech.

3.1 UHPC Preparation

This section discusses the general procedures used in preparing UHPC, including mix design proportions, mix procedures, rheological testing, and curing procedures for UHPC. Placement procedures are not discussed in this particular section because these are highly dependent on the type of specimen.

3.1.1 Mix Proportions

Ductal®, a trademark product of Lafarge, was the UHPC used throughout the entirety of this project. The mix proportions (Table 3-1) are provided with Ductal® premix bags, steel fibers, super plasticizer, and water. No accelerator was utilized in this mix design, in contrast with the proportions previously shown in Section 2.1.5 . Ductal® was supplied in premix bags, such that the Portland cement, fine aggregate, silica fume, and ground quartz were all included in the proper proportions. The super plasticizer used in this project was CHRYSO Fluid Premia 150. The high strength steel fibers were added at 2% by volume, consistent with the recommended optimal amount presented previously in Section 2.1.3 by Richard and Cheyrezy (1995).

Table 3-1: Ductal® mix design proportions.

Material	Weight/Volume (lb/ft^3)
Ductal® Premix	137
Steel Fibers	9.74
Super Plasticizer	1.92
Water	8.61

3.1.2 Mixing Procedures

UHPC was mixed both using an IMER Mortarman 750 and a smaller capacity commercial pan mixer in accordance with the procedures outlined in the *Material Property Characterization of Ultra-High Performance Concrete* report by the U.S. Federal Highway Administration (Graybeal 2006a). These methods were described previously in *Section 2.3.1* and are consistent with the manufacturer recommendations by Lafarge for Ductal®. To ensure a consistent product, Lafarge provided training for the proper mixing operations of Ductal®. The training session was administered by Kyle Nachuk (2008), a Technical Representative of Lafarge North America. Lafarge provides mixing training to all new users of Ductal® to guarantee quality control is maintained. The IMER Mortarman 750 mixer was used for large batches with a volume greater than 1 cubic foot, and a commercial pan mixer with a volume capacity of 2 cubic feet was used for smaller mix quantities (Figure 3-1).

(a) (b)

Figure 3-1: Mixing took place using the (a) IMER Mortarman 750 and (b) a small capacity commercial pan mixer.

3.1.3 Flow Test

Flow was measured for each batch of UHPC to characterize the rheology. The standard testing procedure for flow, ASTM Standard C1437 (2001) for the *Standard Test Method for Flow of Hydraulic Cement Mortar*, was used as a guide to determine flow. Some modifications, as suggested by other researchers and experts, were used to account for differences in UHPC compared to a standard mortar (Graybeal 2006a; Nachuk 2008). First, the flow table and the

flow mold were wiped clean with a damp cloth. The flow mold was filled with UHPC before the cone was lifted upward, allowing the UHPC to flow outward. After the UHPC settled, the diameter of the initial flow was measured at three different locations. Then, the flow table was dropped 20 times in 20 seconds (Graybeal 2006a), differing from the ASTM procedure which requires 25 drops in 15 seconds (ASTM Standard C1437 2001). Once the UHPC settled after the drops (Figure 3-2), the diameter was again measured in three different locations (ASTM Standard C1437 2001). The three measurements were averaged to achieve one approximate diameter of spread. According to Graybeal (2006a), UHPC with a flow of approximately 8 in. and above should require little vibration to ensure proper consolidation in forms. Because little vibration is required, UHPC is considered "easy to cast" with a flow diameter at or above 8 in. This flow diameter was used as a guide in determining the approximate amount of vibration to use for consolidating UHPC. Consolidation is discussed in later sections.

Figure 3-2: The flow test was used to determine the rheology of UHPC.

3.1.4 Curing Procedures

Two different curing regimes were used during this project: untreated and standard steam treatment. For the majority of this project, an untreated curing regime was specified. Specimens were initially covered with plastic to prevent moisture loss immediately following placement. After at least 48 hours, untreated specimens were removed from molds and allowed to cure in

ambient conditions of approximately 70°F and 35% relative humidity. Specimens remained in this ambient condition until testing.

The standard steam treatment, as described previously in Section 2.2.3 , was also used in this project. Steam treated specimens were covered with plastic immediately following placement. After 2 days, specimens were removed from molds and cured in ambient conditions until steam treated. Specimens were transported to the Federal Highway Administration's Turner Fairbank Highway Research Center for steam treatment in a small steam chamber. While in the steam chamber, specimens were subjected to 95% relative humidity (RH) and a temperature of 194°F for 48 hours (Graybeal 2006a), as described previously in Section 2.2.3 (Figure 2-5). This includes two hours of increasing temperature and RH, 44 hours of constant temperature and RH, and two hours of decreasing temperature and RH. Following the steam-treatment, specimens stored in an ambient environment in the Turner-Fairbank Research Center before being transported back to the Thomas M. Murray Structural Engineering Laboratory. Specimens then remained in the same ambient environment as the untreated specimens until testing.

3.2 Material Property Testing

The first phase of testing was focused on material property testing of untreated UHPC. This testing was used primarily to familiarize researchers with the unique mixing procedures associated with UHPC and testing UHPC properties. After the initial phase of material testing, material properties were continually tested as a means of quality control for each additional batch of UHPC. This section describes the placement and testing techniques for each specimen used in characterizing material properties, including compressive strength, tensile strength, modulus of elasticity, Poisson's ratio, and shrinkage. First, an overall note about vibration is discussed to explain this consolidation method used during the initial material characterization.

3.2.1 Vibration

Although UHPC is considered self-consolidating, samples in the initial material characterization were vibrated to ensure proper consolidation in molds as suggested by Nachuk (2008). The designated time on the vibration table was influenced by both the volume of the specimen and the rheology of the UHPC as determined by the flow test. Specimens with a larger volume were placed on the vibrating table for a longer time to ensure the material was well

consolidated in the molds. In each case, caution was taken to prevent over vibration of the samples which could cause steel fibers to sink to the bottom of the molds. The vibration time was also dependent on the rheology of the UHPC. As mentioned previously, a flow of approximately 8 in. was considered "easy to cast" with little vibration (Graybeal 2006a). Therefore, UHPC with a flow of 8 in. or above was set on the vibrating table for a shorter amount of time compared to material with a lower flow diameter. Vibration times were initially determined based on the suggestion by Nachuk (2008) (Table 3-2).

Table 3-2: Vibration Time for Material Property Characterization

Specimen Type	Vibration Time (seconds)
Cube – 2 in.	3
Cylinder – 4 in. diameter x 8 in. high	5
Briquet	3
3rd pt bending	5
Shrinkage beam	5
Biaxial Panel (12 in.)	5

Vibration was not used to consolidate specimens during any other placements throughout the project. This was determined based on observations obtained during the material characterization study and the rheological characterization of the UHPC as determined by the flow test.

3.2.2 Compressive Strength

To determine compressive strength, ASTM Standard C109 (2005) for the *Standard Test Method for Compressive Strength of Hydraulic Cement Mortars (Using 2-in. or [50-mm] Cube Specimens)* was referenced to prepare and test 2 in. cubes. Cubes were chosen in place of standard cylinder specimens because of equipment constraints in the laboratory. Due to this limitation, the compressive strength determined using cubes was assumed to contain an apparent over-strength in comparison to the value typically achieved using standard cylinders. According to Graybeal (2008), the compressive strength achieved when testing UHPC cubes is approximately 5% greater than that of standard cylinders.

To prepare cubes, standard cube molds were filled with UHPC. The surface was not screeded to remove excess concrete, but rather UHPC was removed by pinching. Because of the unique characteristics of fresh UHPC, screeding would have been very difficult. Once cubes

were filled, plastic sheeting was placed on top to contain moisture, and the specimens were cured according to Section 3.1.4

According to the ASTM Standard C109 (2005) test for compressive strength of cubes, a 2 in. cube is to be loaded at a rate between 200 and 400 lb per second, or 50 and 100 psi per second. Because of the high strength of UHPC, a compression test would require much more time than for normal strength concrete using this loading rate. Graybeal (2008) showed that loading specimens at 150 psi/sec was a reasonable alternative to reduce overall testing time without negatively affecting the measured compressive strength. Therefore, a loading rate of 100 to 150 psi per second, or 400 to 600 lb per second, was used to test compressive strength of UHPC using 2 in. cubes (Figure 3-3). The highest load was recorded to determine the ultimate compressive strength of the specimen. During loading, the first recognizable cracking sound was used to record the cracking load during compression testing. The cracking and ultimate compressive strength were computed by dividing the recorded load by the surface area of the cube.

Figure 3-3: Testing compressive strength of UHPC using 2 in. cubes.

3.2.3 Modulus of Elasticity and Poisson's Ratio

The modulus of elasticity of UHPC was determined in accordance to ASTM Standard C469 (2002) for the *Standard Test Method for Static Modulus of Elasticity and Poisson's Ratio of Concrete in Compression*. Standard 4 in. diameter by 8 in. high cylinder specimens were used

for this test. To place cylinders, UHPC was placed vertically in the molds until completely filled. As with the cubes, cylinders were not screeded, but excess UHPC was removed by pinching. Plastic was placed over the individual cylinders, and they were cured according to Section 3.1.4

Prior to testing, the ends of UHPC cylinders were modified to account for uneven surfaces. The top surface of UHPC cylinders was often not level due to shrinkage and uneven contact with the plastic sheets. Therefore, the top surface was first cut using a concrete saw, or a hammer was used to remove rough edges. Next, sulphur caps were molded onto both ends of the specimen to provide a smooth, level surface of bearing. This was especially important for the top surface of the cylinder because it was often uneven due to shrinkage and uneven contact with the plastic sheets.

The compressometer was attached to the middle section of the UHPC cylinder (Figure 3-4). During testing, the cylinders were loaded in compression at a rate of 30 to 40 psi/sec, or 280 to 500 lb/sec for a 4 in. diameter by 8 in. high cylinder. Cylinders were loaded at least once before readings were collected. Then, longitudinal (ε) and transverse (ε_t) strains were recorded during loading. The standard only requires records when the longitudinal strain is at 0.00050 and when the load is at 40 % of the ultimate compressive strength. However, in addition to these values, readings were collected every 10,000 lbs to track the progression of stress and strain during loading. The stress at each point was determined by dividing the load by the cross-section of the cylinder being loaded. Finally, the modulus of elasticity (Equation (3-1)) and Poisson's ratio (Equation (3-2)) were calculated in accordance to the ASTM standard equations (ASTM Standard C469 2002).

Figure 3-4: The compessometer was used to determine the elastic modulus.

$$E = \frac{\left(S_{40\%} - S_{0.000050}\right)}{\left(\varepsilon_{40\%} - 0.000050\right)} \tag{3-1}$$

$$\mu = \frac{\left(\varepsilon_{t,40\%} - \varepsilon_{t,0.000050}\right)}{\left(\varepsilon_{40\%} - 0.000050\right)} \tag{3-2}$$

The cube compressive strength was used to determine the maximum load for the modulus of elasticity test. Because cubes were expected to yield approximately 5 percent over-strength as compared to cylinders in compression testing according to prior research (Graybeal 2006a), the ultimate compressive strength of cylinders was determined by using 90 to 95 percent of the ultimate cube compressive strength. Then, 40 percent of the ultimate compressive strength of cylinders was used to determine the maximum load for an elastic modulus test.

3.2.4 Tensile Strength

Three different methods were used to determine tensile strength of UHPC. Although other properties were measured using only one method, three different methods were initially chosen to test tensile strength because this property can be highly dependent on the chosen test

method. The three methods were compared in the initial material property testing, and a single method was chosen for later UHPC characterizations.

3.2.4.1 *Split Cylinder Tensile Strength*

The first method used to characterize tensile strength of UHPC was the split cylinder test using 4 in. diameter by 8 in. high cylinders. The procedures for this test were followed in accordance to ASTM Standard C496 (2004) for the *Standard Test Method for Splitting Tensile Strength of Cylindrical Concrete Specimens*. Because UHPC cylinders from the elastic modulus and Poisson's ratio tests, previously discussed in Section 3.2.3 were not subjected to damaging compressive loads, they were also used for the split cylinder test.

For the split cylinder test, cylinders were loaded in the Forney testing machine transversely along the cylinder length (Figure 3-5). Wooden strips, measuring 1 in. wide by 1/8 in. thick by 9 in. long, were placed above and below the cylinder at bearing surfaces, and the cylinder was loaded in compression to failure. The ultimate load was used to calculate the split cylinder tensile strength. Additionally, the first recognizable cracking load was recorded to determine a cracking split cylinder tensile strength. Using the equation provided by the ASTM Standard C496 (2004) (Equation (3-3)), the splitting tensile strength ($f_{t,sc}$) was determined by using the load (P) resisted by the cylinder and dimensions of the cylinder, length (l) and diameter (d).

$$f_{t,sc} = \frac{2P}{\pi l d} \tag{3-3}$$

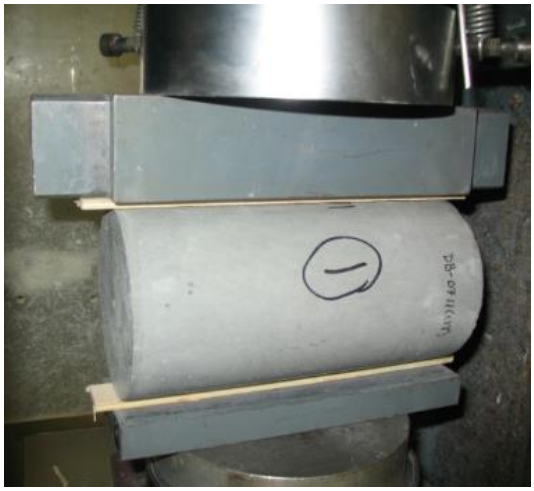

Figure 3-5: Split cylinder test set-up.

3.2.4.2 *Briquet Tensile Strength*

The second method used to determine tensile strength of UHPC was adopted from AASHTO Standard T 132-97 (2004) test for *Tensile Strength of Hydraulic Cement Mortars*. This method was chosen because UHPC resembles a mortar, containing no coarse aggregate. This method was previously used by Graybeal (2006a) during a material characterization study of UHPC. Graybeal found that this method was helpful in evaluating the post-cracking behavior of UHPC, although it was not significantly more accurate than the split cylinder test for determining tensile strength. Therefore, this method was used not only as a comparison for tensile strength, but also as a method for evaluating post-cracking behavior.

Specimens were placed using standard briquet molds. The standard briquets, according to the AASHTO Standard T 132-87 (2004), are 3 in. long and 1 in. thick. They have a curvilinear geometry, but their center cross section is 1 in. wide by 1 in. thick. In preparation of these specimens, the molds were filled completely by dropping UHPC in the center of the molds. Excess UHPC was removed by manual pinching, as described previously for other specimens. Plastic sheets were placed over the specimens, and they were cured according to Section 3.1.4

During testing, specimens were placed into specialized grips (Figure 3-6), as specified by the AASHTO Standard T 132-87 (2004), and preloaded to approximately 5 lbs prior to testing. Specimens were then loaded at a controlled displacement rate of 0.05 in./min using an MTS Insight 150 universal testing machine. Data was collected at a rate of 1 Hz using Testworks 4. The cracking load was considered the highest load before the first significant drop in load as the

specimen was tested, and the ultimate load was considered the highest recorded load. The tensile strength was calculated by dividing the load by the 1 in.^{2} cross-sectional area of the center of the briquet specimen.

Figure 3-6: Briquet tensile test set-up.

3.2.4.3 *Flexure Prism Tensile Strength*

The third method for determining tensile strength was a prism tested in third-point bending. For this test, ASTM Standard C1018 (1997) for the *Standard Test Method for Flexural Toughness and First-Crack Strength of Fiber-Reinforced Concrete (Using Beam With Third-Point Loading)* was referenced. This standard has since been withdrawn from ASTM due to a lack of use by professionals.

In this method, prisms measuring 3 in. by 4 in. by 16 in. were used to determine tensile strength of UHPC (ASTM Standard C1018 1997). These prisms were placed similarly to full-scale UHPC beams (Graybeal 2006b). UHPC was placed at one end of the rectangular prism mold and allowed to flow across the 16-in. length to the opposite end. Placing the UHPC in this way was done for two reasons. The first was that these specimens resembled beams, and beam specimens are typically prepared in this way to align fibers parallel to tensile stresses. The second reason was to facilitate proper consolidation of UHPC in the molds. Kyle Nachuk, a technical representative at Lafarge, noted that UHPC did not mix well when it flowed into itself

(Nachuk 2008), causing problems with fiber alignment and consolidation, as previously discussed in Section 2.2.2 (Figure 2-4). Both of these concerns were important for these specimens, since they were to be tested in flexure. Again, specimens were not screeded to remove excess material, but rather UHPC was manually removed by pinching if molds were overfilled. Plastic sheeting was placed over the exposed surface, and the specimens were cured according to Section 3.1.4

Testing of specimens for the initial material characterization study was performed in the Engineering Science Mechanics Materials Laboratory in Norris Hall. The specimens were loaded at a rate of 100 lbs/sec. Midspan deflection and load were recorded manually every 1000 lbs. The deflection was measured using a dial gauge (Figure 3-7). To facilitate manual data recordings, the machine was intermittently stopped to record data. The load and deflection at initial cracking were recorded, as well as the ultimate load and deflection. The peak load (P) was used to determine the tensile strength of the UHPC, and the cracking load (P_{cr}) was used to determine the cracking tensile strength. These values were determined in accordance with the equation,

$$f_{t,flex} = \frac{Pl}{bh^2} \tag{3-4}$$

Figure 3-7: Preliminary flexure prisms test set-up.

It must be noted that the results of this standard method produce inaccurate results for tensile strength of concrete, due to the same reasons as those previously discussed in Section 2.4.2 on the reported flexural strength of concrete members. As previously discussed, this method uses the maximum load resisted by the member after cracking has occurred. However, the equation used for determining this value is only valid up to the cracking point of concrete. Once the concrete has cracked, the cross section resisting the load has changed and stresses are redistributed throughout the new cross-section. Therefore, the results from this method are inaccurate for determining the actual tensile strength of concrete, and would only be useful when comparing other results using this method. This method would only be accurate for determining the cracking tensile strength of concrete. For this reason, the cracking point was also recorded in this test to determine the first cracking tensile strength of UHPC which should serve as a more accurate representation of strength using this method.

3.2.5 Shrinkage

Long term shrinkage of UHPC was determined in accordance with ASTM Standard C157 (2006) for the *Standard Test Method for Length Change of Hardened Hydraulic-Cement Mortar and Concrete* (ASTM 2006b) and ASTM Standard C490 (2004) for the *Standard Practice for Use of Apparatus for the Determination of Length Change of Hardened Cement Paste, Mortar, and Concrete*. Prisms measuring 2 in. by 2 in. by 11 ¼ in. with gage stud inserts were used for characterizing shrinkage of UHPC. Prisms were filled similarly to those mentioned previously in Section 3.2.4.3 for Flexure Prism Tensile Strength. UHPC was added at one end and allowed to flow to the opposite end. Although fiber orientation was not a primary concern for shrinkage prisms, proper consolidation was best achieved using this method. Shrinkage prisms were not screeded, but excess UHPC was manually removed by pinching. Plastic sheeting was then placed onto the exposed surface, and the prisms were cured according to Section 3.1.4

After form removal, four prisms were placed into a controlled environment drying room immediately following removal from molds. The controlled environment drying room was maintained at a constant temperature of 68 °F and 60% relative humidity. This differed slightly from the ASTM Standard C157 (2006) standard, which specifies a constant temperature and RH of 73 ± 3 °F and 50 ± 4 %. Three other prisms were cured in the laboratory alongside all other material property specimens. Although the ASTM standard only requires prisms to be monitored in a controlled environment drying room, the two sets were used to compare the effects of each

environment. The gage length (G) of all specimens was recorded as 10 in. Prior to measuring each specimen, the reference bar was used to zero the comparator. By placing the prism in the device afterward, the difference in length between the reference bar and the specimen could be determined (CRD) (Figure 3-8). Shrinkage was then determined according to the ASTM Standard C157 (2006) equations by calculating the change in length (ΔL_x) of the specimen over time (Equation (3-5)).

$$\Delta L_x = \frac{CRD - initialCRD}{G} \times 100 \tag{3-5}$$

Figure 3-8: Shrinkage was determined by comparing length changes over time.

3.3 Bending Biaxial Testing

Biaxial testing was performed to establish failure conditions for UHPC in combined tension-compression stress states. Biaxial behavior was identified as a means to evaluate the shear strength of a UHPC structural member since shear cracking occurs due to a biaxial state of stress (Figure 3-9). Two different tests were used to characterize biaxial tension-compression performance. The first of these, the bending biaxial test, is discussed in this section, and the second test, the direct biaxial test, is discussed in Section 3.4 . This section discusses specimen design, preparation, and testing procedures for the bending biaxial test. Methods used to analyze data will also be explained, showing how failure points used to generate a failure envelope were determined.

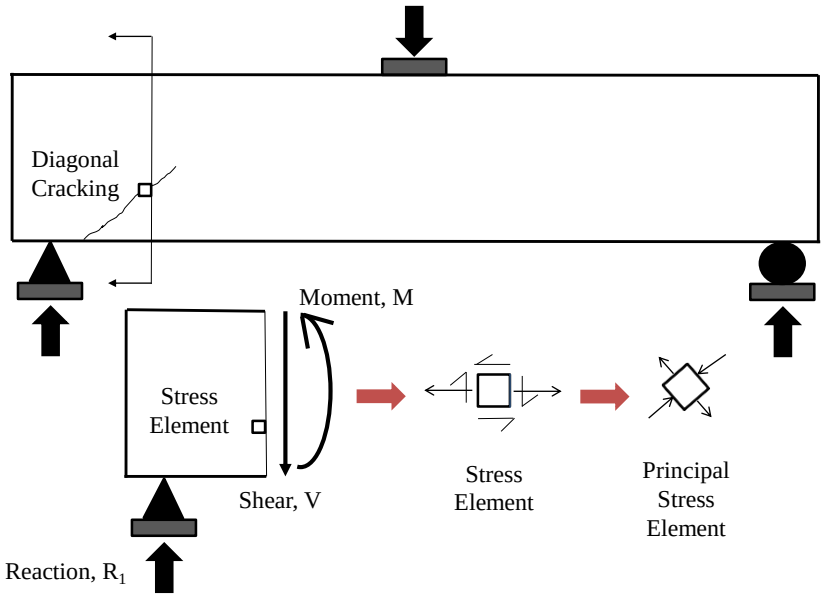

Figure 3-9: Diagonal shear cracking is a result of biaxial principal stresses.

3.3.1 Specimen Design

The bending biaxial test was designed to utilize typical equipment found in most engineering laboratories. The testing specimens were also designed to be simple and easy to form. For this reason, unreinforced, square specimens with constant thickness were used for this test. Resembling small panels, the dimensions were chosen to allow some movement of load placement and to prevent specimens from breaking during form removal. The specimens were designed to have a thickness of 1 in. to provide enough thickness that panels would not be

damaged during form removal. To allow varying load placement during testing, the sides of the specimens were at least 12 in., providing nearly 17 in. of length to place loading points along the diagonal of the specimen.

Fehling et al. (2008) performed biaxial tests on UHPC panels containing mild reinforcement, as previously discussed in Section 2.3.2.4 . Knowledge gained from this research would be useful if UHPC is mildly reinforced; however, UHPC I-beams typically do not contain mild reinforcement for shear. Without this reinforcement, UHPC may act differently in biaxial stress states. Therefore, the specimens in this project do not contain mild reinforcement. Rather, they only contain discrete steel fiber reinforcement as prescribed in the mix design for Ductal®.

3.3.2 Specimen Preparation

Small UHPC panels were cast for preliminary biaxial testing (Figure 3-10). Panels measured 12 in. by 12 in. by 1 in. Wooden forms were used to place trial specimens at the same time the original material characterization specimens were placed. A plastic sheet was fixed to the bottom of the forms to prevent moisture loss through absorption of the wood; however, the wood was left exposed on the 1 in. thick sides.

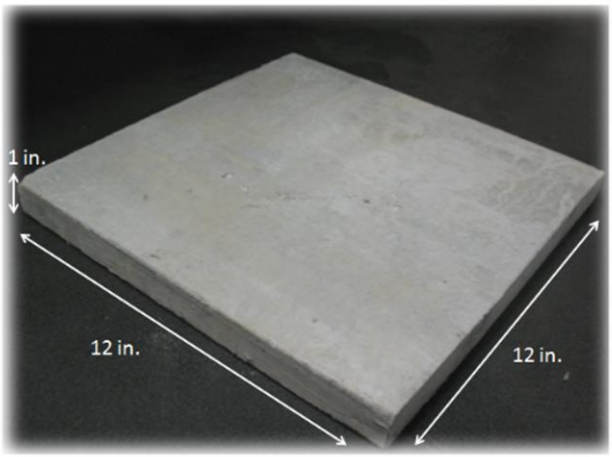

Figure 3-10: UHPC Panels (12x12x1 in.).

UHPC was placed into the middle of the forms, allowing the material to spread outward toward the edges (Figure 3-11). After the forms were filled, they were set on a vibrating table for approximately 5 seconds. Trial specimens were covered with plastic to prevent moisture evaporation. Curing was then performed according to Section 3.1.4 .

Figure 3-11: Placement of small UHPC panels.

3.3.3 Testing Procedures

By loading the panel in compression, tension and compression stresses were generated at the center of the panel orthogonal to one another (Figure 3-12). A loading frame made with HSS 2x2x1/4 steel sections (Figure 3-13, Appendix A) was used to load the small panels in the bending biaxial test. Rubber bearing pads were placed between the testing frame and the specimen to allow pressure application over a 1 in. by 1 in. area. Digital photographs were captured using the Sony XCD SX-90 camera, to be used to investigate digital image correlation techniques for strain.

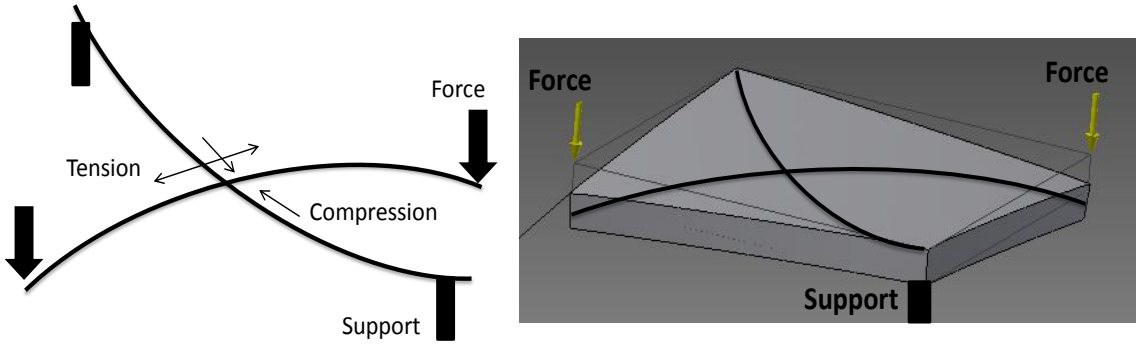

Figure 3-12: Bending biaxial test concept.

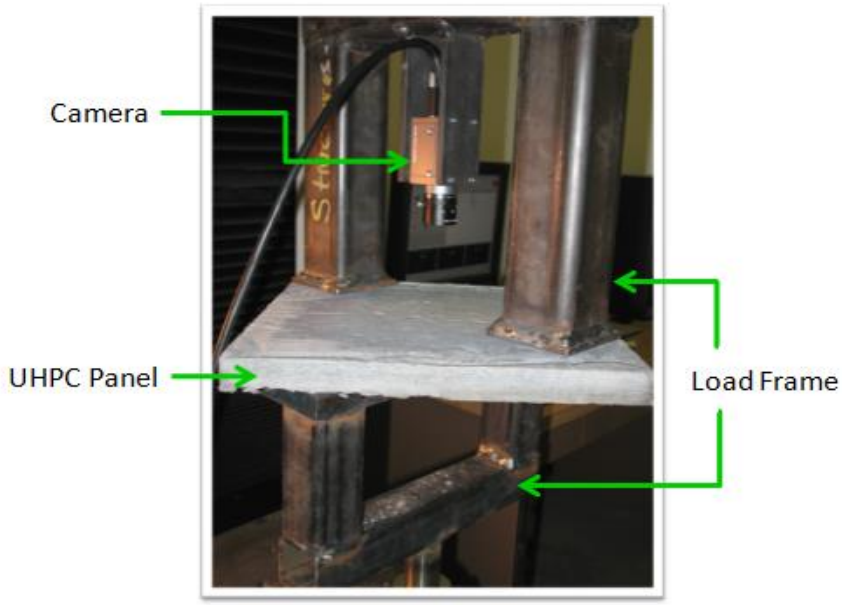

Figure 3-13: Biaxial testing frame and set-up.

Preliminary testing was performed on several trial panels to determine feasibility of this test method. A load rate of was chosen such that critical values, including first cracking and peak load, could be detected easily. Load data was collected at a rate of 1.0 Hz. using MTS Testworks. Images were collected at a rate of 1.0 Hz. using National Instruments Labview. The panel was preloaded to 10.0 lbs at a rate of 0.10 in. per minute and then loaded at 0.03 in. per minute until failure. The first cracking and peak strengths were considered the critical values of the test. The first cracking load was considered the first peak load before a sudden loss in load during testing, indicating a crack had occurred (Figure 3-14). The peak load was considered the maximum load reached during testing. Critical values were later used to generate a failure envelope for first cracking and ultimate strength.

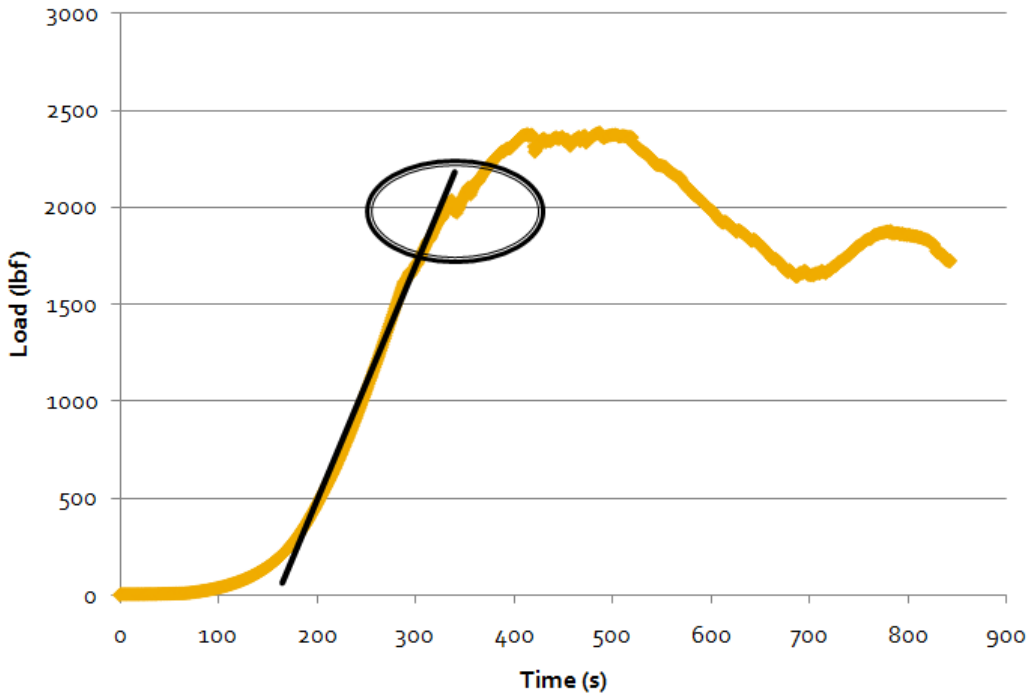

Figure 3-14: Identifying the first cracking load.

3.3.4 Specimen Naming

Specimens were named based on their overall size and loading conditions. The loading conditions were designated by the distances of the top and bottom testing frame supports. A sample name is provided below (Figure 3-15) indicating the meaning for each portion of the name. In this example, a 12 in. by 12 in. by 1 in. panel is loaded with two symmetrically placed point loads at a distance of 8 in. across the top and supported at a distance of 10 in. across the bottom. The support distances and loading points are centered across the diagonals of the panel (Figure 3-16).

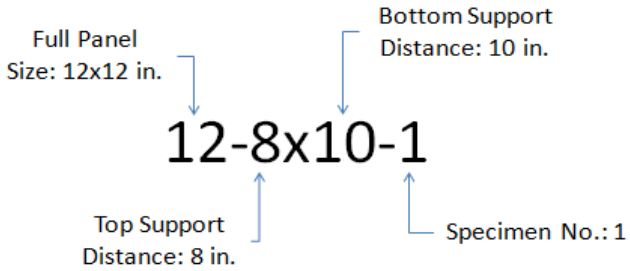

Figure 3-15: Biaxial specimen naming guide.

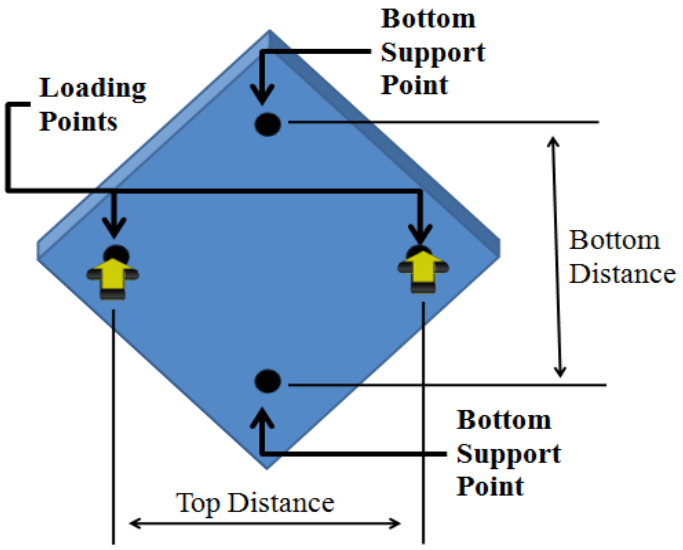

Figure 3-16: Biaxial loading configuration.

3.3.5 Preliminary Biaxial Testing Schedule

For preliminary testing, two different loading configurations were used to generate different tension-to-compression stress ratios on the 12 in. by 12 in. by 1 in. panel. Three panels were tested in each configuration (Table 3-3).

Table 3-3: Bending biaxial testing schedule

Biaxial Specimen Name	No. of Specimens
12-8x10	3
12-10x10	3

3.3.6 Post-processing using Finite Element Analysis

Small panels were analyzed using finite element analysis (FEA) to determine the stresses at the center of the panels due to unit loading. A finite element analysis was necessary because stresses could not be determined theoretically with classical analysis methods. For this analysis, a three-dimensional finite element model (FEM) was created using Abaqus 6.8-2 to simulate the biaxial bending of UHPC panels in the testing frame.

The preliminary analysis was performed using only elastic properties attained from material property testing of untreated UHPC (Table 3-4). These values were fairly consistent with those obtained by Graybeal (2006a) during a similar material study, with the exception of the modulus of elasticity. UHPC was assumed to remain elastic until first cracking. Therefore, the analysis was used to determine the first cracking stresses.

Table 3-4: Material properties for elastic FEA of untreated UHPC.

Material Property	No.	Standard Deviation	Average	FHWA Material Characterization (Graybeal 2006a)
Compressive Strength, f_c (ksi)	3	0.382	21.0	22.9
Split Tensile Strength, f_{ts} (ksi)	2	0.0716	3.39	2.80
Modulus of Elasticity, E (ksi)	2	13.3	8260	6090
Poisson's ratio, μ	2	0.0208	0.184	0.190

The three-dimensional FEM was created such that the top face of the panel was in the x-y plane (Figure 3-17). The top distance indicates the total distance between loading points. The bottom distance indicates the total distance between support points. Support points along the y-axis simulated panel contact with the bottom loading frame, where the specimen was supported during testing. A unit load of 1 kip was applied to the model by applying two 0.5-kip loads in the negative z-direction on the panel at two loading points along the x-axis. The loads were applied over a 1 in. square area in the same location as the rubber bearing pads used in the physical tests. Restraints were used to model the boundary conditions of the panel during loading. The two loading areas, represented by nodes, were restrained from movement in the y-direction. Areas of support were restrained in both the x- and z-directions. All nodes were allowed to freely rotate.

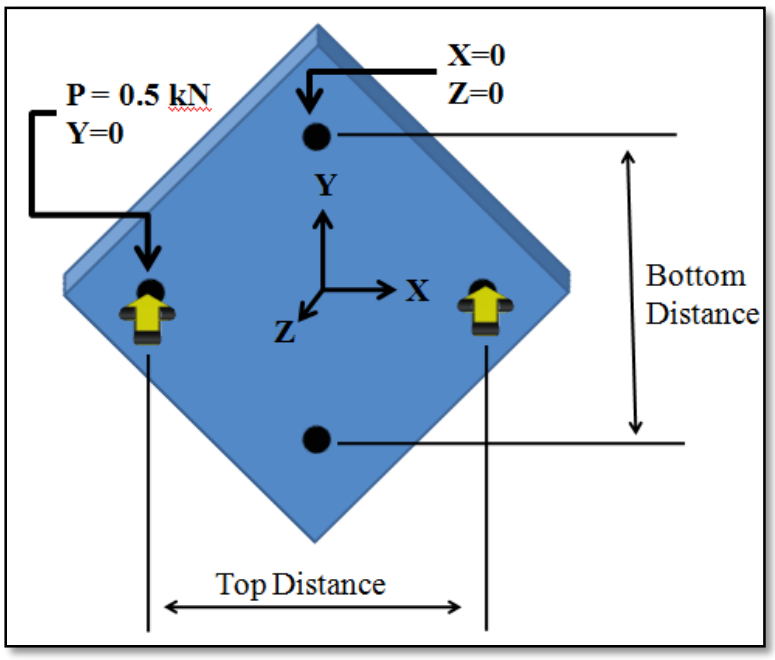

Figure 3-17: FEM model loading and restraint conditions.

Principal stresses at the center of the panel were determined based on the 1 kip loading on the FEM and referred to as "unit principal stresses." The unit principal stresses for the elastic model, located along the x- and y-axes, were used to determine stresses in the panel up to first cracking. The principal stress in the top of the panel along the x-axis (σ_2) was tensile, and the principal stress in the top of the panel along the y-axis (σ_1) was compressive. Cracking stresses were determined by multiplying the cracking load acquired from testing by the unit principal stresses from the FEA. FEA results showed that the typical stress distribution on the surface of a UHPC panel contained a large region of constant stress at the center of the panel, allowing for a significant area of constant strain at the center (Figure 3-18).

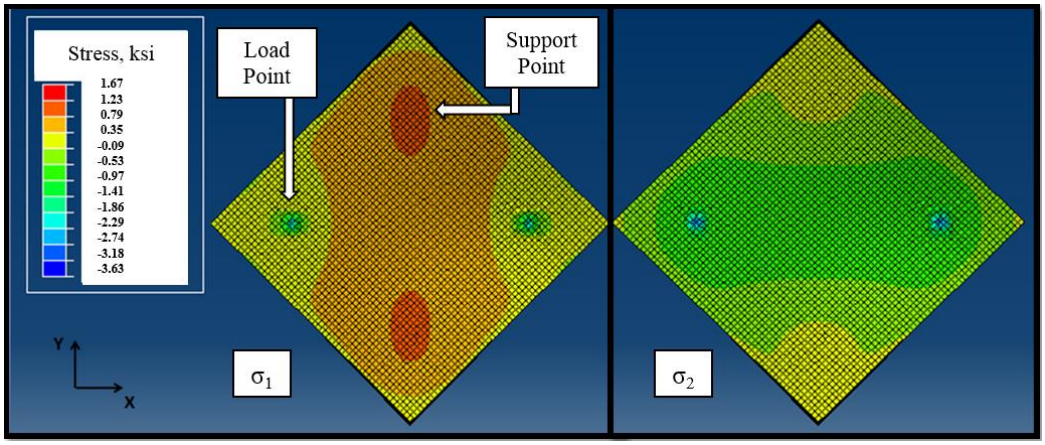

Figure 3-18: FEA principal stress concentrations along top surface.

3.3.7 Generating the Failure Envelope

Multiple points were developed by altering the location of the load application points to create different proportions of compressive and tensile stresses. This was accomplished by changing the dimensions of the loading frame (Figure 3-19). The frame applying load on the top of the panel remained constant, while the frame with support points on the bottom of the panel was altered. The lines A, B, and C on the stress-strain graph indicate the idealized proportions of compressive-to-tensile stresses formed by the different support frame dimensions of configurations A, B, and C above the graph. The failure point for that proportion of compressive-to-tensile stresses ideally falls somewhere along this line. Other points used in the failure model were the uniaxial tensile strength, f_t, and the uniaxial compressive strength, f_c, as determined from material testing results. By using multiple points, a failure envelope for UHPC was created (Figure 3-19).

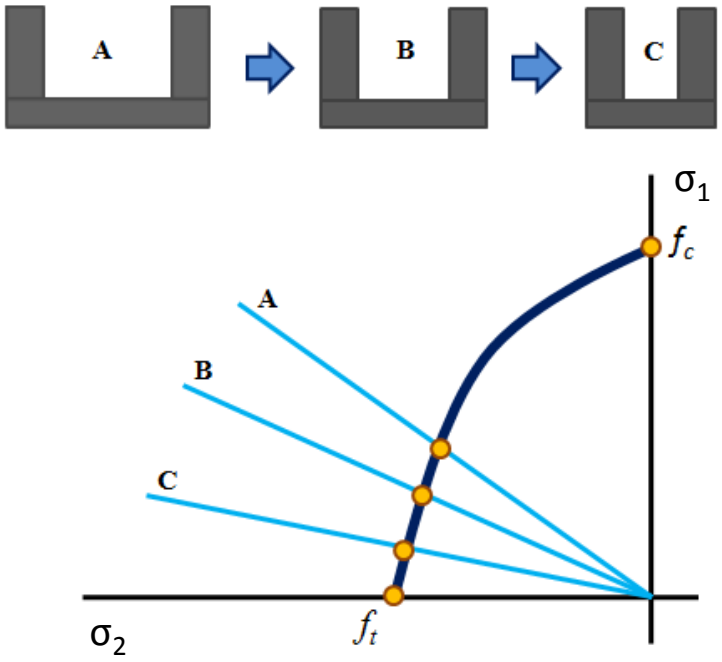

Figure 3-19: A failure model is generated by combining various tension-to-compression stress ratios.

Slope and regression analysis was used to create the failure models and to determine the relationship of compressive and tensile stress interaction of UHPC. These models were then compared to common failure criteria used for conventional concretes and fiber-reinforced concretes to evaluate the differences and similarities in general shape and the relationship between combined tension and compression stress states. Results from the bending biaxial tests were also compared with the direct biaxial test, as discussed in the following section.

3.4 Direct Biaxial Testing

Due to difficulties experienced in the bending biaxial test, a new test procedure was designed to evaluate UHPC using a more direct method. This new test, hereby referred to as the direct biaxial test, was inspired primarily by the AASHTO Standard T 132-87 (2004) test for *Tensile Strength of Hydraulic Cement Mortars*. The aforementioned test was used to test tensile strength of UHPC, as discussed in Section 3.2.4.2 . The biaxial testing methods for fiber-reinforced concrete performed by Demeke and Tegos (1994) also influenced the development of

this test. Biaxial behavior was investigated as a means to identify shear cracking of UHPC (Figure 3-9).

3.4.1 Specimen Design

As mentioned, the direct biaxial test was inspired by the AASHTO Standard T 132-87 (2004) test for *Tensile Strength of Hydraulic Cement Mortars*. In the AASHTO test, the briquet specimen has a center cross-section measuring 1 in. by 1 in., and it is a total of 3 in. in length (Figure 3-20). Since this specimen is extremely small and lacks adequate area to apply compression, the direct biaxial test specimens were designed to have a larger, elongated center cross-section to provide an area sufficient for compressive force application. According to finite element modeling, this size also ensured that there would be an area of constant stress distribution at the center section.

Figure 3-20: Briquet specimen for AASHTO Standard T 132-87 (2004) standard test (lower left) and direct biaxial test specimen (upper right).

The direct biaxial test specimen, or the direct biaxial "dog bone", displays several distinct differences compared to the standard briquet shape (Figure 3-21, Table 3-5). First, a center cross section of 2 in. by 2 in. is provided by the direct biaxial test specimen. The center length is elongated to allow compressive force application over a 2 in. by 2 in. area, also. This area provided adequate area for constant stress distributions to occur at the center of the specimen. Using Abaqus, finite element models were used to determine a proper radius for the fillet between the elongated portion and rounded ends used for tension force application. Fillet radii between 0.5 and 1.5 in. were examined to determine a radius producing the lowest stress concentrations at the tension load application points. Values were varied at 0.25 in., and a radius value of 1.0 in. was chosen based on this analysis.

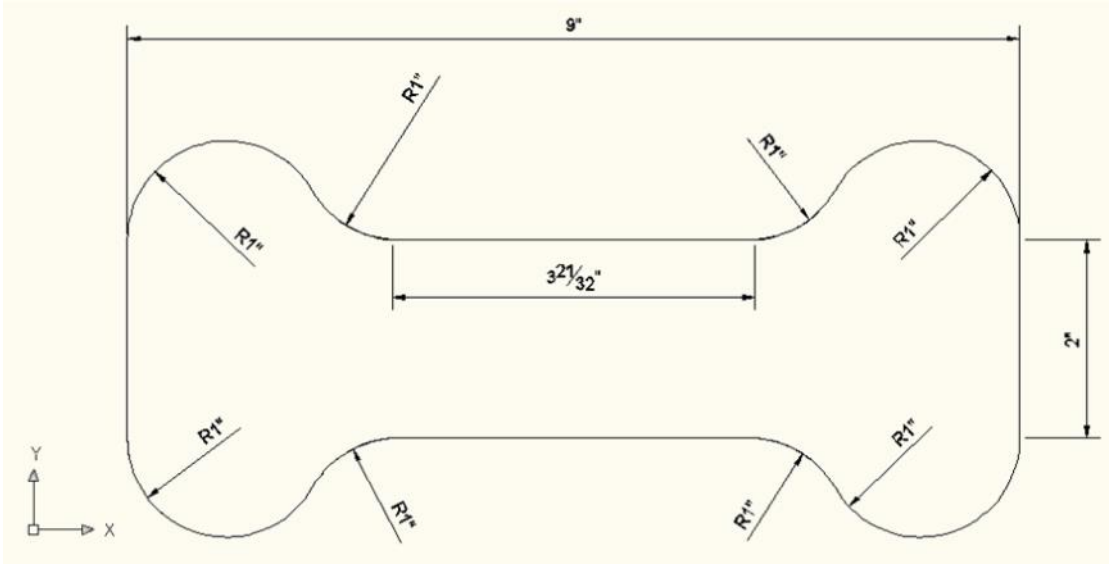

Figure 3-21: Dimensioning of direct biaxial test specimen.

Table 3-5: Dimensional differences between the AASHTO (2004) Briquet and the Direct Biaxial Dog Bone.

Property	AASHTO (2004) Briquet	Direct Biaxial Dog Bone
Total Length (in.)	3	9
Thickness (in.)	1	2
Center Width (in.)	1	2
Center Cross-Sectional Area (in.^{2})	1	4

As mentioned previously, the finite element models of this specimen indicated that an area of constant stress could be achieved at the center using these dimensions. Finite element models for this exercise were performed using elastic properties of UHPC. Three-dimensional, hex-dominated elements were used in the analysis. A converged solution was reached by reducing element sizes. A uniform pressure was applied within the compression area, as shown in the negative y-direction in Figure 3-22. A uniform pressure was also applied in the positive x-direction over an area with a width of 0.125 in. where the rollers were expected to be in contact with the end of the UHPC dog bone. Constraints were set to restrict movement in the y-direction opposite the compression pressure and in the x-direction for the roller supports opposite the pressure from the rollers. The results of this finite element analysis indicated that a sufficient area was available at the center of the section to achieve constant stress distributions.

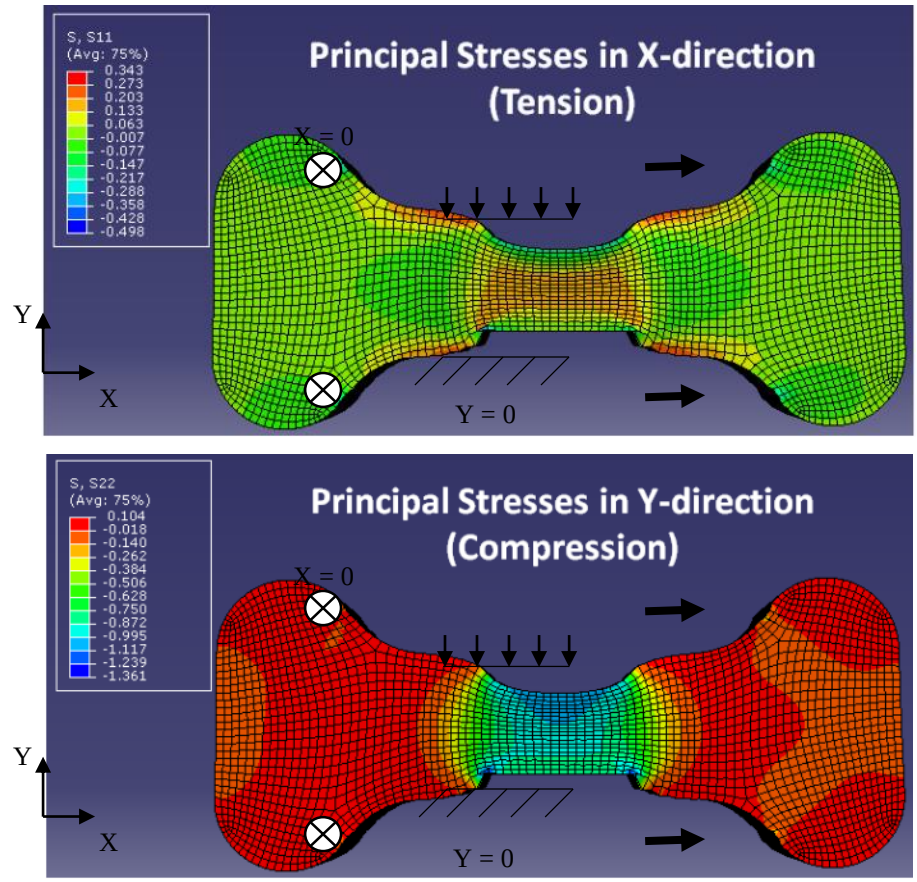

Figure 3-22: Finite element analysis results of the direct biaxial dog bone show principal stress concentrations were sufficient.

3.4.2 Specimen Preparation

Specialized forms were constructed using ultra high molecular weight polyethylene (UHMW-PE). This material was chosen to achieve smooth surfaces and to prevent moisture absorption. A trial form was made using a split-form design (Figure 3-23). Two pieces with mirrored cut outs were bolted together. These pieces were then bolted to an aluminum plate for backing. Potential problems were recognized with this form design during casting of trial specimens. First, the bolts connecting the two plastic mold pieces were a hindrance to placing the concrete. Also, the large exposed surface area resulted in a poor finished surface on the surrounding area to be tested (Figure 3-23). Due to these problems, a revised mold design was produced to reduce the exposed surface area, and to ensure the central area to be tested had a smooth finish on all sides.

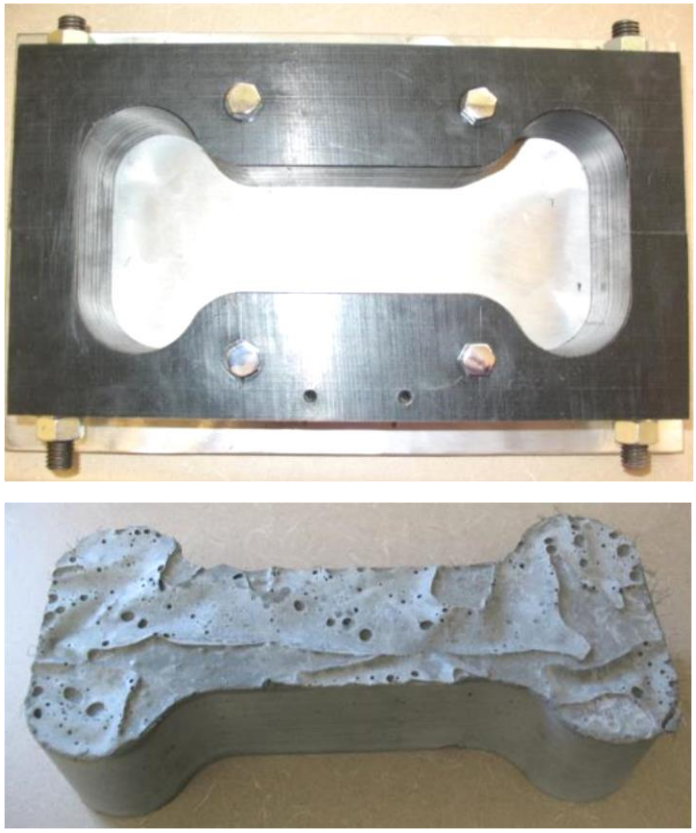

Figure 3-23: The original direct biaxial dog bone form presented potential problems for UHPC specimens.

The revised form design uses the UHMW-PE to form the shape, and clear acrylic glass, composed of poly(methyl methacrylate), walls are bolted along both sides. The clear walls provided a means to view consolidation and fiber orientation during casting, as well as to provide a smooth finished surface surrounding the entire tested area. The dog bone shapes were cast upright along the tensile direction using the new forms. UHPC was added vertically into the forms through a 2 in. by 0.75 in. opening in the top of the form (Figure 3-24). No vibration was used on these specimens due to the high flow valued noted during rheological characterization. Plastic sheeting was placed on the exposed surface to prevent moisture loss. After 24 hours, the bolts were loosened to prevent shrinkage restraint during curing, but specimens remained in the forms until release at 48 hours. Curing resumed as previously discussed in Section 3.1.4

Figure 3-24: UHPC was added vertically into the direct biaxial dog bone test forms.

In the aforementioned description, UHPC was inserted into vertical forms (Figure 3-24). This allowed the UHPC to flow into the form randomly. As the UHPC entered randomly, it created a random fiber orientation. Because UHPC is often placed such that fiber orientation is controlled, it was necessary to simulate controlled fiber orientation in samples, also. Therefore, a frame was constructed to place UHPC on an incline, allowing UHPC to flow horizontally across the biaxial dog bone forms (Figure 3-25). The frame allowed the forms to lie on an angle of 33.9°. The frame could not lie perfectly horizontal because the insertion point of the forms was at the top; however, this did allow for more controlled fiber orientation along the tensile direction of the biaxial dog bone than the previous casting method.

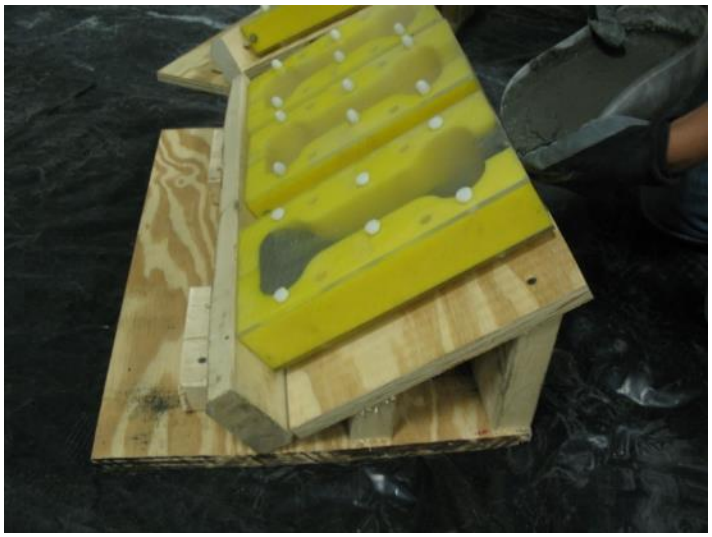

Figure 3-25: UHPC was placed at a 33.9° angle to control fiber orientation.

3.4.3 Direct Biaxial Testing Apparatus

Because the biaxial test was not standardized, specialized equipment was fabricated to test the direct biaxial dog bone specimens. For this section, compression application is assumed to be applied in the vertical direction along the y-axis, and tension is assumed to be applied in the horizontal direction along the x-axis (Figure 3-21).

During testing, restraints were established above and to the left of the specimen to stabilize the specimen against force application (Figure 3-26). A tensile force was first applied using a pair of specialized grips, similar to those used in the AASHTO Standard T 132-87 (2004) testing procedure (Figure 3-6). Similar to the briquet testing apparatus, the tension grips for the direct biaxial test were fabricated to allow load application through non-rigid supports (Figure 3-26). The grips were designed to allow for free rotation in the y- and z-axis as the specimen fractures. The pyramid shaped piece on the tension grips will allow this movement to occur as needed during testing of the specimen. Permitting this movement will prevent restraint in the specimen due to a fixed alignment of the fixtures. Detailed drawings of the tension grip fixture are provided in Appendix A. Similar to compressive force application, tensile force was applied using a hydraulic jack.

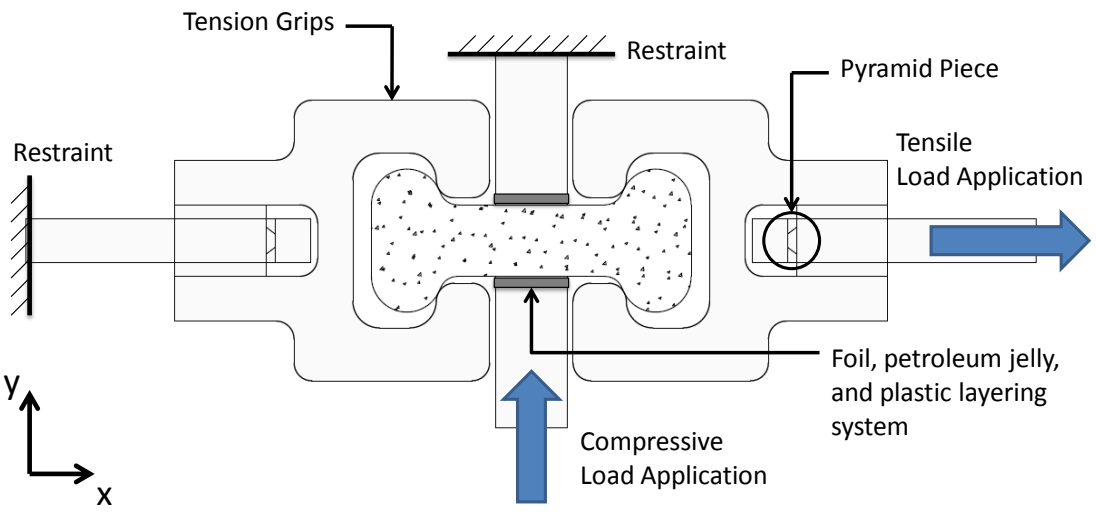

Figure 3-26: Direct biaxial test set-up includes specialized tension grips and a layering system to reduce shear stresses in compression region.

Compression was applied, after a target tensile force was achieved, to the bottom of the specimen in the positive direction along the y-axis (Figure 3-26). A hydraulic actuator was used to apply force through a series of steel plates to produce a constant stress over a 2 in. by 2 in. area at the center of the specimen. The following methods were investigated to reduce friction between the specimen and the compression application:

1. A bare UHMW polyethylene block, 0.25 in. thick, with no lubrication was used, first, due to its high durability and low coefficient of friction.
2. The UHMW polyethylene block, 0.25 in. thick, was lubricated with Vaseline petroleum jelly, and a thin plastic wrap was placed between the lubrication and the specimen.
3. A layered series of foil wrap, plastic wrap, and Vaseline petroleum jelly was investigated to reduce shear stresses between the specimen and the force application by the steel plate. This method was previously used by Demeke and Tegos (1994) in a biaxial test for fiber-reinforced concrete.
4. Finally, an abrasion resistant fiberglass, Teflon-coated tape was applied directly to a steel plate due to the low coefficient of friction and durability of this product.

The coefficient of static friction was determined through one of two ways: a fish scale and small weights or by directly setting the biaxial dog bone in the test setup (Figure 3-27). Through experimental testing, the best option for eliminating friction was accomplished using abrasion resistant fiberglass, Teflon-coated tape on free-floating steel plates (Table 3-6). This could reduce the coefficient of friction to approximately 0.1, as opposed to a value of 0.3 using only a bare polyethylene block.

Figure 3-27: Coefficient of static friction was determine experimentally.

Table 3-6: Coefficient of friction comparison of multiple friction reduction systems.

Method to Reduce Friction	**Coefficient of Static Friction, μ_s**
Polyethylene block (0.25 in. thick) with no lubrication	0.3
Polyethylene block (0.25 in. thick), Vaseline lubrication and thin plastic wrap between block and UHPC	0.2
Free-floating steel plate, Vaseline between plate and support, Teflon tape between plate and UHPC	0.2
Free-floating steel plate, fiberglass and Teflon tape between plate and support, fiberglass and Teflon tape between plate and UHPC	0.1

3.4.4 Direct Biaxial Test Procedures

To perform the direct biaxial test, a pre-selected amount of tension was first applied to the specimen using a hydraulic actuator (Figure 3-28). Hand pumps were chosen for better control of load application. This pre-selected amount was assigned to not exceed the ultimate tensile strength of the UHPC, as determined by an initial series of tests on the specimen for pure tensile strength. After the entire pre-selected tensile force was applied, compressive force was applied using another hydraulic actuator until failure of the specimen occurred. Since the Poisson's effect reduced the amount of tensile force applied along the x-axis as a compressive force was applied along the y-axis, the initial tensile force exceeded the target value for a particular series.

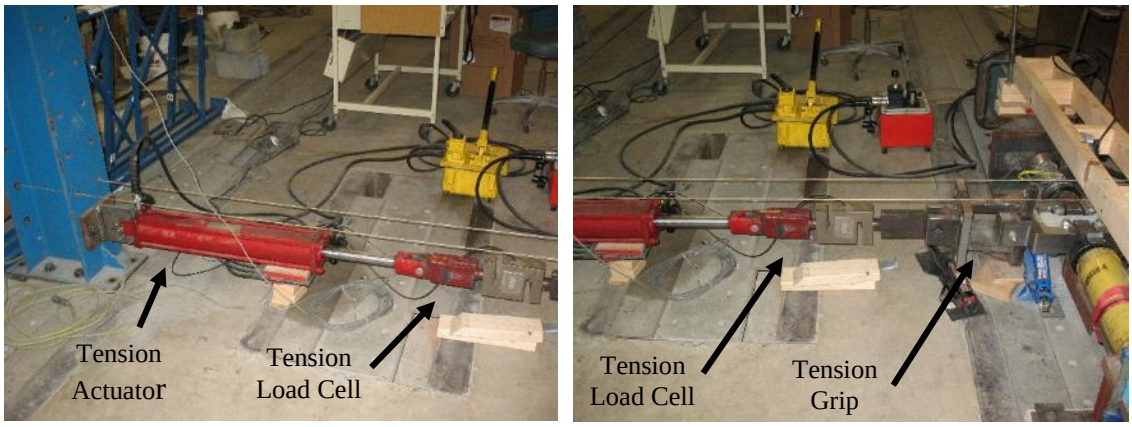

Figure 3-28: Tension was first applied using a hydraulic cylinder.

Data acquisition was accomplished using Labview and the Vishay System 5000. Two load cells were used to monitor the tensile and compressive forced applied to the specimen through the System 5000. Images were collected using the Sony XCD-SX90 camera and the Labview data acquisition system. These images were analyzed after testing using digital image correlation, to be explained in Section 3.5 . A summary of the testing procedures is as follows:

1. The top of the specimen was painted for digital image correlation. A base layer of white paint was applied. Once dry, black speckling was applied.
2. A LVDT was mounted to the underside of the specimen to measure 2 in. along the midsection of the specimen.
3. The specimen was placed in the tensile grips, leveled, and centered in the test frame.

4. The tension grips were extended to provide support to the specimen.
5. The digital camera settings were adjusted to focus the image acquired in Labview.
6. Data acquisition wase initiated for load cells and image collection simultaneously.
7. The specified amount of tension was applied to the specimen.
8. Compression was applied to the member until failure.

Because free-floating steel plates coated in abrasion resistant, Teflon-coated tape were used to eliminate frictional stresses during compression loading, magnets were used to stabilize these blocks until a small amount of compressive force was applied (Figure 3-29). Once an initial force was applied to stabilize the blocks, the magnets were removed and testing resumed up to failure of the specimen.

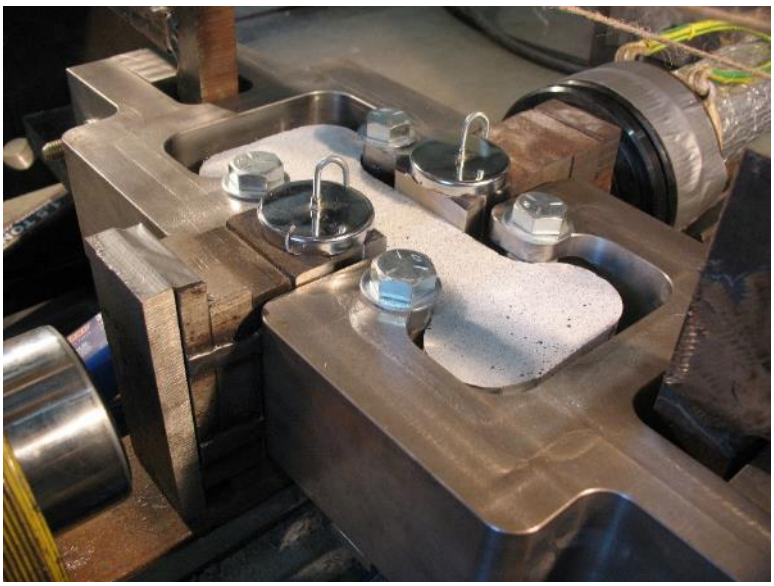

Figure 3-29: Magnets were used to hold free-floating steel blocks in place prior to compression force application.

3.4.5 Testing Schedule & Specimen Naming

The testing schedule was designed to achieve a variety of points along the compression-tension failure planes of both steam treated and untreated UHPC. Because both untreated and steam treated UHPC are used in structures, failure curves for both curing conditions were determined. A specific series of testing is designated by the amount of specified compression and the curing regime. Each series specified testing at least three specimens. In the event that

the standard deviation is considered significant using three specimens, a fourth specimen was tested to identify outliers so long as specimens were available.

The testing schedule (Table 3-7) indicates the 18 series of tests that were performed to construct the biaxial failure envelopes. First, a series of pure compression was tested to determine the uniaxial compressive strength of the specimen. For this test, the specimen was loaded in compression until failure. A uniaxial tension series (DB-PT-UT/ST) was performed for each curing regime to determine the uniaxial tensile strength ($f_{t,DB}$). Using this uniaxial tensile strength of the specimen, the specified tensile values were determined for the remaining tests. Each series was based on a percentage of the uniaxial tensile strength and the curing regime. For instance, the series DB-0.2-UT represents a direct biaxial test performed at 20 percent of the uniaxial tensile strength ($f_{t,DB}$) using untreated (UT) UHPC. The steam treated samples are designated by ST.

Table 3-7: Direct biaxial testing schedule

Series	Specified Tensile Load (k)	No. of Specimens
DB-PC-UT	*0*	3
DB-0.2-UT	$0.2*f_{t,DB}$	3
DB-0.4-UT	$0.4*f_{t,DB}$	3
DB-0.6-UT	$0.6*f_{t,DB}$	3
DB-0.8-UT	$0.8*f_{t,DB}$	3
DB-PT-UT	$f_{t,DB}$ *(load to failure)*	3
DB-PC-ST	*0*	3
DB-0.2-ST	$0.2*f_{t,DB}$	3
DB-0.4-ST	$0.4*f_{t,DB}$	3
DB-0.6-ST	$0.6*f_{t,DB}$	3
DB-0.8-ST	$0.8*f_{t,DB}$	3
DB-PT-ST	$f_{t,DB}$ *(load to failure)*	3
DB-PC-UT-I	*0*	3
DB-0.2-UT-I	$0.2*f_{t,DB}$	3
DB-0.4-UT-I	$0.4*f_{t,DB}$	3
DB-0.6-UT-I	$0.6*f_{t,DB}$	3
DB-0.8-UT-I	$0.8*f_{t,DB}$	3
DB-PT-UT-I	$f_{t,DB}$ *(load to failure)*	3

Where, DB – Direct biaxial test

PC – Pure compression load application

PT – Pure tension load application

UT – Untreated (no steam treatment)

ST – Standard steam treatment

UT-I – Untreated (no steam treatment) placed on a 33.9° incline

3.4.6 Post-Processing and Analysis Techniques

Post-processing and analysis techniques were similar to those previously mentioned for the bending biaxial test in Section 3.3.6 The cracking failure point is considered the combination of loading that causes the member to crack. At this point, Ductal® is considered to have reached its elastic capacity. Post-cracking behavior was investigated to determine the maximum load combination the UHPC specimen is capable of withstanding.

Photogrammetry methods were utilized to evaluate strain during testing and post-cracking behavior. For the direct biaxial test, finite element methods were not necessary to interpret stresses because loads were directly applied to the specimen. Stresses were determined by dividing the force exerted in one direction by the area of force application. In each direction, the area of force application is 4 in.^{2}.

3.4.7 Generating the Failure Envelope

Results from testing were used to generate failure envelopes for biaxial compression and tension stress states for both steam treated and untreated Ductal® UHPC. Both cracking and post-cracking envelopes were developed using slope and regression analysis techniques. Results from the testing schedule (Table 3-7) were used in this analysis. The failure envelope developed using the direct biaxial test was compared to that of the bending biaxial test to determine the degree of consistency in both models. The direct biaxial test model was also compared to models developed for other concretes to evaluate the differences and similarities between the behavior of conventional concretes and Ductal® UHPC.

3.5 Photogrammetry

3.5.1 Digital Image Correlation

For biaxial testing, strains were calculated by analyzing digital photographs with *Digital Image Correlation & Tracking*, a collection of code for use in Matlab (Eberl 2010). This code was developed by researchers at Johns Hopkins University to calculate strains using digital image correlation (DIC), a known method for determining strains in materials, including concrete (Choi and Shah 1997; Küntz et al. 2006; Lecompte et al. 2006). Using DIC to measure strain in concrete was chosen because it required no direct contact with the specimen and provided data collection post-cracking, unlike strain gauges.

Images were captured at a rate of 1 Hz using the Sony XCD-SX90 black and white digital camera and Labview data acquisition. Images were then analyzed by entering a series of commands using the Matlab code for image correlation and tracking (Eberl 2010). First, a file listing all image names was created. Then, a rectangular grid was generated over a base image to identify the location of pixels to be tracked (Figure 3-30). The distance between grid points was altered by defining the raster point distances. These distances determined the number of pixels

between each point. By lowering the raster point distances, a converged solution could be reached.

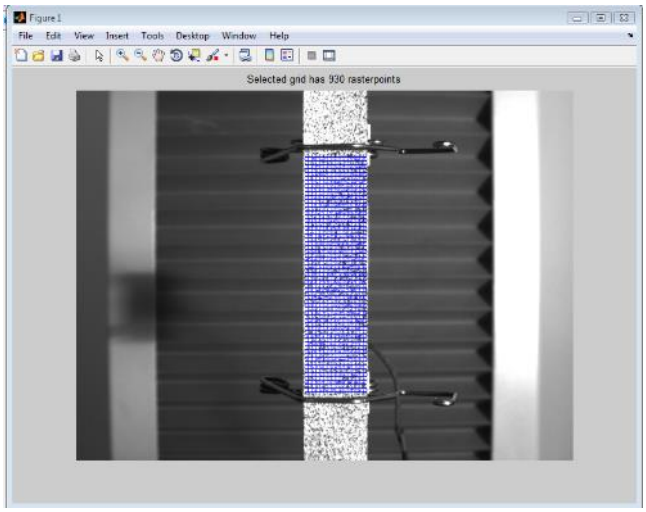

Figure 3-30: Grid generated using DIC program in Matlab.

Once a grid was created, the "automation" function was used to perform the DIC (Figure 3-31). According to the Matlab code, the correlation analysis used the first image as the reference image for all strain calculations. Therefore, each successive image was compared to the first image. For this process to work effectively, the camera had to remain completely stationary so that camera movement would not contribute to the relative movement of the speckling pattern. This process is best known as cross-correlation.

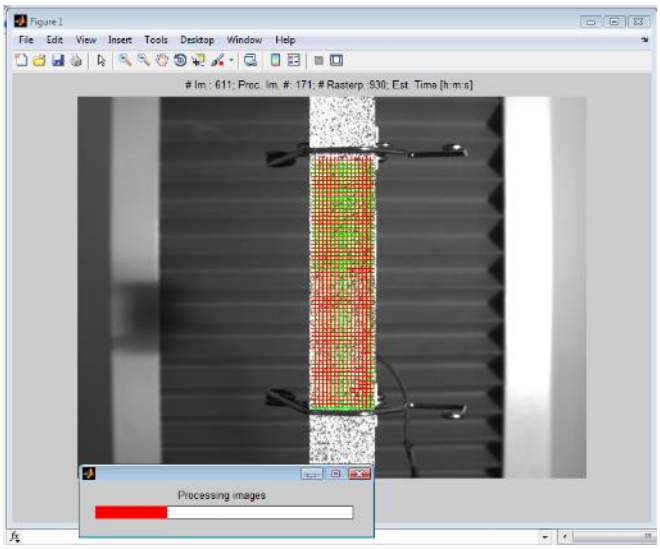

Figure 3-31: Images are processed in Matlab, showing the original grid in green and the movement of the grid points in red.

After all images were cross-correlated, the strains could be measured, using the "displacement" function. The strain between two points could be measured by choosing two different points of interest (Figure 3-32). Another option for measuring strain was to use the average strain function. This function determined the average strain using all points in either the x- or the y-direction. The two points method was used in the strain verification process, as described in the following section. However, the average strain method may also be used in future testing where a constant strain is expected to occur.

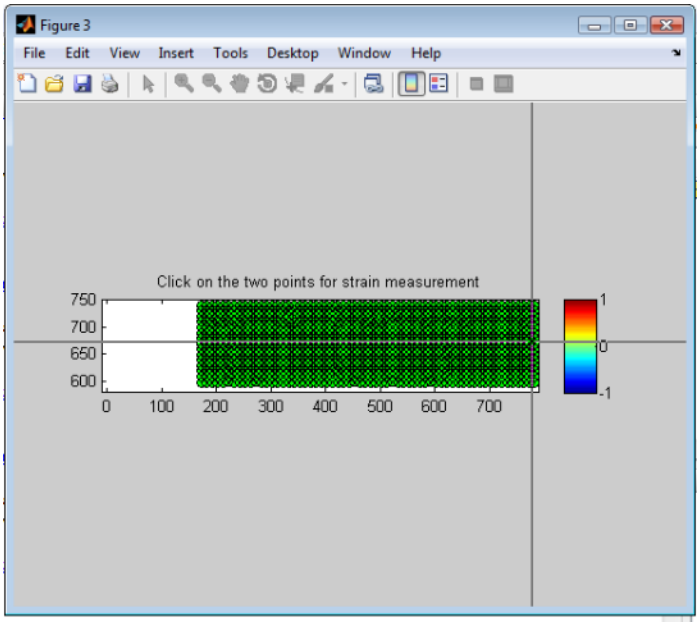

Figure 3-32: Strain measurements can be determined by choosing two points.

3.5.2 DIC Verification using Steel Coupon Specimens

The Matlab program for digital image correlation was verified using steel coupon specimens. The steel coupon specimens were first covered with a light layer of white spray paint. Speckling was accomplished using a multicolor textured black and white spray paint. A light layer of this paint was misted over the specimens until the desired speckling density was achieved. After speckling, the specimens were allowed to dry before being tested within 24 hours.

The specimens were tested using the MTS Insight 150. An extensometer with a gauge length of 2 in. was used to measure strain between two points throughout the test (Figure 3-33). The digital camera was placed so that it could capture images of the specimen between the extensometer connection points throughout the test. Because the extensometer captures only the strain between two points, the two-point method for strain was used in the DIC program for a similar comparison. Results from both the attached extensometer and those determined by the DIC program were compared for the verification to determine whether or not the speckling pattern and the DIC program could be used for future testing of UHPC.

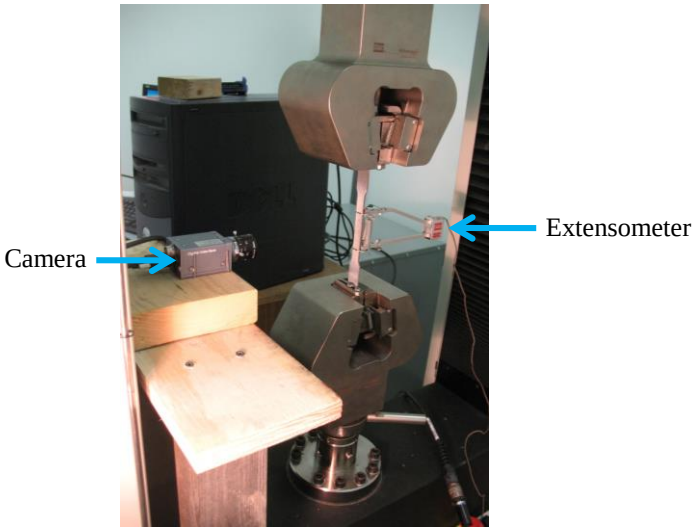

Figure 3-33: Tensile coupon test set-up for DIC verification.

3.6 UHPC Bridge Deck Design

A waffle slab bridge deck was designed using an iterative analysis technique, incorporating structural behavior concepts. An initial design was developed using material models developed by other researchers, but the material models were later altered to reflect data gathered from preliminary tests results. An iterative optimization approach was used to reduce the cross-sectional area of the deck, ultimately reducing the total cost to construct the deck. The deck was also designed to prevent cracking under service loading to best provide long-term durability. Sample calculations for the design process are included in Appendix B.

3.6.1 Deck Design Considerations

Several design considerations were proposed to ensure optimal strength and durability of the waffle slab deck. First, the deck was designed to preclude cracking under service loading. Cracking can make UHPC vulnerable to environmental exposures after cracks form. Such exposures could lead to corrosion of reinforcement, including both corrosion of the discrete steel fibers and primary reinforcement. This parameter was accomplished by limiting strains to make certain that cracking of UHPC would not occur under designated service loads. The deck section was prestressed in the transverse direction, perpendicular to supporting bridge beams, with strands in both the top and bottom of the cross-section to balance the effects of camber and to prevent cracking.

The deck was also designed to minimize the cross-sectional area to take advantage of the strength properties of UHPC and to lower overall costs in construction. Not only does this reduce the material required to place the deck, but it also reduces the dead load due to self-weight which affects the design of other members in the bridge.

Finally, shear connections with steel stringers were designed for durability and strength. Economic feasibility in construction labor and materials was considered to provide a connection detail that would limit overall costs.

3.6.2 Material Properties for Deck Design

For the deck design, the material properties based on the stress-strain model developed by Graybeal (2008) (Table 3-8) and prestressing steel (Table 3-9) were initially used as a guide. The prestressing steel used in the design was a 0.5 in., 270 ksi ultimate stress, low-relaxation steel. An effective prestress value of 52% of the ultimate stress, or 140 ksi, was used as a starting point in the design. This effective prestress value was used in the initial waffle slab bridge deck analysis by Garcia (2007).

Table 3-8: Material properties of UHPC utilized for bridge deck design.

Property	Value
Unit Weight, γ	156 pcf
Modulus of Elasticity, E_c	7600 ksi
Maximum Compressive Stress of UHPC, f_{mc}	24 ksi
Maximum Tensile Stress, f_{mt}	1.5 ksi
Maximum Compressive Strain, ε_{mc}	0.00316
Maximum Tensile Strain, ε_{mt}	0.007

Table 3-9: Material properties of prestressing steel utilized in bridge deck design.

Property	Value
Ultimate Stress, f_{pu} (ksi)	270
Effective Prestress Starting Point, f_{pe} (ksi)	140
Modulus of Elasticity, E_p (ksi)	28,500

The Graybeal (2008) stress-strain model was later compared to results obtained through some preliminary tests involving single cells of the bridge deck section. Modifications to the stress-strain model were made in order to better represent the experimental results from trial testing of placement methods.

3.6.3 Design of Waffle Slab Bridge Deck Cross Section

The waffle slab bridge deck was initially designed using known stress-strain relationships of UHPC previously developed by other researchers. By using an iterative analysis approach, an optimal solution was chosen to maximize capacity while minimizing material. The iterative approach was intended to reduce the cross-sectional area by narrowing portions of the representative T-beam section of the deck. The cross-sectional dimensions were chosen and then analyzed through the use of an Excel spreadsheet.

Although the design was not performed for a specific bridge, the UHPC design was intended to perform similarly to a conventional full-depth concrete bridge deck. The final design was chosen based on comparing performance with this conventional deck. A design was chosen that would maximize flexure and shear strength while minimizing cross-sectional area. The deck was also designed to be fully composite with W36x160 steel girders.

The flexural capacity was determined by analyzing a section of the deck as a T-beam using strain compatibility. The stress-strain relationship developed by Graybeal (2008) was initially used because it was shown to best represent Ductal® beam behavior. Since the deck would actually be a waffle shape with interconnected webs that can provide stiffness to the deck, the results from the analysis were expected to be conservative.

Shear capacity was determined based on known relationships for Ductal®. It was determined that shear capacity would be estimated based on the relationships Graybeal (2006b) identified for shear strength, as previously described in Section 2.4.3.4 . The AFGC and Setra (2002) established several contributing factors for UHPC shear, including the concrete, the fibers, and mild reinforcement. Graybeal (2006b) determined that the shear strength could be predicted by using the area of the web and an approximate angle of the diagonal tensile failure for I-beams without shear reinforcement. This is nearly equivalent to using only the AFGC and Setra fiber contribution to shear. The contribution of the concrete to the shear strength was considered negligible. Since Ductal® contains no coarse aggregate, there would be little to no shear strength contributed due to aggregate interlock. Additionally, the Ductal® I-beams

contained no mild reinforcement for shear, negating this contribution from the overall shear strength (Graybeal 2006b). The waffle slab bridge deck was designed to not require shear reinforcement; therefore, only the contribution due to discrete fiber reinforcement was considered for shear.

3.6.4 Shear Connections to Steel Stringers

The shear connections between the UHPC waffle slab deck and the steel stringers were designed using AASHTO LRFD Bridge Design Specifications (AASHTO 2012) and Virginia Department of Transportation (VDOT) Specifications (VDOT 2007). The deck was designed to be composite with the W36x160 steel stringers using shear studs as horizontal shear connectors encased in grout-filled shear pockets. Shear pockets were rectangular, consistent with previous research on UHPC decks and the proposed two-way ribbed shape. Shear pocket size was determined based on the rib alignment in the waffle shape and the size of the steel stringer flange.

Shear pockets were filled with a basic hydraulic cement grout as defined by VDOT (2007) *Roads and Bridges Specification* to represent typical field processes (Figure 3-34). The grout mix design (Table 3-10) included grading C fine aggregate (Table 3-11) as determined using a sieve analysis (ASTM Standard C136 2006) and Type I/II cement. The aggregate was a graded manufactured sand obtained from Conrock in Blacksburg, VA.

Table 3-10: Grout mix design for shear connections.

Material	Mix 1 (DS-2)	Mix 2 (DS-1)
Fine Aggregate, lb	110	110
Cement, lb	55	55
Water, lb	22.8	22.5
Estimated Moisture from Aggregate, lb	1.44	0.79
Water-to-Cement Ratio	0.44	0.42

Table 3-11: Sieve analysis results for manufactured sand.

Sieve	Sample 1 (% Pass)	Sample 2 (% Pass)	VDOT (2007) Grade C (% Pass)
3/8	100	100	100
No. 4	99.9	99.9	94 to 100
No. 8	93.5	91.2	-
No. 16	44.3	41.2	-
No. 30	19.0	16.5	-
No. 50	8.12	6.08	0 to 25
No. 100	5.22	3.60	-
No. 200	2.61	2.60	-
Pan	0	0	-

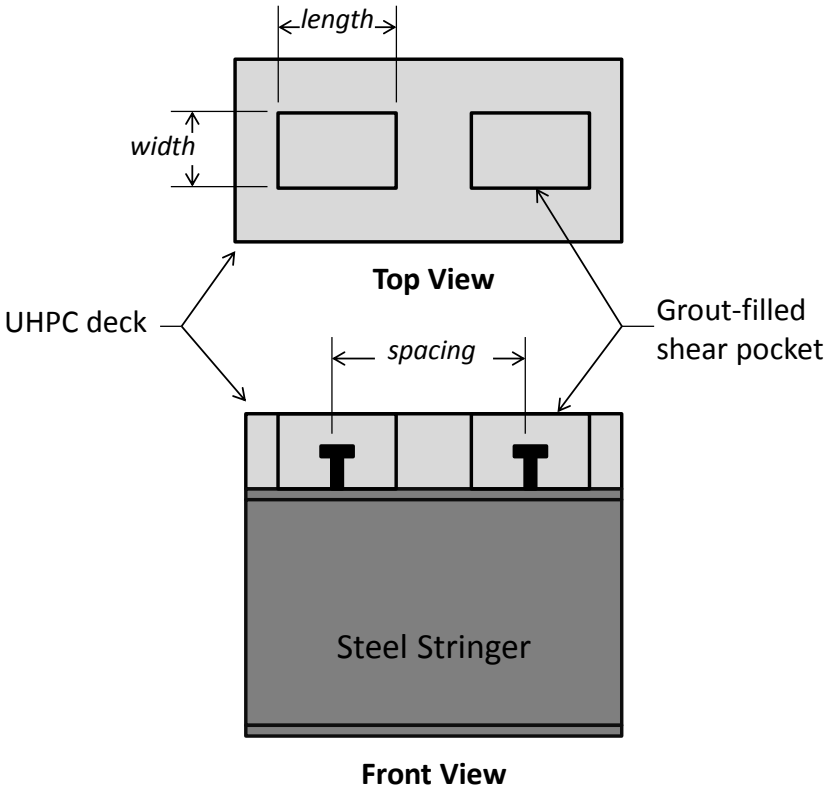

Figure 3-34: Portion of deck showing grout-filled shear pockets with shear studs to develop composite action between the UHPC deck and steel stringers.

3.7 Single Cell Units for Preliminary Testing

Prior to full-scale deck testing, preliminary testing was performed to investigate placement techniques and design assumptions. Single cells of the deck were constructed based on a preliminarily chosen design (Figure 3-35). The purposes for this testing were to investigate casting techniques and form construction of the deck, as well as to verify design assumptions. Placements techniques were investigated to ensure that UHPC would mix properly throughout the single cell. As mentioned previously, UHPC is reported to encounter problems when horizontal flow fronts intersect, resulting in a discontinuity in fiber alignment (Nachuk 2008). Since the deck design is composed of inter-connected individual cells, placing the deck right-side-up would inevitably result in the intersection of horizontal flow of UHPC; however, placing the deck upside-down would not result in this problem. Form construction was also investigated to ensure the most efficient forms are provided for both construction and removal during deck section construction.

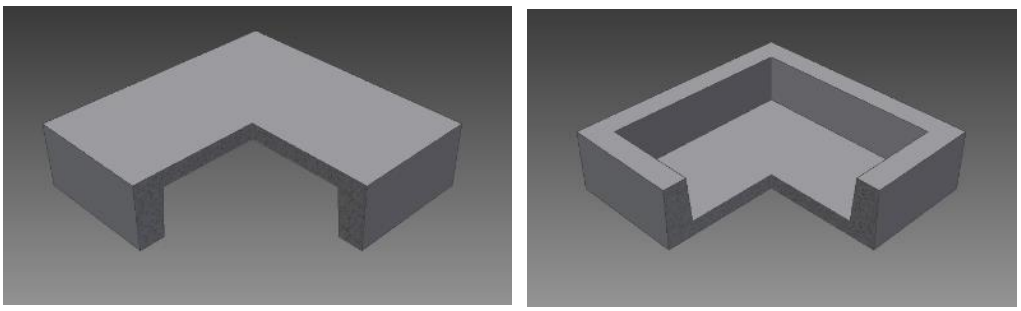

Figure 3-35: Three-quarter view of 8 in. deep single cell showing non-uniform web thickness and 2 in. flange thickness.

3.7.1 Construction of Single Cells

A total of three single cells were constructed based on a chosen deck design. The chosen design was a total depth of 8 in. It had webs spaced at 28 in. on center, a 2 in. thick flange, and the webs varied in thickness from 3 in. at the bottom to a thickness of 4 in. at the intersection with the flange (Figure 3-36).

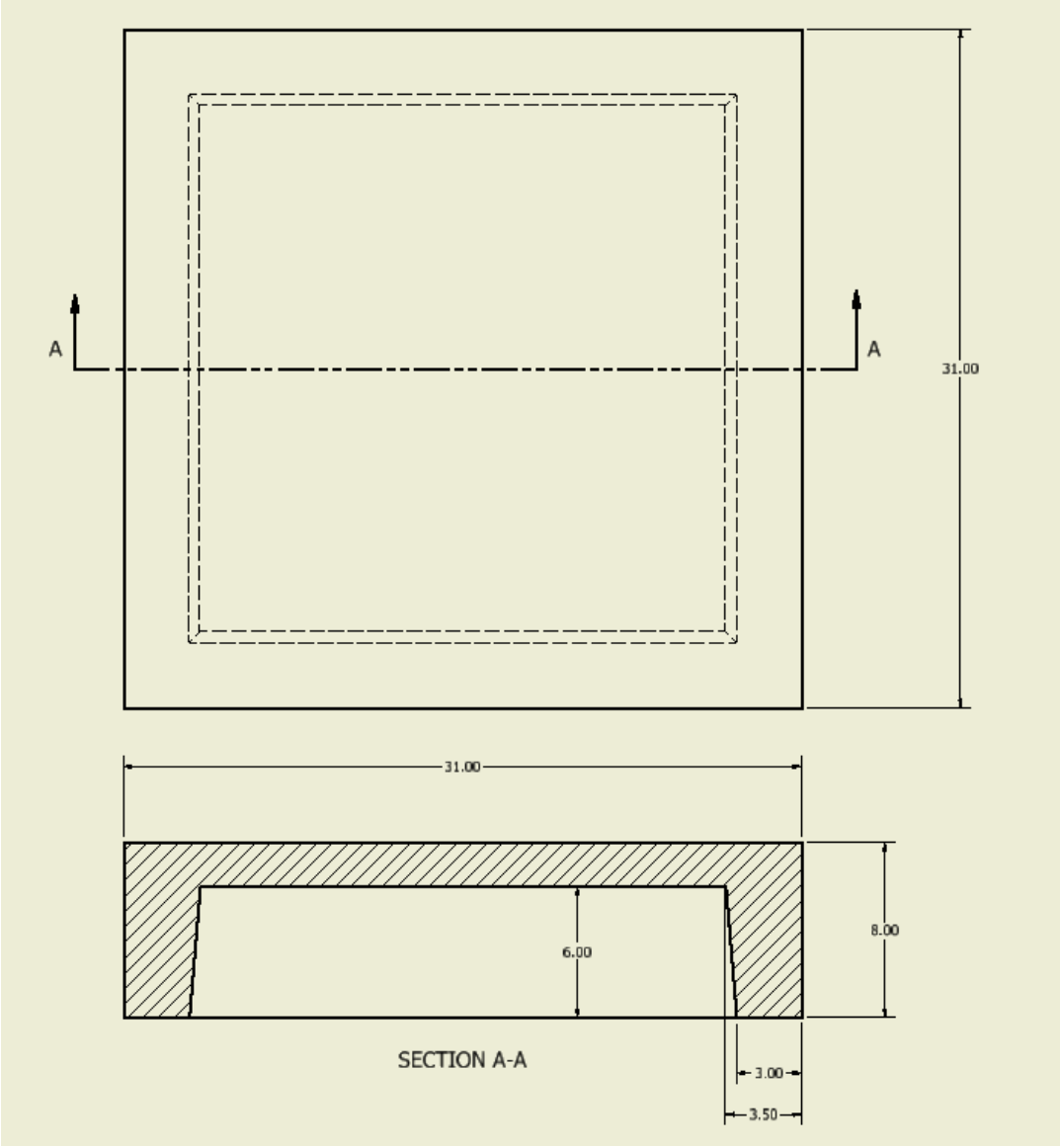

Figure 3-36: Single cells were built to the dimensions of an initial UHPC bridge deck design.

The forms for these cells were constructed using wood and expanded polystyrene foam. The epoxy-based spray paint, Rust-Oleum Appliance Epoxy, was applied to the surface of the wood to prevent moisture absorption. Forms were designed to be efficient during both construction and removal. The base and walls of the formwork were constructed using 0.75-in. plywood and 2x4 lumber; whereas, the center block-out to form the shape of the ribs was constructed using expanded polystyrene foam (Figure 3-37). For two of the three single cells, a thin layer of wall joint filler was applied to the surface of the expanded polystyrene foam before

being covered with a light layer of the epoxy spray paint. The joint filler was applied, allowed to dry, and sanded before painting. In some cases, additional joint filler was required to patch areas, and each patch was sanded before being painted. No special coating or preparation method was used to cover the foam in the third single cell. Joints were filled with a project foam adhesive to ensure leaking would not occur during placement.

Figure 3-37: Single cell formwork containing foam for top-side up placements.

Three different placement scenarios were investigated for the single cells. The first and second scenarios allowed the single cell to be placed top-side up, or right-side up. In these cases, the foam was attached to the bottom of the forms using project foam adhesive. The top surface of these cells would be the driving surface of the bridge deck.

In the first scenario, UHPC was placed in the center of one rib, or web, and allowed to flow around the "waffle" shape created by the foam block-out (Figure 3-38). UHPC flowed through both side ribs before intersecting near the center of the rib opposite the entrance point. UHPC was allowed to flow until the form was completely filled. No external or internal vibration was applied to the UHPC during placement.

Figure 3-38: UHPC was inserted into one rib for the side placement method (Photo by K. Halbe).

The second placement scenario allowed UHPC to flow from one corner while being formed top-side-up; the driving surface was on top. As UHPC was placed in one corner of the form, the material flowed around the "waffle" shape created by the foam block-out into the adjacent ribs (Figure 3-39). The UHPC intersected near the opposite corner of the point of entrance. This method was investigated to consider all conditions that could potentially occur during placement if UHPC were placed top-side-up and concrete flowed from corner to corner.

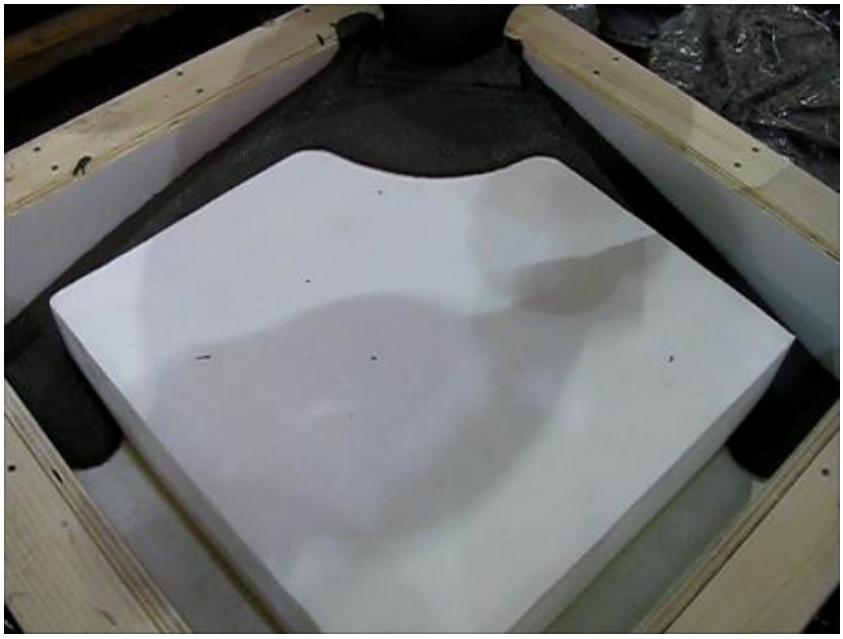

Figure 3-39: UHPC flowed through ribs in the corner placement method (Photo by K. Halbe).

The third method allowed the single cell to be placed upside down. The UHPC was placed into empty formwork, allowing the material to flow from one side to the other transversely; this method was similar to the placement method for a UHPC beam. The empty formwork was filled to a specified height of approximately 4.4 in., ensuring enough material would be placed to fill the entire waffle single cell shape. Then, the "waffle" form was pressed into the partially-filled formwork to form the shape of the cell and forming ribs on all four sides (Figure 3-40, Figure 3-41, and Figure 3-42). A frame was constructed to place the foam in the center of the box, and two steel beams were used to keep the foam and frame in place during initial setting. This upside down placement method was of particular interest because it was used for the first UHPC waffle slab bridge deck in the U.S. for the Wapello Country Bridge in Iowa (Aaleti et al. 2010).

Figure 3-40: UHPC was placed in an open form for the upside down placement (Photo by K. Halbe).

Figure 3-41: The frame was inserted into the form to create the ribs (Photo by K. Halbe).

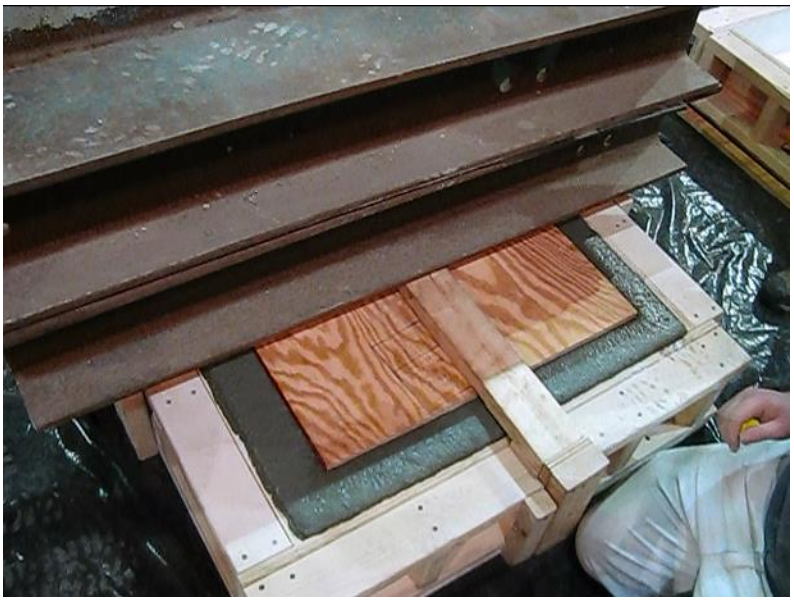

Figure 3-42: Steel beams were placed atop the frame to maintain constant pressure (Photo by K. Halbe).

After the UHPC was placed, the exposed area of the single cells was covered with plastic sheeting and allowed to cure for at least three days prior to form removal (Figure 3-43). The sides of the forms were removed quickly by removing the screws from the base of the form. The foam was removed using a hot knife to remove 3 in. deep sections at a time. The single cells were cured in ambient laboratory conditions prior to testing.

Figure 3-43: Exposed UHPC was covered with plastic sheeting to contain moisture.

Cylinders and cubes were placed alongside the singe cells to determine compressive strength, elastic modulus, and splitting tensile strength (Figure 3-44).

Figure 3-44: Cubes and cylinders were placed to characterize material properties.

3.7.2 Experimental Testing of Single Cells

In order to test quality of consolidation in a non-subjective manner, small beams were cut from the webs of the single cells and tested in third-point bending. First, the sides of the single cell were cut using a walk behind concrete saw (Figure 3-45). Then, a hand-operated concrete saw was used to cut each individual beam from the sides of the cell. Two beams of approximately 3 in. high were cut from the four sides of each single cell, allowing for a total of eight beams per single cell. The beams were approximately 16 in. long, where the center point of the beam corresponded with the center point of the single cell rib. Because the single cell had tapered sides for the interior cell block-out, the beams were not square in cross-section. However, the measured size was recorded for each individual beam in Appendix D.

Figure 3-45: A walk-behind concrete saw cut the webs from the single cell units.

The beams were loaded in a 4-point bending scenario (Figure 3-46). The overall span length of 12 in. was determined based on ASTM Standard C1609 (2006) for the *Standard Test Method for Flexural Performance of Fiber-Reinforced Concrete (Using Beam With Third-Point Loading)*. For each beam, a cracking load and ultimate load were determined to compare tensile strength and ultimate performance post-cracking. For these tests, a beam with a higher flexural capacity was assumed to indicate that the placement technique was more effective in that location. Because improved performance was hypothesized to be affected by fiber orientation and consolidation, a visual investigation was also used to consider both factors.

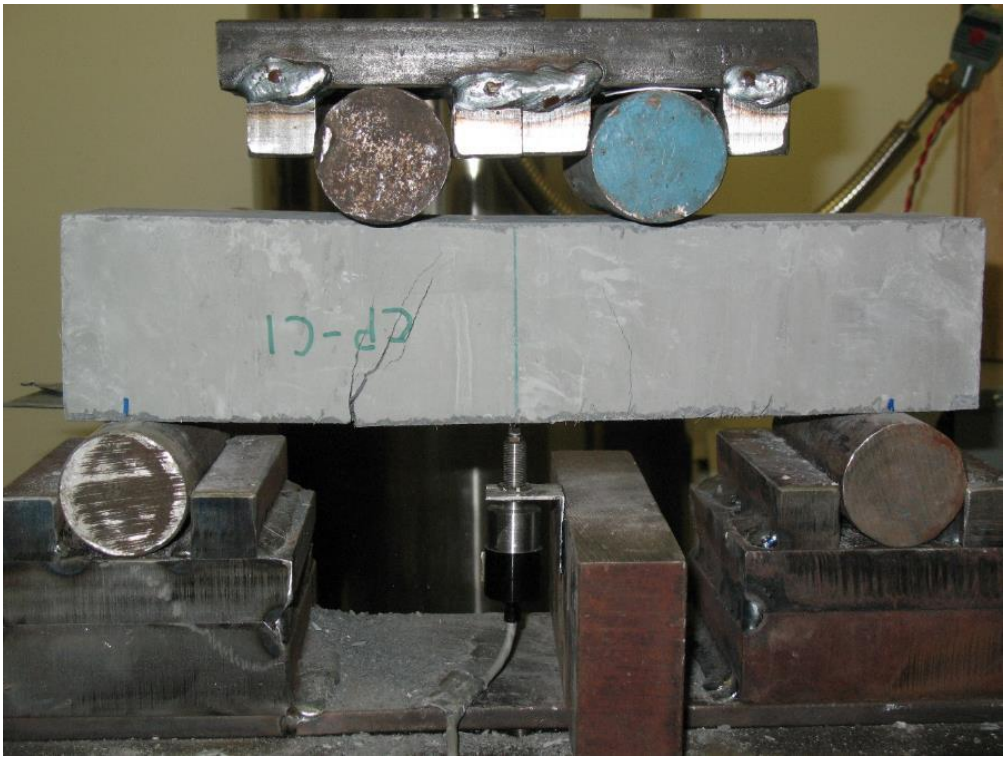

Figure 3-46: Third-point bending test for beams cut from single cells.

3.7.3 Visual Investigation of Single Cells

In addition to experimental testing, a visual investigation was executed to examine the number of fibers bridging cracks and the orientation of fibers at the UHPC intersection points compared to other regions of the single cell. The visual examination was performed on the small beams following flexure testing to evaluate fiber orientation and overall consolidation. This information was used to determine whether the casting technique was effective at providing an adequate amount of fibers in a preferred orientation. This could also indicate whether fiber settling might have occurred during placement, resulting in an unbalanced concentration of fibers throughout the cross section. Because this investigation was partially subjective, more focus was placed on the experimental test results for evaluating the single cells.

3.8 Deck Section Construction and Testing

Finally, a portion of the design bridge deck was constructed and tested to evaluate design parameters and placement methods. A single unit T-shape section was constructed to compare with the AASHTO (2012) equivalent strip design assumption (Figure 3-47). During this investigation, transfer length of prestressing steel reinforcement and placement procedures were also investigated. The upside down and right-side up placement techniques, as previously discussed for single cell units, were each used to place a deck section.

Figure 3-47: Deck sections were constructed and experimentally tested.

3.8.1 Construction of Deck Section

The deck sections were composed of a single web in the transverse direction, six ribs in the longitudinal direction, and two shear pockets to connect with steel girders (Figure 3-47). The longitudinal and transverse ribs formed the waffle shape. Similar to the single cells, wooden formwork was constructed and painted with Rust-Oleum Appliance Epoxy spray paint to prevent moisture absorption. Foam was used to block out the individual cell shapes.

The wooden formwork was used to create the exterior walls and base, outlining the overall width and length of the deck section (Figure 3-48). The walls of the wooden form were constructed 0.25 in. deeper than the 8 in. depth of the intended deck design. This alteration was integrated to account for shrinkage as observed in single cells. Standard 2x4 lumber sections and 0.75 in. thick plywood were used to construct the walls of the form. Holes were drilled in the two 18 in. wide sections to allow placement of prestressing steel. A plywood base was elevated

using 2x4 lumber to align the holes with the stressing abutments, and the walls were screwed to the plywood base.

Figure 3-48: Formwork was constructed using 2x4 lumber and 0.75 in. plywood.

Steel reinforcing bars were placed in the ribs along the longitudinal direction to simulate distribution reinforcement. Although the UHPC contained discrete steel fiber reinforcement throughout the cross-section, two No. 3 reinforcing bars were used as additional distribution reinforcement. Although the location of steel reinforcement was consistent for both deck sections, the methods used to position reinforcement differed.

Foam was used in both the upside down and right-side up deck sections to block out the individual cells, and the method for foam placement was dependent on the placement method. In both cases, 6 in. deep foam sections were cut to size using a vertical band saw rotated at an angle of 4 degrees. Although the joint filler material made foam removal easier than using bare foam in the single cell units, bare foam was used in the deck sections due to the long process involved with applying the joint filler material. The long process involved for application, sanding, and painting made this special coating less effective overall.

The following two sections describe specific formwork alterations and placement procedures as related to the two different deck sections. Prestressing procedures are described in Section 3.8.2 .

3.8.1.1 *Placing the Upside Down Deck Section (DS-1)*

The upside down deck section, DS-1, was constructed to imitate methods previously used for UHPC ribbed slabs. Similar to the upside down single cell unit, UHPC was added up to a predetermined height before the foam was lowered into place to form the individual cells. Prior to UHPC placement, two No. 3 reinforcing bars were placed at the center of each rib location to serve as distribution steel. The two bars were stacked in the rib locations. Because the foam would be lowered into place for DS-1, very limited space was available to place these bars. Additionally, the locations of prestressing steel and the No. 3 bars required that the bars be placed properly. The No. 3 bars were placed on chairs at the center location of each rib (Figure 3-49). The bottom layer of chairs was epoxied to the bottom of the formwork to prevent movement during placement. A second layer of chairs was assembled atop the lower bar to position it at the proper level. Continuous chair supports could not be provided in the deck section due to the path of the foam segments. The top layer of chairs was cut to size before being tied and glued to the bottom reinforcing bar.

Figure 3-49: Reinforcing bars were placed using chairs in DS-1.

After mixing, UHPC was placed into one end of the base form and allowed to flow to the opposite end. No vibration was applied. UHPC filled the form to a height of 4.1 in. to ensure the proper amount of UHPC was placed for the ribs. A frame was constructed to position the foam segments into the proper location (Figure 3-50). The foam was adhered to plywood sheets using foam project adhesive, and wooden guides were installed to the base formwork to ensure proper placement of the frame. The foam was pressed into position using the frame to form the longitudinal ribs and transverse web of the deck section (Figure 3-51). The frame was clamped to the base formwork, and two steel beams were placed on top of the frame to prevent uplift during initial set (Figure 3-52). Once the frame placement was finalized, plastic sheeting was placed over the exposed UHPC to prevent moisture loss while curing. Cylinders and cubes were placed alongside the deck section to determine compressive strength, modulus of elasticity, and splitting tensile strength of the UHPC.

Figure 3-50: Foam was connected to a wooden frame for the upside down placement of DS-1.

Figure 3-51: Foam attached to a frame was placed into DS-1 to create the ribs.

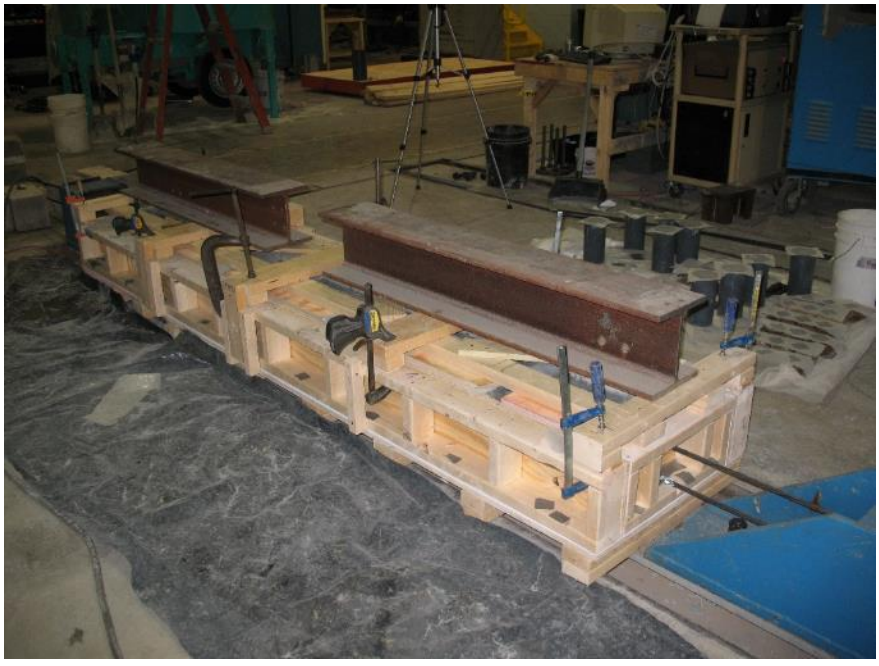

Figure 3-52: The frame was clamped and two steel beams provided additional force along the center section to prevent uplift.

After 48 hours, the sides of the base formwork were detached by removing screws from the base and by using a crowbar to pry the forms from the UHPC. A flat metal scraper was used to remove foam in 4 in. square sections. The deck section was cured in ambient laboratory conditions until testing.

3.8.1.2 *Placing the Right-side Up Deck Section (DS-2)*

The right-side up deck section, DS-2, was constructed because the single cells indicated that tensile capacity was increased for sections placed in this orientation. The base formwork was the same as that used for DS-1; however, the holes for prestressing steel were at different heights due to the change in orientation. Therefore, a new end form was constructed for DS-2 to account for the additional 0.25 in. height necessary for expected shrinkage. To form DS-2, the foam was placed directly into the base form to displace UHPC to form the longitudinal ribs and transverse web (Figure 3-53). Chairs were used to place the first reinforcing bar for distribution reinforcement; these chairs were not glued to the form because a longer chair base could be used to prevent movement during placement (Figure 3-54). Thin metal rods were placed in the foam sections to locate the second layer of distribution reinforcement. The distribution reinforcement was then tied to the chairs and the thin rods for stabilization.

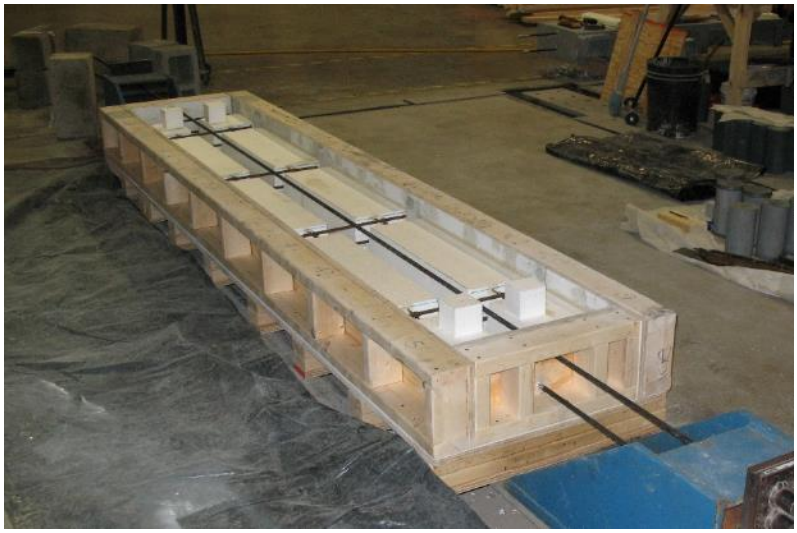

Figure 3-53: Foam was placed directly into the form for DS-2.

(a) (b)

Figure 3-54: Reinforcing bars were placed using thin steel rods between foam sections (a) and using bent chairs near the ends of the formwork (b).

After mixing, UHPC was placed into one end of the base form and allowed to flow to the opposite end. No vibration was applied. The form was filled completely and plastic sheeting was used to cover the exposed UHPC during curing. Cylinders and cubes were placed alongside DS-2 to determine compressive strength, modulus of elasticity, and splitting tensile strength of the UHPC. After 48 hours, the sides of the base form were removed and foam removal began. Only the two center sections of foam were removed prior to cutting the prestressing steel. It was assumed that the foam would not cause any negative impact on measuring surface displacements to determine transfer length and effective prestress. The UHPC was cured in ambient laboratory conditions until testing.

3.8.2 Prestressing Steel for Deck Sections

Prestressing steel was placed through holes drilled in the formwork ends at the desired locations. Steel abutments anchored the strands during tensioning. A load cell was placed at the dead end to measure the force in the strand, and a chuck secured the prestressing strand (Figure 3-55). The steel was stressed using a hydraulic jack and a hand pump for manual control. Each strand was stressed at least twice due to the limited stroke distance of the hydraulic jack. After the jack was first fully extended, the chuck was seated on the strand before the jack was released

and adjusted for the second pull (Figure 3-56). Aluminum spacers were later used between the chuck and the abutment to avoid re-seating the chuck with each additional pull. Re-seating the chuck would produce additional indentations in the strand, possibly leading to a weak section. By seating the chuck once, the strand only has one set of "bite" marks from the gripping mechanism of the chuck. Each strand was stressed to a desired force of approximately 30 kips to account for expected stress losses. After tensioning the strands, construction caulk was used to fill the space between the prestressing tendon and the wooden formwork to prevent leaking.

Figure 3-55: A load cell was placed between the steel abutment and a chuck.

Figure 3-56: Prestressing steel was tensioned using a hydraulic cylinder while chucks and spacers anchored the tensioned steel.

After the UHPC deck section had cured for one week, prestressing steel was cut using an acetylene torch (Figure 3-57). In actuality, the prestressing steel was not cut instantaneously using the torch. Rather, the strands were heated slowly, allowing each individual strand to yield to failure. For each deck section, the top most exposed strand was released, first. In DS-1, the bottom steel was released first because it was located on the top during placement. In DS-2, the top steel was released first because it was located on the top during placement. For both DS-1 and DS-2, the steel was cut on the live end of the deck section.

Figure 3-57: Prestressing steel was cut by heating strands using an acetylene torch.

3.8.3 Transfer Length and Effective Prestress Determination

In order to determine transfer length of prestressing strands in UHPC, two different methods were attempted for the deck sections: DEMEC points and BDI strain gages. For DS-1, DEMEC points were applied along the centerline of the top surface using a basic super glue (Figure 3-58). For DS-1, the top surface was actually the underside of the section. The gages were set at a distance of 1.97 in. (50 mm) using a set bar. A total of 48 DEMEC points were installed to measure surface displacements along each end of the beam. At least three readings were taken prior to cutting the prestressing steel, and three readings were taken after the prestressing steel was released. The three readings were averaged, and the difference between the two readings was used to determine the strain over a specified gage length of 3.94 in. (100 mm).

Figure 3-58: DEMEC points were applied to the exposed surface along the centerline of the web.

Unfortunately, the Wittemore strain gage reader (Figure 3-59) was very unreliable, and confidence was lost in results from this method due to the inconsistency of data readings. Poor data readings could have been attributed to the gage reader or to the rough top surface of the UHPC. Although some measures were taken to smooth the surface, including grinding and

scraping, the surface was still extremely uneven. Regardless of the reason for faulty readings, BDI strain transducers were used for DS-2 to avoid a similar problem.

Figure 3-59: The Wittemore strain gage reader used to measure DEMEC points.

BDI strain transducers (BDI gages) were placed along the top surface of DS-2 to determine surface strain changes after the prestressing steel was cut. Data acquisition utilized the BDI Wireless Structural Testing System (Figure 3-60). The BDI gages had an effective gage length of 3 in. They were installed surrounding the center line of the top surface of the deck section; for DS-2, this surface was actually the top riding surface of the UHPC deck section. A total of 11 gages were used to determine transfer length on the dead end, and a total of 13 gages were used to determine the transfer length on the live end (Figure 3-61). Six BDI gages were used at the center section to estimate the effective prestress force in the section (Figure 3-62). The gages were applied with fast-setting adhesive. The BDI wireless system collected initial readings prior to cutting the steel, and the system continued to collect data from the gages while the steel was cut. After the steel was cut, the deck section was lifted from the base form to ensure no additional friction was preventing the deck section from compressing due to the prestress force transfer.

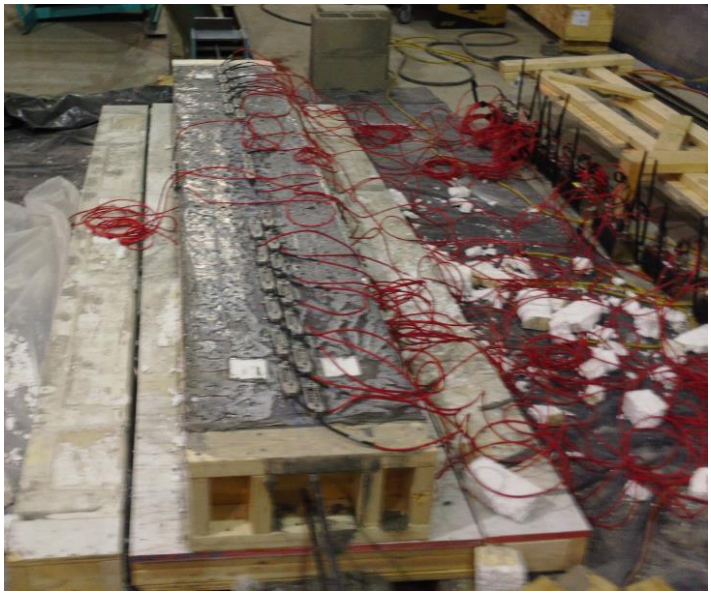

Figure 3-60: BDI gages were attached to DS-2 and measured using the BDI Wireless Structural Testing System as data acquisition.

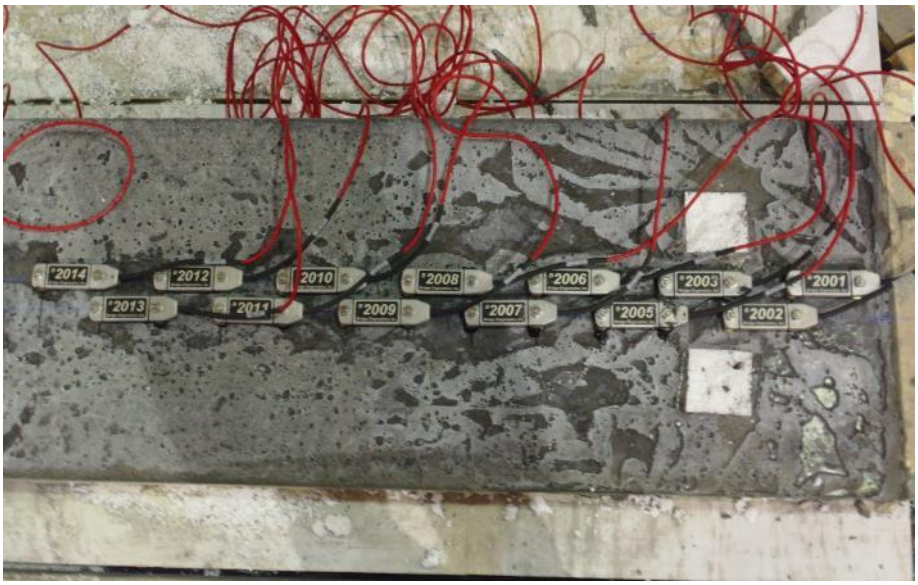

Figure 3-61: BDI gages were placed on the dead and live ends to determine transfer length of the prestressing steel.

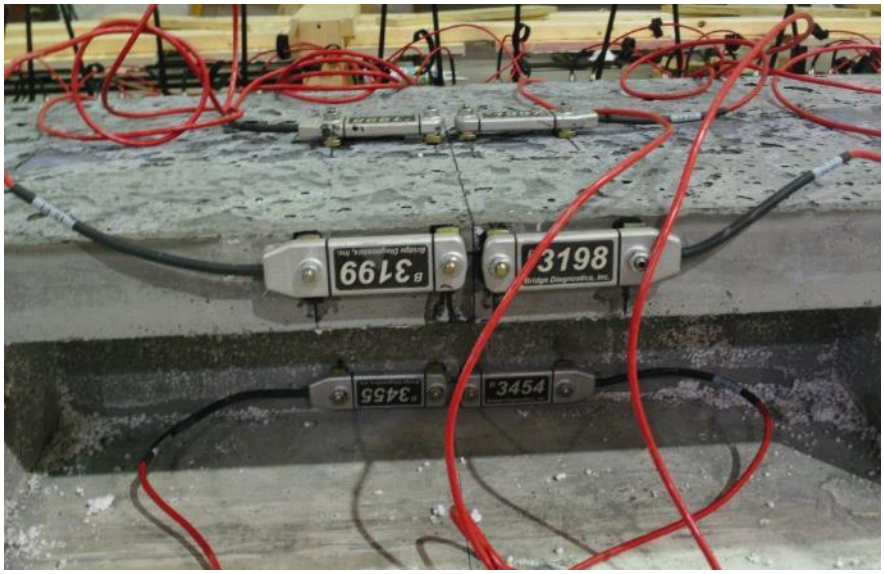

Figure 3-62: BDI gages were placed at the middle of DS-2 to determine the effective prestressing force.

3.8.4 Grout-filled Shear Connections

Shear studs, 0.75 in. diameter by 4 in. high, were welded to a 1 in. thick steel place to simulate a fully composite shear connection with a W36x160 steel girder. The studs were welded such that three studs were spaced at 9 in. along the longitudinal direction (Figure 3-63). This was actually not consistent with the original shear connection design, where three studs were specified to be spaced at 6 in.; however, limited plate dimensions led to the 9 in. spacing alteration in the built connection. The plate and studs were then aligned with the deck section shear pockets in preparation for the grout fill procedure (Figure 3-64).

Figure 3-63: Shear studs were welded to a 1 in. thick steel plate (Photo by M. Maguire).

Figure 3-64: The plates and studs were aligned with the deck section shear pockets.

To enclose the exposed shear pockets on the deck section, plywood was clamped to the sides of the deck section (Figure 3-65). A bottom piece was first clamped, allowing a small ½ in. gap to view consolidation and allow air to adequately escape while consolidating. Once the pocket was filled with grout to the top of this bottom piece, the top piece was clamped to fully enclose the pocket.

Figure 3-65: The top plywood form was added after UHPC filled the shear pocket.

Grout was mixed using the small capacity mixer capable of up to 2 cubic feet of material. The mix design complied with that provided by the VDOT (2007) *Roads and Bridges Specifications* using Grade C sand and Type I/II cement (Table 3-10,Table 3-11). Approximately 1 cubic foot of material was mixed at a time. First, the aggregate was added to the mixer, followed by the cement. The dry ingredients were mixed for several minutes before the water was added. Water was added slowly until a desired consistency was achieved. Although a target flow was not determined, the desired consistency was considered to be easily consolidated without flowing like water; some stiffness was desired in the mix. The mixture was allowed to thoroughly mix before being consolidated in the grout pockets.

The grout pockets were filled through a 3 in. square opening above the shear pocket and consolidated using a 0.625 in. tamping rod (Figure 3-66). The consolidation process did not take place in a specified number of lifts to fill the pocket; rather, several scoops of grout were placed into the pocket hole before frequent consolidation took place to make certain the hole was completely filled. Once filled, the top of the shear pocket opening was troweled. After 30 minutes, the shear pocket opening was examined for early onset shrinkage; additional grout and consolidation was used to account for this at the shear pocket opening. Plastic was used to cover the shear pocket opening while curing. Cube specimens were placed alongside the grout pockets to determine compressive strength; cube specimens were also covered with plastic sheeting while curing. Forms were removed after three days.

Figure 3-66: Grout-filled shear pockets were consolidated using a tamping rod.

3.8.5 Deck Section Experimental Testing

The deck section was tested on a simple span of 8 ft. The deck section was loaded in stages using a hydraulic ram positioned to produce flexure and shear failure types. Cracks were marked to track the progression of failure. The deck section was instrumented to collect information on deflection and strain

A steel frame was constructed on the laboratory strong floor to test the deck sections (Figure 3-67). The steel frame was composed of W12x87 columns and C12x25 sections spanning between the columns to support the hydraulic cylinder loading apparatus. The deck section was supported on pin and roller supports supported by two W21x62 beams (Figure 3-68). A 50 ton hydraulic cylinder controlled by an electric pump was used to apply force to the deck section.

Figure 3-67: A steel frame was constructed to test the deck sections.

(a) **(b)**

Figure 3-68: Roller (a) and pin (b) supports were used to test the deck sections.

3.8.5.1 *Load Placement and Instrumentation*

Two single point, static load tests were performed on each deck section. DS-1 was first tested by placing the load at 30 in. from one support of the deck section (Figure 3-69). For Test 2 of DS-1, the load was placed 18 in. from the opposite support of the deck section. This was the closest distance the column supporting the test frame could be placed to the beam supporting the bridge deck section due to connection constraints on the laboratory strong floor. DS-2 was tested under the same conditions. However, DS-2 was first tested at 18 in. from the support, and the load was placed at 30 in. from the opposite end for Test 2 of DS-2.

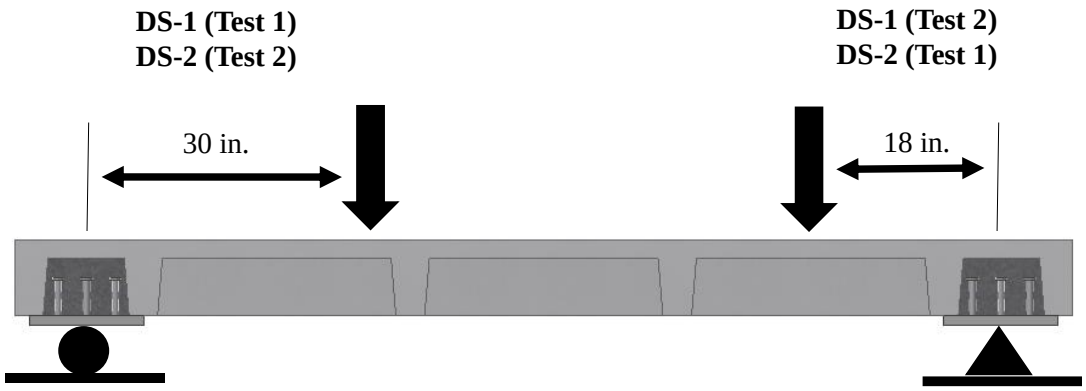

Figure 3-69: Deck section test summary.

An 8 in. square rubber bearing pad was placed on the deck so that the center of the pad was located directly beneath the load application. A series of 8 in. square steel plates were stacked above the bearing pad (Figure 3-70). The hydraulic cylinder was extended to bear on a circular swivel plate placed atop the series of steel plates to transfer the force evenly. The 50 ton canister load cell was placed between the hydraulic cylinder and the support block between the steel channels in the frame. Two steel plates were also added between the cylinder and support block to fill additional space.

Figure 3-70: An 8 in. square bearing pad and steel plates provided pressure.

Cable-extension transducers (CETs) were used to measure deflections during testing (Figure 3-71). Two CETs were located at a distance of 30 in. from the center of each support, such that one CET would be located directly below load application. The third CET was located below the center of the span length. The final CET was located directly below the strain gage rosette, 8 in. from the face of the 1 in. thick steel plate.

Figure 3-71: Four CETs determined deflection at critical locations.

A section of the web was instrumented with a 0.5 in. strain gage rectangular rosette to determine localized principal stresses in a region expected to experience biaxial shear stresses (Figure 3-72). For DS-1, the strain gage rosette was located 8 in. from the face of the 1 in. thick plate for the simulated girder shear connection. It was also centered at 4.25 in. measured from the bottom of the flange. For DS-2, the rosette was located 6 in. from the face of the support and 3.75 in. from the bottom of the flange. Knowing the orientation of the gages, the collected strain gage readings were used to determine principal strains. Using these values in combination with known material properties, the strains were transformed into principal stresses. On the opposite side of the web, images were captured to be analyzed using DIC to determine surface strains (Figure 3-73). As in previous DIC analyses, a base layer of white spray paint was first applied to the concrete, and speckling was accomplished using a black spray paint. Results from the strain gage rosette and the DIC were compared. Image data was collected at 1 Hz using the LabVIEW system; all other data acquisition took place at a rate of 10 Hz using the Vishay System 5000.

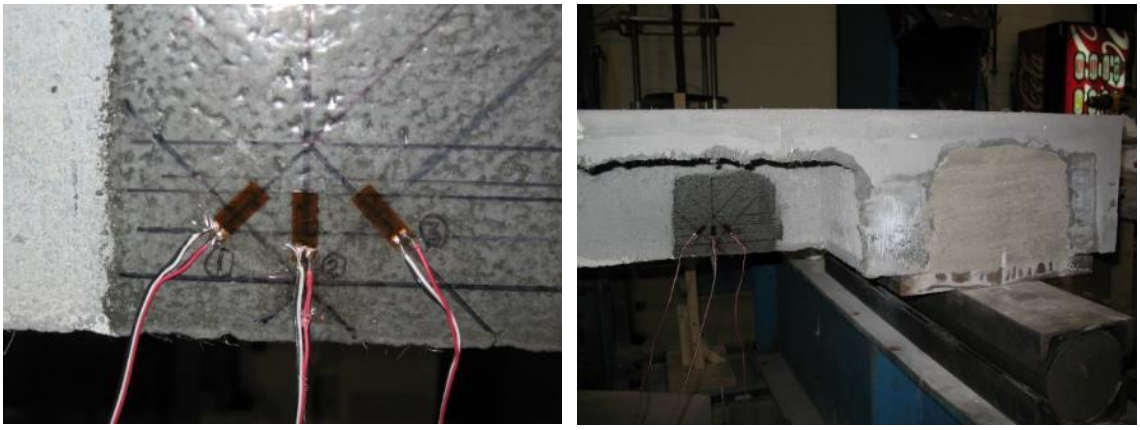

Figure 3-72: A strain gage rosette was used to determine principal stresses at a distance of 8 in. from the face of the 1 in. thick plate.

Figure 3-73: A section of the web 8 in. from the face of the 1 in. thick plate was speckled with spray paints for DIC opposite the strain gage rosette.

3.8.5.2 *Test Protocol*

Load was applied in increments of 500 lbs distributed over the 8 in. square patch created by the bearing pad and steel plates. Once cracking occurred, load was increased by increments of 500 lbs, and cracks were marked for every 1000 lbs of increased load. The test was ended when the plotted load versus displacement curve began to flatten or when crack widths exceeded 0.25 in.

Chapter 4: Results of Preliminary Material Property Characterization

Results presented in this chapter were from the preliminary material property characterization. Results are based on mixing a single batch of UHPC using the IMER Mortarman mixer, and all UHPC was subjected to an untreated curing regime. Additional material property data and observations are included in later chapters, corresponding to each project phase.

4.1 Untreated Material Property Characterization

4.1.1 Mixing and Placement Observations

The mixing procedure described by Graybeal (2006a) was used for the untreated material property characterization. The mixing process took approximately 1 hour to complete from start to finish. As the material was mixed, it transformed from a powder to small balls of material. These balls grew in size until they merged together to form a thick paste. The mixer was stopped briefly to scrape dry material along the exterior and interior of the drum. Once the material was sufficiently moistened, it resembled a paste. Then, fibers were added and mixed for two minutes. Once the mixing process was complete, the mixer was stopped, allowing the UHPC to settle in the drum. The UHPC settled to fill the bottom surface of the drum completely, revealing the self-consolidating nature of the material.

The flow test results (Table 4-1) indicated that the UHPC required minimal vibration. For this reason, the specimens were placed on the vibrating table for approximately 3 to 5 seconds, depending on the size of the specimen (Table 4-2). Since these specimens were untreated, they were covered with plastic and allowed to cure in their forms for 4 days before removal.

Table 4-1: Flow test results of untreated UHPC

Measurement	No.	Diameter (in.)	Average (in.)
Initial	1	7.5	7.8
	2	7.75	
	3	8.25	
After 20 drops	1	9	9.1
	2	9	
	3	9.25	

Table 4-2: Vibration time for untreated UHPC

Specimen	Vibration Time (sec)
Cube – 2x2x2 in.	3
AASHTO (2004) Briquette	3
Cylinder – 4 in. dia. x 8 in. high	5
Prism – 3x4x16 in.	5
Small Panel – 12x12x1 in.	5
Small Panel – 14x14x1 in.	5

Once compression and tensile testing was completed, specimens were further evaluated for any placement problems. It was shown by a split-cylinder compression specimen, that fibers were seemingly oriented in a circular pattern at the center of the 4 in. diameter by 8 in. high cylinder (Figure 4-1). This orientation is hypothesized to be a result of the placement of the UHPC. The circular pattern of fibers may have been caused by folding of the UHPC during placement (Figure 4-2). As the UHPC was placed, UHPC was dropped into the mold along an irregular path, as opposed to dropping in a straight path into the center of the mold. This resulted in folding of the UHPC material during placement.

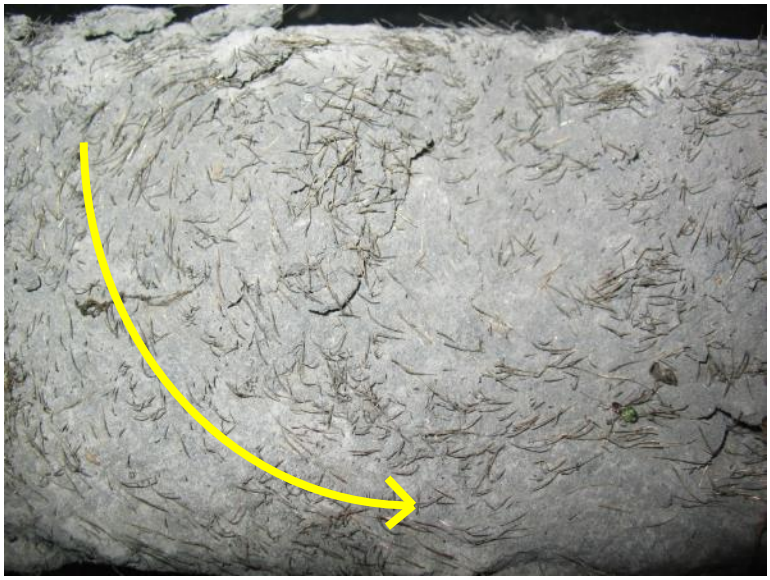

Figure 4-1: Circular fiber orientation in cylinder specimen.

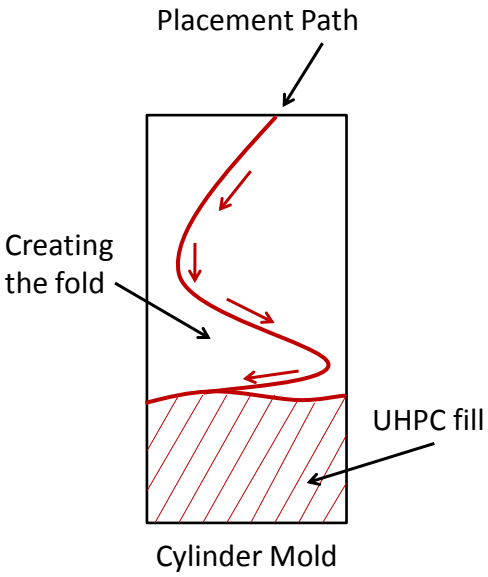

Figure 4-2: Folds in UHPC may have contributed to circular fiber orientation.

Several briquette tension specimens also revealed an irregularity with casting procedures. After the specimens had been tested, the inconsistent fiber concentration through the thickness of the specimen was revealed. It was evident by the high concentration of fibers on the bottom casting face of the briquette that too much vibration had possibly been applied, causing the fibers to sink to the bottom of the mold (Figure 4-3).

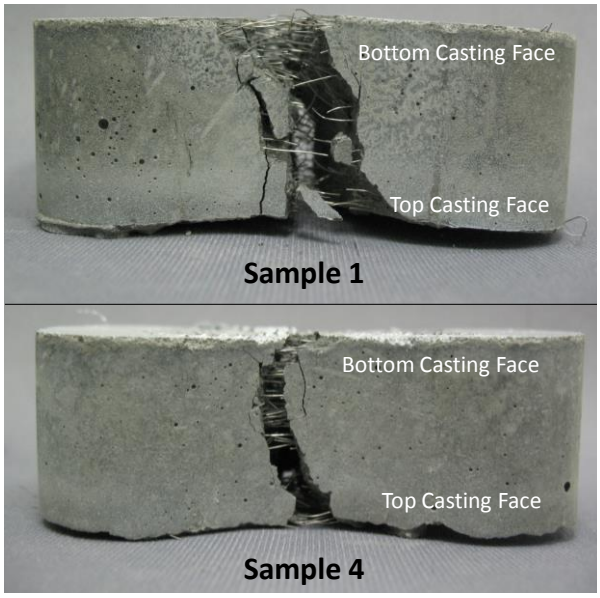

Figure 4-3: High fiber concentration at bottom casting face.

4.1.2 Compressive Strength

Two in. cubes were used to determine the compression strength of the UHPC. Compressive strengths were monitored on the day of release and every 7 days from the day of casting up to 28 days (Table 4-3). A compressive strength at 104 days was also recorded because biaxial tests were performed when the UHPC had reached this age. Three cubes were tested for each day, and an average of these values was used to represent the UHPC compressive strength. The standard deviation is also shown to display the level of consistency in the data. The compressive strength data was shown to be consistently higher than results shown by Graybeal (2006a) by more than 20 percent (Table 4-4). Graybeal (2006a) used an accelerating agent in the UHPC mix design. For this reason, specimens were released within 24 hours of casting. Since the specimens in this study remained in the molds for 4 days, the internal moisture content remained higher for a longer period of time, causing more cement to hydrate while in the molds. In an alternate study on compressive strength compared with age at demolding, Graybeal (2006a) observed the compressive strength of untreated UHPC to increase by 25 to 30 percent when demolded after 47 hours, as opposed to that demolded after 28 hours. Therefore, the later release time likely attributed to the higher compressive strengths observed in this study.

Table 4-3: Compressive strength of untreated UHPC

	Sample f_c (ksi)				
Day	**1**	**2**	**3**	**Average f_c (ksi)**	**Standard Deviation**
4	14.9	13.8	14.9	14.5	0.65
7	18.1	18.5	19.4	18.7	0.64
14	20.6	18.4	19.4	19.5	1.11
21	20.9	20.6	19.5	20.3	0.73
28	20.5	20.8	21.3	20.8	0.38
104	24.3	23.8	26.8	24.9	1.61

Table 4-4: Tested compressive strength compared to Graybeal (2006a)

Day	**Tested f_c (ksi)**	**Graybeal (2006a) f_c (ksi)**	**Difference (%)**
7	18.7	12.9	44.6
14	19.5	16.0	21.9
28	20.8	17.3	20.7

4.1.3 Modulus of Elasticity and Poisson's Ratio

The modulus of elasticity and Poisson's ratio were determined simultaneously by testing 4 in. diameter by 8 in. high cylinders. For initial testing of untreated UHPC, this testing occurred when the concrete was approximately 150 days old, which was considered a mature state for the concrete. The ends of the cylinders were capped with sulphur to create an even contact surface with the universal testing machine (UTM) platens. The compressometer and extensometer were attached to the UHPC cylinder according to the ASTM C469 specification. The resultant modulus of elasticity and Poisson's ratio from two tests are shown (Table 4-5).

Table 4-5: Modulus of Elasticity and Poisson's Ratio of Untreated UHPC

Sample	1	2	Average	Standard Deviation
Age (days)	152	158	-	-
Modulus of Elasticity (ksi)	8280	8240	8260	27
Poisson's Ratio	0.170	0.199	0.180	0.021

The Poisson's ratio was fairly consistent with results by Graybeal (2006a) for steam treated UHPC; however, the modulus of elasticity exceeded recorded results for untreated UHPC. Graybeal (2006a) determined the Poisson's ratio for steam treated UHPC to be approximately 0.199 and the modulus of elasticity for untreated UHPC to be approximately 6200 ksi. A Poisson's ratio for untreated UHPC was not recorded by Graybeal (2006a). The higher modulus of elasticity was consistent with the higher compressive strength values obtained during this initials materials characterization study. The increased values could be attributed to the additional time the specimens remained in their forms before air curing. The impermeable forms contained moisture, leading to better conditions for hydration to occur.

Based on observations from this testing, it was suggested that the top surface of the cylinders from casting be sawn off the cylinder in future testing. The sulphur caps were effective for the majority of the cylinders tested; however, some sulphur caps cracked or broke apart early in the loading process. For these cylinders, new caps were cast on the ends until the loading process could be completed to obtain the modulus of elasticity and Poisson's ratio values. For more effective testing, the ends should be ground down or sawn to provide a smooth surface for sulphur capping.

4.1.4 Testing for Tensile Strength

4.1.4.1 *Split Cylinder Tensile Strength*

Split cylinder testing was performed to determine the tensile strength gain of UHPC (Table 4-6). Split tensile strength was determined at 7 days, 14 days, and at a mature age of 196 days. Three cylinders were used for 7 and 14 days. Due to equipment problems, split tensile strength was not measured at 21 and 28 days. Only two cylinders were used at 196 days because of availability. For this test, only one cylinder split completely apart. All others were held together by fiber bridging at the completion of the tests.

Table 4-6: Split Tensile Strength of Untreated UHPC

	Sample f_t (ksi)				
Age (days)	**1**	**2**	**3**	**Standard Deviation (ksi)**	**Average f_t (ksi)**
7	2.24	2.43	2.37	0.10	2.35
14	2.63	3.03	2.73	0.21	2.79
196	3.49	3.38	-	0.07	3.44

4.1.4.2 *Briquet Tensile Strength*

Briquets were also tested to determine tensile strength of UHPC (Table 4-7). Because the cross-section is 1 in. square, the apparent tensile strength in ksi is equivalent to the load in kips. Samples were loaded at a rate of 0.05 in. per minute. Graybeal (2006a) previously used a load rate of 0.06 in. per minute. Results show that the cracking loads were more than 90% of the peak loads, indicating that the UHPC briquets had some post-cracking tensile strength due to fiber contribution once the specimen cracked.

Table 4-7: Briquet Tensile Strength of Untreated UHPC

Sample	**Age (days)**	**Cracking Load (k)**	**Peak Load (k)**
1	431	1.51	1.58
2	481	1.13	1.20
3	500	1.60	1.60
4	575	1.30	1.41
Standard Deviation		0.21	0.18
Average		1.39	1.45

By evaluating the load versus time curves (Figure 4-4), the post-cracking tensile behavior can be shown more clearly. Once the peak load had been reached, the specimens were able to continue to resist load. For those specimens loaded at 0.05 in. per minute, the load resistance decreased at a rate of 6.75 lb per second. From visual inspection of the specimen during testing, this resistance was considered to be highly dependent on the pull-out strength of the fibers in the concrete matrix.

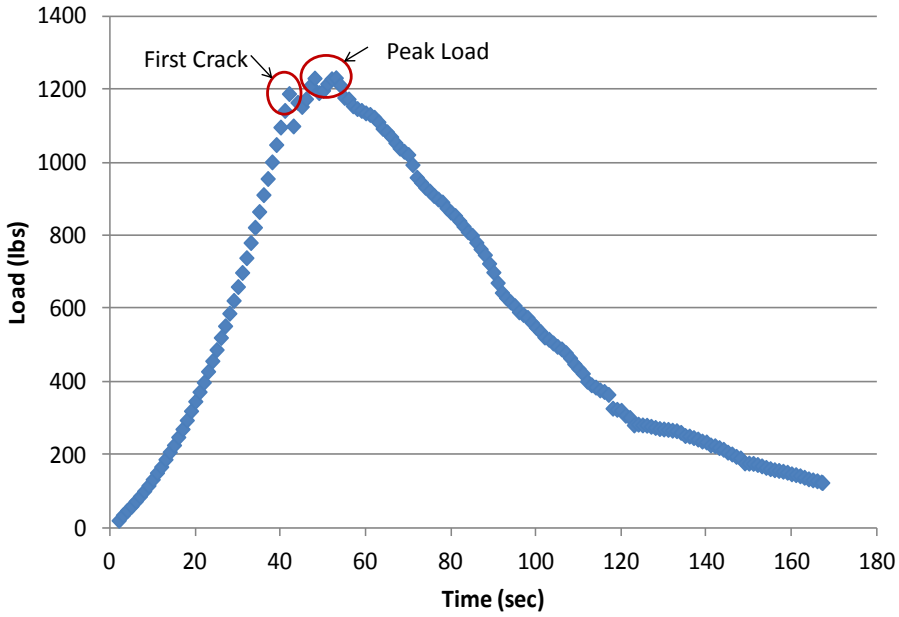

Figure 4-4: Typical briquette tension load versus time relationship (Specimen 1).

4.1.4.3 *Flexure Prism Tensile Strength*

Flexure prism tests were performed as the final comparison test for tensile strength. The tensile strength of the UHPC prism was then determined using Equation (4-1) .

$$f_{t,flex} = \frac{PL}{BD^2} \qquad (4\text{-}1)$$

Where ,

$f_{t,flex}$ = tensile stress of flexure prism (ksi)

P = load (kips)

L = span length (in.)

B = average width of prism (in.)

D = average depth of prism (in.)

Results show that the average cracking load was 5.58 kips, and the average peak load was 9.53 kips (Table 4-8). The cracking point was determined by a sudden drop in load during testing. For samples 1 and 8, a cracking point was not detected prior to the peak load. Therefore, the average cracking load was determined using the remaining six samples. As noted previously in Section 3.2.4.3 , the results of this standard method produce inaccurate results for tensile strength of concrete. This method uses the maximum load resisted by the member after cracking has occurred, assuming the same cross section throughout the test procedure. However, the equation used for determining this value is only valid up to the cracking point of concrete. Once the concrete has cracked, the cross section resisting the load has changed and stresses are redistributed throughout the new cross section. Therefore, the results from this method are inaccurate for determining the actual tensile strength of concrete, and would only be useful when comparing other results using this method. However, because this method is commonly used for concrete testing, this method was implemented for comparison. Using the peak loads ($P_{ultimate}$), the average flexure prism tensile strength was calculated to be 3.18 ksi. The average cracking tensile stress was calculated to be 1.86 ksi. The deflection at peak load was estimated as the nearest recorded deflection within 150 pounds of the recorded peak load.

Table 4-8: Flexure prism test results in third-point bending.

Sample	Age (days)	P_{crack} (k)	$P_{ultimate}$ (k)	Deflection at $P_{ultimate}$* (in.)	$f_{t,\ crack}$ (ksi)	$f_{t,\ ultimate}$ (ksi)
1	470	-	9.26	-	-	3.09
2	470	6.90	11.59	0.060 (=)	2.30	3.86
3	470	4.80	9.14	0.043 (-)	1.60	3.05
4	470	4.80	8.94	0.040 (-)	1.60	2.98
5	495	5.00	10.04	0.043 (-)	1.67	3.35
6	495	6.00	8.40	-	2.00	2.80
7	495	6.00	9.60	-	2.00	3.20
8	495	-	9.28	-	-	3.09
Standard Deviation		0.85	0.96	0.009	0.29	0.32
Average		5.58	9.53	0.047	1.86	3.18

*The following notations indicate whether the recorded deflection is from a (+) load above, (-) load below, or (=) load equal to the peak load.

Load-displacement plots were graphed using manually recorded load and displacement data (Figure 4-5). Both the load and displacement were recorded manually throughout the duration of the test. The average ultimate tensile strength of 3.18 ksi was 28 percent lower than the value determined by Graybeal (2006a). Graybeal (2006a) found the average peak tensile strength to be approximately 4.07 ksi. The 0.047 in. average deflection estimated for peak loads was, however, fairly consistent with the 0.042 in. deflection determined by Graybeal (2006a).

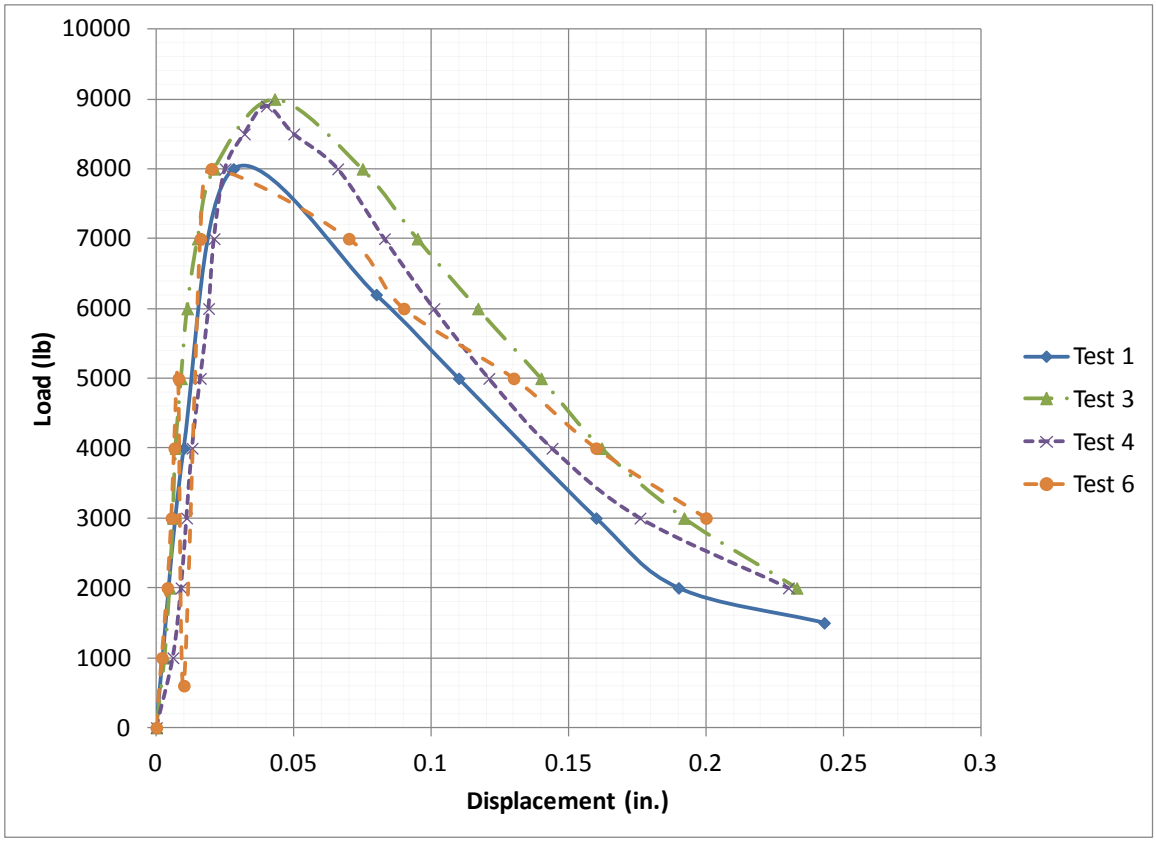

Figure 4-5: Sample load-displacement relationship for third point bending tests.

4.1.4.4 *Evaluation of Tension Testing Methods*

The three aforementioned testing methods were used to determine tensile strength of UHPC. Each method resulted in a different late age tensile strength value, and some values were provided over an age range. The briquet testing method produced significantly lower tensile strength results in comparison to other methods (Table 4-9). These differences were likely affected by the small specimen size of the briquet, preventing proper placement of UHPC in forms. The highest ultimate tensile strength resulted from the split cylinder method, despite the lower age of the specimens at the time of testing. In comparison with the third point bending test method, the split cylinder method resulted in a late age tensile strength approximately 8 percent higher.

Table 4-9: Comparison of Tension Testing Methods

Test Method	Specimen	Age of Specimens (days)	Average Cracking Tensile Strength (ksi)	Average Ultimate Tensile Strength (ksi)
ASTM C 496-04 (2004): Split Cylinder	4 in. diameter by 8 in. high cylinder	196	-	3.44
AASHTO T 132-97 (2004): Briquet	Briquet	431 - 575	1.39	1.45
ASTM C 1018-97 (1997): Third Point Bending	3 in. by 4 in. by 16 in. prism	470 - 495	1.86	3.18

4.1.5 Shrinkage

Shrinkage of UHPC was monitored for specimens in two different locations: an environmentally controlled chamber (Table 4-10) and the laboratory (

Table 4-11) where all other specimens were cured. The specimens in two locations were monitored to identify any differences in shrinkage between the two environments. Shrinkage was determined in comparison to the day of release, Day 4. Results showed that there was negligible difference between the two environments at 7 days; 2 percent. However, the differences between the two environments increased as the age of the UHPC increased. At 28 days, a maximum difference of 8 percent was evident between the two environments, where the laboratory environment had the higher amount of shrinkage.

Table 4-10: Shrinkage of UHPC in environmental chamber

	Shrinkage (microstrain)					
Age (days)	**1**	**2**	**3**	**4**	**Standard Deviation (microstrain)**	**Average (microstrain)**
7	90	80	80	90	5.8	85
14	235	230	240	220	8.5	231
21	275	280	285	260	10.8	275
28	290	295	310	280	12.5	294
1000	365	415	400	380	22.0	390

Table 4-11: Shrinkage of UHPC in laboratory conditions

	Shrinkage (microstrain)				
Age (days)	**1**	**2**	**3**	**Standard Deviation (microstrain)**	**Average (microstrain)**
7	80	80	90	5.8	83
14	230	240	245	7.6	238
21	295	275	285	10.0	285
28	315	320	325	5.0	320
1000	470	490	445	22.5	468

In comparison to research by Graybeal (2006a), the shrinkage in this batch of UHPC was lower. Graybeal (2006a) found untreated UHPC to have an ultimate shrinkage of approximately 555 microstrain. In this study by Graybeal, an accelerator was incorporated into the mix design, and specimens were removed from the molds after 22 hours. In the present study, an accelerator was not used in the mix design, and specimens were removed after 4 days. Because of the later release time, the full amount of shrinkage observed by other researchers was not observed in the present data. It was also observed by Graybeal (2006a) that untreated UHPC experienced a shrinkage rate of 60 microstrain per hour just after it was demolded.

4.2 Bending Biaxial Tests

Bending biaxial tests were performed using two different configurations: 10x10 and 8x10. In the 10x10 configuration, UHPC panels were loaded so that tensile and compressive stresses in each diagonal direction of the panel were equal. In the 8x10 configuration, these diagonal stresses were not equal. Results from this test are explained in the following sub-sections.

4.2.1 Finite Element Analysis of Panels

The finite element analysis was performed for both the 10x10 and 8x10 biaxial bending configurations. Solid, three-dimensional finite element models were created using properties of the UHPC in the bending biaxial panel tests. A uniaxial compressive strength limit of 21.0 ksi was determined using the value determined from 2 in. cube specimens. The uniaxial tensile strength limit of 3.39 ksi was determined using 4 in. diameter by 8 in. high cylinders for the split cylinder test. At the center of the panel, biaxial tension-compression was observed to occur in

the top and bottom faces of the panels. Using the models, a unit load was applied to generate unit stresses through the center of the panels.

The finite element models provided a unit stress for each panel configuration in both tension and compression. Because the material parameters only encompassed the elastic region of the untreated UHPC, the unit stresses as determined from the finite element analyses could only be applied to the cracking load of the UHPC panels. The following table (Table 4-12) provides the unit stresses for both the 8x10 and 10x10 testing configurations, as determined from the finite element analyses.

Table 4-12: Unit stresses determined by finite element analysis.

	Unit Stresses	
Configuration	**Tensile**	**Compressive**
10x10	-0.793	0.793
8x10	-0.901	0.576

4.2.2 Testing Observations

As the UHPC panels were loaded, a crack would first form on the side with dominant tension (Figure 4-6). For the panels loaded in the 10x10 configuration, the tensile and compressive stresses were equal on both the top and bottom of the panels. Therefore, the location of the crack could not be predetermined. For the 8x10 configuration, panels were loaded such that tension would be dominant in the top face of the panels.

Figure 4-6: Cracks first formed in the side with dominant tensile stresses.

Cracking of the panels occurred diagonally between two supports. Theoretically, the cracks should have occurred from corner to corner. However, the cracks primarily occurred from straight edge to straight edge, crossing diagonally through the plate to the opposite side (Figure 4-7 (a)). Although the failure cracks propagated across opposite sides, the cracks in the panels tested in 8x10 configurations were positioned significantly closer to the corner edges than the 10x10 configurations (Figure 4-7 (b)).

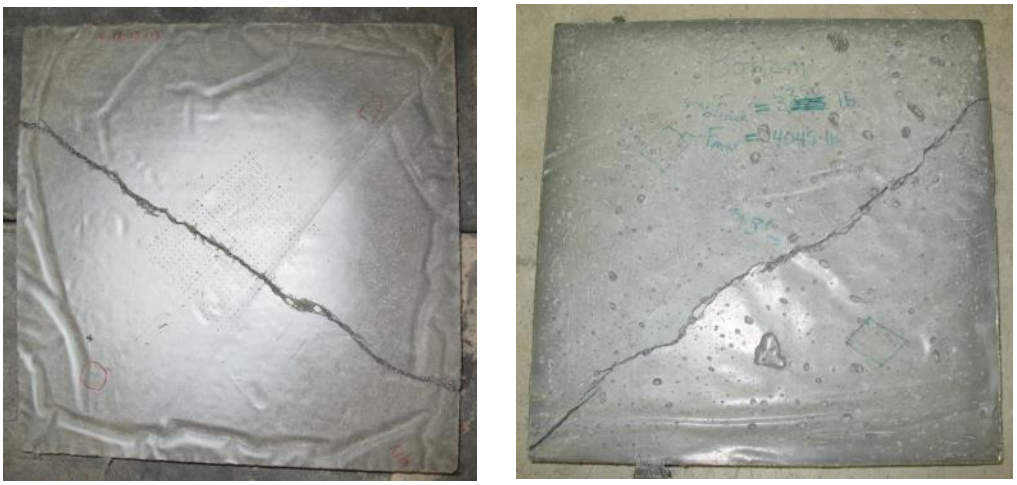

(a) (b)

Figure 4-7: Sample crack patterns of UHPC biaxial panels: (a) 10x10-1, (b) 8x10-1

4.2.3 Experimental Test Results of Panels

The sign convention for biaxial test results assumes that compressive stress (σ_1) is positive and tensile stress (σ_2) is negative. This is a common convention for concrete testing because the compressive strength is much higher in comparison to the tensile strength.

For each of the specimens, a cracking load (P_{cr}) and a maximum load (P_u) were recorded using the MTS Testworks software (Table 4-13, Table 4-14). The cracking load was determined by locating the first sudden drop in load during testing. After initial cracking, the panels continued to resist additional load; therefore, the maximum load occurred after the initial cracking load. Using the stresses in the panels due to unit loading on the finite element models, principal stresses were calculated for the panels by multiplying the idealized stress by the cracking load. The cracking load was used in this case because the finite element model was analyzed within the elastic range of the material.

Table 4-13: Loads and corresponding stresses of 10x10 biaxial bending test.

Specimen	P_{cr} (k)	P_u (k)	σ_1 (ksi)	σ_2 (ksi)
10x10-1	2.19	2.95	1.74	-1.74
10x10-2	2.33	2.39	1.85	-1.85
10x10-3	1.8	2.26	1.43	-1.43
Standard Deviation	0.27	0.37	0.22	0.22
Average	2.11	2.53	1.67	-1.67

Table 4-14: Loads and corresponding stresses of 8x10 biaxial bending test.

Specimen	P_{cr} (k)	P_u (k)	σ_1 (ksi)	σ_2 (ksi)
8x10-1	3.26	4.05	1.87	-2.93
8x10-2	2.31	3.12	1.33	-2.08
8x10-3	3.29	4.64	1.89	-2.96
Standard Deviation	0.55	0.77	0.32	0.50
Average	2.95	3.93	1.70	-2.66

4.2.4 Bending Biaxial Failure Data

The bending biaxial test results and standard material testing results were plotted to begin forming a preliminary failure criterion (Figure 4-8). The uniaxial compressive strength was determined using the compressive strength of cubes, and the uniaxial tensile strength was determined using the third-point bending test results. Standard material testing results were used for the uniaxial failure points because the panels could not be tested in such a way as to produce these results. The third-point bending test was used to represent the tensile strength for this model because this test also incorporated bending to determine tensile strength.

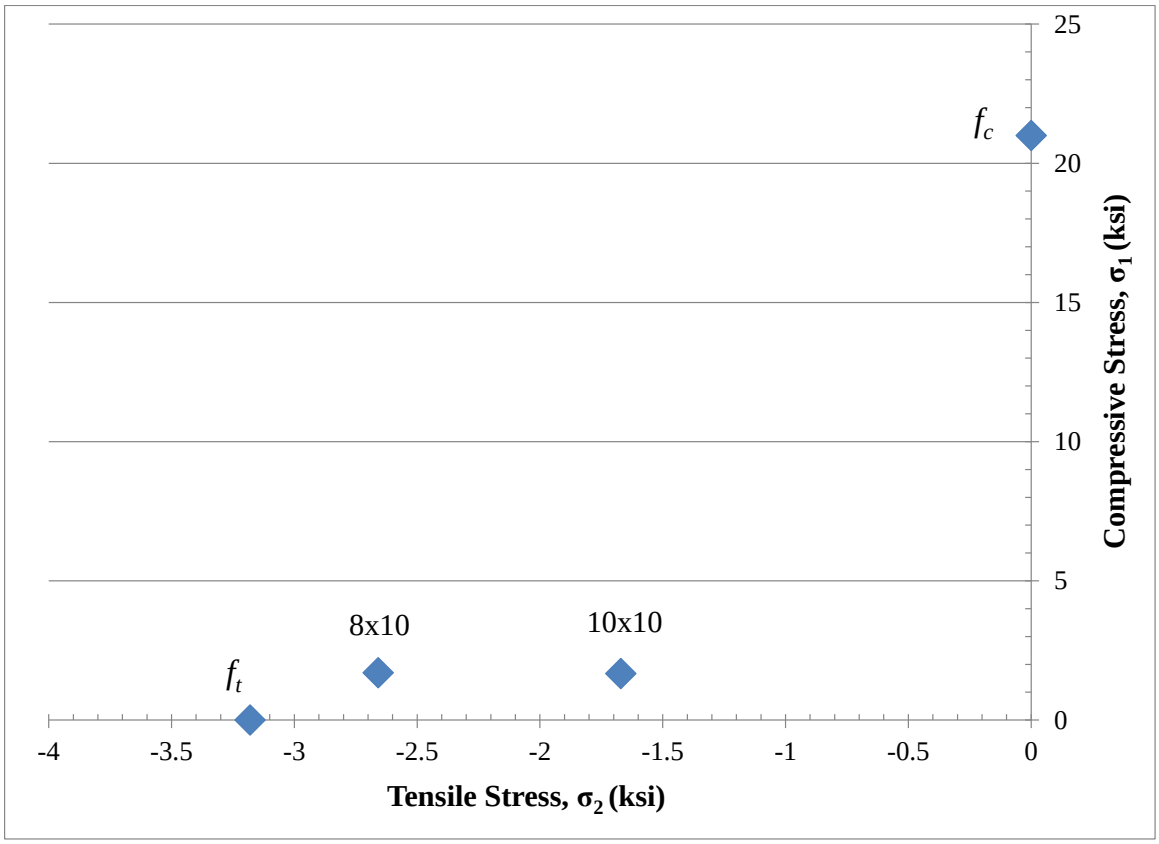

Figure 4-8: Preliminary biaxial failure model based on bending biaxial tests.

Based on models for conventional reinforced concrete and conventional fiber reinforced concrete, the data produced by the panel testing was not expected. According to the bending biaxial failure data, the compressive strength reduced considerably with the addition of orthogonal tension in this model. This drastic change does not resemble typical biaxial tests of either conventional or fiber reinforced concretes. More testing is required to further evaluate this test method. The direct biaxial test, discussed in Chapter 5, was developed to better evaluate the results found using the bending biaxial test.

4.3 Photogrammetry Verification

Tensile coupon specimens were tested to verify the speckling pattern to be used in future testing in conjunction with the DIC program Digital Image Correlation and Tracking (Eberl 2010) in Matlab. The coupon specimens were made of steel, and the testing took place using the MTS Insight universal testing machine.

Prior to testing, the specimens were sprayed with a white spray paint. After drying, a mist of black textured spray paint was misted over the white areas to create a random speckling pattern (Figure 4-9). The specimen was then placed into the grips, and an axial extensometer with a 2 in. gage length was attached to the specimen to calculate strain between two points on the specimen. A standard two-speed test in accordance with ASTM Standard A370 (2006) and ASTM Standard E8 (2004) was used to test the specimen. LabVIEW was used to collect images at a rate of 1 Hz. using the CCD camera. MTS Testworks was used to collect the load and strain data.

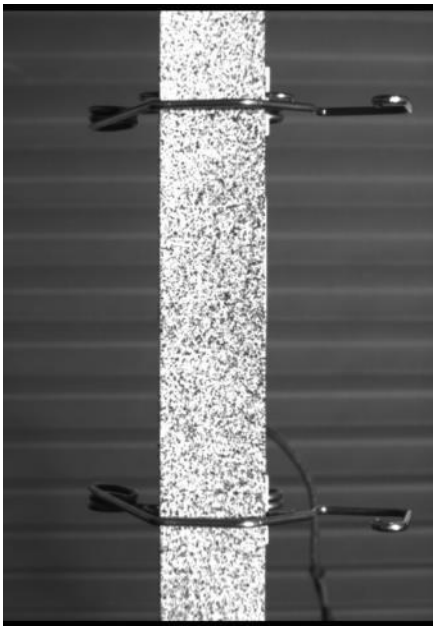

Figure 4-9: Random speckling pattern used for DIC verification.

The images were input into LabVIEW and the DIC program was run to determine strain in the specimen. The strain data from the extensometer and the DIC program results were then compared to verify that both were in agreement with one another. Results (Figure 4-10) showed that the data obtained from MTS Testworks using the extensometer matched the data obtained using the DIC program in Matlab, verifying that the speckling method and the DIC program were reasonable for obtaining data in future tests for UHPC. It is also noted that during these tests, the camera remained stationary in reference to the perpendicular distance to the specimen.

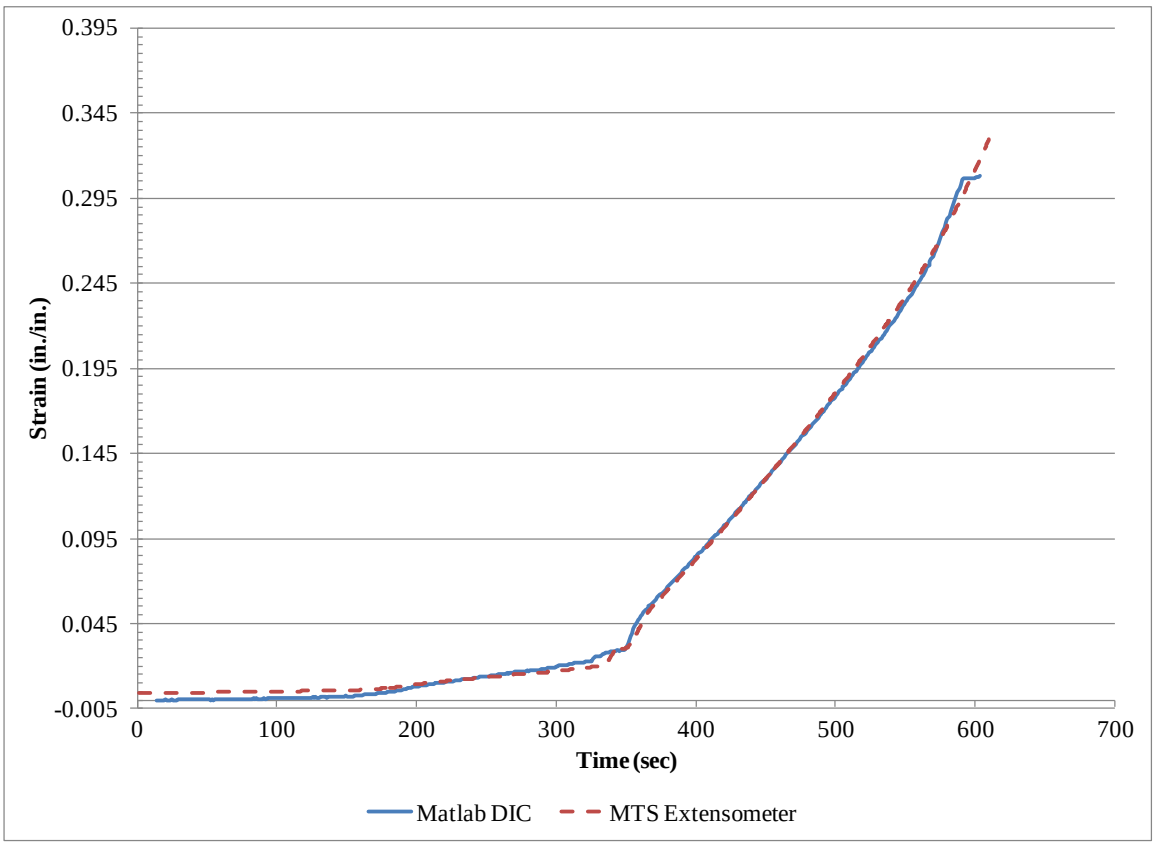

Figure 4-10: DIC verification (Specimen 1).

Based on these results, the DIC methods were used for the direct biaxial test (Chapter 5) and the deck section tests (Chapter 7) to evaluate surface strain of UHPC.

4.4 Conclusions of Preliminary Material Characterization

The remaining parts of this project were more clearly defined using results of the initial material characterization. Through mixing and placing UHPC, the unique rheological properties of the material were shown to affect placement techniques, fiber orientation, and future formwork considerations. It was necessary that UHPC be mixed according to the specified guidelines to ensure consistent results. It was also imperative that forms be made skillfully such that UHPC will not lose moisture during curing and to avoid imperfections in UHPC products due to imperfections in the formwork. UHPC was shown to flow into every crevice of formwork.

The basic material properties, including compressive strength, modulus of elasticity, Poisson's ratio, and tensile strength, either met or exceeded expected values as seen in the research. Due to the simplicity and wide acceptance of the split cylinder tensile test, this method was chosen to determine tensile strength for all future experimental work. Using this widely accepted method will allow direct comparison with a larger collection of research. This ensured that the mixing, placement, and testing procedures were consistent with those established and adopted by other researchers.

Through the results of the bending biaxial test, it was shown that a new method should be developed and investigated to allow more combinations of tensile and compressive stresses and to test uniaxial behavior in tension and compression. A more direct method to determine uniaxial tensile and uniaxial compressive behavior using a consistent specimen was also of interest in the new test method. The direct biaxial test (Chapter 5) was investigated as a possible solution to resolve the difficulties experienced through the preliminary bending test.

Finally, the DIC analysis methods were shown to achieve optimal results while using a random speckling technique achieved with multiple spray paints. These methods were shown to perform well with steel coupon specimens. Further investigation of these methods for determining UHPC strain was later investigated through the direct biaxial test (Chapter 5) and the deck section tests (Chapter 7).

Chapter 5: Biaxial Behavior of UHPC

This chapter presents the findings for the three different direct biaxial test (DBT) scenarios: untreated UHPC with random fiber alignment (UT), steam treated UHPC with random fiber alignment (ST), and untreated UHPC with controlled fiber alignment (UT-I). First, placement observations are discussed in terms of the consolidation and form design. Second, data and representative models for each DBT scenario as determined through regression analysis are presented. Finally, the influence of curing method and placement orientation are discussed, along with a final analysis of UHPC material properties as influenced by the DBT data. All material property test data and supplementary direct biaxial test (DBT) data is provided in Appendix C.

In the following sections, tension is assumed to be in the x-direction and compression is assumed to be in the y-direction (Figure 5-1). Compression was designated as a positive stress because concrete has very high compressive strength compared to the tensile strength. Therefore, the compressive principal stress was considered positive.

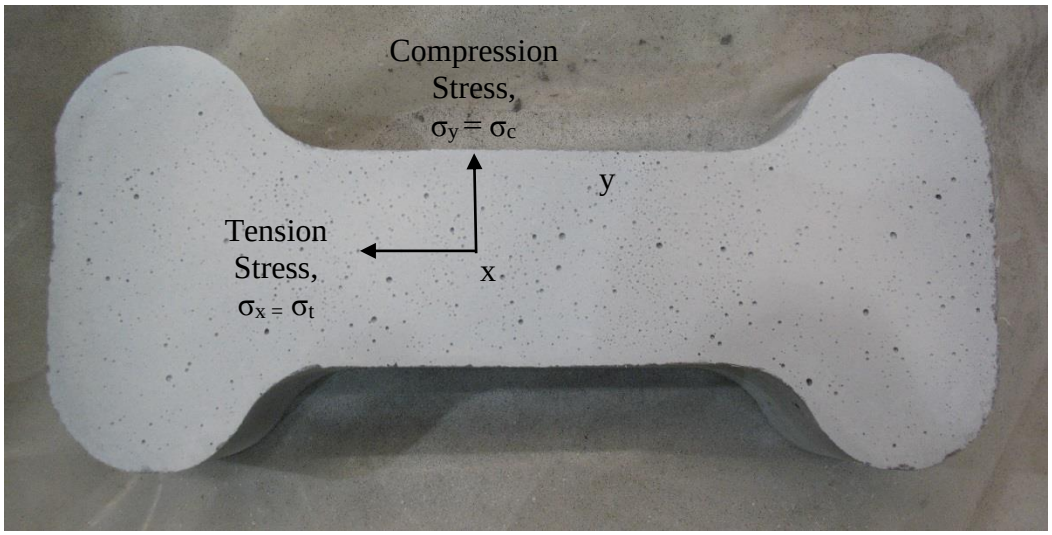

Figure 5-1: Direction of tension and compression stresses.

5.1 Specimen Preparation and General Testing Observations

Two methods were used to place the UHPC for the direct biaxial dog bones: upright at 90° and angled at 33.9° (Figure 5-2). The upright method (UT, ST) resulted in a random fiber orientation. As the UHPC entered the form, it folded over itself. It was later observed through testing that the fibers were randomly aligned. During the inclined placement (UT-I), UHPC flowed along the length of the form, forcing the fibers to align along the length of the biaxial dog bone shape. For each series (UT, ST, and UT-I), at least three different batches of UHPC were used to create all specimens because only nine forms were available. A total of eleven separate batches of UHPC were used to complete all direct biaxial tests.

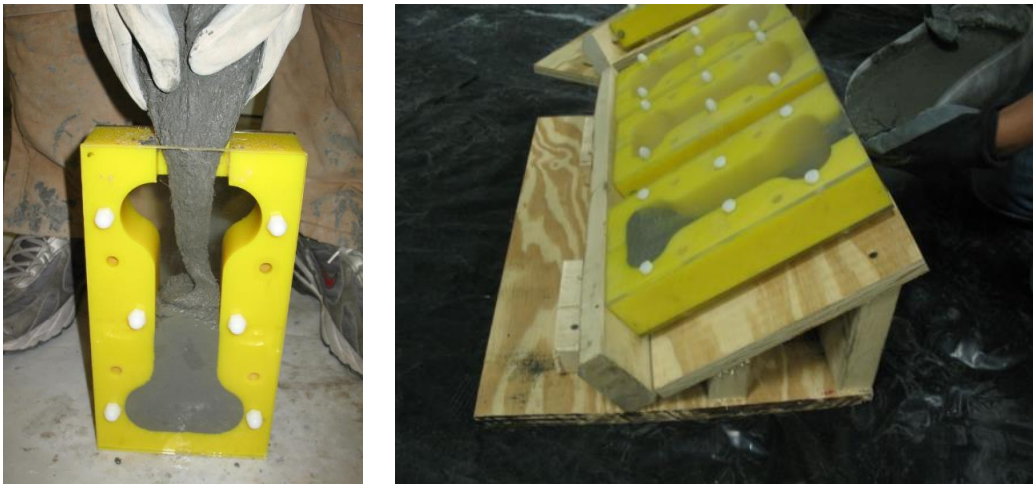

Figure 5-2: UHPC dog bones placed upright at 90° and inclined at 33.9°.

The UHPC was easily self-consolidated, as indicated using the flow test (Table 5-1), and no significant difficulties were noted when consolidating UHPC in the forms. The overall average flow before drop was 8.70 in., and the overall average flow after drops was 9.58 in. This was much higher than values recorded by Graybeal (2006a) who typically had an average of 6.4 in. before the drops and 7.5 in. after the drops. No vibration was applied to any direct biaxial specimens. In some cases, the forms were tapped to accelerate consolidation in the top-most section of the form near the end of placement. The tapping, however, played an insignificant part in the placement process.

Table 5-1: Flow test values for all direct biaxial test mixes.

	Diameter Before 20 Drops (in.)			Diameter After 20 Drops (in.)			Average Diameter (in.)	
Mix ID	**1**	**2**	**3**	**1**	**2**	**3**	**Before**	**After**
DB-063011 (UT)	8.5	9.5	9.3	10.0	10.0	10.0	9.1	10.0
DB-070511 (UT)	9.0	9.5	9.5	10.0	10.0	10.0	9.3	10.0
DB-071111 (UT)	7.5	7.5	7.5	8.5	9.0	9.0	7.5	8.8
DB-080211 (ST)	10.0	9.5	9.8	10.0	10.0	10.0	9.8	10.0
DB-080411 (ST)	9.5	10.0	10.0	10.0	10.0	10.0	9.8	10.0
DB-080611 (ST)	9.5	9.8	10.0	10.0	10.0	10.0	9.8	10.0
DB-061812 (UT)	8.3	8.3	8.5	9.5	9.5	9.5	8.3	9.5
DB-081712 (UT-I)	7.4	8.5	8.3	9.3	9.5	8.1	8.0	9.0
DB-082212 (UT-I)	7.8	7.5	8.0	8.8	9.0	9.5	8.0	9.1
DB-082712 (UT-I)	7.0	7.5	7.8	9.9	9.1	9.5	7.4	9.5
SC-1 (UT-I)	8.5	8.5	8.8	9.5	9.5	9.5	8.6	9.5
Note: 10 in. was the maximum flow possible.						***Average***	**8.7**	**9.6**

The small 2 in. by 0.75 in. opening at the top of the form made it challenging to place the UHPC quickly, especially for the inclined specimens. Because of the unique rheological properties of UHPC, it was possible to place the UHPC through the opening by manually funneling the UHPC. A stationary funnel was experimented with during the first placement; however, manual funneling was optimal for placing the UHPC in the small opening. To funnel the UHPC manually, it was first handled in a metal scoop. A hand was then used to direct the UHPC into the small opening (Figure 5-3). It is suggested that future forms allow for a larger opening to lower the placement time required.

Figure 5-3: UHPC was funneled manually to place into forms.

5.2 Untreated UHPC with Random Fiber Orientation

Results from testing untreated samples with random fiber alignment generally showed that the compressive capacity of UHPC decreased as tensile stress was applied. This was expected based on known failure models for concrete. The amount of scatter of compression data points in the biaxial stress states increased as the tensile stress increased (Table 5-2). The addition of tensile stresses does not significantly reduce the compressive strength of UHPC until more than 60 percent of the tensile stress is applied. The normalized data showed that the uniaxial compressive strength as determined by the DBT was more than 20 percent lower than that obtained from 2 in. cube samples (Table 5-3). This could be attributed to the sensitivity associated with the alignment of the direct biaxial dog bone, the elongated compression area of the direct biaxial dog bone, or the reduction in platen restraint generated in the DBT as compared to the steel fixtures used to test 2 in. cube samples.

Table 5-2: Summary of DBT data for untreated UHPC with random fiber orientation (UT).

		Average (ksi)		*Standard Deviation (ksi)*	
Test ID	**No. Samples**	σ_x	σ_y	σ_x	σ_y
PC	3	0.00	17.17	-	3.21
0.2f_t	3	-0.20	15.86	0.02	1.65
0.4f_t	3	-0.39	16.67	0.01	2.46
0.6f_t	3	-0.59	16.08	0.01	3.15
0.8f_t	2	-0.67	14.04	-	-
PT	3	-1.19	0.00	0.15	-

σ_x = tensile stress (ksi)

σ_y = compressive stress (ksi)

Table 5-3: Summary of normalized DBT data for untreated UHPC with random fiber orientation (UT).

			Average		*Standard Deviation*	
Test ID	**No. Samples**	f_c **(ksi)**	σ_x/f_c	σ_y/f_c	σ_x/f_c	σ_y/f_c
PC	3	22	0.000	0.781	-	0.1460
0.2f_t	3	23	-0.009	0.682	0.0009	0.0872
0.4f_t	3	24	-0.016	0.695	0.0006	0.1026
0.6f_t	3	23	-0.026	0.699	0.0005	0.1369
0.8f_t	2	23	-0.029	0.611	-	-
PT	3	21	-0.056	0.000	0.0072	-

σ_x = tensile stress (ksi)

σ_y = compressive stress (ksi)

f_c = average compressive strength as determined by 2 in. cubes (ksi); values vary based on different batches of UHPC.

It was also difficult to obtain data points with tensile stress in excess of -0.70 ksi due to the large reduction in tensile stress with the addition of compressive stress (Figure 5-4). In many cases, as the tensile stress was raised to 80 to 90 percent of the average ultimate tensile capacity of the UHPC, the specimen would break in pure tension as the tensile force was held constant to set-up the compression blocks. This does suggest that some tensile creep may have attributed to premature failure due to the sustained tensile loading. The tensile force was not adjusted as compressive force was applied. This allowed the tensile stress to decrease due to the Poisson effect. During preliminary direct biaxial tests, failures often occurred in the tensile grips if tension was applied after the addition of compression. To avoid these premature failures due to high stress concentrations at the grip location, no additional tensile force was applied beyond the

initial amount. This limitation also made it difficult to obtain data points with high tensile stresses.

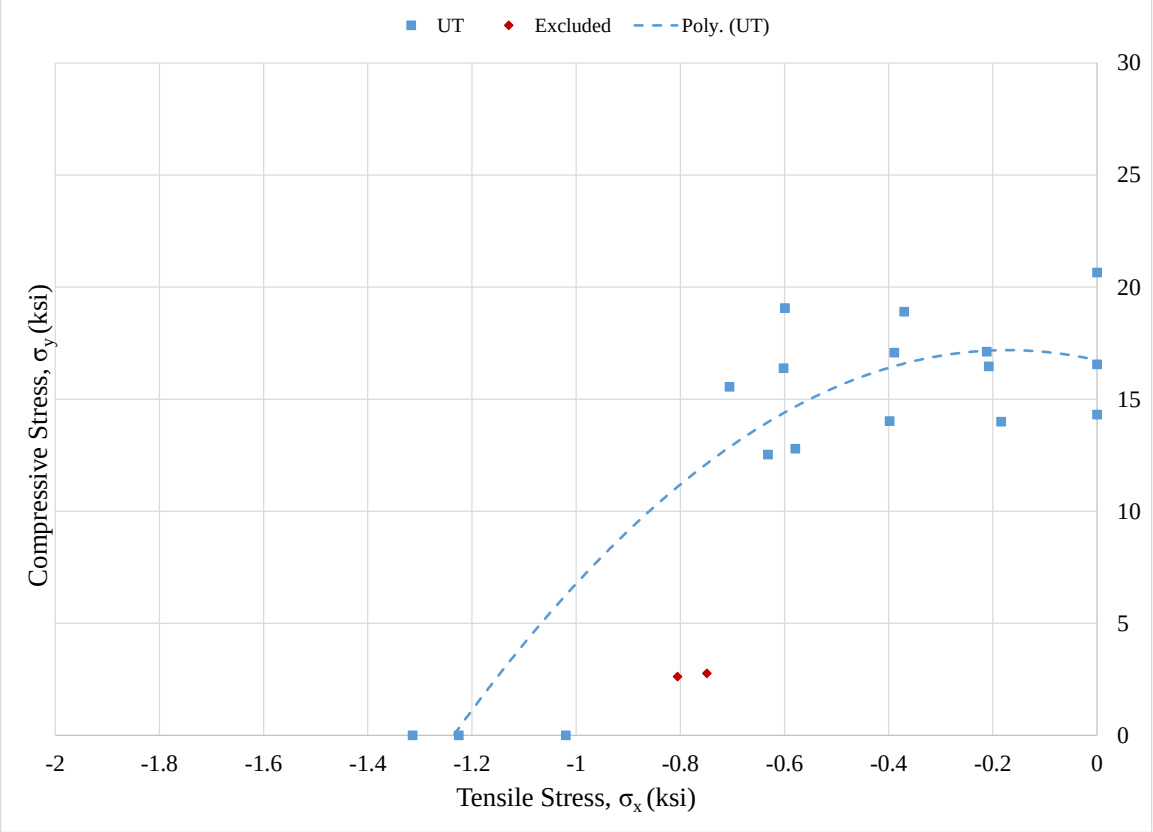

Figure 5-4: Untreated UHPC with random fiber orientation data set.

A two-degree polynomial was first used to represent the UT data set (Figure 5-4, Figure 5-5). The raw UT stress data was represented by Equation (5-1). The normalized UT data can be represented by Equation (5-2). The coefficient of determination, R^2, is approximately 0.82 for both equations. As shown, some points were considered outliers in the overall data set and were excluded from the regression analysis.

$$\sigma_y = -15.21\sigma_x^2 - 5.23\sigma_x + 16.74 \qquad (5\text{-}1)$$

$$R^2 = 0.82$$

$$\psi_1 = -234.2\psi_2^2 - 0.9344\psi_2 + 0.753 \qquad (5\text{-}2)$$

$R^2 = 0.83$

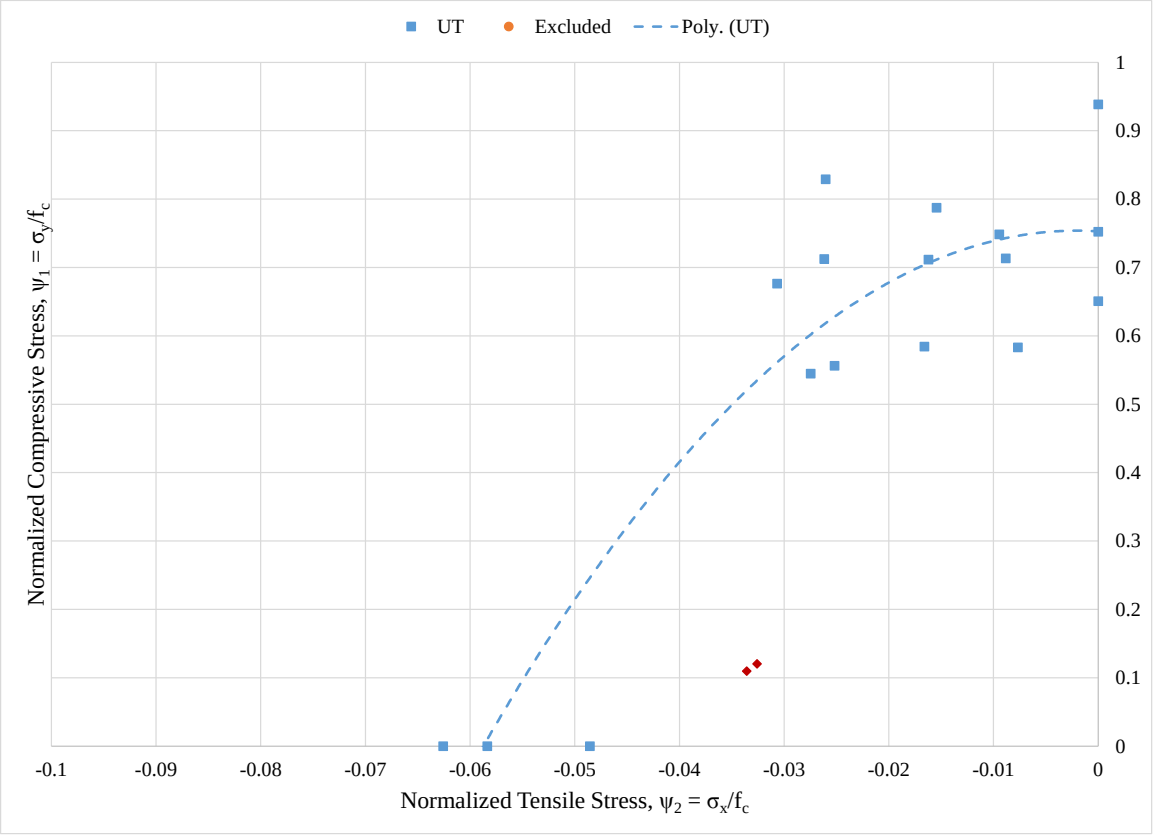

Figure 5-5: Normalized untreated UHPC with random fiber orientation data set.

A simplified bi-linear model was also used to represent the UT data set (Figure 5-6). The bi-linear model neglects two data points from the $0.8f_t$ series because they were considered outliers. The R^2 for Equations (5-3) and (5-4) were 0.87 and 0.12, respectively. Due to the low coefficient of determination for ψ_{1B} (Selection 1), the sum of squares due to error (SSE) was also compared. The SSE for Equations (5-3) and (5-4) were 0.11 and 0.14, respectively. The closer the SSE is to zero indicates that a lower random error is associated with using the fitted line to estimate data response. Both linear models suggest a random error less than 15 percent for the data set.

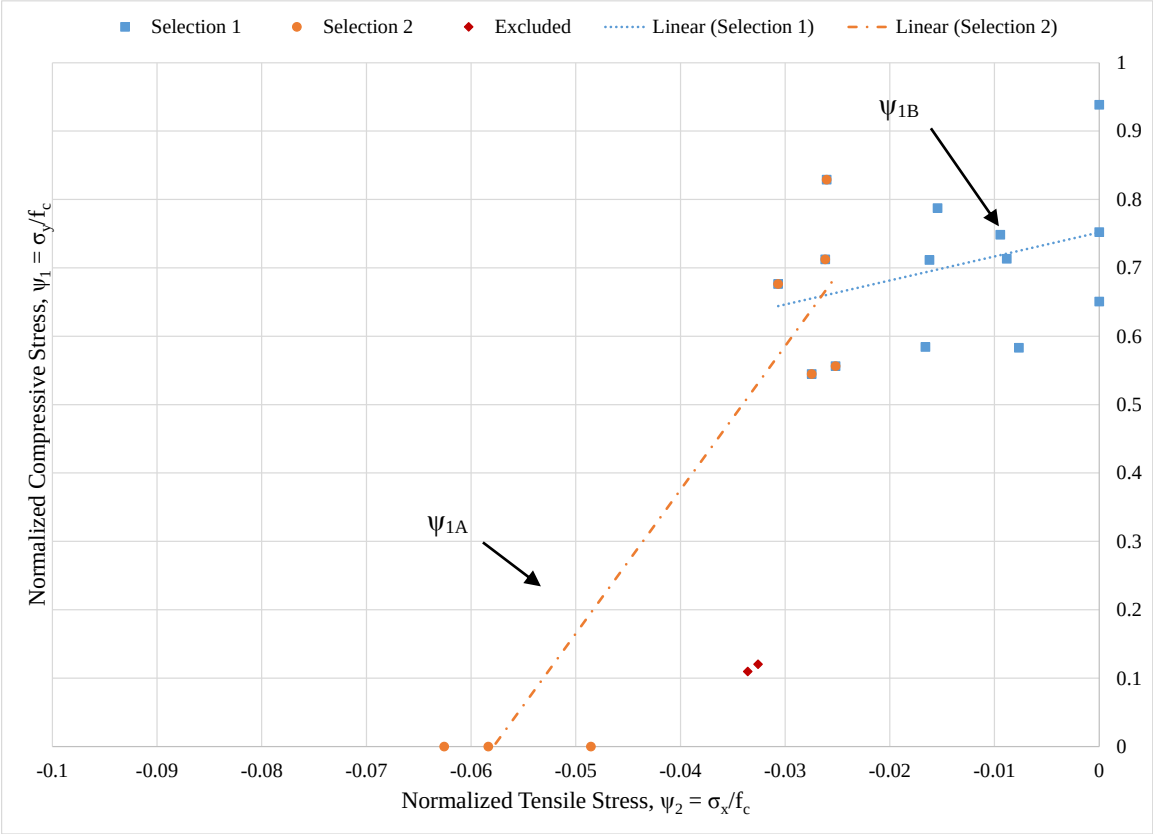

Figure 5-6: Bi-linear model for untreated UHPC with random fiber orientation.

$$\psi_{1A} = 21.02\psi_2 + 1.216 \qquad (5\text{-}3)$$

$$for \quad \psi_2 \leq -0.0265$$

$R^2 = 0.87$, SSE = 0.11

$$\psi_{1B} = 3.514\psi_2 + 0.7519 \qquad (5\text{-}4)$$

$$for \quad -0.0265 < \psi_2 \leq 0$$

$R^2 = 0.12$, SSE = 0.14

The aforementioned bilinear model accounts for some loss in compressive strength with the addition of low tensile stresses. Due to the very small reduction shown by ψ_{1B} (Selection 1) and Equation (5-4), a simplification was also considered to assume no reduction in compressive

strength until Equation (5-3) was applied. For this case, Equation (5-4) was be replaced by Equation (5-5), and the limiting ψ_2 for Equation (5-3) was changed to -0.0246.

$$\psi_{1B} = 0.700 \qquad (5\text{-}5)$$

$$for \quad -0.0246 < \psi_2 \leq 0$$

$R^2 = 0$, SSE = 0.1616

A cracking point was difficult to isolate due to the load-controlled testing method implemented for the direct biaxial test. A displacement controlled test method, similar to that used for tension briquets (AASHTO Standard T 132-87 2004), would be required to identify post-cracking behavior of UHPC. Therefore, only maximum strains were identified for combined tension and compression stresses in this project.

The digital image correlation data for untreated UHPC was summarized to determine maximum strains in the UHPC prior to failure (Table 5-4). Free movement allowed by the pivot point on the tensile grips resulted in some inconsistent data collection through DIC. The UHPC dog bone adjusted orientation suddenly and moved out of the original set-up plane as it pivoted. The LVDT mounted to the underside of the specimen was also used to determine a maximum strain. Using only the pure tension series, a maximum tensile strain was identified as approximately 0.0012 using the LVDT data (Table 5-4). This value was lower than the maximum tensile strain of 0.007 identified for established UHPC stress-strain material models by Garcia (2007) and Graybeal (2008), previously discussed in Section 2.4.1.4 The difference could be attributed to the load controlled test method, the curing method, or the random fiber orientation. Sudden failures occurred as a result of the load controlled test method, leading to an observation of little to no post-cracking behavior. The established stress-strain models were developed for steam treated UHPC. Steam treatment improves the material properties of UHPC by increasing the degree of hydration and refining the microstructure (Cwirzen 2007; Richard and Cheyrezy 1995). Increasing tensile strength and modulus of elasticity could lead to increased ultimate strains. The number of fibers could also affect the tensile strains, allowing for increased post-cracking strengths with more fibers.

Table 5-4: Strain data for untreated UHPC with random fiber alignment.

		Stress (ksi)		Tension		Compression
				LVDT	DIC	DIC
Test ID	**No.**	σ_x	σ_y	$\varepsilon_{x,\ LVDT}$	ε_x	ε_y
PC	1	0.000	20.65	-0.0089	-0.0157	-0.0158
	2	0.000	16.55	-0.0285	-0.0172	-0.0180
	3	0.000	14.31	-0.0244	-0.0200	-0.0245
PT	1n	-1.225	0.00	-0.0017	-	-
	2n	-1.020	0.00	-0.0010	-0.0085	-0.0103
	3n	-1.314	0.00	-0.0010	-0.0151	-0.0144
0.2ft	1	-0.184	13.99	-0.0060	-0.1386	-0.0553
	2	-0.208	16.47	-0.0081	-0.0069	-0.0076
	3	-0.212	17.12	-0.0047	0.1071	-0.0295
0.4ft	1	-0.398	14.02	-0.0035	-0.0697	-0.0692
	2	-0.389	17.08	-0.0224	-0.1440	+0.0309
	3	-0.370	18.90	-0.1578	+0.1214	+0.0217
0.6ft	1	-0.599	19.07	-0.0098	-	-
	2	-0.579	12.79	-0.0078	-	-
	3	-0.602	16.39	-0.0081	+0.1068	-0.0523
0.8ft	1	-0.705	15.56	-0.0079	-	-
	2*	-0.749	2.76	-0.0914	-	-
	3n	-0.632	12.53	+0.0019	+0.0648	-0.0584
	4n*	-0.805	2.63	-0.0505	-	-

*Data point was considered an outlier in the complete data set.
n = notched cross section
Sign Convention – Tension was considered negative.

Although there were many discrepancies in DIC strain data, the LVDT tensile strain data showed consistent values for the PT, $0.2f_t$, and $0.6f_t$ series (Table 5-4). In contrast to the PT series, the ultimate tensile strain increased due the Poisson effect in the biaxial series. From an average ultimate strain of 0.0012 for the PT series, the $0.2f_t$ and $0.6f_t$ series resulted in ultimate tensile strains of approximately 0.0063 and 0.0086, respectively.

5.3 Steam Treated UHPC with Random Fiber Orientation

The steam treated UHPC (ST) with random fiber orientation showed that in some cases, the compressive strength was not negatively affected by the addition of tensile stresses (Table 5-5). The $0.4f_t$ and $0.8f_t$ data sets showed a small increase of 6.4 and 6.5 percent in compressive strength with the addition of tensile stresses. However, the $0.2f_t$ and $0.6f_t$ data sets showed a 3.5

and 26.9 percent decrease in compressive strength with the addition of tensile stresses. The fluctuating responses to tensile stresses appears to further indicate the variability in the data caused by random fiber orientation. It could also indicate that tensile stresses below -0.90 ksi do not significantly affect the compressive strength. The normalized data set also shows the uniaxial compressive strength of the DBT-ST data was 30 percent lower than the compressive strength determined by 2 in. cubes (Table 5-6). This reduction was greater than that determined by DBT-UT data set and could be attributed to the random fiber alignment.

Table 5-5: Summary of DBT data for steam treated UHPC with random fiber orientation.

		Average (ksi)		*Standard Deviation (ksi)*	
Test ID	**No. Samples**	σ_x	σ_y	σ_x	σ_y
PC	3	0.00	23.02	-	2.84
0.2f$_t$	3	-0.30	19.83	0.04	2.49
0.4f$_t$	3	-0.47	21.87	0.02	2.27
0.6f$_t$	2	-0.65	19.31	-	-
0.8f$_t$	3	-0.91	21.50	0.09	5.08
PT	3	-1.38	0.00	0.13	-

σ_x = tensile stress (ksi)

σ_y = compressive stress (ksi)

Table 5-6: Summary of normalized DBT data for steam treated UHPC with random fiber orientation.

			Average		*Standard Deviation*	
Test ID	**No. Samples**	f_c **(ksi)**	σ_x/f_c	σ_y/f_c	σ_x/f_c	σ_y/f_c
PC	3	29.3	0.000	0.787	-	0.0972
0.2f$_t$	3	24.6	-0.012	0.807	0.0016	0.1013
0.4f$_t$	3	26.0	-0.018	0.841	0.0007	0.0873
0.6f$_t$	2	26.0	-0.025	0.743	-	-
0.8f$_t$	3	25.3	-0.036	0.850	0.0035	0.2009
PT	3	27.6	-0.050	0.000	0.0045	-

σ_x = tensile stress (ksi)

σ_y = compressive stress (ksi)

f_c = average compressive strength as determined by 2 in. cubes (ksi)

Several data points appeared to be outliers and were excluded from regression analysis (Figure 5-7, Figure 5-8). Second and third-degree polynomials (Equations (5-6) and (5-7)) were shown to best represent the ST raw and normalized data, respectively. Both equations have an R^2 value greater than 0.80. The normalized ST data model represents the apparent increase in compressive strength with the addition of low tensile stresses that was shown through the $0.4f_t$ and $0.8f_t$ series. Although this increase was shown to occur in two series, the apparent increase is thought to be a result of the random fiber orientation, resulting in more variable results. Because of this variability, a bi-linear model was considered to represent the data set.

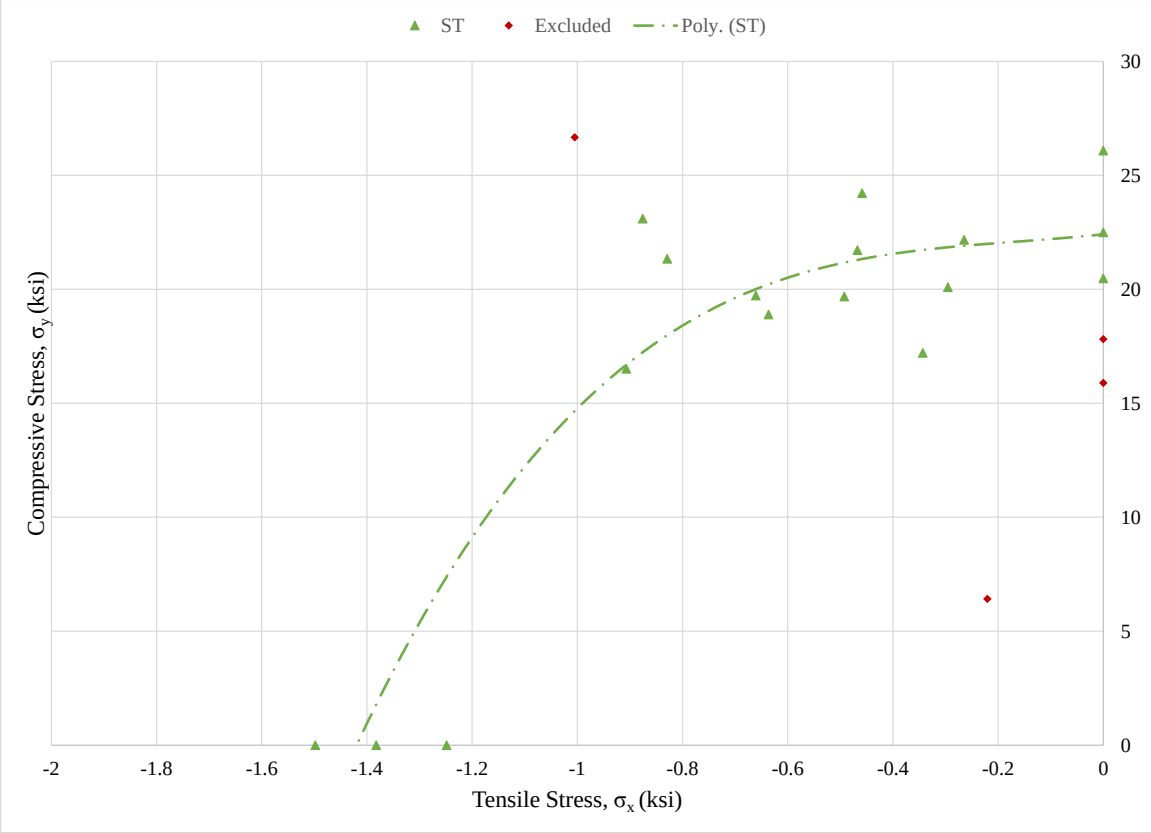

Figure 5-7: Steam treated UHPC with random fiber orientation data set.

$$\sigma_y = 10.06\sigma_x^3 + 4.93\sigma_x^2 + 2.51\sigma_x + 22.42 \qquad (5\text{-}6)$$

$$R^2 = 0.85$$

$$\psi_1 = -605\ \psi_2^2 - 17.012\ \psi_2 + 0.754 \qquad (5\text{-}7)$$

$$R^2 = 0.82$$

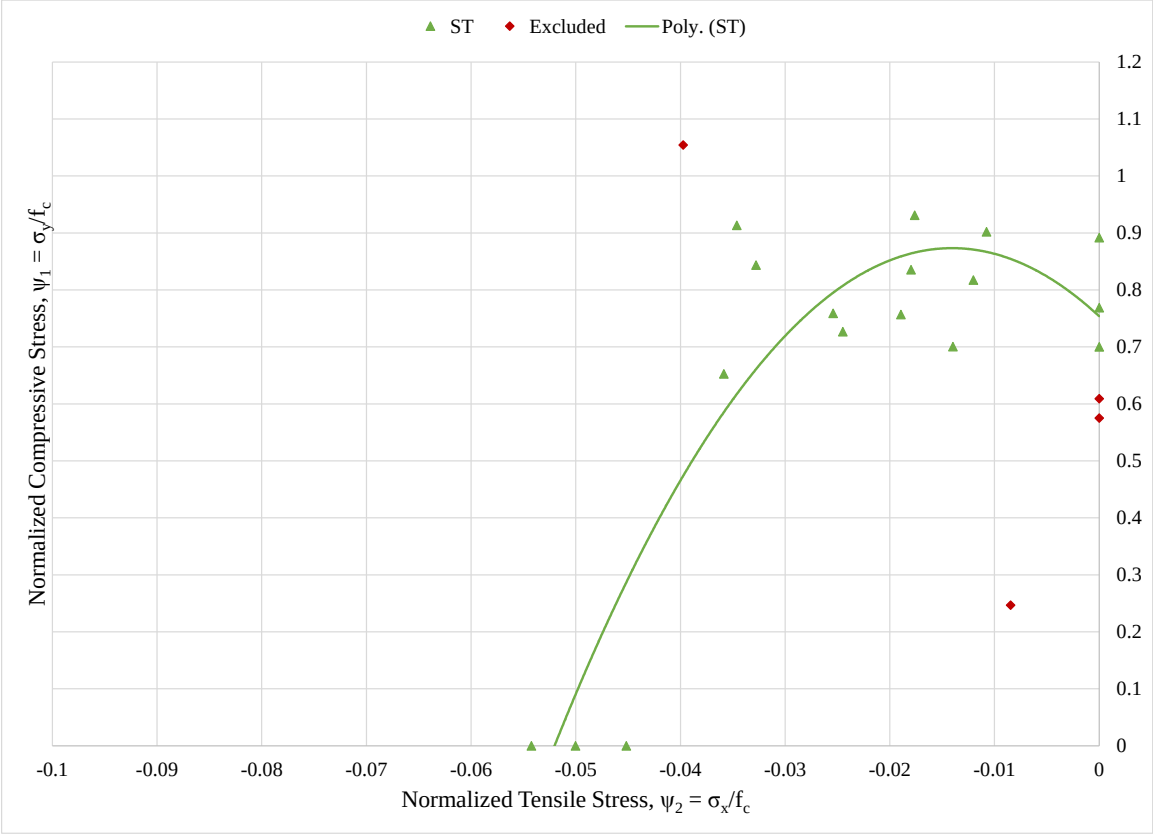

Figure 5-8: Normalized steam treated UHPC with random fiber orientation data set.

A bi-linear model was generated using regression analysis (Figure 5-9). The data set was split into two sections (ψ_{1A} and ψ_{1B}) to obtain two linear models. The slope of ψ_{1B} (Selection 1) was restricted to zero. Without the restriction, ψ_{1B} suggested that the addition of tensile stress increased the compressive stress required for failure. The limitation ensured that the compressive stress would not increase beyond a uniaxial compressive strength as determined using DBT dog bones. The model for ψ_{1A} (Selection 2) was unrestricted. To achieve a slope of zero for ψ_{1B}, Equations (5-8) and (5-9) were generated to represent the normalized ST data. The R^2 for Equations (5-8) and (5-9) are 0.88 and 0.0002, respectively. Due to the low R^2 value, the sum of squares due to error (SSE) was generated to evaluate the model. The SSE for Equations (5-8) and (5-9) are 0.12 and 0.10, respectively, showing that less than 15 percent random error is suggested by the model.

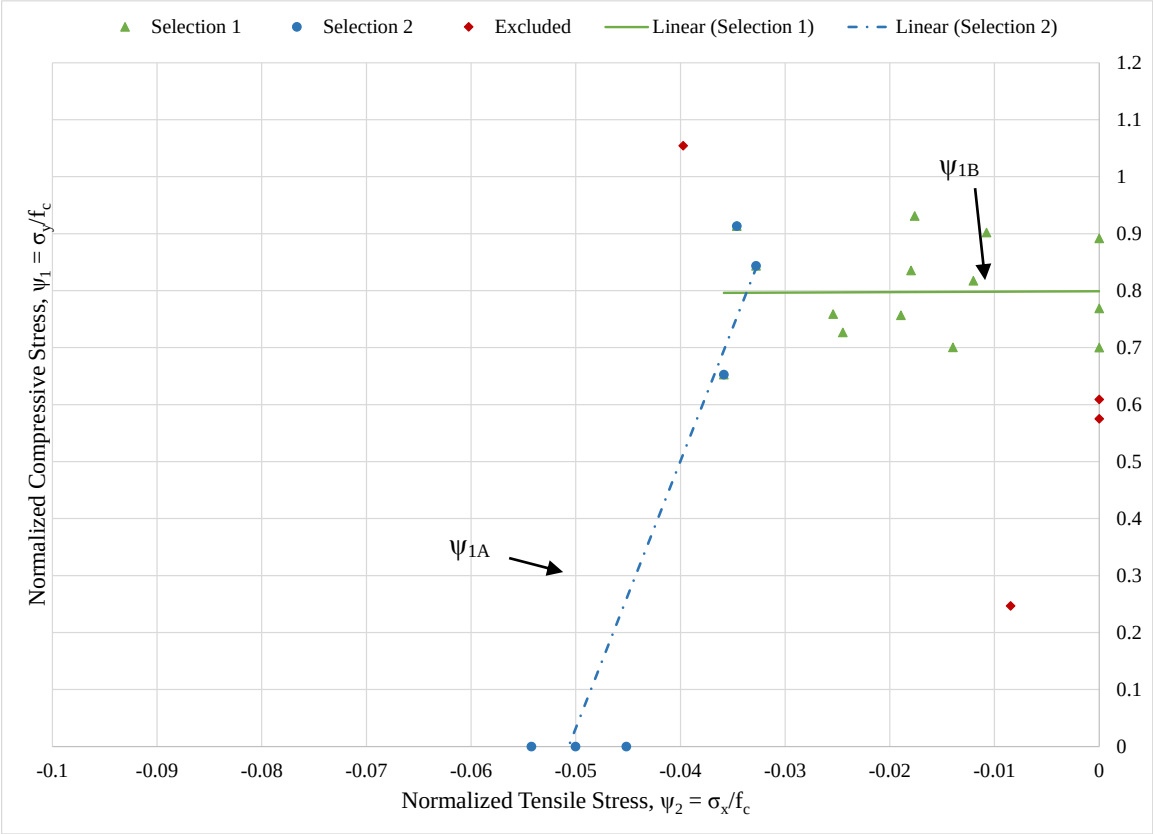

Figure 5-9: Bi-linear model for steam treated UHPC with random fiber orientation.

$$\psi_{1A} = 46.88\psi_2 + 2.376 \qquad \text{(5-8)}$$

$$for \quad \psi_2 \le -0.0322$$

$R^2 = 0.88$, SSE = 0.12

$$\psi_{1B} = 0.800 \qquad \text{(5-9)}$$

$$for \quad -0.0322 < \psi_2 \le 0$$

$R^2 = 0.0002$, SSE = 0.10

5.4 Untreated UHPC with Controlled Fiber Orientation

Untreated UHPC (UT-I) with controlled fiber orientation data showed little reduction in compressive strength with the addition of tensile stresses (Table 5-7). The $0.2f_t$ and $0.4f_t$ series appeared to show a steady reduction in compressive strength; however, the 0.6ft and 0.8ft series

led to the conclusion that the reduction in compressive strength was negligible. The normalized data set also showed the uniaxial compressive strength of the DBT-ST data was approximately five percent below the compressive strength determined by 2 in. cubes (Table 5-8). The variability between the cube compressive strength and the DBT pure compression series reduced with controlled fiber orientation as compared to the aforementioned random fiber orientation scenarios.

Table 5-7: Summary of DBT data for untreated UHPC with controlled fiber orientation.

		Average (ksi)		*Standard Deviation (ksi)*	
Test ID	**No. Samples**	σ_x	σ_y	σ_x	σ_y
PC	3	0.00	21.34	-	1.05
0.2f_t	3	-0.23	19.19	0.03	0.69
0.4f_t	3	-0.48	16.68	0.01	1.40
0.6f_t	3	-0.68	16.94	0.06	2.68
0.8f_t	5	-0.77	18.52	0.11	0.65
PT	4	-1.14	0.00	0.15	-

σ_x = tensile stress (ksi)

σ_y = compressive stress (ksi)

Table 5-8: Summary of normalized DBT data for untreated UHPC with controlled fiber orientation.

			Average		*Standard Deviation*	
Test ID	**No. Samples**	f_c **(ksi)**	σ_x/f_c	σ_y/f_c	σ_x/f_c	σ_y/f_c
PC	3	22.4	0.000	0.953	-	0.0468
0.2f_t	3	22.5	-0.010	0.853	0.0012	0.0307
0.4f_t	3	22.5	-0.021	0.741	0.0624	0.0624
0.6f_t	3	22.4	-0.030	0.756	0.1197	0.1197
0.8f_t	5	21.6	-0.035	0.858	0.0377	0.0377
PT	4	20.0	-0.057	0.000	0.0043	-

σ_x = tensile stress (ksi)

σ_y = compressive stress (ksi)

f_c = average compressive strength as determined by 2 in. cubes (ksi)

Using regression analysis, a third-degree polynomial was considered the best single equation model for the UT-I data set (Figure 5-10). Some data points were excluded from the regression analysis because they were considered outliers. The model for the raw data set, given by Equation (5-10), has an R^2 of 0.76. A second-degree polynomial was developed as a model to represent the normalized UT-I data set (Figure 5-11). Equation (5-11) was used to represent the normalized data set with an R^2 of 0.957. The model represents the reduction in compressive strength with the addition of tensile stresses. By excluding selected data points in the $0.8f_t$ series, the model is considered more conservative.

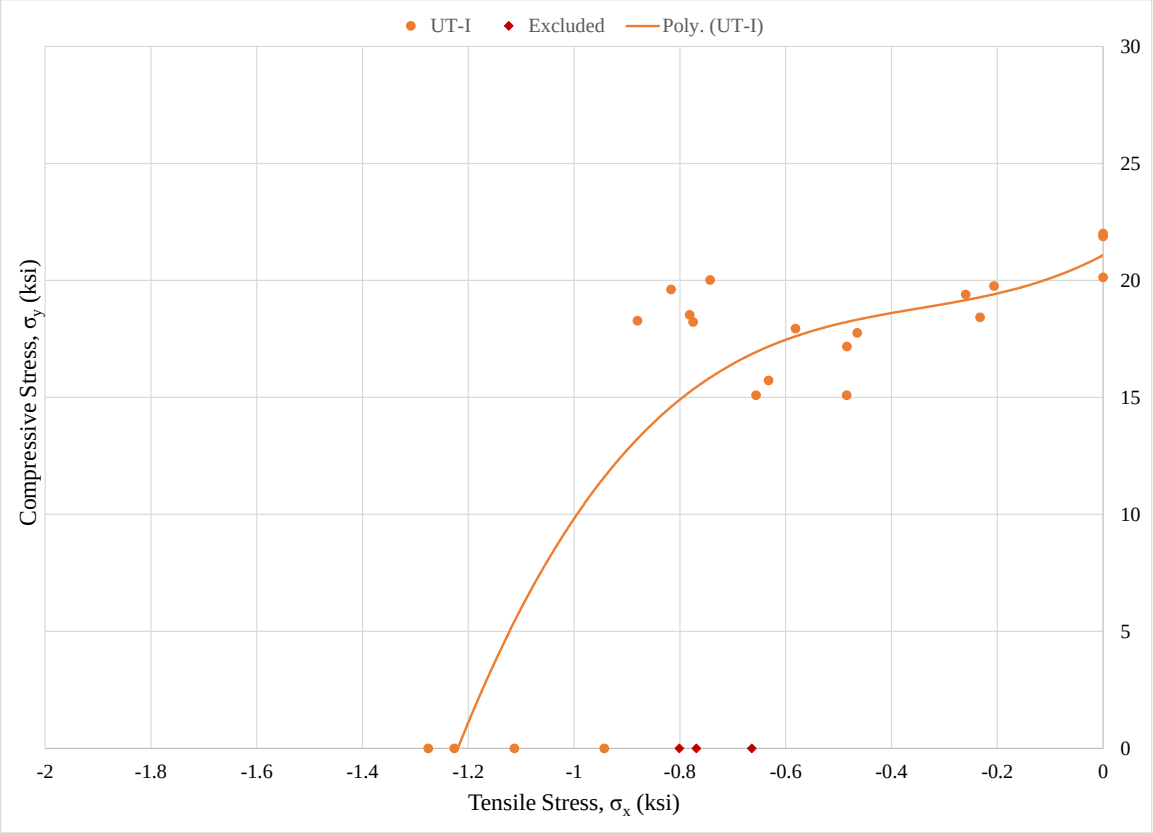

Figure 5-10: Untreated UHPC with controlled fiber orientation data set.

$$\sigma_y = 23.11\sigma_x^3 + 23.90\sigma_x^2 + 12.04\sigma_x + 21.08 \quad (5\text{-}10)$$

$R^2 = 0.76$

$$\psi_1 = -208.4\psi_2^2 + 4.18\psi_2 + 0.946 \quad (5\text{-}11)$$

$R^2 = 0.96$

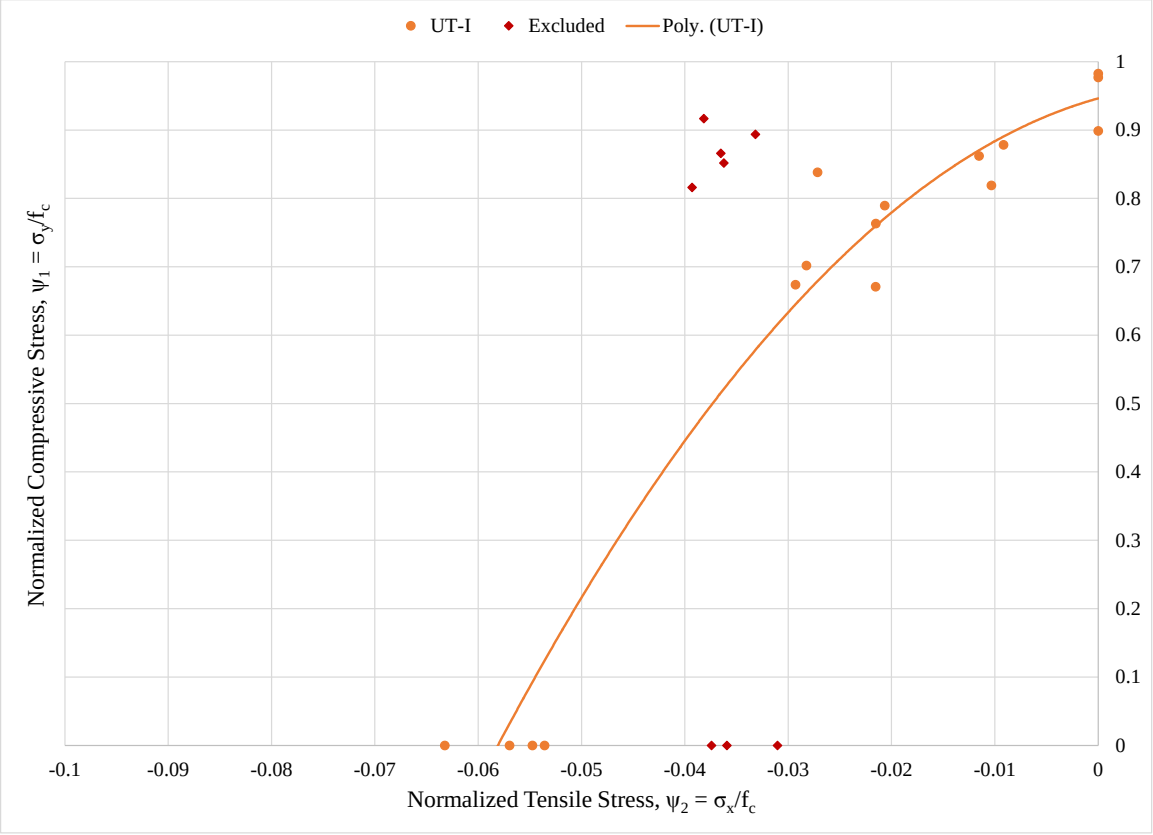

Figure 5-11: Polynomial model for untreated UHPC with controlled fiber orientation.

Again, a bilinear model was constructed to simplify the biaxial stress behavior of untreated UHPC with controlled fiber orientation (Figure 5-12). In the bi-linear model, the $0.8f_t$ series data points were not excluded, but they were used to link Selections 1 and 2. Equations (5-12) and (5-13) were generated to represent the two data sets.

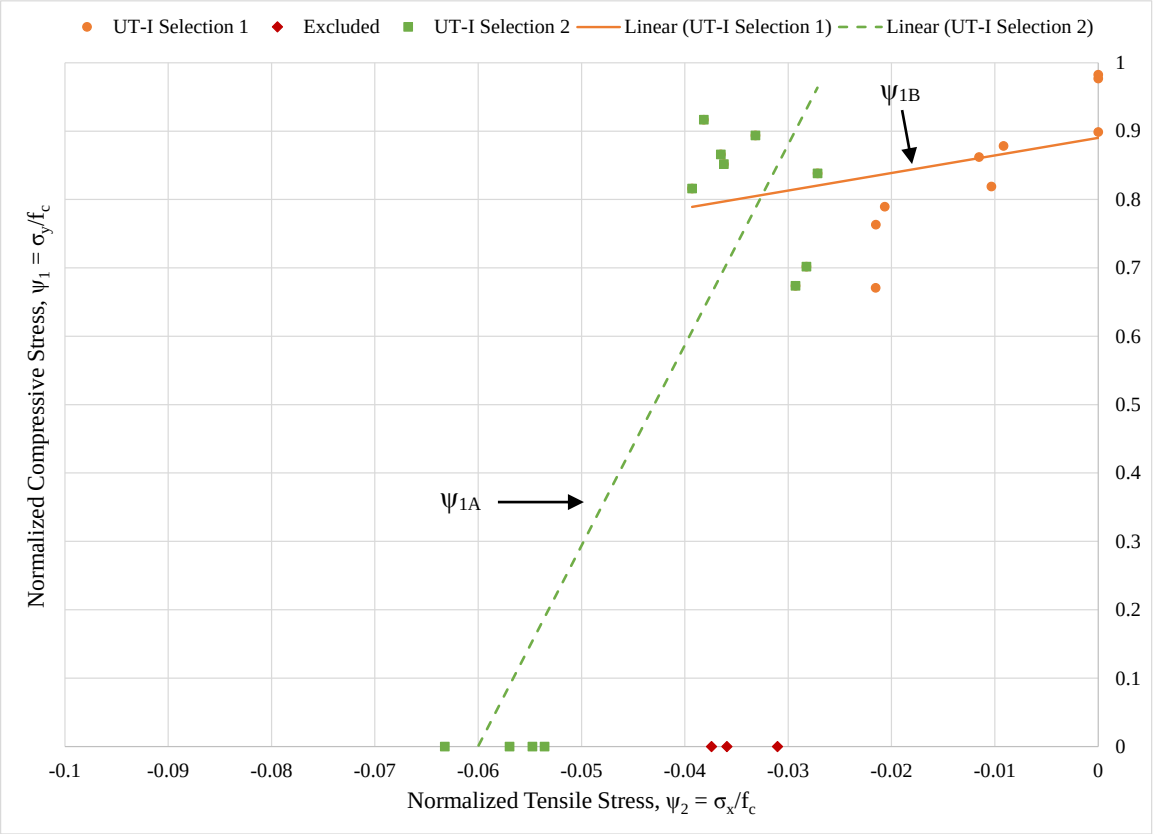

Figure 5-12: Bi-linear model to represent untreated UHPC with controlled fiber orientation (UT-I).

$$\psi_1 = 2.57\psi_2 + 0.89 \qquad (5\text{-}12)$$

$$for \quad -0.0325 < \psi_2 \leq 0$$

$$R^2 = 0.1467$$

$$\psi_1 = 29.33\psi_2 + 1.76 \qquad (5\text{-}13)$$

$$for \quad \psi_2 \leq -0.0325$$

$$R^2 = 0.7928$$

5.5 Influence of Curing Method

5.5.1 Compressive Strength

Six separate batches of UHPC were mixed to complete the random fiber orientation specimens: three for untreated UHPC and three for steam treated UHPC. Steam treatment was completed at the Turner-Fairbank Highway Research Center in McLean, Virginia. Each batch of concrete was subjected to a different delayed steam treatment, based on their casting date. Batches DB-0802, DB-0804, and DB-0806 were steam cured at an age of 8 days, 6 days, and 4 days, respectively.

Compressive strength at 28 days was determined for the steam treated batches of UHPC using 2 in. cubes. Additionally, three 2 in. cube specimens from each of these batches remained at the Thomas M. Murray Structural Engineering Laboratory during the steam treatment to acquire an untreated UHPC compressive strength to serve as a comparison between the effects of each curing method. The results from the 28-day compressive strength testing (Table 5-9) of UHPC in the steam treated batches shows that the steam curing increased the compressive strength by more than 20 percent for each batch.

Table 5-9: Compressive strength at 28-days for steam treated and untreated UHPC from similar batches used in direct biaxial test specimens.

Mix ID	Curing Method	Age of ST (days)	No. of Samples	Standard Deviation (ksi)	Average Compressive Strength, f_c (ksi)	% Increase
DB-0802	UT	-	3	1.56	20.1	-
DB-0804	UT	-	3	0.794	16.4	-
DB-0806	UT	-	3	1.72	18.8	-
DB-0802	ST	8	3	1.18	25.7	28
DB-0804	ST	6	3	1.25	24.1	47
DB-0806	ST	4	3	1.38	23.0	22

UT = untreated, ST = steam treatment

Because there was a delay in the steam treatment process, the UHPC was not able to fully develop compressive strength. Graybeal (2006a) found that delayed steam treated Ductal® UHPC had a compressive strength of approximately 24.8 ksi. The delay between release and steam treatment was 15 days. Due to the rapid turnover required to send all materials to be steam treated, these specimens were not allowed to cure in molds as long as previous mixes,

either. The ST mixes were demolded after 48 hours; whereas, previous mixes were allowed to remain in molds for 72 to 96 hours.

5.5.2 Failure Pattern

Both the ST and UT samples were placed with upright forms, resulting in a random fiber orientation. The random fiber orientation was apparent when failure surfaces were examined after testing. Observing pure tension (PT) samples (Figure 5-13), fibers displayed a seemingly circular pattern similar to that observed previously in split cylinder tests (Figure 4-1). The failure surfaces in tests with compression application often displayed curved failure surfaces (Figure 5-14 to Figure 5-16). This could have been attributed to the folds in the UHPC during placement and the randomized fiber orientation. Both steam treated and untreated samples displayed similar failure patterns; curing method did not appear to affect failure patterns.

Figure 5-13: Randomized fiber orientation in pure tension (PT) sample for steam treated curing.

Figure 5-14: Pure compression failure of untreated UHPC with random fiber orientation (PC-2).

Figure 5-15: Curved failure surface in 0.6ft-2 sample with steam treated curing.

Figure 5-16: Curved failure surface of 0.4ft-3 sample with steam treated curing.

5.5.3 Biaxial Test Results

By examining the raw data, the steam treated failure envelope is larger than the untreated failure envelope (Figure 5-17). The results for the ST data set were consistently more than 10 percent higher than those of the UT data set (Table 5-10), which was expected based on the higher material properties.

Table 5-10: Summary of raw data comparison for UT and ST data sets.

	UT			*ST*			*% Increase*	
Test ID	**No. Samples**	**σ_x**	**σ_y**	**No. Samples**	**σ_x**	**σ_y**	**σ_x**	**σ_y**
PC	3	0	17.17	3	0	23.02	-	34.1
$0.2f_t$	3	-0.20	15.86	3	-0.30	19.83	50.0	25.0
$0.4f_t$	3	-0.39	16.67	3	-0.47	21.87	20.5	31.2
$0.6f_t$	3	-0.59	16.08	2	-0.65	19.31	10.2	20.1
$0.8f_t$	2	-0.67	14.04	3	-0.91	21.5	35.8	53.1
PT	3	-1.19	0	3	-1.38	0	16.0	-

σ_x = tensile stress (ksi)

σ_y = compressive stress (ksi)

% Increase = increase in stress due to steam treatment

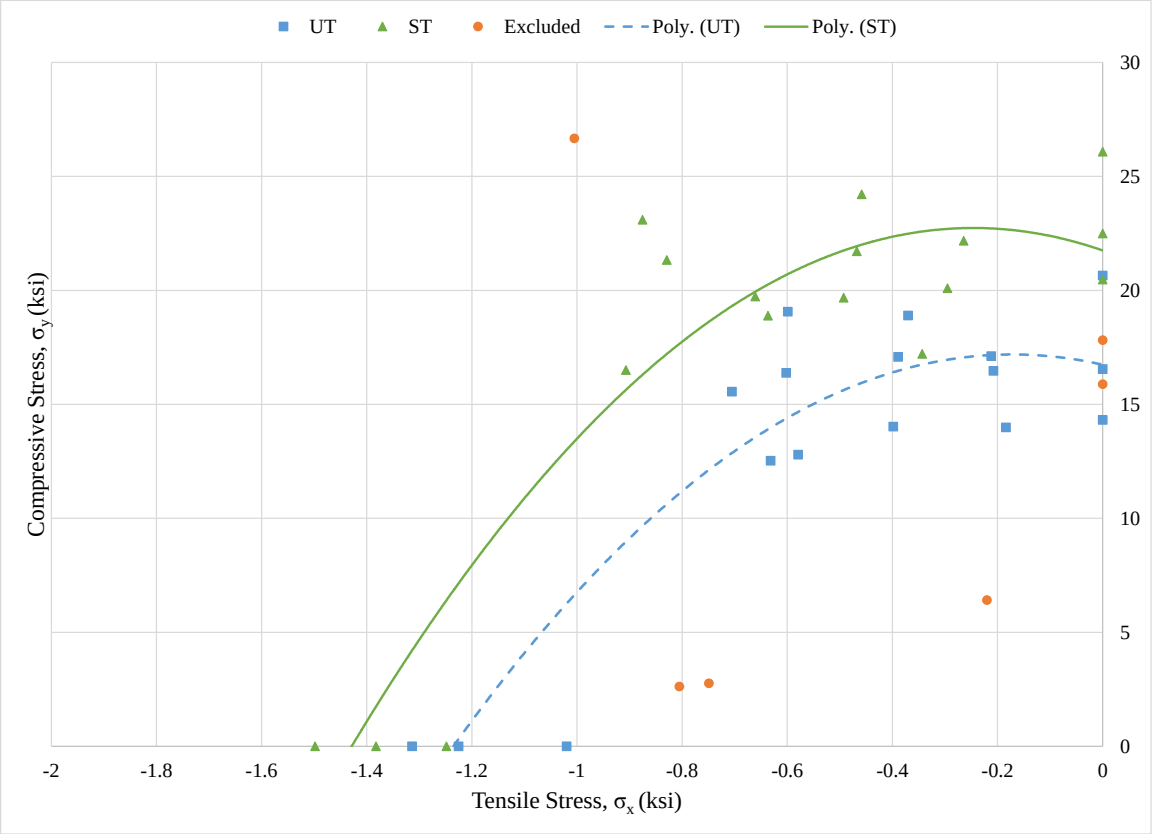

Figure 5-17: Comparison of raw data for steam treated and untreated UHPC with random fiber orientation.

Data was normalized with respect to 2 in. cube compressive strength (Table 5-11). Steam treatment increased compressive strength of UHPC by more than 20 percent (Table 5-9), but steam treatment did not have a significant effect on the direct tensile strength determined by DBT dog bones. The raw data points showed an increase of 16 percent in pure tension (PT) due to steam treatment as compared with a 34.1 percent increase in pure compression (PC) using dog bones. Because the tensile strength did not increase to the same degree as the compressive strength, the normalized pure tensile strength (PT) of steam treated UHPC was lower than untreated UHPC. The failure models for each curing method show these differences (Figure 5-18). The rise in compressive strength of steam treated UHPC increased the y-intercept of ψ_{1B}. The slope and y-intercept of ψ_{1A} increased as a result of steam treatment, and the x-intercept decreased.

Table 5-11: Summarized comparison of normalized UT and ST data sets.

	UT		*ST*		*% Increase*	
Test ID	σ_x/f_c	σ_y/f_c	σ_x/f_c	σ_y/f_c	σ_x/f_c	σ_y/f_c
PC	0	0.781	0	0.787	-	0.8
0.2f_t	-0.009	0.682	-0.012	0.807	33.3	18.3
0.4f_t	-0.016	0.695	-0.018	0.841	12.5	21.0
0.6f_t	-0.026	0.699	-0.025	0.743	-3.8	6.3
0.8f_t	-0.029	0.611	-0.036	0.85	24.1	39.1
PT	-0.056	0	-0.05	0	-10.7	-

σ_x = tensile stress (ksi)

σ_y = compressive stress (ksi)

f_c = compressive strength as determined by 2 in. cubes (ksi)

% Increase = increase in stress due to steam treatment

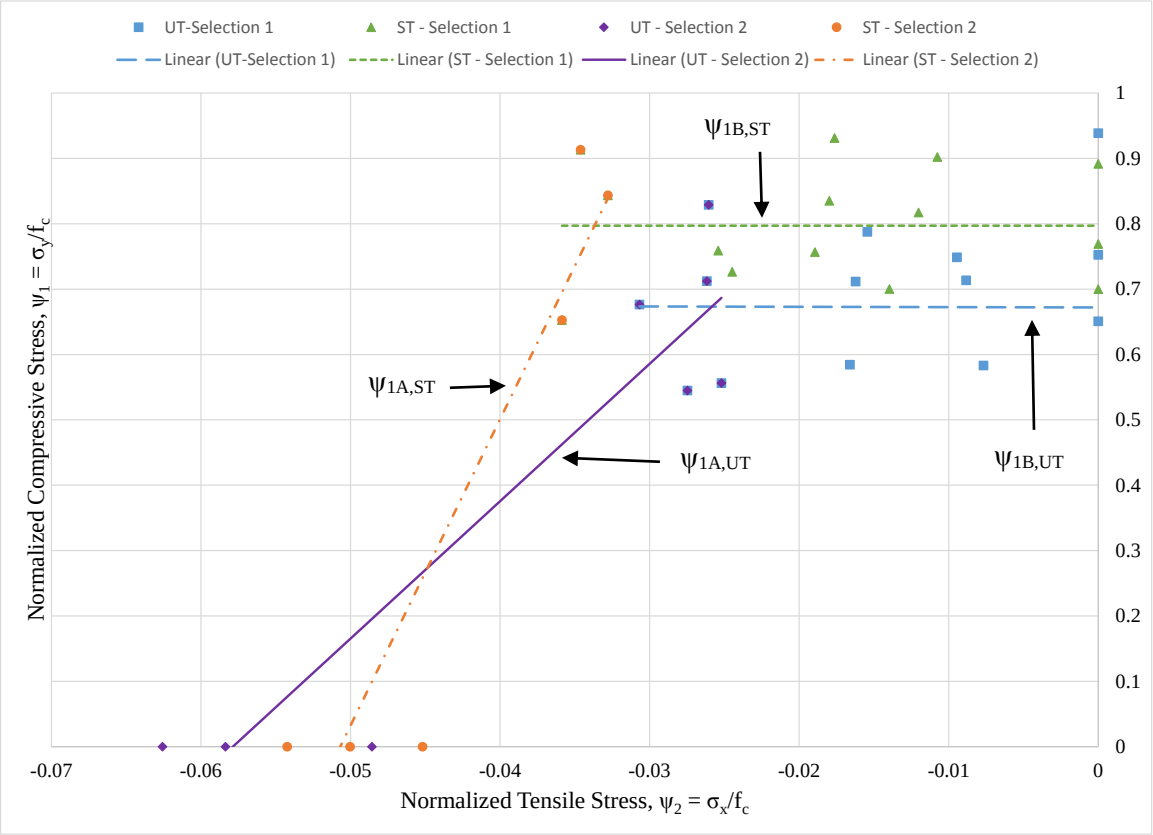

Figure 5-18: Comparison of bi-linear models for normalized UT and ST data.

Using the comparison between UT and ST data sets, a correlation was generated to account for the differences based on varying compressive strength with random fiber orientation. Factors α and β, shown by Equations (5-14) and (5-15), were used to approximate the changes associated with increasing compressive strength. The factors were derived so that only the compressive strength of the mix is required to complete the adjustment for higher compressive strengths. The factors were applied to the UT models to adjust for the ST data set in Equations (5-16) and (5-17). The equations represent the trend from direct biaxial test data of UHPC in this study, and the compressive strength ranged from 23 to 26.5 ksi for untreated and steam treated UHPC, respectively. These correlations should be further tested to determine their ability to predict biaxial behavior of UHPC outside this range.

$$\alpha = \frac{f_c}{23} \qquad (5\text{-}14)$$

f_c in ksi

$$\beta = 0.23\left(f_c - 23\right) + \alpha \qquad (5\text{-}15)$$

f_c in ksi

$$\psi_{1B} = \alpha 0.700 \qquad (5\text{-}16)$$

$$for \quad -0.0246\beta < \psi_2 \le 0$$

$$\psi_{1A} = \beta(21.02\psi_2 + 1.216) \qquad (5\text{-}17)$$

$$for \quad \psi_2 \le -0.0246\beta$$

5.6 Influence of Placement Method

5.6.1 Failure Pattern

A distinct difference was noted in failure patterns of direct biaxial dog bone specimens depending on the placement method. The untreated UHPC placed upright (UT) produced random fiber alignments, as previously shown (Figure 5-13 to Figure 5-16); however, the inclined placement method (UT-I) resulted in a more controlled fiber alignment along the tensile direction of the biaxial dog bone specimen (Figure 5-19). Fewer curved cracking patterns were

noted with the controlled fiber alignment. Vertical, horizontal, and inclined cracks occurred in the specimens (Figure 5-20 to Figure 5-22).

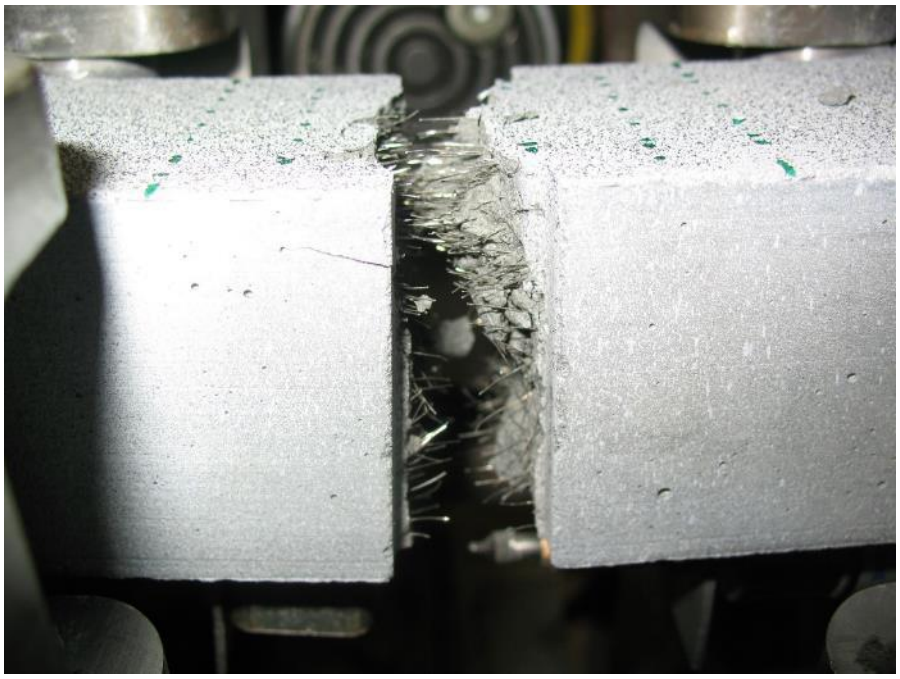

Figure 5-19: Fibers aligned in tensile direction of untreated UHPC with the inclined placement method (PT-1).

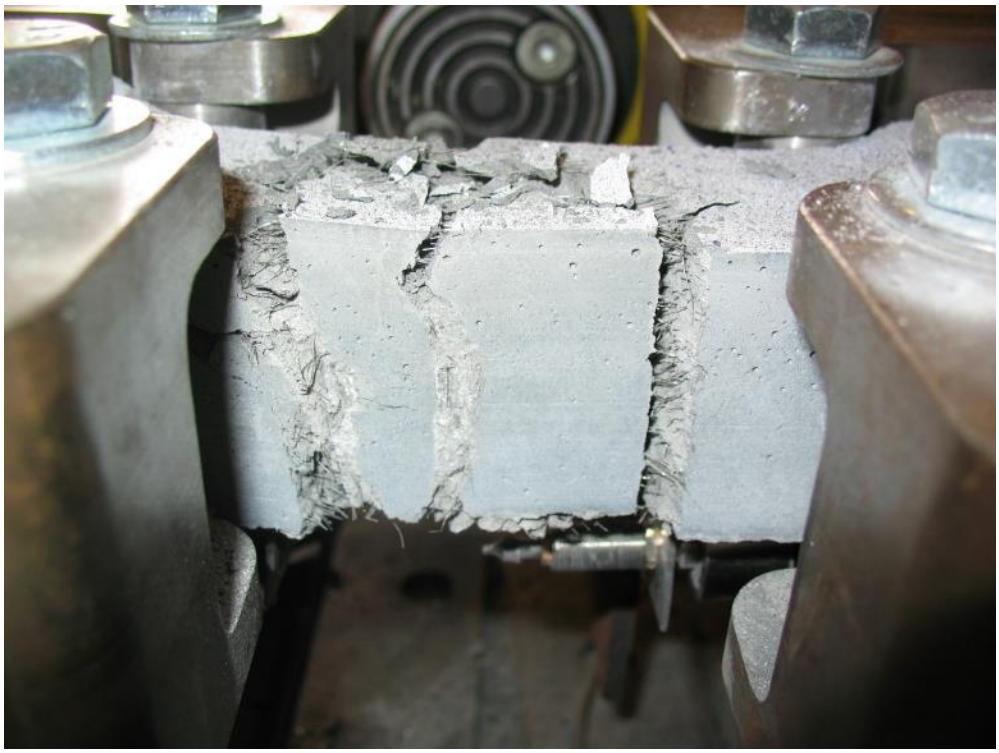

Figure 5-20: Vertical cracking was common with UT-I failures (0.4f_t-2).

Figure 5-21: Inclined cracks were common among UT-I failures (PC-2).

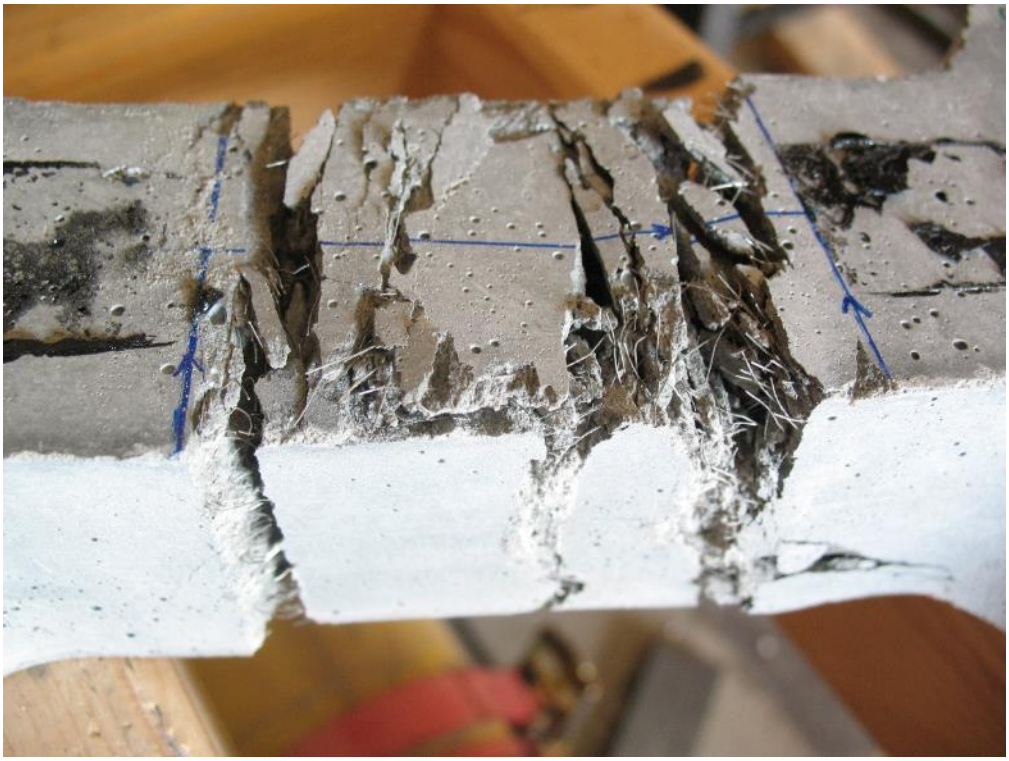

Figure 5-22: Failure surfaces revealed multiple straight cracks at failure with bridging fibers ($0.4f_t$-2).

In this study, Teflon-coated tape was used to reduce platen restraint. In some tests, the failure mode appeared to show some signs of platen restraint. Inclined cracks, as evident by Figure 5-21, could be a sign of platen restraint. The Teflon-coated tape between the floating steel block and the series of steel blocks for compression was minimally damaged during testing. It was replaced after three or more uses to ensure it did not affect the test; although, it rarely showed signs of damage. The tape in direct contact with the specimens was replaced after every test because it showed extreme signs of damage (Figure 5-23).

Figure 5-23: Teflon-coated tape was damaged during testing (UT-I, 0.4f_t-1).

5.6.2 Experimental Test Results

The controlled fiber orientation was expected to increase consistency and possibly the resistance to biaxial tension-compression stresses by increasing the number of fibers bridging cracks. The inclined placement methods improved the resistance to biaxial stress states and pure compression (Table 5-12 and Table 5-13). Graphically, the raw data indicates that the inclined placement method improved the compressive strength but had negligible effect on the tensile strength (Figure 5-24). Although the raw data indicates a 4.2 percent reduction in the pure tension (PT) series using the inclined placement, the normalized data suggests a 1.8 percent increase in pure tensile strength relative to cube compressive strength.

Table 5-12: Comparison of raw data for random and controlled fiber alignments.

	UT			*UT-I*			*% Increase*	
Test ID	**No. Samples**	**σ_x**	**σ_y**	**No. Samples**	**σ_x**	**σ_y**	**σ_x**	**σ_y**
PC	3	0	17.17	3	0	21.34	-	24.3
0.2f_t	3	-0.2	15.86	3	-0.23	19.19	15.0	21.0
0.4f_t	3	-0.39	16.67	3	-0.48	16.68	23.1	0.1
0.6f_t	3	-0.59	16.08	3	-0.68	16.94	15.3	5.3
0.8f_t	2	-0.67	14.04	5	-0.77	18.52	14.9	31.9
PT	3	-1.19	0	4	-1.14	0	-4.2	-

σ_x = tensile stress (ksi)

σ_y = compressive stress (ksi)

% Increase = increase in stress due to controlled fiber alignment

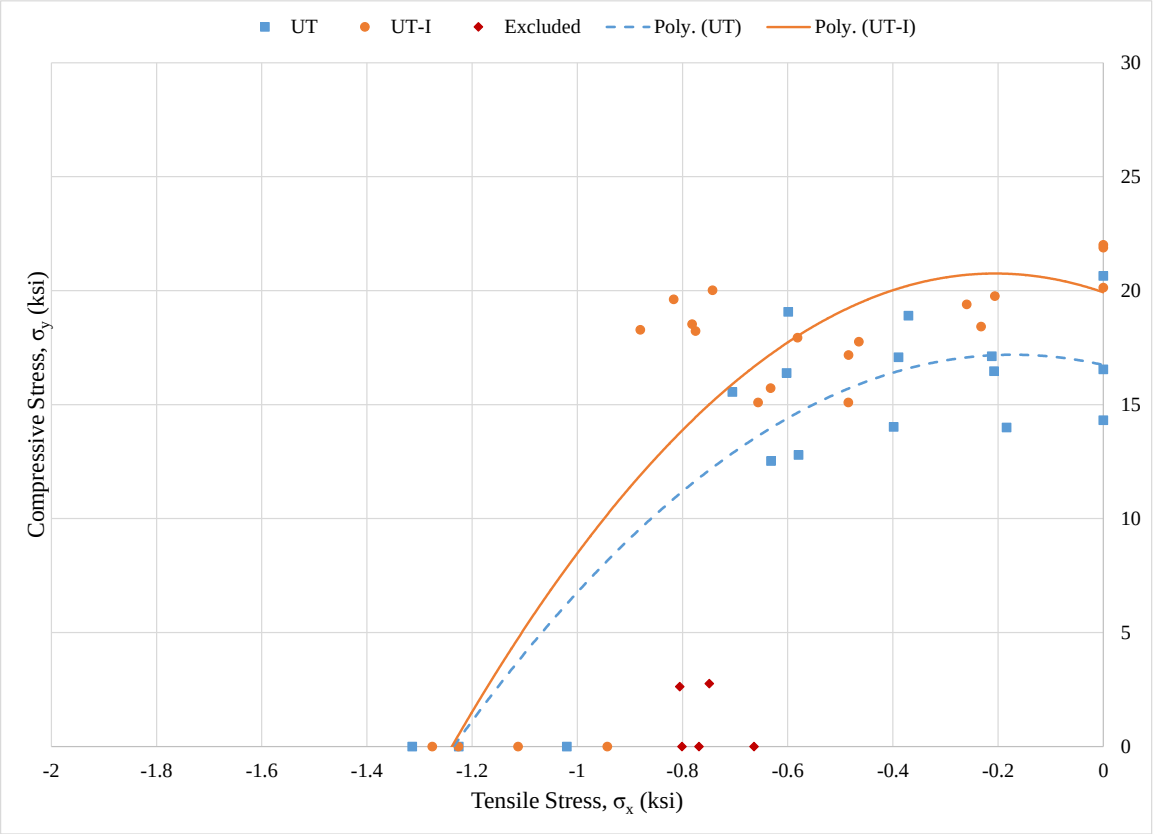

Figure 5-24: Comparison of UT and UT-I raw data sets.

Table 5-13: Summary of comparison for normalized UT and UT-I data sets.

	UT		***UT-I***		***% Increase***	
Test ID	**σ_x/f_c**	**σ_y/f_c**	**σ_x/f_c**	**σ_y/f_c**	**σ_x/f_c**	**σ_y/f_c**
PC	0	0.781	0	0.953	-	22.0
$0.2f_t$	-0.009	0.682	-0.01	0.853	11.1	25.1
$0.4f_t$	-0.016	0.695	-0.021	0.741	31.3	6.6
$0.6f_t$	-0.026	0.699	-0.03	0.756	15.4	8.2
$0.8f_t$	-0.029	0.611	-0.035	0.858	20.7	40.4
PT	-0.056	0	-0.057	0	1.8	-

σ_x = tensile stress (ksi)

σ_y = compressive stress (ksi)

f_c = compressive strength as determined by 2 in. cubes (ksi)

% Increase = increase in stress due to controlled fiber alignment

Normalized data was determined by dividing the direct biaxial test data by the compressive strength, f_c, as determined using 2 in. cubes. This would account for the variable compressive strength data obtained from individual mixes. The normalized models indicated that controlled fiber orientation improved the compressive strength of UHPC (Figure 5-25, Figure 5-26) for the direct biaxial test. Not only was the PC data more consistent, the normalized PC data more closely represented the compressive strength, f_c, as determined by 2 in. cube samples. For the random fiber orientation, the PC data was only 78 percent of f_c on average; whereas, for the controlled fiber orientation, the PC data set was 95 percent of the f_c on average (Table 5-13). Contrary to the original hypothesis that fiber orientation would affect pure tension (PT) tests, these tests were not significantly affected by fiber orientation. Because the direct biaxial tests were completed using a load-controlled test method, fracture was sudden, and a cracking point was not confidently detected. It is hypothesized that the controlled fiber orientation would play a significant role in post-cracking behavior; however, the test method used in this project was not able to detect such behavior. It is suggested that a displacement controlled be used in future tests to better capture post-cracking behavior of UHPC in biaxial stress states.

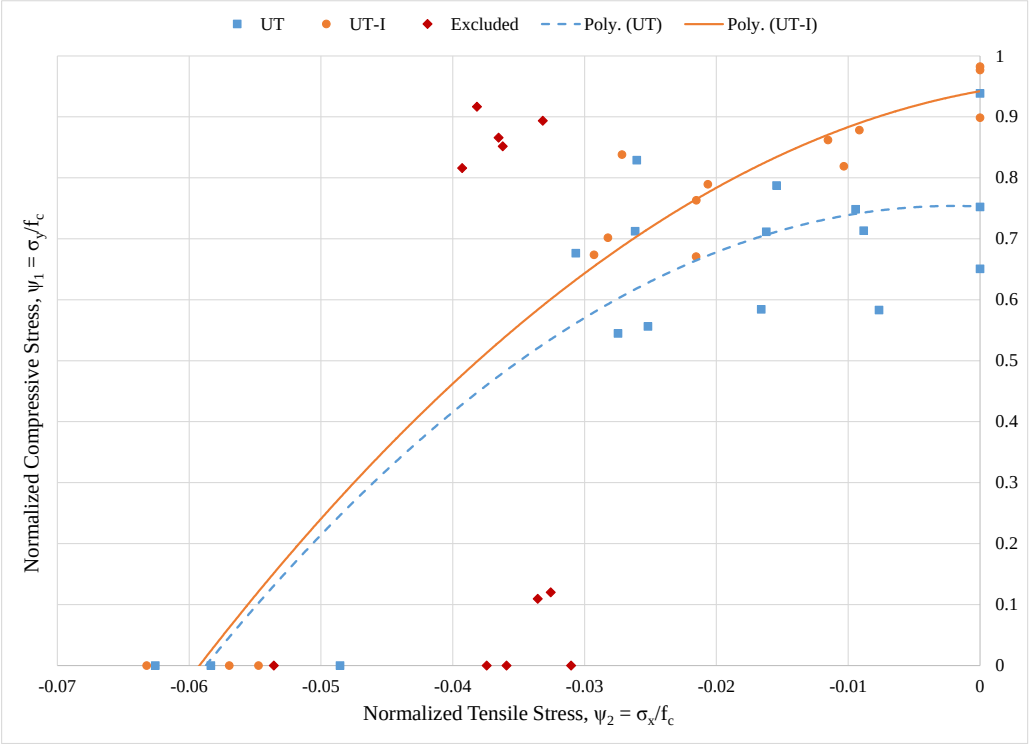

Figure 5-25: Comparison of normalized UT and UT-I data sets (polynomial models).

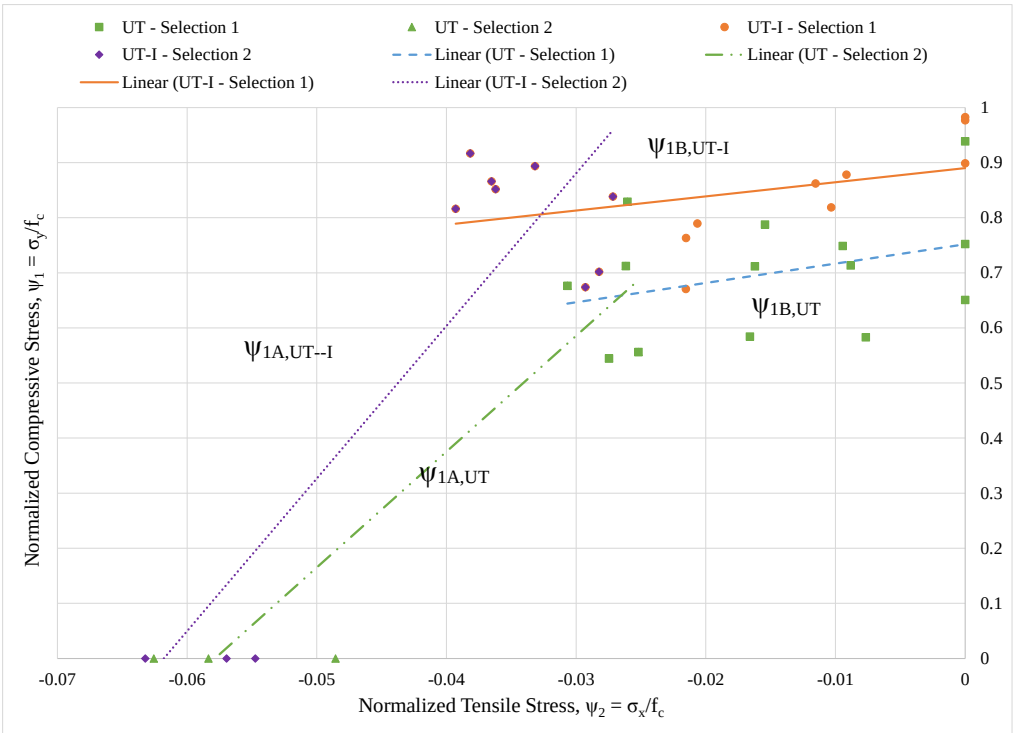

Figure 5-26: Comparison of normalized UT and UT-I data sets (bi-linear models).

The controlled fiber alignment increased the biaxial failure envelope for UHPC. In order to provide a conservative model for UHPC with controlled fiber alignment, it is suggested that either the single two-degree polynomial model or the bi-linear model generated for untreated UHPC with random fiber alignment (UT) be used to represent untreated UHPC with controlled fiber orientation. These models would predict a failure point inside the controlled fiber alignment failure envelope, while also following a similar reduction in compressive strength with the addition of tensile stresses.

5.7 Proposed Biaxial Failure Envelope for UHPC

All biaxial failure data was reviewed to determine the best model to represent UHPC for future applications in this study. The two-degree polynomial failure envelope, shown in Equation (5-2), generated for untreated UHPC with random fiber alignment was considered a possible model for use in future analysis (Figure 5-27). The bi-linear model, provided by Equations (5-3), (5-4), and (5-5), for untreated UHPC with random fiber orientation would also provide a reasonable failure envelope for untreated UHPC with controlled fiber orientation (Figure 5-28). In both cases, the models offer a conservative assumption for controlled fiber orientation, which would most likely be implemented for UHPC applications by controlling placement operations. The two-degree polynomial was chosen as the proposed failure envelope because it provided a single, smooth failure surface, which was seemingly simple compared to the additional information required to use the bi-linear model. The bi-linear model requires that an intersection point be identified to delineate between the two lines defining the failure surface.

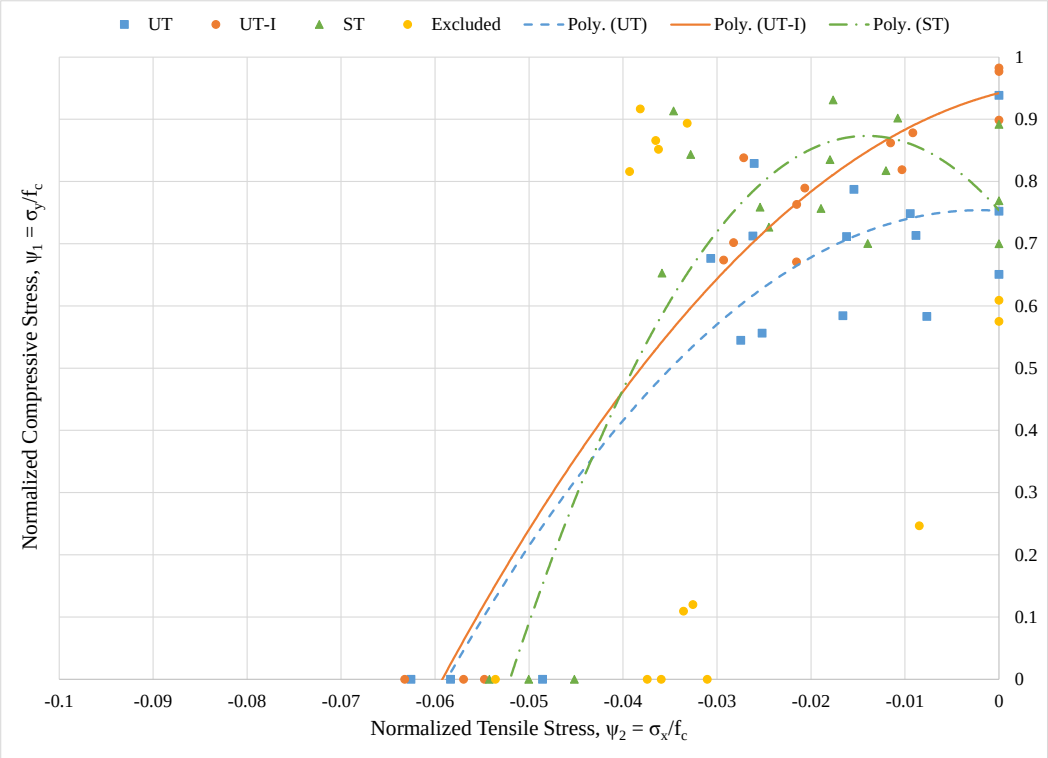

Figure 5-27: Comparison of all normalized DBT data sets (polynomial models).

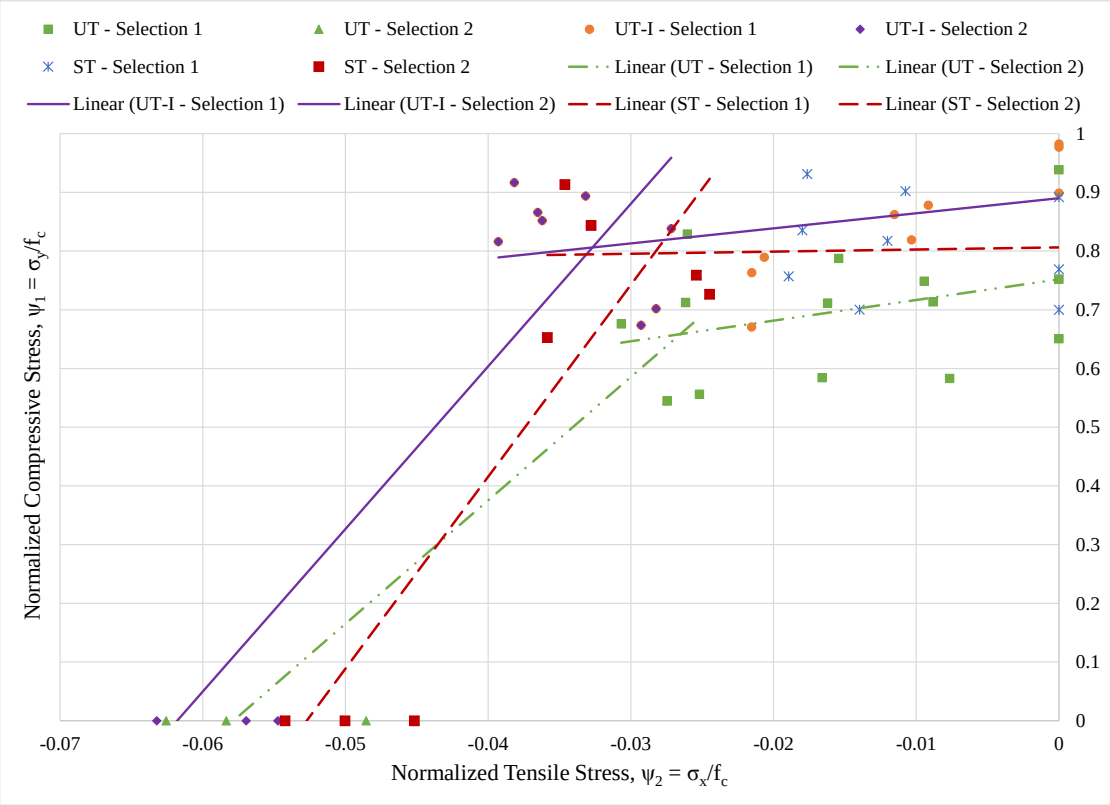

Figure 5-28: Comparison of all normalized DBT data sets (bi-linear models).

It is evident that the proposed model may be less conservative for steam treated UHPC. It is possible that the response was due to the random fiber orientation. It is also possible that the steam treatment has a smaller effect on tensile strength than compressive strength. Because the current study had limited samples of steam treated UHPC, it would be advantageous to investigate this response with additional testing. It would also be advantageous to investigate the proposed alterations for steam treated UHPC with respect to the proposed alteration factors for the bi-linear UHPC model. These factors should be investigated to determine their ability to predict responses for UHPC with compressive strengths above 26.6 ksi.

As previously discussed in the literature, a modified Coulomb model was suggested for another type of UHPC known as Compresit, specifically addressing biaxial compression-compression behavior (Jensen 1999, Nielsen 1995). The Mohr-Coulomb failure criterion suggests that a single, straight line connect the uniaxial compression and uniaxial tension points to form a failure envelope (Dowling 2007). In comparison to the polynomial relationship for untreated UHPC with random fiber orientation, the linear model suggested by the Mohr-

Coulomb failure criteria would provide a more conservative approach to biaxial responses of UHPC (Figure 5-29). If a more conservative response is required for design, the Mohr-Coulomb failure criterion would serve as a reasonable assumption.

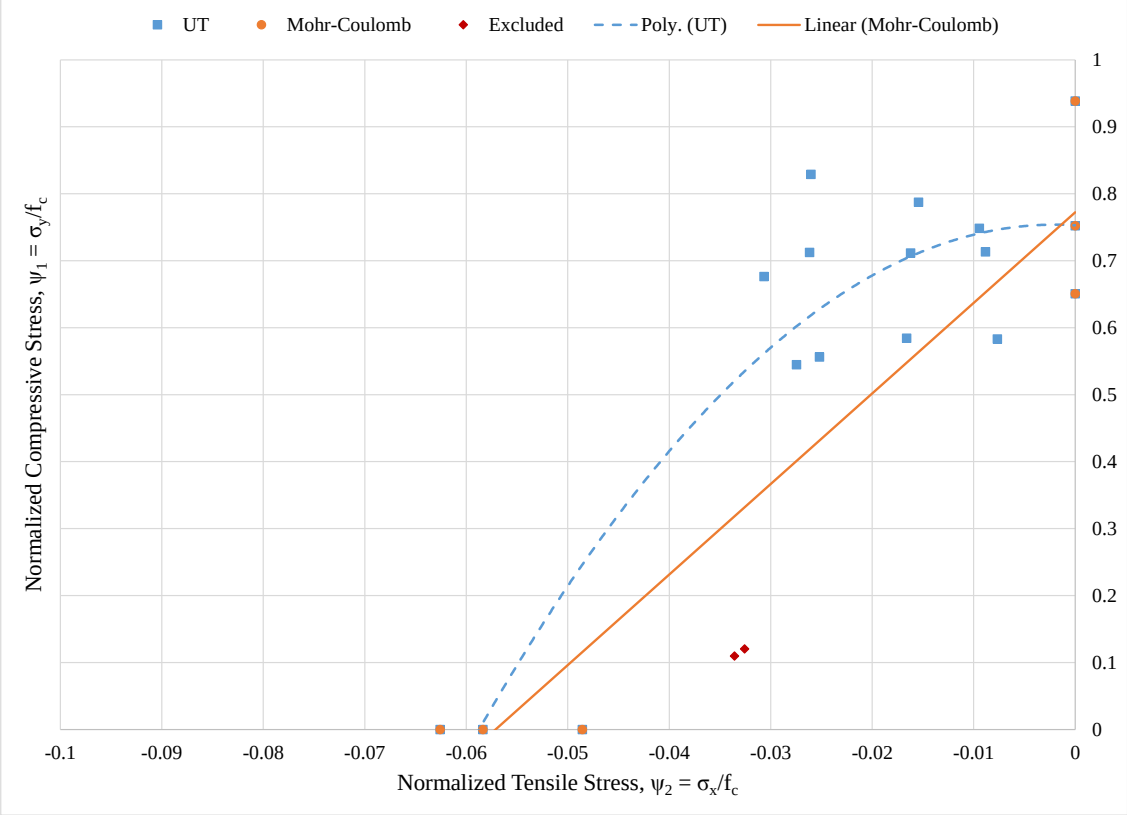

Figure 5-29: Proposed UHPC failure model compared with Mohr-Coulomb failure criterion using direct biaxial test data.

The proposed biaxial failure criterion is suggested as a means to predict whether or not a UHPC structural member will or will not crack under a specified loading resulting in biaxial stresses. For example, if a simply supported beam were loaded with a single point load at midspan, biaxial tension and compression stresses would form in the cross section as shown in Figure 5-30. If the compressive and tensile stresses are normalized according to their compressive strength determined using 2 in. cube specimens and are then plotted on the given axes, the UHPC would be considered uncracked if the point were inside the failure criterion envelope (Figure 5-31). If the plotted point was outside the failure criterion envelope, the section would be considered cracked. This method would ideally be used to identify shear failures, where biaxial stresses result in diagonal cracking (Figure 5-30).

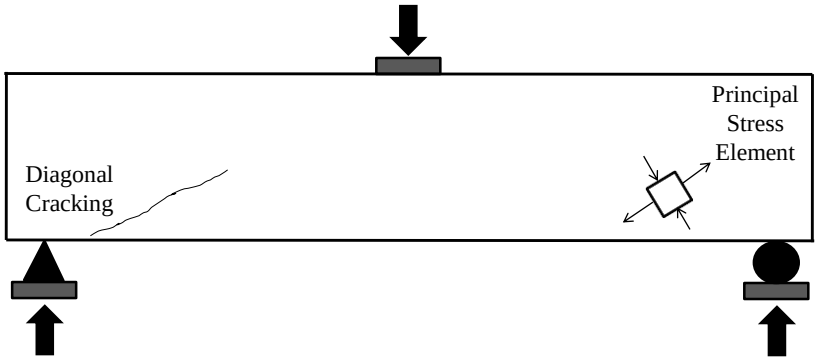

Figure 5-30: Biaxial stress element and diagonal cracking in a simply supported beam loaded at midspan.

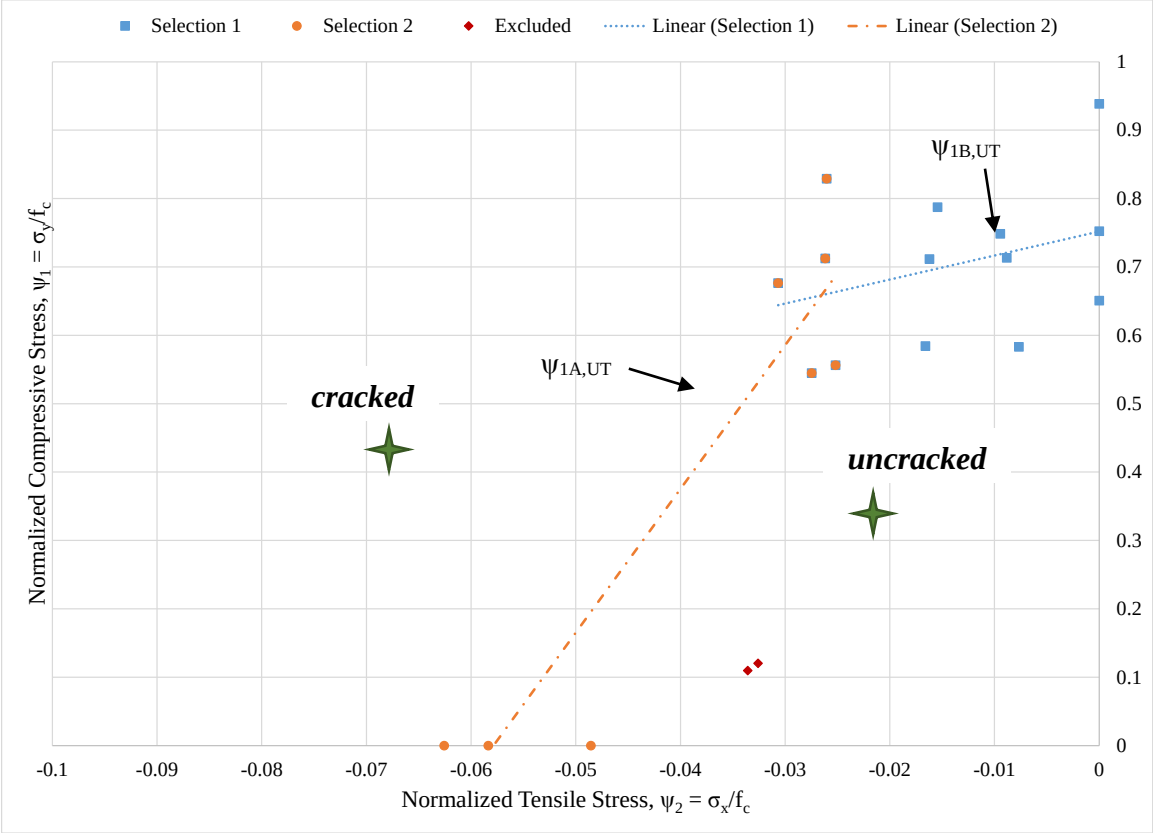

Figure 5-31: Biaxial stresses plotted with bi-linear failure criterion envelope to predict cracked and uncracked UHPC.

5.8 Influence of Material Property Testing and Direct Biaxial Results

5.8.1 Influence of Age on Ductal® Premix

At the time of placement for many of the direct biaxial specimens, the dry premix had been stored in the laboratory for approximately 2.5 years. The specimens placed in August 2011 were removed from the molds after 2 days. This early release from molds, as compared to 4 days, could have contributed to a reduction in compressive strength as compared to the initial characterization mix in 2008. A mix in 2012, however, was released after 4 days to provide a direct comparison with the mix in 2008. Although Lafarge suggests the premix be used within 3 months of delivery (Lafarge 2013), the aged premix bags did not cause any significant reduction in compressive strength (Table 5-14, Figure 5-32). On the contrary, the compressive strength increased at 14 days and beyond, such that the compressive strength had increased by 14 percent at 28 days when using the aged premix. Since the 2008 mix was placed in December, the ambient temperature of the laboratory was approximately 76°F; whereas, the lab remained at a temperature consistently above 85°F while curing of the 2012 mix took place. This increase in curing temperature was likely a factor that also affected the compressive strength.

Table 5-14: Compressive strength comparison for Untreated UHPC using aged Ductal® premix.

Mix Date	Graybeal (2006a)	12/4/2008	8/2/2011	8/4/2011	8/6/2011	6/18/2012
Release Age (days)	2	4	2	2	2	4
28-day Compressive Strength (ksi)	17.3	20.8	20.1	16.4	18.8	23.8

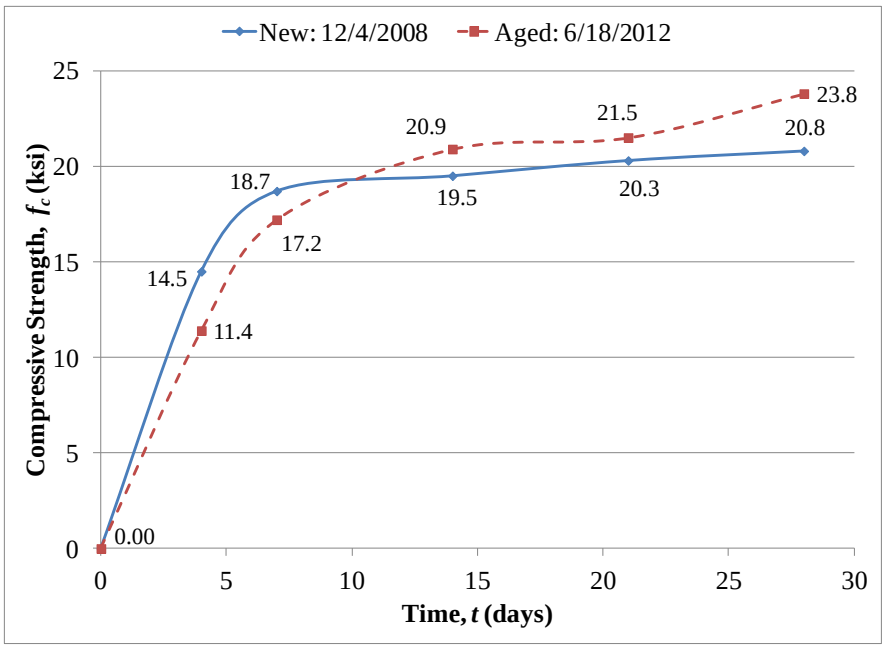

Figure 5-32: Compressive strength gain of UHPC using new and aged Ductal® premix.

5.8.2 Specified Compressive Strength for Untreated UHPC

Data from the direct biaxial (DB) mixes provided further insight into an appropriate specified compressive strength for untreated UHPC. Data from eight different mixes was used in combination with Section 5.3 of ACI 318-11 (ACI Committee 318 2011). The 24 samples yielded an average compressive strength of 20.1 ksi with a standard deviation of 2.60 ksi (

Table 5-15). Using ACI equations (5-1) and (5-3) (Equations (5-18) and (5-19)) and a modification factor (MF) of 1.04, a specified design compressive strength for untreated UHPC was calculated as 16.50 ksi. Based on the ACI 318-11 (ACI Committee 318 2011) specifications, a specified compressive strength value of 16.0 ksi is suggested for design using untreated UHPC.

Table 5-15: 28-day compressive strength data for untreated UHPC.

Mix ID	No.	f_c (ksi)
MC-120408	1	20.50
	2	20.80
	3	21.30
DB-080211	1	19.38
	2	21.88
	3	19.00
DB-080411	1	16.88
	2	15.50
	3	16.88
DB-080611	1	17.25
	2	20.63
	3	18.38
DB-061812	1	23.13
	2	24.38
	3	23.75
DB-081712	1	22.50
	2	22.00
	3	21.63
DB-082212	1	21.88
	2	22.00
	3	22.25
DB-082712	1	17.50
	2	17.13
	3	16.13
Average, f'$_{cr}$ (ksi)		**20.1**
Standard Deviation, s_s (ksi)		**2.60**

$$f_{cr}' = f_c' + 1.34(MF)s_s \tag{5-18}$$

$$f_{cr}' = 0.90 f_c' + 2.33(MF)s_s \tag{5-19}$$

Where,

f_{cr}' = required average compressive strength, psi
f_c' = specified compressive strength, psi
s_s = sample standard deviation, psi
MF = modification factor for sample standard deviation when less than 30 samples are available; MF is 1.04 for 24 samples according to ACI 318-11 Table 5.3.1.2.

5.8.3 Proposed Testing Method for Direct Tensile Strength

The AASHTO Standard T 132-87 (2004) briquet tensile strength from the initial material characterization was shown to most accurately represent the tensile strength obtained from the direct biaxial test (Table 5-16). This method showed a tensile strength only 18.6 percent higher than the direct biaxial responses, whereas other methods exceeded 60 percent. Since the direct biaxial test design was inspired by the briquet tensile strength test, these results are expected. Although the small 1 in. by 1 in. cross-section of the briquet was initially thought to be a hindrance to validate the briquet tensile strength, the direct biaxial test results indicate that the small cross-section did not significantly affect the tensile strength. Rather, tensile strength is grossly over-estimated using the split cylinder and flexure prism tests. The direct biaxial pure tension results could have been affected by the circular fiber alignment, as mentioned previously; however, this fiber alignment would have also affected the split cylinder test results since a similar pattern was found to exist in these specimens.

Table 5-16: Comparison of tensile strength tests to direct biaxial test.

	Standard Tension Tests				**Direct Biaxial (DB)**	
Test	**Split Cylinder (MC)**	**Briquet (MC)**	**Ultimate Flexure Prism (MC)**	**Split Cylinder (DB)**	**Untreated (UT)**	**Untreated Incline (UT-I)**
Average f_t (ksi)	3.44	1.45	3.18	3.36	1.18	1.14
% Difference (above DB-UT)	65.7	18.6	62.9	64.9	-	-

MC – indicates the results of this test were determined from the initial material characterization mix on 12/4/2008 (MC-120408).
DB – indicates the results of this test were from the direct biaxial mix on 06/30/2011 (DB-063011).

5.9 Summary of Direct Biaxial Test Results

The direct biaxial test (DBT) was developed to determine biaxial behavior of UHPC in combined tension and compression. Relationships of biaxial behavior were determined for three different conditions: untreated UHPC with random fiber orientation, steam treated UHPC with random fiber orientation, and untreated UHPC with controlled fiber orientation. For all cases, little interaction between tensile and compressive stresses was observed for tensile stresses below 60 percent of the pure tensile strength. Small decreases in the pure compressive strength were observed up to this point. With the exception of pure tensile strength, few data points were available at high tensile stresses above 60 percent of the pure tensile strength. In some cases, failure occurred as the compression blocks were being set up, suggesting tensile creep could be a cause of failure with sustained tensile stresses.

The effects of compressive strength were evaluated by comparing DBT data of steam treated and untreated UHPC with random fiber orientation. Increasing compressive strength of UHPC through steam treatment increases the normalized pure compressive strength of UHPC. Because tensile strength does not increase to the same degree as compressive strength, the normalized tensile strength of steam treated UHPC decreased as compared to untreated UHPC. Using the data from this study, factors were identified to develop a failure model for UHPC of varying compressive strengths. Additional testing should be completed to determine whether or not these factors are applicable to all UHPC.

The effects of fiber orientation was evaluated by comparing DBT data of untreated UHPC with controlled and random fiber orientations. Contrary to the original hypothesis that fiber orientation would greatly affect the pure tensile strength of UHPC, fiber orientation was shown to negligibly affect tensile strength of UHPC using the DBT method. Controlled fiber orientation was, however, shown to significantly increase the pure compression results of the DBT data set. In both cases, failure of UHPC in biaxial stress states was expressed using both a two-degree polynomial and a bi-linear model. Either model type for untreated UHPC with random fiber orientation would provide a conservative representation for untreated UHPC with controlled fiber orientation. For the purposes of this study, the two-degree polynomial derived for untreated UHPC with random fiber orientation was proposed as a conservative representation of UHPC.

By evaluating compressive strength data from various mixes, aged Ductal® premix did not negatively affect the ultimate compressive strength. Aged premix did reduce early age compressive strength at less than 14 days. Using data from eight different mixes, a specified compressive strength of 16 ksi was proposed for design of untreated UHPC according to ACI 318-11 (ACI Committee 318 2011) specifications.

Chapter 6: UHPC Bridge Deck Design and Preliminary Testing

This chapter presents the methods and criteria used to design a waffle slab UHPC bridge deck. Untreated UHPC was used for the design of the bridge deck. By eliminating the need for steam treatment, an untreated UHPC bridge deck is suggested to provide a more cost-effective solution for using UHPC in bridges by eliminating the need for precast concrete producers to install and maintain specialized steam chambers. Although the maximum benefits of steam treated UHPC would not be possible, untreated UHPC still provides greatly improved material properties as compared with conventional concretes currently implemented for bridge deck construction.

A first iteration design is first presented using established material models for UHPC and appropriate reference to ACI Committee 318 (2011) and AASHTO (2012) specifications. Single cell units of the UHPC bridge deck were used for preliminary testing to investigate possible placement scenarios. Beams were cut from the ribs of the single cell units and tested in third-point bending. Modulus of rupture values were determined based on the third-point bending results to compare placement methods. Based on the single cell unit test results, a second iteration bridge deck design was determined. Design calculations are in Appendix B, and supplementary single cell test results are in Appendix D.

For the purposes of this section, the transverse section of the bridge deck is considered perpendicular to the supporting steel girders spanning the bridge longitudinally (Figure 6-1).

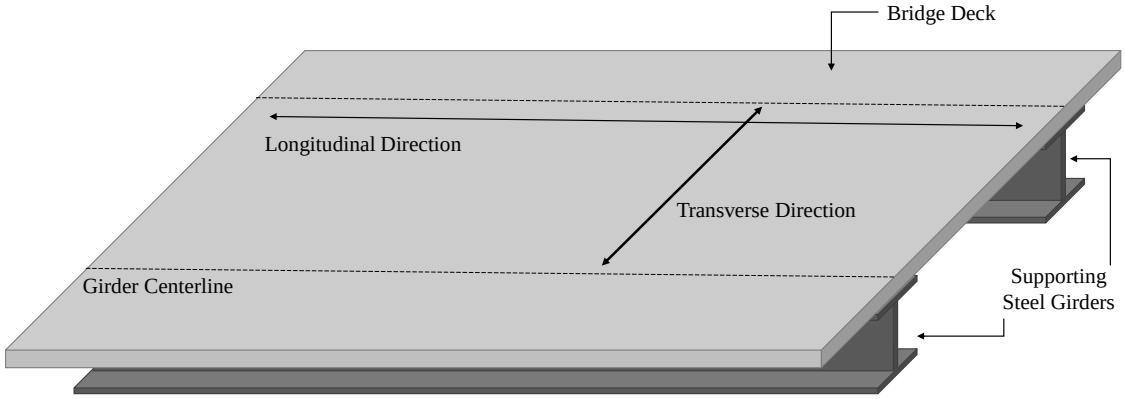

Figure 6-1: Longitudinal and transverse directions of bridge deck.

6.1 First Iteration Design Using Established Material Model

An initial design was determined using the established stress-strain material model by Graybeal (2008) with modifications to account for observed differences with untreated UHPC. Shear strength was determined using the AFGC and Setra (2002) recommendations and recommendations by Graybeal (2006b). The UHPC bridge deck was designed to achieve similar performance levels as compared to a conventional full-depth concrete bridge deck.

A conventional concrete bridge deck design was used as the basis for a deck design using UHPC (Figure 6-2). This cross-section was originally designed by Michael Baker, Inc. for girder spacing of 9 ft, 9 in. and was used in a prior study as a comparison for a UHPC bridge deck analysis by Garcia (2007). The conventional bridge deck was an 8-in. full-depth reinforced concrete deck using a concrete compressive strength, f'_c, of 4000 psi. No. 5 reinforcing bars were placed at 8 in. on center for positive bending, located at a depth of 6-11/16 in. No. 5 reinforcing bars spaced at 6 in. on center were placed at a depth of 2-5/16 in. for negative bending. In order to directly compare this bridge deck to the UHPC deck, the deck was analyzed for a transverse span length of 8 ft using the equivalent strip method defined in AASHTO Section 4.6.2.1 (AASHTO 2012). Design parameters were determined based on the contribution of the deck per foot of longitudinal width (Table 6-1). The conventional concrete deck was considered to be singly-reinforced for determination of bending moments.

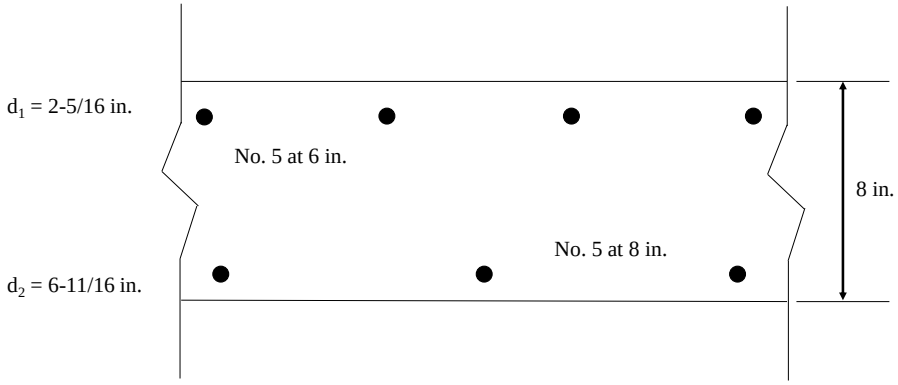

Figure 6-2: Transverse section through conventional reinforced concrete bridge deck (Option 0).

Table 6-1: Conventional concrete bridge deck design parameters for 8 ft girder spacing.

Design Parameter	Units	Conventional Concrete Bridge Deck Panel
Mn+	k-ft / ft	14.75
Mn-	k-ft / ft	-16.22
Vn	k / ft	10.2
EI_g	k-ft^2 / ft	12,818
Δ_i	in. / ft	0.0025
Δ_p	in. / ft	0.2194

6.1.1 Design for Flexure

Both positive and negative bending were considered for the design of the deck. The Graybeal (2008) stress-strain model for UHPC was modified to account for the reduced compressive strength of untreated UHPC as compared to steam-treated UHPC. A maximum compressive stress, f_{mc}, of 16 ksi was used in place of the 24 ksi identified in the Graybeal (2008) model (Figure 6-3). The value of 16 ksi was chosen based on a previous recommendation for modifying the specified compressive strength for untreated UHPC (Section 5.8) using prior data from material testing in this project. Using the linear stress-strain relationship from the Graybeal (2008) model, a corresponding ultimate compressive strain of 0.0021 was chosen for the modified stress-strain model used for the first design iteration. No modifications were made to the tensile region of UHPC in bending for the original design. An effective prestress of 150 ksi, approximately 56 percent of f_{pu}, was used for all prestressing steel. Because similar load factors would be applied to the bridge decks, nominal capacities were compared for this analysis.

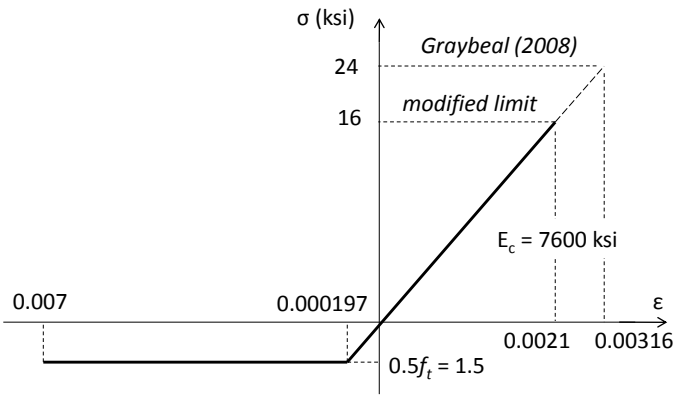

Figure 6-3: Stress-strain relationship used for first deck design iteration using modified limit based on Graybeal (2008) model.

Three design options were compared to determine the optimal prestressed UHPC bridge deck design. The design options used different amounts of prestressing steel. Prestressing steel was used to take advantage of the high compressive strength of UHPC and to initially place the tensile region of the deck into a state of compression. Due to availability, only 0.5 in. and 0.6 in. prestressing steel strands were considered for the designs. In each case, the bridges were designed considering a single T-beam section taken along the transverse direction of the bridge deck. The T-beam section had a flange width equivalent to the rib spacing. Longitudinal ribs were assumed to be spaced similarly to the transverse rib spacing, and the effects of longitudinal ribs were neglected.

The first design, Option 1, had two 0.5 in. low-relaxation prestressing strands with an ultimate tensile stress limit of 270 ksi (Figure 6-4). The cross-sectional area was minimized by spacing ribs at 28 in. center-to-center and making the thickness of the flange 2 in.

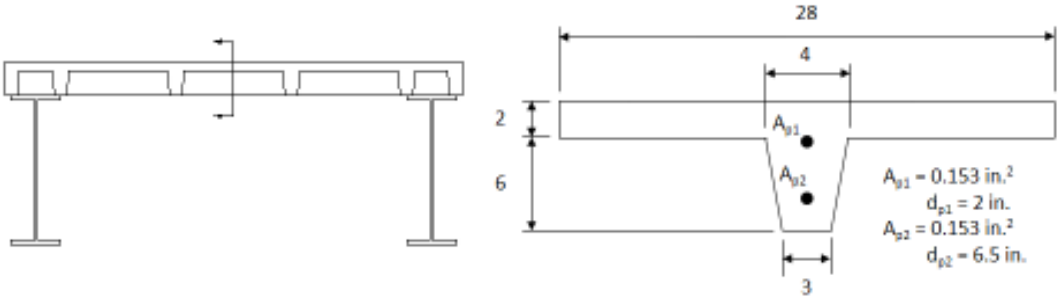

Figure 6-4: UHPC deck design using two 0.5 in. prestressing strands and 28 in. rib spacing; dimensions shown in inches (Option 1).

The second design, Option 2, had a single 0.6 in. prestressing strand with an ultimate tensile stress limit of 270 ksi (Figure 6-5). No reinforcement was used to aid negative bending; rather, the contribution of discrete fiber reinforcement was relied upon for negative bending. Due to the reduced contribution of the prestressing steel as compared to the first design option, the rib spacing was reduced to 24 in. center-to-center. The flange was also made 2 in. thick.

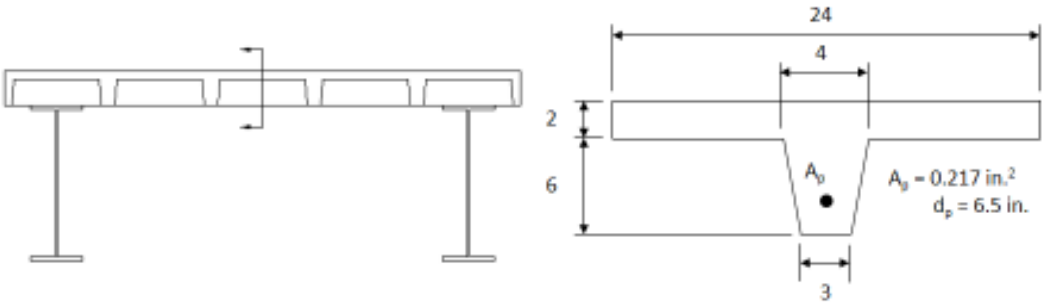

Figure 6-5: UHPC bridge deck design using a single 0.6 in. prestressing strand with 24 in. rib spacing; dimensions shown in inches (Option 2).

The final design, Option 3, had a single 0.5 in. prestressing strand for positive bending and a single No. 11 reinforcing for negative bending (Figure 6-6). As in the second design option, the reduced reinforcement contribution led to a reduction in the rib spacing to 24 in. center-to-center, and a 2 in. flange thickness was chosen.

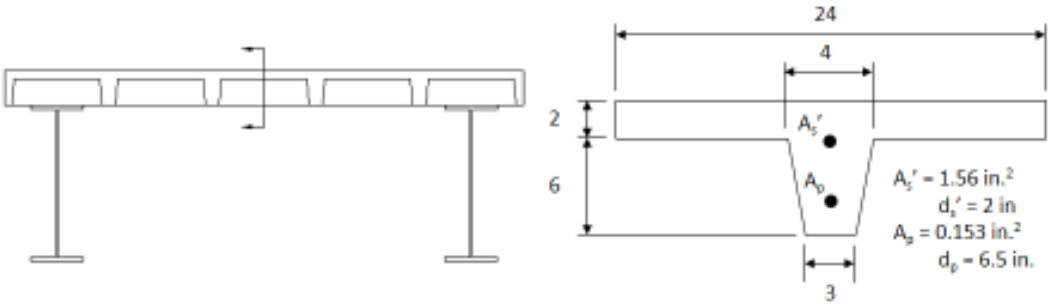

Figure 6-6: UHPC bridge deck design using a single prestressing strand and a reinforcing bar with 24 in. rib spacing; dimensions shown in inches (Option 3).

Option 1 was shown to be the optimal design to achieve the desired moment capacities and reduce the gross cross sectional area of UHPC (Table 6-2). Reducing the area of UHPC was considered a high priority in order to make UHPC bridge decks more feasible for practice. The high cost of raw materials combined with specialized labor during construction could potentially lead to a negative response from the construction industry. Therefore, reducing raw material costs was a high priority in this design. Although there is an added cost due to prestressing steel as compared to conventional reinforcement, these bridge deck panels would be produced in a precast plant that would already be equipped for such practices. Therefore, the additional cost of prestressing steel was not considered to be a deterring factor in choosing a design. The added benefits of prestressing steel over conventional reinforcement should also not be neglected, since it was originally hypothesized that prestressing would aid in reducing the likelihood of shear failure modes in UHPC bridge decks.

Table 6-2: Nominal moment capacity for UHPC bridge deck designs.

Option No.	Description	A_g (in.^{2}/ft)	Mn^+ (k-ft/ft)	% Mn^+ Overstrength	Mn^- (k-ft/ft)	% Mn^- Overstrength
0	Conventional Concrete	96	14.8	0	-16.2	0
1	UHPC with 2 ea. 0.5 in. prestressing steel, 28 in. rib spacing	31.7	15.2	2.7	-19.8	22
2	UHPC with 1 ea. 0.6 in. prestressing steel, 24 in. rib spacing	33	19.9	34	-17.8	9.9
3	UHPC with 1 ea. 0.5 in. prestressing steel, 1 No. 11 reinforcing bar, 24 in. rib spacing	33	18.1	22	-18.6	15

6.1.2 Shear Considerations

The three UHPC designs as mentioned previously in Section 6.1.1 were analyzed for shear (Table 6-3). Research has shown shear failure can occur in UHPC ribbed bridge decks (Saleem et al. 2011), which emphasizes the need for this design consideration. The shear capacity was determined for UHPC using the proposed Graybeal (2006b) recommendations (Section 2.4.3.4). The 1.3 factor of safety in this recommendation was omitted to directly compare nominal shear values. No additional shear reinforcement was provided in the 8 in. thick bridge deck design; therefore, only the discrete fiber contribution to shear strength was considered. However, it should be noted that the effects of prestressing would enhance the overall shear strength.

Table 6-3: Shear capacity of UHPC bridge deck design using only steel fiber contribution.

Option No.	Design	V_n (k / ft)	% Over Conventional Concrete Design
0	Conventional Concrete	10.2	0
1	UHPC with 2 ea. 0.5 in. prestressing steel, 28 in. rib spacing	8.97	-12
2	UHPC with 1 ea. 0.6 in. prestressing steel, 24 in. rib spacing	10.4	2.0
3	UHPC with 1 ea. 0.5 in. prestressing steel, 1 No. 11 reinforcing bar, 24 in. rib spacing	10.4	2.0

The nominal shear strength for Option 1 was lower than Options 2 and 3 because these values were calculated per linear foot along the longitudinal direction (Table 6-3). Although the rib dimensions were equivalent for all options, resulting in a similar shear capacity for each cross-section, Option 1 had a larger rib spacing of 28 in. as compared to both Options 2 and 3. The larger rib spacing decreased the shear contribution provided per linear foot. Although Option 1 had a shear capacity lower than the conventional concrete design, the contribution of the prestress force was not factored into the total shear capacity based on recommendations for UHPC.

Due to the proposed flange thickness of 2 in., punching shear was analyzed to determine whether or not the maximum suggested 28 in. rib spacing would be appropriate for the deck design. According to AASHTO (2012) 3.6.1.2, a standard 10 by 20 in. wheel patch load of 16 kips was considered for punching shear (Figure 6-7). Applying a live load factor (LL) of 1.75 and an impact factor (I) of 1.3 taken from AASHTO (2012) 3.4.1 and 3.6.2, the design patch load was determined to be 36.4 kips. Using a specified compressive strength of 16 ksi, the 2 in. thick flange with a 28 in. rib spacing has a punching shear strength of 51.6 kips (Table 6-4). The 2 in. flange thickness with a rib spacing of either 28 or 24 in. rib spacing was shown to be acceptable for punching shear. The ACI 318-11 (ACI Committee 318 2011) specifications for punching shear are prescribed for conventional concrete, where little data is available based on

concrete with compressive strengths above 10 ksi. Therefore, previous punching shear research for UHPC was consulted.

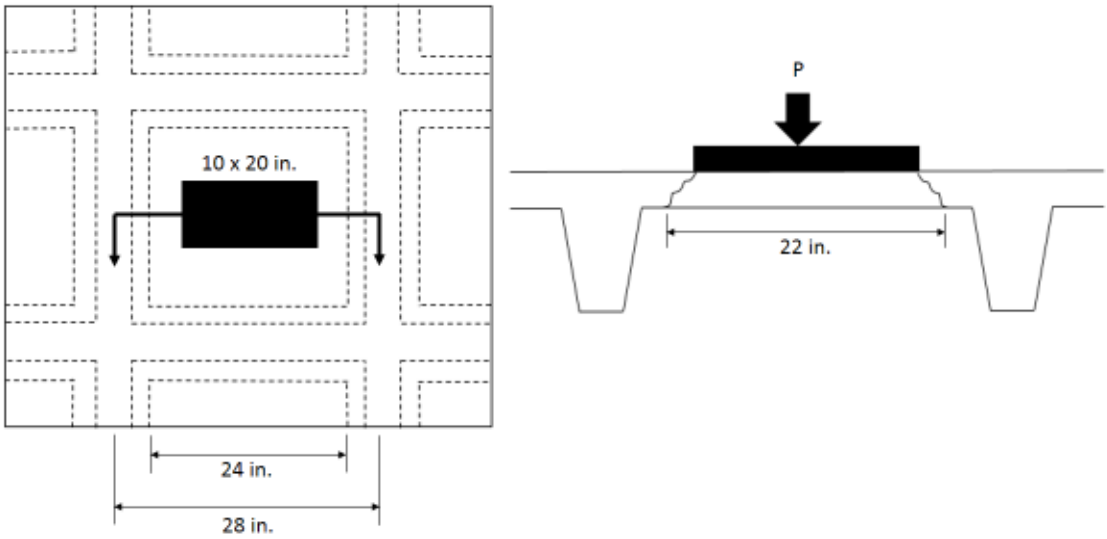

Figure 6-7: Punching shear analysis on 28 in. rib spacing.

Table 6-4: Punching shear comparisons for 24 and 28 in. rib spacing.

Rib Spacing (in.)	Perimeter, b_o (in.^{2})	V_u (k)	φV_n (k)	% Over V_u
28	22 x 12 = 68	36.4	51.6	42
24	20 x 12 = 64	36.4	48.6	34

Harris (2004) showed that a 2.12 in. thick UHPC slab supported at a distance of 36 in. failed at approximately 22 kips using a 1 in. square punch. This punch would be more representative of the area caused by a jack during a tire replacement, which is a more severe punching scenario. The proposed 28 in. rib spacing results in supports located at a 24 in. distance. This distance is 12 in. lower than that used by Harris (2004), and the tire contact area was considerably higher than the 1 in. square punch. Considering these differences, the 2 in. thick flange thickness in the UHPC bridge deck design is suggested to be acceptable for punching shear.

6.1.3 Deflection and Camber Considerations

The goal of this design was to establish similar behavior between the designed UHPC bridge deck and a conventional reinforced concrete bridge deck. To evaluate stiffness, deflection was evaluated for each design alternative. Initial camber and deflection (Δ_i) due to prestressing

and self-weight were determined for each UHPC deck design (Table 6-5). Live load deflections (Δ_{LL}) were also determined using an 8 ft girder spacing with a 16 kip tire patch load at midspan. At the live load, all UHPC decks were considered cracked sections. Option 2 had the lowest deflections, meeting the requirement set by the conventional concrete bridge deck. The deflections from Option 1 were nearly 50 percent more than the conventional concrete bridge deck strip. The contribution of the longitudinal ribs was not included in the deflection calculations. It is assumed that the ribs would reduce deflections; although, the contribution by the ribs should be analyzed using a full panel, not a single strip section.

Table 6-5: Deflection comparisons for UHPC bridge deck designs.

Option No.	Description	E_c (ksi)	I_e (in.^{4}/ft)	Δ_i (in. / ft)	Δ_{LL} (in. / ft)
0	Conventional Concrete	3605	94.3	0.003	0.219
1	UHPC with 2 ea. 0.5 in. prestressing steel, 28 in. rib spacing	7600	21.1	-0.023	0.313
2	UHPC with 1 ea. 0.6 in. prestressing steel, 24 in. rib spacing	7600	37.9	-0.039	0.217
3	UHPC with 1 ea. 0.5 in. prestressing steel, 1 No. 11 reinforcing bar, 24 in. rib spacing	7600	22.5	-0.027	0.404

Δ_i = initial camber/deflection due to prestress forces and self-weight
Δ_p = deflection due to 16 kip patch load at midspan of 8 ft. simple span

6.1.4 Summary of Initial Bridge Deck Design

Design Option 1 using two 0.5 in. prestressing strands was chosen as the first iteration bridge deck design. Option 2 was also considered a possible design because it resulted in similar deflections as the conventional concrete deck, and it resulted in sufficient shear strength. Although Option 1 had higher deflections and lower shear strength, the effect of longitudinal ribs had not been taken into account with this basic design method. The ribs were expected to provide stiffness to transverse bending, and the prestressing forces were expected to improve shear strength. Option 1 resulted in the smallest amount of UHPC material usage, which was important to limit construction costs. The 28 in. rib spacing was also best aligned with the 8 ft

girder spacing. The 24 in. rib spacing of both Options 2 and 3 would require formwork and additional grout fill for shear connections. Preliminary testing was necessary to confirm that sufficient strength and stiffness are provided using the chosen design.

6.2 Preliminary Testing of Bridge Deck Design

Preliminary testing took place on single cell units using the Option 1 geometry as previously discussed (Section 6.1). The single cell units were placed using three different placement methods in order to check the assumed material models and to determine an efficient formwork design for large scale deck section placement. A full collection of material properties for the single cell mixes and supplementary single cell data are provided in Appendix D.

6.2.1 Placement and Formwork Observations

The three different placement scenarios used for the single cells were as follows: A) top-side up placed from a corner, B) top-side up placed from the center of a rib, and C) upside down placed from one side and form inserted from above (Figure 6-8).

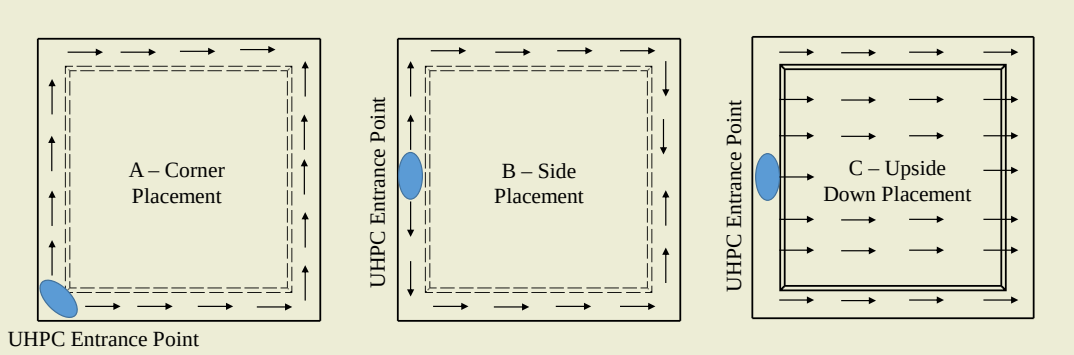

Figure 6-8: Placement scenarios for single cell units.

In scenario A, where the UHPC flowed from a corner, the UHPC intersected at the opposite corner to as the form filled (Figure 6-9). As the entrant corner filled with material, the UHPC began to flow over the bottom foam portion of the form. This inevitably led to another intersection point along the top flange portion atop the foam as the UHPC filled the opposite web and began to overflow over the foam (Figure 6-10).

Figure 6-9: UHPC intersected near the opposite corner of flow entrance for placement scenario A (Photo by K. Halbe).

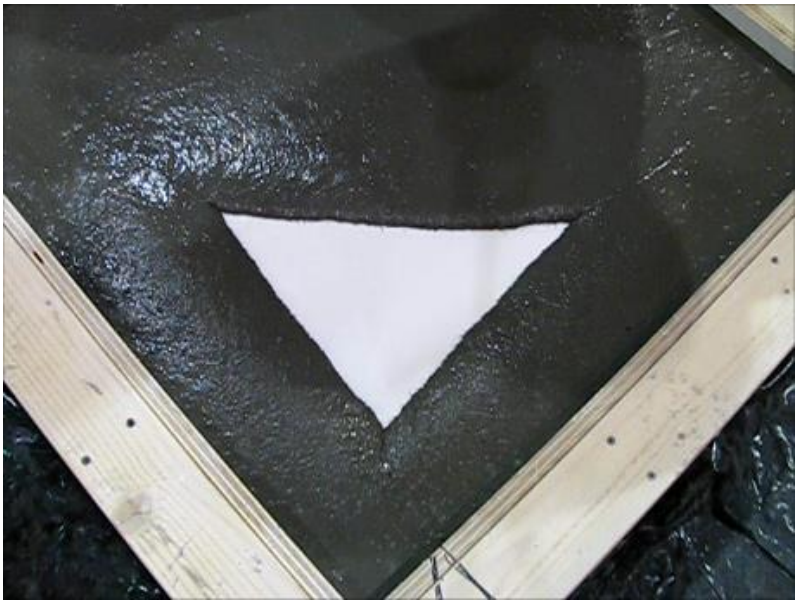

Figure 6-10: UHPC intersected along top flange for placement scenario A (Photo by K. Halbe).

In scenario B, in which the UHPC flowed from the center of a rib, the UHPC intersected at a point nearly centered on the opposite rib (Figure 6-11). Although the UHPC fronts flowed together horizontally, it did not appear as if the UHPC folded as it intersected. As observed, it

easily combined with the opposite horizontal flow. This is of significance because of prior testimony from Nachuk (2008) that UHPC folded in horizontal flow, not allowing the UHPC to intersect properly. This lack of intersection was not witnessed during this placement scenario. Third-point bending tests, discussed in Section 6.2.2 , show the influence this placement technique had on the modulus of rupture. As in the corner placement, the UHPC later intersected atop the foam form as UHPC filled the ribs and the form.

Figure 6-11: UHPC flows intersected near the midsection of the rib for placement scenario B (Photo by K. Halbe).

In the final scenario C where the single cell was placed upside down, a frame was inserted into an open box form filled with UHPC. The UHPC filled the form from one side to the opposite side, allowing no flow intersection points. As the frame containing the foam was placed into the form, the UHPC displaced with ease to form the center void and webs (Figure 6-12). No noted fiber orientation could be determined during this placement; however, it was noted that fibers were present in the extra material that was pinched from the top surface due to overfilling the form. Steel beams were used to hold the inserted formwork in place. Because the steel beams were brought in after the frame had been initially set in the UHPC section, the UHPC in the webs did fluctuate as pressure was released and depressed onto the frame. Since

four people held the four sides of the frame to the UHPC, two of them had to move out of the way to place the steel beams. As they moved away, the frame lifted up due to the loss of force, causing the UHPC fill to fluctuate in height, moving downward. Then, as the steel beam added force to the frame, the UHPC moved back upward to form the webs. This occurred a couple times during the placement before the final beam was set into place.

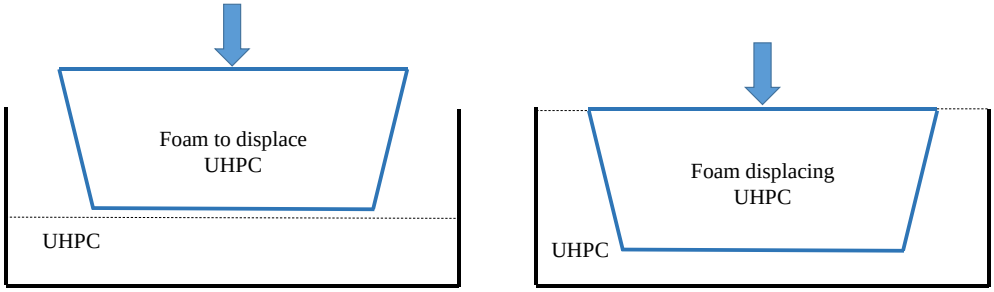

Figure 6-12: UHPC was displaced using foam formwork to form ribs.

Although the upside down placement required additional planning and precision, this method was not considered overly difficult as compared to the top-side placement approaches. However, additional considerations must be taken to accomplish the upside down placement. For instance, the location of the frame must be preset in order to place voids in the proper locations. Uniform pressure should be applied throughout the section when placing the voids; otherwise, the UHPC could fluctuate in height due to the workability and flow of the material. Also, once the section is placed, it must be flipped after the UHPC has set to properly align the top driving surface.

The formwork was fairly consistent for all single cells; however, the surface condition of the foam was different for one scenario. For two of the single cells, the surface of the foam was covered in a thin layer of wall joint filler material and lightly coated with Appliance Epoxy spray paint. The third foam piece was left bare, without any coating. It was noted that during form removal none of the foam sections released immediately. Rather, the foam had to be cut from the interior of the single cell using a hot knife. The interior edges were then removed more precisely using a flat-edged metal scraper. It was noted that the foam did release more easily from the two forms covered with the additional wall joint filler and painted coating. This coating also created a smoother interior surface as opposed to the bare foam. The bare foam caused the surface of the UHPC to mimic the imperfections of the foam. In both cases, no shrinkage

cracking was noted to have occurred in the sections, indicating that the foam did not significantly restrain the UHPC from shrinking. Shrinkage cracking was tested by misting the section with water to investigate the presence of micro-cracking.

Although the coated foam was easier to remove and provided a smoother UHPC finish, it did not save as much time as that used to apply the wall joint filler material and spray paint to the foam. The wall joint filler material required two to three applications. Each application had to fully dry before sanding took place to smooth the surfaces. This process took approximately two days to accomplish in order to allow for multiple coats, each one requiring sanding before the next. Finally, the painting took another day to ensure it was fully dry before attaching to the form. Because the paint would chemically degrade the foam if it were to come in direct contact, careful attention had to be taken to make certain the wall joint filler material completely covered the foam. The lengthy process involved in coating the foam did not significantly affect the removal time, leading to the decision to simply use bare foam in future forms.

The exposed top surface of the UHPC exhibited interesting characteristics as it was placed. At the start of the placement, the UHPC appeared very fluid and smooth along the surface. However, as time progressed throughout the placement, a dry "skin" began to appear along the top surface (Figure 6-13). The shape of the dry "skin" displayed the flow pattern of UHPC. This top surface "skin" formation is characteristic of UHPC.

Figure 6-13: Exposed surface of UHPC during top-side up corner placement, scenario A (Photo by K. Halbe).

6.2.2 Third-Point Bending Tests on Single Cell Ribs

Third-point bending tests were performed on beams cut from the single cell ribs to quantitatively and non-subjectively compare the placement methods. A total of eight beams were cut and tested from each single cell. The location of each beam was relevant to testing. The location was of each beam was noted in reference to the entrance point of UHPC and the direction of flow. Each beam was given a sample identification to indicate its location in the single cell webs and its location in reference to the flange (Figure 6-14, Figure 6-15). For example, a specimen with an identification of UD-A1 was from the upside down placement (UD), located in the web where UHPC entered the formwork (A), and located along the top of the web, nearest the flange (1).

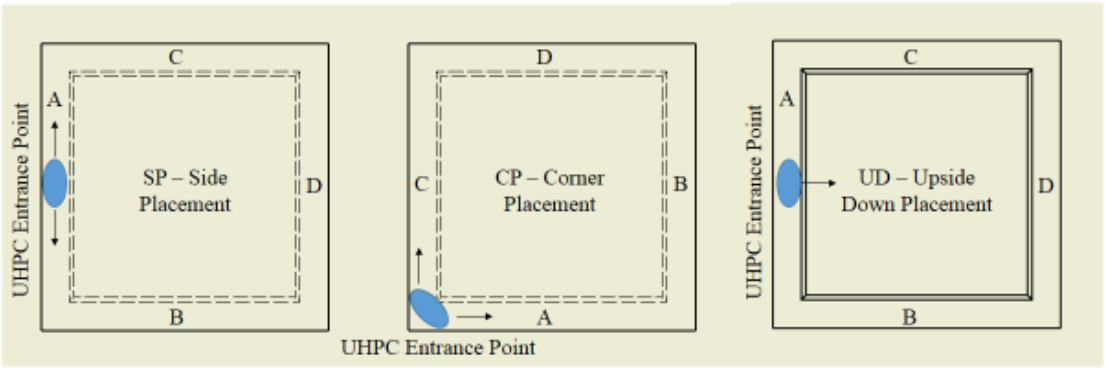

Figure 6-14: Location of beams cut from single cell ribs to indicate Sample ID based on direction of UHPC flow.

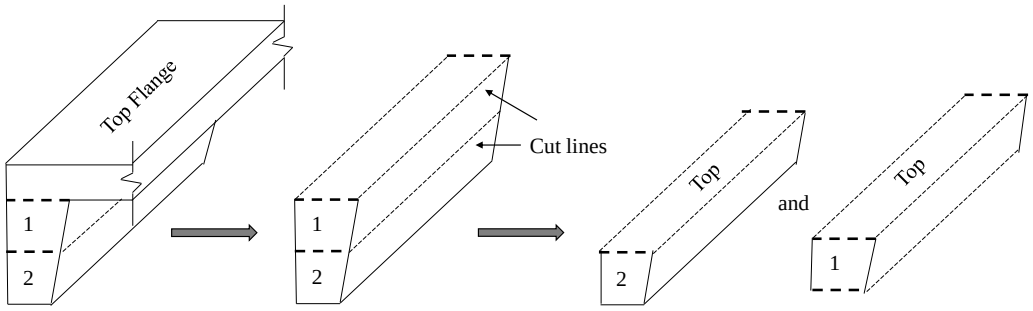

Figure 6-15: Location of beams cut from single cell ribs to indicate Sample ID based on distance from flange.

Prior to performing the test, the beams were measured to determine the average height and width of the sections. Because the sides of the webs were not uniform, varying along the 6 in. web height, the beams cut from the single cell webs were not uniform. Although the beams were measured and marked to be 3 in. high, the concrete saw did not allow for proper precision to ensure all beams were of uniform depth. A detailed collection of the beam dimensions is available in Appendix D. A simplified cross-section measurement was derived based on averaging the detailed dimensional values (Table 6-6). All beams were approximately 3 in. high by 3 in. wide.

Table 6-6: Simplified cross-sections for beams cut from single cell webs.

			Simple Cross Section	
Placement Scenario	**Sample ID**	**Location**	**h (in.)**	**b (in.)**
A	CP-A1	T	3.09	3.14
	CP-A2	B	2.81	3.00
	CP-B1	T	2.98	3.16
	CP-B2	B	2.86	2.97
	CP-C1	T	3.07	3.33
	CP-C2	B	2.78	3.11
	CP-D1	T	2.97	3.19
	CP-D2	B	2.84	3.00
B	SP-A1	T	2.89	3.16
	SP-A2	B	2.91	3.02
	SP-B1	T	2.96	3.25
	SP-B2	B	2.86	3.00
	SP-C1	T	3.01	3.22
	SP-C2	B	2.85	3.00
	SP-D1	T	3.00	3.19
	SP-D2	B	2.80	3.00
C	UD-A1	T	3.00	3.06
	UD-A2	B	2.59	2.88
	UD-B1	T	3.02	3.19
	UD-B2	B	2.70	3.05
	UD-C1	T	3.06	3.25
	UD-C2	B	2.48	3.03
	UD-D1	T	2.94	3.27
	UD-D2	B	2.84	3.00

T = top, B = bottom

Two values for the modulus of rupture were calculated for each sample using the cracking load and the ultimate load. Because UHPC is known to exhibit post-cracking strength gain, both values were determined. The typical load versus cross-head displacement curve shows significant post-cracking strength (Figure 6-16).

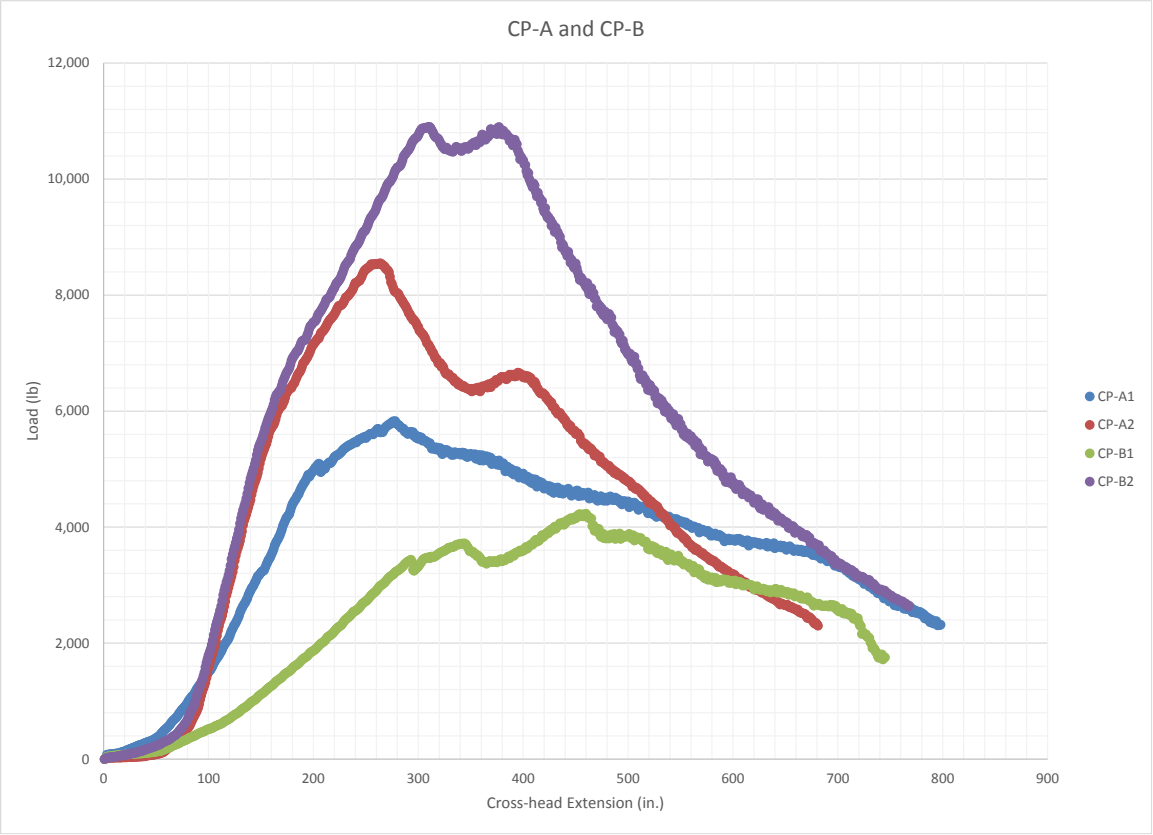

Figure 6-16: Typical load versus cross-head extension relationship for single cell third-point bending tests (placement scenario A, CP).

By comparing the placement methods, the corner placement (CP) method resulted in the highest modulus of rupture values; whereas, the upside down (UD) placement method resulted in much lower modulus of rupture values (Figure 6-17 and Figure 6-18). This was to be expected because the UHPC flowed along the length of every web in the corner placement method, allowing fibers to become aligned in the direction of principal tensile stresses located along the bottom fibers of the beam (Figure 6-19). Although the side placement (SP) method performed below the corner placement method, the webs created by continual flow in one direction (B and C) had values similar to those from the corner placement. Although it was hypothesized that

web SP-D would result in much lower values due to the intersection of horizontal flow, the modulus of rupture value appeared to be minimally affected as compared to values obtained in web CP-C.

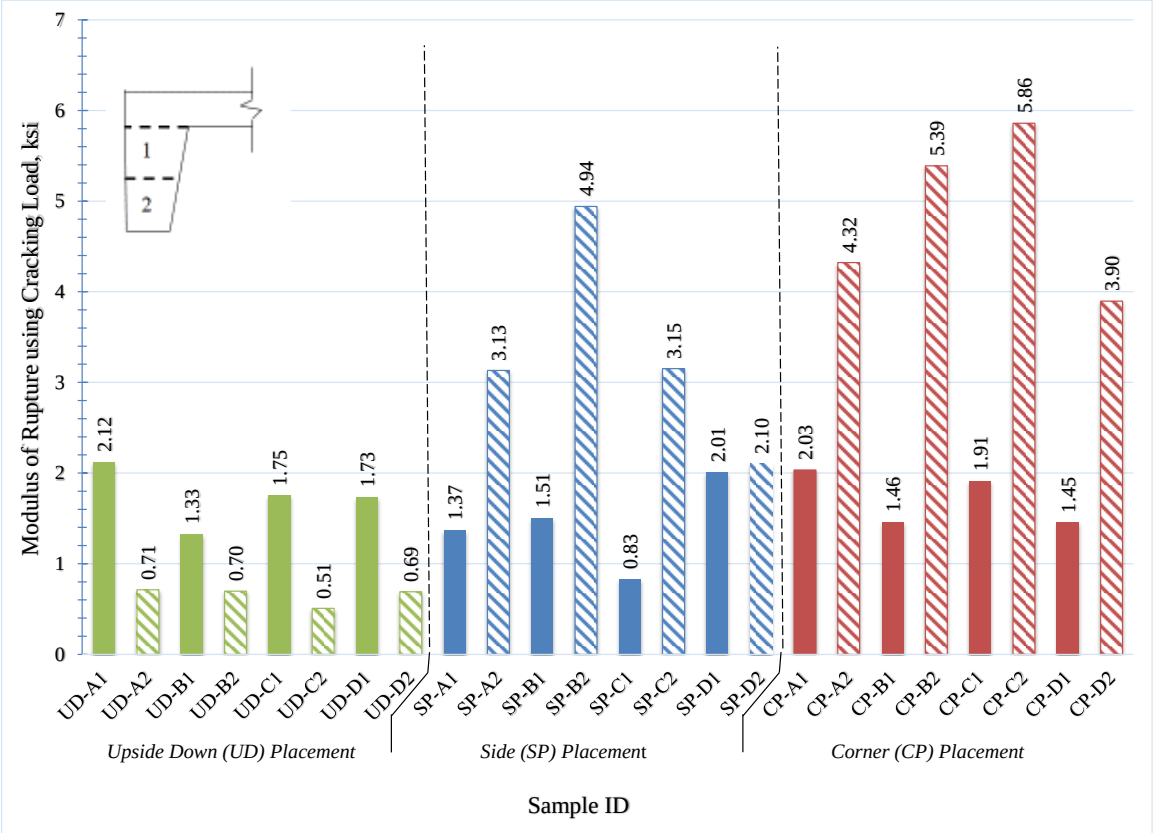

Figure 6-17: Modulus of rupture, $f_{r,cr}$, using cracking load of single cell webs.

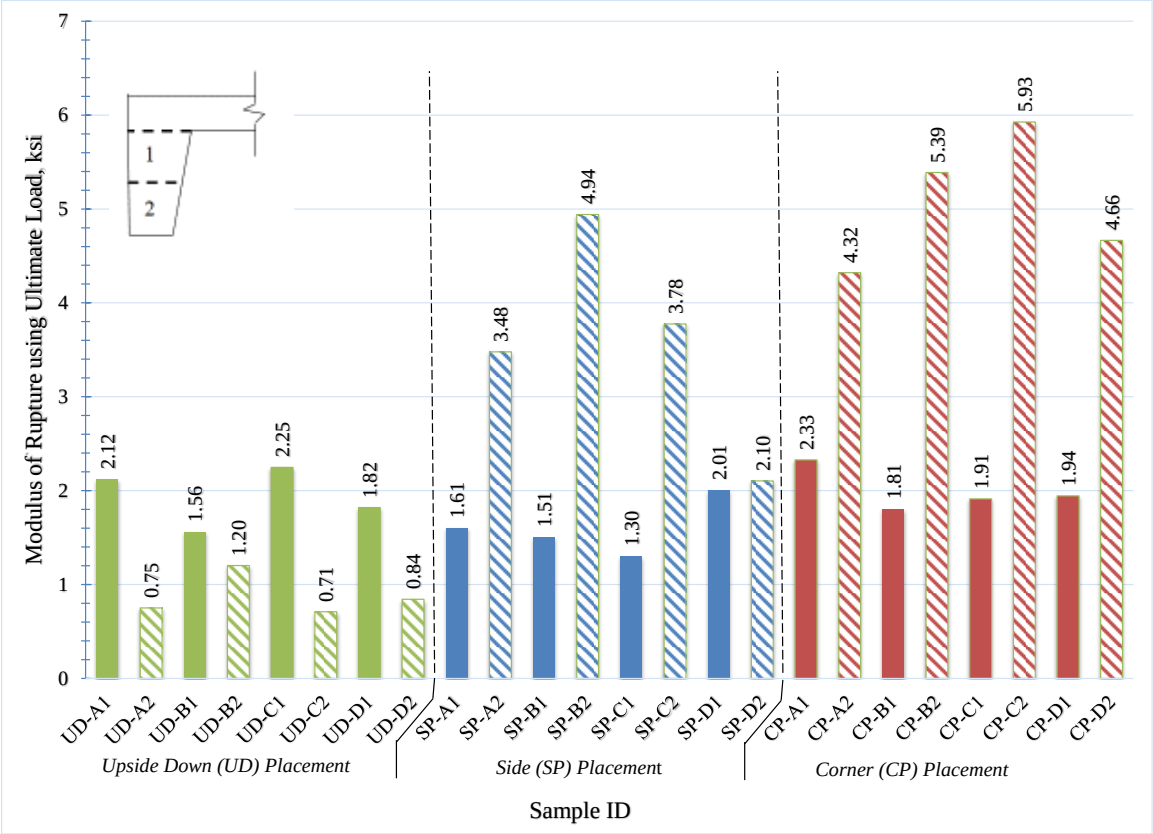

Figure 6-18: Modulus of rupture, f_r, using ultimate load of single cell webs.

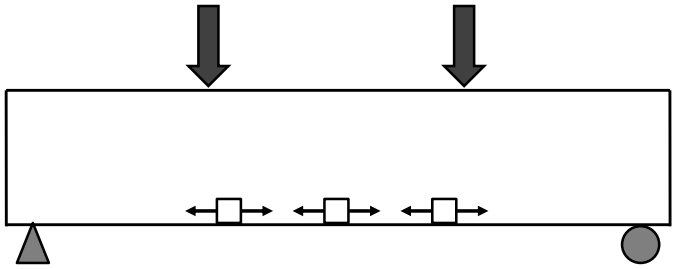

Figure 6-19: Principal tensile stresses along bottom fibers of beam in third-point bending.

In both SP and CP methods, the beams cut from the bottom of the webs (2) had higher modulus of rupture values as compared to the beams cut from the top of the webs (1). In the UD method, the opposite was observed; the beams cut from the bottom of the webs yielded higher modulus of rupture values than those cut from the top of the webs. This indicates that the tensile strength may not be uniform throughout the depth of a UHPC beam; rather, the tensile strength

tended to increases through the depth of the beam, where it is highest along the bottom face of formwork.

6.2.3 Influence of Placement Orientation

A distinct relationship was observed between the modulus of rupture value determined from the single cell webs and the distance from the bottom face of the form. As the distance of the extreme tensile fiber of the beam increased from the bottom face of the form, the modulus of rupture value decreased (Figure 6-20). The data below 5 in. included the CP and SP placements, and the data above 5 in. only included the UD placements.

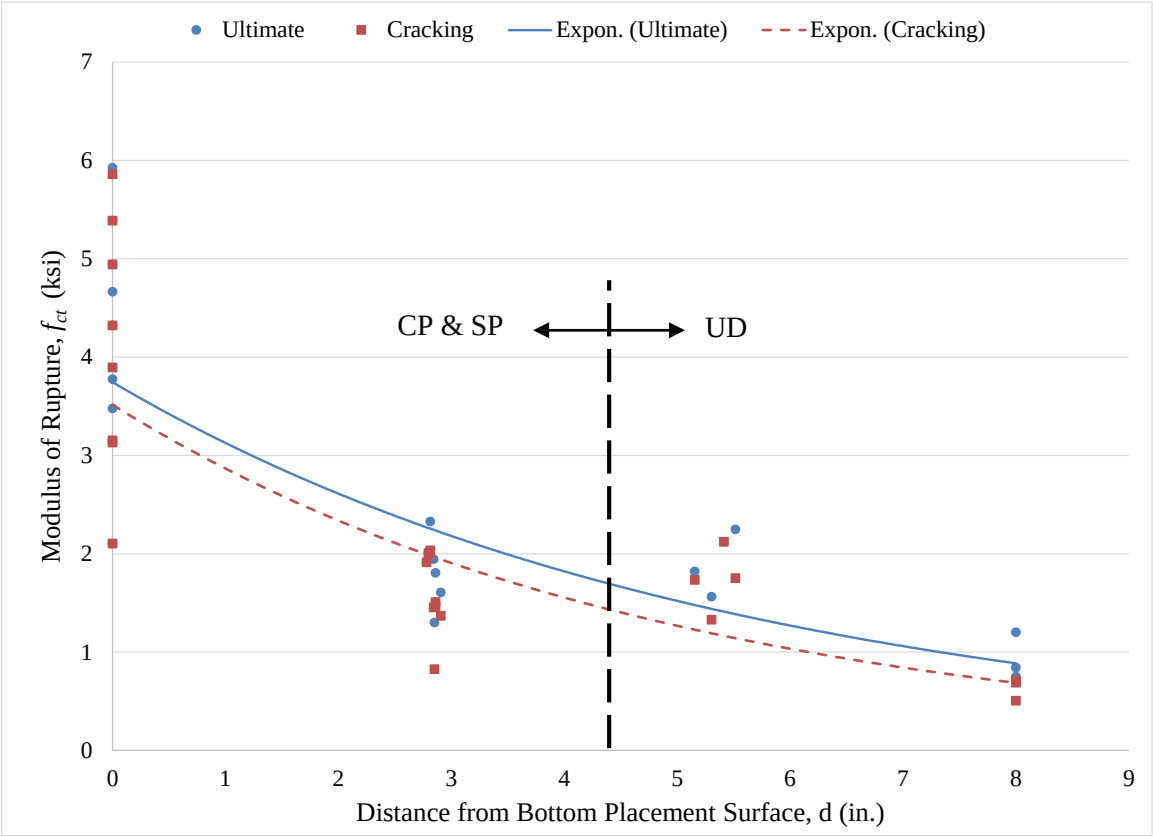

Figure 6-20: Relationship of modulus of rupture and distance from bottom face of form.

6.2.4 Physical Observations

Through a physical examination of the beams, very few fibers were observed in the UD samples, especially those taken from the bottom of the webs (Figure 6-21 to Figure 6-24). On the contrary, a high fiber volume was observed in both the CP and SP samples taken from the

bottom of the webs; the opposite occurred in the bottom web samples (Figure 6-25 to Figure 6-28). The low fiber concentration in the UD samples was either a result of the placement technique itself or a result of fiber sinking. Because the beams cut from the top of the web displayed lower modulus of rupture values in both the SP and CP methods, whereas the opposite was true for the UD placement, it was assumed that fiber sinking may have been a universal problem among all the single cells.

Figure 6-21: Failure crack of UD-A1 (top of web).

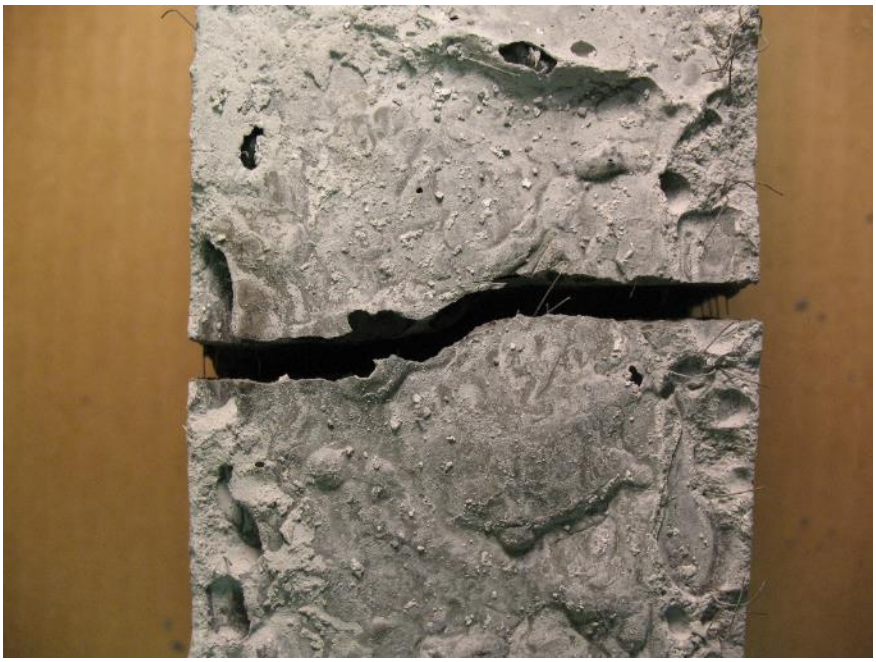

Figure 6-22: Failure crack of UD-D2 (bottom of web).

Figure 6-23: Failure crack of UD-C1 (top of web).

Figure 6-24: Failure pattern of UD-B2 (bottom of web).

Figure 6-25: Failure crack of SP-C1 (top of web).

Figure 6-26: Failure crack of SP-C2 (bottom of web).

Figure 6-27: Failure crack of CP-D1 (top of web).

Figure 6-28: Failure crack of CP-D2 (bottom of web).

Of particular concern were the single cell beams where UHPC intersected horizontally. The SP-D1 and SP-D2 beams were located in a region where an intersection occurred. The intersection point (I) was located between the constant moment region of the beam during testing, and it was the expected weak point of the beam. Failure did not occur directly at the intersection point, indicating that a weak point did not result due to the horizontal flow of UHPC (Figure 6-29 to Figure 6-30). However, the modulus of rupture value for SP-D2 located along the bottom was lower than SP-B2 and SP-C2 where continuous flow of UHPC took place throughout the rib. This did indicate that although the controlling crack did not occur exactly at the initial intersection point (I), a weakened section did result from this placement technique. It is further shown that SP-D1 and SP-D2 outperformed all bottom beam samples (2) from the upside down (UD) placement. More testing should take place in future studies to confirm these findings if horizontal flow is a consideration since there was only one sample available through the current project.

Figure 6-29: Failure surface of SP-D2 (bottom of web), where I is the intersection point of UHPC flow and CL is the center point of the rib.

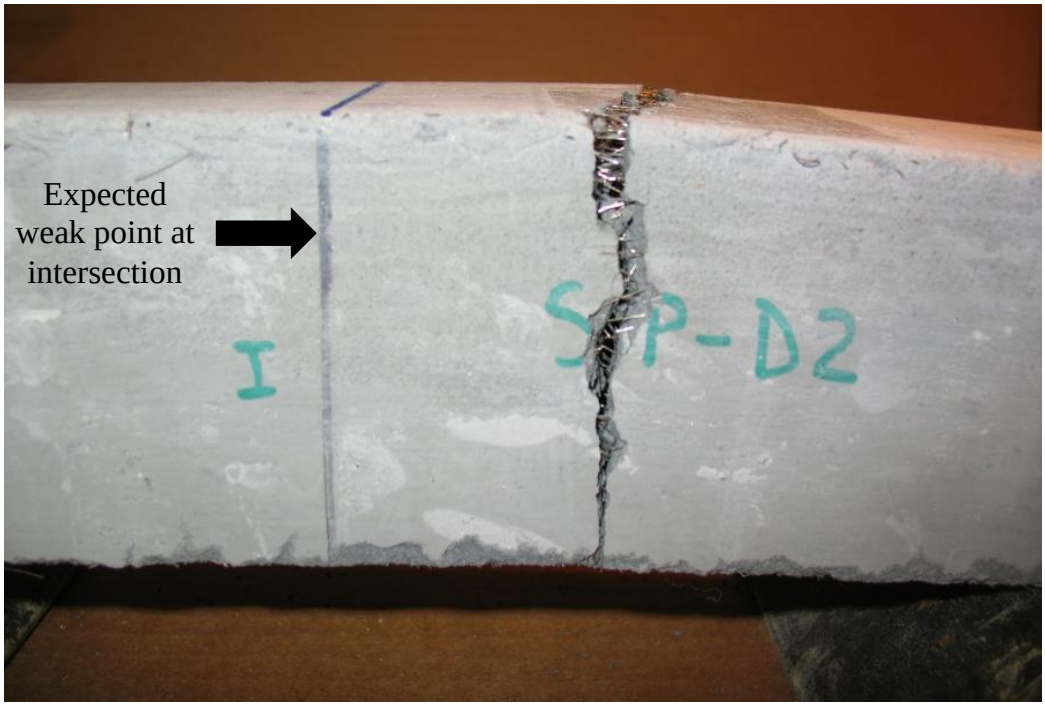

Figure 6-30: Failure pattern of SP-D2 (bottom of web), where I is the intersection point of UHPC flow.

Overall, the upside down placement technique yielded the lowest tensile capacity in bending as compared to both top-side up approaches. Therefore, the lowest modulus of rupture value of 0.5 ksi was incorporated into the second design iteration for the UHPC bridge deck in order to consider the possibility of multiple placement techniques.

6.3 Second Iteration of UHPC Bridge Deck Design

6.3.1 Modification of UHPC Material Parameters

Modifications were made to the UHPC stress-strain model to account for the reduced contribution of UHPC in tension as observed during the preliminary single cell tests. As observed, the upside down placement method resulted in a cracking modulus of rupture ranging between 500 and 700 psi. The modified model accounted for this reduction by using the lowest cracking value of 500 psi as the maximum tensile stress contribution in bending (Figure 6-31). This value would provide a conservative design value to account for either placement method chosen. Because no tensile strain had been determined during the preliminary testing, no modifications were made to the ultimate tensile strain; however, the intermediate tensile strain indicating plastic behavior was changed from 0.000197 to 0.000066 according to the linear relationship signified in the original stress-strain model by Graybeal (2008).

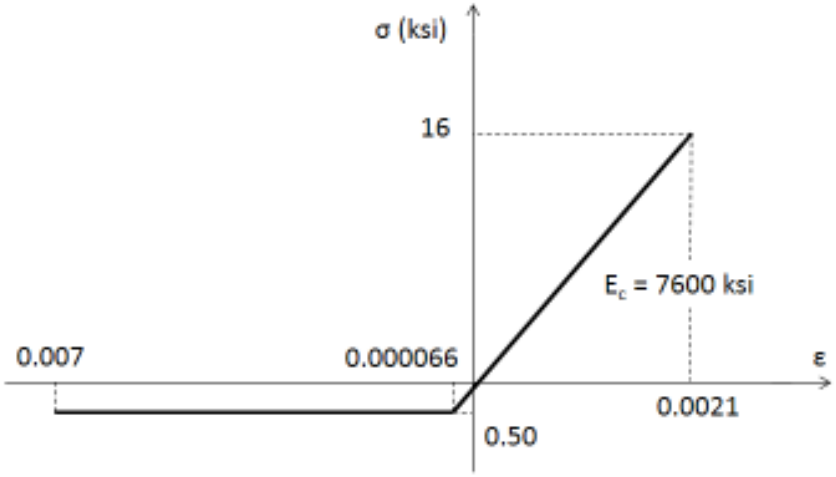

Figure 6-31: Modified UHPC stress-strain model for untreated UHPC and reduced tensile contribution based on preliminary single cells tests.

6.3.2 Final UHPC Bridge Deck Design

Detailed calculations of the final UHPC bridge deck design are presented in Appendix B. In order to accommodate the large reduction in tensile stress contribution, the rib spacing was reduced to 18 in. longitudinally. Because longitudinal spacing of ribs was not considered a contributing factor in the original design, a 28 in. longitudinal rib spacing was maintained to allow for even block-out spacing for composite girder connections (Figure 6-32). Two 0.5 in. prestressing strands were used in the final design to provide reinforcement in the transverse direction. An effective prestress, f_{pe}, of 162 ksi was used in the design, 60 percent of the ultimate stress f_{pu}. Finally, distribution reinforcement was determined according to AASHTO (2012) section 9.7.3.2, and a composite shear connection was designed to connect the UHPC deck panel to a steel girder (Figure 6-33).

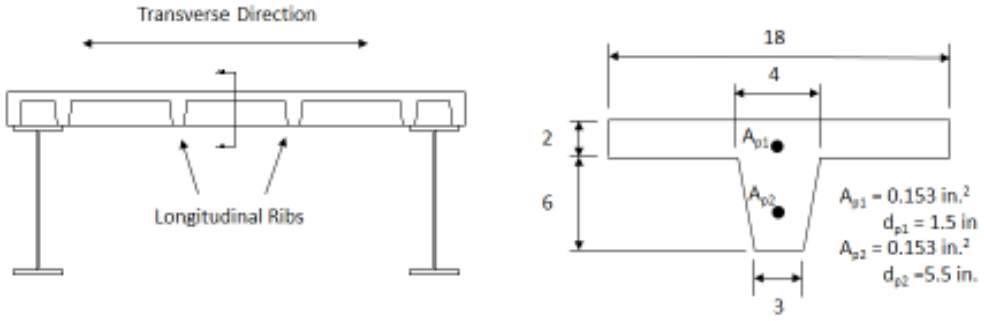

Figure 6-32: Final UHPC bridge deck design using two 0.5 in. prestressing strands and a combination of 28 and 18 in. rib spacing.

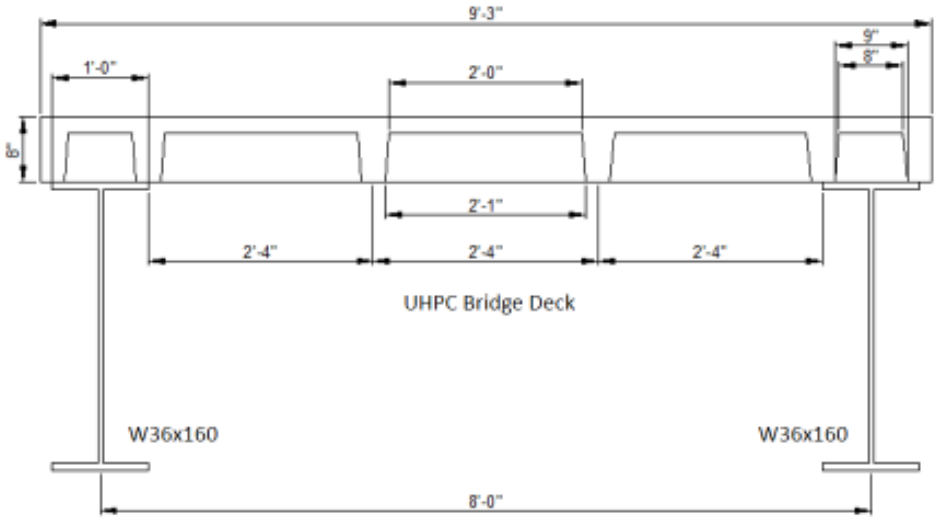

Figure 6-33: Final UHPC bridge deck was designed to be fully composite with W36x160 steel girders.

A summary of the design parameters as compared to the conventional bridge deck design shows that the final design maintained appropriate flexural capacity in both positive and negative moment regions (Table 6-7). It provided ample shear strength using the UHPC fiber contribution alone. However, deflections were expected to be high in comparison to the conventional concrete bridge deck due to low stiffness (EI), indicating that serviceability may be a controlling factor in design for UHPC bridge decks rather than strength parameters. The contribution of longitudinal ribs to the overall stiffness is expected to reduce deflections. Additionally, these deflections were calculated using a T-section with a flange width of 18 in., a width below that identified using the AASHTO (2012) equivalent strip method.

Table 6-7: Final UHPC bridge deck design summary.

Design Parameter	Units	Conventional Concrete	UHPC
M_n^+	k-ft / ft	14.75	15.33
M_n^-	k-ft / ft	-16.22	-17.19
V_n	k / ft	10.2	11.8
EI_c	k-ft^2 / ft	12,820	9080
EI_e	k-ft^2 / ft	2360	950
Δ_i	in. / ft	0.0025	-0.0202
Δ_{LL}	in. / ft	0.219	0.945

Using the AASHTO (2012) equivalent strip method, the section to be analyzed would be 78.8 in. wide. To simplify the analysis based on the 18 in. rib spacing, a 72 in. wide section was analyzed. This 72 in. wide section contained four transverse ribs spaced at 18 in. on center. Using this equivalent section, the UHPC deck would remain uncracked with the 16 kip patch load, resulting in a deflection of only 0.0063 in. per ft (Table 6-8). The total deflection would result in camber of 0.0138 in. per ft with the patch load.

Table 6-8: Final design summary assuming 72 in. wide equivalent strip.

Design Parameter	Units	Conventional Concrete	UHPC
$\mathbf{EI_c}$	k-ft^2 / ft	12,820	9080
$\mathbf{EI_e}$	k-ft^2 / ft	11,220	-
$\mathbf{\Delta_i}$	in. / ft	0.0025	-0.0202
$\mathbf{\Delta_{LL}}$	in. / ft	0.0051	0.0063
$\mathbf{\Delta_{total}}$	in. / ft	0.0076	-0.0139

Chapter 7: UHPC Bridge Deck Section Tests

Two deck sections were constructed and tested to evaluate design parameters for ribbed UHPC bridge deck panels. Each deck section was constructed using a different placement method. DS-1 was constructed using the upside down placement method, and DS-2 was constructed using the right-side up placement method. Both deck sections were tested twice, under two conditions: a single point load located 30 in. from the pin support and a single point load located 18 in. from the pin support. This section discusses the tests, results, and conclusions based on the tests. Supplementary data for experimental testing of deck sections is located in Appendix E.

7.1 Expected Results of Experimental Tests

Material properties of the UHPC used in the two panels were determined. All UHPC was untreated. A summary of the material property testing shows that the measured compressive strength exceeded the assumed design compressive strength of 16 ksi, and the measured modulus of elasticity also exceeded the design value of 7600 ksi for both deck sections (Table 7-1).

Table 7-1: Summarized material properties used to predict structural behavior.

Property	Standard	Sample Geometry	Design Value	DS-1	DS-2*
Compressive Strength, f_c (ksi)	ASTM C 109 (2005)	2 in. cube	16	23.2	26.1
Modulus of Elasticity, E_c (ksi)	ASTM C 469 (2002)	4 in. diameter x 8 in. high cylinder	7600	7800	8000
Tensile Strength, f_t (ksi)	-	-	0.50	-	-
Cracking Split Tensile Strength, $f_{t,sc,cr}$ (ksi)	ASTM C 496 (2004)	4 in. diameter x 8 in. high cylinder	-	1.52	1.32
Ultimate Split Tensile Strength, $f_{t,sc,u}$ (ksi)	ASTM C 496 (2004)	4 in. diameter x 8 in. high cylinder	-	2.30	2.30
Briquet Tensile Strength, $f_{t,b}$ (ksi)	AASHTO T 132-87 (2004)	briquet	-	1.25	0.92

*DS-2 values were based on a weighted average of two separate batches of UHPC implemented in the placement of this deck section.

The aforementioned analysis techniques (Chapter 6) were used to determine expected results for each deck section. The final design was intended to account for the worst possible modulus of rupture for UHPC as determined by single cell testing. Therefore, this design method was considered conservative for the right-side up placement scenario. For DS-1, the stress-strain model previously discussed in Section 6.3 (Figure 6-31) was used to determine expected test results. Because DS-2 was placed right-side up, the tensile capacity of DS-2 was expected to be higher than DS-1. Therefore, the stress-strain model used in the first design iteration, Section 6.1 (Figure 6-3), was used to determine expected results for DS-2.

Using the respective stress-strain models, expected design values were determined for both DS-1 and DS-2. The following values were predicted for each deck section: cracking moment (M_{cr}), cracking load ($P_{cr,30}$) for point load at 30 in. from support, cracking load ($P_{cr,18}$) for point load at 18 in. from support, deflection at cracking ($\Delta_{cr,30}$) beneath point load at 30 in. from support, deflection at cracking ($\Delta_{cr,18}$) beneath point load at 18 in. from support, and nominal positive bending moment capacity (M_n^+) (Table 7-2). The modulus of rupture (f_r) used for DS-1 was 0.5 ksi based on preliminary single cell tests, and the modulus of rupture used for DS-2 was 3 ksi based on preliminary single cell tests.

Table 7-2: Design values and expected behavior for DS-1 and DS-2.

Property	Design Values	DS-1	DS-2
f_r (ksi)	0.5	0.5	3
M_{cr} (k-ft)	10.2	10.1	22.3
$P_{cr,30}$ (k)	6.0	5.9	13.0
$P_{cr,18}$ (k)	8.4	8.3	18.3
$\Delta_{cr,30}$ (in.)	0.04	0.04	0.07
$\Delta_{cr,18}$ (in.)	0.03	0.03	0.05
M_n^+ (k-ft)	23	23	33

Variations in measured dimensions were also taken into consideration for expected values. A summary of measured dimensions is provided in Appendix E. DS-1 was constructed with no more than a 6 percent difference from the design dimension, making it agree well with the design values. DS-2 had a measured flange height (h_f) of 2.4 in., making it 0.4 in. greater than the design thickness of 2 in. This additional material led to a 20 percent increase in flange height. This difference was attributed to the additional height added to the form to account for

early-age shrinkage. The additional height had been added to the forms because a large amount of shrinkage was previously observed in the single cell deck sections.

7.2 Placement & Material Observations

DS-1 was placed using a single batch, 5.75 cu. ft, mixed in the Mortarman 750 mixer. DS-2 was placed using two batches, DS-2A and DS-2B. DS-2A was 5.75 cu. ft and was mixed using the Mortarman 750 mixer. DS-2B was 1 cu. ft and was mixed using the 2 cu. ft capacity pan mixer. Two batches were used to account for additional material placed along the flange to account for early age shrinkage. The flow test for all mixes indicated that the UHPC would be easily consolidated because the flow was greater than 9 in. (Table 7-3), and no vibration was applied to either the material specimens or to the deck sections.

Table 7-3: Flow test results for DS-1 and DS-2 mixes.

	Diameter Before 20 Drops (in.)			Diameter After 20 Drops (in.)			Average Diameter (in.)	
Mix ID	**1**	**2**	**3**	**1**	**2**	**3**	**Before**	**After**
DS-1	9.00	9.19	9.13	10.00	10.00	10.00	9.10	10.00
DS-2A	8.50	9.00	9.50	9.00	9.25	9.88	9.00	9.38
DS-2B	9.50	9.75	10.00	10.00	10.00	10.00	9.75	10.00
Note: 10 in. was the maximum flow possible.						***Average***	**9.28**	**9.79**

Although flow values had been within this range found during direct biaxial test placements, these values were on the upper tier of flow data collected during the study. In the DBT data (Chapter 5), the average flow before and after drops was 8.7 and 9.6 in., respectively. The initial material characterization (Chapter 4) had a flow of 7.8 in. before drops and 9.1 after drops for this single batch. Graybeal (2006a) collected flow values from 43 different batches of UHPC. From this data, the average flow before drops was 6.4 in., and the average flow after 20 drops was 7.5 in. The flow values did not exceed 8.3 in. after drops. The majority if this data was on UHPC with an accelerating admixture; only two batches did not use this admixture (Graybeal 2006a). Since an overdose of an accelerating admixture can result in rapid stiffening of a concrete mix (Kosmatka et al. 2002), it is possible that the high flow was a result of not using the accelerating admixture. Factors, such as humidity, temperature, mixing time, and user error on the flow test, could have also affected the high flow of the mixes, also.

In both deck sections, the UHPC was added into one end of the formwork and allowed to flow horizontally to the other side. For DS-1, the frame containing foam was pressed into the form filled with UHPC to form the ribs of the deck section. The frame was pressed into the form and immediately clamped to the formwork. During preliminary placement using the single cells, the foam and frame for the upside down placement was allowed to uplift during placement. Because of this, the UHPC was disturbed multiple times during the placement process. Unlike the UD single cell, the foam and frame for DS-1 was pressed only once so that the UHPC would only be disturbed once. During this placement, the foam was easily pressed into the UHPC. Because of the frame, it was difficult to place the plastic on the exposed UHPC. In some areas, the frame was a hindrance in placing the plastic (Figure 7-1), resulting in some abnormalities along the exposed surface (Figure 7-2). The placement of plastic is also a concern for commercial production of UHPC bridge decks. Frames should be constructed so that there is adequate space between the frame and the exposed surface to account for the placement of plastic if it is used.

Figure 7-1: Some difficulties occurred in placing plastic on exposed UHPC because of the frame.

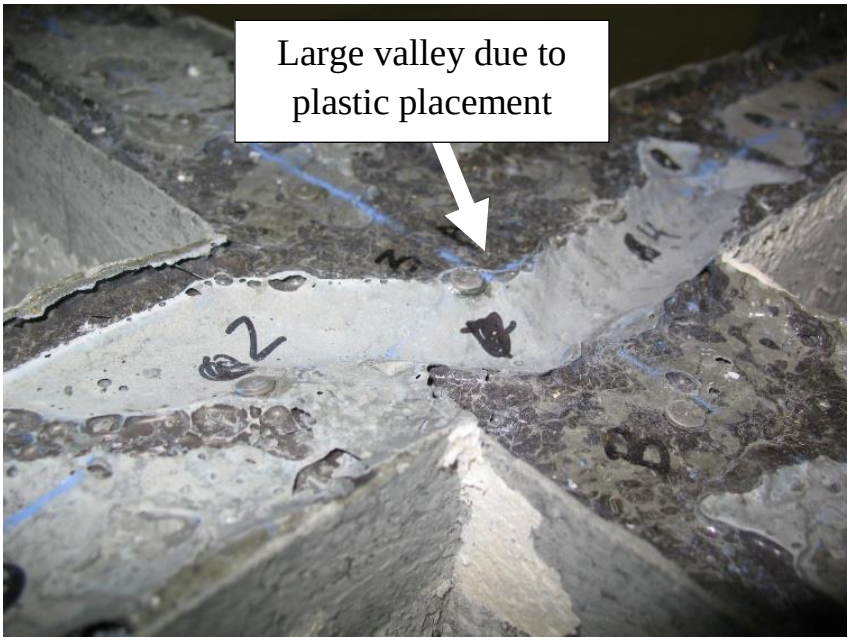

Figure 7-2: Surface abnormalities occurred due to faulty plastic placement.

During the placement for DS-2, the plastic covering the exposed UHPC was easily applied along the top surface, resulting in no major abnormalities. Because the UHPC was placed into only one end of the form to best align fibers with the direction of flow, time was required to allow the UHPC to self-consolidate. At the beginning of placement, the UHPC flowed through the form quickly; however, as less and less UHPC was available at the placement end to provide pressure to fill the form, the form appeared to be filling more slowly. The same surface "skin" as previously observed in the single cell placement also formed atop the deck section. The skin first formed on the opposite end from the UHPC entrance. Again, this surface condition is typical of UHPC.

Due to the observed fiber settlement in single cell test beams, this problem was investigated in the material specimens for the deck section mixes. Fiber settlement was first noticed during compression testing of cubes from mix DS-2B. This mix was observed to be very fluid during placement, more so than previous mixes and DS-2A. Upon investigation of the cubes, it was apparent that few fibers were in the top-most section (Figure 7-3). These samples resulted in sudden, somewhat explosive failures, whereas other UHPC samples would not break apart completely during testing due to the presence of fibers. Although the failure mode was affected for the cylinders, the compressive strength did not appear to be reduced due to the lack

of fibers in the top-most section. The average compressive strength at 28 days was 23.1 ksi, which was consistent with other UHPC mixes.

Figure 7-3: A lack of fibers in cubes resulted in sudden compressive failures.

By observing cylinders, it was apparent that surface conditions showed hints of fiber settling because fibers could be seen on the exterior of cylinders (Figure 7-4). During split tensile testing, however, fiber settling was better displayed by breaking apart these samples. Two samples from each deck section mix were broken apart to examine the amount of fiber settling. Approximate measurements were made from the bottom surface of the cylinders to determine the amount of fiber settling that had occurred in a 4 in. diameter by 8 in. high cylinder (Table 7-4). The results showed that approximately 2 in. of settling occurred in the majority of cylinders, and the maximum amount of settling was 4.75 in. These cylinders showed large concentrations of fibers near the bottom face of the cylinder, and little to no fibers were present in the top section (Figure 7-5, Figure 7-6).

Table 7-4: Fiber settling quantities observed in 8 in. high cylinders.

Mix ID	No.	Distance from top surface to fiber concentration (in.)	Average (in.)
DS-1	1	2.5	2.25
	2	2	
DS-2A	1	2	2
	2	2	
DS-2B	1	4.75	3.5
	2	2.25	

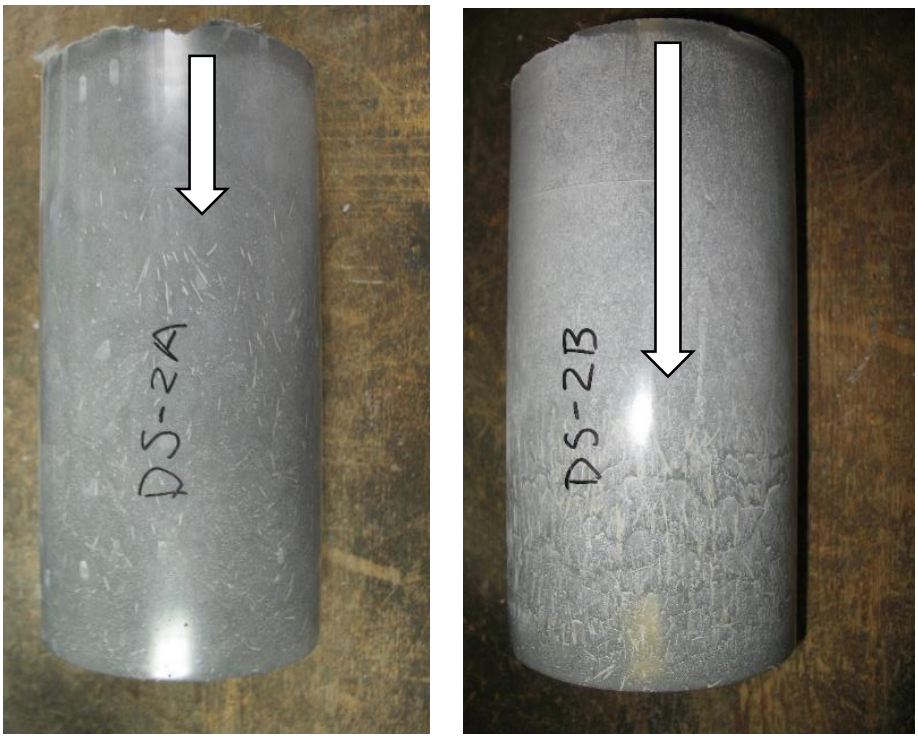

Figure 7-4: Fiber settling was observed on the exterior surface of cylinders.

Figure 7-5: Fibers were observed to be sinking approximately 2 in. from the top surface of an 8 in. high cylinder (DS-2A).

Figure 7-6: Fibers were observed to be concentrated in the bottom 3 in. of an 8 in. high cylinder as the most extreme case of fiber settling (DS-2B).

Fiber settling did not affect compressive strength; however, it did appear to have a small effect on the modulus of elasticity. The largest amount of fiber settling was observed in cylinders from mix DS-2B. The modulus of elasticity of these cylinders was determined to be 7590 ksi, whereas the modulus of elasticity of DS-2A samples was observed as 8020 ksi. On the contrary, the splitting tensile strength of DS-1A and DS-2A were very similar, and fiber settling did not appear to negatively affect this tensile test.

The reason for fiber settling is unknown. Mixing procedures had been followed consistently throughout the study to ensure the material was produced consistently. No vibration or tapping had been applied to any cylinders or cubes for the deck section mixes. Even when the preliminary material characterization implemented vibration, no noted fiber settling had been observed in cylinders. Settling had only been observed in the 1 in. thick briquets (Figure 4-3). As previously discussed, the flow was quite high compared to some previous mixes in this study and those observed by Graybeal (2006a). It is possible that without the use of an accelerator fibers have more time to settle prior to initial set in this material with high flow. It is also possible that moisture has more time to navigate upward without an accelerator, resulting in a weakened top surface in UHPC. Because these are merely speculations, it would be beneficial to

determine the cause of fiber settling in future work so that it can be prevented, or at least mitigated, in future mixes. This is especially important for commercial implementation of the product.

7.3 Transfer Length and Effective Prestress Force

An estimated prestress loss of approximately 34 ksi was initially determined using the refined method from AASHTO (2012) Section 5.9.5 and estimated material properties at transfer (Table 7-5). John et al. (2011) determined that elastic shortening losses in UHPC beams were approximately 25 percent less than those determined by AASHTO, and long-term creep and shrinkage losses were negligible. John et al. (2011) used steam treated UHPC, which was likely the reason for finding such small long term losses. UHPC is known to experience little to no shrinkage after the steam treatment process (Graybeal 2006a). Applying the 25 percent reduction to the predicted elastic shortening loss, the estimated prestress losses were reduced to 31 ksi for the UHPC deck sections. No adjustments were made to creep and shrinkage because the UHPC was untreated. Resultantly, a target jacking force of approximately 30 kips, equivalent to 197 ksi, was determined for the ½ in. diameter strands.

Table 7-5: Prestress losses for single unit UHPC bridge deck section.

Prestress Loss Category	**AASHTO (2012) Refined Losses**	**Adjusted Losses**
Elastic Shortening, ES (ksi)	6.7	4.8
Creep, CR (ksi)	16.8	16.1
Shrinkage, SH (ksi)	6.5	6.5
Relaxation after Transfer, R_2 (ksi)	3.8	4.1
Total Losses after Transfer (ksi)	**33.6**	**31.5**
Relaxation at Transfer, R_1 (ksi)	2.8	2.8
Target Effective Prestress, f_{pe} (ksi)	162	162
Jacking Stress (ksi)	205	197
Target Jacking Force (k)	**31**	**30**

During the prestressing operations, the strand located in the bottom of the form was always stressed first. Because DS-1 was placed upside down, this was actually the strand located in the flange (Figure 7-7). While the top strand was stressed, the stress in the bottom strand reduced. Because the jack used to stress the prestressing steel had a limited stroke distance, each

strand was shimmed, released, and re-stressed during the prestressing process to reach the desired jacking stress (Section 3.8.2). The strands were stressed on the day prior to the placement, and the force in the strands was monitored until they were cut (Table 7-6). The UHPC was thought to be completely set between 24 and 48 hours; however, the strands were not cut until 7 days following placement. Because of the bond between the UHPC and the prestressing steel, shrinkage in the UHPC caused the force measured by the load cell to increase. No visible cracking was observed when the prestressing steel was cut, and no end reinforcement was placed in either deck section to resist bursting stresses.

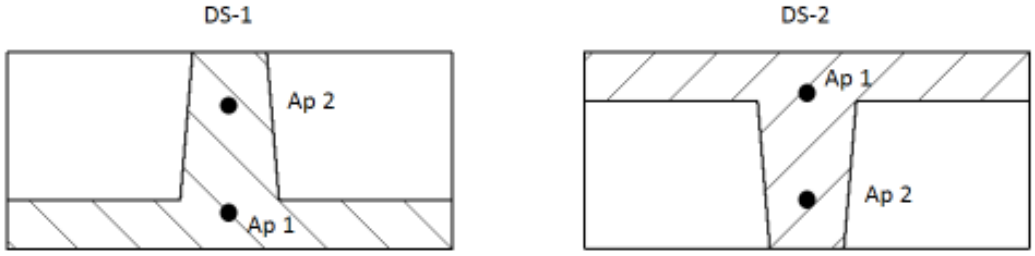

Figure 7-7: Placement orientation and resulting prestressing steel location.

Table 7-6: Prestress forces over time.

		DS-1		DS-2	
Significance	**Time (days)**	**A_p 1 (lb)**	**A_p 2 (lb)**	**A_p 1 (lb)**	**A_p 2 (lb)**
Initial Stress	0	29,400	30,300	30,600	30,300
Placement	1	29,300	30,000	30,300	30,100
	2	29,200	30,000	30,300	30,100
	3	29,000	29,900	30,000	29,800
	4	29,800	30,700	30,600	30,500
	5	-	-	30,800	30,700
	6	-	-	31,000	30,900
Transfer	7	30,000	31,000	31,100	31,000

A_p 1 – located in flange, A_p 2 – located in web

A value of $20d_b$ and $40d_b$ has been suggested as an estimated transfer length for prestressing steel in UHPC (John et al. 2011, Gowripalan and Gilbert 2000). For the ½ in. prestressing steel used in this study, the transfer length was expected to range between 10 and 20 in. Surface strains in DS-1 were determined using DEMEC points and a Whittemore gage reader. The transfer length was determined by plotting the surface strain as determined by the

gage readings and the distance each reading was taken from the end of the beam, as shown in Figure 7-8. The transfer length was considered the point of the intersection of two lines determined by Selections 1 and 2. The first line using Selection 1 assumed a y-intercept of zero and included points up to where the strain values became consistent. The second line using Selection 2 was assumed as having a slope of zero and used the points with consistent strain results. Using principles from the 95% Average Maximum Strain (AMS) analysis method, 95% of the horizontal line resulting from Selection 2 was used to determine the transfer length (Russell and Burns 1993). By finding the intersection point of Selection 1 and 95 percent of selection 2, the transfer length of the live end was estimated as 16.5 in., falling between the estimated range of 10 to 20 in. If the 95% reduction in strain had not been taken in accordance with the 95% AMS method, the transfer length would have been estimated as 17.5 in.

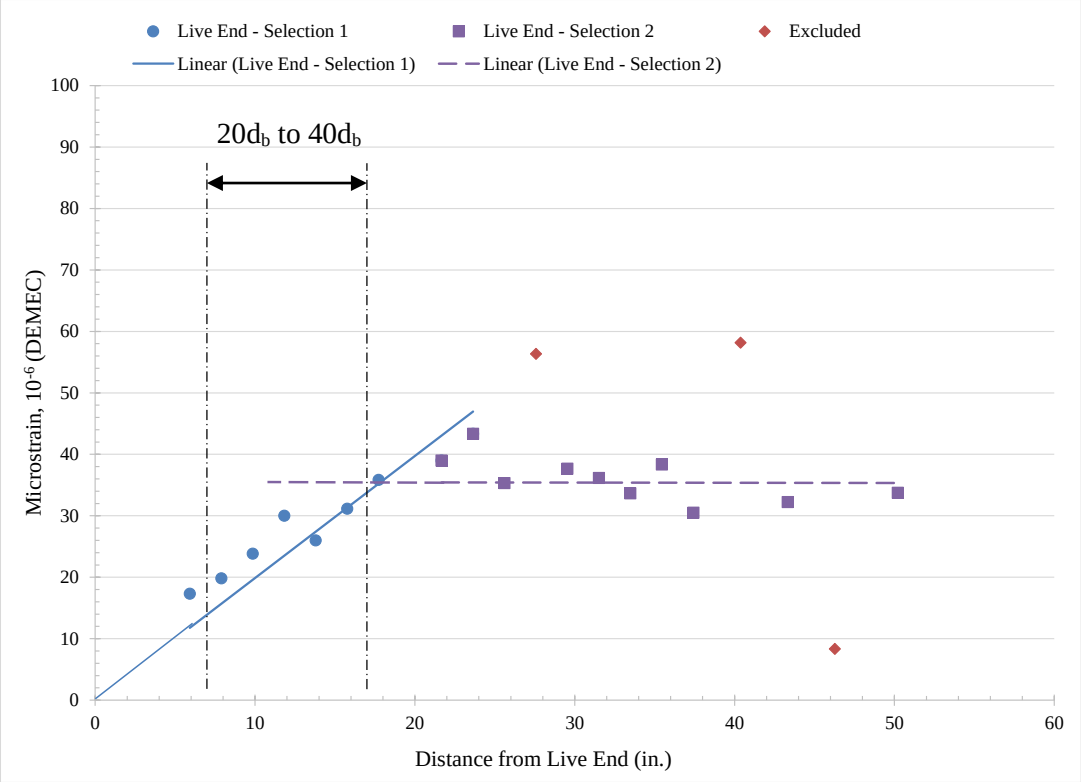

Figure 7-8: Estimated transfer length, L_T, was 16.5 in. using the 95% AMS method and DEMEC points on live end of DS-1 (measurements taken from bottom web).

A transfer length in the dead end of DS-1 was estimated as 9.3 in. using the 95% AMS method (Russell and Burns 1993), falling below the expected length of 10 to 20 in. as shown in Figure 7-9. By not taking the reduction suggested by the 95% AMS method, the transfer length

was estimated as 9.8 in. Both of these values were nearly half the distance estimated by data from the live end. Some points were excluded from the transfer length determination because either they were considered outliers in the data set or the Whittemore gage readings were inconsistent and considered unreliable. In some cases, only two repetitions were used to determine the average DEMEC reading because a third consistent reading could not be taken. The significant difference from the live and dead end transfer length estimations could be a result of the unreliable gage readings and the subjectivity involved in the 95% AMS method suggested by Russell and Burns (1993). Due to inconsistent readings using the Whittemore gage reader, BDI strain transducers were used in place of the DEMEC readings for DS-2.

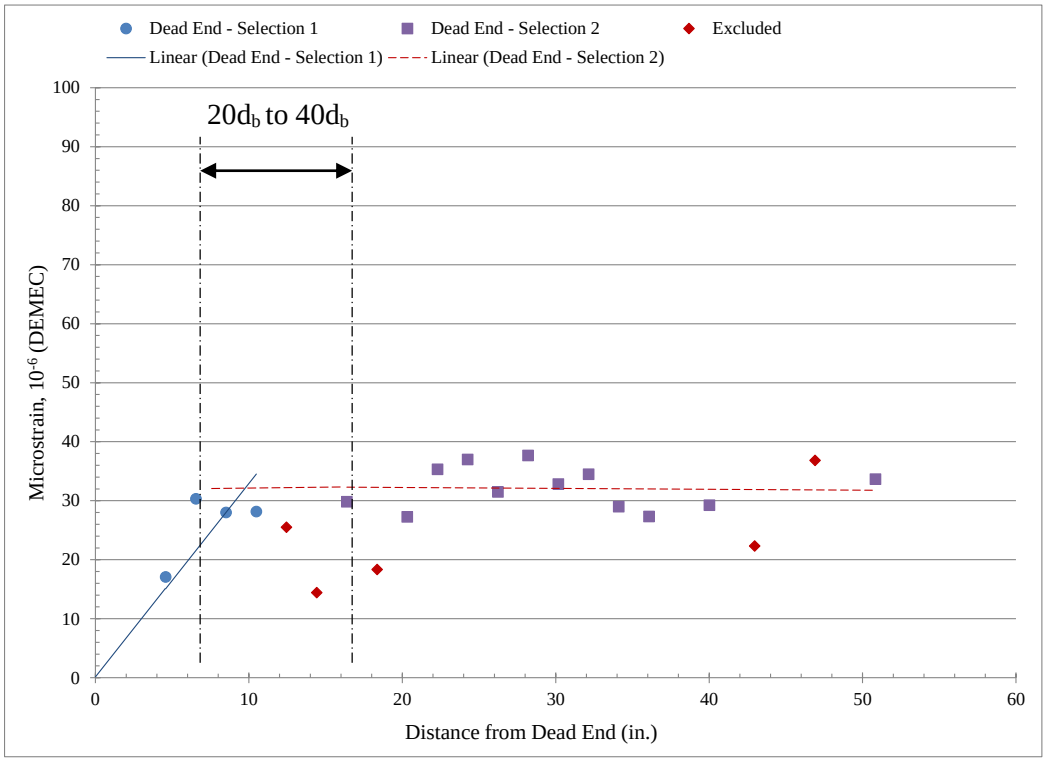

Figure 7-9: Estimated transfer length, L_T, was 9.3 in. using the 95% AMS method and DEMEC points on dead end of DS-1 (measurements taken from bottom web).

Because the strains in DS-2 were measured using BDI strain transducers, data collection took place throughout the cutting process. The strain data showed that the top flange of the deck unit was first put into compression (Figure 7-10). This was expected because the top strand was released first. These large compressive strains reduced as a result of the second strand release; however, because the resultant reading was still negative, the top of the deck was shown to be in

compression. The deck unit was lifted from the bottom face of the form to remove effects from any additional frictional forces along the bottom face of the beam. The additional adjustments in the strain measurements was a result of the lift. However, the reason for the sudden tensile stress increase after the adjustment is unknown. This was consistent on all gages.

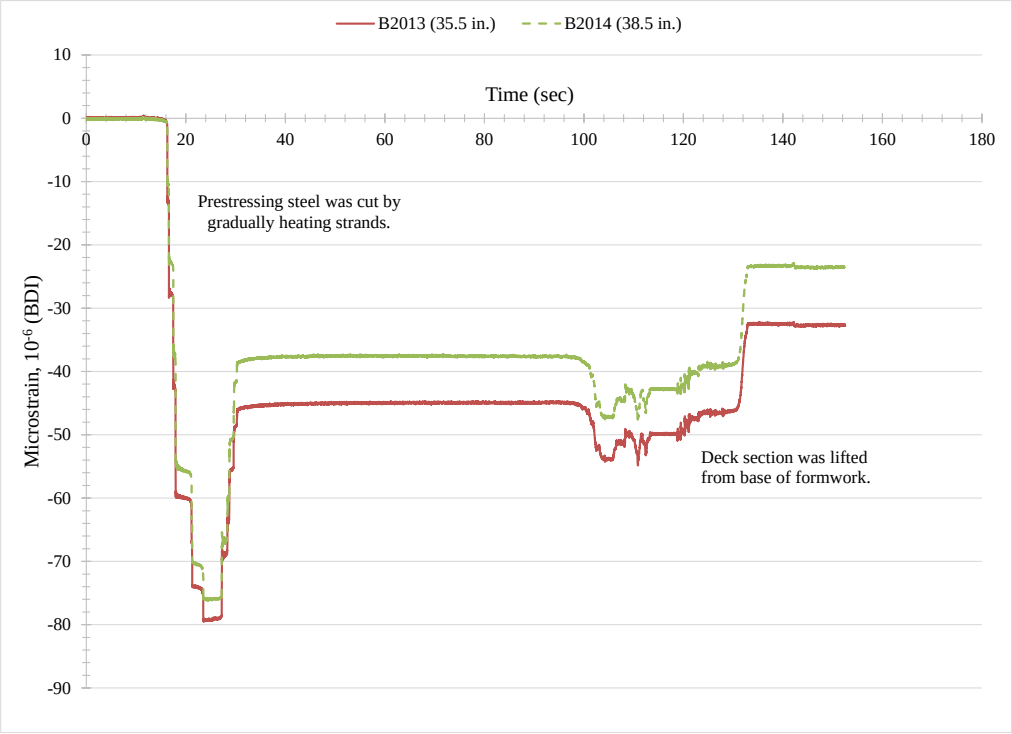

Figure 7-10: Typical BDI strain transducer data from cutting strands and lifting deck section from base of formwork (from live end of DS-2).

The BDI strain transducers did not provide an accurate estimate of the transfer length. However, readings from both the live and dead ends suggest that the transfer length was below 20 in. (Figure 7-11, Figure 7-12). Strain above 50 με was recorded between 5 and 15 in. from the dead end. Consistent strains between 20 and 40 με was recorded beyond 17 in. Due to the consistency beyond 20 in. from the dead end, the data suggested that the transfer length was below 20 in. Data from the live end suggests that transfer length could have been much lower; however, a clear trend was not apparent, leading to the conclusion that transfer length was likely below 20 in. Again, a transfer length below 20 in. is consistent with the recommendations of Gowripalan and Gilbert (2000), suggesting a transfer length of $20d_b$ and $40d_b$.

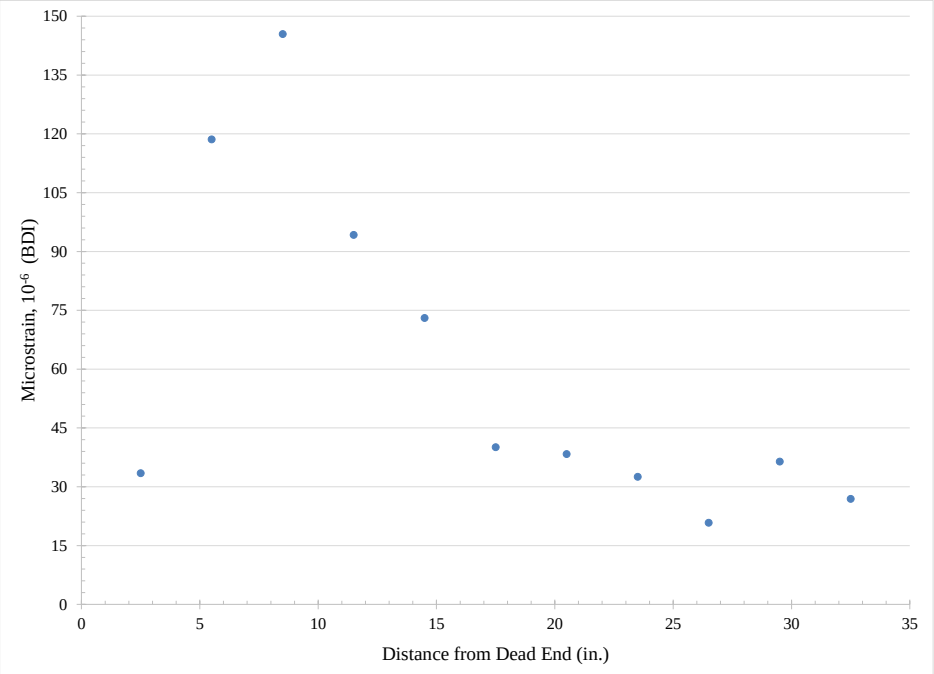

Figure 7-11: BDI strain transducer measurements from dead end of DS-2 suggest transfer length below 20 in. (measurements taken from top of flange).

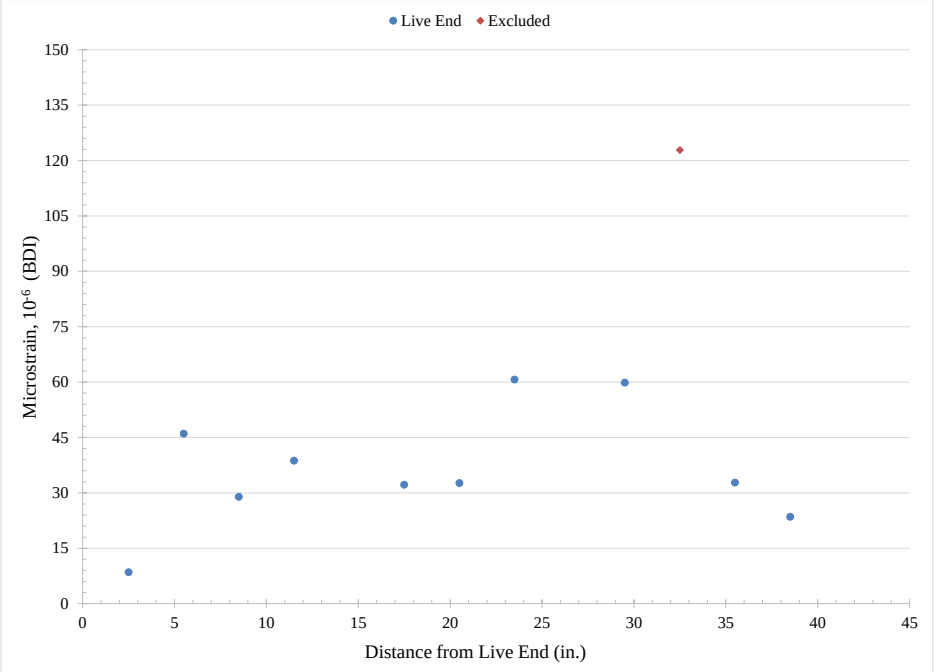

Figure 7-12: BDI strain transducer measurements from live end lead to an inconclusive transfer length estimate (measurements taken from top of flange).

A summary of all transfer lengths determined for DS-1 and DS-2 this study are provided in Table 7-7. In all cases, transfer length was estimated to be below 20 in. The dead and live ends of DS-1 showed significant difference in transfer length, where the dead end had values below the lower limit of $20d_b$ for transfer length as suggested by previous research (John et al. 2011, Gowripalan and Gilbert 2000). Although a specific transfer length estimation was inconclusive using the DBI gages on DS-2, the transfer length was predicted to be less than 20 in., within the upper limit of $40d_b$ suggested by previous research (John et al. 2011, Gowripalan and Gilbert 2000). Based on all results, the suggested range for transfer length of UHPC ($20d_b$ to $40d_b$) is a reasonable estimation for design.

Table 7-7: Summary of transfer length (l_t) determination for DS-1 and DS-2.

Deck Section	End Type	Transfer Length using 95% AMS, $l_{t,95\%}$ (in.)	Transfer Length using no reduction, $l_{t,nr}$ (in.)
DS-1	Live	16.5	17.5
	Dead	9.3	9.8
DS-2	Live	< 20	< 20
	Dead	< 20	< 20

An effective prestress of DS-2 was estimated using data collected from BDI gages adhered to the cross section at mid-span. The gages were used to determine strains near the top and bottom of the deck section in order to develop a strain profile through the center cross section (Figure 7-13). Using the strain profile, strains at the top and bottom fibers of the section were determined. Then, the equations used to determine decompression strains were used to determine the effective prestress force in each strand. Using this method, the effective prestress force, P_{e1}, in A_{p1} (flange) was estimated to be 27.8 kips, and the effective prestress force, P_{e2}, in A_{p2} (web) was estimated to be 25.6 kips (Figure 6-13). Ninety percent of the initial prestress is typically used to estimate an effective prestress force. Assuming a transfer stress of $0.9f_{pi}$, where f_{pi} is the initial prestress in the tendon, the measured values were within 5 percent of predicted values. (Figure 7-14,

Table 7-8). The initial prestress was based on the lowest force measured in the strands prior to transfer; this force occurred on Day 3, 48 hours after UHPC placement (Table 7-6). An effective prestress was not determined for DS-1 due to inconclusive data using DEMEC points.

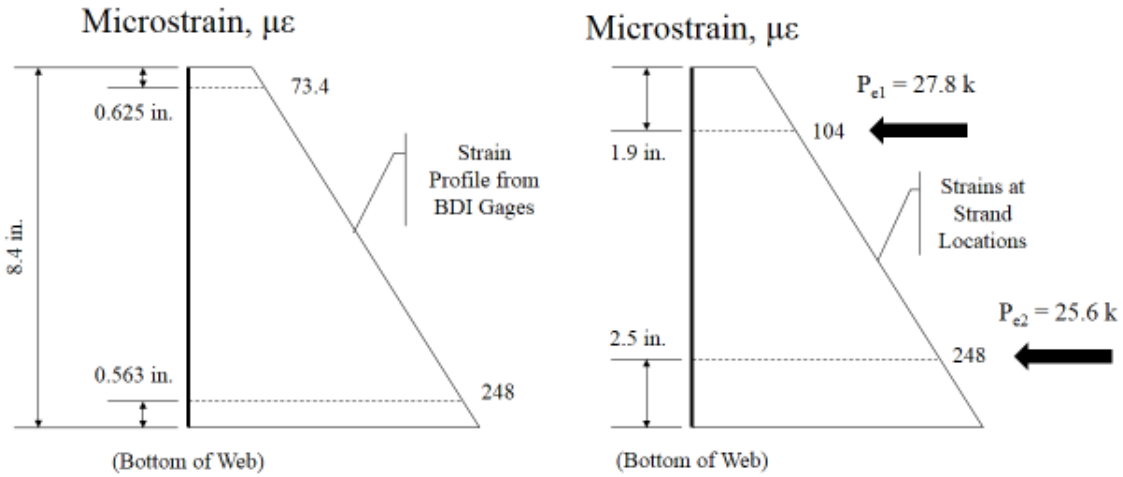

Figure 7-13: Strain profile generated using BDI gages to determine effective prestress forces.

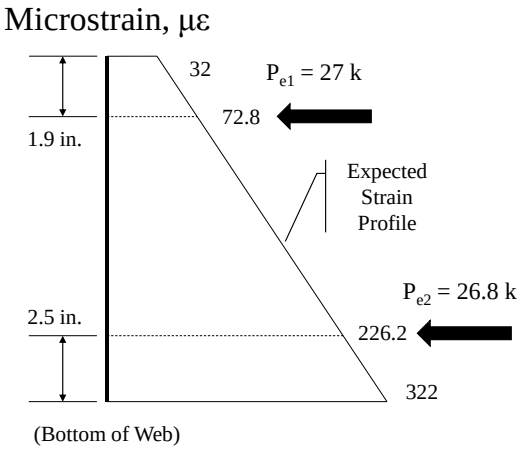

Figure 7-14: Predicted strain profile for DS-2 at mid-section.

Table 7-8: Summary of measured and predicted effective prestress values.

	Location in Cross Section	
Measured and Estimated Values	**Top**	**Bottom**
Distance* to BDI Gage (in.)	0.63	7.84
Measured BDI Gage Strain (με)	73.4	248
Distance* to Prestressing Steel from Top, (in.)	1.9	6.9
Strain at Prestressing Steel from BDI Gage (με)	104	248
Prestress Force from BDI Gages (k)	**27.8**	**25.6**
Predicted Strain in Prestressing Steel (με)	73	226
Predicted Prestress Force (k)	**27.0**	**26.8**

**Distances taken from top flange of cross section.*

7.4 DS-1 Tests for Upside Down Placement Method

For each test, DS-1 was supported on a simple pin and roller support over a span length of 8 ft. Load was increased incrementally by 500 lbs. Once visual cracks were detected, crack growth was marked for every 1000 lbs of increased load.

7.4.1 Test 1: Load Point at 30 in. Distance

DS-1 failed in flexure with the single point load at 30 in. from the support, exceeding the nominal positive moment capacity calculated for design. The first audible detection of a crack was at 8 kips, equivalent to a cracking moment (M_{cr}) of 13.8 k-ft. A second audible crack was heard at 10.5 kips; however, no visible cracks were detected until 12 kips. Cracks were first detected between the pin support and the load point. Beginning at 14 kips, a large crack formed directly below the load, and additional flexure cracks formed (Figure 7-15). No diagonal cracks were detected near the strain gage rosette or near the supports, and the absence of cracks indicated that the beam had sufficient shear strength under the test conditions. Cracking did

extend into the flange at 18 kips, indicating a depth to the neutral axis of approximately 1.2 in. For this deck section, the calculated neutral axis depth was approximately 1.1 in. for the design moment capacity. UHPC beams typically result in tightly spaced crack networks of relatively small crack widths (Graybeal 2008, Graybeal 2009a, Graybeal 2009b, Yang et al. 2010). However, DS-1 did not display typical UHPC cracking behavior. The cracks were not closely spaced. At the maximum deflection of nearly 1.4 in., the dominant crack grew to approximately 0.25 in. in width (Figure 7-16). Few fibers were visible in the crack, similar to the single cell units placed upside down. The lack of fibers in the bottom of the web was most likely the reason for the uncharacteristic crack patterns. The discrete fiber reinforcement in UHPC is expected to bridge cracks and reduce crack growth.

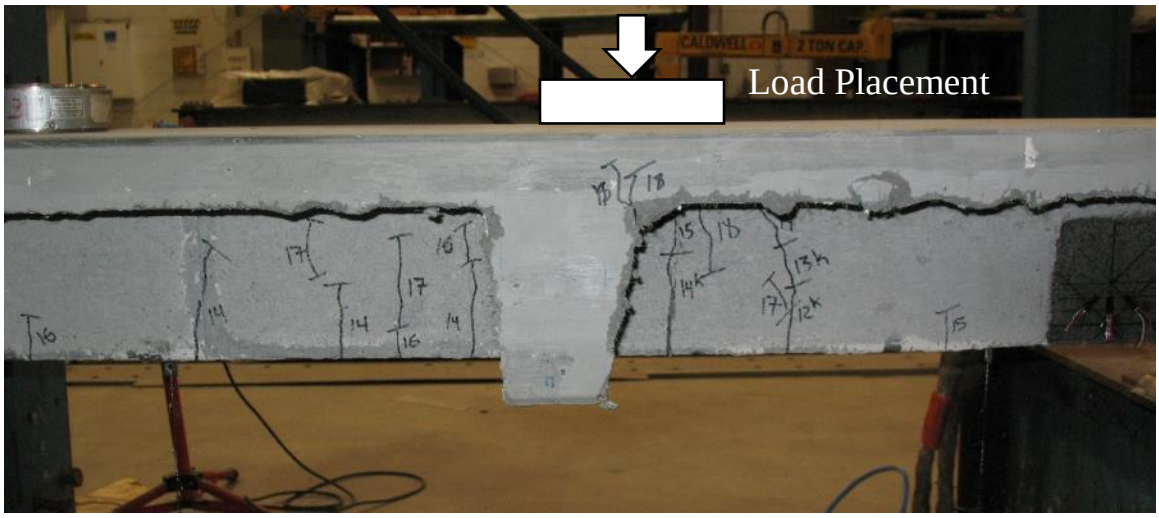

Figure 7-15: Cracking patterns of DS-1 Test 1 (load placed 30 in. from support).

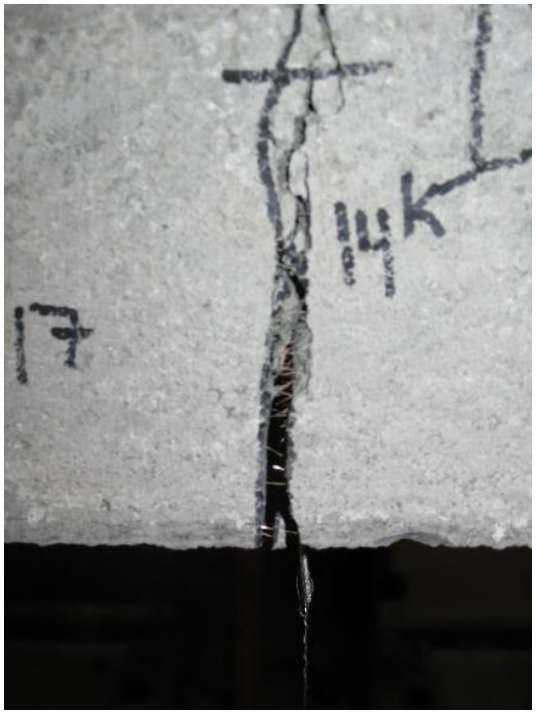

Figure 7-16: Dominant failure crack for DS-1 Test 1 was approximately 0.25 in. wide and showed few fibers.

The maximum load achieved during Test 1 of DS-1 was 18 kips, resulting in a maximum applied moment of approximately 30 k-ft. Deflection increased with little to no increase in load carrying capacity beyond this point (Figure 7-17). The applied moment exceeded the design moment capacity of 23 k-ft by 30.4 percent (Figure 7-18), suggesting that the iterative design process using the modified stress-strain curve could be a conservative design method for positive flexural capacity. Although the design moment capacity was achieved, the deck did not withstand the design patch load of 36.4 kips (16 kips including appropriate load factors). The deck section was tested over a simple span of 8 ft, consistent with the assumed girder spacing. Simple span conditions were used to simplify analysis of the testing procedures. Not only would a composite shear connection be implemented between the steel girders and the UHPC deck panel, but the deck panels would also span over multiple girders. Because more rigid end conditions and continuous spans would result in a reduction of applied moments, further testing would be required to determine how the full deck panels behave when introduced to service conditions. The section tested was also narrower than the required AASHTO strip width for one axle (AASHTO 2012). According to AASHTO (2012), the strip width required for this deck

would be 78.8 in. for positive bending, assuming this deck would qualify for the "precast, post-tensioned" category. This full width should be considered to compare with design loads.

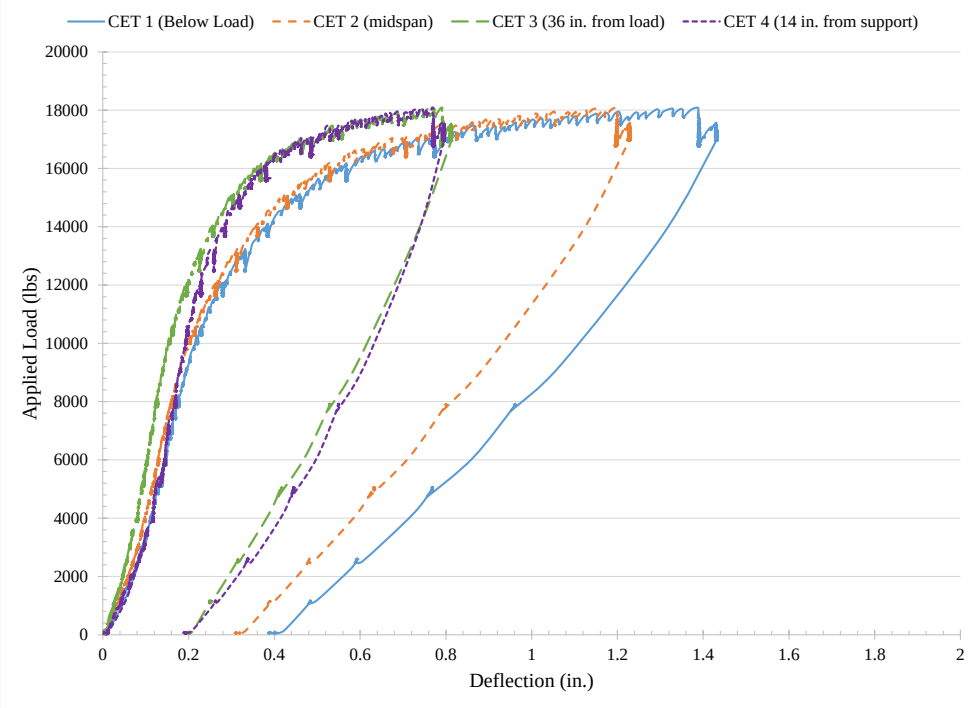

Figure 7-17: Load-deflection plot for DS-1 Test 1.

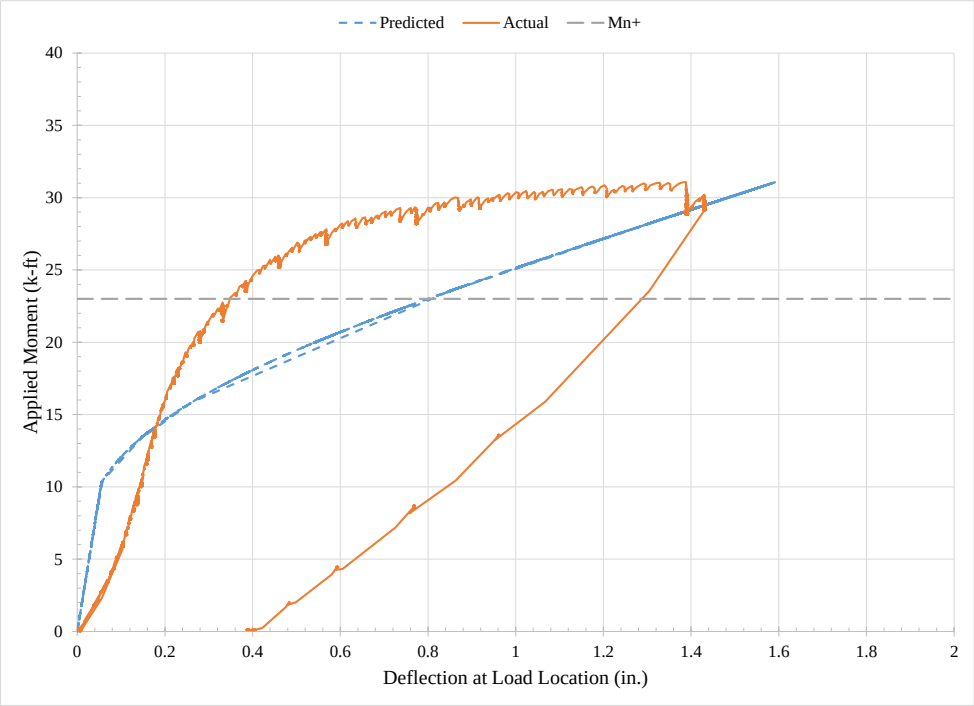

Figure 7-18: Maximum applied moment versus maximum deflection for DS-1 Test 1 (30 in. from support).

Predicted deflections were calculated using the gross moment of inertia (I_g) up to when the section met the predicted cracking moment, and the effective moment of inertia (I_e) was used once the section exceeded the predicted cracking moment. The equation for I_e in ACI 318-11 (ACI Committee 318 2011) was developed by Branson (1965) for conventional concrete. Because no alternative is currently advised for UHPC, the equation for I_e in ACI 318-11 (ACI Committee 318 2011) was used in this study to predict deflections in a cracked section. A small, non-linear portion of deflection was shown at the start of each test. This was likely due to settling of the supports. Because of this non-linear region, the predicted deflections all began higher than those measured during each test.

A ductile failure mode was observed, showing large deflections and increased crack widths before the test was stopped. At the completion of the test, the ratio of the ultimate deflection (Δ_u = 1.39 in.) to the deflection at first crack (Δ_{cr} = 0.20 in.) was 6.95. Because a second test was intended for DS-1, the deck section was not tested to ultimate failure to best preserve the specimen for the second test scenario.

Principal strains were determined at 14 in. from the support nearest the load point using the strain gage rosette. The rosette was located 4.25 in. below the top of the web. Strains were also estimated using DIC on the opposite side of the beam. Principal stresses were then determined by transforming the principal strains assuming a linear-elastic relationship. In the case of the DIC, only two strains were able to be interpreted through the analysis. The program was written to determine strain in the x and y directions for a set of digital images (Figure 7-19). Because only two strains were able to be interpreted using the DIC program, a shear stress was estimated based on the load scenario using Equation (7-1) and transformed into a shear strain using Equation (7-2). This shear strain was then combined with the two strains determined through DIC to generate principal strains and principal stresses. The individual points marked on the deck section in Figure 7-19 were location markers for choosing the area to be analyzed. The deck was speckled using black and white spray paints for the DIC program.

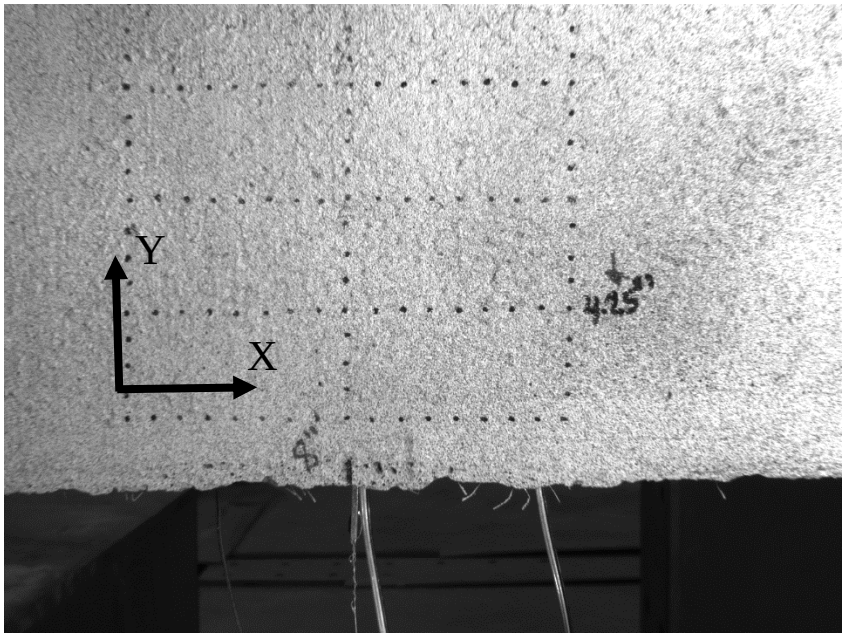

Figure 7-19: Strain could only be determined in the x and y directions.

$$\tau_{xy} = \frac{VQ}{Ib} \qquad (7\text{-}1)$$

$$\gamma_{xy} = \frac{\tau_{xy}}{G} \quad (7\text{-}2)$$

Where,

τ_{xy} = shear stress (ksi)

V = shear (kips)

Q = first moment of area ($in.^3$)

I = moment of inertia ($in.^4$)

b = width of section (in.)

γ_{xy} = shear strain

G = shear modulus (ksi); $E/[2(1+\upsilon)]$

E = elastic modulus (ksi)

υ = Poisson's ratio

DIC strain data was plotted with the polynomial biaxial failure model proposed for untreated UHPC (Chapter 5). By plotting this data with the proposed biaxial failure curve, it was apparent that no shear cracking would occur according to the strain gage rosette because the principal stresses were well within the failure surface (Figure 7-20). The DIC stresses followed the same path; however, they extended well beyond the stresses observed in the rosette. Three strains and their respective orientations are necessary to determine principal strains. Because only two strains could be measured using the DIC method, the estimated shear strain could be the reason for this discrepancy. The initial stress state was estimated assuming a linear-elastic relationship and included the effects of prestressing forces and the self-weight of the deck section. The centroid of the strain gage rosette was estimated to be in a state of uniaxial compression. The initial compressive stress of 1.90 ksi was added to the DIC and rosette stresses to evaluate the deck section with the biaxial failure envelope.

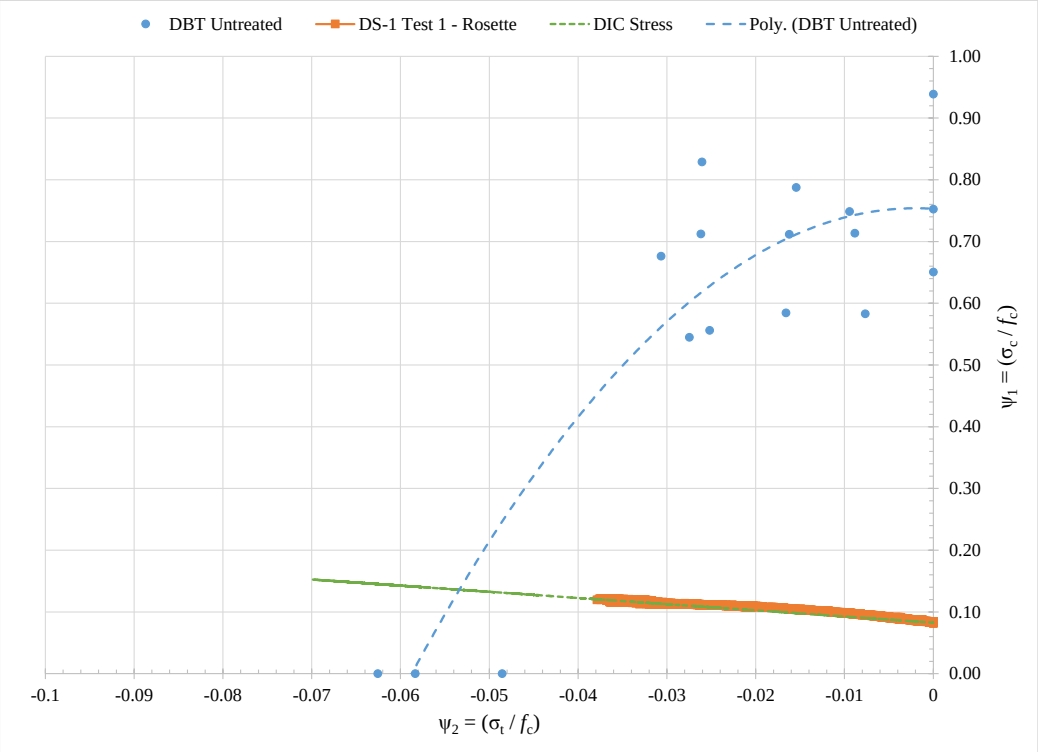

Figure 7-20: Stresses determined using strain gage rosette and DIC for DS-1 Test 1.

7.4.2 Test 2: Load Point at 18 in. Distance

The second static test was completed on DS-1 using a single point load located 18 in. from the pin support, and the deck section again failed in flexure. The first audible crack was heard at 10 kips, equivalent to a 12.2 k-ft moment. Visible cracks were not noted until 15 kips, equivalent to a moment of 18.3 k-ft. Cracks were marked on the deck section during testing. Cracks were not tightly spaced and displayed a clear flexure failure pattern (Figure 7-21). Cracking extended into the flange at 24 kips, indicating a depth to the neutral axis of approximately 1.3 in., and cracking was contained within the end cell unit (Figure 7-22). The dominant failure crack was visible at 15 kips and was located 21.5 in. from the support. Few fibers were seen in the dominant crack, showing little fiber bridging (Figure 7-23). No indication of shear cracking occurred throughout the test.

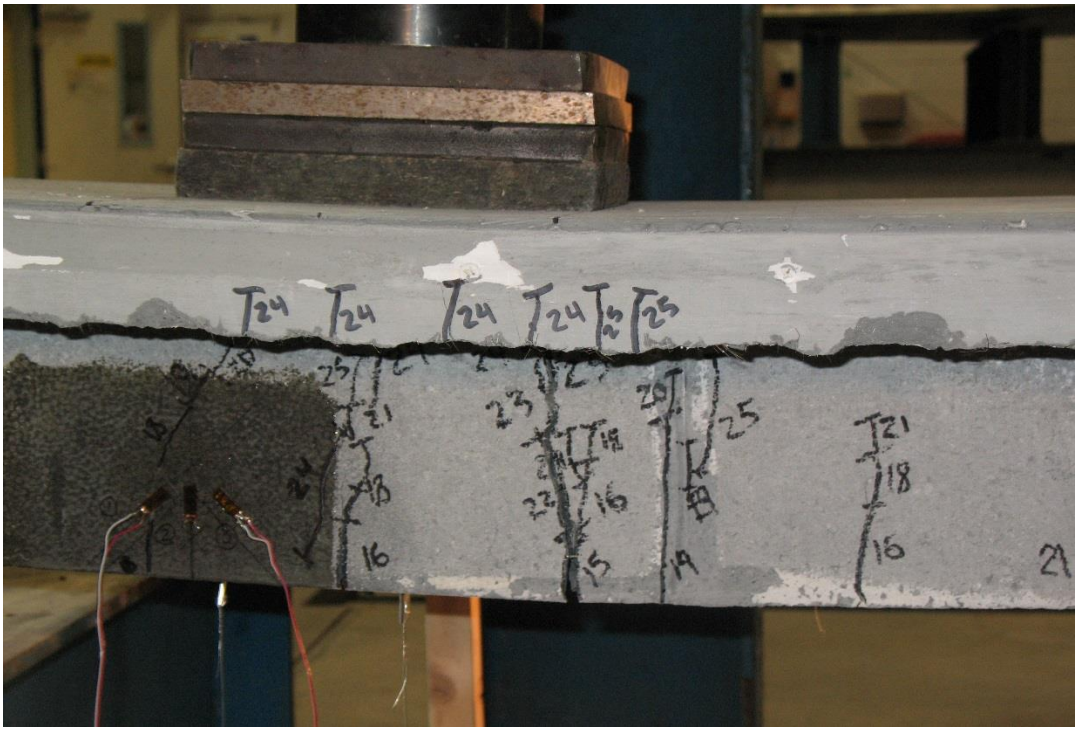

Figure 7-21: Cracking network extends into flange.

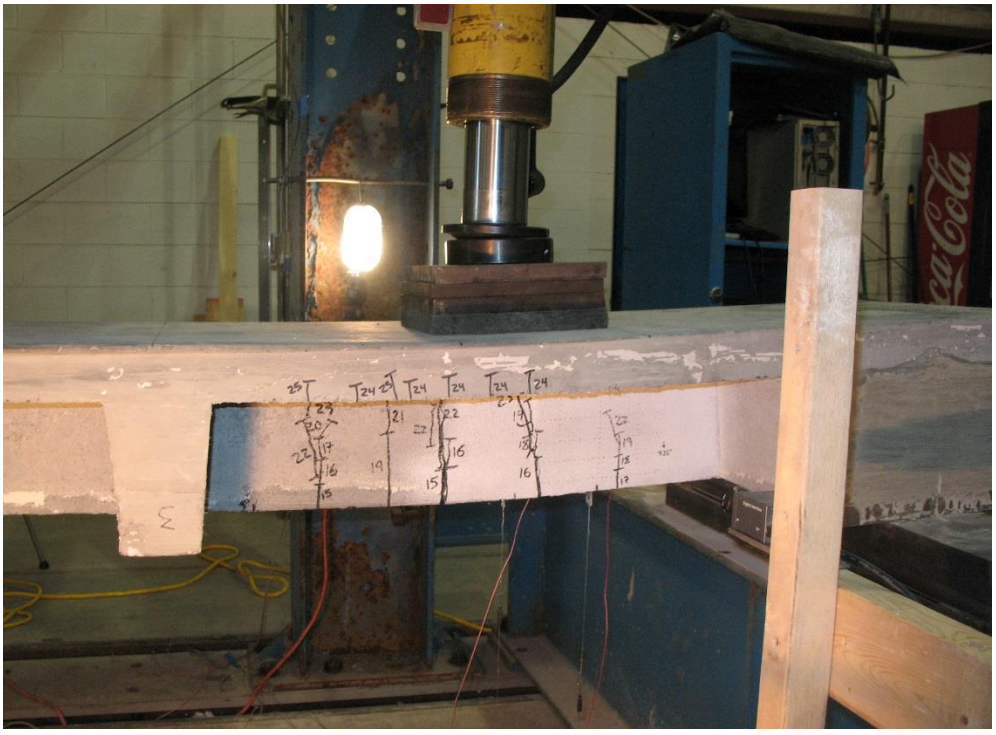

Figure 7-22: Cracking contained within end cell unit.

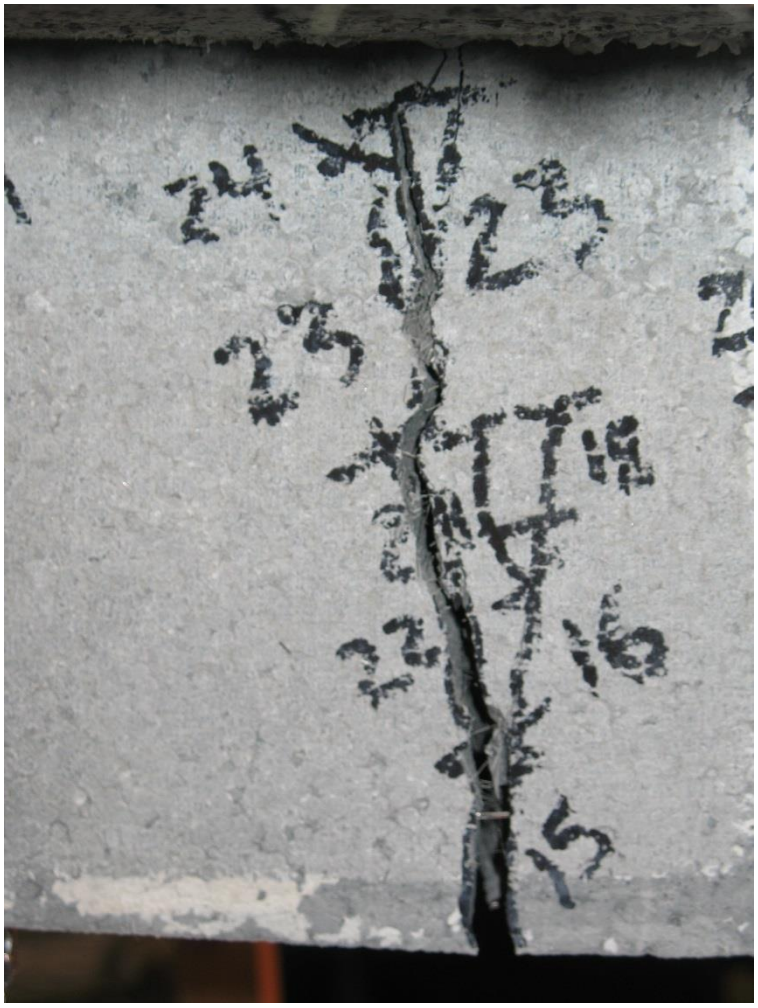

Figure 7-23: Dominant crack in DS-2 displayed little fiber bridging.

The maximum load resisted throughout the test was approximately 25 kips (Figure 7-24), equivalent to an applied moment of 30 k-ft at the location of the applied load (Figure 7-25). The maximum applied moment of 30 k-ft exceeded the design moment of 23 k-ft by 30.4 percent. Again, the failure model used to design the deck cross section in flexure was conservative for the upside down placement method. The ductile behavior of the deck section was evident by increasing deflections and crack widths. At the completion of the test, the ratio of the ultimate deflection (Δ_u = 1.14 in.) to the deflection at first crack (Δ_{cr} = 0.25 in.) was 4.56.

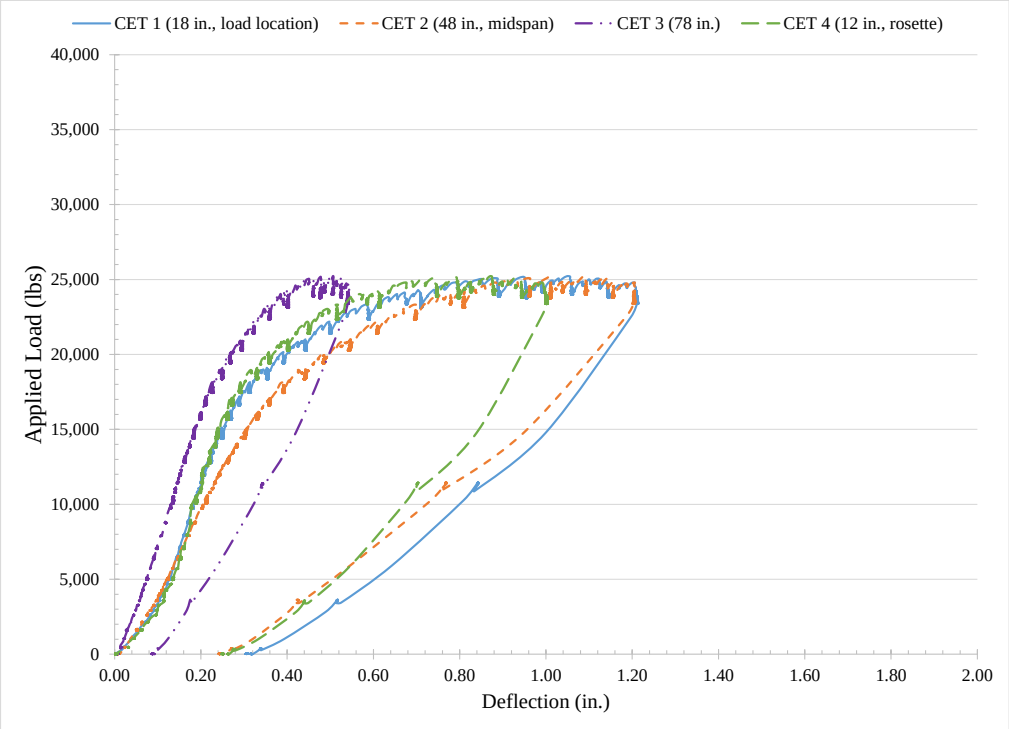

Figure 7-24: Load versus deflection for all CETs (DS-1 Test 2)

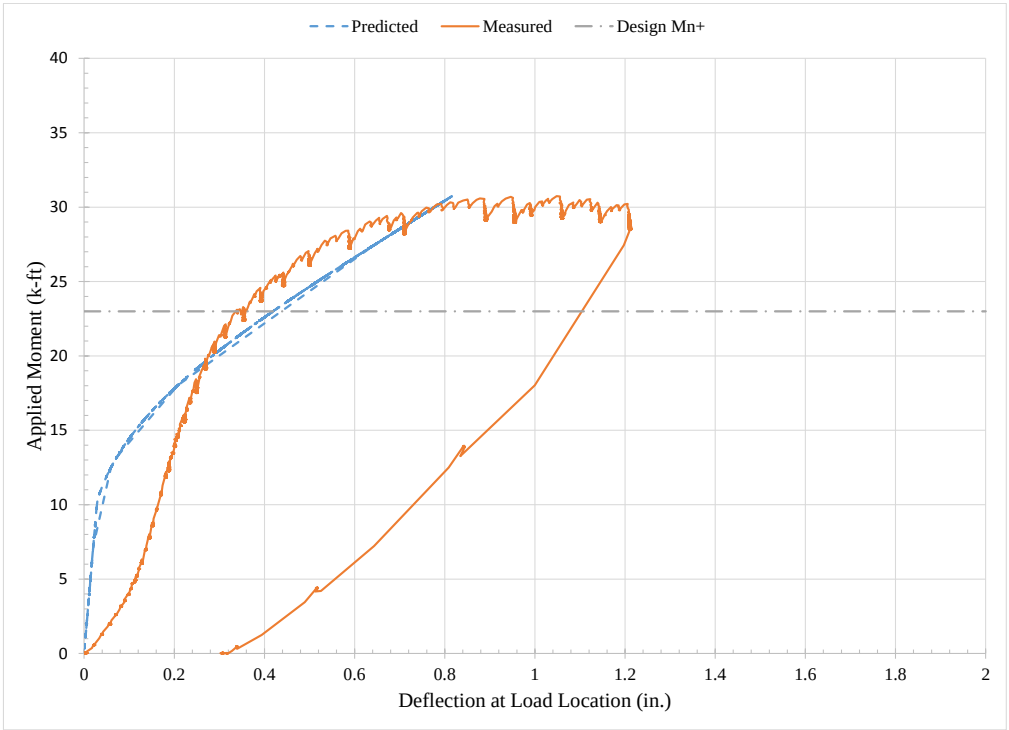

Figure 7-25: Applied moment versus deflection at load location (DS-1 Test 2).

The applied moment versus deflection plot in Figure 7-25 shows some sudden jumps, which could be a result of the prestressing strands slipping, rather than yielding. With the load placed 18 in. from the support, it was embedded 31.5 in up to the point of the load. Reported development lengths for prestressing steel in UHPC vary from less than 18 in. (Lubbers 2003) to less than 37 in. (Graybeal 2006b) for 0.5 in. low-relaxation prestressing steel with an ultimate stress of 270 ksi. Lubbers (2003) determined the limit of 18 in. using pull-out tests with non-stressed prestressing steel. Graybeal (2006b) determined the limit of 27 in. based on I-girder tests. John et al. (2011) reported development length to be less than 35 in. for 0.6 in. prestressing strands in UHPC beams. It is possible that the prestressing strand did slip during this test, since the development length could have been more than 31.5 in. Slip should be measured in future tests to better determine the failure mode and the development length of prestressing steel in UHPC.

During Test 2 of DS-1, a crack went through the area where the strain gage rosette was located. The gages were located 14 in. from the support, and 4.25 in. below the top of the web. A visible crack formed at the location of strain gage 1, nearest the pin support (Figure 7-26). The crack was first detected visibly at 18 kips; however, the gage began to show signs of possible micro-cracking at 15 kips, when a sudden jump in strain occurred. A change in strain from 97 με to 860 με was shown in gage 1, and a change from 100 με to 860 με in gage 2. Gage 3 showed a small decrease in strain at the same time, from 90 με to 60 με. This sudden change in strain also occurred at the time when the first visible crack was noted during the test. The sudden change in strain could have been due to the redistribution of stresses throughout the section with the growth of the crack.

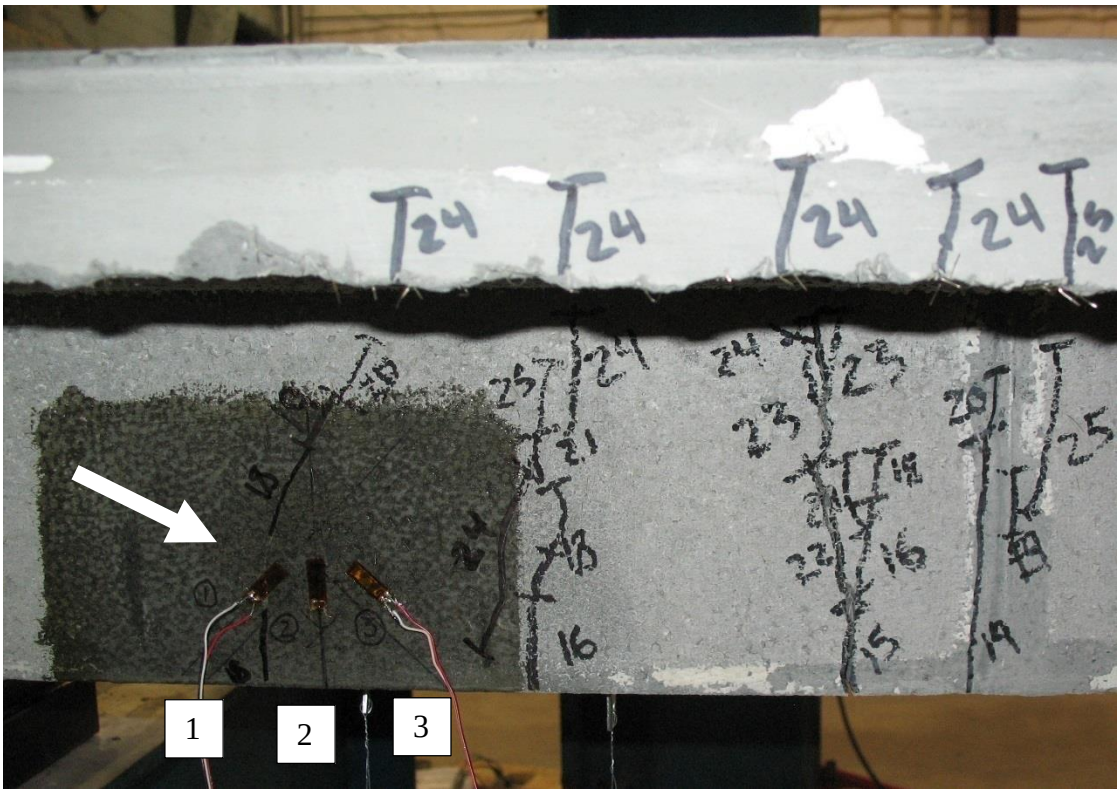

Figure 7-26: Cracking occurred beneath strain gage 1.

The crack at gage 1 was likely the reason for the gage reading failure. Prior to this gage failure, gage 2 lost contact with the system, and the principal strains could no longer be determined beyond 16 kips using the rosette. Principal strains and stresses were determined using the rosette up to this point of gage failure. In plotting the principal stresses with the polynomial biaxial failure curve for untreated UHPC, the sudden strain changes due to cracking were evident (Figure 7-27). The initial stress state was estimated assuming a linear-elastic relationship and included the effects of prestressing forces and the self-weight of the deck section. The centroid of the strain gage rosette was estimated to be in a state of uniaxial compression. The initial compressive stress of 1.90 ksi was added to the rosette stress to evaluate the deck section with the biaxial failure envelope.

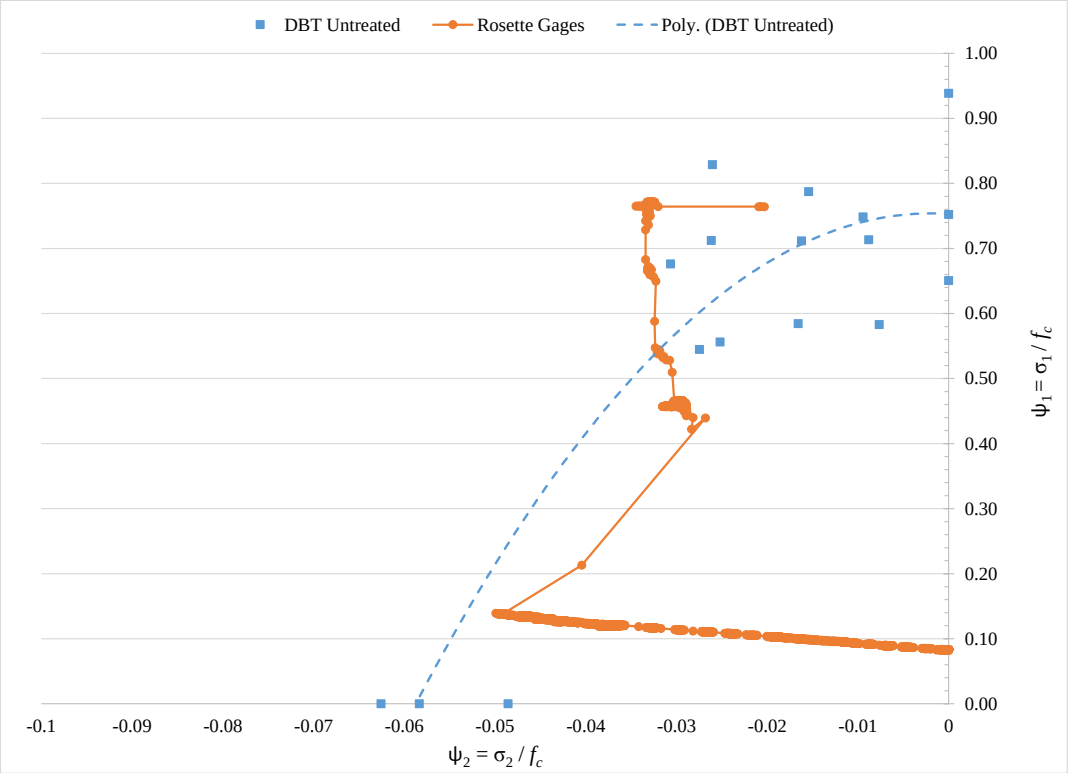

Figure 7-27: Stresses generated from strain gage rosette plotted with biaxial failure model for untreated UHPC.

Principal stresses were also generated using the DIC methods. Because only two strains were determined using DIC, a shear stress was used to estimate principal strains and stresses. Principal stresses were then plotted with the biaxial failure model proposed for untreated UHPC (Figure 7-28). The DIC stresses were separated into two selections. The first selection, DIC Method (1), only included the data prior to the 15 kip crack. The second selection, DIC Method (2), included all remaining data points after the initial 15 kip crack. Up to the 15 kip crack, both the strain gage rosette and DIC data approached the failure curve. After the crack, DIC stresses continued beyond the failure model.

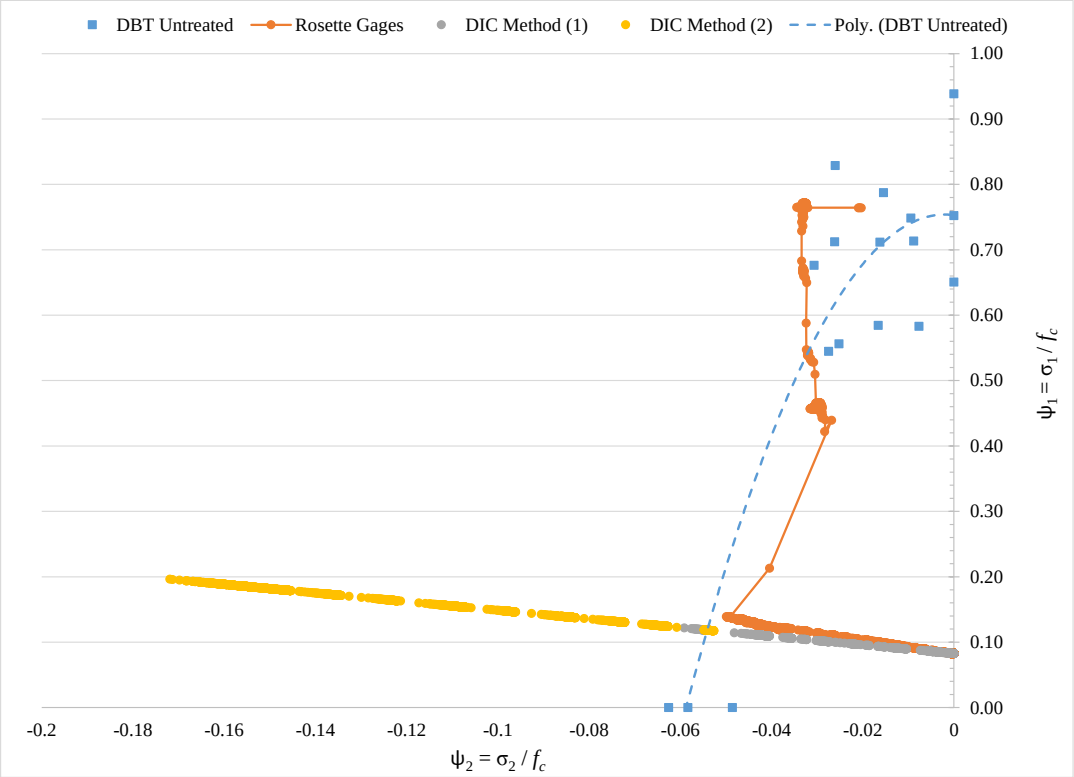

Figure 7-28: Stresses generated using DIC data plotted with the biaxial failure model for untreated UHPC.

7.5 DS-2 Tests for Right-side Up Placement Method

For each test, DS-2 was tested on a simple pin and roller support over a span length of 8 ft. Load was increased incrementally by 500 lbs. Once visual cracks were detected, crack growth was marked for every 1000 lbs of increased load.

7.5.1 Test 1: Load Point at 18 in. Distance

The first static test performed on DS-2 used a point load located 18 in. from the support. Unlike DS-1, no audible cracking was noted prior to visible cracking. At 29 kips, a crack extended nearly the full-depth of the web on the rosette strain gage side of the beam directly below the load (Figure 7-29). Vertical cracks were also observed in the web on both sides of the beam (Figure 7-30). More tightly spaced crack networks were observed near the dominant failure crack than previously observed in DS-1 tests. The more dense fiber network was primarily observed on the DIC side of the deck section (Figure 7-31, Figure 7-32). On the opposite side, the first full-depth crack in the web grew independently as additional load was

applied beyond 29 kips. This dominant crack was located approximately 15 in. from the nearest support and 3 in. from the center of the 8 by 8 in. patch load. Unlike DS-1, numerous fibers were observed bridging cracks in DS-2 (Figure 7-33).

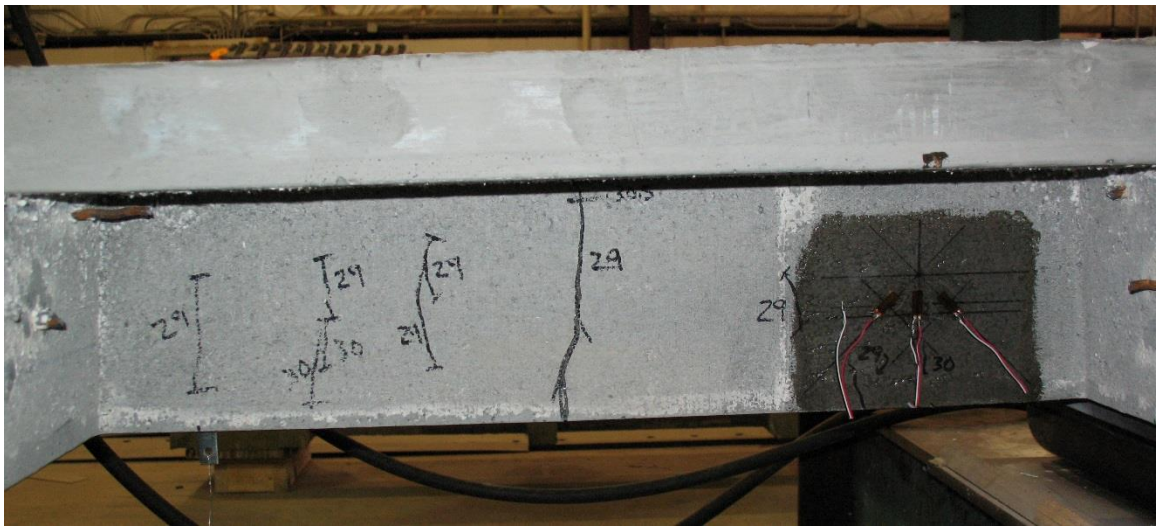

Figure 7-29: Crack pattern on rosette side of the beam (DS-2 Test 1).

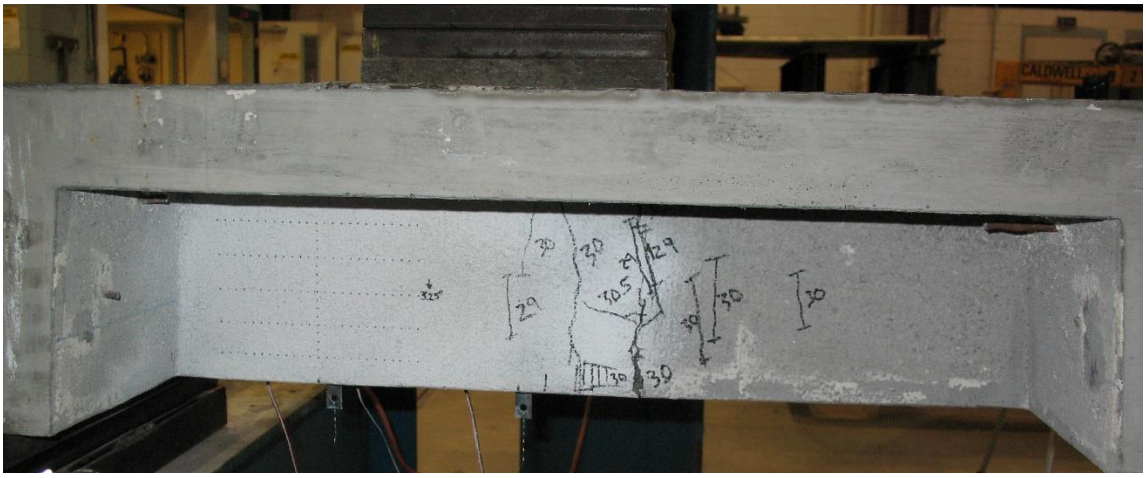

Figure 7-30: Cracking pattern on DIC side of the beam (DS-2 Test 1).

Figure 7-31: More dense fiber network on DIC side of beam displayed fiber bridging.

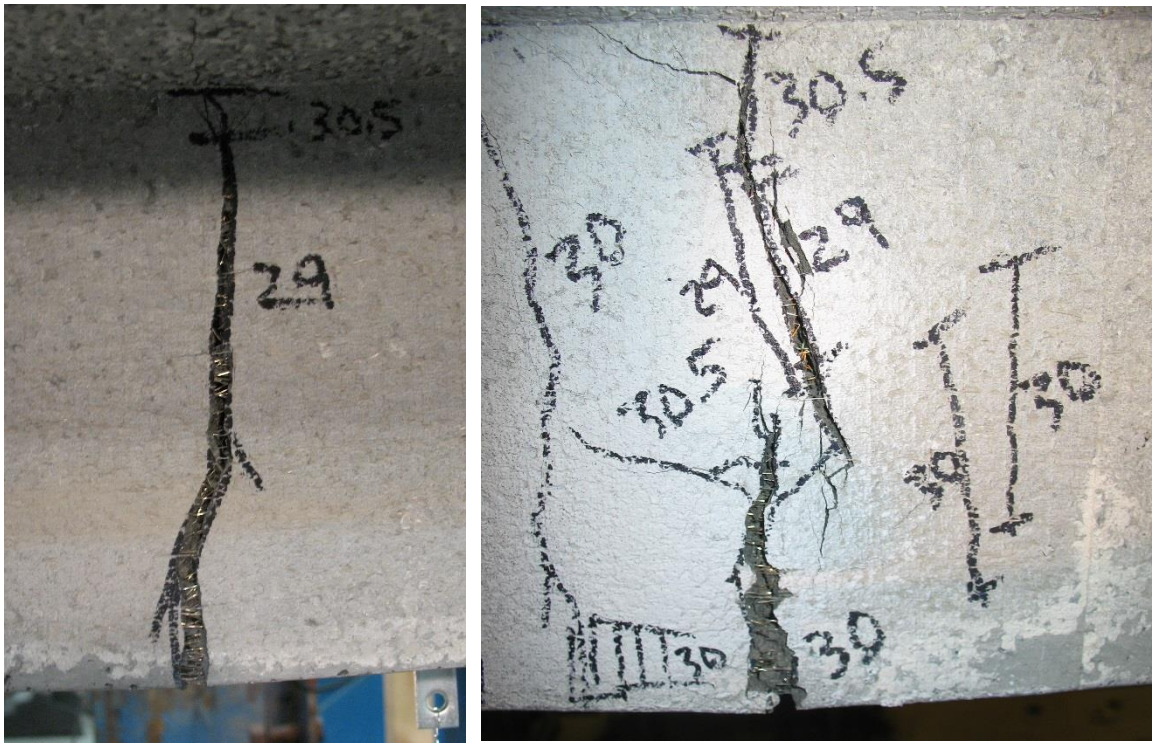

(a) (b)

Figure 7-32: A single dominant flexure crack was on the rosette side (a), and a more dense fiber network was observed on the DIC side (b).

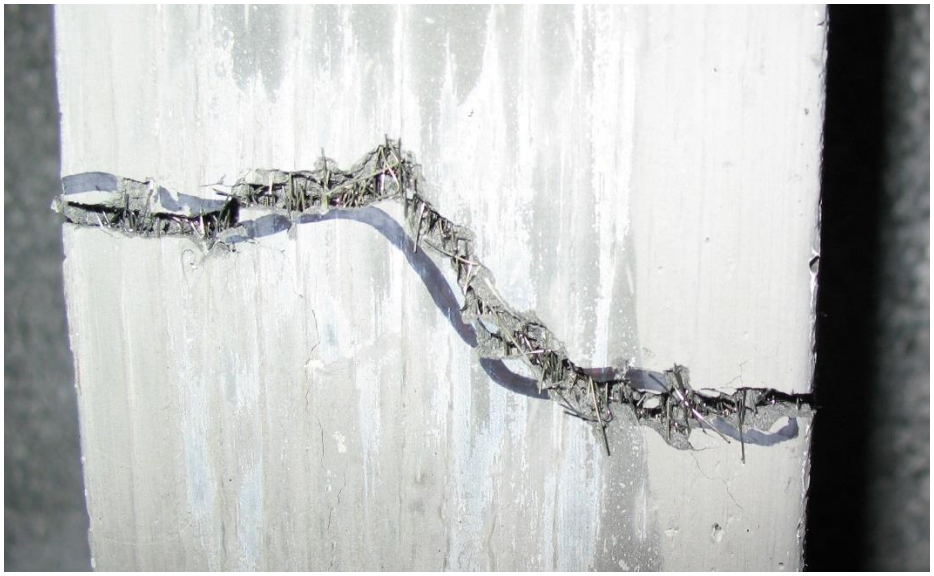

Figure 7-33: Underside of the web showed a high concentration of fibers bridging the dominant flexure crack.

The test was ended after reaching a maximum load of 31 kips (Figure 7-34), equivalent to an applied moment of 36 k-ft at the location of load application (Figure 7-35). This maximum applied moment exceeded the design moment capacity of 23 k-ft by 56.5 percent. Recall, the predicted moment capacity for the right-side up deck section was identified as 33 k-ft using a maximum tensile stress of 1.5 ksi. The deck section exceeded this expected moment capacity by 9.1 percent. The deck section was unable to resist additional load beyond the maximum 31 kips. Cracks grew and deflections increased throughout this time, indicating ductile behavior. At the completion of the test, the ratio of the ultimate deflection (Δ_u = 0.82 in.) to the deflection at first crack (Δ_{cr} = 0.21 in.) was 3.90.

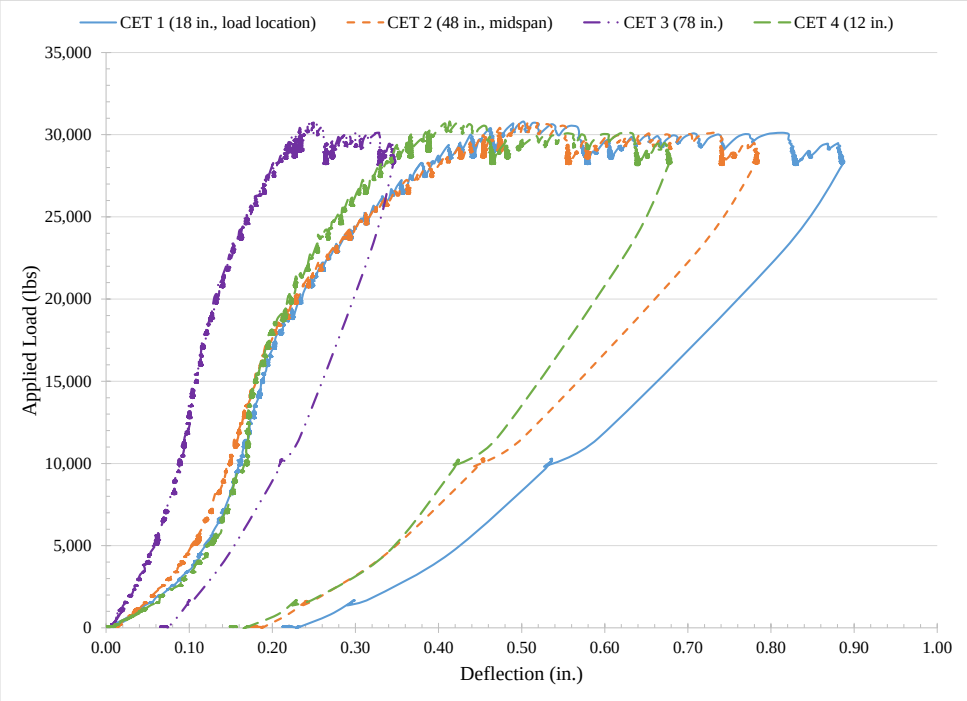

Figure 7-34: Load versus deflection for all CETs (DS-2 Test 1), indicating distance from support nearest load application.

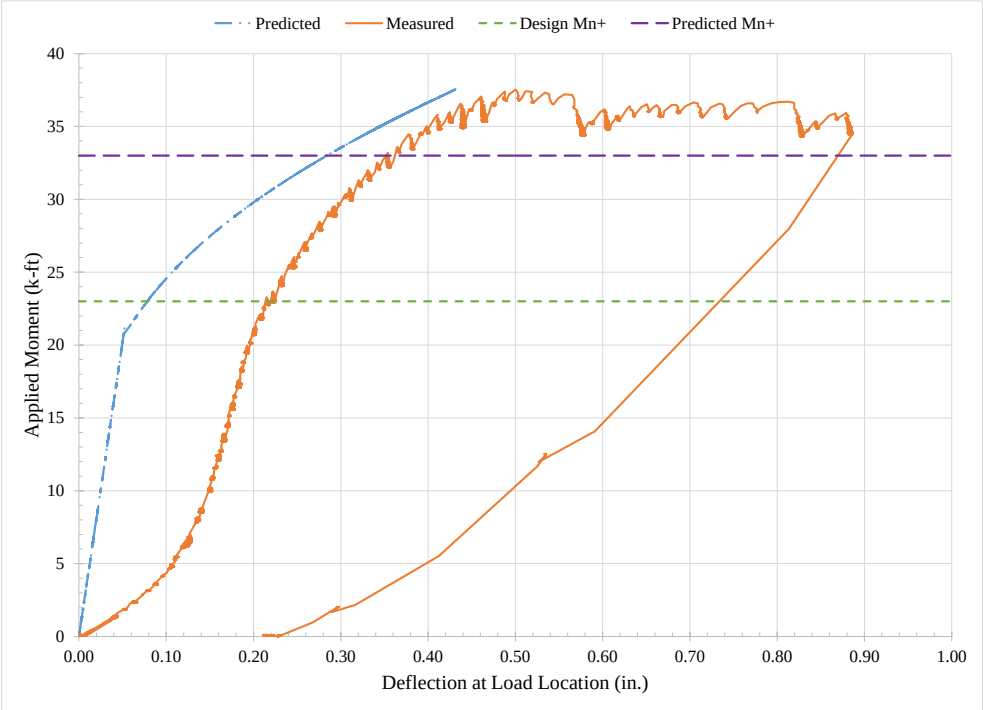

Figure 7-35: Applied moment versus deflection at location of load (DS-2 Test 1).

As in DS-1 Test 2, the embedment length at the location of the load was 31.5 in. Because the development length for 0.5 prestressing strands could be higher than this value (Section 7.4.2), it is possible that the strands experienced slipping during Test 1 of DS-2. Observing the applied moment versus deflection plot in Figure 7-35, sudden jumps in the maximum applied moment imply that slipping may have occurred.

Principal strains were determined using the strain gage rosette. Because the loading point was very close to the strain gage location in DS-1 Test 2, the strain gage rosette was relocated for DS-2 Test 1 and DS-2 Test 2. The rosettes for DS-2 were located 2 in. closer to the support, making them 12 in. from the support. They were also moved 1 in. higher on the web so that the centerline was located 3.25 in. below the top of the web. The strains were transformed into principal strains and stresses assuming a linear elastic relationship. The principal stresses were plotted with the biaxial failure criterion proposed for untreated UHPC with random fiber orientation (Figure 7-36). This model was considered conservative for UHPC with controlled fiber orientation. The stresses generated using the rosette strains remained well inside the biaxial failure curve, indicating no failure in this location. The initial stress state was estimated assuming a linear-elastic relationship and included the effects of prestressing forces and the self-weight of the deck section. The centroid of the strain gage rosette was estimated to be in a state of uniaxial compression. The initial compressive stress of 1.63 ksi was added to the rosette stress to evaluate the deck section with the biaxial failure envelope.

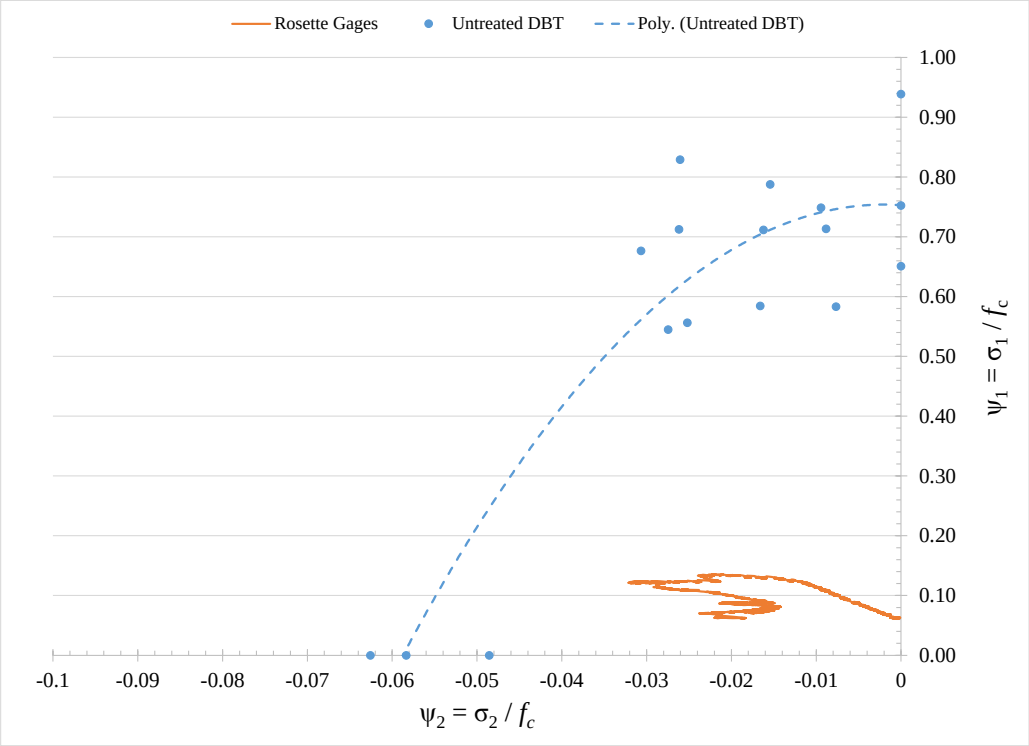

Figure 7-36: Principal strains of the rosette gage plotted with biaxial failure model for UHPC.

Principal strains were also determined using the DIC data and an estimated shear strain. The strains were transformed into stresses and plotted with the biaxial failure criterion developed for untreated UHPC with random fiber orientation. The stresses generated using the DIC methods showed no clear pattern for DS-2 Test 1 (Figure 7-37). It is possible that the movement of the deck section affected the DIC measurements. As the deck was loaded, it moved at an angle in reference to the original photograph. Similar problems were experienced previously during direct biaxial tests.

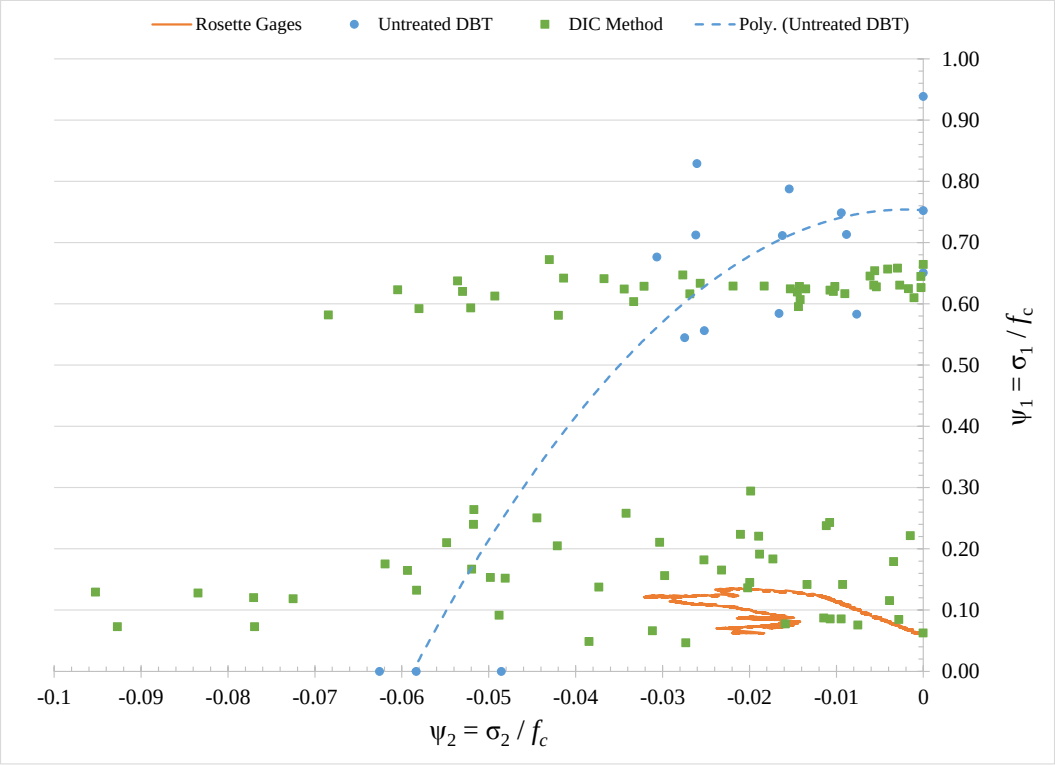

Figure 7-37: DIC stresses displayed no clear pattern (DS-2 Test 1)

7.5.2 Test 2: Load Point at 30 in. Distance

The second static test was completed on DS-2 using a single point load located 30 in. from the pin support. Again, no audible cracking was noted for Test 2 prior to detecting cracks on one side at 17 kips, equivalent to a moment of 29 k-ft. Multiple small flexure cracks occurred on one side of the deck section, but one dominant flexure crack approximately 25.6 in. from the support led to failure (Figure 7-38 to Figure 7-41). A small crack network propagated around this dominant crack, and fiber bridging was observed (Figure 7-42). Cracks primarily occurred near the corner intersecting the nearest longitudinal rib.

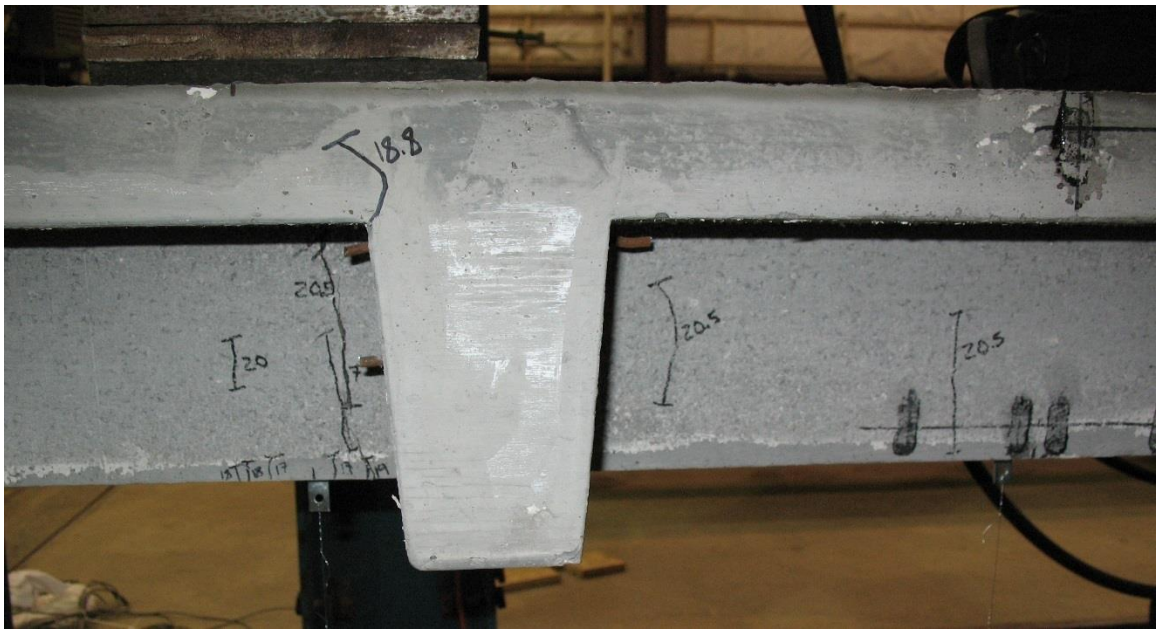

Figure 7-38: Crack pattern on DIC side of deck section (DS-2 Test 2).

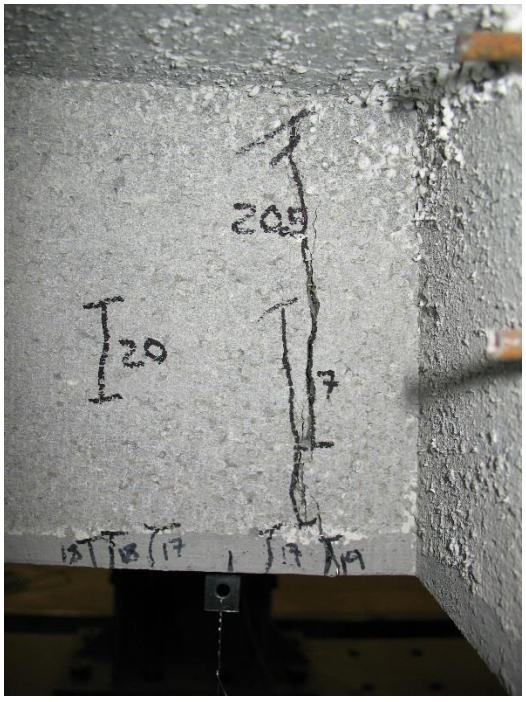

Figure 7-39: Primary failure crack on DIC side of deck section (DS-2 Test 2).

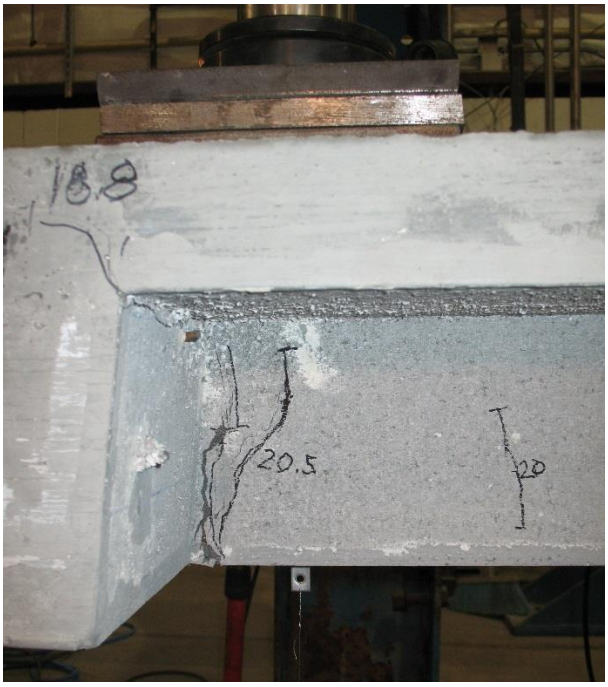

Figure 7-40: Crack pattern on rosette side of deck section (DS-2 Test 2).

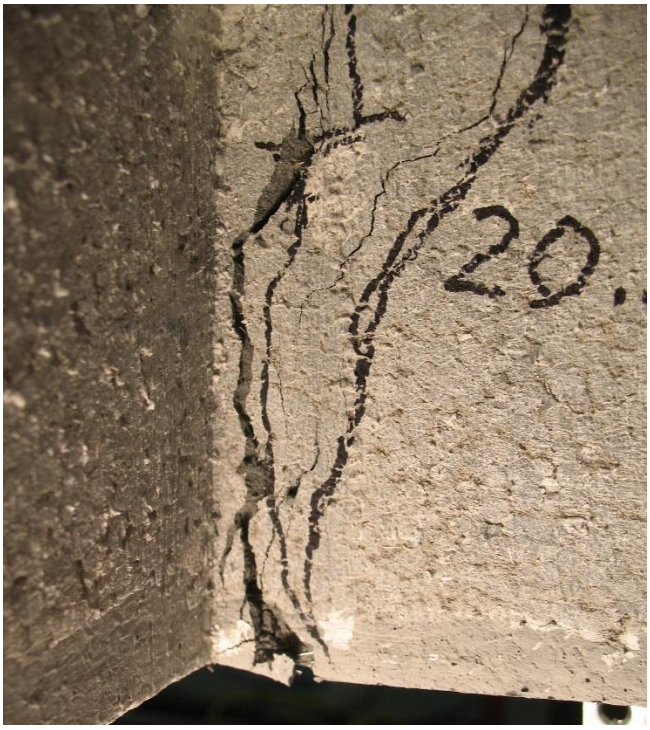

Figure 7-41: Tightly spaced crack network propagated from primary crack.

Figure 7-42: Fiber bridging on bottom of web (DS-2 Test 2).

During Test 2 of DS-2, the maximum applied load was approximately 21 kips (Figure 7-43), equivalent to an applied moment of 35 k-ft at the location of load application (Figure 7-44). The maximum applied moment exceeded the design moment capacity of 23 k-ft by 52.2 percent. The predicted bending moment using a maximum tensile stress of 1.5 ksi was 33 k-ft, and the applied moment capacity exceeded this value by only 6 percent. The deck section was resisting the maximum load steadily until a crack extended into the flange. Once this crack extended into the flange, the load could not be raised above 18 kips without sudden drops in load. The sudden drops could indicate slipping of the strand. The crack that led to failure was 26.5 in. from the support, allowing the strand to have an embedment length of 34 in. Based on the observations of Graybeal (2006b) who set a limiting embedment length as 37 in. in steam treated UHPC, it is possible that the strand was not fully developed at the 34 in. embedment provided in this deck section. Future testing should incorporate measurements for strand slipping to better determine whether failure is due to slipping of the strand or yielding. This testing would also better establish a development length for prestressing steel in UHPC. In this test, deflections increased after the initial cracking point. However, the sudden drops did not

allow a constant load to be sustained for an extended duration after the peak load had been reached. At the completion of the test, the ratio of the ultimate deflection at the peak sustained load (Δ_u = 0.59 in.) to the deflection at first crack (Δ_{cr} = 0.23 in.) was 2.57.

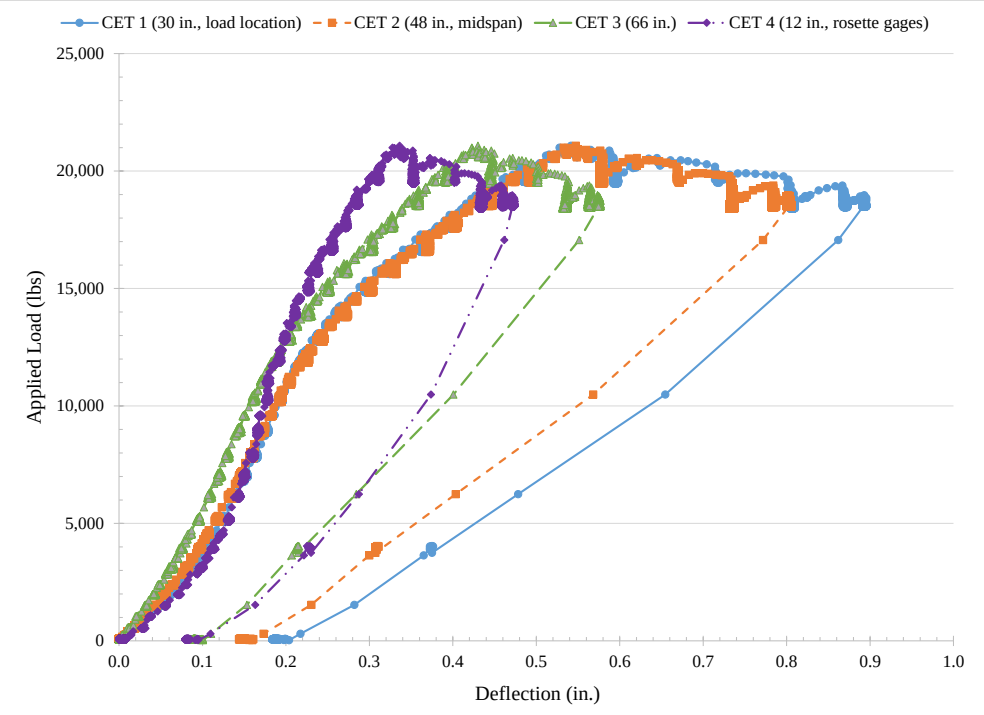

Figure 7-43: Applied load versus deflection for all CETs (DS-2 Test 2).

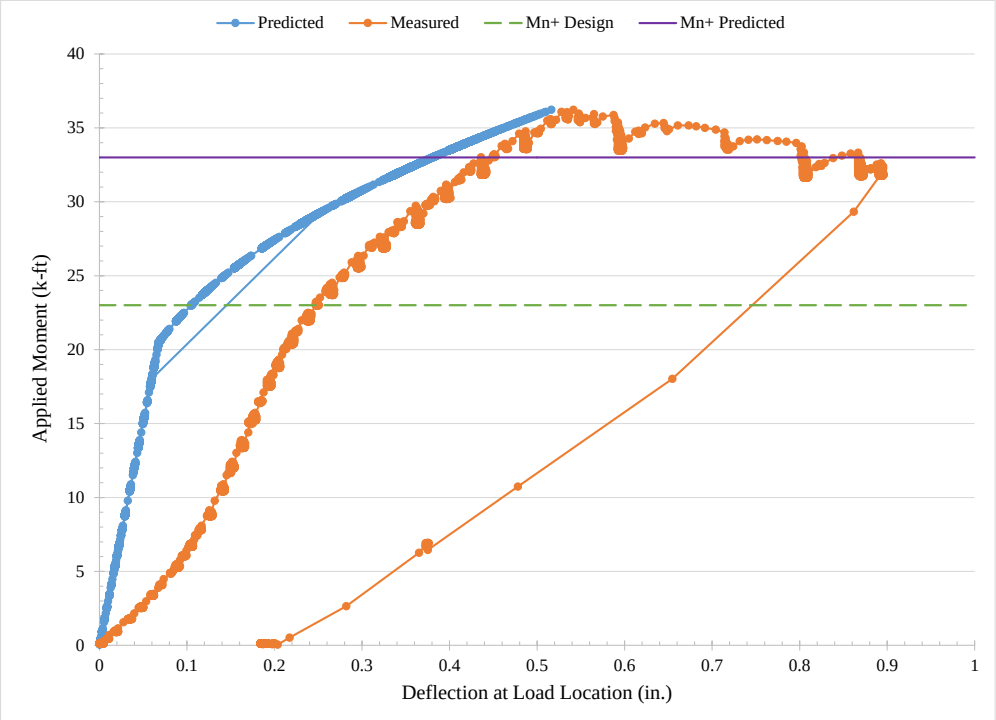

Figure 7-44: Applied moment versus deflection at load location (DS-2 Test 2).

Strains were again monitored using a strain gage rosette on one side of the deck section. The rosette strains were transformed into principal stresses and plotted with the UHPC biaxial failure model (Figure 7-45). Principal stresses were shown to be well below the failure stress conditions for biaxial failure. Observations showed no cracking in the strain gage area, further corroborating that there was no cracking or biaxial failure at the rosette. As in DS-2 Test 1, the DIC strains did not show any clear pattern. This was likely a result of the very low stresses and the estimated shear stress used to determine principal stresses. The movement of the deck in the digital images could have also been a factor in the inconclusive DIC data. The initial stress state was estimated assuming a linear-elastic relationship and included the effects of prestressing forces and the self-weight of the deck section. The centroid of the strain gage rosette was estimated to be in a state of uniaxial compression. The initial compressive stress of 1.63 ksi was added to the rosette stress to evaluate the deck section with the biaxial failure envelope.

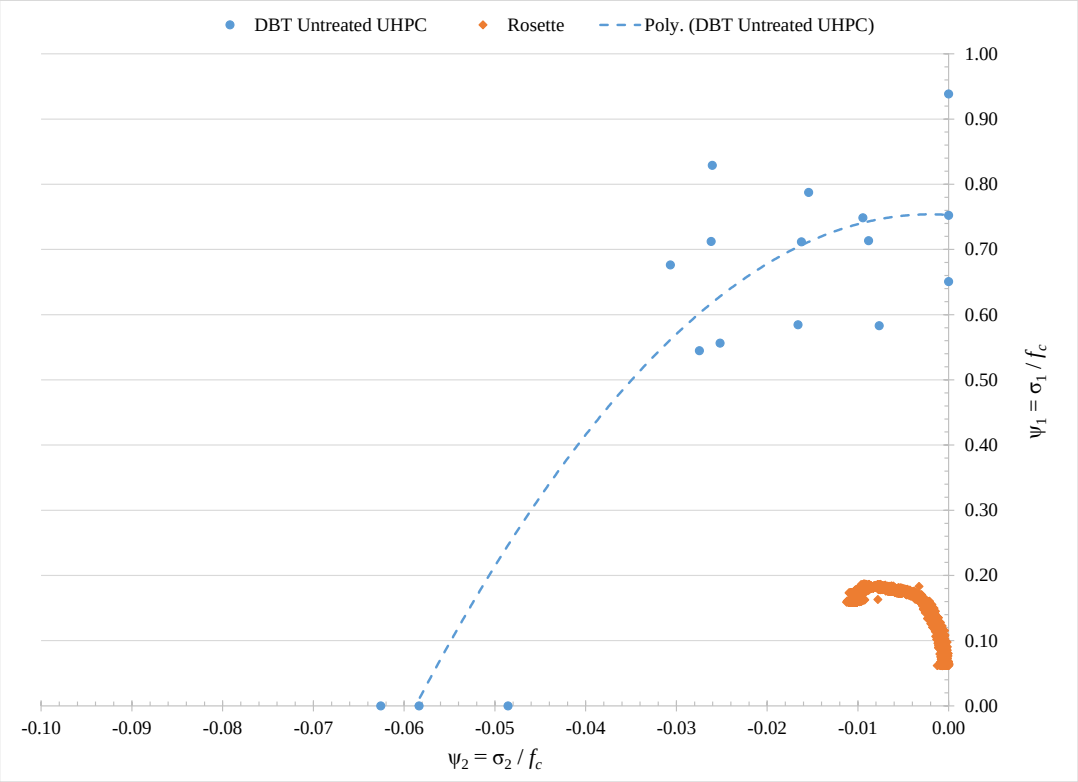

Figure 7-45: Principal stresses determined using rosette gages plotted with biaxial failure model for untreated UHPC (DS-2 Test 2).

7.6 Influence of Placement Orientation

It was evident through experimental testing that placement orientation affected the structural behavior of the deck sections. Both deck sections failed in flexure with an identifiable dominant crack controlling the failure mode. In both cases, ductile behavior was identified through increasing deflections and crack width prior to an ultimate failure situation. In all tests, the deck sections were not tested to ultimate failure to preserve the deck sections for additional tests and analyses.

7.6.1 Positive Bending Moment Capacity

The maximum applied moment capacity exceeded the design moment capacity for all deck sections (Table 7-9). The stress-strain model implementing a maximum tensile stress of 0.5 ksi provided a conservative design for positive moment capacity (M_n^+). Because this maximum tensile stress was based on results from the upside down (UD) single cell units, this model was quite conservative for predicting behavior of DS-2. Using this model, DS-1 resisted applied

moments ($M_{a,max}$) of approximately 30 percent more than the design moment capacity, and DS-2 resisted applied moments of more than 55 percent the design moment capacity.

Table 7-9: Maximum applied moments exceeded design moment capacity.

Deck Section	Test Scenario	$M_{a,max}$ (k-ft)	M_n^+ (k-ft)	% Increase	$M_{n,pred}^+$ (k-ft)	% Increase
DS-1	Test 1 (30 in.)	30	23	30.4	23	30.4
	Test 2 (18 in.)	30	23	30.4	23	30.4
DS-2	Test 1 (18 in.)	36	23	56.5	33	9.1
	Test 2 (30 in.)	35	23	52.2	33	6.1

Because the design moment capacity was considered conservative for the right-side up placement scenario, a refined prediction of positive bending moment capacity was determined using the first-iteration design stress-strain model using a maximum tensile stress of 1.5 ksi. Using this methodology for analysis of the cross section, the difference between the applied moments and the predicted moment capacity ($M_{n,pred}^+$) was greatly reduced to less than 10 percent difference (Table 7-9).

The cracking moments from visual and audible observations exceeded those predicted using traditional analysis methods. In each case, the observed cracking moment exceeded the predicted values by more than 20 percent (Table 7-10). It is likely that micro-cracking took place prior to either audible or visible cracking. The cracking moment was also estimated using the load-deflection plots by identifying the point at which the load-deflection plot becomes non-linear (

Table 7-11, Figure 7-46). In these cases, the cracking moments for DS-1 exceeded the predicted values by more than 60 percent; whereas, the cracking moments for DS-2 were within 5 percent of predicted values.

Table 7-10: Cracking moments observed physically and audibly during tests.

Deck Section	Test Scenario	$M_{cr,pred}$ (k-ft)	$P_{cr,obs}$ (k)	$M_{cr,obs}$ (k-ft)	% Increase
DS-1	Test 1 (30 in.)	10.1	8	13.8	37
	Test 2 (18 in.)	10.1	10	12.2	21
DS-2	Test 1 (18 in.)	22.3	29	35.3	58
	Test 2 (30 in.)	22.3	17	29.2	31

Table 7-11: Cracking moments determined using load-deflection plots.

Deck Section	Test Scenario	$M_{cr,pred}$ (k-ft)	$P_{cr,graph}$ (k)	$M_{cr,graph}$ (k-ft)	% Increase
DS-1	Test 1 (30 in.)	10.1	9.5	16.3	61.4
	Test 2 (18 in.)	10.1	14	17.1	69.3
DS-2	Test 1 (18 in.)	22.3	17.5	21.3	-4.48
	Test 2 (30 in.)	22.3	12.5	21.5	-3.59

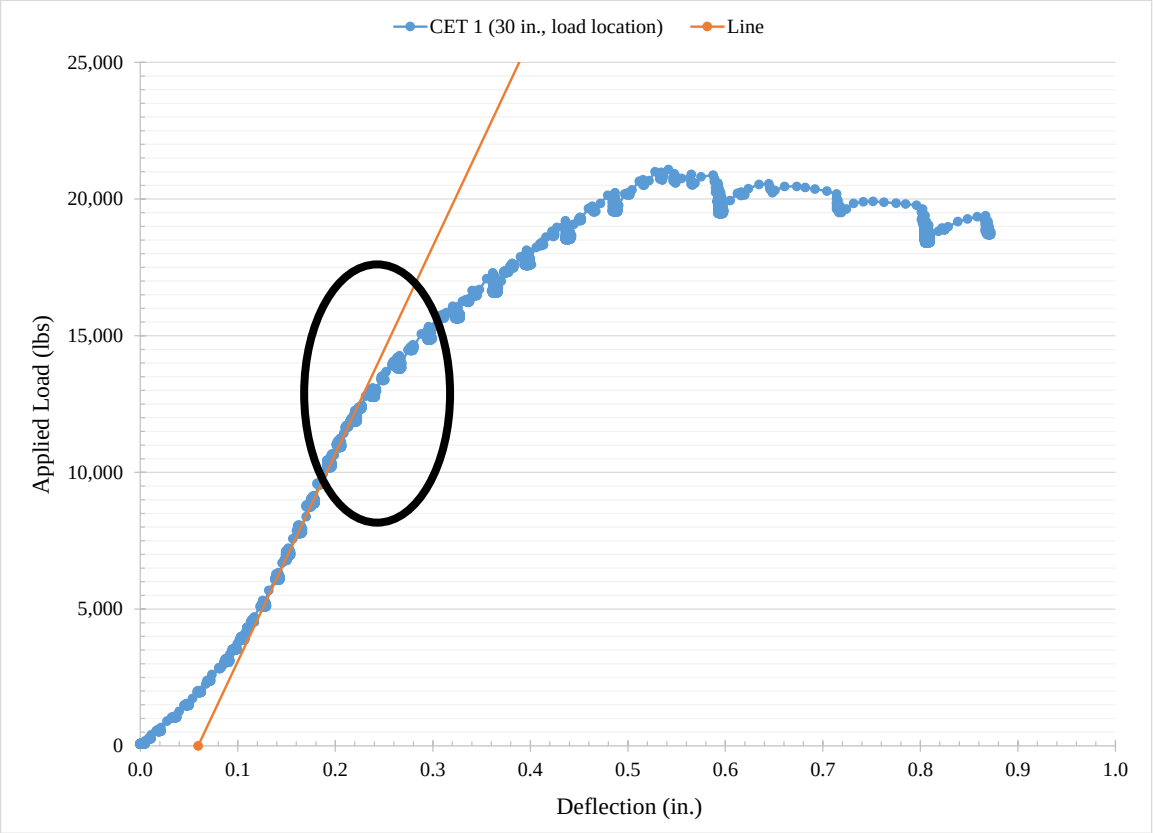

Figure 7-46: Cracking load estimated using load-displacement plots (DS-2 Test 2).

DS-2 provided a significant amount of additional moment capacity as compared with DS-1. In considering the two placement methods, it was shown to be advantageous to utilize the right-side up placement method for maximum positive bending moment capacity. On average, the observed cracking moment was increased by nearly 150 percent, the graphical cracking moment was increased by 28 percent, and the maximum applied moment was increased by 18 percent using the right-side up placement method (Table 7-12). The 150 percent increase from

the observed cracking moment was largely a results of the observations on DS-2 Test 1. The observed cracking moment was 35 k-ft and the graphical cracking moment was 21 k-ft. Because cracks were not heard during the DS-2 tests, visual cracks were the only indicator during the test that the beam had cracked. Since visual cracks are typically not seen until well after microcracking has taken place, the error increases a great deal when visual cracks are relied upon for an estimate of the cracking moment.

Table 7-12: Average differences in cracking moments and maximum applied moment for DS-1 and DS-2.

Deck Section	$M_{cr,obs}$ (k-ft)	$M_{cr,graph}$ (k-ft)	$M_{a,\ max}$ (k-ft)
DS-1	13.0	16.7	30
DS-2	32.3	21.4	35.5
% Increase	149	28	18

7.6.2 Deflections

Deflections were observed to be reduced in DS-2 using the right-side up placement method. Deflections measured beneath the load point at the design moment capacity of 23 k-ft were identified for each test scenario (Table 7-13). An approximate measured deflection directly beneath the load at the start of the maximum applied moment was also identified. The deflections in DS-2 were more than 30 percent less than the deflections for DS-1. This reduction in deflections was likely attributed to the fiber bridging action observed in DS-2, leading to improved bending tensile capacity.

Table 7-13: Deflections observed beneath the load at specified applied moments.

Deck Section	Test Scenario	M_n^+ (k-ft)	Δ_{23} (in.)	$M_{a,\ max}$ (k-ft)	$\Delta_{Ma,max}$ (in.)
DS-1	Test 1 (30 in.)	23	0.363	30	0.949
	Test 2 (18 in.)	23	0.359	30	0.782
DS-2	Test 1 (18 in.)	23	0.220	36	0.411
	Test 2 (30 in.)	23	0.248	35	0.487

7.6.3 Shear of Deck Sections

Shear failure was not observed in any of the deck sections; however, shear was a concern based on research involving shear failures in UHPC single unit, two-way ribbed bridge deck sections (Saleem et al. 2011). Saleem et al. (2011) experimentally tested single unit UHPC bridge decks over a simple span of 4 ft, half the span length used in the current study. The bridge deck used by Saleem et al. (2011) was reinforced with non-prestressed reinforcement in both the web and flange. A single No. 7 reinforcing bar was placed in the 2 in. thick web, and three No. 4 reinforcing bars were spaced evenly throughout the 12 in. wide by 1.25 in. thick flange. The total height of the bridge deck was 5 in. Partial-depth longitudinal ribs were spaced at 16 in. and were only 3 in. deep.

In the current study, the design shear strength was determined to be 11.8 kips using only the contribution of discrete fiber reinforcement in UHPC. The contribution of prestressing steel was not taken into account for these values; although, it is expected that prestressing would increase the shear capacity of the deck section due to the addition of compression stresses in the UHPC prior to loading. Shear estimations were made from the experimental tests at the cracking and maximum applied moment. The shear at cracking was determined for both the observed (obs) and graphically determined (graph) cracking loads. With the exception of DS-2 Test 1, the shear at cracking was lower than the design shear strength of 11.8 kips, preventing shear failures of the deck section under the test conditions (Table 7-14).

Table 7-14: Maximum shear at cracking and maximum applied moments.

Deck Section	Test Scenario	V_{design} (k)	$V_{cr,obs}$ (k)	$V_{cr,graph}$ (k)	$V_{a,max}$ (k)
DS-1	Test 1 (30 in.)	11.8	5.56	6.53	12.0
	Test 2 (18 in.)	11.8	8.13	11.4	20.1
DS-2	Test 1 (18 in.)	11.8	19.4	14.2	24.1
	Test 2 (30 in.)	11.8	6.84	8.59	13.9

7.7 Waffle Slab Bridge Deck System Overview

Using the average results from each bridge deck section, the ability of this design to work as a bridge deck system was estimated assuming the equivalent strip width approximate method of the AASHTO (2012) LRFD Bridge Design Specifications. It was assumed that this method

could be applied to the UHPC bridge deck; although, no guidelines specify that this approximate method should or should not be used with UHPC waffle slabs.

As previously mentioned in Section 6.3.2, the equivalent strip width according to AASHTO (2012) would be 78.8 in. To simplify the analysis based on the 18 in. transverse rib spacing, four single unit deck sections were used for the analysis with a total width of 72 in. According to AASHTO (2012) 3.6.1.2, a standard 10 by 20 in. wheel patch load of 16 kips was considered for the analysis. Applying a live load factor (LL) of 1.75 and an impact factor (I) of 1.3 taken from AASHTO (2012) 3.4.1 and 3.6.2, the design patch load was determined to be 36.4 kips. Using this load, the required shear and moment at midspan are 19.3 kips and 75.0 kip-ft assuming an 8-ft girder spacing and including self-weight. The load placed at midspan provided the largest bending moment; however, this configuration did not provide a maximum shear condition. Required shear increases as the load is placed closer to the support. With two tire patch loads placed 6 ft apart along the beam, the required shear was increased to 36.4 kips. The self-weight was based on a density of 156 pcf for the UHPC cross section and a load factor of 1.25.

Average test results for each deck section were used to estimate the nominal moment and shear capacity of a 72 in. section of the waffle slab bridge deck system (

Table 7-11, Table 7-12, and Table 7-14). Assuming the longitudinal ribs would transfer load equally across the equivalent strip width, the waffle slab deck system would be expected to crack at a moment of 66.8 k-ft if placed upside down and 85.6 k-ft if placed right-side up (Table 7-15). Based on average test results, the deck system placed upside down would be sufficient at ultimate conditions, but it would be expected to crack under the factored loading. The deck placed right-side up is expected to be sufficient in both bending moment and shear. No cracking is expected for this deck section under the factored loading.

Table 7-15: UHPC waffle slab deck system comparison.

		Shear				Moment			
Deck System	**Placement Method**	**$V_{u,8in.}$ (k)**	**V_{cr} (k)**	**φV_{cr} (k)**	**φV_n (k)**	**$M_{u,mid}$ (k-ft)**	**M_{cr} (k-ft)**	**φM_{cr} (k-ft)**	**φM_n (k-ft)**
DS-1	UD	**37.8**	45.5	34.1	60.3	**75.5**	66.8	60.1	108
DS-2	RU	**37.8**	56.9	42.7	72.3	**75.5**	85.6	77.0	128

UD = upside down, RU = right-side up

$\varphi_{shear} = 0.75$, $\varphi_{moment} = 0.90$

According to this comparison, the untreated UHPC waffle slab bridge deck system is expected to be sufficient under the assumption that the connecting longitudinal ribs between each single unit deck section are capable of providing proper load distribution. If fiber settling is considered a potential risk to the system, using the right-side up placement method would ensure the deck would not crack under positive bending moment. Additional testing should be carried out to investigate the contribution of the longitudinal ribs in the waffle deck panel system. Additional testing should also investigate negative bending, shear connections, and panel-to-panel connections.

Chapter 8: Conclusions and Recommendations

8.1 Project Summary

The central purpose of this study was to investigate the potential for UHPC in bridge deck applications. First, an initial material characterization identified the need for proper mixing and placement procedures necessary for UHPC (Chapter 4). The biaxial failure pattern of UHPC, identifying the influence of curing method and fiber orientation, was investigated, and a failure model was proposed for untreated UHPC (Chapter 5). A preliminary design for an untreated UHPC bridge deck was completed (Chapter 6). Fiber settling was identified as a potential placement problem, showing great reductions in modulus of rupture values in the single cell unit placed upside down. The UHPC bridge deck was redesigned based on preliminary testing results, and single unit bridge deck sections were constructed and experimentally tested to evaluate behavior over a simple span of 8 ft (Chapter 7).

8.2 Conclusions

8.2.1 Material Behavior of UHPC

Although this study was not seeking to specifically characterize the material behavior of UHPC, several conclusions can be made based on results from the current study:

1. The AASHTO Standard T 132-87 (2004) test for mortar using briquets to determine tensile strength was identified as the best method to determine a direct tensile strength of UHPC. Both the ASTM Standard C496 (2004) method for splitting tensile strength of cylinders and the ASTM Standard C1609 (2006) method for fracture of fiber-reinforced concrete were shown to over predict the direct tensile capacity of UHPC to a greater degree than by using briquets.

2. A specified compressive strength of 16 ksi was identified for untreated UHPC based on ACI 318-11 (ACI Committee 318 2011) provisions. Although the majority of compressive strengths observed throughout this project exceeded 20 ksi, the design compressive strength would provide a conservative value to account for material variations.

3. The self-consolidating nature of UHPC and fiber concentrations make UHPC sensitive to placement methods. With no vibration, UHPC was shown to exhibit fiber settling, possibly due to high flow combined with a long initial set time. The unique rheological properties of UHPC made it possible to place UHPC products upside down by inserting formwork from the top down with ease.

4. Although the upside down construction practice was possible, fiber settling was observed. A high fiber concentration was observed in samples nearest the bottom face of the formwork, and a very low fiber concentration was observed in samples taken nearest the top surface of the placement.
    a. Single cell units were placed both upside down and right-side up to quantitatively compare the placement methods by testing beams cut from the ribs. A reduction in modulus of rupture was observed in samples placed upside down compared to samples placed right-side up. A direct correlation was observed between fiber concentration and the modulus of rupture. Modulus of elasticity of UHPC was negatively affected by fiber settling; however, fiber settling showed little to no negative impact on either compressive strength or splitting tensile strength of UHPC.
    b. Fiber settling impacted the failure mode for both compressive strength and tensile strength; a more sudden, brittle failure mode was observed compared to UHPC without fiber settling.
    c. The cause of fiber settling was not identified. Regimented mix procedures had been followed to ensure UHPC was produced consistently. It was suggested that the cause of fiber settling be identified in future work to ensure this placement problem does not negatively impact the potential for UHPC in future designs.

8.2.2 Biaxial Behavior of UHPC

Three different conditions were investigated for the biaxial tension-compression failure of UHPC: untreated with random fiber orientation, steam treated with random fiber orientation, and untreated with controlled fiber orientation. Based on the results, failure models were developed for each scenario, and the effect of both fiber orientation and curing method were identified. The following are conclusions based on the biaxial testing of UHPC:

1. The direct biaxial test (DBT) was shown to be a reasonable method to determine biaxial behavior of UHPC. Biaxial tension-compression failure of UHPC were represented using both a two-degree polynomial and a bi-linear model.

2. The failure models developed for untreated UHPC with random fiber orientation could be used as a conservative model for untreated UHPC with controlled fiber orientation. With more controlled fiber orientation, where fibers are aligned in the direction of tensile stresses, the interaction between tensile and compressive stresses decreased, showing little reduction in compressive strength with the addition of tensile stresses. Due to the sensitivity of UHPC to placement methods, it is likely that most UHPC applications would incorporate specific placement procedures to align fibers along the principal tensile direction.

3. Knowing the direct tensile strength and compressive strength of UHPC, the Mohr-Coulomb model (Dowling 2007) could serve as a more conservative model for UHPC, especially for UHPC products containing random or unknown fiber orientation. This model identifies that the compressive strength is completely dependent on the level of tensile stresses applied. Although it was shown through biaxial testing of untreated UHPC with random fiber orientation that little reduction in compressive strength is experienced when combined with up to 40 percent of the direct tensile stress, the Mohr-Coulomb model would provide a conservative estimate for UHPC in all possible placement scenarios.

4. Steam treating UHPC resulted in an evident increase in compressive strength, and a reduction in the interaction between compressive and tensile stress. However, the tensile capacity of UHPC did not increase to the same degree as the compressive strength due to steam treatment. Therefore, the normalized biaxial failure model showed that steam treatment had a negative effect on the normalized failure tensile stresses. A single bi-linear failure curve was proposed for both untreated and steam treated UHPC with random fiber orientation as previously discussed in Chapter 5, Section 5.5. More data is required to verify the accuracy of the proposed factors used to identify a single failure model for UHPC using these equations.

5. Digital image correlation was shown to be difficult to implement on specimens that move in and out of their original plane. Movement of the specimens led to the DIC methods calculating excessively large strains.

6. The load controlled test method implemented for the direct biaxial test made it difficult to identify post-cracking behavior. Although cracking did occur in some tests prior to ultimate failure and was identified visually through image acquisition, it was not possible to confidently identify a first-cracking point using the presented data. Failure in pure tension (PT) tests was sudden, and no cracking was observed prior to failure of these specimens.

8.2.3 Design and Experimental Tests of UHPC Bridge Deck

A UHPC bridge deck was designed based on known UHPC structural behavior in bending and shear. Preliminary testing took place to investigate three different placement scenarios. Using these results, two single unit bridge deck sections were constructed and experimentally tested on a simple span of 8 ft to evaluate structural behavior. Two tests were performed on each bridge deck section by placing a single point load at a designated distance from the support, 30 in. and 18 in.

1. The stress-strain model identifying a maximum compressive stress of 16 ksi and a maximum tensile stress of 0.5 ksi was shown to be a conservative design model for untreated UHPC. If placement methods will ensure fibers are located in tension regions, the maximum tensile stress could be increased to 1.5 ksi to better represent untreated UHPC achieving full tensile capacity. This model was based on the stress-strain curve identified by Graybeal (2008).

2. All experimental tests of the single unit deck sections resulted in flexure failures. The shear capacity was estimated using only the discrete fiber contribution; however, prestressing was expected to increase the shear capacity of the deck sections.

3. Placement method was shown to influence ultimate moment capacity and deflections. Although all deck sections exceeded the design moment capacity, the ultimate moment capacity of the right-side up placement method resulted in a 20 percent increase over the upside down placement method. Deflections were reduced by approximately 30 percent with the right-side up placement method as compared to the upside down method. Based on preliminary testing using single cells and observations of cylinders, fiber settling was likely a major influence attributing to differences observed between experimental tests of the two placement techniques in this study.

8.3 Recommendations

8.3.1 Recommendations for Material Properties

1. A specified compressive strength, f_c', of 16 ksi should be used for untreated UHPC.

2. The AASHTO Standard T 132-87 (2004) test for tensile strength of hydraulic mortars should be used to determine a direct tensile strength of UHPC.

3. A polynomial or bi-linear failure model, as previously discussed in Chapter 5, should be utilized for analyzing UHPC in biaxial stress states.

4. To account for the possibility of fiber settling in UHPC, the modified stress-strain model using a maximum tensile stress of 0.5 ksi should be used for flexure analysis of UHPC bridge decks. Because the bridge deck would experience both positive and negative bending, this reduced tensile stress would provide a more conservative design for one of the two conditions if fiber settling were to occur.

5. If a flow above 9 in. is measured, precautions should be taken to guarantee no excessive vibration is applied to the mix during placement. If fiber settling is observed, a Ductal® representative should be contacted to discuss methods to reduce flow. Best judgment should be used to determine whether or not to use any high flow mix in practice.

8.3.2 Recommendations for Future Biaxial Testing

1. Platen restraint should be reduced in the compression region. In this study, the use of Teflon-coated tape was used to reduce platen restraint. In some cases, the failure appeared to show some signs of platen restraint. To further reduce platen restraint, additional cost-effective methods should be investigated.

2. Out-of-plane movement negatively affected digital image correlation analysis. To reduce the amount of out-of-plane movement of the biaxial "dog bone," it would be beneficial to align tension vertically upright. This would allow gravity to initially align the specimen in the tension direction. To accomplish this in the Thomas M. Murray Structural Engineering Laboratory, a connection should be made directly to the strong floor, and the tension actuator should be located directly above this connection.

3. Notches should be cut at the center section to prevent premature failures at the grips when more than 60 percent of the ultimate tensile capacity is applied to a specimen. When a very high compressive strength is achieved in a mix, notches should be used

when more than 50 percent of the ultimate tensile capacity is applied. Tensile strength does not increase to the same degree as compressive strength in UHPC, as evident by the steam treated data set. In this study, notches were only cut into the two sides where compression was applied; however, it could be useful to investigate using notches on all sides to further reduce the center cross sectional area.

4. In order to better identify the post-cracking behavior of UHPC in biaxial tension-compression stress states, a displacement controlled test regime should be developed for the direct biaxial test. It was difficult to capture post-cracking behavior using the load-controlled test regime in this study. However, post-cracking behavior was identified using the displacement controlled method for tensile strength using briquets (AASHTO Standard T 132-87 2004).

8.3.3 Recommendations for UHPC Bridge Deck Design

1. UHPC waffle slab bridge decks should be designed for bending moment capacity using an iterative design approach, using a single T-beam strip in the transverse direction, and neglecting the contribution of longitudinal ribs.
    a. For untreated UHPC, the stress-strain relationship identified by Graybeal (2008) for flexure analysis should be modified to account for the reduced compressive strength. The maximum compressive stress should be limited to 16 ksi. If fiber settling is expected to negatively impact the tensile region, the maximum tensile stress should be limited to 0.5 ksi for a conservative analysis. The maximum tensile stress could be limited to 0.5 ksi for all analyses for the most conservative prediction.
    b. To predict flexural cracking, a modulus of rupture, f_r, of 3 ksi should be used if fiber settling is not expected to be a problem. A value of 0.5 ksi should be used as the modulus of rupture if fiber settling is suspected or considered a potential placement problem.

2. The full equivalent strip width as defined by AASHTO (2012) guidelines should be used to analyze limiting deflections of the UHPC bridge deck.

3. Shear analysis of prestressed UHPC bridge decks can be accomplished by considering only the contribution of discrete fiber reinforcement, as previously discussed in Section 2.4.3

8.4 Future Research

1. Additional testing should be completed for UHPC in biaxial tension-compression stress states to identify limiting strains and to better identify the effect of high tensile stresses on compressive strength. The interaction of compressive strength with tensile stresses was difficult to obtain in the present study due to high stress concentrations at the gripping locations and possibly tensile creep effects at high tensile stresses.

2. A displacement controlled test method should be developed for the direct biaxial test to investigate post-cracking behavior of UHPC in biaxial stress states. Using pure tension tests, UHPC is known to exhibit significant post-cracking tensile strength.

3. Additional testing should be performed to identify the effects of connecting UHPC fronts due to intersecting horizontal flow paths. Single cell tests in this study showed a decrease in modulus of rupture; however, the degree of reduction did not indicate a significant problem due to intersecting horizontal flow paths. Because only one data point was available in this study, additional testing is necessary to confirm the presented hypothesis that intersecting flow paths do not significantly affect the performance of UHPC in bending. Additional testing could also include the direct biaxial test to identify how intersecting flow paths affect combined stress states.

4. The cause of fiber settling should be identified, and mitigation techniques should be investigated for this potential placement problem. Methods to reduce flow should be investigated, potentially including: reducing high-range water reducer, increasing dry material content, adding an accelerating admixture, and altering mix procedures.

5. The effects of fiber settling should be investigated beyond the results presented in this study. Although this placement problem should be avoided in practice, it would be advantageous to understand both the mechanism of how fiber settling occurs and potential risks associated with fiber settling.

6. Experimental testing should be completed on full-scale UHPC bridge deck panels to confirm the proposed design method. Both static and fatigue testing should be performed on the panels and connections.
    a. The equivalent strip method should be evaluated in these tests for predicting deflections, and the interaction of the connecting longitudinal ribs should be investigated.
    b. The designed shear connection using a basic cementitious grout should be experimentally tested. Push-off tests simulating the connection could be used in conjunction with the full-scale panel tests. Push-off tests could be performed under both static and fatigue conditions.

7. Panel-to-panel connections should be designed and experimentally tested. It is suggested that a hybrid bolted and UHPC-filled connection be investigated to improve construction efficiency. This connection would reduce the amount of joint fill material required on site.

References

Aaleti, S., Sritharan, S., Rouse, M., and Wipf, T. (2010). "Structural Characterization of UHPC Waffle Bridge Deck Panels and Connections." Iowa Department of Transportation, Iowa Research Board, 54.

AASHTO Standard T 132-87 (2004). "Tensile Strength of Hydraulic Cement Mortars." American Association of State Highway and Transportation Officials, Washington, D.C., 8.

AASHTO (2008). "Bridging the Gap: Restoring and Rebuilding the Nation's Bridges." American Association of State Highway and Transportation Officials, Washington, D.C., July 2008, ftp://ftp.mdt.mt.gov/research/LIBRARY/BTG-1-BRIDGING-GAP-AASHTO.PDF, (August 2013).

AASHTO (2012). "AASHTO LERD Bridge Design Specifications, 6th Edition, with 2013 Interim Revisions." American Association of State Highway and Transportation Officials, ed., Washington, D.C.

ACI Committee 318 (2011). "Building Code Requirements for Structural Concrete (ACI 318-11) and Commentary." American Concrete Institute, Farmington Hills, MI.

ACI Committee 363 (1992). "State-of-the-Art Report on High Strength Concrete." ACI 363R-92, American Concrete Institute.

Association Française de Génie Civil (AFGC) and Service d'études techniques des routes et autoroute (Setra) (2002). *Ultra High Performance Fibre-Reinforced Concretes: Interim Recommendations*. Service d'études techniques des routes et autoroutes (Setra) and Association Française de Génie Civil (AFGC), Paris, France, 152.

ASTM Standard A370 (2006). "Standard Test Methods and Definitions for Mechanical Testing of Steel Products." ASTM International, West Conshohocken, PA, 2006, DOI: 10.1520/A0370-06, www.astm.org.

ASTM Standard C109 (2005). "Standard Test Method for Compressive Strength of Hydraulic Cement Mortars (Using 2-in. or [50-mm] Cube Specimens)." ASTM International, West Conshohocken, PA, 2005, DOI: 10.1520/C0109_C0109M-05, www.astm.org.

ASTM Standard C136 (2006). "Standard Test Method for Sieve Analysis of Fine and Coarse Aggregates." ASTM International, West Conshohocken, PA, 2006, DOI: 10.1520/C0136-06, www.astm.org.

ASTM Standard C157 (2006). "Standard Test Method for Length Change of Hardened Hydraulic-Cement Mortar and Concrete." ASTM International, West Conshohocken, PA, 2006, DOI: 10.1520/C0157_C0157M-06, www.astm.org.

ASTM Standard C469 (2002). "Standard Test Method for Static Modulus of Elasticity and Poisson's Ratio of Concrete in Compression." ASTM International, West Conshohocken, PA, 2002, DOI: 10.1520/C0469-02, www.astm.org.

ASTM Standard C490 (2004). "Standard Practice for Use of Apparatus for the Determination of Length Change of Hardened Cement Paste, Mortar, and Concrete." ASTM International, West Conshohocken, PA, 2004, DOI: 10.1520/C0490-04, www.astm.org.

ASTM Standard C496 (2004). "Standard Test Method for Splitting Tensile Strength of Cylindrical Concrete Specimens." ASTM International, West Conshohocken, PA, 2004, DOI: 10.1520/C0496_C0496M-04, www.astm.org.

ASTM Standard C1018 (1997). "Standard Test Method for Flexural Toughness and First-Crack Strength of Fiber-Reinforced Concrete (Using Beam With Third-Point Loading)." ASTM International, West Conshohocken, PA, 1997, DOI: 10.1520/C1018-97, www.astm.org.

ASTM Standard C1437 (2001). "Standard Test Method for Flow of Hydraulic Cement Mortar." ASTM International, West Conshohocken, PA, 2001, DOI: 10.1520/C1437-01, www.astm.org.

ASTM Standard C1609 (2006). "Standard Test Method for Flexural Performance of Fiber-Reinforced Concrete (Using Beam With Third-Point Loading)." ASTM International, West Conshohocken, PA, 2006, DOI: 10.1520/C1609_C1609M-06, www.astm.org.

ASTM Standard E8 (2004). "Standard Test Methods for Tension Testing of Metallic Materials." ASTM International, West Conshohocken, PA, 2004, DOI: 10.1520/E0008-04, www.astm.org.

Barnett, S. J., Lataste, J.-F., Parry, T., Millard, S. G., and Soutsos, M. N. (2010). "Assessment of fibre orientation in ultra high performance fibre reinforced concrete and its effect on flexural strength." *Materials and Structures*, 43(7), 1009-1023.

Belarbi, A. and Hsu, T. T. C. (1995). "Constitutive Laws of Softened Concrete in Biaxial Tension-Compression." *ACI Structural Journal*, 92(5), 562-573.

Bierwagen, D., and Abu-Hawash, A. (2005). "Ultra High Performance Concrete Highway Bridge." *Mid-Continent Transportation Research Symposium*, Ames, Iowa, August 18-19, 14.

Bischoff, P. H. (2003). "Tension stiffening and cracking of steel fiber-reinforced concrete." *Journal of Materials in Civil Engineering*, 15(2), 174-182.

Blais, P. Y., and Couture, M. (1999). "Precast, prestressed pedestrian bridge - world's first Reactive Powder Concrete structure." *PCI Journal*, 44(5), 60-71.

Branson, D. E. (1965). "Instantaneous and Time-Dependent Deflections on Simple and Continuous Reinforced Concrete Beams." *HPR Report* No. 7, Part 1, Alabama Highway Department, Bureau of Public Records, August 1965, 1-78.

Brouwer, G. (2001). "Bridge to the Future." *Civil Engineering*, 71(11), 50-55.

Chanvillard, G. and Rigaud, S. (2003). "Complete Charterisation of Tensile Properties of Ductal UHPFRC According to the French Recommendations." *Fourth International RILEM Workshop: High Performance Fiber Reinforced Cement Composites (HPFRCC4)*, Ann Arbor, USA, 21-34.

Chen, W. F. (1982). *Plasticity in Reinforced Concrete*, McGraw-Hill, Inc., ed., New York.

Choi, S., and Shah, S. (1997). "Measurement of Deformations on Concrete Subjected to Compression Using Image Correlation." *Experimental Mechanics*, 37(3), 307-313.

Chuan-zhi, W., Zhen-hai, G., and Xiu-qin, Z. (1987). "Experimental Investigation of Biaxial and Triaxial Compressive Concrete Strength." *ACI Materials Journal*, 84(2), 92-100.

Correlated Solutions (2009). "Correlated Solutions: Non-Contacting Measuring Solutions." Correlated Solutions, Inc., www.correlatedsolutions.com, (August 2009).

Cwirzen, A. (2007). "The effect of the heat-treatment regime on the properties of reactive powder concrete." *Advances in Cement Research*, 19(1), 25-33.

Dallaire, E., Aitcin, P., and Lachemi, M. (1998). "High-Performance Powder." *Civil Engineering*, 68(1), 48-51.

Demeke, A., and Tegos, I. A. (1994). "Steel fiber reinforced concrete in biaxial stress tension-compression conditions." *ACI Materials Journal*, 91(5), 579-584.

Dowling, N. E. (2007). *Mechanical Behavior of Materials: Engineering Methods for Deformation, Fracture, and Fatigue, Third Edition,* Pearson Prentice Hall, Upper Saddle River, NJ.

Eberl, C. (2010). "Digital Image Correlation and Tracking." http://www.mathworks.com/matlabcentral/fileexchange/12413-digital-image-correlation-and-tracking, (March 2011).

Fehling, E., Bunje, K., and Schmidt, M. (2009). "Gärtnerplatz - Bridge over River Fulda in Kassel - Multispan Hybrid UHPC - Steel Bridge -." *UHPFRC 2009*, Marseille, France, November 17-18.

Fehling, E., Roder, F., Leutbecher, T., and Sturwald, S. (2008). "Structural behavior of UHPC under biaxial loading." *Second International Symposium on Ultra High Performance Concrete*, Kassel, Germany, March 5-7, 569-576.

Garcia, H. M. (2007). "Analysis of an Ultra-High Performance Concrete Two-Way Ribbed Bridge Deck Slab." Report No. *FHWA-HRT-07-056*, Federal Highway Administration, United States, August 2007, 61.

Gerstle, K. H. (1981). “Simple Formulation of Biaxial Concrete Behavior.” *ACI Journal*, 78(1), 62-68.

Gowripalan, N., and Gilbert, R. I. (2000). *Design Guidelines for RPC Prestressed Concrete Beams*. The University of New South Wales, ed., VSL (Aust) Pty. Ltd., Sydney, Australia.

Graybeal, B., and Tanesi, J. (2007a). "Durability of Ultrahigh-Performance Concrete." *Journal of Materials in Civil Engineering*, 19(10), 848-854.

Graybeal, B. A. (2004). “Fabrication of an Optimized UHPC Bridge.” *PCI National Bridge Conference (CD Proceedings)*, Atlanta, GA, USA, October 17-20.

Graybeal, B. A. (2006a). "Material Property Characterization of Ultra-High Performance Concrete." Report No. *FHWA-HRT-06-103*, Federal Highway Administration, United States, August 2006, 186.

Graybeal, B. A. (2006b). "Structural Behavior of Ultra-High Performance Concrete Prestressed I-Girders." Report No. *FHWA-HRT-06-115*, Federal Highway Administration, United States, August 2006, 104.

Graybeal, B. A. (2007b). "Compressive behavior of ultra-high-performance fiber-reinforced concrete." *ACI Materials Journal*, 104(2), 146-152.

Graybeal, B. A. (2008). "Flexural Behavior of an Ultrahigh-Performance Concrete I-Girder." *Journal of Bridge Engineering*, 13(6), 602-610.

Graybeal, B. A. (2009a). "Structural Behavior of a 2nd Generation Ultra-High Performance Concrete Pi-Girder." Report No. *FHWA-HRT-10-026*, Federal Highway Administration, United States, November 2009, 114.

Graybeal, B. A. (2009b). "Structural Behavior of a Prototype Ultra-High Performance Concrete Pi-Girder." Report No. *FHWA-HRT-10-027*, Federal Highway Administration, United States, November 2009, 146.

Graybeal, B. A. (2009c). "UHPC Making Strides." Roads and Bridges, U.S. Department of Transportation - Federal Highway Administration, 72(4), www.fhwa.dot.gov/publications/publicroads/09janfeb/03.cfm, (August 2013).

Grunberg, J., Ertel, C., Lohaus, L., Wefer, M., Curbach, M., Speck, K., Niedermeier, R., and Fitik, B. (2010). “Failure models for ultra high performance concrete (UHPC).” *Proceedings of Third fib International Congress incorporating the PCI Annual Convention and Bridge Conference*, May 29 – June 2, Washington, D.C., United States.

Hale, W. M., and Tackett, A. M. (2010). "Examining the Effects of Mixer Type and Temperature on the Properties of Ultra-High Performance Concrete." Arkansas Univ., Fayetteville. Mack-Blackwell Transportation Center, United States, 97.

Harris, D. K. (2004). “Characterization of Punching Shear Capacity of Thin UHPC Plates.” M.S. thesis, Virginia Polytechnic Institute and State University, Blacksburg, VA.

Harryson, P. (2003). "High Performance Joints for Concrete Bridge Applications." *Structural Engineering International*, 13(1), 69-75.

Heimann, J., and Schuler, G. (2010). "The Implementation of Full Depth UHPC Waffle Bridge Deck Panels, Phase 1 Report." Federal Highway Administration, 13.

Helm, J. D. (2008). “Digital Image Correlation for Specimens with Multiple Growing Cracks.” *Experimental Mechanics*, 48(6), 753-762.

Hussein, A. and Marzouk, H. (2000). “Behavior of High-Strength Concrete under Biaxial Stresses.” *ACI Materials Journal*, 97(1), 27-36.

Japan Society of Civil Engineers (2004). "Recommendations for Design and Construction of Ultra High Strength Fiber Reinforced Concrete Structures (Draft)." J. Niwa, ed., Subcommittee on Research of Ultra High Strength Fiber Reinforced Concrete, Tokyo.

Jensen, B. C. (1999). "Applications of Steel-Fibre-Reinforced Ultra-High-Strength Concrete." *Structural Engineering International*, 9(2), 143-146.

John, E. E., Ruiz, E. D., Floyd, R. W., and Hale, W. M. (2011). “Transfer and Development Lengths and Prestress Losses in Ultra-High-Performance Concrete Beams.” *Journal of the Transportation Research Board*, No. 2251, Washington, D.C., 76-81.

Keierleber, B., Bierwagen, D., Wipf, T., and Abu-Hawash, A. . (2010). "FHWA, Iowa Optimize Pi Girder." *ASPIRE*, Precast/Prestressed Concrete Institute, Chicago, IL, 24-26.

Khayat, K. H., and Roussel, Y. (2000). "Testing and performance of fiber-reinforced, self-consolidating concrete." *Materials and Structures*, 33(6), 391-397.

Kosmatka, S. H., Kerkhoff, B., and Panarese, W.C. (2002). *Design and Control of Concrete Mixtures*, Portland Cement Association, Skokie, IL.

Küntz, M., Jolin, M., Bastien, J., Perez, F., and Hild, F. (2006). "Digital image correlation analysis of crack behavior in a reinforced concrete beam during a load test." *Canadian Journal of Civil Engineering*, 33, 1418-1425.

Kupfer, H., Hilsdorf, H. K., and Rusch, H. (1969). "Behavior of Concrete Under Biaxial Stresses." *ACI Journal Proceedings*, 66(8), 656-666.

Lafarge (2013). "Ductal." www.ductal-lafarge.com, (August 2013).

Lecompte, D., Vantomme, J., and Sol, H. (2006). "Crack Detection in a Concrete Beam using Two Different Camera Techniques." *Structural Health Monitoring*, 5(1), 59-68.

Li, V. C. (2003). "On Engineered Cementitious Composites (ECC): A Review of the Material and its Applications." *Advanced Concrete Technology*, 1(3), 215-230.

Linder, W. (2009). *Digital Photogrammetry: A Practical Course*. Springer Berlin Heidelberg, Berlin.

Liu, T. C. Y., Nilson, A. H., and Slate, F. O. (1972). "Stress-Strain Response and Fracture of Concrete in Uniaxial and Biaxial Compression." *ACI Journal Proceedings*, 69(5), 291-295.

Lü, P., Li, Q., and Song, Y. (2007). "Behavior of Concrete Under Nonproportional Biaxial Fatigue Stresses with One Constant." *ACI Materials Journal*, 104(1), 3-12.

Lubbers, A. (2003). "Bond Performance Between Ultra-High Performance Concrete and Prestressing Strands." MS thesis, Ohio University, Athens, OH.

Ma, J., Dehn, F., Tue, N. V., Orgass, M., and Schmidt, D. (2004). "Comparative Investigations on Ultra-High Performance Concrete with and without Coarse Aggregates." *Proceedings of the International Symposium on Ultra-High Performance Concrete,* Kassel, Germany, September 13-15, 205-212.

Magureanu, C., Sosa, I., Negrutiu, C., and Heghes, B. (2010). "Bending and shear behavior of ultra-high performance fiber reinforced concrete." *5th International Conference on High Performance Structures and Materials, HPM 2010*, Tallinn, Estonia, July 28-30, 79-89.

Mindess, S., Young, F., and Darwin, D. (2003). *Concrete: Second Ed.* Prentice Hall, Upper Saddle River, NJ.

Nachuk, K. (2008). "Technical Representative, Ductal." Personal interview, December 4, 2008.

Nielsen, C. V. (1995). "Ultra High-Strength Steel Fibre Reinforced Concrete, Part I and Part II." Reports Nos. 323 and 324, Department of Structural Engineering, Technical University of Denmark.

Nishikawa, K., and Morita, T. (2006). "The First Highway Bridge Applying Ultra High Strength Fiber Reinforced Concrete in Japan." *7th International Conference on Short and Medium Span Bridges*, Montreal, Quebec, Canada, August 23-25, AM-012-1 - AM-012-9.

Ottosen, N. S. (1977). "A Failure Criterion for Concrete." *ASCE Journal of the Engineering Mechanics Division*, 103(4), 527-535.

Pauw, A. (1960). "Static Modulus of Elasticity of Concrete as Affected by Density." *ACI Journal Proceedings*, 57(12), 679-687.

Perry, V. (2005). "The Use of UHPC for Precast Bridge Decks: The Technology, Applications and Challenges Facing Commercialization." *National Bridge Conference*, Palm Springs, CA, October 16-19, 13.

Perry, V., and Weiss, G. (2009) "Innovative Field Cast UHPC Joints for Precast Bridge Decks - Design, Prototype Testing and Projects." *UHPFRC 2009*, Marseille, France, November 17-18.

Richard, P., and Cheyrezy, M. (1995). "Composition of Reactive Powder Concretes." *Cement and Concrete Research*, 25(7), 1501-1511.

Richardson, I. G. (1999). "The nature of C-S-H in hardened cements." *Cement and Concrete Research*, 29(8), 1131-1147.

Robins, P., Austin, S., Chandler, J., and Jones, P. (2001). "Flexural strain and crack width measurement of steel-fibre-reinforced concrete by optical grid and electrical gauge methods." *Cement and Concrete Research*, 31(5), 719-729.

Rosenthal, I. and Glucklich, J. (1970). "Strength of Plain Concrete Under Biaxial Stress." *ACI Journal Proceedings*, 67(11), 903-914.

Roux, N., Andrade, C., and Sanjuan, M. A. (1996). "Experimental study of durability of reactive powder concretes." *Journal of Materials in Civil Engineering*, 8(1), 1-6.

Russell, B. W. and Burns, N. H. (1993). *Design Guidelines for Transfer, Development and Debonding of Large Diameter Seven Wire Strands in Pretensioned Concrete Girders.* Report 1210-5F, Center for Transportation Research, University of Texas at Austin, Austin TX, 464.

Saleem, M. A., Mirmiran, A., Xia, J., and Mackie, K. (2011). "Ultra-High-Performance Concrete Bridge Deck Reinforced with High-Strength Steel." *ACI Structural Journal*, 105(5), 601-609.

Shaheen, E., and Shrive, N. G. (2007). "Cyclic loading and fracture mechanics of Ductal concrete." *International Journal of Fracture*, 148(3), 251-60.

Shim, C., Choi, K., and Chang, S. (2001). "Design of Transverse Joints in Composite Bridges with Precast Decks." *KSCE Journal of Civil Engineering*, 5(1), 17-27.

Sorelli, L. G., Fanning, P.,and Toutlemonde, F. (2006). "Innovative Bridge System of Ultra High Performance Fibre Reinforced Cocnrete: Experiments, Modeling and Design." *7th International Conference on Short and Medium Span Bridges*, Montreal, Quebec, Canada, August 23-25, AM-026-1 - AM-026-10.

Sorelli, L. G., Ulm, F. J., and Toutlemonde, F. (2007). "Fracture Stability and Micromechanics of Strain Hardening Cementitious Composites." *6th International Conference on Fracture Mechanics of Concrete and Concrete Structures*, Taylor and Francis/Balkema, Catania, Italy, 1403-1411.

Steinberg, E. (2010). "Structural Reliability of Prestressed UHPC Flexure Models for Bridge Girders." *Journal of Bridge Engineering*, 15(1), 65-72.

Su, E. C. M. and Hsu, T. T. C. (1988). “Biaxial Compression Fatigue and Discontinuity of Concrete.” *ACI Materials Journal*, 85(3), 178-188.

Sutton, M. A. (2008). "Digital Image Correlation for Shape and Deformation Measurements." *Springer Handbook of Experimental Solid Mechanics*, W. N. Sharpe, Jr., ed., Springer US, 565-600.

Sutton, M. A., Schreier, H. W., and Orteu, J. J. (2009). *Image correlation for shape, motion and deformation measurements Basic concepts, theory and applications*. Springer, New York.

Tao, X. and Phillips, D. V. (2005). “A simplified isotropic damage model for concrete under bi-axial stress states.” *Cement and Concrete Composites*, 27(6), 716-726.

Tasuji, M. E., Slate, F. O., and Nilson, A. H. (1978). “Stress-Strain Response and Fracture of Concrete in Biaxial Loading.” *ACI Journal Proceedings*, 75(7), 306-312.

Thompson, R. J. (2007). "HighCorr High Temperature Digital Image Correlation Software for Matlab: A User's Guide." Johns Hopkins University, MathWorks MATLAB Central. http://www.mathworks.com/matlabcentral/fx_files/14850/1/content/HighCorr%20guide%20files/RJT_HighCorr_guide.htm, (January 2009).

Toutlemonde, F., Lauvin, L., Behloul, M., Resplendino, J., Renaud, J., Simon, A., and Bouteille, S. (2008). "Experimental validation of a ribbed UHPFRC bridge deck." *Second International Symposium on Ultra High Performance Concrete*, Kassel, Germany, March 5-8, 771-778.

Toutlemonde, F., Lauvin, L., Renaud, J., Kretz, T., and Brisard, S. (2007). "Fatigue Performance of an UHPFRC Ribbed Slab Applied as a Road Bridge Deck Verified According to the Eurocodes." *5th International Conference on Concrete Under Severe Conditions: Environment and Loading*, Tours, France, June 4-6, 1191-1200.

Toutlemonde, F., Resplendino, J., Sorelli, L., Bouteille, S., and Brisard, S. (2005). "Innovative Design of Ultra High-Performance Fiber Reinforced Concrete Ribbed Slab: Experimental Validation and Preliminary Detailed Analysis." *ACI Special Publication*, 228(76), 1187-1206.

Transportation Research Board. (2003). "NCHRP Synthesis 324: Prefabricated Bridge Elements and Systems to Limit Traffic Disruption During Construction." National Cooperative Highway Research Program, Washinton, D.C., http://onlinepubs.trb.org/onlinepubs/nchrp/nchrp_syn_324.pdf.

Transportation Research Board. (2007). "NCHRP Report 584: Full-Depth Precast Concrete Bridge Deck Panel Systems." National Cooperative Highway Research Program, Washington, D.C., http://onlinepubs.trb.org/onlinepubs/nchrp/nchrp_rpt_584.pdf.

VDOT (2007). *Roads and Bridges Specifications.* Virginia Department of Transportation, Richmond, VA.

Voo, Y. L., Poon, W. K., and Foster, S. J. (2010). "Shear Strenght of Steel Fiber-Reinforced Ultrahigh-Performance Concrete Beams without Stirrups." *Journal of Structural Engineering*, 136(11), 1393-1400.

Whiteman, T., Lichti, D.D., and Chandler, I. (2002). "Measurement of Deflections in Concrete Beams by Close-Range Digital Photogrammetry." *ISPRS Commission IV, Symposium 2002: Geospatial Theory, Processing and Applications*, Ottowa, Canada, July 9-12.

Yang, I. H., Joh, C., and Kim, B. S. (2010). "Structural behavior of ultra high performance concrete beams subjected to bending." *Engineering Structures*, 32(11), 3478-3487.

Yin, W. S., Su, E. C. M., Mansur, M. A., and Hsu, T. T. C. (1989). "Biaxial Tests of Plain and Fiber Concrete." *ACI Materials Journal*, 86(3), 236-243.

Zanni, H., Cheyrezy, M., Maret, V., Philippot, S., and Nieto, P. (1996). "Investigation of hydration and pozzolanic reaction in Reactive Powder Concrete (RPC) using 29Si NMR." *Cement and Concrete Research*, 26(1), 93-100.

Zhang, D., Luo, M., and Arola, D.D. (2006). "Displacement/strain measurements using an optical microscope and digital image correlation." *Optical Engineering*, 45(3), 9.

Appendix A: Drawings for Designed Test Fixtures

All dimensions in this section are in inches, unless otherwise noted.

Bending Biaxial Test Frame:

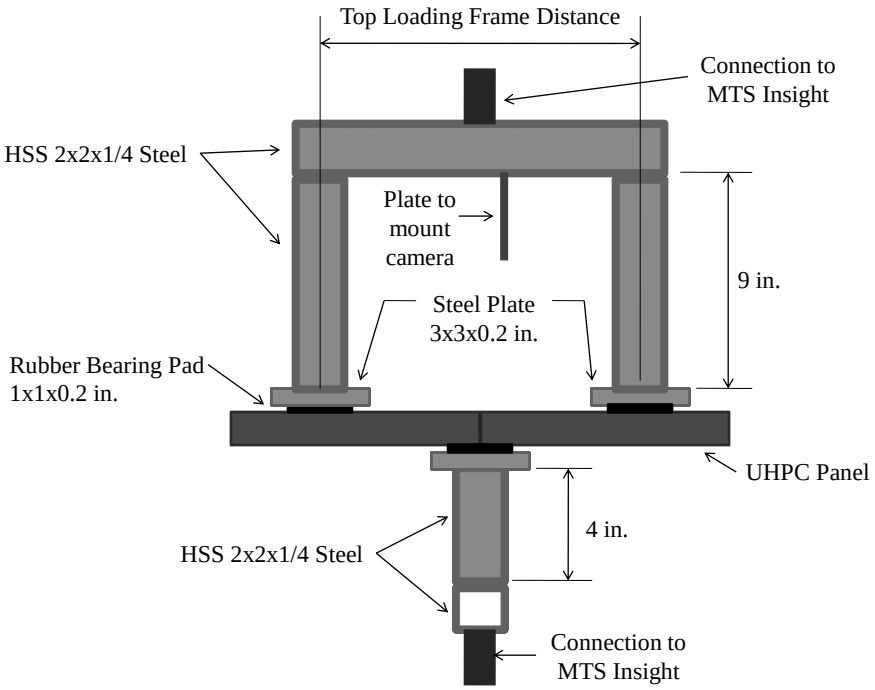

Figure A-1: Top test frame for bending biaxial test.

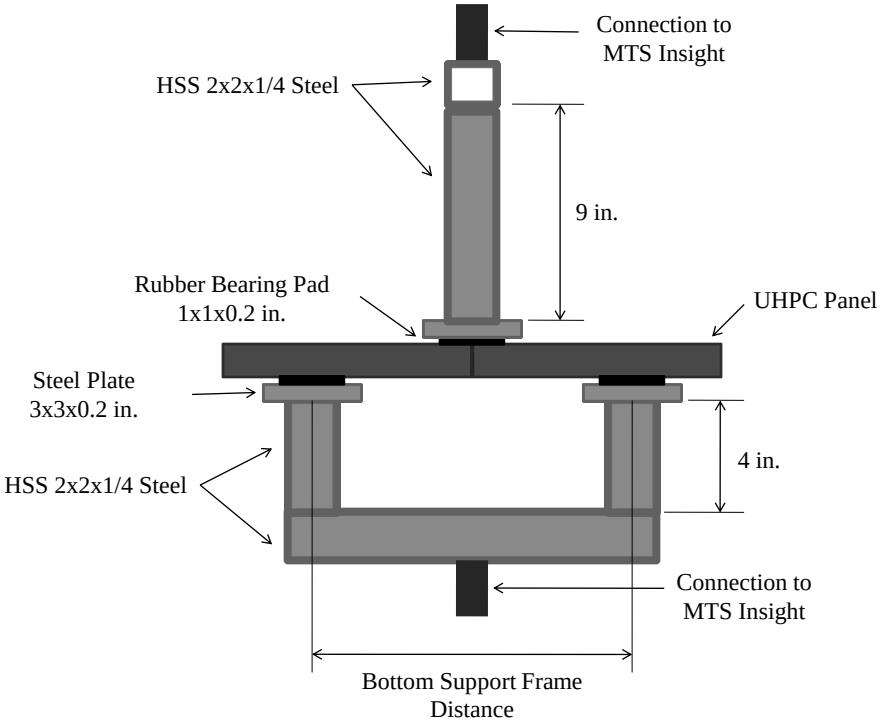

Figure A-2: Bottom test frame for bending biaxial test.

Direct Biaxial Test (DBT) Manufactured Fixtures:

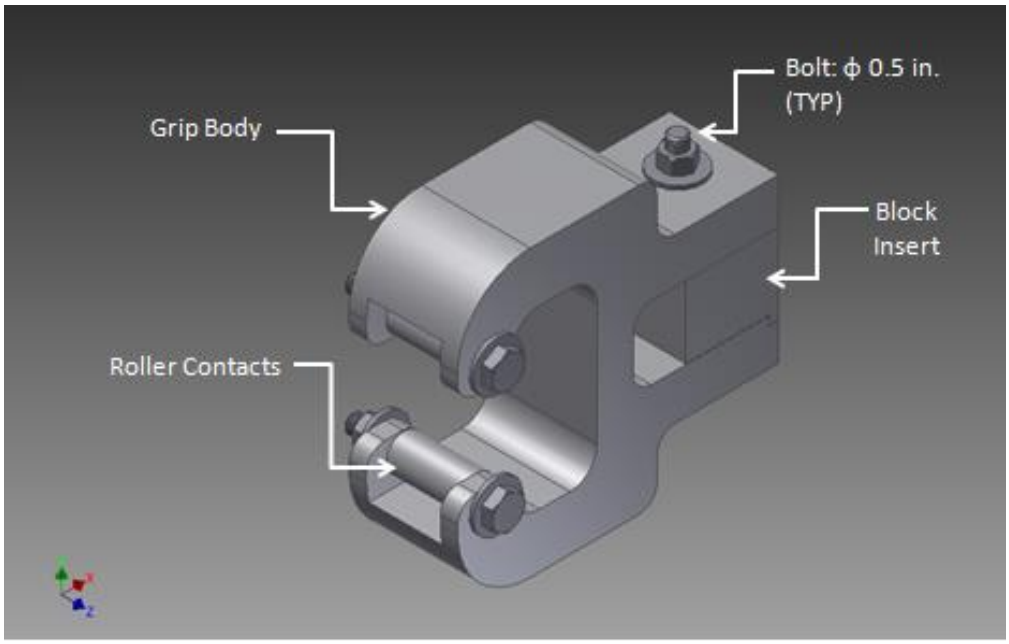

Figure A-3: Fully assembled tension grip for direct biaxial test (DBT).

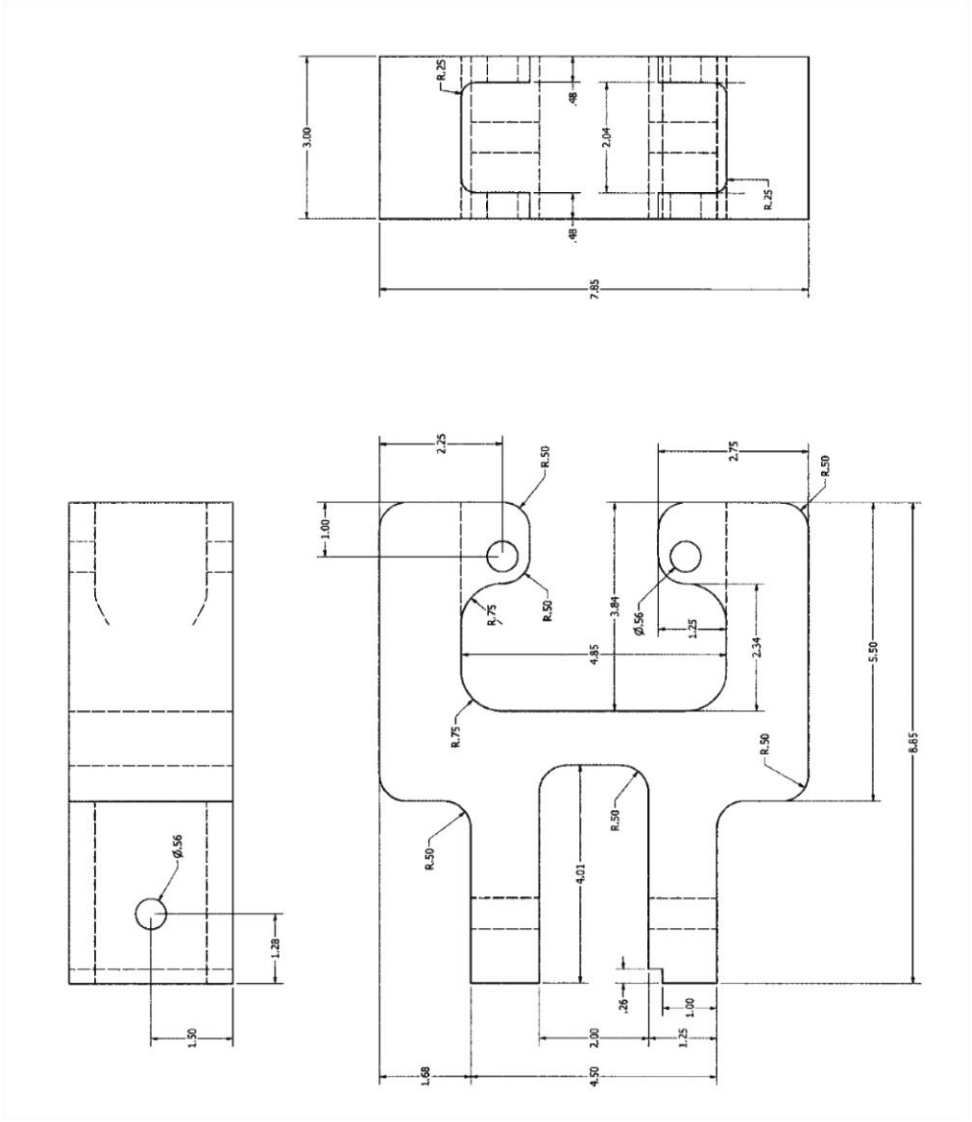

Figure A-4: Direct biaxial test (DBT) grip body.

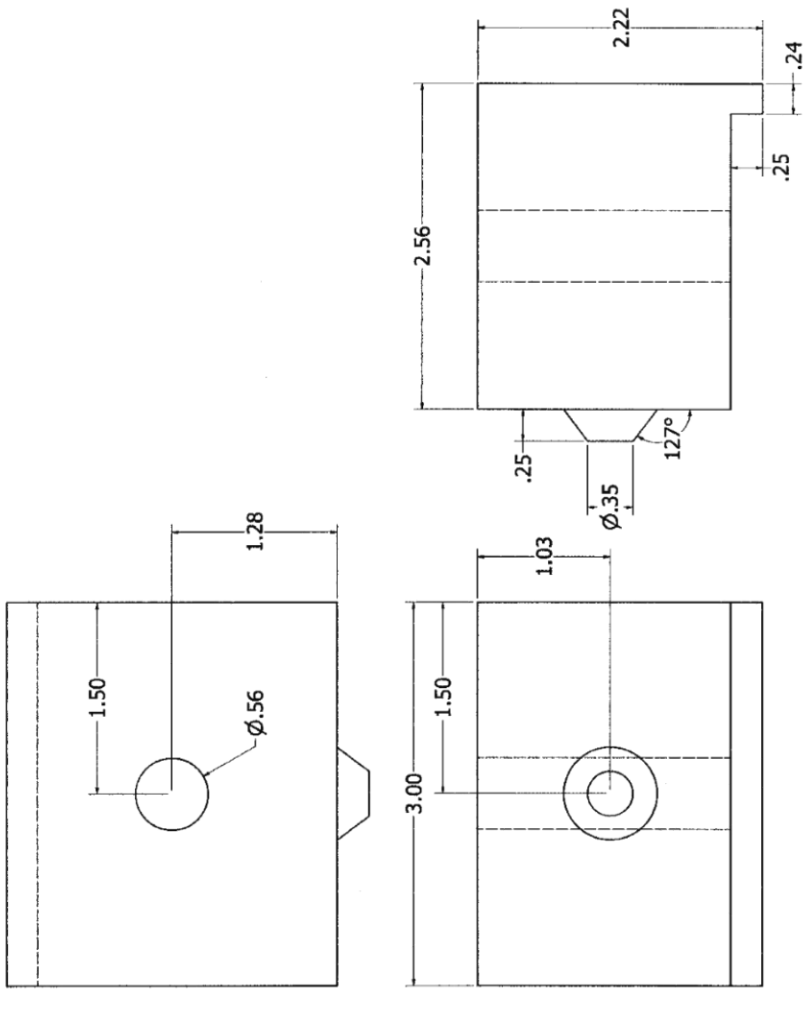

Figure A-5: DBT block insert for grips.

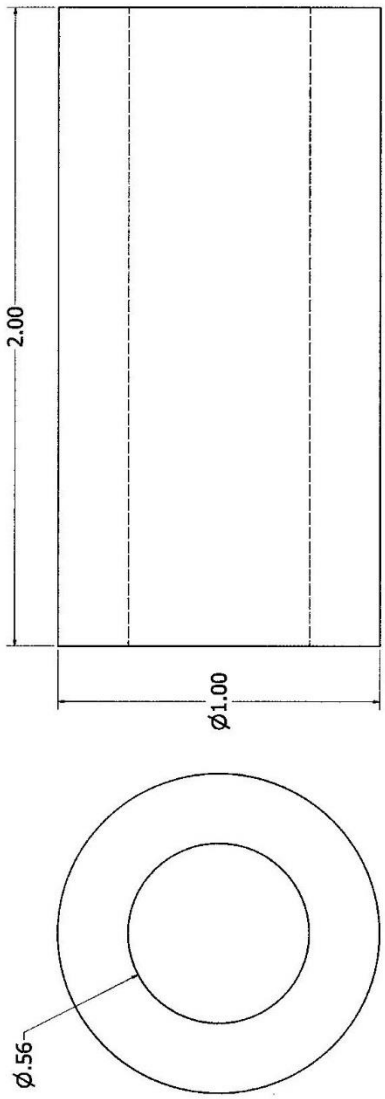

Figure A-6: DBT roller support for grips.

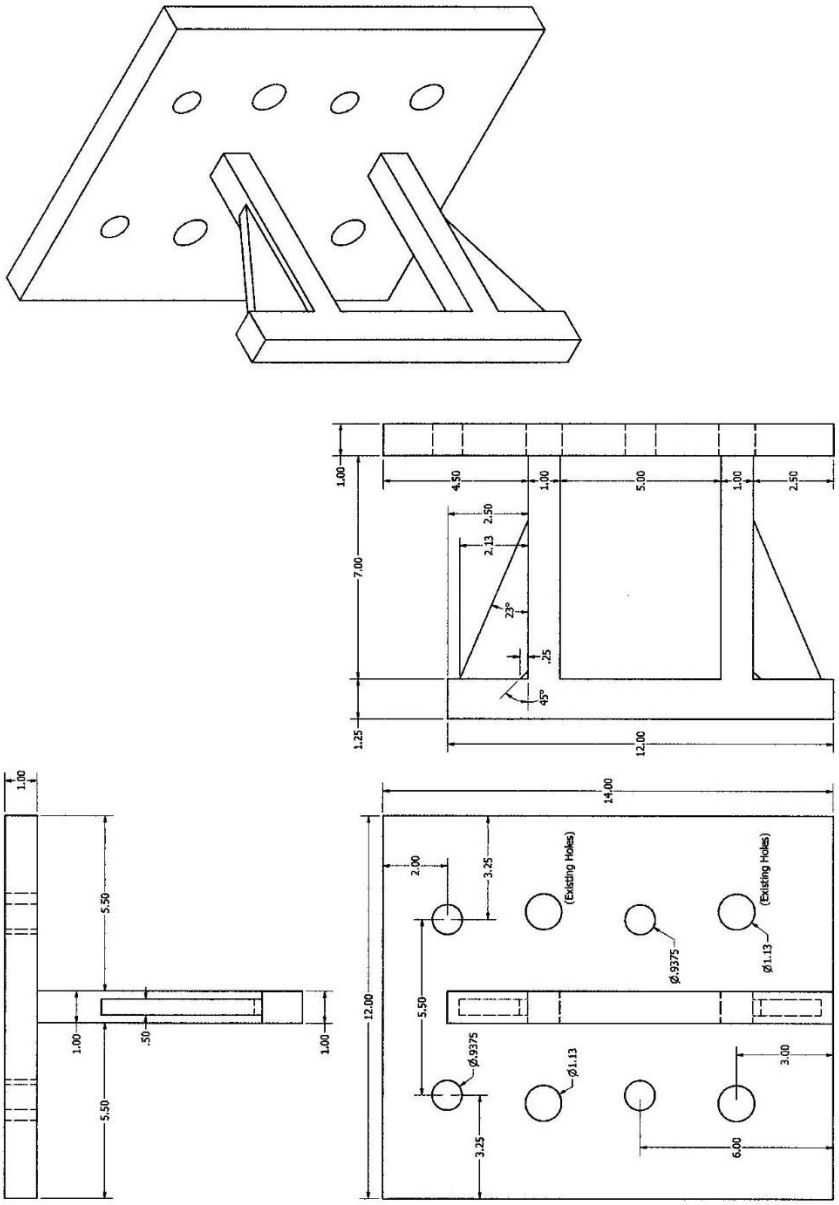

Figure A-7: Connection plate system to connect DBT grip to column support.

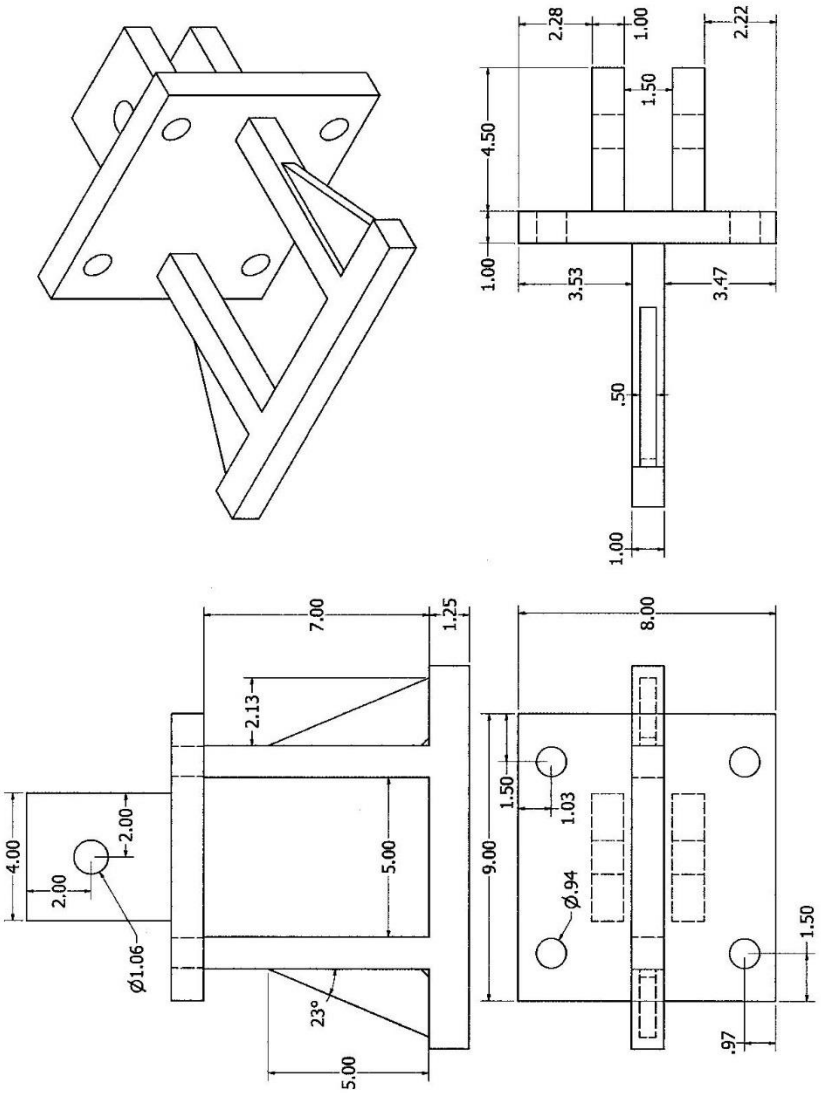

Figure A-8: Connection plate system to connect DBT grip to tension load cell and hydraulic cylinder.

Deck Section Drawings:

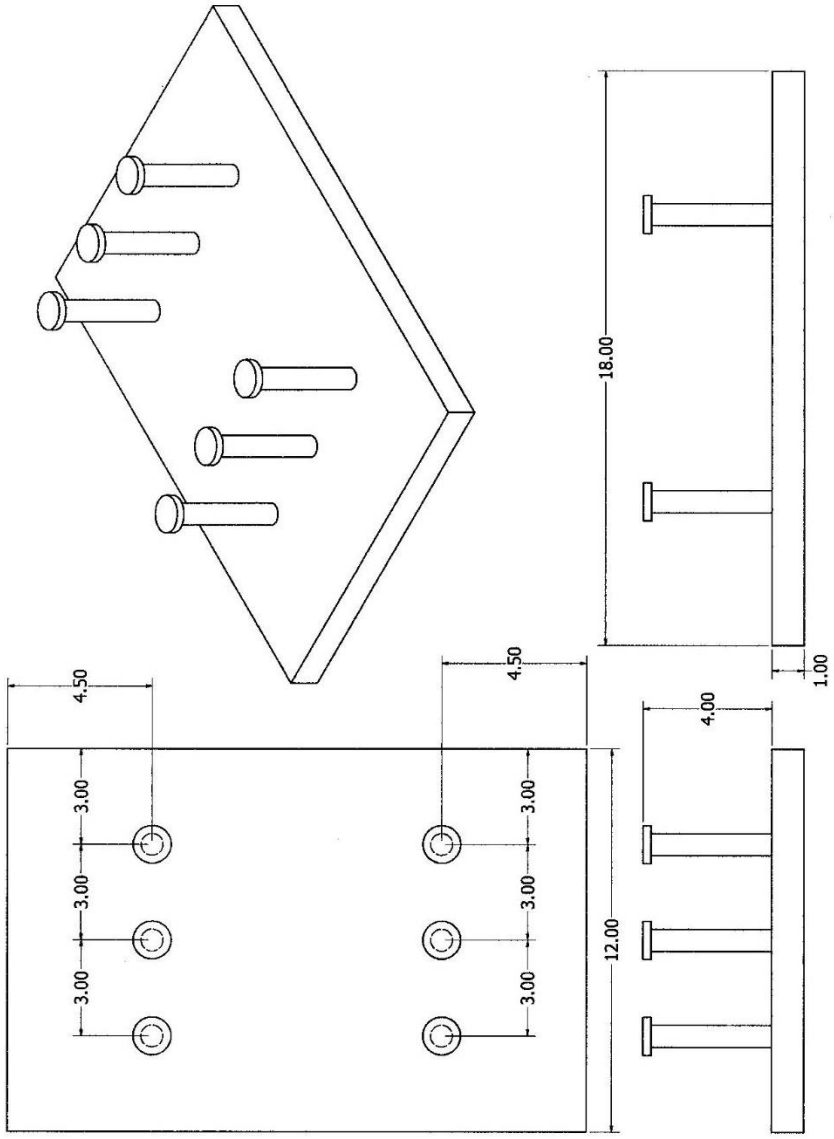

Figure A-9: Shear stud detail for deck section shear connection.

Appendix B: Bridge Deck Design Examples

Design Iteration 1:

UHPC Material Model:

Use the Graybeal (2008) stress-strain curve for UHPC with modifications to maximum compressive stress for untreated UHPC.

$E_c := 7600\ \textbf{ksi}$ $\varepsilon_{mc} := 0.00211$ $\varepsilon_{mt} := 0.007$

$f_{mc} := 16\ \textbf{ksi}$ $f_{mt} := 1.5\ \textbf{ksi}$

Prestressing Steel Material Properties:

Prestressing steel acquired from Rettco Steel, LLC. Product test certificate available in Appendix E.

$f_{pu} := 270\ \textbf{ksi}$ $f_{pe} := 140\ \textbf{ksi}$ $A_p := 0.153\ \textbf{in}^2$

$E_p := 28500\ \textbf{ksi}$ $P_e := f_{pe} \cdot A_p = 21.42\ \textbf{kip}$

Cross Section Properties of Single Unit Deck Section:

$b_f := 28\ \textbf{in}$ $h_f := 2\ \textbf{in}$ $d_{p1} := 2\ \textbf{in}$

$b_w := 3\ \textbf{in}$ $h_w := 6\ \textbf{in}$ $d_{p2} := 6.5\ \textbf{in}$

$h := h_f + h_w = 8\ \textbf{in}$

Geometric Properties of Cross Section:

Gross Concrete Area:

$$A_c := h_f \cdot b_f + h_w \cdot b_w = 74\ \textbf{in}^2$$

$$y_{bar} := \frac{h_f \cdot b_f \cdot 0.5 \cdot h_f + h_w \cdot b_w \cdot (h_f + 0.5 \cdot h_w)}{A_c} = 1.973\ \textbf{in}$$

$$I_g := \frac{1}{12} \cdot b_f \cdot h_f^{\,3} + (b_f \cdot h_f) \cdot \left(y_{bar} - \frac{h_f}{2}\right)^2 + \frac{1}{12} \cdot b_w \cdot h_w^{\,3} + (b_w \cdot h_w) \cdot (h_f + 0.5 \cdot h_w - y_{bar})^2$$

$I_g = 290.613\ \textbf{in}^4$

$r := \sqrt{\frac{I_g}{A_c}} = 1.982\ \textbf{in}$ $r^2 = 3.927\ \textbf{in}^2$

Eccentricity of Prestressing Steel:

$e_{p1} := d_{p1} - y_{bar} = 0.027\ \textbf{in}$ $e_{p2} := d_{p2} - y_{bar} = 4.527\ \textbf{in}$

Positive Bending Moment Capacity, M_n+:

Use strain compatibility to determine positive bending moment capacity.

Prestressing Steel:

Effective Prestress Strain: $\varepsilon_{pe} := \frac{f_{pe}}{E_p} = 0.004912$

Decompression Strain: $f_c := \frac{P_e}{A_c} + \left(\frac{P_e \cdot e^2}{I_g} \cdot \left(\frac{A_c}{A_c}\right)\right)$ $\varepsilon_{decomp} := \frac{f_c}{E_c}$

$M_p := P_e \cdot e_{p1} + P_e \cdot e_{p2} = 97.548\ (\textbf{kip} \cdot \textbf{in})$

$M_p = 8.129\ (\textbf{kip} \cdot \textbf{ft})$

Top Strand: $\varepsilon_{2t} := \frac{1}{A_c \cdot E_c} \cdot \left(2 \cdot P_e + \frac{M_p \cdot e_{p1}}{r^2}\right) = 0.00007737$

Bottom Strand: $\varepsilon_{2b} := \frac{1}{A_c \cdot E_c} \cdot \left(2 \cdot P_e + \frac{M_p \cdot e_{p2}}{r^2}\right) = 0.0002761$

Type of failure mode is dependent on location of neutral axis, c, in reference to the balanced failure condition.

Balanced Failure Neutral Axis (NA) Location:

$c_{bt} := \frac{\varepsilon_{mc}}{\varepsilon_{mc} + \varepsilon_{mt}} \cdot h = 1.853\ \textbf{in}$

If $c < c_{bt}$, the UHPC has reached its limiting tensile strain.

If $c > c_{bt}$, the UHPC has reached its limiting compressive strain.

Assume: $c_{pos} := 1.08524062741043\ \text{in}$ and $\varepsilon_t := \varepsilon_{mt}$

Assume also that (c + y) is less than than height of flange.

$$\varepsilon_{cc} := \frac{c_{pos}}{h - c_{pos}} \cdot \varepsilon_{mt} = 0.001099$$

$$f_{cc} := E_c \cdot \varepsilon_{cc} = 8.35\ \text{ksi}$$

$$y := 0.000197 \cdot \left(\frac{h - c_{pos}}{\varepsilon_{mt}} \right) = 0.195\ \text{in}$$

Where, y is the distance to reach constant tensile stress for UHPC in tension.

$$C_c := \frac{1}{2} \cdot f_{cc} \cdot c_{pos} \cdot b_f = 126.857\ \text{kip}$$

$$T_{c1} := \frac{1}{2} \cdot f_{mt} \cdot y \cdot b_f = 4.087\ \text{kip}$$

$$T_{c2} := f_{mt} \cdot b_f \cdot (h_f - c_{pos} - y) = 30.247\ \text{kip}$$

$$T_{c3} := f_{mt} \cdot h_w \cdot b_w = 27\ \text{kip}$$

$$\varepsilon_{pt} := \frac{\varepsilon_{mt}}{h - c_{pos}} \cdot (d_{p1} - c_{pos}) + \varepsilon_{pe} + \varepsilon_{2t} = 5.916 \cdot 10^{-3}$$

$$T_{s1} := \text{if } \varepsilon_{pt} < 0.0086 \quad = 25.795\ \text{kip}$$
$$\quad A_p \cdot E_p \cdot \varepsilon_{pt}$$
$$\text{else}$$
$$\quad \left(f_{pu} - \frac{0.04\ \text{ksi}}{\varepsilon_{pt} - \varepsilon_{mt}} \right) \cdot A_p$$

$$\varepsilon_{pb} := \frac{\varepsilon_{mt}}{h - c_{pos}} \cdot (d_{p2} - c_{pos}) + \varepsilon_{pe} + \varepsilon_{2b} = 10.67 \cdot 10^{-3}$$

$$T_{s2} := \text{if } \varepsilon_{pb} < 0.0086 \quad = 39.642\ \text{kip}$$
$$\quad A_p \cdot E_p \cdot \varepsilon_{pb}$$
$$\text{else}$$
$$\quad \left(f_{pu} - \frac{0.04\ \text{ksi}}{\varepsilon_{pb} - \varepsilon_{mt}} \right) \cdot A_p$$

Check assumptions:

$T_{tot} := T_{c1} + T_{c2} + T_{c3} + T_{s1} + T_{s2} = 126.771$ **kip**

$Check := C_c - T_{tot} = 0.086$ **kip** Check value is close to zero; therefore, c value is OK.

Calculate Positive Moment Capacity if (c + y) is less than height of flange:

$M\_C_c := C_c \cdot \frac{2}{3} \cdot c_{pos} = 91.78$ **kip · in**

$M\_T_{c1} := T_{c1} \cdot \frac{2}{3} \cdot y = 0.53$ **kip · in**

$M\_T_{c2} := T_{c2} \cdot \left(y + \frac{1}{2} \cdot (h_f - c_{pos} - y)\right) = 16.777$ **kip · in**

$M\_T_{c3} := T_{c3} \cdot \left(h_f - c_{pos} + \frac{1}{2} \cdot h_w\right) = 105.699$ **kip · in**

$M\_T_{s1} := T_{s1} \cdot (d_{p1} - c_{pos}) = 23.597$ **kip · in**

$M\_T_{s2} := T_{s2} \cdot (d_{p2} - c_{pos}) = 214.654$ **kip · in**

$M_{npos} := M\_C_c + M\_T_{c1} + M\_T_{c2} + M\_T_{c3} + M\_T_{s1} + M\_T_{s2} = 453.037$ **kip · in**

$M_{npos} = 37.753$ **kip · ft**

Negative Bending Moment Capacity, M_n-:

Use strain compatibility to determine negative bending moment capacity.

Balanced Failure Neutral Axis (NA) Location:

$$c_{bb} := \frac{\varepsilon_{mt}}{\varepsilon_{mc} + \varepsilon_{mt}} \cdot h = 6.147 \text{ in}$$

If $c < c_{bb}$, the UHPC has reached its limiting tensile strain.

If $c > c_{bb}$, the UHPC has reached its limiting compressive strain.

Assume: $c_{neg} := 5.8053801619425 \text{ in}$ and $\varepsilon_c := \varepsilon_{mc}$

Assume also that c is less than height of web and (c + y) is greater than than height of web.

$$y := 0.000197 \cdot \frac{c_{neg}}{\varepsilon_{mc}} = 0.542 \text{ in}$$

$$x_2 := h_w - c_{neg} = 0.195 \text{ in}$$

$$f_{x2} := \frac{x_2}{c_{neg}} \cdot (f_{mc}) = 0.536 \text{ ksi}$$

$$C_c := \frac{1}{2} \cdot f_{mc} \cdot c_{neg} \cdot b_w = 139.329 \text{ kip}$$

$$T_{c1} := \frac{1}{2} \cdot f_{x2} \cdot x_2 \cdot b_w = 0.157 \text{ kip}$$

$$T_{c2} := b_f \cdot \left(\frac{1}{2} \cdot (f_{mt} - f_{x2}) \cdot (y - x_2) + f_{x2} \cdot (y - x_2) \right) = 9.904 \text{ kip}$$

$$T_{c3} := f_{mt} \cdot b_f \cdot (h - c_{neg} - y) = 69.409 \text{ kip}$$

$$\varepsilon_{pt} := \frac{d_{p1} - c_{neg}}{h - c_{neg}} \cdot (-\varepsilon_{mc}) + \varepsilon_{pe} + \varepsilon_{2t} = 8.648 \cdot 10^{-3}$$

$$T_{s1} := \text{if } \varepsilon_{pt} < 0.0086 \quad = 37.597\ \text{kip}$$
$$\quad \| A_p \cdot E_p \cdot \varepsilon_{pt}$$
$$\quad \text{else}$$
$$\quad \| \left(f_{pu} - \frac{0.04\ \text{ksi}}{\varepsilon_{pt} - \varepsilon_{mt}} \right) \cdot A_p$$

$$\varepsilon_{pb} := \frac{d_{p2} - c_{neg}}{h - c_{neg}} \cdot (-\varepsilon_{mc}) + \varepsilon_{pe} + \varepsilon_{2b} = 4.521 \cdot 10^{-3}$$

$$T_{s2} := \text{if } \varepsilon_{pb} < 0.0086 \quad = 19.712\ \text{kip}$$
$$\quad \| A_p \cdot E_p \cdot \varepsilon_{pb}$$
$$\quad \text{else}$$
$$\quad \| \left(f_{pu} - \frac{0.04\ \text{ksi}}{\varepsilon_{pb} - \varepsilon_{mt}} \right) \cdot A_p$$

Check assumptions:

$$T_{tot} := T_{c1} + T_{c2} + T_{c3} + T_{s1} + T_{s2} = 136.779\ \text{kip}$$

$$\text{Check} := C_c - T_{tot} = 2.55\ \text{kip}$$

Check value is close to zero; therefore, c value is OK.

Calculate Negative Moment Capacity if c is less than height of web (c + y) is greater than height of web:

Area 1 of C_c: $$A_1 := \frac{1}{2} \cdot (f_{mt} - f_{x2}) \cdot (y - x_2) = 0.167\ \frac{\text{kip}}{\text{in}}$$

Area 2 of C_c: $$A_2 := f_{x2} \cdot (y - x_2) = 0.186\ \frac{\text{kip}}{\text{in}}$$

Centroid of C_c: $$z := \frac{A_1 \cdot \left(\frac{2}{3} \cdot (y - x_2) \right) + A_2 \cdot \left(\frac{1}{2} \cdot (y - x_2) \right)}{A_1 + A_2} = 0.201\ \text{in}$$

$$M\_C_c := -C_c \cdot \frac{2}{3} \cdot c_{neg} = -539.239\ \text{kip} \cdot \text{in}$$

$$M\_T_{c1} := -T_{c1} \cdot \frac{2}{3} \cdot x_2 = -0.02\ \text{kip} \cdot \text{in}$$

$$M\_T_{c2} := -T_{c2} \cdot (x_2 + z) = -3.919 \text{ kip} \cdot \text{in}$$

$$M\_T_{c3} := -T_{c3} \cdot \left(y + \frac{h - c_{neg} - y}{2}\right) = -94.974 \text{ kip} \cdot \text{in}$$

$$M\_T_{s1} := -T_{s1} \cdot (h - c_{neg} - d_{p1}) = -7.317 \text{ kip} \cdot \text{in}$$

$$M\_T_{s2} := T_{s2} \cdot (d_{p2} - (h - c_{neg})) = 9588.707 \text{ J}$$

$$M_{nneg} := M\_C_c + M\_T_{c1} + M\_T_{c2} + M\_T_{c3} + M\_T_{s1} + M\_T_{s2} = -560.603 \text{ kip} \cdot \text{in}$$

$$M_{nneg} = -46.717 \text{ kip} \cdot \text{ft}$$

Shear Strength of UHPC assuming only discrete fiber reinforcement:

$$S := 0.9 \cdot (b_w \cdot d_{p2}) = 17.55 \text{ in}^2$$

$$\beta_u := 40°$$

$$\gamma_{bf} := 1.3$$

$$\sigma_p := 1.0 \text{ ksi}$$

$$V_f := \frac{S \cdot \sigma_p}{\gamma_{bf} \cdot \tan(\beta_u)} = 16.09 \text{ kip}$$

$$V_n := V_f \cdot \gamma_{bf} = 20.92 \text{ kip}$$

$$V_{n\_per\_ft} := \frac{V_n}{\left(\frac{b_f}{12 \text{ in}}\right) 1 \text{ ft}} = 8.96 \frac{\text{kip}}{\text{ft}}$$

Punching Shear Strength of 2 in. UHPC flange with 28 in. rib spacing:

Calculate design load for shear:

$P_{LL} := 16\ \text{kip}$ $l_p := 20\ \text{in}$ $b_p := 10\ \text{in}$

$LL := 1.75$ $t := 2\ \text{in}$

$I := 1.3$ $f_c := 16000\ \textit{psi}$

$P_u := P_{LL} \cdot LL \cdot I = 36.4\ \text{kip}$ $w_u := \frac{P_u}{l_p \cdot b_p} = 0.182\ \text{ksi}$

Assume two-way bending for punching shear:

Check that punching influence area is within cell width of 24 in. for 28 in. rib spacing:

$l_p + t = 22\ \text{in}$ < 24 in.; therefore, within cell width

$b_p + t = 12\ \text{in}$ < 24 in.; therefore, within cell width

$A_{Infl} := (l_p + t) \cdot (b_p + t) = 264\ \text{in}^2$

$V_u := w_u \cdot A_{Infl} = 48.05\ \text{kip}$

$\phi := 0.75$

$$V_n := 4 \cdot \sqrt{f_c}\ \frac{\text{lb}}{\text{in}^2} \cdot \frac{(2 \cdot (b_p + t) + 2 \cdot (l_p + t)) \cdot 2\ \text{in}}{1000\ \frac{\text{lb}}{\text{kip}}} = 68.81\ \text{kip}$$

$\phi \cdot V_n = 51.61\ \text{kip}$ $> V_u$

Deflection of UHPC due to 16 kip patch live load at midspan, assuming single unit section:

The single unit section is based on the rib spacing, assuming a T-beam section with flange width equivalent to the rib spacing. Deflections were checked to evaluate the response of the UHPC deck as compared with the conventional concrete bridge deck.

Determine moment due to live load:

$P_{LL} = 16\ \mathbf{kip}$ $\quad l_{span} := 8\ \mathbf{ft}$

$M_a := \frac{P_{LL} \cdot l_{span}}{4} = 32\ \mathbf{kip \cdot ft}$

Determine whether section is cracked or uncracked:

$A_c = 74\ \mathbf{in}^2$

$y_{bar} = 1.973\ \mathbf{in}$ (from top of flange)

$c_b := h - y_{bar} = 6.027\ \mathbf{in}$ $\quad y_t := c_b = 6.027\ \mathbf{in}$ $\quad c_t := y_{bar} = 1.973\ \mathbf{in}$

$w_{sw} := 0.153 \frac{\mathbf{kip}}{\mathbf{ft}^3} \cdot A_c = 0.079 \frac{\mathbf{kip}}{\mathbf{ft}}$

$I_g = 290.613\ \mathbf{in}^4$ $\quad r^2 = 3.927\ \mathbf{in}^2$ $\quad E_c = 7600\ \mathbf{ksi}$

$f_r := 1.5\ \mathbf{ksi}$ *Assume modulus of rupture is equivalent to maximum tensile stress according to stress-strain model used for analysis.*

$$M_{cr} := \frac{I_g}{y_t} \cdot \left(\frac{P_e}{A_c} \cdot \left(1 + \frac{e_{p1} \cdot c_b}{r^2} + 1 + \frac{e_{p2} \cdot c_b}{r^2} \right) + f_r \right) = 197.79\ \mathbf{kip \cdot in}$$

$M_{cr} = 16.48\ \mathbf{kip \cdot ft}$ $< M_a$, section is cracked.

$n_p := \frac{E_p}{E_c} = 3.75$ $\quad A_{ps1} := A_p = 0.153\ \mathbf{in}^2$ $\quad A_{ps2} := A_p = 0.153\ \mathbf{in}^2$

$d_{p1} = 2\ \mathbf{in}$ $\quad d_{p2} = 6.5\ \mathbf{in}$

$\rho_{p1} := \frac{A_{ps1}}{b_w \cdot d_{p1}} = 0.0255$ $\quad \rho_{p2} := \frac{A_{ps2}}{b_w \cdot d_{p2}} = 0.00785$

$$I_{cr} := \left(n_p \cdot A_{ps1} \cdot d_{p1}^{\,2} + n_p \cdot A_{ps2} \cdot d_{p2}^{\,2}\right) \cdot \left(1 - 1.6 \cdot \sqrt{n_p \cdot \rho_{p1} + n_p \cdot \rho_{p2}}\right) = 11.522\ \text{in}^4$$

$$I_e := I_{cr} + \left(\frac{M_{cr}}{M_a}\right)^3 \cdot \left(I_g - I_{cr}\right) = 49.66\ \text{in}^4$$

$$n := \frac{E_p}{E_c} = 3.75$$

$$A_{tr} := h_f \cdot b_f + A_{ps1} \cdot (n-1) + A_{ps2} \cdot (n-1) + b_w \cdot h_w = 74.842\ \text{in}^2$$

$$y_{tr} := \frac{h_f \cdot b_f \cdot \left(h_w + \frac{h_f}{2}\right) + A_{ps2} \cdot (n-1) \cdot (h - d_{p2}) + A_{ps1} \cdot (n-1) \cdot (h - d_{p1}) + b_w \cdot h_w \cdot \frac{h_w}{2}}{A_{tr}}$$

$$y_{tr} = 6.001\ \text{in}$$

(y_{tr} is from bottom of web)

$$I_{gtr\_web} := \frac{1}{12} \cdot b_w \cdot h_w^{\,3} + \left(b_w \cdot h_w\right) \cdot \left(y_{tr} - \frac{h_w}{2}\right)^2$$

$$I_{gtr\_flange} := \frac{1}{12} \cdot b_f \cdot h_f^{\,3} + \left(b_f \cdot h_f\right) \cdot \left(y_{tr} - \left(h_w + \frac{h_f}{2}\right)\right)^2$$

$$I_{gtr\_top\_strand} := (n-1) \cdot A_{ps1} \cdot \left(h - y_{tr} - d_{p1}\right)^2$$

$$I_{gtr\_bottom\_strand} := (n-1) \cdot A_{ps2} \cdot \left(h - y_{tr} - d_{p2}\right)^2$$

$$I_{gtr} := I_{gtr\_web} + I_{gtr\_flange} + I_{gtr\_top\_strand} + I_{gtr\_bottom\_strand} = 299.187\ \text{in}^4$$

$$P_{e1} := P_e = 21.42\ \text{kip} \qquad P_{e2} := P_e = 21.42\ \text{kip}$$

$$e_1 := h - y_{tr} - d_{p1} = -0.001\ \text{in} \qquad e_2 := h - y_{tr} - d_{p2} = -4.501\ \text{in}$$

$$I_{etr} := I_{cr} + \left(\frac{M_{cr}}{M_a}\right)^3 \cdot \left(I_{gtr} - I_{cr}\right) = 50.832\ \text{in}^4$$

$$\Delta_{camber} := \frac{P_{e1} \cdot e_1 \cdot l_{span}}{8 \cdot E_c \cdot I_{gtr}} + \frac{P_{e2} \cdot e_2 \cdot l_{span}}{8 \cdot E_c \cdot I_{gtr}} = -0.0489 \text{ in}$$

$$\Delta_{sw} := \frac{5 \cdot w_{sw} \cdot l_{span}^4}{384 \cdot E_c \cdot I_{gtr}} = 0.003187 \text{ in}$$

Negative deflection is upward, camber.

$$\Delta_{inet} := \Delta_{camber} + \Delta_{sw} = -0.046 \text{ in}$$

$$\Delta_{inet\_per\_ft} := \frac{\Delta_{inet}}{\left(\frac{b_f}{\left(\frac{12 \text{ in}}{1 \text{ ft}}\right)}\right)} = -0.0196 \frac{\text{in}}{\text{ft}}$$

$$\Delta_{LL} := \frac{P_{LL} \cdot l_{span}^3}{48 \cdot E_c \cdot I_{etr}} = 0.763 \text{ in}$$

$$\Delta_{LL\_per\_ft} := \frac{\Delta_{LL}}{\left(\frac{b_f}{\left(\frac{12 \text{ in}}{1 \text{ ft}}\right)}\right)} = 0.3272 \frac{\text{in}}{\text{ft}}$$

$$\Delta_{tot} := \Delta_{inet} + \Delta_{LL} = 0.718 \text{ in}$$

$$\Delta_{tot\_per\_ft} := \frac{\Delta_{tot}}{\left(\frac{b_f}{\left(\frac{12 \text{ in}}{1 \text{ ft}}\right)}\right)} = 0.3076 \frac{\text{in}}{\text{ft}}$$

Deflection of UHPC due to 16 kip patch load at midspan, assuming the AASHTO (2012) equivalent strip width:

$b_{fs} := 56 \text{ in}$ AASHTO (2012) equivalent strip width was 78.8 in., but simplified to 56 in. for this calculation to use the equivalent of two T-beam sections with 28 in. flanges.

$$I_{g\_s} := \frac{1}{12} \cdot b_{fs} \cdot h_f^3 + (b_{fs} \cdot h_f) \cdot \left(y_{bar} - \frac{h_f}{2}\right)^2 + \frac{1}{12} \cdot b_w \cdot h_w^3 \cdot 2 + b_w \cdot h_w \cdot 2 \cdot \left(h - \frac{h_w}{2} - y_{bar}\right)^2$$

$$M_{cr\_s} := \left(\frac{I_{g\_s}}{y_t}\right) \cdot \left(2 \cdot \frac{P_e}{A_c} \cdot \left(1 + \frac{e_{p1} \cdot c_b}{r^2} + 1 + \frac{e_{p2} \cdot c_b}{r^2}\right) + f_r\right) = 53.875 \text{ kip} \cdot \text{ft}$$

$M_{cr} > M_a = 32$ ***kip*ft***, section is uncracked

$$\Delta_{LLs} := \frac{P_{LL} \cdot l_{span}^3}{48 \cdot E_c \cdot I_{g\_s}} = 0.067 \text{ in}$$

$$\Delta_{LLs\_per\_ft} := \frac{\Delta_{LLs}}{\left(\frac{b_{fs}}{\left(\frac{12 \text{ in}}{1 \text{ ft}}\right)}\right)} = 0.014 \frac{\text{in}}{\text{ft}}$$

$$\Delta_{tots\_per\_ft} := \Delta_{LLs\_per\_ft} + \Delta_{inet\_per\_ft}$$

$$\Delta_{tots\_per\_ft} = -0.00527 \frac{\text{in}}{\text{ft}}$$

Design Iteration 2:

UHPC Material Model:

Use the Graybeal (2008) stress-strain curve for UHPC with modifications to maximum compressive stress for untreated UHPC and modifications based on single cell tests.

$E_c := 7600\ \text{ksi}$ $\varepsilon_{mc} := 0.00211$ $\varepsilon_{mt} := 0.007$

$f_{mc} := 16\ \text{ksi}$ $f_{mt} := 0.5\ \text{ksi}$

Prestressing Steel Material Properties:

Prestressing steel acquired from Rettco Steel, LLC. Product test certificate available in Appendix E.

$f_{pu} := 270\ \text{ksi}$ $f_{pe} := 0.6 \cdot f_{pu} = 162\ \text{ksi}$ $A_p := 0.153\ \text{in}^2$

$E_p := 28500\ \text{ksi}$ $P_e := f_{pe} \cdot A_p = 24.786\ \text{kip}$

Cross Section Properties of Single Unit Deck Section:

$b_f := 18\ \text{in}$ $h_f := 2\ \text{in}$ $d_{p1} := 1.5\ \text{in}$

$b_w := 3\ \text{in}$ $h_w := 6\ \text{in}$ $d_{p2} := 5.5\ \text{in}$

$h := h_f + h_w = 8\ \text{in}$

Geometric Properties of Cross Section:

Gross Concrete Area:

$$A_c := h_f \cdot b_f + h_w \cdot b_w = 54\ \text{in}^2$$

$$y_{bar} := \frac{h_f \cdot b_f \cdot 0.5 \cdot h_f + h_w \cdot b_w \cdot (h_f + 0.5 \cdot h_w)}{A_c} = 2.333\ \text{in}$$

$$I_g := \frac{1}{12} \cdot b_f \cdot h_f^3 + (b_f \cdot h_f) \cdot \left(y_{bar} - \frac{h_f}{2}\right)^2 + \frac{1}{12} \cdot b_w \cdot h_w^3 + (b_w \cdot h_w) \cdot (h_f + 0.5 \cdot h_w - y_{bar})^2$$

$I_g = 258\ \text{in}^4$

$r := \sqrt{\frac{I_g}{A_c}} = 2.186\ \text{in}$ $r^2 = 4.778\ \text{in}^2$

Eccentricity of Prestressing Steel:

$e_{p1} := d_{p1} - y_{bar} = -0.833$ **in**

$e_{p2} := d_{p2} - y_{bar} = 3.167$ **in**

Positive Bending Moment Capacity, M_n+:

Use strain compatibility to determine positive bending moment capacity.

Prestressing Steel:

Effective Prestress Strain: $\varepsilon_{pe} := \frac{f_{pe}}{E_p} = 0.005684$

Decompression Strain: $f_c := \frac{P_e}{A_c} + \left[\left(\frac{P_e \cdot e^2}{I_g}\right) \cdot \left(\frac{A_c}{A_c}\right)\right]$ $\varepsilon_{decomp} := \frac{f_c}{E_c}$

$M_p := P_e \cdot e_{p1} + P_e \cdot e_{p2} = 57.834$ **(kip · in)**

$M_p = 4.82$ **(kip · ft)**

Top Strand: $\varepsilon_{2t} := \frac{1}{A_c \cdot E_c} \cdot \left(2 \cdot P_e + \frac{M_p \cdot e_{p1}}{r^2}\right) = 0.00009621$

Bottom Strand: $\varepsilon_{2b} := \frac{1}{A_c \cdot E_c} \cdot \left(2 \cdot P_e + \frac{M_p \cdot e_{p2}}{r^2}\right) = 0.0002142$

Type of failure mode is dependent on location of neutral axis, c, in reference to the balanced failure condition.

Balanced Failure Neutral Axis (NA) Location:

$c_{bt} := \frac{\varepsilon_{mc}}{\varepsilon_{mc} + \varepsilon_{mt}} \cdot h = 1.853$ **in**

If $c < c_{bt}$, the UHPC has reached its limiting tensile strain.

If $c > c_{bt}$, the UHPC has reached its limiting compressive strain.

Assume: $c_{pos} := 1.09611056604428\ \textbf{in}$ and $\varepsilon_t := \varepsilon_{mt}$

Assume also that (c + y) is less than than height of flange.

$$\varepsilon_{cc} := \frac{c_{pos}}{h - c_{pos}} \cdot \varepsilon_{mt} = 0.001111$$

$$f_{cc} := E_c \cdot \varepsilon_{cc} = 8.446\ \textbf{ksi}$$

$$y := 0.000066 \cdot \left(\frac{h - c_{pos}}{\varepsilon_{mt}} \right) = 0.065\ \textbf{in}$$

Where, y is the distance to reach constant tensile stress for UHPC in tension.

$$C_c := \frac{1}{2} \cdot f_{cc} \cdot c_{pos} \cdot b_f = 83.324\ \textbf{kip}$$

$$c_{pos} + y = 1.161\ \textbf{in}$$

$$T_{c1} := \frac{1}{2} \cdot f_{mt} \cdot y \cdot b_f = 0.293\ \textbf{kip}$$

$$T_{c2} := f_{mt} \cdot b_f \cdot (h_f - c_{pos} - y) = 7.549\ \textbf{kip}$$

$$T_{c3} := f_{mt} \cdot h_w \cdot b_w = 9\ \textbf{kip}$$

$$\varepsilon_{pt} := \frac{\varepsilon_{mt}}{h - c_{pos}} \cdot (d_{p1} - c_{pos}) + \varepsilon_{pe} + \varepsilon_{2t} = 6.19 \cdot 10^{-3}$$

$$T_{s1} := \text{if } \varepsilon_{pt} < 0.0086 \quad = 26.991\ \textbf{kip}$$
$$\quad A_p \cdot E_p \cdot \varepsilon_{pt}$$
$$\text{else}$$
$$\quad \left(f_{pu} - \frac{0.04\ \textbf{ksi}}{\varepsilon_{pt} - \varepsilon_{mt}} \right) \cdot A_p$$

$$\varepsilon_{pb} := \frac{\varepsilon_{mt}}{h - c_{pos}} \cdot (d_{p2} - c_{pos}) + \varepsilon_{pe} + \varepsilon_{2b} = 10.364 \cdot 10^{-3}$$

$$T_{s2} := \text{if } \varepsilon_{pb} < 0.0086 \quad = 39.491\ \textbf{kip}$$
$$\quad A_p \cdot E_p \cdot \varepsilon_{pb}$$
$$\text{else}$$
$$\quad \left(f_{pu} - \frac{0.04\ \textbf{ksi}}{\varepsilon_{pb} - \varepsilon_{mt}} \right) \cdot A_p$$

Check assumptions:

$$T_{tot} := T_{c1} + T_{c2} + T_{c3} + T_{s1} + T_{s2} = 83.324 \text{ kip}$$

$$Check := C_c - T_{tot} = 0 \text{ kip}$$

Check value is zero; therefore, c value is OK.

Calculate Positive Moment Capacity if (c + y) is less than height of flange:

$$M\_C_c := C_c \cdot \frac{2}{3} \cdot c_{pos} = 60.888 \text{ kip} \cdot \text{in}$$

$$M\_T_{c1} := T_{c1} \cdot \frac{2}{3} \cdot y = 0.013 \text{ kip} \cdot \text{in}$$

$$M\_T_{c2} := T_{c2} \cdot \left(y + \frac{1}{2} \cdot (h_f - c_{pos} - y) \right) = 3.658 \text{ kip} \cdot \text{in}$$

$$M\_T_{c3} := T_{c3} \cdot \left(h_f - c_{pos} + \frac{1}{2} \cdot h_w \right) = 35.135 \text{ kip} \cdot \text{in}$$

$$M\_T_{s1} := T_{s1} \cdot (d_{p1} - c_{pos}) = 10.901 \text{ kip} \cdot \text{in}$$

$$M\_T_{s2} := T_{s2} \cdot (d_{p2} - c_{pos}) = 173.912 \text{ kip} \cdot \text{in}$$

$$M_{npos} := M\_C_c + M\_T_{c1} + M\_T_{c2} + M\_T_{c3} + M\_T_{s1} + M\_T_{s2} = 284.507 \text{ kip} \cdot \text{in}$$

$$M_{npos} = 23.709 \text{ kip} \cdot \text{ft}$$

Negative Bending Moment Capacity, M_n-:

Use strain compatibility to determine negative bending moment capacity.

Balanced Failure Neutral Axis (NA) Location:

$$c_{bb} := \frac{\varepsilon_{mt}}{\varepsilon_{mc} + \varepsilon_{mt}} \cdot h = 6.147 \text{ in}$$

If $c < c_{bb}$, the UHPC has reached its limiting tensile strain.

If $c > c_{bb}$, the UHPC has reached its limiting compressive strain.

Assume: $c_{neg} := 2.97818454302582 \text{ in}$ and $\varepsilon_c := \varepsilon_{mc}$

Assume also that (c + y) is less than height of web

$$y := 0.000066 \cdot \frac{c_{neg}}{\varepsilon_{mc}} = 0.093 \text{ in} \qquad c_{neg} + y = 3.071 \text{ in}$$

$$C_c := \frac{1}{2} \cdot f_{mc} \cdot c_{neg} \cdot b_w = 71.476 \text{ kip}$$

$$T_{c1} := \frac{1}{2} \cdot f_{mt} \cdot y \cdot b_w = 0.07 \text{ kip}$$

$$T_{c2} := f_{mt} \cdot b_w \cdot (h_w - (y + c_{neg})) = 4.393 \text{ kip}$$

$$T_{c3} := f_{mt} \cdot b_f \cdot h_f = 18 \text{ kip}$$

$$\varepsilon_{pt} := \frac{d_{p1} - c_{neg}}{h - c_{neg}} \cdot (-\varepsilon_{mc}) + \varepsilon_{pe} + \varepsilon_{2t} = 6.402 \cdot 10^{-3}$$

$$T_{s1} := \begin{cases} A_p \cdot E_p \cdot \varepsilon_{pt} & \text{if } \varepsilon_{pt} < 0.0086 \\ \left(f_{pu} - \frac{0.04 \text{ ksi}}{\varepsilon_{pt} - \varepsilon_{mt}}\right) \cdot A_p & \text{else} \end{cases} = 27.914 \text{ kip}$$

$$\varepsilon_{pb} := \frac{d_{p2} - c_{neg}}{h - c_{neg}} \cdot \left(-\varepsilon_{mc}\right) + \varepsilon_{pe} + \varepsilon_{2b} = 4.839 \cdot 10^{-3}$$

$$T_{s2} := \text{if } \varepsilon_{pb} < 0.0086 \quad = 21.1 \text{ kip}$$
$$\left\| A_p \cdot E_p \cdot \varepsilon_{pb} \right.$$
$$\text{else}$$
$$\left\| \left(f_{pu} - \frac{0.04 \text{ ksi}}{\varepsilon_{pb} - \varepsilon_{mt}}\right) \cdot A_p \right.$$

Check assumptions:

$$T_{tot} := T_{c1} + T_{c2} + T_{c3} + T_{s1} + T_{s2} = 71.476 \text{ kip}$$

$$\text{Check} := C_c - T_{tot} = 0 \text{ kip}$$

Check value is close to zero; therefore, c value is OK.

Calculate Negative Moment Capacity if c is less than height of web (c + y) is greater than height of web:

$$M\_C_c := -C_c \cdot \frac{2}{3} \cdot c_{neg} = -141.913 \text{ kip} \cdot \text{in}$$

$$M\_T_{c1} := -T_{c1} \cdot \frac{2}{3} \cdot y = -0.004 \text{ kip} \cdot \text{in}$$

$$M\_T_{c2} := -T_{c2} \cdot \left(y + \frac{h_w - c_{neg} - y}{2}\right) = -6.842 \text{ kip} \cdot \text{in}$$

$$M\_T_{c3} := -T_{c3} \cdot \left(\frac{h_f}{2} + \left(h_w - c_{neg}\right)\right) = -72.393 \text{ kip} \cdot \text{in}$$

$$M\_T_{s1} := -T_{s1} \cdot \left(h - c_{neg} - d_{p1}\right) = -98.307 \text{ kip} \cdot \text{in}$$

$$M\_T_{s2} := T_{s2} \cdot \left(d_{p2} - \left(h - c_{neg}\right)\right) = 10.09 \text{ kip} \cdot \text{in}$$

$$M_{nneg} := M\_C_c + M\_T_{c1} + M\_T_{c2} + M\_T_{c3} + M\_T_{s1} + M\_T_{s2} = -309.37 \text{ kip} \cdot \text{in}$$

$$M_{nneg} = -25.781 \text{ kip} \cdot \text{ft}$$

Shear Strength of UHPC assuming only discrete fiber reinforcement:

$$S := 0.9 \cdot (b_w \cdot d_{p2}) = 14.85\ \text{in}^2$$

$$\beta_u := 40\ °$$

$$\gamma_{bf} := 1.3$$

$$\sigma_p := 1.0\ \text{ksi}$$

$$V_f := \frac{S \cdot \sigma_p}{\gamma_{bf} \cdot \tan(\beta_u)} = 13.61\ \text{kip}$$

$$V_n := V_f \cdot \gamma_{bf} = 17.7\ \text{kip}$$

$$V_{n\_per\_ft} := \frac{V_n}{\left(\frac{b_f}{12\ \text{in}}\right) 1\ \text{ft}} = 11.8\ \frac{\text{kip}}{\text{ft}}$$

Punching Shear Strength of 2 in. flange with 28 in. rib spacing:

Calculate design load for shear:

$P_{LL} := 16\ \text{kip}$ $l_p := 20\ \text{in}$ $b_p := 10\ \text{in}$

$LL := 1.75$ $t := 2\ \text{in}$

$I := 1.3$ $f'_c := 16000\ \textit{psi}$

$P_u := P_{LL} \cdot LL \cdot I = 36.4\ \text{kip}$ $w_u := \frac{P_u}{l_p \cdot b_p} = 0.182\ \text{ksi}$

Assume two-way bending for punching shear:

Check that punching influence area is within cell width of 24 in. for 28 in. longitudinal rib spacing and 14 in. for 18 in. transverse rib spacing:

$l_p + t = 22\ \text{in}$ < 24 in.; therefore, within cell width

$b_p + t = 12\ \text{in}$ < 14 in.; therefore, within cell width

$A_{Infl} := (l_p + t) \cdot (b_p + t) = 264\ \text{in}^2$

$V_u := w_u \cdot A_{Infl} = 48.05\ \text{kip}$

$\phi := 0.75$

$$V_n := 4 \cdot \sqrt{f'_c}\ \frac{\text{lb}}{\text{in}^2} \cdot \frac{(2 \cdot (b_p + t) + 2 \cdot (l_p + t)) \cdot 2\ \text{in}}{1000\ \frac{\text{lb}}{\text{kip}}} = 68.81\ \text{kip}$$

$\phi \cdot V_n = 51.61\ \text{kip}$ $> V_u$

Deflection of UHPC due to 16 kip patch live load at midspan, assuming single unit section:

The single unit section is based on the rib spacing, assuming a T-beam section with flange width equivalent to the rib spacing.

Determine moment due to live load:

$P_{LL} = 16\ \mathbf{kip}$ $\quad l_{span} := 8\ \mathbf{ft}$

$$M_a := \frac{P_{LL} \cdot l_{span}}{4} = 32\ \mathbf{kip \cdot ft}$$

Determine whether section is cracked or uncracked:

$A_c = 54\ \mathbf{in}^2$

$y_{bar} = 2.333\ \mathbf{in}$ (from top of flange)

$c_b := h - y_{bar} = 5.667\ \mathbf{in}$ $\quad y_t := c_b = 5.667\ \mathbf{in}$

$c_t := y_{bar} = 2.333\ \mathbf{in}$

$$w_{sw} := 0.156\ \frac{\mathbf{kip}}{\mathbf{ft}^3} \cdot A_c = 0.059\ \frac{\mathbf{kip}}{\mathbf{ft}}$$

$I_g = 258\ \mathbf{in}^4$ $\quad r^2 = 4.778\ \mathbf{in}^2$ $\quad E_c = 7600\ \mathbf{ksi}$

$f_r := 0.5\ \mathbf{ksi}$ *Assume modulus of rupture is equivalent to maximum tensile stress according to stress-strain model used for analysis.*

$$M_{cr} := \frac{I_g}{y_t} \cdot \left(\frac{P_e}{A_c} \cdot \left(1 + \frac{e_{p1} \cdot c_b}{r^2} + 1 + \frac{e_{p2} \cdot c_b}{r^2} \right) + f_r \right) = 122.395\ \mathbf{kip \cdot in}$$

$M_{cr} = 10.2\ \mathbf{kip \cdot ft}$ $\quad < M_a$, section is cracked.

$$n_p := \frac{E_p}{E_c} = 3.75$$

$A_{ps1} := A_p = 0.153\ \mathbf{in}^2$ $\quad A_{ps2} := A_p = 0.153\ \mathbf{in}^2$

$d_{p1} = 1.5\ \mathbf{in}$ $\quad d_{p2} = 5.5\ \mathbf{in}$

$$\rho_{p1} := \frac{A_{ps1}}{b_w \cdot d_{p1}} = 0.034 \qquad \rho_{p2} := \frac{A_{ps2}}{b_w \cdot d_{p2}} = 0.00927$$

$$I_{cr} := \left(n_p \cdot A_{ps1} \cdot d_{p1}^{\,2} + n_p \cdot A_{ps2} \cdot d_{p2}^{\,2}\right) \cdot \left(1 - 1.6 \cdot \sqrt{n_p \cdot \rho_{p1} + n_p \cdot \rho_{p2}}\right) = 6.628\ \text{in}^4$$

$$I_e := I_{cr} + \left(\frac{M_{cr}}{M_a}\right)^3 \cdot \left(I_g - I_{cr}\right) = 14.768\ \text{in}^4$$

$$n := \frac{E_p}{E_c} = 3.75$$

Assume transformed section to take advantage of prestressing steel.

$$A_{tr} := h_f \cdot b_f + A_{ps1} \cdot (n-1) + A_{ps2} \cdot (n-1) + b_w \cdot h_w = 54.842\ \text{in}^2$$

$$y_{tr} := \frac{h_f \cdot b_f \cdot \left(h_w + \frac{h_f}{2}\right) + A_{ps2} \cdot (n-1) \cdot (h - d_{p2}) + A_{ps1} \cdot (n-1) \cdot (h - d_{p1}) + b_w \cdot h_w \cdot \frac{h_w}{2}}{A_{tr}}$$

$$y_{tr} = 5.649\ \text{in}$$

(y_{tr} is from bottom of web)

$$I_{gtr\_web} := \frac{1}{12} \cdot b_w \cdot h_w^{\,3} + \left(b_w \cdot h_w\right) \cdot \left(y_{tr} - \frac{h_w}{2}\right)^2$$

$$I_{gtr\_flange} := \frac{1}{12} \cdot b_f \cdot h_f^{\,3} + \left(b_f \cdot h_f\right) \cdot \left(y_{tr} - \left(h_w + \frac{h_f}{2}\right)\right)^2$$

$$I_{gtr\_top\_strand} := (n-1) \cdot A_{ps1} \cdot \left(h - y_{tr} - d_{p1}\right)^2$$

$$I_{gtr\_bottom\_strand} := (n-1) \cdot A_{ps2} \cdot \left(h - y_{tr} - d_{p2}\right)^2$$

$$I_{gtr} := I_{gtr\_web} + I_{gtr\_flange} + I_{gtr\_top\_strand} + I_{gtr\_bottom\_strand} = 262.494\ \text{in}^4$$

$$P_{e1} := P_e = 24.786\ \text{kip} \qquad P_{e2} := P_e = 24.786\ \text{kip}$$

$$e_1 := h - y_{tr} - d_{p1} = 0.851\ \text{in} \qquad e_2 := h - y_{tr} - d_{p2} = -3.149\ \text{in}$$

$$I_{etr} := I_{cr} + \left(\frac{M_{cr}}{M_a}\right)^3 \cdot \left(I_{gtr} - I_{cr}\right) = 14.914\ \text{in}^4$$

$$\Delta_{camber} := \frac{P_{e1} \cdot e_1 \cdot l_{span}^{2}}{8 \cdot E_c \cdot I_{gtr}} + \frac{P_{e2} \cdot e_2 \cdot l_{span}^{2}}{8 \cdot E_c \cdot I_{gtr}} = -0.0329 \text{ in}$$

$$\Delta_{sw} := \frac{5 \cdot w_{sw} \cdot l_{span}^{4}}{384 \cdot E_c \cdot I_{gtr}} = 0.002702 \text{ in}$$

Negative deflection is upward, camber.

$$\Delta_{inet} := \Delta_{camber} + \Delta_{sw} = -0.03 \text{ in}$$

$$\Delta_{inet\_per\_ft} := \frac{\Delta_{inet}}{\left(\frac{b_f}{\left(\frac{12 \text{ in}}{1 \text{ ft}}\right)}\right)} = -0.0201 \frac{\text{in}}{\text{ft}}$$

$$\Delta_{LL} := \frac{P_{LL} \cdot l_{span}^{3}}{48 \cdot E_c \cdot I_{etr}} = 2.602 \text{ in}$$

$$\Delta_{LL\_per\_ft} := \frac{\Delta_{LL}}{\left(\frac{b_f}{\left(\frac{12 \text{ in}}{1 \text{ ft}}\right)}\right)} = 1.7346 \frac{\text{in}}{\text{ft}}$$

$$\Delta_{tot} := \Delta_{inet} + \Delta_{LL} = 2.572 \text{ in}$$

$$\Delta_{tot\_per\_ft} := \frac{\Delta_{tot}}{\left(\frac{b_f}{\left(\frac{12 \text{ in}}{1 \text{ ft}}\right)}\right)} = 1.7145 \frac{\text{in}}{\text{ft}}$$

Deflection of UHPC due to 16 kip patch load at midspan, assuming the AASHTO (2012) equivalent strip width:

$b_{fs} := 72 \text{ in}$ AASHTO (2012) equivalent strip width was 78.8 in., but simplified to 72 in. for this calculation to use the equivalent of four T-beam sections.

$$I_{g\_s} := \frac{1}{12} \cdot b_{fs} \cdot h_f^{3} + (b_{fs} \cdot h_f) \cdot \left(y_{bar} - \frac{h_f}{2}\right)^{2} + \frac{1}{12} \cdot b_w \cdot h_w^{3} \cdot 4 + b_w \cdot h_w \cdot 4 \cdot \left(h - \frac{h_w}{2} - y_{bar}\right)^{2}$$

$$M_{cr\_s} := \left(\frac{I_{g\_s}}{y_t}\right) \cdot \left(4 \cdot \frac{P_e}{A_c} \cdot \left(1 + \frac{e_{p1} \cdot c_b}{r^2} + 1 + \frac{e_{p2} \cdot c_b}{r^2}\right) + f_r\right) = 140.428 \text{ kip} \cdot \text{ft}$$

$M_{cr} > M_a$ = 32 kip*ft, section is uncracked

$$\Delta_{LLs} := \frac{P_{LL} \cdot l_{span}^{3}}{48 \cdot E_c \cdot I_{g\_s}} = 0.038 \text{ in}$$

$$\Delta_{LLs\_per\_ft} := \frac{\Delta_{LLs}}{\left(\frac{b_{fs}}{\left(\frac{12 \text{ in}}{1 \text{ ft}}\right)}\right)} = 0.0063 \frac{\text{in}}{\text{ft}}$$

$$\Delta_{tot\_per\_ft} := \Delta_{LLs\_per\_ft} + \Delta_{inet\_per\_ft}$$

$$\Delta_{tot\_per\_ft} = -0.0139 \frac{\text{in}}{\text{ft}}$$

Estimate Prestress Losses for UHPC Deck Section:

Use the AASHTO (2012) refined method to estimate prestress losses.

Elastic Shortening:

$A_{ps\_tot} := A_{ps1} + A_{ps2} = 0.306\ \mathbf{in^2}$

$f_{pbt} := 0.75 \cdot f_{pu} = 202.5\ \mathbf{ksi}$

$e_{avg} := \text{mean}\left(e_{p1}, e_{p2}\right) = 1.167\ \mathbf{in}$

$M_g := \frac{w_{sw} \cdot l_{span}^{\ 2}}{8} = 5.616\ \mathbf{kip \cdot in}$

$E_{ci} := 6000\ \mathbf{ksi}$ E_{ci} estimated based on approximately 80 percent of E_c.

$$ES := \frac{A_{ps\_tot} \cdot f_{pbt} \cdot \left(I_g + e_{avg}^{\ 2} \cdot A_c\right) - e_{avg} \cdot M_g \cdot A_c}{A_{ps\_tot} \cdot \left(I_g + e_{avg}^{\ 2} \cdot A_c\right) + \frac{A_c \cdot I_g \cdot E_{ci}}{E_p}} = 6.653\ \mathbf{ksi}$$

Creep:

$$f_{cgp} := \frac{\frac{A_{ps\_tot} \cdot f_{pbt}}{A_c} \cdot \left(1 + \frac{e_{avg}^{\ 2} \cdot A_c}{I_g}\right) - \frac{M_g \cdot e_{avg}}{I_g}}{1 + \frac{A_{ps\_tot} \cdot E_p}{A_c \cdot E_{ci}} \cdot \left(1 + \frac{e_{avg}^{\ 2} \cdot A_c}{I_g}\right)} = 1.401\ \mathbf{ksi}$$

$\Delta f_{cdp} := 0\ \mathbf{ksi}$

$CR := 12.0 \cdot f_{cgp} - 7 \cdot \Delta f_{cdp} = 16.807\ \mathbf{ksi}$

Shrinkage:

$H := 70\ \ \%$

$SH := (17.0 - 0.15 \cdot H)\ \mathbf{ksi} = 6.5\ \mathbf{ksi}$

Relaxation after Transfer:

$$R_2 := 0.3 \cdot (20.0\ \text{ksi} - 0.4 \cdot ES - 0.2 \cdot (SH + CR)) = 3.803\ \text{ksi}$$

30% applied for relaxation after transfer for low-relaxation strands

Relaxation at Transfer:

$time := 7$ *days*

$f_{pj} := 205\ \text{ksi}$

$$f_{py} := \frac{39.4\ \text{kip}}{A_p} = 257.516\ \text{ksi}$$

Yield point determined from prestressing steel material data sheet (Appendix E)

$$R_1 := \frac{\log(24.0 \cdot time)}{40.0} \cdot \left(\frac{f_{pj}}{f_{py}} - 0.55\right) \cdot f_{pj} = 2.806\ \text{ksi}$$

Total Prestress Losses after Transfer:

$$\Delta_{fpTot} := ES + CR + SH + R_2 = 33.76\ \text{ksi}$$

Determine Jacking Force:

$$Jack\_Stress := f_{pbt} + R_1 = 205.306\ \text{ksi}$$

$$Jack\_Force := Jack\_Stress \cdot A_p = 31.41\ \text{kip}$$

Estimate Prestress Losses for UHPC Deck Section with Adjustments:

Use the AASHTO (2012) refined method with adjustments for UHPC according to research by Emerson (2011).

Elastic Shortening:

$$A_{ps\_tot} := A_{ps1} + A_{ps2} = 0.306\ \text{in}^2$$

$$f_{pbt} := 0.72 \cdot f_{pu} = 194.4\ \text{ksi}$$

$e_{avg} := \text{mean}(e_{p1}, e_{p2}) = 1.167\ \textbf{in}$

$M_g := \frac{w_{sw} \cdot l_{span}^{2}}{8} = 5.616\ \textbf{kip} \cdot \textbf{in}$

$E_{ci} := 6000\ \textbf{ksi}$ E_{ci} estimated based on approximately 80 percent of E_c.

$$ES := 0.75 \cdot \frac{A_{ps\_tot} \cdot f_{pbt} \cdot \left(I_g + e_{avg}^{2} \cdot A_c\right) - e_{avg} \cdot M_g \cdot A_c}{A_{ps\_tot} \cdot \left(I_g + e_{avg}^{2} \cdot A_c\right) + \frac{A_c \cdot I_g \cdot E_{ci}}{E_p}} = 4.786\ \textbf{ksi}$$

Creep:

$$f_{cgp} := \frac{\frac{A_{ps\_tot} \cdot f_{pbt}}{A_c} \cdot \left(1 + \frac{e_{avg}^{2} \cdot A_c}{I_g}\right) - \frac{M_g \cdot e_{avg}}{I_g}}{1 + \frac{A_{ps\_tot} \cdot E_p}{A_c \cdot E_{ci}} \cdot \left(1 + \frac{e_{avg}^{2} \cdot A_c}{I_g}\right)} = 1.344\ \textbf{ksi}$$

$\Delta f_{cdp} := 0\ \textbf{ksi}$

$CR := 12.0 \cdot f_{cgp} - 7 \cdot \Delta f_{cdp} = 16.123\ \textbf{ksi}$

Shrinkage:

$H := 70\ \%$

$SH := (17.0 - 0.15 \cdot H)\ \textbf{ksi} = 6.5\ \textbf{ksi}$

Relaxation after Transfer:

$R_2 := 0.3 \cdot (20.0\ \textbf{ksi} - 0.4 \cdot ES - 0.2 \cdot (SH + CR)) = 4.068\ \textbf{ksi}$

30% applied for relaxation after transfer for low-relaxation strands

Relaxation at Transfer:

$time := 7$ *days*

$f_{pj} := 205\ \textbf{ksi}$

$f_{py} := \frac{39.4\ \text{kip}}{A_p} = 257.516\ \text{ksi}$ *Yield point determined from prestressing steel material data sheet (Appendix E)*

$R_1 := \frac{\log(24.0 \cdot \text{time})}{40.0} \cdot \left(\frac{f_{pj}}{f_{py}} - 0.55\right) \cdot f_{pj} = 2.806\ \text{ksi}$

Total Prestress Losses after Transfer:

$\Delta_{fpTot} := ES + CR + SH + R_2 = 31.48\ \text{ksi}$

Determine Jacking Force:

$\text{Jack\_Stress} := f_{pbt} + R_1 = 197.206\ \text{ksi}$

$\text{Jack\_Force} := \text{Jack\_Stress} \cdot A_p = 30.17\ \text{kip}$

Design Shear Connection to Steel Girder:

Geometric Constraints:

$s := 3.5\ \text{in}$ *spacing center-to-center between connectors in a row*

$d_e := 2.5\ \text{in}$ *edge distance*

$n_s := 2$ *number of spaces*

$\text{dia} := \frac{3}{4}\ \text{in}$ *diameter of shear stud*

$4 \cdot \text{dia} = 3\ \text{in}$ *spacing must be greater than (4d) - OK*

Other constraints:
- *At least 2 in. of concrete cover over top of shear connector*
- *Shear stud should extend 2 in. into concrete deck*
- *Ratio of length-to-depth should not be less than 4*

Fatigue:

$n := 1$ *number of stress-range cycles per truck passage; assume single-span girders*

$\rho := 0.85$ *fraction of truck traffic in a single lane; assume 2 lanes are available to trucks*

$ADT := 20000$ *average daily traffic, estimated as 20,000 vehicles per lane per day*

$fraction := 0.2$ *fraction of trucks in traffic (AASHTO (2012) Table 3.6.1.4.2-1); assumed as a rural interstate*

$ADTT_{SL} := \rho \cdot ADT \cdot fraction = 3400$ *average daily truck traffic in a single lane*

$N := 365 \cdot 75 \cdot n \cdot \rho \cdot ADTT_{SL} = 79113750$ *number of loading cycles*

$$V := \frac{36.4\ \text{kip}}{2} = 18.2\ \text{kip}$$

$I_{composite} := 22000\ \text{in}^4$ *I and Q determined using transformed composite girder and deck section.*

$Q := 847\ \text{in}^3$

$$S_r := \frac{V \cdot Q}{I_{composite}} = 0.701\ \frac{\text{kip}}{\text{in}}$$ *range of horizondal shear at deck-beam interface*

$$\alpha := 34.5\ \text{ksi} - 4.28\ \text{ksi} \cdot \log(N) = 0.695\ \text{ksi}$$

$$Z_r := \text{if } \alpha \cdot dia^2 \geq \frac{5.5\ \text{ksi} \cdot dia^2}{2} = 1.547\ \text{kip}$$

$$\left\| \alpha \cdot dia^2 \right.$$

$$\text{else}$$

$$\left\| \frac{5.5\ \text{ksi} \cdot dia^2}{2} \right.$$

$$pitch := \frac{3 \cdot Z_r}{S_r} = 6.623\ \text{in} \quad > 6\ \text{in.}$$

Therefore, spacing 3 studs at 6 in. is OK for fatigue.

Strength:

$A_{stud} := \pi \cdot \left(\frac{dia}{2}\right)^2 = 0.442\ \mathbf{in}^2$ *Area of shear stud*

$f_c := 16000\ \mathbf{psi}$ $E_c = 7600000\ \mathbf{psi}$

$F_u := 60000\ \mathbf{psi}$ *Specified tensile strength of shear stud*

$$Q_n := \text{if } 0.5 \cdot \frac{\pi}{4} \cdot dia^2 \cdot \sqrt{16\ \mathbf{ksi} \cdot 7600\ \mathbf{ksi}} \le A_{stud} \cdot F_u = 26.507\ \mathbf{kip}$$
$$\left\| 0.5 \cdot \frac{\pi}{4} \cdot dia^2 \cdot \sqrt{16\ \mathbf{ksi} \cdot 7600\ \mathbf{ksi}} \right.$$
$$\text{else}$$
$$\left\| A_{stud} \cdot F_u \right.$$

Q_n is nominal shear resistance of a single shear stud

$Q_r := 0.85 \cdot Q_n = 22.531\ \mathbf{kip}$

Q_r is factored shear resistance of one shear connector; 0.85 is the factor

$A_{girder} := 47\ \mathbf{in}^2$ $f_{y\_girder} := 60\ \mathbf{ksi}$

$P_1 := f_{y\_girder} \cdot A_{girder} = 2820\ \mathbf{kip}$ *tension force in steel girder*

$$P_2 := \frac{1}{2} \cdot f_c \cdot h \cdot b_w + (b_f - b_w) \cdot \left(h_f \cdot \left(\frac{h_w \cdot f_c}{h}\right) + \frac{1}{2} \cdot \left(f_c - \frac{h_w \cdot f_c}{h}\right) \cdot h_f\right) = 612\ \mathbf{kip}$$

ultimate compression force in deck

$P := \min(P_1, P_2) = 612\ \mathbf{kip}$

$n_s := \frac{P}{Q_r} = 27.2$ *number of shear connectors required for one side*

$n_{s\_tot} := 2 \cdot n_s = 54.32$ *total number of shear connectors*

Therefore, use shear connector spacing of 6 in. with 3 studs per row.

Although the design was specified as listed above, the shear studs were spaced at 8 in. in the simulated connection using the 1 in. thick plate. This connection detail is specified in Appendix A.

Distribution Reinforcement:

Distribution reinforcement was determined based on AASHTO (2012) section 9.7.3.2, where primary reinforcement is perpendicular to traffic.

$$S_{dr} := 8 \ ft$$

$$Percent := \begin{cases} \dfrac{220}{\sqrt{S_{dr}}} & \text{if } \dfrac{220}{\sqrt{S_{dr}}} \le 67 \\ 67 & \text{else} \end{cases} = 67$$

$$Distr\_Reinf := \frac{Percent}{100} \cdot (A_p + A_p) = 0.205 \ in^2$$

Discrete fiber reinforcement is provided at 2 percent by volume in UHPC and may also contribute to distribution reinforcement.

$$Fiber_{Possible\_Contribution} := 0.02 \cdot \left(\frac{h_f \cdot 28 \ in}{\left(\frac{28 \ in}{12 \ \frac{in}{ft}} \right)} + \frac{b_w \cdot h_w}{\left(\frac{28 \ in}{12 \ \frac{in}{ft}} \right)} \right) = 0.634 \ \frac{in^2}{ft}$$

Provide 2 each No. 3 reinforcing bars per rib and assume distribution reinforcement will provide adequate contribution. This assumption should be tested in future research.

Appendix C: Direct Biaxial Test Data

Untreated UHPC with Random Fiber Alignment (UT):

Table C-1: Compressive strength of DB-063011 (UT)

DB-063011 (UT) Age (days)	Compressive Strength, f_c (ksi)		
	299	335	344
1	21.13	20.38	21.88
2	22.38	19.00	23.13
3	19.38	-	-
4	20.63	-	-
Average f_c (ksi)	**20.90**	**19.70**	**22.50**
Standard Deviation (ksi)	**1.24**	**0.97**	**0.88**

Table C-2: Compressive strength of DB-070511 (UT).

DB-070511 (UT) Age (days)	Compressive Strength, f_c (ksi)	
	339	**374**
1	**20.50**	**22.88**
2	**23.38**	**22.75**
3	**-**	**22.00**
Average f_c (ksi)	**21.95**	**22.55**
Standard Deviation (ksi)	**2.03**	**0.47**

Table C-3: Compressive strength of DB-071111 (UT).

DB-071111 (UT) Age (days)	Compressive Strength, f_c (ksi)	
	333	368
1	22.13	24.75
2	24.38	25.63
3	24.25	23.75
Average f_c (ksi)	**23.60**	**24.70**
Standard Deviation (ksi)	**1.26**	**0.94**

Table C-4: Compressive strength of DB-061812 (UT).

DB-061812 (UT)	Compressive Strength, f_c (ksi)					
Age (days)	4	7	14	21	28	37
1	11.13	17.13	20.75	21.25	23.13	22.88
2	11.50	17.63	20.50	22.38	24.38	24.25
3	11.63	16.88	21.38	21.00	23.75	23.63
4	-	-	-	-	-	22.50
5	-	-	-	-	-	22.13
6	-	-	-	-	-	23.63
Average f_c (ksi)	**11.40**	**17.20**	**20.90**	**21.55**	**23.75**	**23.20**
Standard Deviation (ksi)	**0.26**	**0.38**	**0.45**	**0.73**	**0.63**	**0.80**

Table C-5: Compressive strength of KH-062612 (UT).

KH-062612 (UT)	Compressive Strength, f_c (ksi)		
Age (days)	7	14	28
1	17.00	22.50	24.38
2	18.13	21.50	23.75
3	17.88	22.88	24.63
Average f_c (ksi)	**17.67**	**22.29**	**24.25**
Standard Deviation (ksi)	**0.59**	**0.71**	**0.45**

Mix data for KH-062612 (UT) courtesy of K. Halbe.

Table C-6: Cracking split tensile strength of untreated (UT) mixes.

					Cracking			
Mix ID	**Age (days)**	**No.**	**d (in.)**	**l (in.)**	**P_{cr} (k)**	**$f_{ts,cr}$ (ksi)**	**Average $f_{ts,cr}$ (ksi)**	**Standard Deviation (ksi)**
DB-0630 (UT)	392	1	4	7 3/4	--	--	1.64	0.03
		2	4	7 25/32	--	--		
	393	3	4	7 11/16	80	1.66		
		4	4	7 5/8	77.5	1.62		
DB-0705 (UT)	388	1	4	7 3/4	60	1.23	1.60	0.24
		2	4	7 5/8	87.5	1.83		
		3	4	7 9/16	67.5	1.42		
		4	4	7 25/32	70	1.43		
		5	4	7 9/16	81	1.70		
		6	4	7 25/32	92.5	1.89		
		7	4	7 3/4	81	1.66		
DB-0711 (UT)	386	1	4	7 13/16	79.5	1.62	1.69	0.22
		2	4	7 13/16	95	1.94		
		3	4	7 29/32	75	1.51		
DB-061812 (UT)	38	1	4	7 7/8	--	--	1.63	--
		2	4	7 3/4	--	--		
		3	4	7 13/16	--	--		
		4	4	7 7/8	--	--		
		5	4	7 7/8	--	--		
		6	4	7 13/16	80	1.63		
KH-062612 (UT)		1	4	7 5/8	--	--	--	--
		2	4	7 13/16	--	--		
		3	4	7 3/4	--	--		
Totals for Cracking Split Tensile Test							**1.63**	**0.20**

Table C-7: Ultimate splitting tensile strength of untreated (UT) mixes

					Ultimate			
Mix ID	**Age (days)**	**No.**	**d (in.)**	**l (in.)**	**P_u (k)**	**$f_{ts,u}$ (ksi)**	**Average $f_{ts,u}$ (ksi)**	**Standard Deviation (ksi)**
DB-0630 (UT)	392	1	4	7 3/4	175	3.59	3.42	0.15
		2	4	7 25/32	165.5	3.39		
	393	3	4	7 11/16	166.5	3.45		
		4	4	7 5/8	155	3.24		
DB-0705 (UT)	388	1	4	7 3/4	127	2.61	3.03	0.38
		2	4	7 5/8	163	3.40		
		3	4	7 9/16	153	3.22		
		4	4	7 25/32	156	3.19		
		5	4	7 9/16	115.5	2.43		
		6	4	7 25/32	164	3.35		
		7	4	7 3/4	145	2.98		
DB-0711 (UT)	386	1	4	7 13/16	151.5	3.09	3.03	0.14
		2	4	7 13/16	154	3.14		
		3	4	7 29/32	143	2.88		
DB-061812 (UT)	38	1	4	7 7/8	140	2.83	3.00	0.31
		2	4	7 3/4	171	3.51		
		3	4	7 13/16	148.5	3.03		
		4	4	7 7/8	148	2.99		
		5	4	7 7/8	127.5	2.58		
		6	4	7 13/16	151.5	3.09		
KH-062612 (UT)	28	1	4	7 5/8	159	3.31	2.95	0.31
		2	4	7 13/16	139	2.83		
		3	4	7 3/4	133	2.72		
Totals for Ultimate Split Tensile Test							**3.07**	**0.31**

Table C-8: Modulus of Elasticity for Untreated DBT mixes (UT).

Mix ID	Age (days)	No.	E_c (ksi)	Average (ksi)	Standard Deviation (ksi)
DB-063011 (UT)	299	1	7680	7600	166
		2	7410		
		3	7710		
	345	4	7910	7720	190
		5	7830		
		6	7640		
		7	7490		
DB-070511 (UT)	340	1	7780	7560	193
		2	7420		
		3	7480		
	367	4	7870	7920	109
		5	7820		
		6	7910		
		7	8080		
DB-071111 (UT)	371	1	7720	7860	126
		2	7880		
		3	7970		
DB-061812 (UT)	31	1	7760	7830	171
		2	7700		
		3	8020		
	37	4	7850	7830	64
		5	7760		
		6	7890		
KH-062612 (UT)	28	1	7290	7220	--
		2	7150		
		3	--		
Total Average E_c (ksi)			**7720**		
Total Standard Deviation (ksi)			**232**		

Table C-9: DBT data of untreated UHPC with random fiber orientation.

			Failure Load		Stress		Normalized Stress	
Test ID	**No.**	f_c **(ksi)**	**T (kips)**	**C (kips)**	**T Stress, σ_x (ksi)**	**C Stress, σ_y (ksi)**	**$\Psi_2 = \sigma_x/f_c$**	**$\Psi_1 = \sigma_y/f_c$**
PC	1	22	0.000	82.60	0.000	20.65	0.000	0.939
	2	22	0.000	66.20	0.000	16.55	0.000	0.752
	3	22	0.000	57.26	0.000	14.31	0.000	0.651
0.2ft	1	24	-0.736	55.98	-0.184	13.99	-0.008	0.583
	2	22	-0.831	65.87	-0.208	16.47	-0.009	0.749
	3	24	-0.848	68.48	-0.212	17.12	-0.009	0.713
0.4ft	1	24	-1.593	56.10	-0.398	14.02	-0.017	0.584
	2	24	-1.557	68.32	-0.389	17.08	-0.016	0.712
	3	24	-1.482	75.60	-0.370	18.90	-0.015	0.788
0.6ft	1	23	-2.396	76.27	-0.599	19.07	-0.026	0.829
	2	23	-2.318	51.17	-0.579	12.79	-0.025	0.556
	3	23	-2.408	65.54	-0.602	16.39	-0.026	0.712
0.8ft	1	23	-2.821	62.23	-0.705	15.56	-0.031	0.676
	2	23	-2.997	11.05	-0.749	2.76	-0.033	0.120
	3n	23	-1.895	46.99	-0.632	12.53	-0.027	0.545
	4n	24	-2.416	9.85	-0.805	2.63	-0.034	0.109
PT	1n	21	-3.566	0.00	-1.225	0.00	-0.058	0.000
	2n	21	-3.039	0.00	-1.020	0.00	-0.049	0.000
	3n	21	-3.863	0.00	-1.314	0.00	-0.063	0.000

T = tension, C = compression, n = notched specimen

Table C-10: Mix ID for DBT tests of untreated UHPC.

Test ID	No.	Mix ID	f_c
PC	1	DB-070511	22
	2	DB-070511	22
	3	DB-070511	22
0.2ft	1	DB-071111	24
	2	DB-070511	22
	3	DB-071111	24
0.4ft	1	DB-071111	24
	2	DB-071111	24
	3	DB-071111	24
0.6ft	3	DB-061812	23
	4	DB-061812	23
	5	DB-061812	23
0.8ft	3	DB-061812	23
	2	DB-061812	23
	6n	DB-061812	23
	7n	KH-062612	24
PT	1n	DB-063011	21
	2n	DB-063011	21
	3n	DB-063011	21

Steam Treated UHPC with Random Fiber Alignment (ST):

Table C-11: Compressive strength of DB-0802 (ST).

DB-0802 (ST)	Compressive Strength, f_c (ksi)		
Age (days)	28	385	401
1	26.1	28.7	28.1
2	26.6	25.2	30.1
3	24.4	28.9	29.5
4	-	28.4	27.7
Average f_c (ksi)	**25.71**	**27.63**	**29.25**
Standard Deviation (ksi)	**1.18**	**2.06**	**1.02**

Table C-12: Compressive strength of DB-0804 (ST).

DB-0804 (ST)	Compressive Strength, f_c (ksi)		
Age (days)	28	400	404
1	25.5	24.0	26.5
2	23.1	24.9	27.5
3	23.6	24.9	24.0
4	-	25.2	20.9
5	-	-	25.7
Average f_c (ksi)	24.08	24.58	26.00
Standard Deviation (ksi)	1.25	0.51	1.80

Table C-13: Compressive strength of DB-0806 (ST).

DB-0806 (ST)	Compressive Strength, f_c (ksi)			
Age (days)	28	403	419	422
1	21.7	22.6	23.0	26.1
2	22.9	25.4	22.5	26.2
3	24.5	27.9	27.2	24.4
4	-	25.5	-	-
Average f_c (ksi)	23.04	25.34	24.25	25.58
Standard Deviation (ksi)	1.38	2.15	2.61	1.05

Table C-14: Cracking splitting tensile strength of steam treated UHPC.

				Cracking			
Mix ID	**No.**	**d (in.)**	**l (in.)**	**Pcr (k)**	**$f_{ts,cr}$ (k)**	**Average $f_{ts,cr}$ (ksi)**	**Standard Deviation (ksi)**
DB-0802 (ST)	1	4	7 3/4	77.5	1.59	1.62	0.32
	2	4	7 13/16	92.5	1.88		
	3	4	7 7/8	67.5	1.36		
	4	4	7 13/16	102.5	2.09		
	5	4	7 7/8	62	1.25		
	6	4	7 3/4	74	1.52		
DB-0804 (ST)	1	4	7 11/16	70.5	1.46	1.55	0.17
	2	4	7 19/32	73.5	1.54		
	3	4	7 1/2	70	1.49		
	4	4	7 1/2	82	1.74		
	5	4	7 5/8	84.5	1.76		
	6	4	7 11/16	64.5	1.34		
DB-0806 (ST)	1	4	7 5/8	103.5	2.16	1.80	0.25
	2	4	7 9/16	90	1.89		
	3	4	7 27/32	85	1.72		
	4	4	7 15/16	78.5	1.57		
	5	4	7 13/16	--	--		
	6	4	7 7/8	70	1.41		
	7	4	7 3/4	96	1.97		
	8	4	7 3/4	89.5	1.84		
Totals for Cracking Split Tensile Test						**1.66**	**0.26**

Table C-15: Ultimate splitting tensile strength of steam treated UHPC.

				Ultimate			
Mix ID	**No.**	**d (in.)**	**l (in.)**	**Pu (k)**	**$f_{ts,u}$ (ksi)**	**Average $f_{ts,u}$ (ksi)**	**Standard Deviation (ksi)**
DB-0802 (ST)	1	4	7 3/4	152.5	3.13	3.31	0.20
	2	4	7 13/16	170	3.46		
	3	4	7 7/8	160	3.23		
	4	4	7 13/16	153.5	3.13		
	5	4	7 7/8	161.5	3.26		
	6	4	7 3/4	177.5	3.65		
DB-0804 (ST)	1	4	7 11/16	150.5	3.12	3.48	0.34
	2	4	7 19/32	169	3.54		
	3	4	7 1/2	154	3.27		
	4	4	7 1/2	193.5	4.11		
	5	4	7 5/8	161	3.36		
	6	4	7 11/16	169	3.50		
DB-0806 (ST)	1	4	7 5/8	180.5	3.77	3.37	0.24
	2	4	7 9/16	161	3.39		
	3	4	7 27/32	176	3.57		
	4	4	7 15/16	158	3.17		
	5	4	7 13/16	163.5	3.33		
	6	4	7 7/8	146.5	2.96		
	7	4	7 3/4	164	3.37		
	8	4	7 3/4	165	3.39		
Totals for Ultimate Split Tensile Test						**3.38**	**0.26**

Table C-16: Modulus of elasticity of steam treated UHPC.

Mix ID	Age (days)	No.	E_c (ksi)	Average E_c (ksi)	Standard Deviation (ksi)
DB-0802 (ST)	402	1	8370	8270	138
		2	8110		
		3	8320		
DB-0804 (ST)	401	1	7880	7840	72
		2	7890		
		3	7760		
	404	4	7810	7870	55
		5	7920		
		6	7870		
DB-0806 (ST)	404	1	8350	8530	180
		2	8710		
		3	8540		
	424	4	8450	8260	-
		5	8070		
Total Average (ksi)			**8150**		
Total Standard Deviation (ksi)			**306**		

Table C-17: DBT data of steam treated UHPC with random fiber orientation.

			Load		Stress		Stress / f_c	
Test ID	**No.**	**f_c (ksi)**	**T (kips)**	**C (kips)**	**T Stress, σ_x (ksi)**	**C Stress, σ_y (ksi)**	**$\Psi_2 = \sigma_x/f_c$**	**$\Psi_1 = \sigma_y/f_c$**
PC	1*	28	0.000	63.55	0.000	15.89	0.000	0.575
	2	29	0.000	104.34	0.000	26.09	0.000	0.892
	3*	29	0.000	71.26	0.000	17.81	0.000	0.609
	4	29	0.000	81.90	0.000	20.47	0.000	0.700
	5	29	0.000	89.97	0.000	22.49	0.000	0.769
0.2ft	1	25	-1.373	68.85	-0.343	17.21	-0.014	0.700
	2	25	-1.181	80.37	-0.295	20.09	-0.012	0.817
	3	25	-1.058	88.69	-0.265	22.17	-0.011	0.902
0.4ft	1	26	-1.970	78.71	-0.493	19.68	-0.019	0.757
	2	26	-1.834	96.85	-0.459	24.21	-0.018	0.931
	3	26	-1.870	86.87	-0.468	21.72	-0.018	0.835
0.6ft	1*	26	-0.881	25.67	-0.220	6.42	-0.008	0.247
	2	26	-2.546	75.56	-0.637	18.89	-0.024	0.727
	3	26	-2.643	78.92	-0.661	19.73	-0.025	0.759
0.8ft	1	25	-3.317	85.33	-0.829	21.33	-0.033	0.844
	2	25	-3.627	66.04	-0.907	16.51	-0.036	0.653
	3*	25	-3.502	86.62	-0.876	23.10	-0.035	0.913
	4	25	-4.020	99.99	-1.005	26.66	-0.040	1.054
PT	1n	28	-3.511	0.00	-1.248	0.00	-0.045	0.000
	2n	28	-3.974	0.00	-1.382	0.00	-0.050	0.000
	3n	28	-4.261	0.00	-1.498	0.00	-0.054	0.000

T = tension, C = compression, n = notched specimen, * = considered possible outliers

Table C-18: Mix ID for DBT tests of steam treated UHPC.

Test ID	No.	Mix ID	f_c (ksi)
PC	1	DB-0802	28
	2	DB-0802	29
	3	DB-0802	29
	4	DB-0802	29
	5	DB-0802	29
0.2ft	1	DB-0804	25
	2	DB-0804	25
	3	DB-0804	25
0.4ft	1	DB-0804	26
	2	DB-0804	26
	3	DB-0804	26
0.6ft	1	DB-0804	26
	2	DB-0804	26
	3	DB-0804	26
0.8ft	1	DB-0806	25
	2	DB-0806	25
	3	DB-0806	25
	4	DB-0806	25
PT	1n	DB-0802	28
	2n	DB-0802	28
	3n	DB-0802	28

n = notched specimen

Untreated UHPC with Controlled Fiber Alignment (UT-I):

Table C-19: Compressive strength of DB-081712 (UT-I).

DB-081712 (UT-I)	Compressive Strength, f_c (ksi)		
Age (days)	28	45	47
1	22.5	22.4	22.4
2	22.0	23.8	23.4
3	21.6	21.0	22.0
Average f_c (ksi)	22.0	22.4	22.6
Standard Deviation (ksi)	0.44	1.38	0.71

Table C-20: Compressive strength of DB-082212 (UT-I).

DB-082212 (UT-I)	Compressive Strength, f_c (ksi)		
Age (days)	28	44	48
1	21.9	22.6	23.3
2	22.0	21.4	21.4
3	22.3	23.5	22.5
Average f_c (ksi)	22.0	22.5	22.4
Standard Deviation (ksi)	0.19	1.07	0.94

Table C-21: Compressive strength of DB-082712 (UT-I).

DB-082712 (UT-I)	Compressive Strength, f_c (ksi)		
Age (days)	28	44	47
1	17.5	18.1	16.6
2	17.1	17.4	18.38
3	16.1	17.3	17.00
Average f_c (ksi)	16.9	17.6	17.33
Standard Deviation (ksi)	0.71	0.47	0.92

Table C-22: Compressive strength of SC-1.

SC-1	Compressive Strength, f_c (ksi)		
Age (days)	28	30	50
1	25.0	22.6	25.3
2	21.6	19.9	23.1
3	21.8	21.6	24.5
4	-	-	24.6
Average f_c (ksi)	22.8	21.4	24.4
Standard Deviation (ksi)	1.91	1.39	0.90

Table C-23: Cracking splitting tensile strength of untreated UHPC for DBT with controlled fiber orientation.

					Cracking			
Mix ID	**Age (days)**	**No.**	**d (in.)**	**l (in.)**	**Pcr (k)**	**$f_{ts,cr}$ (k)**	**Average $f_{ts,cr}$ (k)**	**Standard Deviation (ksi)**
DB-081712 (UT-I)	46	1	4	7 11/16	56.5	1.17	1.46	0.42
		2	4	7 7/8	--	--		
		3	4	7 9/16	83.5	1.76		
DB-082212 (UT-I)	44	1	4	7 3/4	--	--	1.59	0.28
		2	4	7 13/16	78.5	1.60		
		3	4	7 5/8	62.5	1.30		
	48	4	4	7 13/16	--	--		
		5	4	7 13/16	92	1.87		
		6	4	7 3/4	--	--		
DB-082712 (UT-I)	44	1	4	7 9/16	87.5	1.84	1.46	0.54
		2	4	7 5/8	--	--		
	47	3	4	7 7/16	--	--		
		4	4	7 3/8	50	1.08		
SC-1	50	1	4	7 7/8	94.5	1.91	1.33	0.52
		2	4	7 13/16	56.5	1.15		
		3	4	7 3/4	45	0.92		

Table C-24: Ultimate splitting tensile strength of untreated UHPC for DBT with controlled fiber orientation.

					Ultimate			
Mix ID	**Age (days)**	**No.**	**d (in.)**	**l (in.)**	**Pu (k)**	**$f_{ts,u}$ (ksi)**	**Average $f_{ts,u}$ (ksi)**	**Standard Deviation (ksi)**
DB-081712 (UT-I)	46	1	4	7 11/16	149.5	3.10	3.11	0.14
		2	4	7 7/8	147.5	2.98		
		3	4	7 9/16	154.5	3.25		
DB-082212 (UT-I)	44	1	4	7 3/4	157.5	3.23	3.13	0.30
		2	4	7 13/16	145.5	2.96		
		3	4	7 5/8	126	2.63		
	48	4	4	7 13/16	166	3.38		
		5	4	7 13/16	168.5	3.43		
		6	4	7 3/4	154	3.16		
DB-082712 (UT-I)	44	1	4	7 9/16	142	2.99	2.98	0.21
		2	4	7 5/8	144	3.01		
	47	3	4	7 7/16	126	2.70		
		4	4	7 3/8	149	3.22		
SC-1	50	1	4	7 7/8	135.00	2.73	2.83	0.19
		2	4	7 13/16	133.00	2.71		
		3	4	7 3/4	148.00	3.04		

Table C-25: Modulus of elasticity of untreated UHPC for DBT with controlled fiber orientation.

Mix ID	Age (days)	No.	E_c (ksi)	Average E_c (ksi)	Standard Deviation (ksi)
DB-081712 (UT-I)	45	1	7750	7750	198
		2	7550		
		3	7950		
	46	4	7910	7850	63
		5	7780		
		6	7850		
DB-082212 (UT-I)	44	1	7550	7550	46
		2	7590		
		3	7500		
	48	4	7740	7800	68
		5	7880		
		6	7790		
DB-082712 (UT-I)	44	1	7070	7270	--
		2	7470		
	47	3	7300	7290	--
		4	7290		
SC-1	50	1	8100	8050	41
		2	8040		
		3	8020		
Total Average (ksi)			**7690**		
Total Standard Deviation (ksi)			**282**		

Table C-26: DBT data of untreated UHPC with controlled fiber orientation.

			Failure Load		Stress		Stress / f_c	
Test ID	**No.**	**f_c (ksi)**	**T (kips)**	**C (kips)**	**T Stress, σ_x (ksi)**	**C Stress, σ_y (ksi)**	**$\Psi_2 = \sigma_x/f_c$**	**$\Psi_1 = \sigma_y/f_c$**
PC	1	22	0.00	87.53	0.000	21.882	0.000	0.977
	2	22	0.00	88.03	0.000	22.006	0.000	0.982
	3	22	0.00	80.53	0.000	20.133	0.000	0.899
PT	1n	22	3.51	0.00	-1.276	0.000	-0.057	0.000
	2n*	22	3.75	0.00	-1.226	0.000	-0.055	0.000
	3n*	18	3.00	0.00	-0.943	0.000	-0.054	0.000
	4n	18	3.14	0.00	-1.048	0.000	-0.060	0.000
	5n	18	3.29	0.00	-1.113	0.000	-0.063	0.000
0.2ft	1	23	1.04	77.59	-0.259	19.398	-0.012	0.862
	2	23	0.93	73.70	-0.232	18.425	-0.010	0.819
	3	23	0.82	79.04	-0.206	19.760	-0.009	0.878
0.4ft	1	23	1.86	71.05	-0.465	17.762	-0.021	0.789
	2	23	1.94	60.37	-0.485	15.091	-0.022	0.671
	3	23	1.94	68.69	-0.484	17.172	-0.022	0.763
0.6ft	1	22	2.53	62.89	-0.632	15.723	-0.028	0.702
	2*	22	2.97	80.08	-0.743	20.019	-0.033	0.894
	3	22	2.62	60.37	-0.656	15.091	-0.029	0.674
0.8ft	1	22	3.52	73.12	-0.880	18.280	-0.039	0.816
	2n	21	1.76	71.75	-0.581	17.938	-0.027	0.838
	3n*	21	2.25	78.46	-0.817	19.615	-0.038	0.917
	4n	21	2.30	72.91	-0.775	18.228	-0.036	0.852
	5n*	21	2.30	74.11	-0.782	18.528	-0.037	0.866

T = tension, C = compression, n = notched specimen, * = considered possible outliers

Table C-27: Mix ID for untreated UHPC for DBT with controlled fiber orientation.

Test ID	No.	Mix ID	f_c (ksi)
PC	1	DBI-081712	22
	2	DBI-081712	22
	3	DBI-081712	22
0.2ft	1	DBI-081712	23
	2	DBI-081712	23
	3	DBI-081712	23
0.4ft	1	DBI-082212	23
	2	DBI-082212	23
	3	DBI-082212	23
0.6ft	1	DBI-082212	22
	2	DBI-082212	22
	3	DBI-082212	22
0.8ft	1	DBI-082212	22
	2n	SC-1	21
	3n	SC-1	21
	4n	SC-1	21
	5n	SC-1	21
PT	1n	DBI-081712	22
	2n	DBI-081712	22
	3n	DBI-082712	18
	4n	DBI-082712	18
	5n	DBI-082712	18

n = notched specimen

Appendix D: Supplementary Single Cell Test Data

UHPC Material Properties of Single Cell Mixes:

Table D-1: Compressive Strength of SC-1.

SC-1	Compressive Strength, f_c (ksi)		
Age (days)	28	30	50
1	25.0	22.6	25.3
2	21.6	19.9	23.1
3	21.8	21.6	24.5
4	-	-	24.6
Average f_c (ksi)	22.8	21.4	24.4
Standard Deviation (ksi)	1.91	1.39	0.90

Table D-2: Compressive Strength of SC-2.

SC-2	Compressive Strength, f_c (ksi)	
Age (days)	28	50
1	23.0	26.9
2	24.8	24.5
3	23.8	25.4
4	-	23.4
Average f_c (ksi)	23.8	25.0
Standard Deviation (ksi)	0.88	1.48

Table D-3: Cracking split cylinder tensile strength of SC-1 and SC-2.

					Cracking			
Mix ID	**Age (days)**	**No.**	**d (in.)**	**l (in.)**	**P_{cr} (k)**	**$f_{ts,cr}$ (k)**	**Average $f_{ts,cr}$ (k)**	**Standard Deviation (ksi)**
SC-1	50	1	4	7 7/8	94.5	1.91	1.33	0.52
		2	4	7 13/16	56.5	1.15		
		3	4	7 3/4	45	0.92		
SC-2	50	1	4	7 13/16	51.5	1.05	1.05	--
		2	4	7 7/8	--	--		

Table D-4: Ultimate split cylinder tensile strength of SC-1 and SC-2.

					Ultimate			
Mix ID	**Age (days)**	**No.**	**d (in.)**	**l (in.)**	**P_u (k)**	**$f_{ts,u}$ (ksi)**	**Average $f_{ts,u}$ (ksi)**	**Standard Deviation (ksi)**
SC-1	50	1	4	7 7/8	135.00	2.73	2.83	0.19
		2	4	7 13/16	133.00	2.71		
		3	4	7 3/4	148.00	3.04		
SC-2	50	1	4	7 13/16	133.00	2.71	2.89	0.25
		2	4	7 7/8	151.50	3.06		

Table D-5: Modulus of elasticity of SC-1 and SC-2.

Mix ID	**Age (days)**	**No.**	**E_c (ksi)**	**Average E_c (ksi)**	**Standard Deviation (ksi)**
SC-1	50	1	8100	8050	41
		2	8040		
		3	8020		
SC-2	50	1	7980	7990	--
		2	8000		
Total Average (ksi)			**8030**		
Total Standard Deviation (ksi)			**46**		

Third-Point Bending Test Data of Single Cell Ribs:

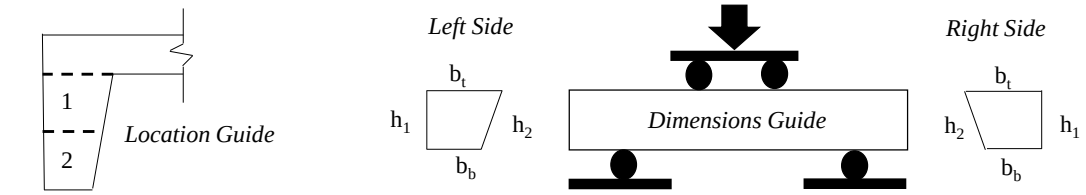

1 – Beam was on top section of the web, nearest the flange
2 – Beam was on the bottom section of the web

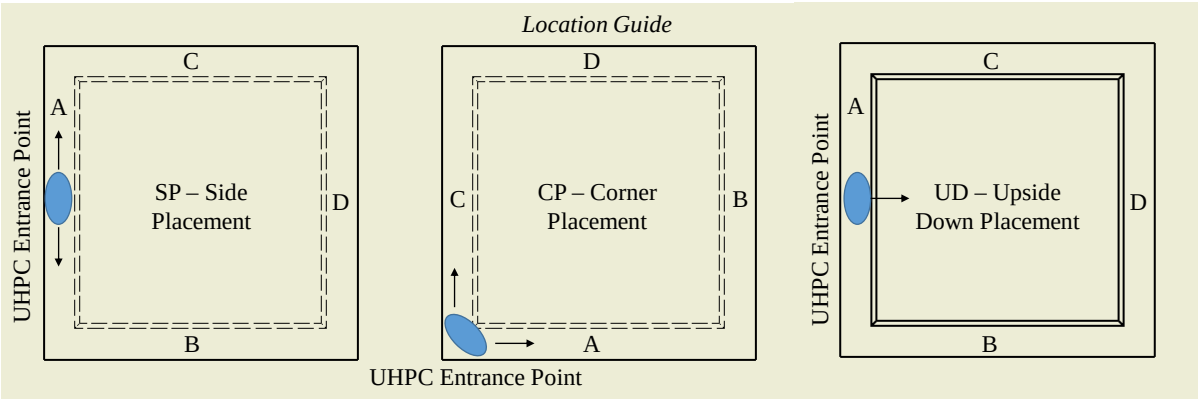

Figure D-1: Single cell beam location and dimensional guides.

Table D-6: Detailed dimensions of single cell ribs.

		Left Dimensions (in.)				Right Dimensions (in.)			
Sample ID	**Mix ID**	h_1	h_2	b_t	b_b	h_1	h_2	b_t	b_b
UD-A1	SC-1	3.13	2.94	3.25	3.00	3.06	2.88	3.31	3.13
UD-A2	SC-1	2.63	2.63	3.00	2.81	2.63	2.47	3.06	2.94
UD-B1	SC-1	3.00	2.94	3.34	3.19	3.06	3.06	3.31	3.19
UD-B2	SC-1	2.63	2.69	3.13	3.03	2.72	2.75	3.19	3.06
UD-C1	SC-1	3.06	3.03	3.50	3.25	3.00	3.16	3.53	3.25
UD-C2	SC-1	2.06	2.75	3.25	3.00	2.56	2.56	3.25	3.06
UD-D1	SC-1	3.00	2.94	3.44	3.19	2.94	2.88	3.56	3.34
UD-D2	SC-1	2.75	2.88	3.13	2.88	2.88	2.88	3.31	3.13
SP-A1	SC-2	2.94	2.81	3.31	3.19	2.94	2.88	3.19	3.13
SP-A2	SC-2	2.94	2.94	3.19	3.03	2.88	2.88	3.06	3.00
SP-B1	SC-2	2.97	2.88	3.44	3.25	3.06	2.94	3.44	3.25
SP-B2	SC-2	2.81	2.94	3.25	3.00	2.88	2.81	3.25	3.00
SP-C1	SC-2	3.00	2.94	3.44	3.25	3.09	3.00	3.31	3.19
SP-C2	SC-2	2.88	2.84	3.25	3.06	2.75	2.94	3.13	2.94
SP-D1	SC-2	3.00	2.88	3.38	3.19	3.13	3.00	3.44	3.19
SP-D2	SC-2	2.88	2.88	3.19	3.00	2.69	2.75	3.19	3.00
CP-A1	SC-2	3.06	2.94	3.31	3.13	3.25	3.13	3.31	3.16
CP-A2	SC-2	2.88	2.88	3.13	3.00	2.75	2.75	3.13	3.00
CP-B1	SC-2	3.00	2.88	3.25	3.19	3.06	3.00	3.25	3.13
CP-B2	SC-2	2.94	2.94	3.19	3.00	2.75	2.81	3.03	2.94
CP-C1	SC-2	3.06	2.94	3.50	3.28	3.19	3.09	3.50	3.38
CP-C2	SC-2	2.81	2.81	3.19	3.03	2.75	2.75	3.38	3.19
CP-D1	SC-2	3.00	2.88	3.50	3.25	3.06	2.94	3.44	3.13
CP-D2	SC-2	2.81	2.88	3.25	3.06	2.81	2.88	3.13	2.94

UD – upside down placement
SP – side placement
CP – corner placement

Table D-7: Cracking tensile strength of single cell beam samples.

				Simple Cross Section		Cracking		
Sample ID	**Mix ID**	f_c **(ksi)**	E_c **(ksi)**	**h (in.)**	**b (in.)**	P_{cr} **(lb)**	$f_{ct,flexure,cr}$ **(ksi)**	$f_{ct,cr}$ **(ksi)**
UD-A1	SC-1	24.4	8054	3.00	3.06	4873	2.12	1.32
UD-A2	SC-1	24.4	8054	2.59	2.88	1143	0.71	0.43
UD-B1	SC-1	24.4	8054	3.02	3.19	3211	1.33	0.83
UD-B2	SC-1	24.4	8054	2.70	3.05	1286	0.70	0.42
UD-C1	SC-1	24.4	8054	3.06	3.25	4450	1.75	1.10
UD-C2	SC-1	24.4	8054	2.48	3.03	790	0.51	0.30
UD-D1	SC-1	24.4	8054	2.94	3.27	4070	1.73	1.07
UD-D2	SC-1	24.4	8054	2.84	3.00	1394	0.69	0.42
SP-A1	SC-2	25	7990	2.89	3.16	3006	1.37	0.84
SP-A2	SC-2	25	7990	2.91	3.02	6646	3.13	1.93
SP-B1	SC-2	25	7990	2.96	3.25	3580	1.51	0.94
SP-B2	SC-2	25	7990	2.86	3.00	10101	4.94	3.04
SP-C1	SC-2	25	7990	3.01	3.22	2007	0.83	0.52
SP-C2	SC-2	25	7990	2.85	3.00	6409	3.15	1.94
SP-D1	SC-2	25	7990	3.00	3.19	4800	2.01	1.25
SP-D2	SC-2	25	7990	2.80	3.00	4115	2.10	1.29
CP-A1	SC-2	25	7990	3.09	3.14	5095	2.03	1.28
CP-A2	SC-2	25	7990	2.81	3.00	8547	4.32	2.65
CP-B1	SC-2	25	7990	2.98	3.16	3415	1.46	0.91
CP-B2	SC-2	25	7990	2.86	2.97	10899	5.39	3.31
CP-C1	SC-2	25	7990	3.07	3.33	4999	1.91	1.20
CP-C2	SC-2	25	7990	2.78	3.11	11744	5.86	3.58
CP-D1	SC-2	25	7990	2.97	3.19	3404	1.45	0.90
CP-D2	SC-2	25	7990	2.84	3.00	7876	3.90	2.39

$f_{ct,\,flexure,\,cr}$ = cracking tensile strength from bending test from ASTM C1609 (2012)
$f_{ct,\,cr}$ = cracking tensile strength from bending test using modification for UHPC (Graybeal 2006a)
UD – upside down placement
SP – side placement
CP – corner placement

Table D-8: Ultimate tensile strength of single cell beam samples.

				Simple Cross Section		Ultimate		
Sample ID	**Mix ID**	f_c **(ksi)**	E_c **(ksi)**	**h (in.)**	**b (in.)**	P_{max} **(lb)**	$f_{ct,flexure}$ **(ksi)**	f_{ct} **(ksi)**
UD-A1	SC-1	24.4	8054	3.00	3.06	4873	2.12	1.32
UD-A2	SC-1	24.4	8054	2.59	2.88	1203	0.75	0.45
UD-B1	SC-1	24.4	8054	3.02	3.19	3779	1.56	0.98
UD-B2	SC-1	24.4	8054	2.70	3.05	2217	1.20	0.73
UD-C1	SC-1	24.4	8054	3.06	3.25	5709	2.25	1.41
UD-C2	SC-1	24.4	8054	2.48	3.03	1108	0.71	0.42
UD-D1	SC-1	24.4	8054	2.94	3.27	4273	1.82	1.13
UD-D2	SC-1	24.4	8054	2.84	3.00	1706	0.84	0.52
SP-A1	SC-2	25	7990	2.89	3.16	3530	1.61	0.99
SP-A2	SC-2	25	7990	2.91	3.02	7381	3.48	2.15
SP-B1	SC-2	25	7990	2.96	3.25	3580	1.51	0.94
SP-B2	SC-2	25	7990	2.86	3.00	10101	4.94	3.04
SP-C1	SC-2	25	7990	3.01	3.22	3157	1.30	0.81
SP-C2	SC-2	25	7990	2.85	3.00	7676	3.78	2.32
SP-D1	SC-2	25	7990	3.00	3.19	4800	2.01	1.25
SP-D2	SC-2	25	7990	2.80	3.00	4115	2.10	1.29
CP-A1	SC-2	25	7990	3.09	3.14	5828	2.33	1.46
CP-A2	SC-2	25	7990	2.81	3.00	8547	4.32	2.65
CP-B1	SC-2	25	7990	2.98	3.16	4230	1.81	1.12
CP-B2	SC-2	25	7990	2.86	2.97	10899	5.39	3.31
CP-C1	SC-2	25	7990	3.07	3.33	4999	1.91	1.20
CP-C2	SC-2	25	7990	2.78	3.11	11879	5.93	3.62
CP-D1	SC-2	25	7990	2.97	3.19	4553	1.94	1.21
CP-D2	SC-2	25	7990	2.84	3.00	9431	4.66	2.87

$f_{ct,\ flexure}$ = ultimate tensile strength from bending test from ASTM C1609 (2012).
f_{ct} = ultimate tensile strength from bending test using modification for UHPC (Graybeal 2006a)
UD – upside down placement
SP – side placement
CP – corner placement

Appendix E: Supplementary Deck Section Test Data

UHPC Material Property Test Results:

Table E-1: Compressive strength results for DS-1 (upside down placement) mixed in Mortarman 750.

DS-1	Compressive Strength, f_c (ksi)				
	Prestress Transfer	-	28-day	Test 1	Test 2
Age (days)	7	22	28	79	84
1	15.75	21.25	22.00	19.25	24.75
2	16.25	21.00	21.50	25.00	21.50
3	15.75	20.50	20.38	24.00	23.38
4	-	-	-	23.63	-
Average (ksi)	15.90	20.90	21.30	23.00	23.20
Standard Deviation (ksi)	0.29	0.38	0.83	2.55	1.63

Table E-2: Compressive strength results for DS-2A (right-side up placement) mixed in Mortarman 750.

DS-2A	Compressive Strength, f_c (ksi)				
	Prestress Transfer	-	28-day	Test 1	Test 2
Age (days)	7	14	28	71	72
1	16.25	22.88	23.38	24.38	28.13
2	17.88	20.75	25.38	27.50	25.88
3	17.75	22.50	24.75	25.13	24.50
4	-	23.38	-	-	-
Average (ksi)	17.30	22.40	24.50	25.70	26.20
Standard Deviation (ksi)	0.90	1.14	1.02	1.63	1.83

Table E-3: Compressive strength results for DS-2B (right-side up placement) mixed in 2 cu. ft pan mixer.

DS-2B	Compressive Strength, f_c (ksi)				
	Prestress Transfer	-	28-day	Test 1	Test 2
Age (days)	7	14	28	71	72
1	20.38	22.63	22.38	27.38	24.25
2	17.25	21.00	22.13	24.88	25.88
3	17.00	25.38	24.88	22.00	26.13
Average (ksi)	18.20	23.00	23.10	24.75	25.40
Standard Deviation (ksi)	1.88	2.21	1.52	2.69	1.02

Table E-4: Compressive strength results for G-1, grout used in DS-2 connections.

G-1	Compressive Strength, f_c (ksi)	
	Test 1	Test 2
Age (days)	24	25
1	9.88	9.63
2	8.25	10.00
3	9.63	9.88
Average (ksi)	9.25	9.80
Standard Deviation (ksi)	0.88	0.19

Table E-5: Compressive strength results for G-2, grout used in DS-1 connections.

G-2	Compressive Strength, f_c (ksi)	
	Test 1	Test 2
Age (days)	17	22
1	8.63	8.75
2	8.25	8.63
3	8.63	9.00
Average (ksi)	8.50	8.80
Standard Deviation (ksi)	0.22	0.19

Table E-6: Modulus of Elasticity results for DS-1 and DS-2.

Mix ID	Significance	Age (days)	No.	E_c (ksi)	Average (ksi)	Standard Deviation (ksi)
DS-1	Prestress Transfer	8	1 2 3	6660 6810 7470	6980	431
	Test 1 & 2	79	1 2 3	7920 7900 7810	7880	59
DS-2A	Prestress Transfer	8	1 2 3	7630 - 7420	7530	-
	28-day Strength	29	1 2 3	8040 7910 -	7980	-
	Test 1 & 2	74	1 2 3	7940 8040 8080	8020	72
DS-2B	Prestress Transfer	8	1 2 3	6800 6840 5580	6410	716
	28-day Strength	29	1 2 3	7500 7450 -	7480	-
	Test 1 & 2	74	1 2 3	7520 7660 -	7590	-
Total Average E_c (ksi)				7450		
Total Average Standard Deviation (ksi)				630		

Table E-7: Cracking splitting tensile test results for DS-1 and DS-2.

					Cracking			
Mix ID	**Age (days)**	**No.**	**d (in.)**	**l (in.)**	**P_{cr} (k)**	**$f_{ts,cr}$ (ksi)**	**Average (ksi)**	**Standard Deviation (ksi)**
DS-1	84	1	4	7 15/16	44	0.88	1.54	0.57
		2	4	7 15/16	93.5	1.87		
		3	4	7 15/16	92.5	1.85		
	89	4	4	8	97	1.93	1.49	0.62
		5	4	7 7/8	52	1.05		
DS-2A	74	1	4	7 15/16	93.5	1.87	1.29	0.54
		2	4	7 15/16	40	0.80		
		3	4	7 5/8	57.5	1.20		
DS-2B	74	1	4	7 13/16	75	1.53	1.97	0.63
		2	4	7 3/4	117.5	2.41		
Totals for Cracking Split Tensile Test							1.54	0.53

Table E-8: Ultimate splitting tensile test results for DS-1 and DS-2.

					Ultimate			
Mix ID	**Age (days)**	**No.**	**d (in.)**	**l (in.)**	**P_u (k)**	**$f_{ts,u}$ (ksi)**	**Average (ksi)**	**Standard Deviation (ksi)**
DS-1	84	1	4	7 15/16	128.5	2.58	2.55	0.10
		2	4	7 15/16	121.5	2.44		
		3	4	7 15/16	131.5	2.64		
	89	4	4	8	100	1.99	1.92	0.10
		5	4	7 7/8	91.5	1.85		
DS-2A	74	1	4	7 15/16	115	2.31	2.30	0.17
		2	4	7 15/16	106	2.13		
		3	4	7 5/8	118	2.46		
DS-2B	74	1	4	7 13/16	90	1.83	2.36	0.75
		2	4	7 3/4	141	2.90		
Totals for Ultimate Split Tensile Test							2.31	0.36

Table E-9: Briquet tensile test results for DS-1 and DS-2.

Mix ID	**Age (days)**	**No.**	**$f_{t,b}$ (ksi)**	**Average $f_{t,b}$ (ksi)**	**Standard Deviation (ksi)**
DS-1	84	1	1.32	1.25	0.12
		2	1.34		
		3	1.08		
		4	1.24		
DS-2A	69	1	0.74	0.89	0.13
		2	1.00		
		3	1.00		
		4	0.84		
DS-2B	69	1	2.32	1.53	0.54
		2	1.46		
		3	1.16		
		4	1.20		
Totals for Briquet Tensile Test				1.22	0.40

Prestressing Steel Material Data:

Rettco Steel, LLC
24 Herring Road, Newnan, GA 30265
770-252-5525

Product Test Certification

CUSTOMER: Virginia Tech

DATE 02/05/2013

LOCATION: Murray Structural Lab
105 Plantation Road
Blacksburg, VA 24060

CERTIFICATION # QA 14532-020513

PURCHASE ORDER: Donation

CERTIFICATION STANDARD- ASTM A416/A416M-10

PRODUCT DESCRIPTION:

1/2" DIAMETER 270K GRADE LOW RELAXATION SEVEN WIRE STRAND

COIL IDENTIFICATION:

COIL # S	HEAT # S	MOE
14532-4	120384	28.8

TESTS AND SAMPLE INFORMATION:

THE ATTACHED CURVES ARE REPRESENTATIVE OF THE MATERIAL PROVIDED IN THIS SHIPMENT.

PRESTRESSED CONCRETE STRAND IDENTIFIED ON THIS CERTIFICATION WAS PRODUCED BY RETTCO STEEL, LLC AND MEETS THE REQUIREMENTS FOR "DOMESTIC ORIGIN" AS DEFINED BY THE "SURFACE TRANSPORTATION ACT" OF 1978, AND AMENDED 1982, AND MEETS ALL OF THE REQUIREMENTS SET FORTH IN FEDERAL HIGHWAY ADMINISTRATION RULES AND REGULATIONS WITH THE REGARDS TO "DOMESTIC ORIGIN". AS IT IS STATED IN AND REQUIRED BY THE "SURFACE TRANSPORTATION ACT", THE RAW MATERIAL USED IN THE MANUFACTURING OF THESE PRODUCTS WAS MELTED IN THE UNITED STATES OF AMERICA AND THE MANUFACTURING OF THE FINISHED PRODUCT OCCURRED IN THE UNITED STATES OF AMERICA.

"THE MATERIAL DESCRIBED IN THIS CERTIFICATION WILL BOND TO CONCRETE OF NORMAL STRENGTH AND CONSISTENCY IN CONFORMANCE WITH THE PREDICTIONS FOR TRANSFER AND DEVELOPMENT LENGTH GIVEN IN THE ACI/AASHTO SPECIFICATIONS."

RACHEL H RIGGINS
NOTARY PUBLIC
COWETA COUNTY, GEORGIA
MY COMMISSION EXPIRES
JUNE 3, 2015

CERTIFICATION PREPARED BY:
Thomas Bellflower / QA Tech.

Figure E-1: Prestressing steel product test certificate.

Figure E-2: Prestressing steel product test data sheet.

Supplementary BDI Gage Data for DS-2:

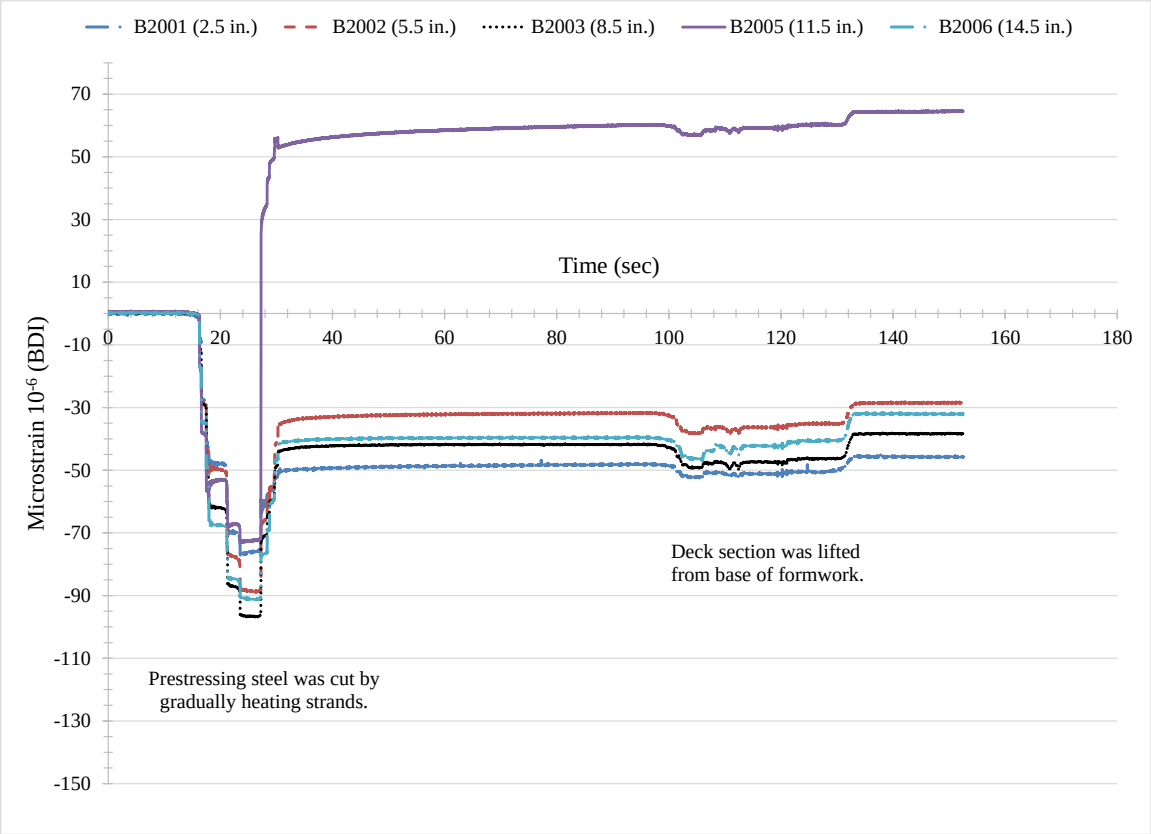

Figure E-3: BDI gages along live end of deck section starting at 2.5 in. (DS-2).

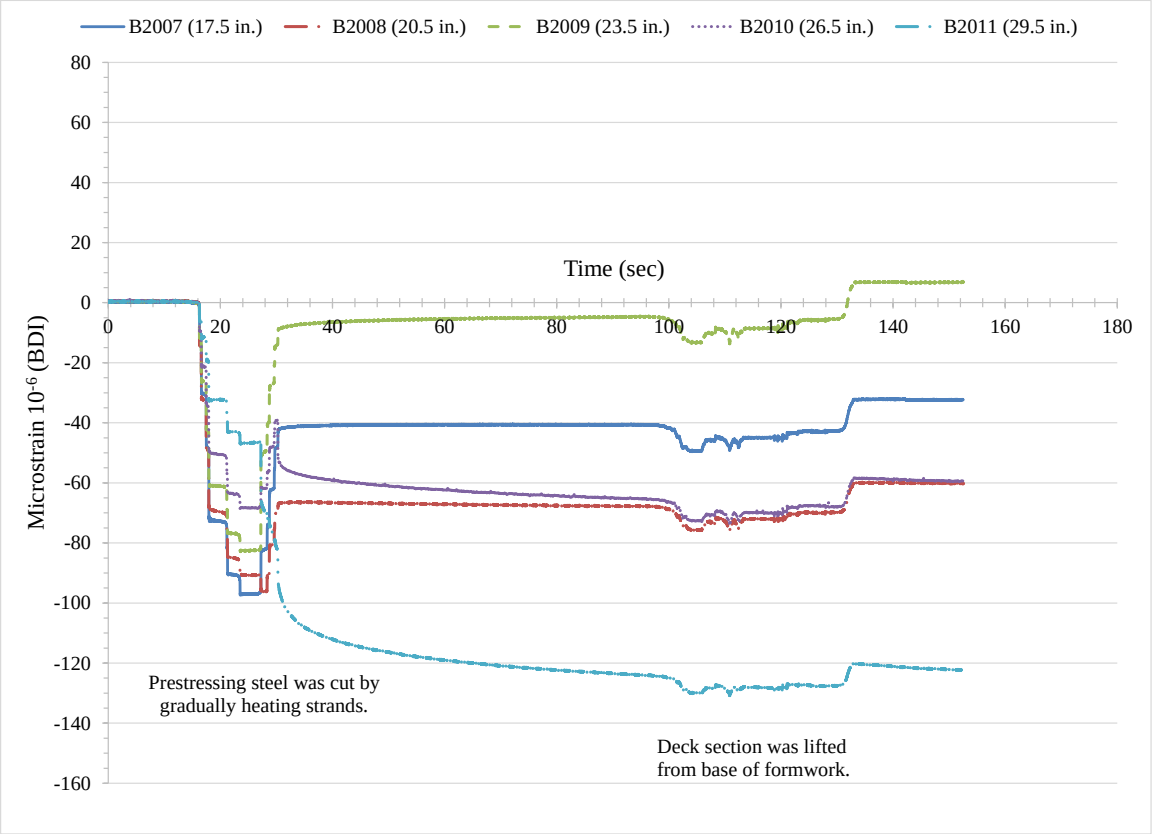

Figure E-4: BDI gages along live end of deck section starting at 17.5 in. (DS-2).

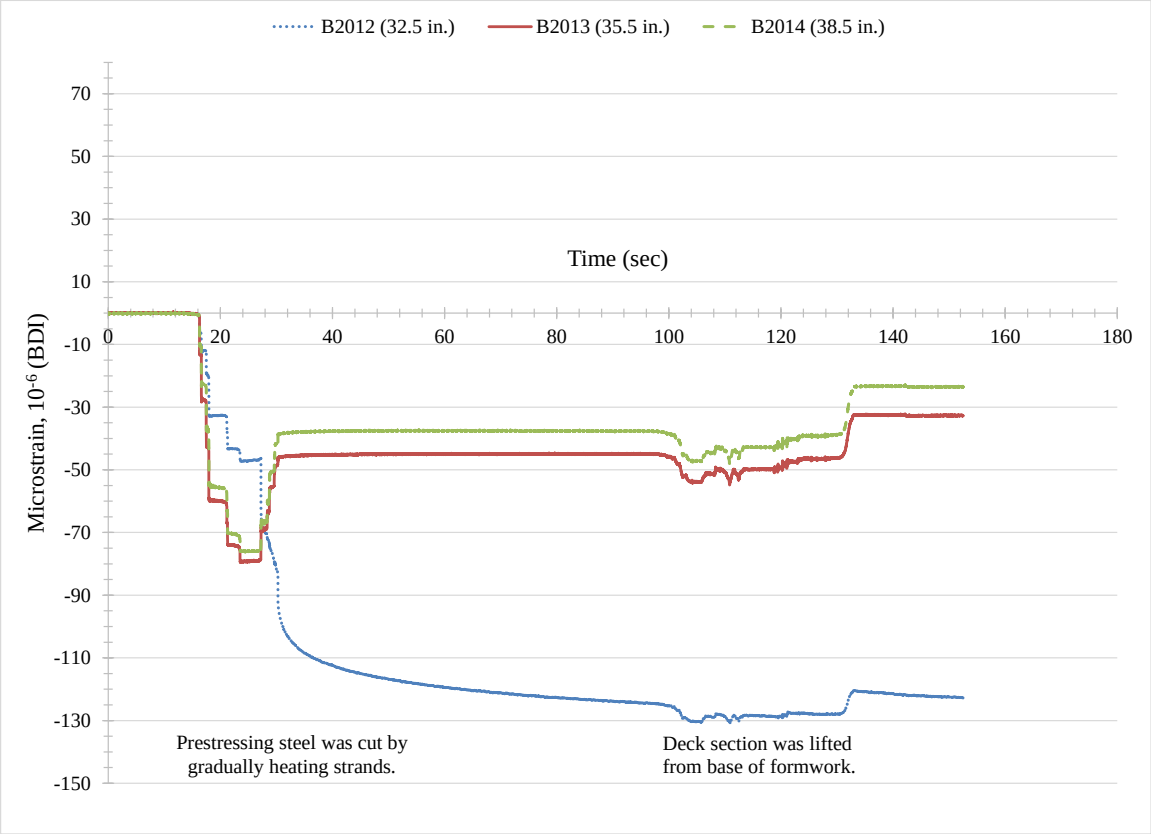

Figure E-5: BDI gages along live end of deck section starting at 32.5 in. (DS-2).

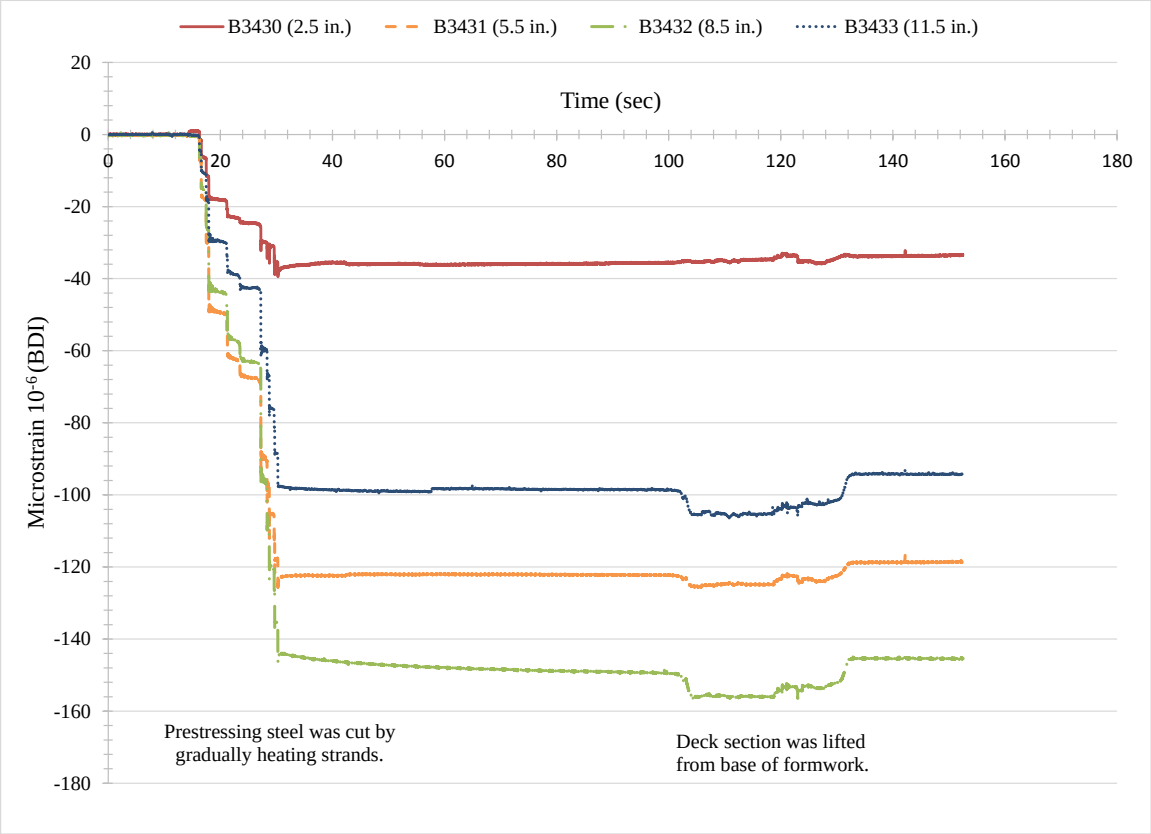

Figure E-6: BDI gages from dead end of deck section starting at 2.5 in. (DS-2).

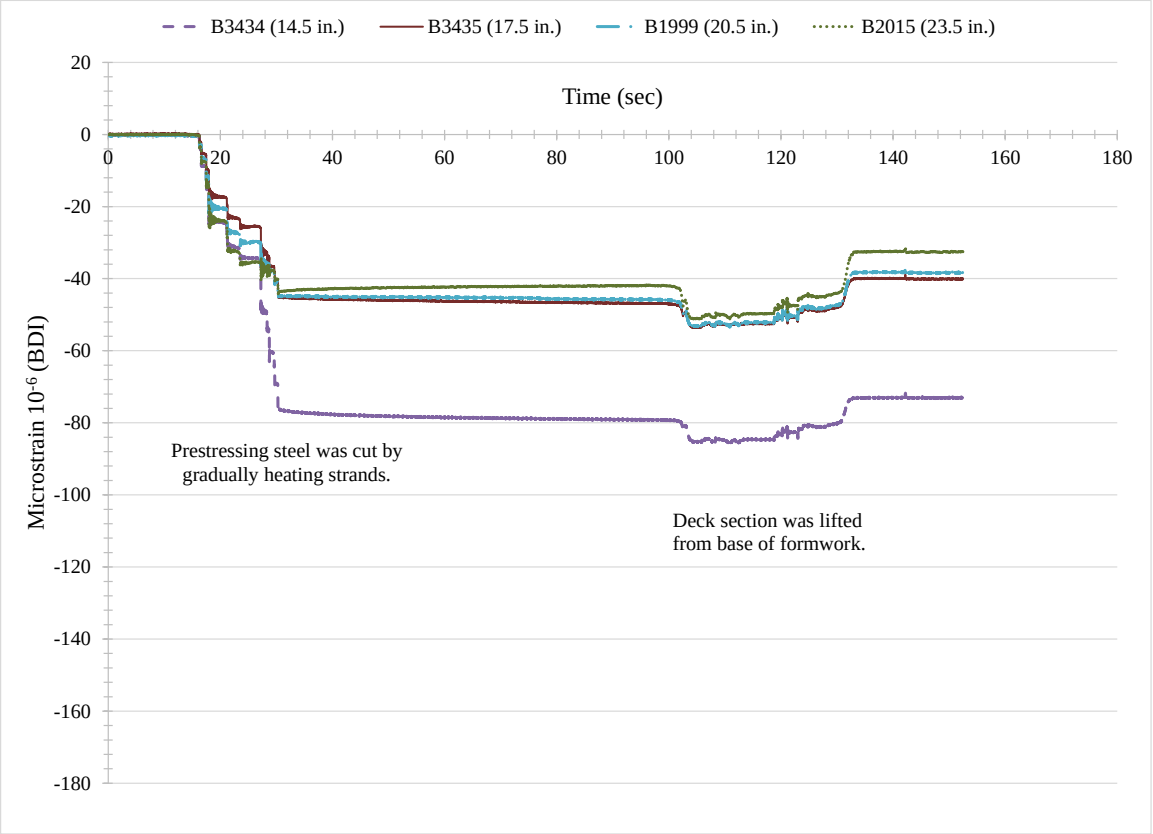

Figure E-7: BDI gages from dead end of deck section starting at 14.5 in. (DS-2).

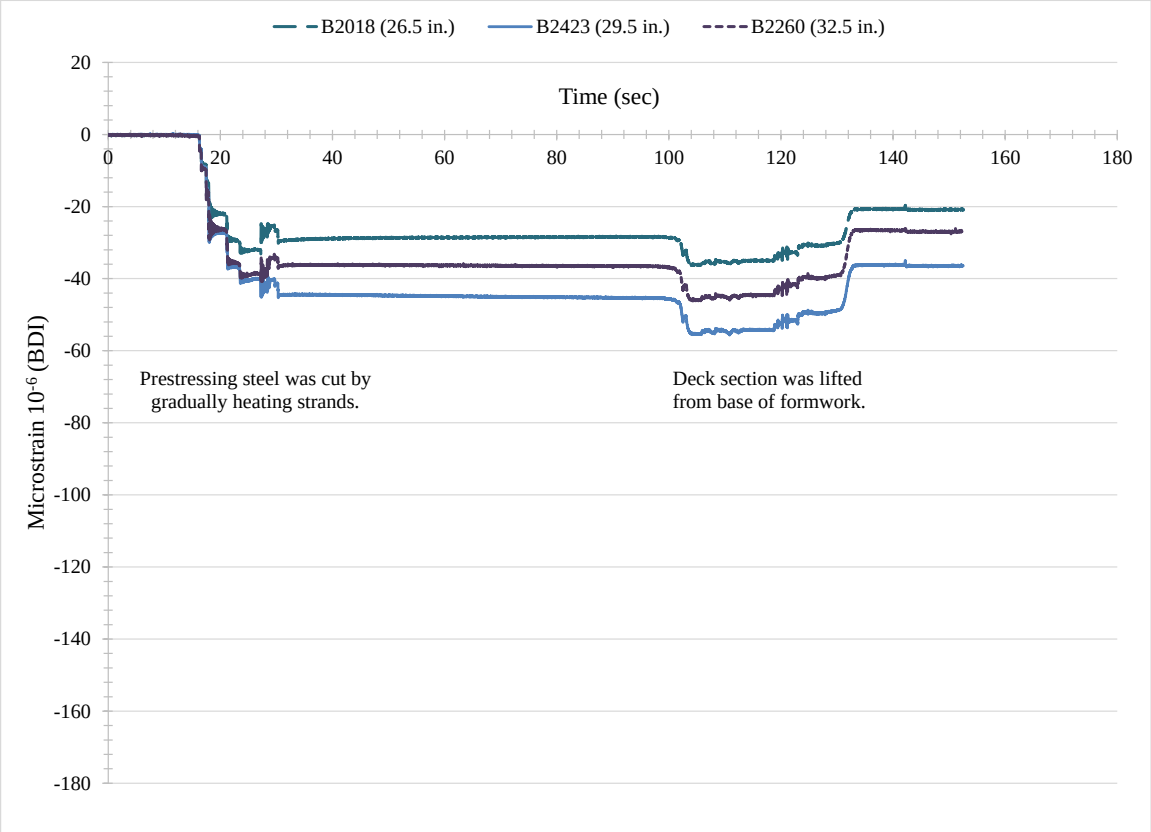

Figure E-8: BDI gages from dead end of deck section starting at 26.5 in. (DS-2).

Deck Section As-Built Dimensions:

Table E-10: Overall as-built dimensions for DS-1 and DS-2.

	Total Height, *h* (in.)		**Flange Width, b_f (in.)**		**Length, *L* (in.)**
Deck Section	Live	Dead	Live	Dead	(at centerline)
DS-1	8.00	7.88	18.06	18.06	111.06
DS-2	8.38	8.31	18.00	18.00	110.94

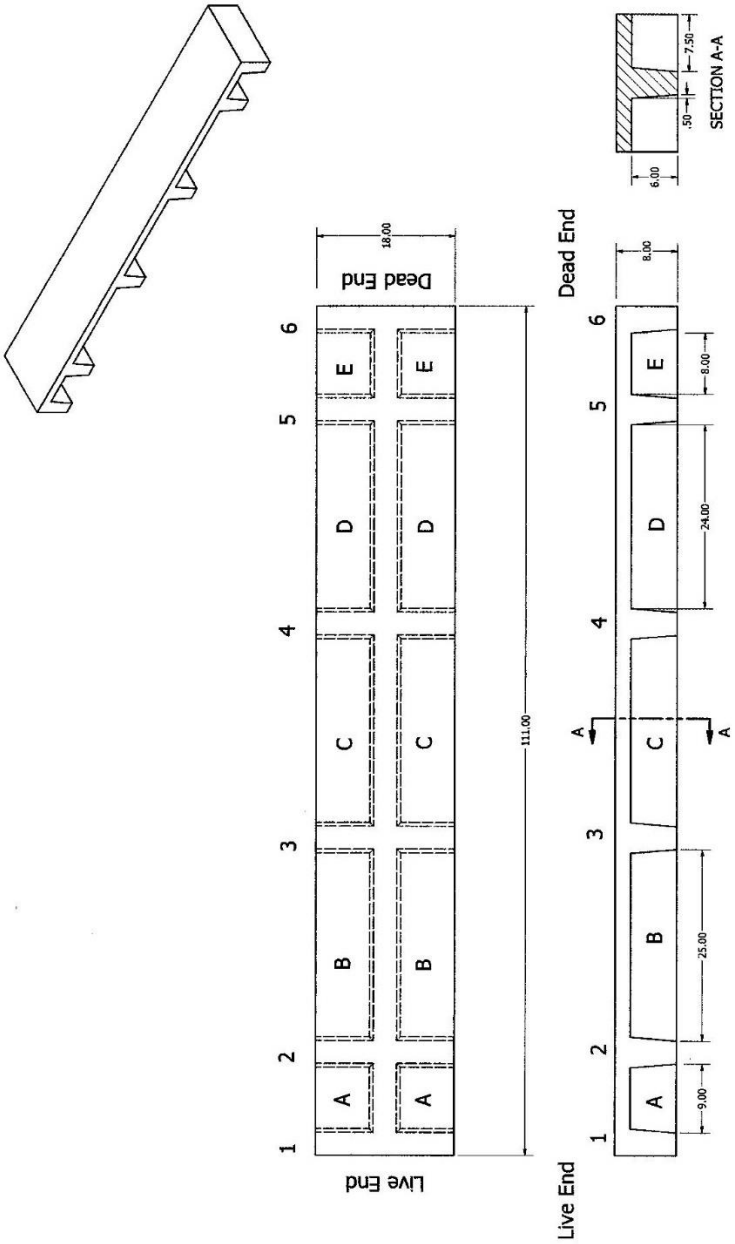

Figure E-9: Guide for measuring "as-built dimensions" for DS-1 and DS-2.

Table E-11: As-built dimensions at rib locations of DS-1 and DS-2.

Deck Section	Side of Deck Section	Rib No.	$b_{w,b}$ (in.)	$b_{w,t}$ (in.)	h (in.)	b_f (in.)
DS-1	Left of Live End	1	3.19	3.50	8.00	18.00
		2	3.06	4.00	8.00	18.00
		3	3.13	4.06	8.06	18.13
		4	3.00	4.00	8.06	18.19
		5	3.19	4.13	8.06	18.06
		6	3.50	3.88	7.88	18.06
	Right of Live End	1	3.25	3.75	8.00	18.00
		2	3.13	4.13	8.06	18.00
		3	3.13	4.06	8.06	18.13
		4	3.38	4.00	8.00	18.19
		5	3.38	4.00	7.88	18.06
		6	3.44	3.75	7.88	18.06
DS-2	Left of Live End	1	3.03	3.56	8.38	18.06
		2	3.06	4.00	8.38	18.00
		3	3.00	3.88	8.38	17.94
		4	3.06	4.00	8.50	18.06
		5	3.13	4.00	8.50	18.13
		6	3.00	3.44	8.50	18.06
	Right of Live End	1	2.94	3.50	8.50	18.06
		2	3.19	4.13	8.50	18.00
		3	2.44	3.88	8.50	17.94
		4	3.00	4.00	8.44	18.06
		5	3.00	4.03	8.38	18.13
		6	2.94	3.94	8.38	18.06

$b_{w,b}$ = bottom width of rib
$b_{w,t}$ = top width of rib
h = total height of deck section (web/rib + flange)
b_f = flange width

Table E-12: As-built h_f dimensions of DS-1 and DS-2 between ribs.

			h_f *(in.)*			
Deck Section	**Location**		**1**	**2**	**3**	**Average**
DS-1	Left of Live End	A	1.88	2.25	2.06	2.06
		B	2.13	2.13	2.13	2.13
		C	2.19	2.19	2.13	2.17
		D	2.25	2.25	2.19	2.23
		E	2.25	2.25	2.31	2.27
	Right of Live End	A	2.25	2.25	2.31	2.27
		B	2.06	2.06	2.00	2.04
		C	2.13	2.13	2.13	2.13
		D	2.13	2.06	2.13	2.10
		E	2.13	2.13	2.13	2.13
DS-2	Left of Live End	A	2.38	2.38	2.38	2.38
		B	2.38	2.41	2.44	2.41
		C	2.44	2.38	2.28	2.36
		D	2.38	2.28	2.25	2.30
		E	2.25	2.13	2.13	2.17
	Right of Live End	A	2.50	2.50	2.50	2.50
		B	2.44	2.50	2.56	2.50
		C	2.56	2.50	2.44	2.50
		D	2.44	2.44	2.44	2.44
		E	2.38	2.34	2.44	2.39

h_f = height of flange

Supplementary Test Data – DS-1 Test 1, Point load at 30 in.:

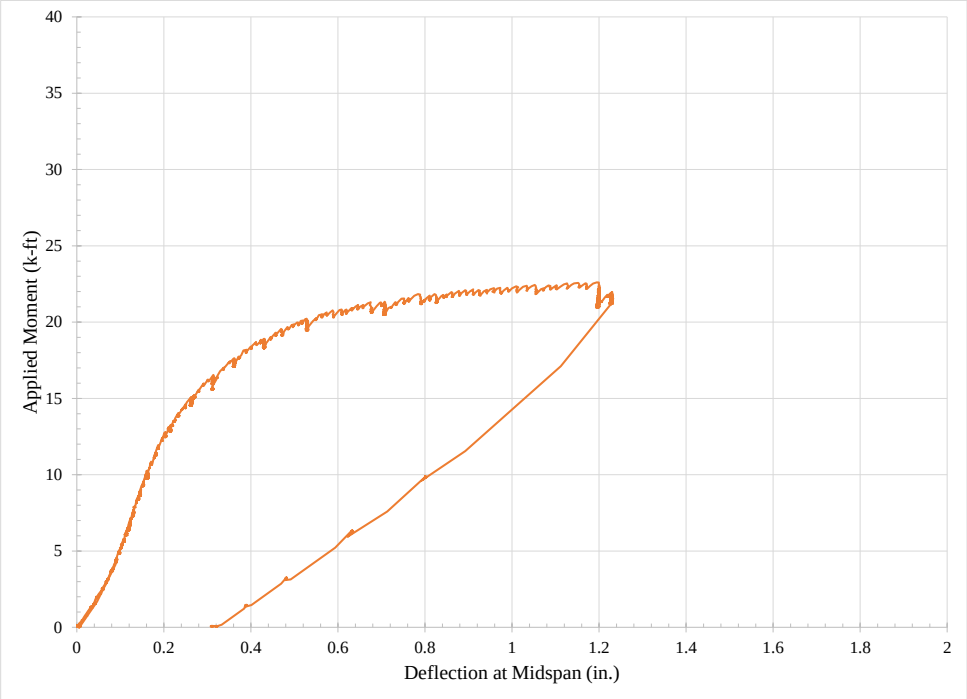

Figure E-10: Applied moment versus deflection at midspan (DS-1 Test 1).

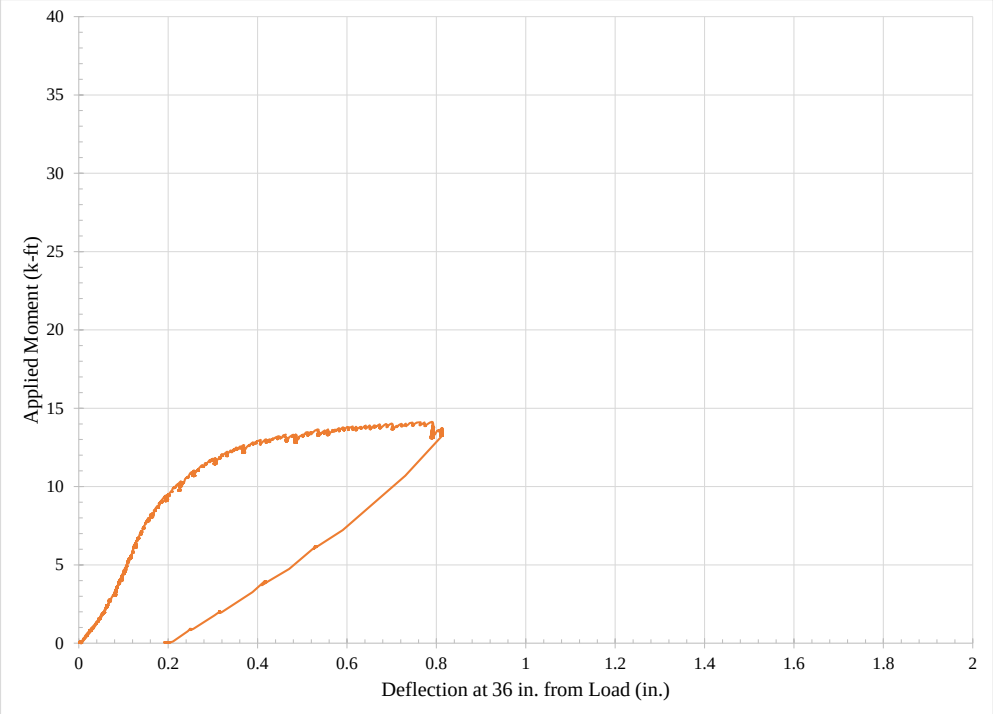

Figure E-11: Applied moment versus deflection at 36 in. from point load (DS-1 Test 1).

Supplementary Test Data – DS-1 Test 2, Point load at 18 in.:

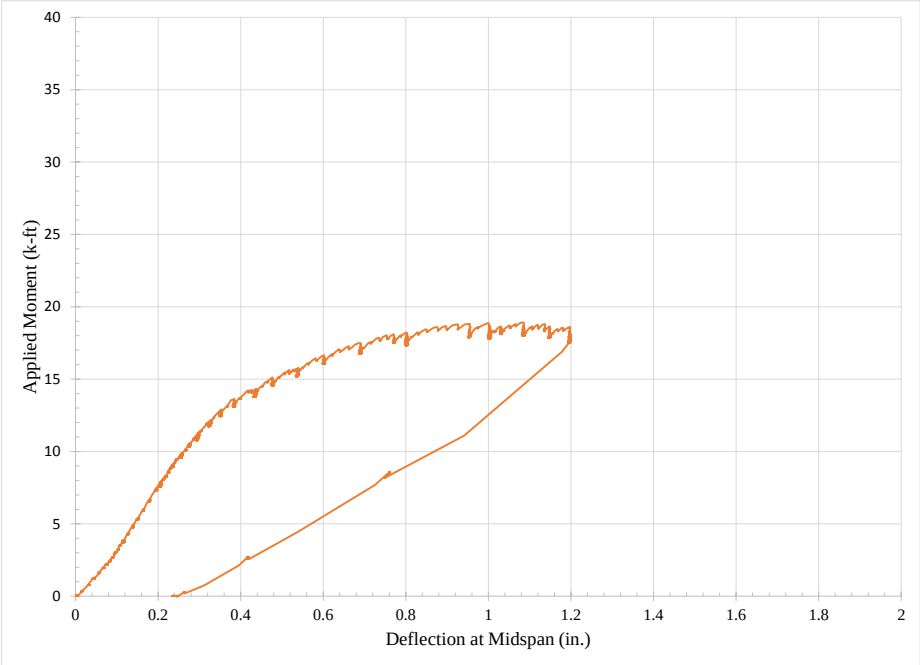

Figure E-12: Applied moment versus deflection at midspan (DS-1 Test 2).

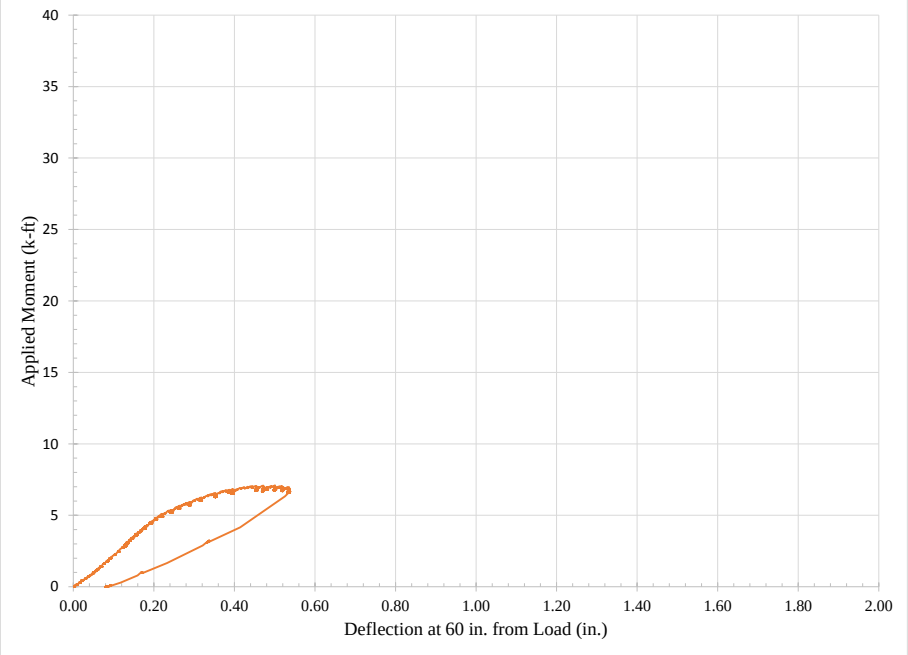

Figure E-13: Applied moment versus deflection at 60 in. from point load (DS-1 Test 2).

Supplementary Test Data – DS-2 Test 1, Point load at 18 in.:

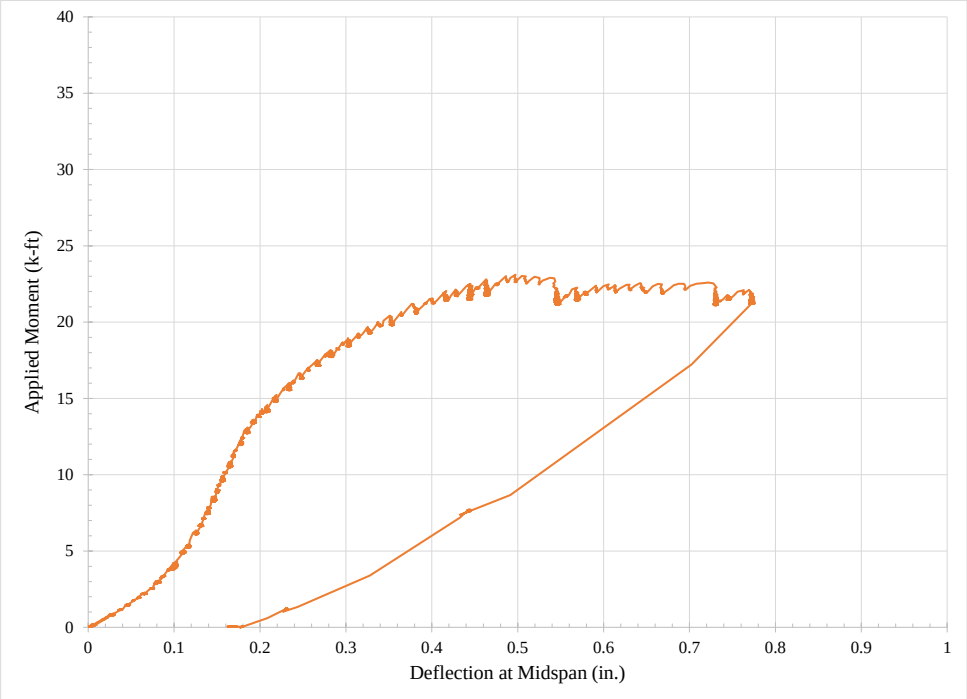

Figure E-14: Applied moment versus deflection at midspan (DS-2 Test 1).

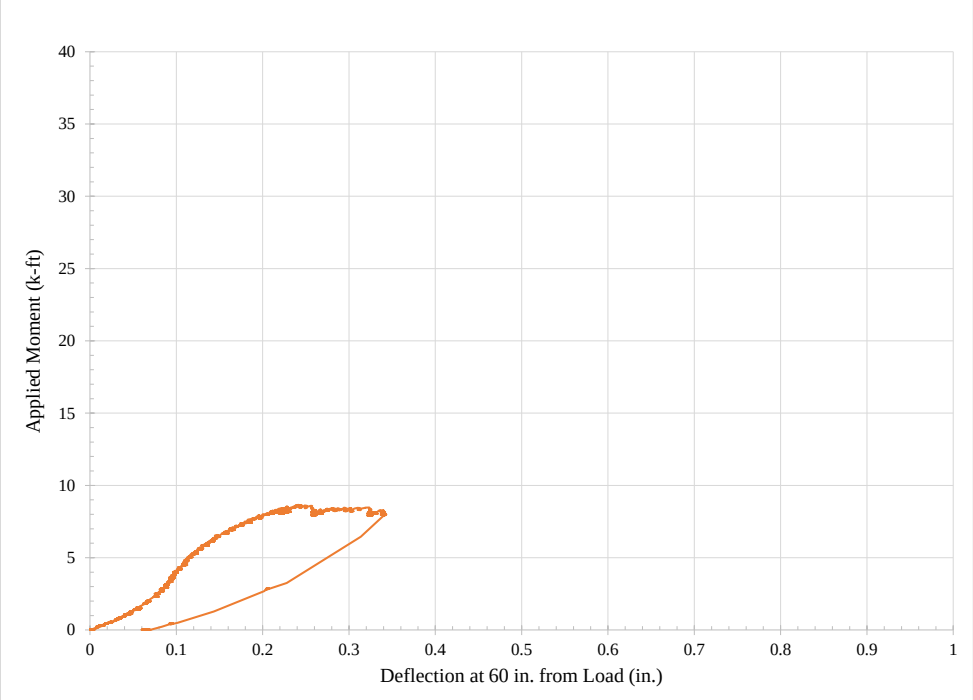

Figure E-15: Applied moment versus deflection at 60 in. from point load (DS-2 Test 1).

Supplementary Test Data – DS-2 Test 2, Point load at 30 in.:

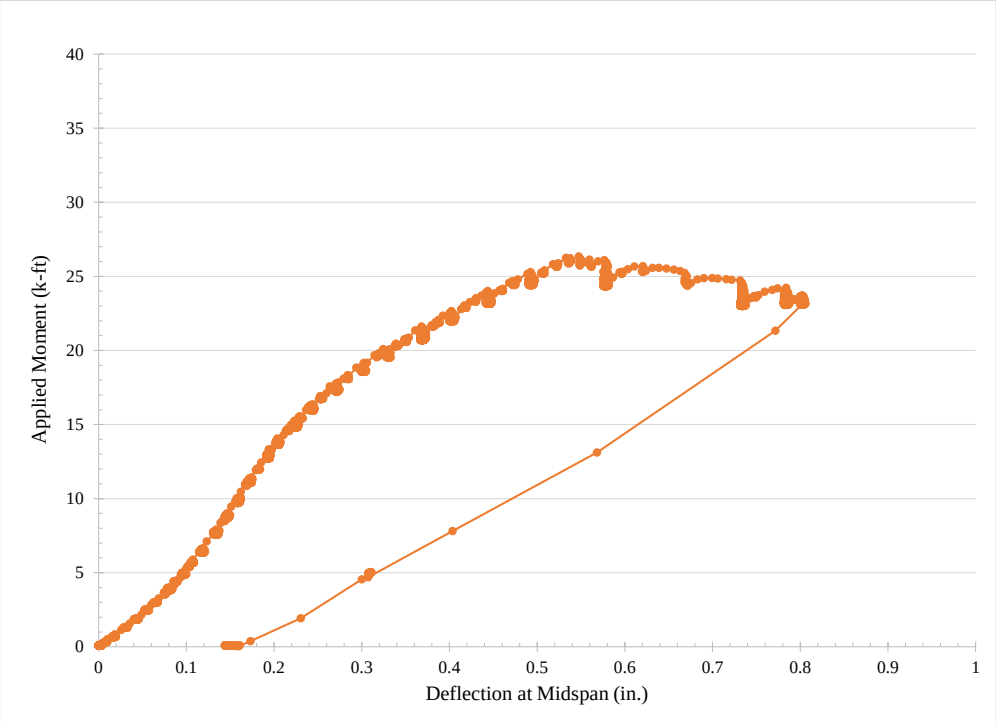

Figure E-16: Applied moment versus deflection at midspan (DS-2 Test 2).

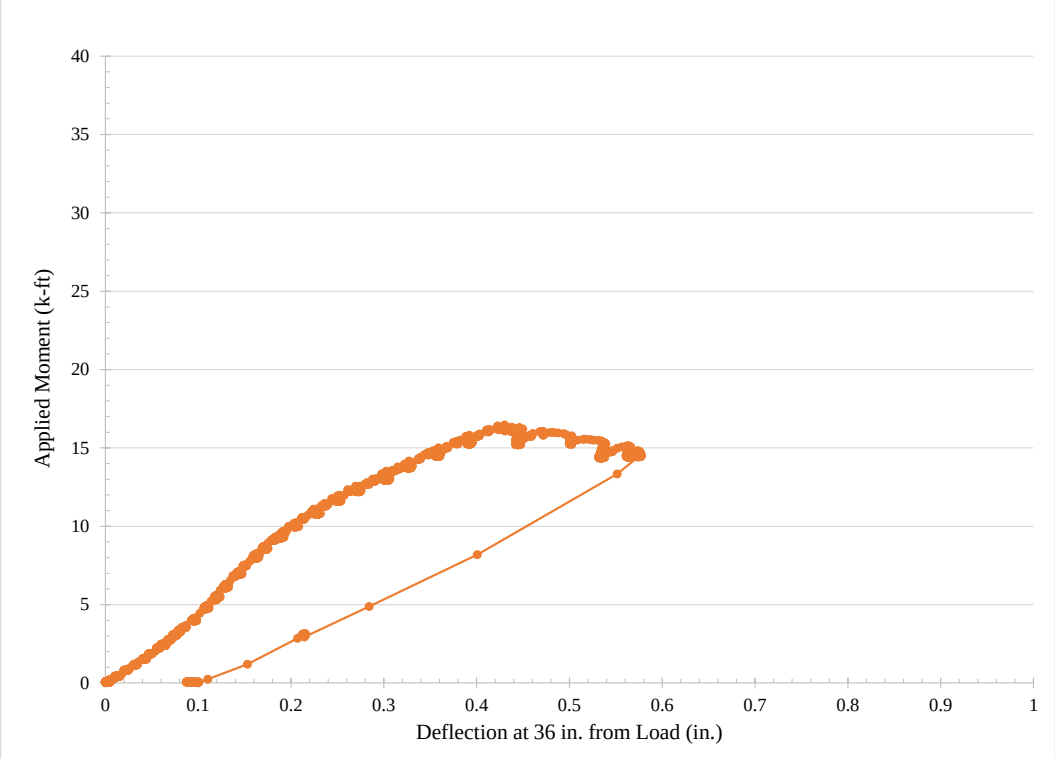

Figure E-17: Applied moment versus deflection at 36 in. from point load (DS-2 Test 2).